Proceedings Of

12th ARMY SYMPOSIUM ON SOLID MECHANICS

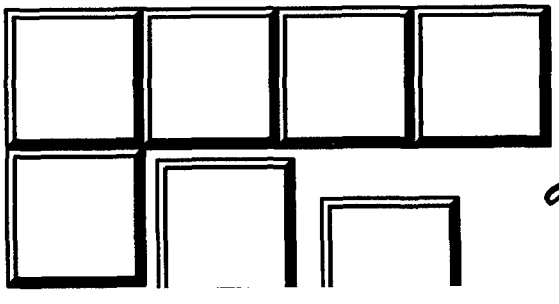

"Synergism of Mechanics, Mathematics and Materials"

Edited by Dr. Shun-Chin Chou

4-7 November 1991
Plymouth, Massachusetts

TWELFTH ARMY SYMPOSIUM ON SOLID MECHANICS PROCEEDINGS

"SYNERGISM OF MECHANICS, MATHEMATICS AND MATERIALS"

4-7 November 1991

Plymouth, Massachusetts

Edited by: *Dr. Shun-chin Chou*

The findings in this report are not to be construed as an official Department of the Army position, unless so designated by other authorized documents.

Mention of any trade names or manufacturers in this report shall not be construed as advertising nor as an official endorsement or approval of such products or companies by the United States Government.

PREFACE

This proceeding contains the papers presented at the 1991 Army Symposium on Solid Mechanics, held at Plymouth, Massachusetts, November 4 - 7, 1991. It was the twelfth in a series of biennial symposia with focus on solid mechanics research achievements which impact defense system needs. The symposia series which dates back to 1966 has been sponsored by the Army Materials Technology Laboratory in its role as the US Army lead laboratory for solid Mechanics research and exploratory development.

Each symposium has its theme which emphasizes a particular subject of interest. The theme of 1991 symposium is "Synergism of Mechanics, Mathematics and Materials." The need to interact among these three disciplines are well known, and the derived benefits have long been demonstrated. The symposium is organized into seven technical sessions covering subjects from basic research to applications. Many papers amplify the importance and benefits of synergism among the three disciplines. These papers have been subjected to the usual review process and revisions, if any required.

The Symposium Chairman wishes to thank Dr. Gordon A. Bruggerman, Acting Director of MTL and Dr. George H. Bishop, Jr. Director of Materials Reliability Division of MTL for their support and encouragement required to take on the task of running the Symposium. I want to thank the members of The

Technical Program Committee particular to Dr. Julian Wu of The Army Research office and Professor Thomas C.T. Ting of University of Illinois at Chicago, for many of the ideas for the symposium and for putting together the individual sessions. I wish to acknowledge Miss Karen Kaloostian, MTL Conference Coordinator for the arrangements before and during the Symposium. Universal Technology Corporation, the Symposium Administrator's effort for assembling the programs, abstracts and the proceedings for publication should be acknowledged.

Watertown, Massachusetts

SHUN-CHIN CHOU

CONTENTS

SESSION III: Failure and Damage

SESSION IV: Penetration Mechanics

SESSION V: Plasticity

SESSION VI: Structural Mechanics

SYMPOSIUM AND TECHNICAL PROGRAM COMMITTEES

ARMY SYMPOSIUM ON SOLID MECHANICS

"Synergism of Mechanics, Mathematics and Materials"

Symposium Committee

SYMPOSIUM CHAIRMAN

DR. SHUN-CHIN CHOU
U.S. ARMY MATERIALS TECHNOLOGY LABORATORY
(617) 923-5115, DSN 955-5115

SYMPOSIUM COORDINATORS

KAREN KALOOSTIAN
U.S. ARMY MATERIALS TECHNOLOGY LABORATORY
(617) 923-5043, DSN 955-5043

TOM GILROY
U.S. ARMY MATERIALS TECHNOLOGY LABORATORY
(617) 923-5525, DSN 955-5525

SYMPOSIUM ADMINISTRATION

MS. FAYE GEIDNER
UNIVERSAL TECHNOLOGY CORPORATION
(513) 426-8530

SYMPOSIUM SECRETARIES

SUSAN RODKEY
U.S. ARMY MATERIALS TECHNOLOGY LABORATORY
(617) 923-5742, DSN 955-5742

LUCY OHANNESIAN
U.S. ARMY MATERIALS TECHNOLOGY LABORATORY
(617) 923-5427, DSN 955-5427

ANN BARATTA
U.S. ARMY MATERIALS TECHNOLOGY LABORATORY
(617) 923-5115, DSN 955-5115

TECHNICAL PROGRAM COMMITTEE

Paul Cavallaro
U.S. Army Materials Technology Laboratory

Dattatraya P. Dandekar
U.S. Army Materials Technology Laboratory

Colin E. Freese
U.S. Army Materials Technology Laboratory

Arthur R. Johnson
U.S. Army Materials Technology Laboratory

Donald W. Oplinger
Federal Aviation Administration

Theordore H. H. Pian
Massachusetts Institute of Technology

Steven Serabian
U.S. Army Materials Technology Laboratory

Alexander Tessler
U.S. Army Materials Technology Laboratory

Thomas C. T. Ting
University of Illinois at Chicago

Charles S. White
U.S. Army Materials Technology Laboratory

Julian Wu
U.S. Army Research Office

SYMPOSIUM AGENDA

Final Agenda

ARMY SYMPOSIUM ON SOLID MECHANICS

"Synergism of Mechanics, Mathematics and Materials"

4-7 November 1991

MONDAY, 4 NOVEMBER 1991

5:00-7:00 p.m.	CONFERENCE REGISTRATION
5:00 p.m.	WELCOME RECEPTION

TUESDAY, 5 NOVEMBER 1991

7:00-8:00 a.m.	CONFERENCE REGISTRATION Coffee and Danish
8:00-8:30 a.m.	WELCOME *Dr. Gordon A. Bruggeman*, Acting Director, U.S. Army Materials Technology Laboratory
	SESSION I: CONTINUUM MECHANICS Session Chairman: *Dr. Julian Wu*
8:30-9:15 a.m.	SYNERGISM OF MECHANICS, MATHEMATICS AND ANISOTROPIC ELASTIC MATERIALS *T. Ting*, University of Illinois at Chicago
9:15-10:00 a.m.	TWO-PHASE CONTINUUM MECHANICS WITH MASS TRANSPORT AND STRESS *M. Gurtin*, Carnegie Mellon University *P. Voorhees*, Northwestern University
10:00-10:15 a.m.	BREAK
10:15-11:00 a.m.	FINDING THE RANGE OF POSSIBLE ELASTIC MODULI OF ANISOTROPIC COMPOSITES USING THE TRANSLATION METHOD *G. Milton*, New York University (Joint Paper with R. Kohn)
11:00-11:30 a.m.	DEVELOPMENT AND APPLICATION OF AN ELASTIC-PLASTIC CONSTITUTIVE RELATION INVOLVING STRAIN INDUCED ANISOTROPY BASED ON NON-PROPORTIONAL STRAINING EXPERIMENTS *E. Lee* and *Y. Suh*, Rensselaer Polytechnic Institute (Paper Not Available)
11:30-12:00 noon	THE MATHEMATICAL HIERARCHY UNDERLYING POLYNOMIAL-BASIS AND MATRIX REPRESENTATION MODEL REDUCTION *L. Flippen*, Naval Research Laboratory
12:00-12:30 p.m.	TIME RATES OF GENERALIZED STRAIN TENSORS WITH APPLICATIONS TO ELASTICITY *M. Scheidler*, US Army Ballistic Research Laboratory

12:30-2:00 p.m.	OPEN LUNCH
	NOTE: SESSION IIA & IIB (Concurrent Sessions)
	SESSION IIA: MICRO-MECHANICS Session Chairman: *Dr. A. Mayer*
2:00-2:45 p.m.	EXTREMAL MICROSTRUCTURES FOR COMPOSITE MATERIALS *R. Kohn*, New York University, Courant Institute of Mathematical Science
2:45-3:15 p.m.	TOUGHENING AND DEGRADATION EFFECTS OF MICROCRACKING IN A CERAMIC COMPOSITE AT HIGH TEMPERATURES *S. Suresh*, Brown University and *M. Kachanov*, Tufts University (Paper Not Available)
3:15-3:45 p.m.	MICROMECHANICS OF CRITICAL STATES *D. Krajcinovic, M. Basista* and *K. Mallick*, Arizona State University
3:45-4:00 p.m.	BREAK
4:00-4:30 p.m.	A STATISTICAL-MICROMECHANICS MODEL FOR PARTICULATE MATERIAL *C. Chang*, University of Massachusetts
4:30-5:00 p.m.	THE ROLE OF MICROSTRUCTURE IN THE DEFORMATION AND FAILURE OF TUNGSTEN HEAVY ALLOYS UNDER DYNAMIC LOADING CONDITIONS *J. Lankford, A. Bose, H. Couque* and *C. Anderson*, Southwest Research Institute
5:00-5:30 p.m.	ON THE RELATIONSHIP BETWEEN FRACTURING OF BRITTLE MICROCRACKING SOLID AND ITS EFFECTIVE ELASTIC PROPERTIES *M. Kachanov*, Tufts University
	SESSION IIB: APPLICATION Session Chairman: *Dr. D. Tracey*
2:00-2:30 p.m.	ESTIMATION OF RESIDUAL STRESSES IN RAILROAD RAILS *A. Perlman*, Tufts University, *J. Gordon* and *O. Orringer*, US Department of Transportation, *M. Zamora*, Dynatrend and *J. Orkisz*, Cracow, Poland
2:30-2:55 p.m.	SIMPLIFIED DAMAGE TOLERANCE LIFE CALCULATIONS FOR A LIGHT WEIGHT TWIN ENGINE AIRPLANE BASED ON PUBLICLY AVAILABLE DATA *Y. Tang, M. Violette* and *O. Orringer*, US Department of Transportation

2:55-3:20 p.m.	DEVELOPMENT OF A FATIGUE LIFE INDICATION SYSTEM *G. Samavedam* and *D. Thomson*, Foster-Miller, Inc. *B. Hornbeck*, US Army Belvoir Research, Development & Engineering Center
3:20-3:45 p.m.	STATIC AEROELASTIC AND DYNAMIC ANALYSIS OF T-38 WING *J. Woo*, US Army Ballistic Research Laboratory
3:45-4:00 p.m.	BREAK
4:00-4:25 p.m.	A HIGH PURITY ALUMINA WITH EXCEPTIONAL COMPRESSIVE AND FLEXURE STRENGTH BEHAVIOR OR ALUMINA REVISITED - BUT MUCH BETTER THAN EVER *J. Staehler, W. Predebon, B. Pletka*, Michigan Technological University
4:25-4:50 p.m.	NONLINEAR DYNAMIC RESPONSE ANALYSIS OF COMMUNICATION SHELTER SUBJECTED TO BLAST LOADS *L. Serdar, R. Yaghiayan*, Kaman Sciences Corporation *E. Patnaik*, US Army Harry Diamond Laboratories
4:50-5:15 p.m.	STRUCTURAL ANALYSIS OF PERISHING 1A OVERPACK SHIPPING CONTAINER *D. Gray*, Kaman Sciences Corporation
5:15-5:40 p.m.	ADVANCED COMPOSITE HELICOPTER MISERS GOLD POST-TEST ANALYSIS *M. Partridge, M. Atkinson* and *L. Mente*, Kaman Sciences Corporation and *K. Unsworth*, US Army Aviation Systems Command (Paper Not Available)
6:30 p.m.	NO-HOST RECEPTION

WEDNESDAY, 6 NOVEMBER 1991

7:30-8:00 a.m.	CONFERENCE REGISTRATION Coffee and Danish

SESSION III: FAILURE AND DAMAGE
Session Chairman: *Dr. U. Lindholm*

8:00-8:45 a.m.	DYNAMIC RESPONSE AND FAILURE MODES OF CERAMICS AND CERAMIC COMPOSITES *S. Nemat-Nasser*, University of California at San Diego
8:45-9:15 a.m.	EFFECT OF GRAIN SIZE ON THE DYNAMIC TENSILE DEFORMATION AND FAILURE OF COPPER *D. Lassila* and *W. Gourdin*, University of California, Lawrence Livermore National Laboratory
9:15-9:45 a.m.	ADIABATIC SHEAR BANDS IN AISI 4340 STEEL: MICROSTRUCTURAL OBSERVATION *C. Mgbokwere, S. Nutt* and *J. Duffy*, Brown University

9:45-10:15 a.m.	THERMOMECHANICAL SIMULATION OF ADIABATIC SHEAR BAND IN HIGH SPEED FORMING *A. Tseng, P. Chou and J. Hashemi*, Drexel University
10:15-10:30 a.m.	BREAK
10:30-11:00 a.m.	ADIABATIC SHEAR-BANDING IN HIGH-STRENGTH ALLOYS *J. Beatty*, US Army Materials Technology Laboratory *Y. Li, M. Meyers* and *S. Nemat-Nasser*, University of California at San Diego
11:00-11:30 a.m.	STRAIN ENERGY DENSITY APPROACH TO STABLE CRACK EXTENSION UNDER NET SECTION YIELDING *D. Jeong* and *O. Orringer*, US Department of Transportation and *G. Sih*, Lehigh University
11:30-12:00 p.m.	A CAVITATION LOCUS SURROUNDING A MODE 1 PLANE STRAIN CRACK IN A NEO-HOOKEAN MATERIAL *C. Quigley*, US Army Materials Technology Laboratory and *D. Parks*, Massachusetts Institute of Technology
12:00-1:30 p.m.	OPEN LUNCH

SESSION IV: PENETRATION MECHANICS

Session Chairman: *Dr. K. Iyer*

1:30-2:15 p.m.	EFFECT OF MATERIAL ELASTICITY AND FRICTIONAL FORCES ON THE STEADY STATE AXISYMMETRIC DEFORMATIONS OF A THICK TARGET *R. Batra, X. Chen* and *R. Jayachandran*, University of Missouri-Rolla
2:15-2:45 p.m.	EXPERIMENTAL INVESTIGATION OF RHA PLATE PERFORATION BY A SHAPED CHARGE JET *M. Raftenberg*, Ballistic Research Laboratory
2:45-3:15 p.m.	PENETRATION ANALYSIS OF HY100 STEEL PLATE *E. Chen*, Sandia National Laboratories
3:15-3:30 p.m.	BREAK
3:30-4:00 p.m.	MATERIAL PARAMETERS FOR SHAPED CHARGE LINERS AND EFP WARHEADS IN ARMOR PENETRATION *C. Feng*, US Army Armament Research, Development and Engineering Center (Paper Not Available)
4:00-4:30 p.m.	DETERMINATION OF THE CONTACT FORCES BETWEEN A PROJECTILE AND A HARD TARGET *R. Thomas, V. Bateman* and *T. Carne*, Sandia National Laboratories
4:30-5:00 p.m.	MODELING DEFORMATION AND DAMAGE IN ARMOR CERAMICS *C. White* and *J. McLaughlin*, US Army Materials Technology Laboratory
6:00-7:00 p.m.	RECEPTION
7:00-9:00 p.m.	BANQUET*

*Additional Banquet tickets may be purchased on-site at the Conference Registration Desk

THURSDAY, 7 NOVEMBER 1991

7:30-8:00 a.m. CONFERENCE REGISTRATION
Coffee and Danish

SESSION V: PLASTICITY
Session Chairman: *Prof. P. Symonds*

8:00-8:45 a.m. DYNAMIC DUCTILE RUPTURE IN SPHEROIDIZED 1045 STEEL
M. Zhou and *R. Clifton*, Brown University

8:45-9:15 a.m. MODELING PLASTIC ANISOTROPY FOR PLANAR POLYCRYSTALLINE AGGREGATES USING ORIENTATION AVERAGING
V. Prantil, P. Dawson and *J. Jenkins*, Cornell University (Paper Not Available)

9:15-9:45 a.m. PLASTICALLY INDUCED SURFACE ROUGHNESS: PHENOMENA AND MECHANISM
Y. Dai, Brown and Sharpe Co. and *F. Chiang*, State University of New York at Stony Brook

9:45-10:15 a.m. ELASTO-PLASTIC FINITE ELEMENT ANALYSIS OF 2-D ROLLING PLUS SLIDING CONTACT WITH TEMPERATURE DEPENDENT BEARING STEEL MATERIAL PROPERTIES
V. Gupta, P. Bastias, G. Hahn and *C. Rubin*, Vanderbilt University

10:15-10:30 a.m. BREAK

10:30-11:00 a.m. THE INFLUENCE OF PRESTRAIN ON THE STRESS RESPONSE OF AN Al/Mg ALLOY TO A POLYGONAL STRAIN PATH
E. Krempl and *S. Cheng*, Rensselaer Polytechnic Institute

11:00-11:30 a.m. A RE-EXAMINATION OF THE PLASTIC FLOW CRITERION FOR COPPER
N. Huffington, US Army Ballistic Research Laboratory

11:30-12:00 a.m. A CLASS OF CONSTITUTIVE MODELS FOR RATE-DEPENDENT INELASTICITY IN METALS
M. Rashid, University of California at San Diego

12:00-1:30 p.m. OPEN LUNCH

SESSION VI: STRUCTURAL MECHANICS
Session Chairman: *Dr. R. Singleton*

1:30-2:00 p.m. LOW-VELOCITY IMPACT DAMAGE IN GRAPHITE/EPOXY LAMINATED COMPOSITES
H. Choi and *F. Chang*, Stanford University

2:00-2:25 p.m. THE EFFECT OF LOW TEMPERATURE ON THE FLEXURAL FATIGUE AND FRACTURE OF UNIDIRECTIONAL GRAPHITE/EPOXY COMPOSITES
P. Dutta, US Army Cold Regions Research and Engineering Laboratory

2:25-2:50 p.m.	COUPLED HYDRO-STRUCTURAL ANALYSIS OF NON-PERFORATING IMPACTS *N. Ari* and *D. Gray*, Kaman Sciences Corporation
2:50-3:10 p.m.	BREAK
3:10-3:35 p.m.	CONTINUUM AND MOLECULAR MODELS FOR RUBBER VISCOELASTICITY *A. Johnson* and *R. Stacer*, Army Materials Technology Lab
3:35-4:00 p.m.	[1,2] - ORDER THEORY FOR HOMOGENEOUS ORTHOTROPIC SHELLS *T. Tsui* and *A. Tessler*, US Army Materials Technology Laboratory
4:00-4:25 p.m.	PLYCRACKS AND LOAD REDISTRIBUTION IN LAMINATED COMPOSITES *S. Chatterjee* and *C. Yen*, Materials Sciences Corporation
4:25 p.m.	ADJOURN

CONFERENCE PRESENTATIONS

SESSION I: CONTINUUM MECHANICS

Session Chairman: *Dr. Julian Wu*

SYNERGISM OF MECHANICS, MATHEMATICS AND ANISOTROPIC ELASTIC MATERIALS

T. C. T. Ting

Department of Civil Engineering, Mechanics and Metallurgy,
University of Illinois at Chicago, Box 4348, Chicago, IL 60680

INTRODUCTION

Anisotropic elastic materials are interesting materials. A simple tensile stress applied to the material produces not only an extensional strain but also a shear strain. Likewise, a pure shear stress applied to the material produces a shear strain and an extensional (or compression) strain. Therefore a loading which is symmetric (or antisymmetric) with the x_2–axis, say, in general does not produce a deformation which is symmetric (or antisymmetric) with the x_2–axis. There are surprises in which anisotropic materials behave like isotropic materials. These will be pointed out in the paper.

In contrast to isotropic elastic materials which have two elastic constants, anisotropic elastic materials may have as many as twenty one elastic constants. When two–dimensional deformations are considered, the analysis still requires fifteen elastic constants. In view of this, there is a wide spread and justifiable misconception that the analysis of anisotropic elastic materials is much more complicated than that of isotropic elastic materials. This is not necessarily true if one employs the Stroh formalism. With the Stroh formalism the solutions to anisotropic elasticity problems are in most cases simpler than those for isotropic elasticity problems. The reason is simply that isotropic materials are more than a special case of anisotropic materials. They are mathematically **degenerate** materials.

Much progress has been made since Stroh's two pioneering papers appeared in 1958 and 1962 [1,2]. We will point out in the paper the integral formalism of Barnett–Lothe [3] which allows us to compute three Barnett–Lothe tensors **S**, **H** and **L**, which are real, without finding the Stroh eigenvalues p and the associated eigenvectors **a**, **b**, which are complex. We will also point out some identities which enable us to convert certain combinations of p, **a** and **b** to **S**, **H**, **L** and other real quantities. Owing to these identities, several existing complex form solutions are simplified to real form solutions and solutions are obtained for some heretofore unsolved problems. As a result, many physically interesting and unexpected phenomena, which have been shrouded in the complex form solutions, have been discovered recently. Most of the unexpected phenomena defy an intuitive explanation.

The Stroh formalism is not only mathematically elegant and technically powerful, but some of its mathematical quantities such as the eigenvalues p and the eigenvectors **a** and **b** have physical meanings. The mathematical structure of **S**, **H** and **L** provides us a rare insight into the relations between anisotropic and isotropic materials.

For isotopic materials the in–plane displacement and the antiplane displacement are uncoupled. The in–plane displacement (u_1, u_2) and the associated surface traction vector on any boundary Γ are polarized on the (x_1, x_2) plane while the antiplane displacement u_3 and the associated surface traction are polarized along the x_3 axis. For general anisotropic materials under the assumption of two–dimensional deformations, the u_3 component is in general non–zero and cannot be uncoupled from the in–plane displacements u_1, u_2. This does not mean that there are no planes or axes on which the displacement and the surface traction are polarized. There are, as we will show, oblique planes and axes on which the displacement and the surface traction are polarized.

The synergism of mathematics and mechanics appears to work very well for anisotropic elastic materials. Examples presented in the paper illustrate that this is indeed the case.

1. THE STROH FORMALISM. In a fixed rectangular coordinate system x_i (i = 1, 2, 3) let u_i, σ_{ij} be, respectively, the displacement and stress in an anisotropic elastic material. The stress strain laws and the equations of equilibrium are

$$\sigma_{ij} = C_{ijks} u_{k,s}\,, \tag{1.1}$$

$$C_{ijks} u_{k,sj} = 0, \tag{1.2}$$

where a comma stands for differentiation, repeated indices imply summation and C_{ijks} are the elasticity constants which are assumed to possess the symmetry property

$$C_{ijks} = C_{jiks} = C_{ijsk} = C_{ksij}\,.$$

For two–dimensional deformations in which u_i (i = 1, 2, 3) depends on x_1, x_2 only, a general solution to (1.2) is, in matrix notation,

$$\mathbf{u} = \mathbf{a}\, f(z), \quad z = x_1 + p x_2. \tag{1.3}$$

In the above f is an arbitrary function of z, and p and **a** are determined by inserting (1.3) into (1.2). We have

$$\{\mathbf{Q} + p(\mathbf{R} + \mathbf{R}^T) + p^2\mathbf{T}\}\,\mathbf{a} = 0 \tag{1.4}$$

where the superscript T denotes the transpose and **Q**, **R**, **T** are 3x3 real matrices whose components are

$$Q_{ik} = C_{i1k1},\quad R_{ik} = C_{i1k2},\quad T_{ik} = C_{i2k2}. \tag{1.5}$$

We note that **Q** and **T** are symmetric and, subject to the positiveness of strain energy, positive definite. The stresses obtained by substituting (1.3) into (1.1) can be written in terms of the stress function $\boldsymbol{\phi}$ as

$$\sigma_{i1} = -\phi_{i,2},\quad \sigma_{i2} = \phi_{i,1}, \tag{1.6}$$

in which

$$\boldsymbol{\phi} = \mathbf{b}\, f(z), \tag{1.7}$$

$$\mathbf{b} = (\mathbf{R}^T + p\mathbf{T})\mathbf{a} = -\frac{1}{p}(\mathbf{Q} + p\mathbf{R})\mathbf{a}. \tag{1.8}$$

The second equality in (1.8) follows from (1.4). It suffices therefore to consider the stress function $\boldsymbol{\phi}$ because the stresses σ_{ij} can be obtained by differentiation.

There are six eigenvalues p and six eigenvectors **a** from (1.4). Since p cannot be real if the strain energy is positive [4], there are three pairs of complex conjugates for p. If p_α, $\mathbf{a}_\alpha$, $\mathbf{b}_\alpha$ ($\alpha = 1, 2,..,6$) are the eigenvalues and the associated eigenvectors we let

$$\text{Im}\, p_\alpha > 0,\quad p_{\alpha+3} = \overline{p}_\alpha,\quad \mathbf{a}_{\alpha+3} = \overline{\mathbf{a}}_\alpha,\quad \mathbf{b}_{\alpha+3} = \overline{\mathbf{b}}_\alpha, \tag{1.9}$$

($\alpha = 1, 2, 3$), where Im stands for the imaginary part, the overbar denotes the complex conjugate and $\mathbf{b}_\alpha$ is related to $\mathbf{a}_\alpha$ through (1.8). Assuming that the p_α are distinct, the general solutions for **u** and $\boldsymbol{\phi}$ obtained by superposing six solutions of the form (1.3) and (1.7) are

$$\begin{aligned}\mathbf{u} &= \sum_{\alpha=1}^{3}\left\{\mathbf{a}_\alpha f_\alpha(z_\alpha) + \overline{\mathbf{a}}_\alpha f_{\alpha+3}(\overline{z}_\alpha)\right\},\\ \boldsymbol{\phi} &= \sum_{\alpha=1}^{3}\left\{\mathbf{b}_\alpha f_\alpha(z_\alpha) + \overline{\mathbf{b}}_\alpha f_{\alpha+3}(\overline{z}_\alpha)\right\}.\end{aligned} \tag{1.10}$$

In (1.10) $f_1, f_2,..., f_6$ are arbitrary functions of their argument and

$$z_\alpha = x_1 + p_\alpha x_2.$$

The above formalism is due to Stroh [1,2]. In applications all we have to determine is the form of the arbitrary functions f_α. What distinguishes the Stroh formalism from others is that there are relations between $\mathbf{a}_\alpha$ and $\mathbf{b}_\alpha$ which allow us to find the solution easily and/or to simplify the solution obtained. These relations and the Barnett–Lothe integral formalism are presented next.

In closing this section we note that, in most applications, f_α has the same function form so that we may write

$$f_\alpha(z_\alpha) = q_\alpha f(z_\alpha),$$

$$f_{\alpha+3}(z_\alpha) = \bar{q}_\alpha \bar{f}(\bar{z}_\alpha), \quad \alpha = 1, 2, 3,$$

where q_α are arbitrary constants. The second equation is for obtaining real solutions for $\mathbf{u}$ and ϕ. Equations (1.10) can then be written as

$$\mathbf{u} = 2\,\mathrm{Re}\sum_{\alpha=1}^{3} \mathbf{a}_\alpha q_\alpha f(z_\alpha), \quad \phi = 2\,\mathrm{Re}\sum_{\alpha=1}^{3} \mathbf{b}_\alpha q_\alpha f(z_\alpha). \tag{1.11}$$

2. THE BARNETT–LOTHE TENSORS. The two equations in (1.8) can be rewritten as

$$\begin{bmatrix} -\mathbf{R}^{\mathrm{T}} & \mathbf{I} \\ -\mathbf{Q} & \mathbf{0} \end{bmatrix} \begin{bmatrix} \mathbf{a} \\ \mathbf{b} \end{bmatrix} = p \begin{bmatrix} \mathbf{T} & \mathbf{0} \\ \mathbf{R} & \mathbf{I} \end{bmatrix} \begin{bmatrix} \mathbf{a} \\ \mathbf{b} \end{bmatrix}$$

where I is the 3x3 identity matrix. Multiplying both sides by the matrix

$$\begin{bmatrix} \mathbf{T}^{-1} & \mathbf{0} \\ -\mathbf{R}\mathbf{T}^{-1} & \mathbf{I} \end{bmatrix}$$

leads to the standard eigenrelation [5,6]

$$\mathbf{N}\xi = p\xi, \tag{2.1}$$

$$\mathbf{N} = \begin{bmatrix} \mathbf{N}_1 & \mathbf{N}_2 \\ \mathbf{N}_3 & \mathbf{N}_1^{\mathrm{T}} \end{bmatrix}, \quad \xi = \begin{bmatrix} \mathbf{a} \\ \mathbf{b} \end{bmatrix}, \tag{2.2}$$

$$N_1 = -T^{-1}R^T, \quad N_2 = T^{-1}, \quad N_3 = RT^{-1}R^T - Q. \tag{2.3}$$

It is clear that $\mathbf{N}_2$ and $\mathbf{N}_3$ are symmetric and $\mathbf{N}_2$ is positive definite. It can be shown that $-\mathbf{N}_3$ is positive semi–definite [7]. Moreover, $-\mathbf{N}_1$ and $-\mathbf{N}_3$ have the structure

$$-\mathbf{N}_1 = \begin{bmatrix} * & 1 & * \\ * & 0 & * \\ * & 0 & * \end{bmatrix}, \quad -\mathbf{N}_3 = \begin{bmatrix} * & 0 & * \\ 0 & 0 & 0 \\ * & 0 & * \end{bmatrix}, \tag{2.4}$$

in which the * denotes a possibly non–zero element. These * elements have surprisingly simple expressions in terms of elastic compliances [7]. The structure of $\mathbf{N}_1$, $\mathbf{N}_3$ shown in (2.4) plays important roles in solving problems and interpreting the final solutions.

The vector $\xi = (\mathbf{a}, \mathbf{b})$ in (2.2) is the right eigenvector of $\mathbf{N}$. It can be shown that $(\mathbf{b}, \mathbf{a})$ is the left eigenvector. The left and right eigenvectors associated with different eigenvalues are orthogonal to each other. The orthogonality relations can be normalized such that

$$\mathbf{a}_\alpha \cdot \mathbf{b}_\beta + \mathbf{b}_\alpha \cdot \mathbf{a}_\beta = \delta_{\alpha\beta} \tag{2.5}$$

where $\delta_{\alpha\beta}$ is the Kronecker delta. Introducing the 3x3 matrices $\mathbf{A}$ and $\mathbf{B}$ by

$$\mathbf{A} = [\mathbf{a}_1, \mathbf{a}_2, \mathbf{a}_3], \quad \mathbf{B} = [\mathbf{b}_1, \mathbf{b}_2, \mathbf{b}_3], \tag{2.6}$$

and employing (1.9), the orthogonality relations (2.5) take the form

$$\begin{bmatrix} \mathbf{B}^T & \mathbf{A}^T \\ \overline{\mathbf{B}}^T & \overline{\mathbf{A}}^T \end{bmatrix} \begin{bmatrix} \mathbf{A} & \overline{\mathbf{A}} \\ \mathbf{B} & \overline{\mathbf{B}} \end{bmatrix} = \begin{bmatrix} \mathbf{I} & 0 \\ 0 & \mathbf{I} \end{bmatrix}. \tag{2.7}$$

The two 6x6 matrices on the left are the inverses of each other and their product can be interchanged. The interchanged product is

$$\begin{aligned} \mathbf{A}\mathbf{B}^T + \overline{\mathbf{A}\mathbf{B}}^T &= \mathbf{I} = \mathbf{B}\mathbf{A}^T + \overline{\mathbf{B}\mathbf{A}}^T, \\ \mathbf{A}\mathbf{A}^T + \overline{\mathbf{A}\mathbf{A}}^T &= 0 = \mathbf{B}\mathbf{B}^T + \overline{\mathbf{B}\mathbf{B}}^T. \end{aligned} \tag{2.8}$$

Equations (2.8) tell us that the real part of $\mathbf{A}\mathbf{B}^T$ is $\mathbf{I}/2$ and that $\mathbf{A}\mathbf{A}^T$ and $\mathbf{B}\mathbf{B}^T$ are purely imaginary. Hence the three matrices $\mathbf{S}$, $\mathbf{H}$, $\mathbf{L}$, defined by

$$\mathbf{S} = i(2\mathbf{A}\mathbf{B}^T - \mathbf{I}), \quad \mathbf{H} = 2i\mathbf{A}\mathbf{A}^T, \quad \mathbf{L} = -2i\mathbf{B}\mathbf{B}^T, \tag{2.9}$$

are real. It is clear that **H** and **L** are symmetric. It can be shown that they are positive definite, the products

$$\mathbf{SH}, \quad \mathbf{LS}, \quad \mathbf{H}^{-1}\mathbf{S}, \quad \mathbf{SL}^{-1}$$

are antisymmetric, and the relation

$$\mathbf{HL} - \mathbf{SS} = \mathbf{I} \tag{2.10}$$

holds [3,6].

The formulation presented so far assumes that the eigenvalues p are distinct. If $p_1 = p_2$, say, and $\mathbf{a}_1 = \mathbf{a}_2$, the solution (1.10) is not general. The matrices **A** and **B** would be singular and the orthogonality relation (2.7) is not valid. Anisotropic materials for which $p_1 = p_2$ and $\mathbf{a}_1 = \mathbf{a}_2$ are called **degenerate** materials. They are degenerate in the mathematical sense, not necessarily in the physical sense. Isotropic materials are a special case of degenerate materials for which $p_1 = p_2 = p_3 = i$ and $\mathbf{a}_1 = \mathbf{a}_2 \neq \mathbf{a}_3$. In many applications however the final solution depends only on the three real matrices **S**, **H**, **L** defined in (2.9). Barnett and Lothe [3] devised an integral formalism of these three real matrices which circumvented the need of determining the eigenvalues and the eigenvectors. Thus the problem of degenerate materials disappears. The integral formalism is as follows. Define the three real matrices

$$Q_{ik}(\theta) = C_{ijks}n_jn_s, \quad R_{ik}(\theta) = C_{ijks}n_jm_s, \quad T_{ik}(\theta) = C_{ijks}m_jm_s, \tag{2.11}$$

in which θ is a real parameter and

$$n_i = [\cos\theta, \sin\theta, 0], \quad m_i = [-\sin\theta, \cos\theta, 0].$$

Equations (2.11) reduce to (1.5) when $\theta = 0$. Next consider the incomplete integrals

$$\mathbf{S}(\theta) = \frac{1}{\pi}\int_0^\theta \mathbf{N}_1(\omega)\mathrm{d}\omega, \quad \mathbf{H}(\theta) = \frac{1}{\pi}\int_0^\theta \mathbf{N}_2(\omega)\mathrm{d}\omega,$$

$$\mathbf{L}(\theta) = \frac{1}{\pi}\int_0^\theta -\mathbf{N}_3(\omega)\mathrm{d}\omega, \tag{2.12}$$

where

$$\mathbf{N}_1(\theta) = -\mathbf{T}^{-1}(\theta)\mathbf{R}^{\mathrm{T}}(\theta), \quad \mathbf{N}_2(\theta) = \mathbf{T}^{-1}(\theta),$$

$$\mathbf{N}_3(\theta) = \mathbf{R}(\theta)\mathbf{T}^{-1}(\theta)\mathbf{R}^{\mathrm{T}}(\theta) - \mathbf{Q}(\theta).$$

$\mathbf{N}_i(\theta)$ reduce to $\mathbf{N}_i$ in (2.3) when $\theta = 0$. When $\theta = \pi$ we have the complete integrals $\mathbf{S}(\pi)$, $\mathbf{H}(\pi)$, $\mathbf{L}(\pi)$. Barnett and Lothe proved that $\mathbf{S}$, $\mathbf{H}$, $\mathbf{L}$ of (2.9) are identical to the complete integrals, i.e.,

$$\mathbf{S} = \mathbf{S}(\pi), \quad \mathbf{H} = \mathbf{H}(\pi), \quad \mathbf{L} = \mathbf{L}(\pi). \tag{2.13}$$

Thus $\mathbf{S}$, $\mathbf{H}$, $\mathbf{L}$ are called the Barnett–Lothe tensors and $\mathbf{S}(\theta)$, $\mathbf{H}(\theta)$, $\mathbf{L}(\theta)$ the associated tensors. In the sequel, dependence of $\mathbf{S}(\theta)$, $\mathbf{H}(\theta)$, $\mathbf{L}(\theta)$ on θ will be given explicitly unless $\theta = \pi$, and dependence of $\mathbf{N}_i(\theta)$ on θ will be given explicitly unless $\theta = 0$.

As we see from the integrals in (2.12), there is no need to determine the eigenvalues p and the associated eigenvectors $\mathbf{a}$ and $\mathbf{b}$. This is a remarkable result which has been widely used in the analysis of anisotropic elasticity. It should be pointed out that there are cases in which the final solution cannot be presented entirely in terms of Barnett–Lothe tensors and their associated tensors. In that case we have to modify the general solution (1.10) for degenerate materials [8,9].

For isotropic elastic materials use of (2.12) leads to

$$\mathbf{S} = s\begin{bmatrix} 0 & -1 & 0 \\ 1 & 0 & 0 \\ 0 & 0 & 0 \end{bmatrix}, \quad \mathbf{H} = \frac{1}{\mu}\begin{bmatrix} \frac{1-s^2}{\kappa} & 0 & 0 \\ 0 & \frac{1-s^2}{\kappa} & 0 \\ 0 & 0 & 1 \end{bmatrix}, \quad \mathbf{L} = \mu\begin{bmatrix} \kappa & 0 & 0 \\ 0 & \kappa & 0 \\ 0 & 0 & 1 \end{bmatrix}, \tag{2.14}$$

where μ is the shear modulus,

$$\kappa = \frac{1}{1-\nu}, \quad s = \frac{1-2\nu}{2(1-\nu)},$$

and ν is the Poisson ratio. For general anisotropic materials the structure of $\mathbf{S}$, $\mathbf{H}$, $\mathbf{L}$ is more complicated. For orthotropic materials and for monoclinic materials with the plane of symmetry at $x_3 = 0$, explicit expressions of $\mathbf{S}$, $\mathbf{H}$, $\mathbf{L}$ are obtained in [10,11]. We will show later that, if a proper oblique coordinate system is chosen as the natural base of the tensors $\mathbf{S}$, $\mathbf{H}$, $\mathbf{L}$, the tensor components $S^i{}_j$, H^{ij} and L_{ij} for general anisotropic materials have the exact expressions as that shown in (2.14) for isotropic materials.

3. PHYSICAL MEANINGS OF THE EIGENVECTORS a AND b. Let $\mathbf{a}'$, $\mathbf{a}''$ be the real and imaginary parts of $\mathbf{a}$,

$$\mathbf{a} = \mathbf{a}' + i\mathbf{a}''.$$

A complex vector is also called a bivector [12,13]. The real vectors $\mathbf{a}'$

and $\mathbf{a}''$ span a plane. If $\hat{\mathbf{a}}$ is obtained by multiplying $\mathbf{a}$ by a complex factor $e^{i\psi}$ where ψ is real,

$$\hat{\mathbf{a}} = e^{i\psi}\mathbf{a} = \hat{\mathbf{a}}' + i\hat{\mathbf{a}}'',$$

in which

$$\begin{aligned} \hat{\mathbf{a}}' &= \mathbf{a}'\cos\psi - \mathbf{a}''\sin\psi, \\ \hat{\mathbf{a}}'' &= \mathbf{a}'\sin\psi + \mathbf{a}''\cos\psi. \end{aligned} \tag{3.1}$$

Thus the real and imaginary parts of $\hat{\mathbf{a}}$ lie on the plane spanned by $\mathbf{a}'$ and $\mathbf{a}''$. Therefore the plane is called the polarization plane of $\mathbf{a}$, or simply the plane $\mathbf{a}$, which is invariant with the multiplication factor on $\mathbf{a}$. As ψ varies (3.1) show that $\hat{\mathbf{a}}'$ and $\hat{\mathbf{a}}''$ trace an ellipse. A pair of diameters in an ellipse is said to be conjugate if all chords parallel to one diameter are bisected by the other diameter. Therefore the tangent at the extremity of one diameter is parallel to the other diameter. It can be shown that $\hat{\mathbf{a}}'$ and $\hat{\mathbf{a}}''$ form a pair of conjugate radii. One could choose a ψ such that $\hat{\mathbf{a}}'$ and $\hat{\mathbf{a}}''$ are orthogonal and hence are the principal radii of the ellipse [14].

It is clear that the bivector $\mathbf{a}$ and its complex conjugate $\bar{\mathbf{a}}$ define the same polarization plane.

Consider now the solution (1.3). The displacement $\mathbf{u}$ is a bivector $\mathbf{a}$ multiplied by $f(z)$. Regardless of the position (x_1, x_2), $f(z)$ is a complex factor of the form $\rho e^{i\psi}$ where ρ is real. Whether we take the real or imaginary part of $\mathbf{a}\, f(z)$, $\mathbf{u}$ is polarized on the plane $\mathbf{a}$ for all (x_1, x_2). Likewise, the stress function $\boldsymbol{\phi}$ of (1.7) is polarized on the plane $\mathbf{b}$. If $\mathbf{t}_\Gamma$ is the surface traction vector on a curved boundary Γ, it can be shown from (1.6) that

$$\mathbf{t}_\Gamma = \frac{\partial \boldsymbol{\phi}}{\partial \eta} \tag{3.2}$$

where η is the arclength of Γ measured in the direction such that the material is located on the right hand side of Γ. Equations $(1.6)_1$ and $(1.6)_2$ are special cases of (3.2) when Γ is the surface x_1 = constant and x_2 = constant, respectively. Since $\boldsymbol{\phi}$ is polarized on the plane $\mathbf{b}$, (3.2) tells us that the surface traction $\mathbf{t}_\Gamma$ is polarized on the plane $\mathbf{b}$.

The general solution (1.10) or (1.11) implies that there are three polarization planes $\mathbf{a}_1$, $\mathbf{a}_2$, $\mathbf{a}_3$ for the displacement $\mathbf{u}$ and three

polarization planes $\mathbf{b}_1$, $\mathbf{b}_2$, $\mathbf{b}_3$ for the surface traction $\mathbf{t}_\Gamma$. For monoclinic materials with the plane of symmetry at $x_3 = 0$, $\mathbf{a}_1$, $\mathbf{a}_2$, $\mathbf{b}_1$, $\mathbf{b}_2$ all define the same plane, namely, the (x_1, x_2) plane. As to $\mathbf{a}_3$ and $\mathbf{b}_3$, their real and imaginary parts are parallel. The polarization planes degenerate into lines parallel to the x_3–axis. The displacement associated with $\mathbf{a}_3$ and the surface traction $\mathbf{t}_\Gamma$ associated with $\mathbf{b}_3$ are in the x_3 direction.

In summary, there are three independent (or three one–component) solutions for general anisotropic materials. The displacement of a one–component solution is polarized on the plane **a** while the surface traction on any boundary is polarized on the plane **b**. To satisfy a prescribed boundary condition, all three one–component solutions are in general needed. In surface waves, there are one–component surface waves [15, 16] and two–component surface waves [17, 18]. For Green's functions for the infinite space due to a line force and a line dislocation, there are one–component Green's functions. The latter will be discussed in Section 5.

4. THE S TENSOR. Of the three Barnett–Lothe tensors, the tensor **S** is the most interesting one. By writing **S** as

$$\mathbf{S} = \mathbf{L}^{-1}(\mathbf{LS}), \tag{4.1}$$

S is the product of the symmetric positive definite tensor $\mathbf{L}^{-1}$ and the antisymmetric tensor **LS**. It has the property that

$$\text{tr } \mathbf{S} = 0, \quad \det \mathbf{S} = 0.$$

Therefore the eigenvalues of **S** are 0 and $\mp is$ where

$$s = \left\{-\frac{1}{2} \text{tr } (\mathbf{S}^2)\right\}^{1/2}. \tag{4.2}$$

Denoting the associated eigenvectors by $\mathbf{e}_3$ and $\mathbf{e}_1 \pm i\mathbf{e}_2$ where $\mathbf{e}_1$, $\mathbf{e}_2$, $\mathbf{e}_3$ are real, we have

$$\mathbf{S}(\mathbf{e}_1 \pm i\mathbf{e}_2) = \mp is(\mathbf{e}_1 \pm i\mathbf{e}_2), \quad \mathbf{Se}_3 = \mathbf{0}. \tag{4.3}$$

Thus $\mathbf{e}_3$ is the **right null vector** of **S** and $\mathbf{e}_1 \pm i\mathbf{e}_2$ are the right eigenvectors. The new right eigenvectors $\hat{\mathbf{e}}_1 \pm i\hat{\mathbf{e}}_2$ obtained by multiplying $\mathbf{e}_1 \pm i\mathbf{e}_2$ by a complex factor span the same plane as $\mathbf{e}_1 \pm i\mathbf{e}_2$. Therefore the plane spanned by $(\mathbf{e}_1, \mathbf{e}_2)$ is called the **right eigenplane**.

Let $\mathbf{e}^1$, $\mathbf{e}^2$, $\mathbf{e}^3$ be the reciprocal of $\mathbf{e}_1$, $\mathbf{e}_2$, $\mathbf{e}_3$ so that

$$\mathbf{e}^i \cdot \mathbf{e}_j = \delta^i{}_j. \tag{4.4}$$

Consider the following tensor components of **S**, **H**, **L** :

$$\mathbf{S} = S^i{}_j\, \mathbf{e}_i \otimes \mathbf{e}^j, \quad \mathbf{H} = H^{ij}\, \mathbf{e}_i \otimes \mathbf{e}_j, \quad \mathbf{L} = L_{ij}\, \mathbf{e}^i \otimes \mathbf{e}^j. \tag{4.5}$$

Using (2.10) and the fact that **SH**, **LS** are antisymmetric, the matrices formed by $S^i{}_j$, H^{ij}, L_{ij} can be shown to have the structure given in (2.14) where s, μ, κ are now independent constants [19]. Thus as far as the Barnett–Lothe tensors are concerned, anisotropic materials are identical to isotropic materials if we choose an oblique coordinate system represented by $\mathbf{e}_1$, $\mathbf{e}_2$, $\mathbf{e}_3$. For isotropic materials $\mathbf{e}_1$, $\mathbf{e}_2$, $\mathbf{e}_3$ are unit vectors in the direction of the x_1, x_2, x_3 axis, respectively.

It should be pointed out that $(\mathbf{e}^1, \mathbf{e}^2)$ and $\mathbf{e}^3$ are, respectively, the **left eigenplane** and the **left null vector** of **S**. Do $\mathbf{e}_i$, $\mathbf{e}^j$ have physical interpretations? They do. They are explained in the next Section.

5. GREEN'S FUNCTIONS FOR LINE FORCES AND LINE DISLOCATIONS IN THE INFINITE SPACE. There are several interesting properties associated with Green's functions for the infinite space due to a line force f and a line dislocation with Burgers vector b applied along the x_3 axis. The basic solution is obtained from (1.11) by choosing the function $f(z_\alpha)$ such that

$$\mathbf{u} = \frac{1}{\pi}\,\mathrm{Im}\sum_{\alpha=1}^{3}\mathbf{a}_\alpha q_\alpha \ln z_\alpha, \quad \phi = \frac{1}{\pi}\,\mathrm{Im}\sum_{\alpha=1}^{3} b_\alpha q_\alpha \ln z_\alpha. \tag{5.1}$$

Since $\ln z_\alpha$ is a multi–valued function we introduce a cut along the negative x_1–axis. In the polar coordinate system

$$x_1 = r\cos\theta, \quad x_2 = r\sin\theta, \tag{5.2}$$

the solution (5.1) applies to

$$-\pi < \theta < \pi, \qquad r > 0.$$

Therefore

$$\ln z_\alpha = \ln r \pm i\pi \quad \text{at} \quad \theta = \pm\pi, \ \text{for } \alpha = 1, 2, 3. \tag{5.3}$$

Equations (5.1) represent three one–component Green's functions. For each α, $\mathbf{u}$ is polarized on the plane $\mathbf{a}_\alpha$ and the surface traction $\mathbf{t}_\Gamma$ is polarized on the plane $\mathbf{b}_\alpha$. The discontinuities in $\mathbf{u}$ and ϕ across $\theta = \pm\pi$ are, respectively, the line dislocation b^α and the line force

f^{α} for the one–component Green's function. Hence by (5.3),

$$b^{\alpha} = 2\,\mathrm{Re}(\mathbf{a}_{\alpha}q_{\alpha}), \quad f^{\alpha} = 2\,\mathrm{Re}(\mathbf{b}_{\alpha}q_{\alpha}), \tag{5.4}$$

which show that b^{α} is on the plane $\mathbf{a}_{\alpha}$ and f^{α} is on the plane $\mathbf{b}_{\alpha}$. We therefore have the result that the one–component Green's function has $\mathbf{u}$ and b^{α} polarized on the plane $\mathbf{a}_{\alpha}$ and has f^{α} and the surface traction $\mathbf{t}_{\Gamma}$ polarized on the plane $\mathbf{b}_{\alpha}$.

To obtain a one–component Green's function we may assume an arbitrary complex constant q_{α}. Equations (5.4) then provide b^{α} and f^{α} required for the one–component Green's function. Alternately we may prescribe an f^{α} which lies on the plane $\mathbf{b}_{\alpha}$. Equation $(5.4)_2$ can be solved for q_{α} and $(5.4)_1$ gives the associated b^{α}. To solve $(5.4)_2$ for q_{α}, let the real and imaginary parts of $\mathbf{b}_{\alpha}$ and q_{α} be written as

$$\mathbf{b}_{\alpha} = \mathbf{b}'_{\alpha} + i\mathbf{b}''_{\alpha}, \quad q_{\alpha} = q'_{\alpha} + iq''_{\alpha}.$$

We then have

$$f^{\alpha} = 2(\mathbf{b}'_{\alpha}q'_{\alpha} - \mathbf{b}''_{\alpha}q''_{\alpha})$$

from which q'_{α} and q''_{α} can be determined.

When f and b are prescribed arbitrarily, we need all three one–component Green's functions for the solution. Making use of (2.6), (5.1) are rewritten as

$$\mathbf{u} = \frac{1}{\pi}\,\mathrm{Im}\{\mathbf{A}\langle \ln z\rangle \mathbf{q}\}, \quad \boldsymbol{\phi} = \frac{1}{\pi}\,\mathrm{Im}\{\mathbf{B}\langle \ln z\rangle \mathbf{q}\}, \tag{5.5}$$

in which

$$\mathbf{q}^{\mathrm{T}} = [q_1, q_2, q_3]$$

and

$$\langle \ln z\rangle = \mathrm{diag}[\ln z_1, \ln z_2, \ln z_3]$$

is a diagonal matrix. Equations (5.5) must satisfy the conditions

$$\mathbf{u}(\pi) - \mathbf{u}(-\pi) = b,$$

$$\boldsymbol{\phi}(\pi) - \boldsymbol{\phi}(-\pi) = f,$$

which lead to

$$2\,\mathrm{Re}(\mathbf{Aq}) = \boldsymbol{b}, \quad 2\,\mathrm{Re}(\mathbf{Bq}) = \boldsymbol{f}. \tag{5.6}$$

This can be written as

$$\begin{bmatrix} \mathbf{A} & \overline{\mathbf{A}} \\ \mathbf{B} & \overline{\mathbf{B}} \end{bmatrix} \begin{bmatrix} \mathbf{q} \\ \overline{\mathbf{q}} \end{bmatrix} = \begin{bmatrix} \boldsymbol{b} \\ \boldsymbol{f} \end{bmatrix}.$$

It follows from (2.7) that

$$\begin{bmatrix} \mathbf{q} \\ \overline{\mathbf{q}} \end{bmatrix} = \begin{bmatrix} \mathbf{B}^{\mathrm{T}} & \mathbf{A}^{\mathrm{T}} \\ \overline{\mathbf{B}}^{\mathrm{T}} & \overline{\mathbf{A}}^{\mathrm{T}} \end{bmatrix} \begin{bmatrix} \boldsymbol{b} \\ \boldsymbol{f} \end{bmatrix}.$$

Hence

$$\mathbf{q} = \mathbf{A}^{\mathrm{T}}\boldsymbol{f} + \mathbf{B}^{\mathrm{T}}\boldsymbol{b}, \tag{5.7a}$$

or

$$q_\alpha = \mathbf{a}_\alpha \cdot \boldsymbol{f} + \mathbf{b}_\alpha \cdot \boldsymbol{b}. \tag{5.7b}$$

Inserting (5.7b) into (5.4) gives us $\boldsymbol{b}^\alpha$ and $\boldsymbol{f}^\alpha$ in terms of $\boldsymbol{b}$ and $\boldsymbol{f}$.

We show next that the solution (5.5) together with (5.7a) can be rewritten into a real form. Equations (2.9) are identities which convert certain combinations of complex quantities involving **A**, **B** to real quantities **S**, **H** and **L**. The following identities are useful for problems related to line forces and line dislocations [20].

$$\begin{aligned}
2\,\mathbf{A}\langle \ln z\rangle \mathbf{A}^{\mathrm{T}} &= -\mathrm{i}[(\ln r)\mathbf{I} + \pi\mathbf{S}(\theta)]\mathbf{H} + \pi\mathbf{H}(\theta)[\mathbf{I} - \mathrm{i}\mathbf{S}^{\mathrm{T}}], \\
2\,\mathbf{B}\langle \ln z\rangle \mathbf{A}^{\mathrm{T}} &= [(\ln r)\mathbf{I} + \pi\mathbf{S}^{\mathrm{T}}(\theta)][\mathbf{I} - \mathrm{i}\mathbf{S}^{\mathrm{T}}] + \mathrm{i}\pi\mathbf{L}(\theta), \\
2\,\mathbf{A}\langle \ln z\rangle \mathbf{B}^{\mathrm{T}} &= [(\ln r)\mathbf{I} + \pi\mathbf{S}(\theta)][\mathbf{I} - \mathrm{i}\mathbf{S}] + \mathrm{i}\pi\mathbf{H}(\theta)\mathbf{L}, \\
2\,\mathbf{B}\langle \ln z\rangle \mathbf{B}^{\mathrm{T}} &= \mathrm{i}[(\ln r)\mathbf{I} + \pi\mathbf{S}^{\mathrm{T}}(\theta)]\mathbf{L} - \pi\mathbf{L}(\theta)[\mathbf{I} - \mathrm{i}\mathbf{S}].
\end{aligned} \tag{5.8}$$

These identities allow us to convert the complex expressions on the left to real quantities shown on the right which are obtainable directly in terms of elasticity constants through (2.12) and (2.13). With the identities (5.8), the solution (5.5) together with (5.7a) is converted into a real form as

$$2\mathbf{u} = -\frac{1}{\pi}(\ln r)\mathbf{h} - \mathbf{S}(\theta)\mathbf{h} + \mathbf{H}(\theta)\mathbf{g},$$
$$2\boldsymbol{\phi} = \frac{1}{\pi}(\ln r)\mathbf{g} + \mathbf{L}(\theta)\mathbf{h} + \mathbf{S}^{\mathrm{T}}(\theta)\mathbf{g}, \tag{5.9}$$

where

$$\mathbf{g} = \mathbf{L}\boldsymbol{b} - \mathbf{S}^{\mathrm{T}}\boldsymbol{f}, \quad \mathbf{h} = \mathbf{S}\boldsymbol{b} + \mathbf{H}\boldsymbol{f}. \tag{5.10}$$

From (3.2), the surface traction $\mathbf{t}_\theta$ on any radial plane θ = constant is in the direction of $\mathbf{g}$ which is invariant with the choice of the radial plane. The infinite displacement $\mathbf{u}_0$ at r = 0 is in the direction of $\mathbf{h}$. Moreover, the relation [14]

$$\mathbf{g}\cdot\mathbf{h} = \boldsymbol{f}\cdot\boldsymbol{b}$$

is easily established using (2.10) and the anti–symmetric property of **LS** and **SH**.

We now present physical interpretations of $\mathbf{e}_i$ and $\mathbf{e}^i$. Using (4.5) and the discussions following (5.10), (5.10) can be written as

$$2\pi r\mathbf{t}_\theta = \mathbf{g} = [L_{ij}(\mathbf{e}^j\cdot\boldsymbol{b}) - S^j{}_i(\mathbf{e}_j\cdot\boldsymbol{f})]\mathbf{e}^i,$$
$$-2\pi(\ln r)^{-1}\mathbf{u}_0 = \mathbf{h} = [S^i{}_j(\mathbf{e}^j\cdot\boldsymbol{b}) + H^{ij}(\mathbf{e}_j\cdot\boldsymbol{f})]\mathbf{e}_i.$$

With the structure of $S^i{}_j$, H^{ij}, L_{ij} shown in (2.14) and using (4.4), it can be shown that if $\boldsymbol{b}$ is along $\mathbf{e}_3$ and $\boldsymbol{f}$ is along $\mathbf{e}^3$, $\mathbf{u}_0$ is in the direction of $\mathbf{e}_3$ and $\mathbf{t}_\theta$ in the direction of $\mathbf{e}^3$. On the other hand, if $\boldsymbol{b}$ is on the right eigenplane ($\mathbf{e}_1$, $\mathbf{e}_2$) and $\boldsymbol{f}$ is on the left eigenplane ($\mathbf{e}^1$, $\mathbf{e}^2$), $\mathbf{u}_0$ is polarized on the right eigenplane and $\mathbf{t}_\theta$ is polarized on the left eigenplane. More relations between $\mathbf{e}_1$, $\mathbf{e}_2$, $\mathbf{e}^1$,$\mathbf{e}^2$ and $\boldsymbol{b}$ and $\boldsymbol{f}$ can be found in [14].

6. BIMATERIALS AND INTERFACE CRACKS. Let $\theta = \theta_0$ be the interface between two materials in the bimaterial. The half–space $\theta_0 < \theta < \theta_0+\pi$ is occupied by material 1 and the other half–space $\theta_0-\pi < \theta < \theta_0$ is occupied by material 2. They are rigidly bonded together along $\theta = \theta_0$. For a line force $\boldsymbol{f}$ and a line dislocation $\boldsymbol{b}$ applied at the origin r = 0, (5.9) is a basic solution which applies to both materials. We may add constant terms to the right hand sides of (5.9) which produce a rigid body displacement but no stresses. Therefore consider the solution

$$2\,\mathbf{u}_1(r,\theta) = -\frac{1}{\pi}(\ln r)\mathbf{h} - [\mathbf{S}_1(\theta)-\mathbf{S}_1(\theta_0)]\mathbf{h} + [\mathbf{H}_1(\theta)-\mathbf{H}_1(\theta_0)]\mathbf{g},$$
$$2\,\boldsymbol{\phi}_1(r,\theta) = \frac{1}{\pi}(\ln r)\mathbf{g} + [\mathbf{L}_1(\theta)-\mathbf{L}_1(\theta_0)]\mathbf{h} + [\mathbf{S}_1^{\mathrm{T}}(\theta)-\mathbf{S}_1^{\mathrm{T}}(\theta_0)]\mathbf{g}, \tag{6.1}$$

for material 1 in $\theta_0 < \theta < \theta_0+\pi$. The subscript 1 denotes material 1. The solution for material 2 is obtained from (6.1) by replacing the subscript 1 by 2 while keeping the same constants $\mathbf{g}$ and $\mathbf{h}$. It is readily shown that the continuity of $\mathbf{u}$ and $\boldsymbol{\phi}$ at $\theta = \theta_0$ is automatically satisfied. The discontinuity in $\mathbf{u}$ and $\boldsymbol{\phi}$ across $\theta = \theta_0 \pm \pi$, which should be equal to $\boldsymbol{b}$ and $\boldsymbol{f}$, respectively, leads to two equations for $\mathbf{g}$ and $\mathbf{h}$ which are independent of θ_0 [21]. Therefore, the stresses obtained by substituting $\boldsymbol{\phi}_1$ of (6.1) and similar equation for $\boldsymbol{\phi}_2$ into (1.6) are independent of the location θ_0 of the interface ! This unexpected phenomenon defies an intuitive explanation even for isotropic bimaterials.

One of the most studied problems in anisotropic elasticity is the problem of interface cracks in bimaterials [22–33]. Let $x_2 > 0$ be occupied by material 1 and $x_2 < 0$ be occupied by material 2. The interface crack of length $2a$ is located at

$$x_2 = 0, \quad |x_1| < a.$$

The bimaterial is subject to a uniform traction $\mathbf{t}_\Gamma$ and $-\mathbf{t}_\Gamma$ at the crack surfaces $x_2 = +0$ and -0, respectively. The stress singularities near a tip of the interface crack is proportional to r^δ where r is the radial distance from the crack tip and δ is a constant depending on the material property of the bimaterial. It is shown in [24] that there are three singularities given by

$$\delta = -\frac{1}{2}, \quad -\frac{1}{2} + i\gamma, \quad \text{and} \quad -\frac{1}{2} - i\gamma,$$

where

$$\gamma = \frac{1}{2\pi} \ln\frac{1+\beta}{1-\beta} = \frac{1}{\pi} \tanh^{-1}\beta,$$

$$\beta = \left[-\frac{1}{2} \operatorname{tr}(\hat{\mathbf{S}}^2)\right]^{1/2} < 1. \tag{6.2}$$

In the above

$$\hat{\mathbf{S}} = \mathbf{D}^{-1}\mathbf{W}, \tag{6.3}$$

$$\mathbf{D} = \mathbf{L}_1^{-1} + \mathbf{L}_2^{-1}, \quad \mathbf{W} = \mathbf{S}_1\mathbf{L}_1^{-1} - \mathbf{S}_2\mathbf{L}_2^{-1},$$

in which $\mathbf{D}$ is symmetric, positive definite and $\mathbf{W}$ is anti–symmetric. Thus $\hat{\mathbf{S}}$ has the same properties as the $\mathbf{S}$ tensor. The eigenvalues of $\hat{\mathbf{S}}$ are $\mp i\beta$ and 0 and the associated right eigenvectors are denoted by $\mathbf{d}_1 \pm i\mathbf{d}_2$ and $\mathbf{d}_0$, respectively. The left eigenvectors can be shown to be $\mathbf{D}(\mathbf{d}_1 \mp i\mathbf{d}_2)$ and $\mathbf{D}\mathbf{d}_0$ [34]. Hence $\mathbf{d}_0$, $\mathbf{D}\mathbf{d}_0$ are, respectively, the right and left null vectors while the planes spanned by $(\mathbf{d}_1, \mathbf{d}_2)$ and $(\mathbf{D}\mathbf{d}_1, \mathbf{D}\mathbf{d}_2)$ are the right and left eigenplanes.

The two materials in the bimaterial are said to be **mismatched** when $\mathbf{W} \neq \mathbf{0}$. $\mathbf{W} = \mathbf{0}$ if and only if $\beta = 0$ (and hence $\gamma = 0$) [24, 25]. For mismatched bimaterials ($\gamma \neq 0$), the displacement at the crack surface is oscillatory. This leads to the physically unacceptable interpenetration of the crack surfaces.

When $\beta = 0$ the solution in materials 1 and 2 both have the expression

$$\begin{aligned} \mathbf{u} &= \mathrm{Re}\,\{\mathbf{A}\langle f(z)\rangle \mathbf{B}^{-1}\}\mathbf{t}_\Gamma, \\ \boldsymbol{\phi} &= \mathrm{Re}\,\{\mathbf{B}\langle f(z)\rangle \mathbf{B}^{-1}\}\mathbf{t}_\Gamma, \end{aligned} \tag{6.4}$$

in which

$$f(z) = \sqrt{z^2 - a^2} - z.$$

Of course **A**, **B** and z in material 1 and material 2 would be different. There is no oscillation in displacement and the stress has the square root singularities.

The following results are taken from [34]. When $\beta \neq 0$, the solution is still given by (6.4) if the applied traction $\mathbf{t}_\Gamma$ is the null vector of **W**, i.e., if

$$\mathbf{W}\mathbf{t}_\Gamma = 0,$$

or, by (6.3),

$$\hat{\mathbf{S}}\mathbf{t}_\Gamma = 0.$$

Thus when the applied traction is in the direction of the right null vector $\mathbf{d}_0$, there is no oscillation in displacement. The crack surface opening

$$\Delta\mathbf{u} = \mathbf{u}(x_1, +0) - \mathbf{u}(x_1, -0), \quad |x_1| < a,$$

is in the direction of the left null vector $\mathbf{D}\mathbf{d}_0$ and the surface traction on the surface $x_2 = 0$ outside the crack is in the direction of the right null vector $\mathbf{d}_0$.

If the applied traction is not in the direction of $\mathbf{d}_0$, we decompose it into two components. One is along the right null vector $\mathbf{d}_0$ and the other is on the right eigenplane ($\mathbf{d}_1$, $\mathbf{d}_2$). Explicit solutions associated with the one on the right eigenplane can be found in [34] in which the displacement is oscillatory. It suffices to mention that the crack surface opening $\Delta\mathbf{u}$ lies on the left eigenplane of $\hat{\mathbf{S}}$ while the surface traction along the surface $x_2 = 0$ lies on the right eigenplane of $\hat{\mathbf{S}}$.

DISCUSSION

We have shown that, in many respects, anisotropic elastic materials have properties which are similar to, or generalization of, the properties of isotropic materials. Analogous to the antiplane deformations of isotropic materials, anisotropic materials have deformations which are polarized in one direction while the surface traction vector on any boundary is polarized on a different direction. Similar to the in–plane deformations of isotropic materials, anisotropic materials can have deformations which are polarized on one oblique plane while the surface traction vector on any boundary is polarized on another oblique plane.

Simple problems for which we thought we have understood them thoroughly still yield new information due to the simplification of the solutions by the Stroh formalism. For example, consider the Griffith crack of length $2a$ located at $x_2 = 0$, $|x_1| < a$ in the infinite anisotropic elastic medium. When the traction applied at the crack surfaces is in the direction of the x_2 axis, the crack opening is in general not symmetric with the x_2 axis as expected. However, the x_1 axis outside the crack remains a straight line (i. e., the u_2 component of the displacement along the x_1 axis vanishes). If the traction applied at the crack surface is the null vector of $\mathbf{SL}^{-1}$, all three displacement components along the x_1 axis vanish. If the applied traction is in the direction of the vector formed from the second column of $\mathbf{L}$, the hoop stress vector along the crack surface is independent of x_1 [21].

Other interesting properties worth mentioning are the physical implications of the eigenvalues p. For the Green's functions for a half–space subject to a singularity in the form of line forces and line dislocations, the solution can be obtained by a superposition of the Green's function due to the same singularity for the infinite space and several image singularities located outside of the space occupied by the material. The locations of the image singularities are determined exclusively by the eigenvalues p. Moreover, the locations of the image singularities are independent of the nature of the singularities concerned [35]. If the singularities are line forces and line dislocations, the image singularities are also line forces and line dislocations. For degenerate materials for which isotropic materials are a special case, two or more of the image singularities coalesce into one singularity, creating a new singularity in the form of a double force, a concentrated couple, and/or a higher order singularity which are well known for isotropic materials [36] but have not been satisfactorily explained in the past.

ACKNOWLEDGEMENTS. The work presented here is supported by the U. S. Army Research Office through grant DAAL 03–91–G–0082.

REFERENCES

[1] A. N. Stroh, "Dislocations and cracks in anisotropic elasticity," Phil Mag. **3**, 625–646 (1958).

[2] A. N. Stroh, "Steady state problems in anisotropic elasticity," J. Math. Phys. **41**, 77–103 (1962).

[3] D. M. Barnett and J. Lothe, "Synthesis of the sextic and the integral formalism for dislocations, Greens functions and surface waves in anisotropic elastic solids," Phys. Nor., **7**, 13–19 (1973).

[4] J. D. Eshelby, W. T. Read, and W. Shockley, "Anisotropic elasticity with applications to dislocation theory," Acta Metall. **1**, 251–259 (1953).

[5] K. Malen and J. Lothe, "Explicit expressions for dislocation derivatives," Phys. Status Solidi. **39**, 287–296 (1970).

[6] P. Chadwick and G. D. Smith, "Foundations of the theory of surface waves in anisotropic elastic materials," Adv. Appl. Mech. **17**, 303–376 (1977).

[7] T. C. T. Ting, "Some identities and the structure of $\mathbf{N}_i$ in the Stroh formalism of anisotropic elasticity," Q. Appl. Math. **46**, 109–120 (1988).

[8] T. C. T. Ting, "Effects of change of reference coordinates on the stress analyses of anisotropic elastic materials," Int. J. Solids Structures. **18**, 139–152 (1982).

[9] T. C. T. Ting and Chyanbin Hwu, "Sextic formalism in anisotropic elasticity for almost non–semisimple matrix **N**," Int. J. Solids Structures. **24**, 65–76 (1988).

[10] Changsong Dongye and T. C. T. Ting, "Explicit expressions of Barnett–Lothe tensors and their associated tensors for orthotropic materials," Q. Appl. Math. **47**, 723–734 (1989).

[11] T. C. T. Ting, "Barnett–Lothe tensors and their associated tensors for monoclinic materials with the symmetry plane at $x_3 = 0$," J. Elasticity. **27**, 143–165 (1992).

[12] J. W. Gibbs, "Elements of Vector Analysis," Dover, N.Y. (1961).

[13] Ph. Boulanger and M. Hayes, "Bivectors and inhomogeneous plane waves in anisotropic elastic bodies," in Modern Theory of

Anisotropic Elasticity and Applications. SIAM Proceedings Series. SIAM, Phila. 280–289 (1991).

[14] T. C. T. Ting, "The eigenvectors of the **S** matrix and their relations with line dislocations and forces in anisotropic elastic solids," in Micromechanics and Inhomogeneity, The Toshio Mura Anniversary Volume. Springer–Verlag, N.Y. 449–467 (1990).

[15] D. M. Barnett, P. Chadwick and J. Lothe, "The behavior of elastic surface waves polarized in a plane of material symmetry. I. Addendum," Proc. R. Soc. Lon. A **433**, 699–710 (1991).

[16] D. M. Barnett and P. Chadwick, "The existence of one–component surface waves and exceptional subsequent transonic states of type 2, 4 and E1 in anisotropic elastic media," in Modern Theory of Anisotropic Elasticity and Applications. SIAM Proceedings Series. SIAM, Phila. 199–214 (1991).

[17] D. M. Barnett, J. Lothe and S. A. Gundersen, "Zero curvature transonic states and free surface waves in anisotropic elastic media," Wave Motion. **12**, 341–360 (1990).

[18] S. A. Gundersen, L. Wang and J. Lothe, "Secluded supersonic surface waves," in Modern Theory of Anisotropic Elasticity and Applications. SIAM Proceedings Series. SIAM, Phila. 186–198 (1991).

[19] P. Chadwick and T. C. T. Ting, "On the structure and invariance of the Barnett–Lothe tensors," Q. Appl. Math. **45**, 419–427 (1987).

[20] T. C. T. Ting, "Line forces and dislocations in anisotropic elastic composite wedges and spaces," Phys. Status Solidi. B **146**, 81–90 (1988).

[21] T. C. T. Ting, "The Stroh formalism and certain invariances in two–dimensional anisotropic elasticity," in Modern Theory of Anisotropic Elasticity and Applications. SIAM Proceedings Series. SIAM, Phila. 3–32 (1991).

[22] D. L. Clements, "A crack between dissimilar anisotropic media," Int. J. Eng. Sci. **9**, 257–265 (1971).

[23] J. R. Willis, "Fracture mechanics of interface cracks," J. Mech. Phys. Solids. **19**, 353–368 (1971).

[24] T. C. T. Ting, "Explicit solution and invariance of the singularities at an interface crack in anisotropic composites," Int. J. Solids Structures. **22**, 965–983 (1986).

[25] J. L. Bassani and J. Qu, "Finite cracks on bimaterial and bicrystal interfaces," J. Mech. Phys. Solids. **37**, 435–453 (1989).

[26] V. K. Tewary, R. H. Wagoner and J. P. Hirth, "Elastic Green's function for a composite solid with a planar crack in the interface" J. Mater. Res. **4**, 124–136 (1989).

[27] Zhigang Suo, "Singularities, interfaces and cracks in dissimilar anisotropic media," Proc. R. Soc. Lon. A **427**, 331–358 (1990).

[28] K. C. Wu, "Stress intensity factor and energy release rate for interfacial cracks between dissimilar anisotropic materials," J. Appl. Mech. **57**, 882–886 (1990).

[29] T. C. T. Ting, "Interface cracks in anisotropic bimaterials," J. Mech. Phys. Solids. **38**, 505–513 (1990).

[30] Chyanbin Hwu, "Collinear cracks in anisotropic bodies," Int. J. Fracture. **54**, 239–256 (1991).

[31] L. Ni and S. Nemat–Nasser, "Interface cracks in anisotropic dissimilar materials: an analytic solution," J. Mech. Phys. Solids. **39**, 113–144 (1991).

[32] H. Gao, M. Abbudi and D. M. Barnett, "On interfacial crack–tip field in anisotropic elastic solids," J. Mech. Phys. Solids. **40**, 393–416 (1992).

[33] Jianmin Qu and Qianqian Li, "Interfacial dislocation and its applications to interface cracks in anisotropic bimaterials," J. Elasticity. **26**, 169–195 (1991).

[34] T. C. T. Ting, "Interface cracks in anisotropic elastic bimaterials – a decomposition principle," George Herrmann 70th Anniversary Issue, Int. J. Solids Structures. **29**, 1989–2003 (1992).

[35] T. C. T. Ting, "Image singularities of Green's functions for anisotropic elastic half–spaces and bimaterials," Q. J. Mech. Appl. Math. **45**, 119–139 (1992).

[36] J. Dundurs, "Elastic interaction of dislocations with inhomogeneities," in Mathematical Theory of Dislocations. T. Mura, ed. ASME, N. Y. 70–115 (1969).

TWO-PHASE CONTINUUM MECHANICS WITH MASS TRANSPORT AND STRESS

Morton E. Gurtin[1]
Peter W. Voorhees[2]

[1]Mathematics, Carnegie Mellon University,
Pittsburgh, PA 15213
[2]Materials Science and Engineering, Northwestern University
Evanston, IL 60208

1. Introduction

There are multiphase processes that are essentially isothermal with kinetics driven by mass transport and stress, an example being coarsening or Ostwald ripening, in which a phase, quenched into a metastable state, exhibits late-stage kinetics characterized by the dissolution of second-phase domains with large interfacial curvature at the expense of domains with low interfacial curvature. In [1] we developed a continuum-mechanical framework within which such processes can be discussed. We here discuss the results of [1].

We consider a two-phase system consisting of bulk regions separated by a sharp interface endowed with energy and capable of supporting force, following — and in certain respects generalizing — the framework set out in [2-5]. We base our discussion on balance laws for mass and force in conjunction with a version of the second law appropriate to a mechanical system out of equilibrium. We assume that mass transport is characterized by the bulk diffusion of a *single* independent species; we neglect mass diffusion within the interface.

2. Theory without deformation.

We neglect deformation and bulk stress, but allow the diffusion potential (chemical potential) to be discontinuous across the interface. We develop a heirarchy of free-boundary problems at various levels of approximation, framed in terms of the departure $u = \mu - \mu_0$ of the diffusion potential μ from the transition μ_0, which is the potential at which the phase change would occur were interfacial structure neglected. For small departures from μ_0 the basic system of equations, neglecting diffusional transients, consists of a PDE in bulk supplemented by three interface conditions. The PDE has the form

$$div\mathbf{h} = 0\,, \tag{1}$$

where $\mathbf{h}$, the mass flux, is given by

$$\begin{aligned} \mathbf{h} &= -\mathbf{D}_\alpha \nabla u \text{ in phase } \alpha, \\ \mathbf{h} &= -\mathbf{D}_\beta \nabla u \text{ in phase } \beta, \end{aligned} \tag{2}$$

with $\mathbf{D}_\alpha$ and $\mathbf{D}_\beta$ constant mobility tensors. The first interface condition is balance of mass

$$\mathbf{h}^- \cdot \boldsymbol{\nu} - AV = \mathbf{h}^+ \cdot \boldsymbol{\nu} - BV \equiv J, \tag{3}$$

in which $\mathbf{h}^-$ and $\mathbf{h}^+$, respectively, represent the limits of $\mathbf{h}$ from the α and β phases, A and B are constants representing the density in the α and β phases at the potential μ_0, $\boldsymbol{\nu}$ is the unit normal to the interface directed out of phase α, and V is the normal velocity and K the curvature of the interface. The second interface condition, essentially constitutive, characterizes the net mass flux J *defined* in (3):

$$J = -b_{21}(\boldsymbol{\nu})V - b_{22}(\boldsymbol{\nu})[\![u]\!], \tag{4}$$

where $b_{21}(\boldsymbol{\nu})$ and $b_{22}(\boldsymbol{\nu})$ are constitutive moduli, while $[\![\,]\!]$ (in boldface) denotes the jump across the interface (β minus α). The third interface condition generalizes the classical "Gibbs-Thomson relation" to situations in which the chemical potential is discontinuous across the interface:

$$Bu^+ - Au^- = f(\boldsymbol{\nu})K + div_s \mathbf{c}(\boldsymbol{\nu}) - b_{11}(\boldsymbol{\nu})V - b_{12}(\boldsymbol{\nu})[\![u]\!], \tag{5}$$

where $f(\boldsymbol{\nu})$ is the interfacial energy,

$$\mathbf{c}(\boldsymbol{\nu}) = -\partial_\nu f(\boldsymbol{\nu}) \tag{6}$$

is the surface shear, $b_{11}(\boldsymbol{\nu})$ and $b_{12}(\boldsymbol{\nu})$ are constitutive moduli, and div_s is the surface divergence.

We also establish global growth relations for solutions of the underlying equations. In particular, solutions of the quasi-static equations (1)–(6) consistent with the boundary condition

$$\mathbf{h} \cdot \mathbf{n} \text{ on } \partial\Omega \tag{7}$$

satisfy

$$vol(\Omega_\alpha)^{\cdot} = 0, \qquad \{\int_s f(\boldsymbol{\nu}) da\}^{\cdot} \leq 0. \tag{8}$$

Here $\Omega_\alpha(t)$ is the region occupied by phase α, while $s(t) = \partial\Omega_\alpha(t)$ represents the interface. The relations (8) yield a formal justification for the statical *Wulff problem*, which, in the present context, is to

$$\text{minimize} \qquad \int_s f(\nu)da \tag{9}$$

over all interfaces $s = \partial\Omega_\alpha$ with $vol(\Omega_\alpha)$ prescribed.

3. Theory with deformation and bulk diffusion.

We include deformation and stress, but limit our discussion to a continuous potential and to a coherent interface. In addition, we consider only infinitesimal deformations, neglecting inertia. We derive a quasi-static theory analogous to (1) – (6). The bulk equations of this theory are

$$Div\mathbf{T} = 0, \qquad div\mathbf{h} = 0 \tag{10}$$

supplemented by (2), where $\mathbf{T}$, the stress, is given by the stress-strain relations

$$\begin{aligned} \mathbf{T} &= \mathbf{L}_\alpha[\mathbf{E} - \mathbf{E}_{0\alpha}] \text{ in phase } \alpha, \\ \mathbf{T} &= \mathbf{L}_\beta[\mathbf{E} - \mathbf{E}_{0\beta}] \text{ in phase } \beta, \end{aligned} \tag{11}$$

with $\mathbf{L}_\alpha$ and $\mathbf{L}_\beta$ the (constant) elasticity tensors,

$$\mathbf{E} = \frac{1}{2}(\nabla\mathbf{u} + \nabla\mathbf{u}^T) \tag{12}$$

the strain tensor, and $\mathbf{E}_{0\alpha}$ and $\mathbf{E}_{0\beta}$ the (constant) stress-free strains in phases α and β. The corresponding interface conditions are

$$\begin{aligned} \ell u &= [W(\mathbf{E} - \mathbf{E}_0)] - \mathbf{T}\nu \cdot [\nabla\mathbf{u}]\nu + f(\nu)K + div_s\mathbf{c}(\nu) - b(\nu)V, \\ \ell V &= [\mathbf{h}] \cdot \nu, \qquad\qquad [\mathbf{T}]\nu = 0, \end{aligned} \tag{13}$$

where $W(\mathbf{E} - \mathbf{E}_0)$ is the strain energy, defined, e.g., in phase α by $\frac{1}{2}[\mathbf{E} - \mathbf{E}_{0\alpha}] \cdot \mathbf{L}_\alpha[\mathbf{E} - \mathbf{E}_{0\alpha}]$, $b(\nu)$ is a constitutive modulus, and ℓ is a constant. We consider solutions of (10) – (13) consistent with (7) and the dead-load condition

$$\mathbf{u} = \mathbf{0} \text{ on a portion } U \text{ of } \partial\Omega, \ \mathbf{Tn} = \mathbf{T}^*\mathbf{n} \text{ on the remainder}, \tag{14}$$

with $\mathbf{T}^*(=$ constant$)$ prescribed, where Ω, with outward unit normal $\mathbf{n}$, is the fixed region of space occupied by the body. We prove that such solutions satisfy the global growth relations

$$\begin{aligned} &vol(\Omega_\alpha)^{\cdot} = 0, \\ &\Big\{\int_\Omega \{W(\mathbf{E} - \mathbf{E}_0) - \mathbf{T}^* \cdot (\mathbf{E} - \mathbf{E}_0)\}dv + \int_s f(\nu)da\Big\}^{\cdot} \leq 0, \end{aligned} \tag{15}$$

relations that suggest the following variational problem: given $vol(\Omega_\alpha)$ and boundary displacements $\mathbf{g}(\mathbf{x})$ on U,

$$\text{minimize} \int_\Omega \{W(\mathbf{E}-\mathbf{E}_0) - \mathbf{T}^* \cdot (\mathbf{E}-\mathbf{E}_0)\} dv + \int_s f(\nu) da \qquad (16)$$

over all interfaces $s = \partial\Omega_\alpha$ and all displacement fields $\mathbf{u}$ that are continuous across s and satisfy $\mathbf{u} = \mathbf{g}$ on U. This problem – a natural generalization of the Wulff problem – is purely mechanical: the diffusion potential is not involved.

We also discuss a quasi-linear theory in which the elliptic equations (2), $(10)_2$ are replaced by parabolic equations. This theory leads to the following variational problem, in which the diffusion potential plays an important role:

minimize

$$\mathbf{T}^* \cdot [\mathbf{E}_0] vol(\Omega_\alpha) + \int_\Omega \{W(\mathbf{E}-\mathbf{E}_0) - \mathbf{T}^* \cdot (\mathbf{E}-\mathbf{E}_0) + Cu^2\} dv + \int_s f(\nu) da \qquad (17)$$

subject to

$$-[\Lambda] vol(\Omega_\alpha) + \int_\Omega \{2Cu + \mathbf{G} \cdot (\mathbf{E}-\mathbf{E}_0)\} dv = m_0$$

over all interfaces $s = \partial\Omega_\alpha$ and all displacement fields $\mathbf{u}$ that are continuous across s and satisfy $\mathbf{u} = \mathbf{g}$ on U. Here C is a constitutive modulus having values C_α and C_β in phase α and β, while m_0 is a prescribed constant.

Acknowledgement. This work was supported by the Army Research Office and by the National Science Foundation. We would like to thank David Kinderlehrer for valuable comments.

References.

[1] Gurtin, M. E. and P. W. Vorhees, The continuum mechanics of two-phase systems with mass transport and stress, Forthcoming.

[2] Gurtin, M. E., Multiphase thermomechanics with interfacial structure. 1. Heat conduction and the capillary balance law, Arch. Rational Mech. Anal. **104**, 195–221 (1988).

[3] Gurtin, M. E., On thermomechanical laws for the motion of a phase interface, Zeit. angew. Math. Phys. Forthcoming.

[4] Gurtin, M. E. and A. Struthers, Multiphase thermomechanics with interfacial structure. 3. Evolving phase boundaries in the presence of bulk deformation, Arch. Rational Mech. Anal. **112**, 97–160 (1990).

[5] Davi, F. and M. E. Gurtin, On the motion of a phase interface by surface diffusion, Zeit. angew. Math. Phys. **41**, 782–811 (1990).

THE MATHEMATICAL HIERARCHY UNDERLYING POLYNOMIAL-BASIS AND MATRIX-REPRESENTATION MODEL REDUCTION

L. D. Flippen, Jr.

Naval Research Laboratory, Code 6386, 4555 Overlook Ave., S.W., Washington, D. C. 20375

INTRODUCTION

Model reduction methods are useful in cases where the most complete mathematical model known for some physical system is so intricate in its details so as to become essentially intractable. Predictions from such models are "costly" to extract and usually contain information well in excess of one's needs. A model reduction process mathematically produces a simpler model from the original complex model such that the simpler model contains only the "essential physics" of the physical system. (It is usually assumed that the source of the complications in the original model is not associated with the applied external stimuli; that is, the complications are inherent in the physical system itself.) An abstract mathematical framework [1-2] exists for systematically synthesizing simpler mathematical models from complex ones. Model reduction methods which lie within this framework have been applied to a number of diverse areas. As an important example, model reduction methods have been applied, (under the names homogenization [3-4], effective medium and self-consistent theories [5], variational bounds (for bulk properties) theories [6], differential scheme [7], and others), to the synthesis of effective macroscale constitutive relations from specified inclusion-matrix scale constitutive relations for composite materials. The constitutive relations synthesized reflect an "equivalent", homogeneous material which responds, on the macroscale, just as the original composite material does. Model reduction methods have also been applied to problems in nonequilibrium statistical mechanics [8] and the reduction of particle (kinetic) models to diffusional (hydrodynamic-like) models [9].

Most mathematical models of the physical systems of interest in engineering and applied science take the generic form

$$\Lambda q = f \tag{1}$$

and

$$q = \Sigma u \,, \tag{2}$$

where the physical system itself is modeled by the mappings Λ and Σ, all of the dependent variables of the mathematical model are contained in q with a subset of them contained in u, and where f contains the source or load functions driving the system response. Equation (1) represents the material-composition-independent, fundamental (usually conservation) laws of the system and its boundary conditions. Equation (2) represents the constitutive relations for the specific material composition of the system. The combination of equations (1) and (2) as given by

$$Lu = f, \tag{3}$$

where

$$L = \Lambda\Sigma, \tag{4}$$

usually takes the form of one or more governing differential or integro-differential equations, boundary conditions, and initial conditions (if relevant). (In the common notation used here, Lu is shorthand for the mapping, by L, of u into $L(u)$. Similarly, $\Lambda\Sigma u$ is shorthand for $\Lambda(\Sigma(u))$, and so on.)

In model simplification one synthesizes a new mathematical model

$$L_{eff}u_0 = f \tag{5}$$

from (3) by a mathematical process [1]. The new model (5) is synthesized in such a way that it does not have the complexity originally found in (3) which made (3) difficult. The new model (5) also approximates (3) in some sense, where the L_{eff} mapping is an "effective" version of the L of (4) and where u_0 is an effective version of the u of (2) and (3). In most cases it is desirable that (1) be preserved as part of (5) so that one synthesizes [2]

$$\Lambda q_0 = f \tag{6}$$

and

$$q_0 = \Sigma_{eff}u_0 \tag{7}$$

from (1) and (2), with

$$L_{eff} = \Lambda\Sigma_{eff}. \tag{8}$$

The q_0 and Σ_{eff} are "effective" versions of the q and Σ, respectively, of (1) and (2). In this case the model reduction process becomes a synthesis of effective constitutive relations for the particular material in question. The model reduction process special-

izes to an homogenization, or smoothing, process in the common case of a system composed of a heterogeneous material, such as a composite, for which Σ is spatially rapidly-fluctuating and Σ_{eff} is spatially constant or slowly-varying.

The model reduction process of [2] is based on the idea of producing a Σ_{eff} for which the predicted responses u_0 and q_0 of (6) and (7) are filtered versions, respectively, of the predicted responses u and q of (1) and (2). Specific filters are chosen for a given problem by the person applying the model reduction process so as to suit his information needs concerning responses of the system over some given range of stimulii. Taking P_L and P_σ as the mappings which act as the chosen filters for u and q, respectively, means that

$$u_0 = P_L u \tag{9}$$

and

$$q_0 = P_\sigma q \, . \tag{10}$$

The P_L and P_σ mappings are idempotent, so that $P_L P_L = P_L$ and similarly for P_σ. In addition, compatibility [2] between P_L and P_σ means that they should commute (with respect to mapping composition). At its most abstract level the general model reduction process [2] is basically a search for a "solution" mapping Ω to algebraic (with respect to mapping composition) equations of mappings given by

$$\Lambda \Sigma \Omega P_L = \Lambda P_\sigma \Sigma \Omega P_L \tag{11}$$

and by

$$P_L \Omega P_L = P_L \, . \tag{12}$$

Obtaining the Ω mapping which satisfies (11) and (12) simultaneously constitutes the bulk of the work in applying any model reduction process to a given model. Once found, the solution mapping Ω can be used to construct Σ_{eff} by

$$\Sigma_{eff} = P_\sigma \Sigma \Omega P_L \, . \tag{13}$$

The Ω mapping can also be used to "reconstruct" the solution u to (1) and (2) from the solution u_0 to (6) and (7) by

$$u = \Omega P_L u_0 \tag{14}$$

(probably) to within an accuracy comparable to that of u_0 and to that with which Ω satisfies (11). (The Ω can usually be made to satisfy (12) exactly.)

In general, there is no universal, systematic way known to the author to directly solve (11) for the unknown mapping Ω. This difficulty suggests an approach which translates the problem of finding Ω into one that is more familiar and for which systematic means of solution are available. The group-homomorphic theory of model reduction is developed in this paper with this purpose in mind. The polynomial-basis [10] and matrix-representation model reduction methods discussed in this paper can be most economically understood within the common setting of the group-homomorphic theory. The basic idea of the group-homomorphic theory is to make the search for the Ω solution to (11) correspond to the search for a solution to governing equations of a kind with which engineers and scientists are more familiar, such as boundary value problems. In other words, for a given Λ, Σ, P_L, and P_σ, one would like fixed, known set G, $f^* \in G$, mapping L^*: $G \rightarrow G$, and $\tilde{\Omega}$: $G \rightarrow H$, where H = {set of possible mapping "candidates" for solving (11)}, such that $\Omega(\beta)$, for some $\beta \in G$, satisfies (11) as the solution precisely whenever β satisfies

$$L^* \beta = f^* . \tag{15}$$

The search for Ω then reduces to the search for solutions β to (15). The idea is to design the scenario such that (15) is something for which systematic solution techniques are available, such as for boundary value problems.

DISCUSSION

An axiomatic approach to the group-homomorphic theory of model reduction is taken since it is a flexible scheme under which new model reduction methods might suggest themselves and under which some current methods can be unified. It is based on the following set of definitions and axioms:

1. G is an abelian group.

2. Φ is a homomorphism which maps elements of G into an abelian group of mappings H so that $\Phi(\beta) \in H$ for each $\beta \in G$. As a homomorphism, Φ preserves the group operation of G so that $\Phi(\alpha + \beta) = \Phi(\alpha) + \Phi(\beta)$ for each $\alpha \in G$ and each $\beta \in G$.

3. W is a nonempty set of mappings for which a T_G: $G \rightarrow G$ mapping exists for each $T \in W$ such that $T\Phi(\beta) = \Phi(T_G \beta)$ is true for all $\beta \in G$.

The above collection of G, H, Φ, and W will be referred to as a group-homomorphic structure. For each group G and H in the structure, the binary group operation will be denoted by addition, the inverse by negation, and the group identity by zero, with context distinguishing between the groups. (An abelian group is one for which the group

elements commute with respect to the group binary operation. Also, $\Phi(-\beta) = -\Phi(\beta)$ for all $\beta \in G$ and $\Phi(0) = 0$ both follow [11] from the second axiom. Some rigor has been sacrificed in the above definitions, such as preciseness concerning the ranges and domains involved, but too much formalism at this point might obscure the main ideas involved.)

For a given Λ, Σ, P_L, and P_σ of (1), (2), (9), and (10) respectively, a model reduction method can be constructed from a given group-homomorphic structure, such that the problem of solving (11) reduces to that of solving (15), under the conditions:

1. The mappings Λ, Σ, P_L, and P_σ are each elements of W.

2. A fixed $\mu \in G$ is known such that $\Phi(\mu) P_L = P_L$ and $\Pi\mu = \mu$, where Π is defined as $\Pi = (P_L)_G$ so that $P_L \Phi(\beta) = \Phi(\Pi\beta)$ for each $\beta \in G$.

3. To be consistent with the idempotent property of P_L and P_σ and the fact that they must commute, the associated mappings Π and Γ must be idempotent and commute, where Γ is defined as $\Gamma = (P_\sigma)_G$ so that $P_\sigma \Phi(\beta) = \Phi(\Gamma\beta)$ for each $\beta \in G$, and hence

$$\Pi^2 = \Pi, \Gamma^2 = \Gamma, \text{and } \Gamma\Pi = \Pi\Gamma.$$

4. The mapping Π is also a homomorphism so that $\Pi(\alpha + \beta) = \Pi\alpha + \Pi\beta$.

With the candidate Ω mappings defined, as a function of $\beta \in G$, by

$$\Omega(\beta) = \Phi(\mu + [I - \Pi]\beta) \tag{16}$$

equation (12) is automatically satisfied. This can be seen by

$$\begin{aligned} P_L \Omega(\beta) P_L &= P_L \Phi(\mu + [I - \Pi]\beta) P_L \\ &= \Phi(\Pi\{\mu + [I - \Pi]\beta\}) P_L \\ &= \Phi(\Pi\mu + \Pi[I - \Pi]\beta) P_L \\ &= \Phi(\mu + 0) P_L = \Phi(\mu) P_L = P_L \ , \end{aligned}$$

where $\Pi[I - \Pi] = \Pi - \Pi^2 = \Pi - \Pi = 0$ has been used. Substituting (16) into each side of (11) leads to

$$\Lambda\Sigma\Omega P_L = \Phi(\Lambda_G\Sigma_G\{\mu + [I-\Pi]\beta\})P_L$$

and

$$\Lambda P_\sigma\Sigma\Omega P_L = \Phi(\Lambda_G\Gamma\Sigma_G\{\mu + [I-\Pi]\beta\})P_L .$$

Equation (11) is hence satisfied by

$$\Phi(\Lambda_G\Sigma_G\{\mu + [I-\Pi]\beta\}) = \Phi(\Lambda_G\Gamma\Sigma_G\{\mu + [I-\Pi]\beta\}) ,$$

which is equivalent to

$$\begin{aligned} 0 &= \Phi(\Lambda_G\Sigma_G\{\mu + [I-\Pi]\beta\} - \Lambda_G\Gamma\Sigma_G\{\mu + [I-\Pi]\beta\}) \\ &= \Phi(L^*\beta - f^*) \end{aligned}$$

because, by postulate, Φ is a homomorphism and H, the range of Φ, is an abelian group. The mapping 0 in the above relation is the zero element of H and the L^* and f^* are defined by

$$L^* = \Lambda_G\Sigma_G[I-\Pi] - \Lambda_G\Gamma\Sigma_G[I-\Pi] \tag{17}$$

and

$$f^* = \Lambda_G\Gamma\Sigma_G\mu - \Lambda_G\Sigma_G\mu . \tag{18}$$

Equation (11) is hence satisfied if β satisfies (15) for L^* and f^* as defined by (17) and (18). Equation (16) and the solution β to (15) can then be substituted into (13) to give

$$\Sigma_{eff} = \Phi(\Gamma\Sigma_G\{\mu + [I-\Pi]\beta\})P_L \tag{19}$$

as the effective constitutive mapping for this model reduction scheme.

The group-homomorphic theory is the underlying mathematical framework for operator-polynomial methods of model reduction [12], from which the multiple scales homogenization method can be obtained [12]. It also forms a convenient structure for organizing symbolic programming implementations of model reduction methods [12]. The focus of this paper, however, is on variable basis model reduction methods, from which the polynomial-basis and matrix-representation model reduction methods can be obtained. The variable basis methods will be constructed in terms of the above group-homomorphic theory. This requires some definitions with which to build the appropriate underlying group-homomorphic structure.

For a given abstract vector space V and a given (fixed) positive integer N, the group-homomorphic structure associated with the variable basis methods consists of the following sequence of definitions:

1. Define S to be the scalar field associated with the vector space V.

2. Define V^* = {all linear functionals: $V \rightarrow S$}. (The V^* is called the algebraic dual space associated with the vector space V.)

3. Define $\beta \bullet \gamma$, γ^T, and η^{-1} as notational shorthand for the matrix multiplication of β and γ, the transpose of γ, and the inverse of (square) η, respectively, for any given matrices β, γ, and (square) η.

4. Define $\langle x, y \rangle$ as notational shorthand for the M by K matrix $\{x_i(y_j)\}$, with (i,j) component formed by mapping y_j into $x_i(y_j)$, for any $y \in V^K$ and any ordered set x of M mappings, each of whose domain is V, for some positive integers M and K. (The values of M and K will vary according to the x and y input to $\langle x, y \rangle$.)

5. Define G by $G = V^N$, so that, for any given $\beta \in G$, β is an ordered set of N elements of V. (Each element of G is to be viewed as a single-row matrix.)

6. Choose fixed, known $\phi \in V^{*N}$ so that $\langle \phi, \mu \rangle$ is a matrix of constant scalars for any $\mu \in V^K$ and positive integer K.

7. Define Φ by

$$\Phi(\beta)f = \beta \bullet \langle \phi, f \rangle \tag{20}$$

for all $\beta \in G$ for each $f \in V^M$ for some positive integer M. (The value of M may vary according to the f input. Note that $\Phi(\beta)f$ is an element of $\{\text{span of components of } \beta\}^M$ and so each β whose components form a linearly independent set is a basis for each of the components of the range of $\Phi(\beta)$, hence the name "variable basis" method.)

8. Define W as the set of all mappings T such that

$$Tf \equiv \lambda \bullet \langle \psi, f \rangle \tag{21}$$

is well defined for some $\lambda \in V^K$, some positive integer K, and some ordered set ψ of K linear mappings, each of whose domain is V, and

where $f \in V^M$ for some positive integer M. (The values of M and K will vary according to the particular λ and ψ used and according to the f input.)

By definition any vector space is an abelian group with respect to vector addition. Since V^N is a vector space if V is a vector space then G is an abelian group. It is readily seen that $\Phi(\alpha+\beta) = \Phi(\alpha) + \Phi(\beta)$ so that Φ is a homomorphism. It is also readily seen that

$$\begin{aligned}\langle \phi, (f+g) \rangle &= \{\phi_i (f_j + g_j)\} \\ &= \{\phi_i (f_j) + \phi_i (g_j)\} \\ &= \{\phi_i (f_j)\} + \{\phi_i (g_j)\} \\ &= \langle \phi, f \rangle + \langle \phi, g \rangle\end{aligned}$$

because of the linearity of each of the components of ϕ. This relation, along with the distributive property of matrix multiplication, implies that $\Phi(\beta)$ is a linear mapping (and hence a homomorphism) for each $\beta \in G$. In an appendix it is shown that, for any $T \in W$,

$$T(\alpha \bullet \gamma) = (T\alpha) \bullet \gamma \tag{22}$$

is true for all $\alpha \in V^K$ and all K by J matrices γ of constant scalar components for any given choice of positive integers K and J. This leads to

$$\begin{aligned}T\Phi(\beta) f &= T(\beta \bullet \langle \phi, f \rangle) \\ &= (T\beta) \bullet \langle \phi, f \rangle \\ &= \Phi(T\beta) f\end{aligned}$$

for any $T \in W$, with W defined by 8 above and Φ by (20), upon using the choice

$$\gamma = \langle \phi, f \rangle$$

in (22), for which γ consists of constant scalar components for any given f. The W set of this group-homomorphic structure hence consists of elements T such that

$$T\Phi(\beta) = \Phi(T\beta) \tag{23}$$

for all $\beta \in G$, so that

$$T_G = T$$

for this particular group-homomorphic structure. The result

$$\Phi(\beta) \in W \tag{24}$$

for each $\beta \in G$ follows from taking the choices

$$\lambda = \beta$$
$$\psi = \phi$$

in (21). Relations (23) and (24) imply

$$\Phi(\alpha)\Phi(\beta) = \Phi(\Phi(\alpha)\beta) \tag{25}$$

for all $\alpha \in G$ and $\beta \in G$.

One can build idempotent mappings from Φ for potential use as P_L and P_σ candidates. For any fixed $\mu \in G$ for which $\langle \phi, \mu \rangle$ is nonsingular one has

$$\begin{aligned}\Phi(\mu \bullet \langle \phi, \mu \rangle^{-1})\,\mu \bullet \langle \phi, \mu \rangle^{-1} &= [\Phi(\mu \bullet \langle \phi, \mu \rangle^{-1})\,\mu] \bullet \langle \phi, \mu \rangle^{-1} \\ &= [\mu \bullet \langle \phi, \mu \rangle^{-1} \bullet \langle \phi, \mu \rangle] \bullet \langle \phi, \mu \rangle^{-1} \\ &= \mu \bullet \langle \phi, \mu \rangle^{-1}\end{aligned}$$

by using

$$\beta = \mu \bullet \langle \phi, \mu \rangle^{-1}$$
$$\alpha = \mu$$
$$\gamma = \langle \phi, \mu \rangle ,$$

in (22) and (24) and by (20). This can be summarized by

$$\begin{aligned}\Phi(\mu')\,\mu' &= \mu' \\ \mu' &= \mu \bullet \langle \phi, \mu \rangle^{-1} .\end{aligned} \tag{26}$$

The mapping $\Phi(\mu')$ is idempotent, as can be seen by combining (26) and (25), with $\alpha = \beta = \mu'$, to get

$$\begin{aligned}\Phi(\mu')\Phi(\mu') &= \Phi(\Phi(\mu')\mu') \\ &= \Phi(\mu') .\end{aligned} \tag{27}$$

The above group-homomorphic structure can be built into a model reduction method for any problem (1) and (2) for which

$$\Lambda \in W$$
$$\Sigma \in W$$

and for which the projector choice

$$P_L = \Phi(\mu \bullet \langle \phi, \mu \rangle^{-1}) \tag{28}$$

is taken for some fixed $\mu \in G$ so that $\Phi(\mu') P_L = P_L$ from (26) and (27). The choice (28) implies

$$\Pi = \Phi(\mu \bullet \langle \phi, \mu \rangle^{-1}) \tag{29}$$

because of (25), so that $\Pi\mu' = \mu'$ and $\Pi^2 = \Pi$ from (26) and (27). There is still a lot of freedom remaining in (28) since one is still free to choose the μ and ϕ. The model reduction method based on (28), (29), and

$$P_\sigma = P_L ,$$

which implies

$$\Gamma = \Pi$$

because of (25) and (29), is always available. Other P_σ choices, however, such as

$$P_\sigma = \Phi(\upsilon \bullet \langle \phi, \upsilon \rangle^{-1})$$

for fixed $\upsilon \in G$, which in turn implies

$$\Gamma = \Phi(\upsilon \bullet \langle \phi, \upsilon \rangle^{-1}) ,$$

may be useful, assuming that $\Gamma\Pi = \Pi\Gamma$ is satisfied for the particular choice of υ.

The special case for which V is a Hilbert space offers certain simplifications. For a given (bounded) linear functional ψ on a Hilbert space V, with inner product (α,β) for any $\alpha \in V$ and $\beta \in V$, the most general form for ψ, by Riesz's theorem [13], is $\psi(f) = (f,\alpha)$ for an $\alpha \in V$ uniquely determined by ψ. The ϕ_i's (components of ϕ from definition 6) then have the form $\phi_i(f) = (f,z_i)$ for each i, with each z_i uniquely determined by ϕ_i. The special case for which $z = \mu$ in (28) makes P_L into a Mori-Zwanzig type of projector used extensively in model reduction in nonequilibrium statistical mechanics and described in [9] for example. The most convenient choice for μ in such a case is one whose (orthonormal) components satisfy $(\mu_i,\mu_j) = \delta_{ij}$, where δ is the Kronecker delta with components 1 for $i = j$ and 0 otherwise.

The polynomial-basis model reduction method [10] consists of a variable basis method using (20), (28), and (29) for which the components of μ are polynomials and the components of ϕ are (except for the first) averages of derivatives. As an example, the specific case of first order polynomials $1, x_1 = x, x_2 = y$, and $x_3 = z$ in a cartesian coordinate system was used [10] to homogenize the problem of steady heat conduction in an isotropic, heterogeneous material which obeys Fick's law of heat diffusion. In this case the ϕ and μ specialize to

$$\phi_j = P_0 \begin{bmatrix} I & \text{for } j = 1 \\ \dfrac{\partial}{\partial x_{j-1}} & \text{for } j = 2,3,4 \end{bmatrix}$$

and

$$\mu_j = \begin{bmatrix} 1 & \text{for } j = 1 \\ (I - P_0)\, x_{j-1} & \text{for } j = 2,3,4 \end{bmatrix} ,$$

where I is the identity operator and P_0 is a linear, idempotent functional for which $P_0(1) = 1$. (The simplest physically meaningful P_0 is a volume average.) The projector choice

$$P_\sigma = \Gamma = \Phi(\eta) = \langle P_0, \quad \rangle$$
$$\eta = \{1, 0, 0, 0\}$$

was used so as to produce constant effective thermal conductivities for an equivalent (anisotropic) homogeneous material. In specializing to the periodic medium case the same bulk properties are synthesized [10] as that from the method of multiple scales. The commutation requirement

$$\Gamma\Pi = \Pi\Gamma = \Gamma$$

is satisfied because of

$$\langle \phi, \mu \rangle = \delta$$
$$\mu \bullet \langle \phi, \eta \rangle = \eta$$
$$\Gamma\mu = \eta$$

for this case, where δ is the identity matrix.

The matrix-representation model reduction method is also a variable basis method for which the basis is constrained to the same subspace for all cases. The homomorphism

$$\Psi(\alpha) = \Phi(\mu \bullet \langle \phi, \mu \rangle^{-1} \bullet \alpha) , \tag{30}$$

for Φ from (20), is more convenient in this case than Φ itself. The $\mu \in G$ in (30) is fixed and the α, an N by N matrix of constant scalars, is allowed to vary. The components of

$$\beta = \mu \bullet \langle \phi, \mu \rangle^{-1} \bullet \alpha$$

in (30) are hence each constrained to the subspace (of V) formed by the span of the components of μ. The new homomorphism given by (30) has the two important properties

$$\Psi(\alpha)\Psi(\beta) = \Psi(\alpha \bullet \beta) , \tag{31}$$

for any two N by N matrices α and β of constant scalar components, and

$$\begin{aligned} PTP &= \Psi(\tau) \\ \tau &= \langle \phi, T\mu \rangle \bullet \langle \phi, \mu \rangle^{-1} \\ P &= \Phi(\mu \bullet \langle \phi, \mu \rangle^{-1}) \end{aligned} \tag{32}$$

for any $T \in W$, using the same μ and ϕ as in (30). Equation (31) is proven by

$$\begin{aligned} \Psi(\alpha)\Psi(\beta) &= \Phi(\mu \bullet \langle \phi, \mu \rangle^{-1} \bullet \alpha)\, \Phi(\mu \bullet \langle \phi, \mu \rangle^{-1} \bullet \beta) \\ &= \Phi(\Phi(\mu \bullet \langle \phi, \mu \rangle^{-1} \bullet \alpha)\, [\mu \bullet \langle \phi, \mu \rangle^{-1} \bullet \beta]) \\ &= \Phi([\Phi(\mu \bullet \langle \phi, \mu \rangle^{-1} \bullet \alpha)\, \mu] \bullet [\langle \phi, \mu \rangle^{-1} \bullet \beta]) \\ &= \Phi([\mu \bullet \langle \phi, \mu \rangle^{-1} \bullet \alpha \bullet \langle \phi, \mu \rangle] \bullet [\langle \phi, \mu \rangle^{-1} \bullet \beta]) \\ &= \Phi(\mu \bullet \langle \phi, \mu \rangle^{-1} \bullet \alpha \bullet \beta) \\ &= \Psi(\alpha \bullet \beta) \end{aligned}$$

and (32) by

$$\begin{aligned} PTP &= PT\Phi(\mu \bullet \langle \phi, \mu \rangle^{-1}) \\ &= \Phi(\mu \bullet \langle \phi, \mu \rangle^{-1})\, \Phi(T(\mu \bullet \langle \phi, \mu \rangle^{-1})) \\ &= \Phi(\Phi(\mu \bullet \langle \phi, \mu \rangle^{-1})\, [(T\mu) \bullet \langle \phi, \mu \rangle^{-1}]) \\ &= \Phi([\Phi(\mu \bullet \langle \phi, \mu \rangle^{-1})\, (T\mu)] \bullet \langle \phi, \mu \rangle^{-1}) \\ &= \Phi(\mu \bullet \langle \phi, \mu \rangle^{-1} \bullet \langle \phi, T\mu \rangle \bullet \langle \phi, \mu \rangle^{-1}) \\ &= \Psi(\langle \phi, T\mu \rangle \bullet \langle \phi, \mu \rangle^{-1}) . \end{aligned}$$

The N by N matrices of constant scalar components (algebraically) form a ring, call it G', with respect to matrix addition and multiplication. Equation (31) and

$$\begin{aligned}\Psi(\alpha+\beta) &= \Phi(\mu \bullet \langle\phi,\mu\rangle^{-1} \bullet [\alpha+\beta]) \\ &= \Phi([\mu \bullet \langle\phi,\mu\rangle^{-1} \bullet \alpha] + [\mu \bullet \langle\phi,\mu\rangle^{-1} \bullet \beta]) \\ &= \Phi(\mu \bullet \langle\phi,\mu\rangle^{-1} \bullet \alpha) + \Phi(\mu \bullet \langle\phi,\mu\rangle^{-1} \bullet \beta) \\ &= \Psi(\alpha) + \Psi(\beta)\end{aligned}$$

establish Ψ as a homomorphism over the ring G'. (This method is hence ring-homomorphic as well as group-homomorphic.)

The projector P of (32) maps onto the subspace formed by the span of the components of μ. The projector Θ, defined by $\Theta(T) = PTP$ for P of (32), projects each $T \in W$ into an operator under which this subspace is invariant. The τ of (32) can be thought of as a matrix representation [13, p. 113] of the corresponding T (of W) with respect to the basis consisting of the components of μ. In addition, equation (31) shows that mapping composition corresponds to multiplication of the corresponding matrices. The matrix representation τ of T reduces to $\{(T\mu_j,\mu_i)\}$ for the special case of a Hilbert space upon the use of Riesz's theorem (as mentioned earlier) and orthonormal components for μ.

If the subspace onto which P of (32) projects is "large enough", so that PTP is an adequate approximation to T for each $T \in W$ of interest, then a matrix-representation model reduction method, with Ψ of (30) playing the role of Φ and G' playing the role of G in the group-homomorphic setting, is feasible. An important example consists of

$$P_L = P_\sigma = \Psi(\pi)$$
$$\pi \bullet \pi = \pi,$$

with the fixed matrix π playing the role of μ, and

$$(I - P_L) L \Omega P_L = 0 \tag{33}$$

as the replacement for (11) for the case, assumed here, for which the complete system mapping L of (3) is not to be subdivided into Λ and Σ. Equation (33) is equivalent to the artifice of taking $\Lambda \rightarrow I$ and $\Sigma \rightarrow L$ in (11). The importance of this example stems from the fact that

$$\Omega(\beta) P_L = \Psi(\Omega')$$
$$\Omega' = \pi + [\delta - \pi] \bullet \beta \bullet \pi,$$

which makes Ω', as opposed to β, the unkown, to-be-determined matrix, leads to

$$[\delta - \pi] \bullet L' \bullet \Omega' = 0$$

as the matrix analogue to (33), where L' is the matrix representation of L in the sense of (32) with $PLP \approx L$. This reformulation of the matrix-representation model reduction problem into a discrete model reduction problem allows one to utilize a known systematic approach [1] to such problems.

References

1. L. D. Flippen, "Abstract Zwanzig Model Reduction Theory with Application to Discretized Linear Systems", accepted by Mathl. Comput. Modelling.

2. L. D. Flippen, "Fundamental Law Preservation in Model Reduction", submitted to Mathl. Comput. Modelling.

3. A. Maewal, "Homogenization for Transient Heat Conduction", J. Appl. Mech., 46 (1979), pp. 945-946.

4. E. Sanchez-Palencia and A Zaoui (Ed.), Homogenization Techniques for Composite Media, Lecture Notes in Physics No. 272, Springer-Verlag, Berlin (1987).

5. J. E. Gubernatis, "Scattering Theory and Effective Medium Approximations to Heterogeneous Materials", AIP Conf. Proc., No. 40 (1978), pp. 84-98.

6. J. R. Willis, "Variational and related methods for the overall properties of composites", Advances in Applied Mechanics, Vol. 21, Academic Press, New York (1981), pp. 1-78.

7. Z. Hashin, "The Differential Scheme and its Application to Cracked Materials", J. Mech. Phys. Solids, 36 (1988), pp. 719-734.

8. P. Resibois and M. DeLeener, Classical Kinetic Theory of Fluids, Wiley, New York (1977), pp. 205-207.

9. J. J. Duderstadt and W. R. Martin, Transport Theory, Wiley, New York (1979), pp. 37, 193-194, and 236-250.

10. L. D. Flippen, "Polynomial-Basis Model Reduction", submitted to Mathl. Comput. Modelling.

11. R. Geroch, Mathematical Physics, Univ. of Chicago Press, Chicago (1985), pp. 16-17.

12. L. D. Flippen, "Group-Homomorphic-Structured Symbolic Programming of Model Reduction Methods in Mathematica with Application to Multiple Scales Homogenization", in preparation.

13. E. Kreyszig, Introductory Functional Analysis with Applications, Wiley, New York (1978), p. 188.

APPENDIX

Proof of $T(\beta \bullet \gamma) = (T\beta) \bullet \gamma$

Let ψ have only a single component. For any single-row matrices γ and β of equal length

$$\langle \psi, (\beta \bullet \gamma^T) \rangle = \psi(\beta \bullet \gamma^T) = \langle \psi, \beta \rangle \bullet \gamma^T \tag{A1}$$

is a statement of the linearity of ψ for γ of constant scalar components only. This can be extended to multi-rowed γ's of constant scalar components by

$$\begin{aligned} &\langle \psi, (\beta \bullet \gamma) \rangle \\ &= \langle \psi, \{ [\beta \bullet (\text{column 1 of } \gamma)], [\beta \bullet (\text{column 2 of } \gamma)], \ldots \} \rangle \\ &= \{ \psi(\beta \bullet (\text{column 1 of } \gamma)), \psi(\beta \bullet (\text{column 2 of } \gamma)), \ldots \} \\ &= \{ [\langle \psi, \beta \rangle \bullet (\text{column 1 of } \gamma)], [\langle \psi, \beta \rangle \bullet (\text{column 2 of } \gamma)], \ldots \} \\ &= \langle \psi, \beta \rangle \bullet \gamma , \end{aligned} \tag{A2}$$

where (A1) has been used for each column of γ. This, in turn, can be extended to multi-component ψ's by

$$\begin{aligned} \langle \psi, (\beta \bullet \gamma) \rangle &= \{ \langle \psi_i, (\beta \bullet \gamma) \rangle \} \\ &= \{ \langle \psi_i, \beta \rangle \bullet \gamma \} \\ &= \{ \langle \psi_i, \beta \rangle \} \bullet \gamma \\ &= \langle \psi, \beta \rangle \bullet \gamma , \end{aligned} \tag{A3}$$

where (A2) has been used for each component of ψ. Pre-matrix-multiplying (A3) by λ produces (22) upon using (21).

TIME RATES OF GENERALIZED STRAIN TENSORS WITH APPLICATIONS TO ELASTICITY

Mike Scheidler

US Army Ballistic Research Laboratory
Aberdeen Proving Ground, MD 21005-5066

1 Introduction

Consider a smooth motion with deformation gradient $\mathbf{F}$. Since $\det \mathbf{F} > 0$, $\mathbf{F}$ has two unique polar decompositions

$$\mathbf{F} = \mathbf{RU} = \mathbf{VR}\,, \tag{1.1}$$

in which $\mathbf{R}$, the *rotation tensor*, is proper orthogonal, and $\mathbf{U}$ and $\mathbf{V}$, the *right* and *left stretch tensors*, are symmetric positive-definite; cf. [1–6]. The stretch tensors have spectral decompositions

$$\mathbf{U} = \sum_{i=1}^{3} \lambda_i\, \mathbf{u}_i \otimes \mathbf{u}_i \quad \text{and} \quad \mathbf{V} = \sum_{i=1}^{3} \lambda_i\, \mathbf{v}_i \otimes \mathbf{v}_i\,, \tag{1.2}$$

where the *principal stretches* λ_i are the principal values of $\mathbf{U}$ and $\mathbf{V}$. The principal directions $\mathbf{u}_i$ of $\mathbf{U}$ are called the *principal axes of strain in the reference configuration* or the *Lagrangian triad*; the principal directions $\mathbf{v}_i = \mathbf{R}\mathbf{u}_i$ of $\mathbf{V}$ are called the *principal axes of strain in the current configuration* or the *Eulerian triad*. The numbers $\lambda_i - 1$ are scalar measures of strain in the principal directions. If $\mathbf{I}$ denotes the identity tensor, then $\mathbf{U} - \mathbf{I}$ and $\mathbf{V} - \mathbf{I}$ may be interpreted as strain tensors.

For finite deformations, various other scalar and corresponding tensor strain measures have been proposed; cf. Truesdell and Toupin[1, §31-33A]. Here we focus on a general class of strain measures introduced by Hill[6–8]. Hill takes as a *scalar strain measure* any sufficiently smooth function f defined on the positive reals with the properties

$$f(1) = 0\,, \quad f'(1) = 1\,, \quad f' > 0\,. \tag{1.3}$$

Corresponding to the scalar strain measure f is a *Lagrangian strain tensor*

$$\mathbf{f}(\mathbf{U}) \equiv \sum_{i=1}^{3} f(\lambda_i)\, \mathbf{u}_i \otimes \mathbf{u}_i \tag{1.4}$$

and an *Eulerian strain tensor*

$$\mathbf{f}(\mathbf{V}) \equiv \sum_{i=1}^{3} f(\lambda_i)\, \mathbf{v}_i \otimes \mathbf{v}_i\,. \tag{1.5}$$

Their principal directions are the Lagrangian and Eulerian triads, respectively, and their principal values are the numbers $f(\lambda_i)$. By (1.3), $f(\lambda_i)$ is a strictly increasing function of λ_i which differs from $\lambda_i - 1$ by a term of order $(\lambda_i - 1)^2$:

$$f(\lambda_i) = \lambda_i - 1 + \mathcal{O}\big((\lambda_i - 1)^2\big) \,. \tag{1.6}$$

It follows that $\mathbf{f}(\mathbf{V})$, for example, is an invertible function of $\mathbf{V}$ which differs from $\mathbf{V} - \mathbf{I}$ by a term of order $\|\mathbf{V} - \mathbf{I}\|^2$:

$$\mathbf{f}(\mathbf{V}) = \mathbf{V} - \mathbf{I} + \mathcal{O}\big(\|\mathbf{V} - \mathbf{I}\|^2\big) \,. \tag{1.7}$$

Some traditional strain measures included in (1.3) are $f(\lambda) = \ln \lambda$ and

$$f(\lambda) = f_n(\lambda) \equiv \frac{1}{n}(\lambda^n - 1) \,, \tag{1.8}$$

where n is some nonzero integer. For example, by taking $n = 1$ in (1.8) we recover the strain tensors $\mathbf{U} - \mathbf{I}$ and $\mathbf{V} - \mathbf{I}$. The Lagrangian strain tensor corresponding to the choice $n = 2$ in (1.8) is the *Green-St. Venant strain tensor*

$$\mathbf{f}_2(\mathbf{U}) = \frac{1}{2}(\mathbf{C} - \mathbf{I}) \,, \tag{1.9}$$

where

$$\mathbf{C} = \mathbf{U}^2 = \mathbf{F}^{\mathrm{T}}\mathbf{F} \tag{1.10}$$

is the *right Cauchy-Green tensor*. The Eulerian strain tensor corresponding to the choice $n = -2$ in (1.8) is the *Almansi-Hamel strain tensor*

$$\mathbf{f}_{-2}(\mathbf{V}) = \frac{1}{2}(\mathbf{I} - \mathbf{B}^{-1}) \,, \tag{1.11}$$

where

$$\mathbf{B} = \mathbf{V}^2 = \mathbf{F}\mathbf{F}^{\mathrm{T}} \tag{1.12}$$

is the *left Cauchy-Green tensor*.

Hill's class of generalized strain tensors has found important applications in the formulation of constitutive equations and constitutive inequalities for elastic and plastic material response; cf. Hill[6–9], Wang and Truesdell[3], Ogden[5], Havner[10], Nemat-Nasser[11,12], Guo and Dubey[13]. In these applications it is useful to express the time-rate of change of a strain tensor in terms of the *stretching* and *spin tensors* $\mathbf{D}$ and $\mathbf{W}$, which are the symmetric and skew parts of the velocity gradient. For some choices of f, expressions for the time-rate of change of $\mathbf{f}(\mathbf{U})$ and $\mathbf{f}(\mathbf{V})$ follow easily from well-known formulas for the material time derivative of $\mathbf{C}$ and $\mathbf{B}$. For example, the material time derivative of the Green-St. Venant strain tensor $\mathbf{f}_2(\mathbf{U})$ is [1, §95]

$$\mathbf{f}_2(\mathbf{U})^{\cdot} = \mathbf{F}^{\mathrm{T}}\mathbf{D}\mathbf{F} = \mathbf{U}(\mathbf{R}^{\mathrm{T}}\mathbf{D}\mathbf{R})\mathbf{U} \,. \tag{1.13}$$

The material time derivative of the Almansi-Hamel strain tensor $\mathbf{f}_{-2}(\mathbf{V})$ is

$$\mathbf{f}_{-2}(\mathbf{V})^{\cdot} = \frac{1}{2}(\mathbf{B}^{-1}\mathbf{D} + \mathbf{D}\mathbf{B}^{-1} + \mathbf{B}^{-1}\mathbf{W} - \mathbf{W}\mathbf{B}^{-1}) \,; \tag{1.14}$$

this can also be written as [1, §95]

$$\mathbf{f}_{\text{-}2}(\mathbf{V})^{\circ} = \mathbf{D} - \mathbf{f}_{\text{-}2}(\mathbf{V})\,\mathbf{D} - \mathbf{D}\,\mathbf{f}_{\text{-}2}(\mathbf{V})\,, \tag{1.15}$$

where

$$\mathbf{A}^{\circ} \equiv \dot{\mathbf{A}} + \mathbf{AW} - \mathbf{WA} \tag{1.16}$$

is the *Jaumann rate* of a tensor field $\mathbf{A}$.

Formulas of the type (1.13)–(1.15), which are written in direct tensor notation, will be referred to as *direct formulas* for the time-rates. For a general strain measure f, direct formulas for $\mathbf{f}(\mathbf{U})^{\cdot}$ and $\mathbf{f}(\mathbf{V})^{\cdot}$ or $\mathbf{f}(\mathbf{V})^{\circ}$ are much more difficult to derive and also much more complicated than (1.13)–(1.15). On the other hand, Hill[6,7] found a simple formula for the components of $\mathbf{f}(\mathbf{U})^{\cdot}$ relative to the Lagrangian triad. Hill's component formula and its analogue for $\mathbf{f}(\mathbf{V})^{\circ}$ are discussed in Section 2. In Section 3 we indicate how these component formulas can be used to derive approximate direct formulas for $\mathbf{f}(\mathbf{U})^{\cdot}$ and $\mathbf{f}(\mathbf{V})^{\circ}$ as well as bounds for the error in the approximations. We then apply the general results to the logarithmic strain tensors $\ln\mathbf{U}$ and $\ln\mathbf{V}$, which are obtained by setting $f = \ln$ in (1.4) and (1.5). In Section 4 we use the approximate formula for $(\ln\mathbf{V})^{\circ}$ to derive an approximate formula for the rate of the deviatoric stress tensor in an isotropic elastic material. These approximate formulas provide good estimates when the shear strain is small, with no restrictions on the volumetric strain. In Section 5 we indicate how the component formulas for $\mathbf{f}(\mathbf{U})^{\cdot}$ and $\mathbf{f}(\mathbf{V})^{\circ}$ can be used to derive exact direct formulas for these rates analogous to the formulas obtained by Hoger[14] for the case $f = \ln$.

2 Component Formulas

Hill[6,7] derived the following simple formula for the material time derivative of the Lagrangian strain tensor $\mathbf{f}(\mathbf{U})$:

$$\mathbf{f}(\mathbf{U})^{\cdot} = \sum_{i,j=1}^{3} L_f(\lambda_i,\lambda_j)\,D_{ij}\,\mathbf{u}_i \otimes \mathbf{u}_j\,, \tag{2.1}$$

where

$$\begin{aligned} L_f(\lambda_i,\lambda_j) &= \lambda_i\,f'(\lambda_i) \quad \text{if } \lambda_i = \lambda_j \\ &= \frac{2\lambda_i\lambda_j}{\lambda_i+\lambda_j}\,\frac{f(\lambda_i)-f(\lambda_j)}{\lambda_i-\lambda_j} \quad \text{if } \lambda_i \neq \lambda_j\,. \end{aligned} \tag{2.2}$$

D_{ij} are the components of the stretching tensor $\mathbf{D}$ relative to the Eulerian triad, or the components of the rotated stretching tensor $\mathbf{R}^{\mathrm{T}}\mathbf{D}\mathbf{R}$ relative to the Lagrangian triad. Observe that the term $L_f(\lambda_i,\lambda_j)\,D_{ij}$ in (2.1) is the ij-component of $\mathbf{f}(\mathbf{U})^{\cdot}$ relative to the Lagrangian triad. It turns out that the derivation of (2.1)–(2.2) given by Hill[6,7] is rigorous only for those instants at which the principal stretches are distinct. As described in detail in Scheidler[15], there are problems with the "limiting process" proposed by Hill for obtaining (2.2) when $i \neq j$ and $\lambda_i = \lambda_j$. In discussing Hill's formula, subsequent authors have either repeated Hill's argument [13] or simply considered the case of distinct principal stretches only [5,10,11,12].

There is an equally simple analogue of (2.1)–(2.2) for the Jaumann rate of $\mathbf{f}(\mathbf{V})$:

$$\mathbf{f}(\mathbf{V})^\circ = \sum_{i,j=1}^{3} E_f(\lambda_i, \lambda_j)\, D_{ij}\, \mathbf{v}_i \otimes \mathbf{v}_j \,, \tag{2.3}$$

where

$$\begin{aligned} E_f(\lambda_i, \lambda_j) &= \lambda_i\, f'(\lambda_i) \quad \text{if } \lambda_i = \lambda_j \\ &= \frac{\lambda_i^2 + \lambda_j^2}{\lambda_i + \lambda_j}\, \frac{f(\lambda_i) - f(\lambda_j)}{\lambda_i - \lambda_j} \quad \text{if } \lambda_i \neq \lambda_j \,. \end{aligned} \tag{2.4}$$

Observe that the term $E_f(\lambda_i, \lambda_j)\, D_{ij}$ in (2.3) is the ij-component of $\mathbf{f}(\mathbf{V})^\circ$ relative to the Eulerian triad. Hill[6–9] did not derive formulas for the time-rates of Eulerian strain tensors. For the case of distinct principal stretches a result equivalent to (2.1)–(2.2) was obtained by Nemat-Nasser[11,12] using Hill's methods.

In a recent paper [15], I showed that the above formulas hold for any C^2 motion and any C^1 strain measure f, regardless of whether or not the principal stretches are distinct. The proof utilizes a component formula for the derivative of an isotropic tensor function due to Bowen and Wang[16] and Chadwick and Ogden[17],[1] together with a theorem due to Ball[18] which is used to establish the sufficiency of the aforementioned smoothness conditions.

3 Approximate Direct Formulas

The component formulas presented in the previous section can be used to derive approximate direct formulas for the time-rates of generalized strain tensors. An example of such a formula is

$$\mathbf{f}(\mathbf{V})^\circ = -x^2 f''(x)\, \mathbf{D} + \frac{f'(x) + x f''(x)}{2} (\mathbf{DV} + \mathbf{VD}) + \mathcal{O}(\varepsilon_x{}^2) \,. \tag{3.1}$$

Here x can be any positive number, and ε_x is the largest of the distances from x to the three principal stretches:

$$\varepsilon_x \equiv \max_{i=1,2,3} |\lambda_i - x| \,. \tag{3.2}$$

By neglecting the remainder term $\mathcal{O}(\varepsilon_x{}^2)$ in (3.1), we obtain an approximate formula for $\mathbf{f}(\mathbf{V})^\circ$. As the notation indicates, this remainder term is of order $\varepsilon_x{}^2$, i.e., $\|\mathcal{O}(\varepsilon_x{}^2)\|/\varepsilon_x{}^2$ remains bounded as $\varepsilon_x \to 0$. While this limiting behavior is of theoretical interest, it is of little practical use since it provides no information on the size of the remainder term for a given (nonzero) value of ε_x. What is needed is an explicit bound on the remainder term in (3.1). It can be shown that

$$\|\mathcal{O}(\varepsilon_x{}^2)\| \leq \|\mathbf{D}\| \left[\frac{f'(x) + \lambda_{max}\, |f''(x)|}{(\lambda_{max} + \lambda_{min})/2} + \delta \lambda_{max} \max|f'''| \right] \varepsilon_x{}^2 \tag{3.3}$$

for any $x > 0$. Here λ_{min} and λ_{max} are the minimum and maximum values of the principal stretches; $\delta = 1/2$ if f''' has constant sign and $\delta = 1$ otherwise; $\max|f'''|$

[1] Cf. also Wang and Truesdell[3, §6.4] and Ogden[5, §6.1.4].

is the maximum value of $|f'''|$ over the smallest interval containg x and the principal stretches. To derive (3.1)–(3.3) and the results below, we use the component formula (2.3)–(2.4), Taylor's formula applied to f' with Lagrange's form of the remainder, and a variation of the Taylor-Lagrange formula due to Hummel and Seebeck[19]. Details can be found in Scheidler[20]. The error bound (3.3), which is new, is sharper than the corresponding bound in [20]. The derivation of (3.3) is similar to the derivation in [20] but requires a bit more work; details will be reported in a forthcoming paper [21]. It is also worth noting that the derivation of the bounds in [20] utilized the assumption that $\varepsilon_x < x$; for some choices of x this places restrictions on the motion. The new bound (3.3) holds for any C^2 motion and any C^3 strain measure f.

As mentioned above, we are free to choose the parameter x in (3.1). The simplest choice is $x = 1$, in which case ε_x is just the maximum of the absolute values of the principal strains $\lambda_i - 1$. Of course, better approximations will generally be obtained by choosing x to lie between λ_{min} and λ_{max}. It is easily shown that

$$\frac{1}{2}(\lambda_{max} - \lambda_{min}) \leq \varepsilon_x \leq \lambda_{max} - \lambda_{min}\,, \quad \text{if } \lambda_{min} \leq x \leq \lambda_{max}\,. \tag{3.4}$$

Since $(\lambda_{max} - \lambda_{min})/2$ can be interpreted as the *maximum shear strain*, (3.4) states that ε_x is bounded below by the maximum shear strain and bounded above by twice the maximum shear strain, provided that x lies between the minimum and maximum principal stretches. Then regardless of the volumetric strain, (3.1) yields a good approximation to $\mathbf{f}(\mathbf{V})^\circ$ if the maximum shear strain is sufficiently small. The best choice for x in (3.1) will depend on the particular application of the approximate formula. We mention three reasonable choices for x, all of which satisfy the condition $\lambda_{min} \leq x \leq \lambda_{max}$. First, we could take x to be the arithmetic mean of the principal stretches:

$$x = \frac{1}{3}(\lambda_1 + \lambda_2 + \lambda_3) = \frac{1}{3}\mathrm{tr}\,\mathbf{U} = \frac{1}{3}\mathrm{tr}\,\mathbf{V}\,. \tag{3.5}$$

Second, we could take x to be the *volumetric stretch*, which is defined as the geometric mean of the principal stretches:

$$x = (\lambda_1\lambda_2\lambda_3)^{1/3} = (\det\mathbf{U})^{1/3} = (\det\mathbf{V})^{1/3} = (\det\mathbf{F})^{1/3} = \left(\frac{\rho_0}{\rho}\right)^{1/3}, \tag{3.6}$$

where ρ_0 and ρ are the densities in the reference and current configurations, respectively. Finally, we could take

$$x = \min_{x>0}\varepsilon_x = \frac{1}{2}(\lambda_{max} + \lambda_{min})\,, \tag{3.7}$$

in which case $\varepsilon_x = (\lambda_{max} - \lambda_{min})/2$ is the maximum shear strain.

Since the left stretch tensor $\mathbf{V} = (\mathbf{F}\mathbf{F}^{\mathrm{T}})^{1/2}$ is an irrational function of the deformation gradient $\mathbf{F}$, a formula analogous to (3.1), but with $\mathbf{V}$ on the right-hand side replaced with $\mathbf{B} = \mathbf{F}\mathbf{F}^{\mathrm{T}}$, may be more useful for computational purposes. The result is

$$\mathbf{f}(\mathbf{V})^\circ = \frac{xf'(x) - x^2f''(x)}{2}\,\mathbf{D} + \left[\frac{f'(x)}{4x} + \frac{f''(x)}{4}\right](\mathbf{DB} + \mathbf{BD}) + \mathcal{O}(\varepsilon_x{}^2)\,. \tag{3.8}$$

The bound (3.3) does not apply to the remainder term in (3.8), but a similar bound can be obtained [21]. By utilizing Hill's component formula (2.1)–(2.2), analogous results

can be obtained for $\mathbf{f}(\mathbf{U})^{\cdot}$. Indeed, (3.1) and (3.8) remain valid under the replacements $\mathbf{f}(\mathbf{V})^{\circ} \to \mathbf{f}(\mathbf{U})^{\cdot}$, $\mathbf{D} \to \mathbf{R}^{\mathrm{T}}\mathbf{D}\mathbf{R}$, $\mathbf{V} \to \mathbf{U}$ and $\mathbf{B} \to \mathbf{C}$. Of course, the remainder terms are different in this case, but they satisfy the same bounds as before [20,21].

Now consider the logarithmic strain tensors. For $f = \ln$, (3.1) and (3.8) reduce to

$$(\ln \mathbf{V})^{\circ} = \mathbf{D} + \mathcal{O}(\varepsilon_x{}^2) \,. \tag{3.9}$$

Furthermore, in this case we have the following simple bound for the remainder term in (3.9):

$$\left\| \mathcal{O}(\varepsilon_x{}^2) \right\| \leq \|\mathbf{D}\| \, \frac{3}{4} \, \frac{\lambda_{max}}{\lambda_{min}} \left(\frac{\lambda_{max}}{\lambda_{min}} - 1 \right)^2 . \tag{3.10}$$

This follows from (3.3) by setting $f = \ln$ and choosing x as in (3.7). Similarly,

$$(\ln \mathbf{U})^{\cdot} = \mathbf{R}^{\mathrm{T}}\mathbf{D}\mathbf{R} + \mathcal{O}(\varepsilon_x{}^2) \,, \tag{3.11}$$

where the remainder term in (3.11) also satisfies (3.10). Observe that $\lambda_{max}/\lambda_{min}$, and thus the bound (3.10), is independent of the dilatational part of the deformation. Also note that since

$$\frac{\lambda_{max}}{\lambda_{min}} - 1 = \frac{2}{\lambda_{min}} \, \frac{\lambda_{max} - \lambda_{min}}{2} \,, \tag{3.12}$$

$\lambda_{max}/\lambda_{min} - 1$ is a measure of shear strain which is independent of the dilatational part of the deformation. By means of his component formula, Hill[6,7] showed (at least for distinct principal stretches) that $(\ln \mathbf{U})^{\cdot}$ differs from $\mathbf{R}^{\mathrm{T}}\mathbf{D}\mathbf{R}$ by a term whose components are of order $(\lambda_i/\lambda_j - 1)^2$, and he observed that this remainder term is independent of the dilatational part of the deformation. Using a different method, Gurtin and Spear[22] proved that for a family of motions depending on a small parameter ε,

$$(\ln \mathbf{V})^{\circ} = \mathbf{D} + \mathcal{O}(\varepsilon^3) \quad \text{if} \quad \mathbf{F} - \mathbf{I} = \mathcal{O}(\varepsilon) \;\&\; \dot{\mathbf{F}} = \mathcal{O}(\varepsilon) \,. \tag{3.13}$$

We can easily recover this result from (3.9) and (3.10); cf. [20]. Neither Hill nor Gurtin and Spear obtained bounds for the remainder terms in their approximate formulas.

4 Approximate Rate Equation for Isotropic Elasticity

Isotropic solids such as polycrystalline metals and ceramics exhibit elastic response only for small shear strains. Under the assumption that the shear strains are within this elastic range, we will give a rigorous derivation of an approximate rate equation for the deviatoric stress tensor. The assumption of small shear strains is often seen as justification for invoking the linear theory of elasticity, in which

$$\mathbf{T}_* = 2\mu_0 \mathbf{E}_* \,. \tag{4.1}$$

Here $\mathbf{T}$ denotes the *Cauchy stress tensor*, the constant μ_0 is the *shear modulus*, $\mathbf{E}$ is the *infinitesimal strain tensor*, and an asterisk subscript denotes the deviatoric part of a tensor. For terminal ballistics applications the linear theory is invalid for two reasons. First, material rotations may be large, in which case the linear theory fails to be properly invariant. Second, the high pressures generate large compressive volume changes, and it is known (see below) that large volumetric strains can influence the deviatoric stress.

A properly invariant consitutive equation for the deviatoric stress can be obtained simply by replacing $\mathbf{E}_*$ in (4.1) with the deviatoric part of any Eulerian strain tensor:

$$\mathbf{T}_* = 2\mu_0 \mathbf{f}(\mathbf{V})_* = 2\mu_0 \mathbf{V}_* + \mathcal{O}(\|\mathbf{V} - \mathbf{I}\|^2) \ , \tag{4.2}$$

where the equation on the right follows from (1.7). Thus, to within terms of order $\|\mathbf{V} - \mathbf{I}\|^2$, the constitutive equation $(4.2)_1$ is insensitive to the choice of the strain measure f. Note, however, that $\|\mathbf{V} - \mathbf{I}\|^2$ is small iff both the shear strains and the volumetric strains are small. For large volume changes, the constitutive equation $(4.2)_1$ is sensitive to the choice of the strain measure; in other words, different strain measures will yield different deviatoric stress/volumetric strain effects. Thus for a given material, use of $(4.2)_1$ would require the determination of an appropriate strain measure f. We will take a different approach below.

For finite deformations, the *shear modulus* μ of an isotropic elastic material is commonly defined as follows. Let $c_s(\rho)$ denote the *shear wave speed* in the material when it is under hydrostatic compression at density ρ, so that $\mathbf{T} = -p\mathbf{I}$, where p is the *pressure*, and $\lambda_1 = \lambda_2 = \lambda_3 = (\rho_0/\rho)^{1/3}$. Then

$$\mu = \hat{\mu}(p) = \bar{\mu}(\rho) \equiv \rho\, c_s(\rho)^2 \ . \tag{4.3}$$

If $\mu_0 \equiv \bar{\mu}(\rho_0)$, then the shear wave speed in the undeformed material is given by $c_s(\rho_0) = \sqrt{\mu_0/\rho_0}$, in agreement with the linear theory. For sufficiently low pressures ($\approx$ 1GPa or less), $c_s(\rho)$ is typically obtained from ultrasonic measurements with the pressure generated in a piston-cylinder apparatus. Such experiments reveal that c_s, and hence μ, increases with density, or equivalently, with pressure; indeed, for many solids $\partial\mu/\partial p|_{p=0}$ lies between 1/3 and 3 [23,24]. Direct measurements of the shear wave speed are difficult to obtain at high pressures. For metals and ceramics, Steinberg *et al.* [24,25] have proposed the following constitutive relation[2] for μ:

$$\mu = \mu_0 + a\, p \left(\frac{\rho_0}{\rho}\right)^{1/3} \ , \tag{4.4}$$

where the constant $a = \partial\mu/\partial p|_{p=0}$. The relation (4.4) is based on theoretical calculations. For pressure-density relations appropriate to metals and ceramics, (4.4) implies that μ increases with p, whereas $\partial\mu/\partial p$ decreases with p. Steinberg *et al.* [24,25,26] have found that (4.4) yields results consistent with wave profiles from plate impact experiments. For example, for 6061-T6 aluminum at a pressure of 41 GPa, (4.4) predicts that the shear modulus increases by a factor of 3 and that the shear wave speed increases by a factor of 3/2. Steinberg *et al.* [24,26] found that calculations based on (4.4) correctly predicted the arrival time of elastic release waves in Al shock-loaded to 41 GPa, and that the calculated elastic release arrived much too late when the pressure dependence of μ was reduced by 75%.

Any class of constitutive relations intended for high pressure applications should be general enough to accommodate any physically reasonable shear modulus function $\mu = \bar{\mu}(\rho)$. One such class is given by (4.7) below. The analysis is based on the following

[2]They also include a linear temperature dependence. They find that the temperature term is typically on the order of 10% of the pressure term in shock-wave experiments.

formulas for $\bar{\mu}$, which are valid for any isotropic elastic material:[3]

$$\begin{aligned}\bar{\mu}(\rho) &= \frac{\lambda_i}{2}\left(\frac{\partial t_i}{\partial \lambda_i} - \frac{\partial t_i}{\partial \lambda_j}\right)\Bigg|_{\lambda_1=\lambda_2=\lambda_3=(\rho_0/\rho)^{1/3}} \\ &= \frac{\lambda_i}{2}\left(\frac{\partial t_i^*}{\partial \lambda_i} - \frac{\partial t_i^*}{\partial \lambda_j}\right)\Bigg|_{\lambda_1=\lambda_2=\lambda_3=(\rho_0/\rho)^{1/3}}\end{aligned} \tag{4.5}$$

for any distinct $i, j \in \{1, 2, 3\}$. Here t_i and t_i^* are the principal stresses and the principal deviatoric stresses, respectively. In particular, from $(4.5)_2$ it follows that the shear modulus is completely determined by the deviatoric response of the material. On the other hand, there are infinitely many constitutive relations for $\mathbf{T}_*$ which yield the same shear modulus. With the aid of (4.5) it may be shown that [21]

$$\mathbf{T}_* = 2\bar{\mu}(\rho)(\ln \mathbf{V})_* + \mathcal{O}\left(\left(\frac{\lambda_{max}}{\lambda_{min}} - 1\right)^2\right) \tag{4.6}$$

for any isotropic elastic material with shear modulus $\mu = \bar{\mu}(\rho)$. It follows that two isotropic elastic materials have the same shear modulus iff the deviatoric stress in these materials differs by a term of order $(\lambda_{max}/\lambda_{min} - 1)^2$. In particular, for a given function $\bar{\mu}$ the constitutive relation

$$\mathbf{T}_* = 2\bar{\mu}(\rho)(\ln \mathbf{V})_* \tag{4.7}$$

has the following properties:

1. This relation defines a material whose deviatoric response is isotropic elastic with shear modulus $\mu = \bar{\mu}(\rho)$.

2. For any other isotropic elastic material with shear modulus $\mu = \bar{\mu}(\rho)$, the deviatoric stress differs from (4.7) by a term of order $(\lambda_{max}/\lambda_{min} - 1)^2$.

The component form of (4.7) is

$$t_i^* = \frac{2\mu}{3}(2\ln\lambda_i - \ln\lambda_j - \ln\lambda_k)\,, \tag{4.8}$$

for any permutation (ijk) of (123). Then from $(4.5)_2$ it is easily verified that the shear modulus for such a material is indeed equal to μ. It is interesting to note that the properties 1 and 2 above fail to hold if $\ln \mathbf{V}$ in (4.7) is replaced by any other Eulerian strain tensor $\mathbf{f}(\mathbf{V})$, or equivalently, if the logarithm function in (4.8) is replaced by any other scalar strain measure f. This can be verified with the aid of $(4.5)_2$.

For the remainder of this section we focus on the constitutive relation (4.7). On taking the Jaumann rate of (4.7), we obtain

$$\begin{aligned}\mathbf{T}_*^\circ &= 2\mu\,(\ln \mathbf{V})_*^\circ + 2\dot{\mu}\,(\ln \mathbf{V})_* \\ &= 2\mu\,(\ln \mathbf{V})_*^\circ + \frac{\dot{\mu}}{\mu}\,\mathbf{T}_*\,,\end{aligned} \tag{4.9}$$

[3] Cf. [3, (5.25)], where an equation equivalent to $(4.5)_1$, but in terms of the squares of the principal stretches, is derived for acceleration waves. As discussed in [2, §73], acceleration waves obey the same laws of propagation as infinitesimal plane waves.

where the second equation follows by solving (4.7) for $(\ln \mathbf{V})_*$. Then from $(4.9)_2$, (3.9) and (3.10), it follows that

$$\mathbf{T}_*^\circ = 2\mu \mathbf{D}_* + \frac{\dot{\mu}}{\mu}\mathbf{T}_* + \mathcal{O}\left(\left(\frac{\lambda_{max}}{\lambda_{min}} - 1\right)^2\right), \tag{4.10}$$

where an explicit bound for the remainder term is given by the expression on the right-hand side of (3.10). Therefore, to within a term of order $(\lambda_{max}/\lambda_{min} - 1)^2$ the material time derivative of the deviatoric stress tensor is given by

$$\dot{\mathbf{T}}_* = 2\mu \mathbf{D}_* + \frac{\dot{\mu}}{\mu}\mathbf{T}_* + \mathbf{W}\mathbf{T}_* - \mathbf{T}_*\mathbf{W}. \tag{4.11}$$

Alternate expressions for the term $\dot{\mu}/\mu$ are

$$\frac{\dot{\mu}}{\mu} = \frac{1}{\mu}\frac{\partial \mu}{\partial \rho}\dot{\rho} = \frac{\rho}{\mu}\frac{\partial \mu}{\partial \rho}(-\mathrm{tr}\,\mathbf{D}) = \frac{\kappa}{\mu}\frac{\partial \mu}{\partial p}(-\mathrm{tr}\,\mathbf{D}), \tag{4.12}$$

where

$$\kappa \equiv \rho \frac{\partial p}{\partial \rho} \tag{4.13}$$

is the *bulk modulus*. For many metals and ceramics, $\frac{\kappa}{\mu}\frac{\partial \mu}{\partial p} \sim 1$–10. In view of $(4.12)_{2,3}$, the right-hand side of (4.11) involves three different rates: $\mathbf{D}_*$, a measure of distortional strain rate ; $-\mathrm{tr}\,\mathbf{D}$, a measure of the rate of compression; and $\mathbf{W}$, a measure of the rate of rotation. In general these rates are independent, so that none of the terms in (4.11) should be omitted.

From the above results we may draw the following conclusions. Within the elastic range of an isotropic metal or ceramic with shear modulus μ (as defined by (4.3)), the constitutive relation (4.7) provides a good approximation to the deviatoric stress $\mathbf{T}_*$, and (4.11) provides a good approximation to the time-rate of change of $\mathbf{T}_*$; in particular, these approximations are good regardless of the volumetric strain. Furthermore, for metals it is typically assumed that prior plastic deformation does not alter the elastic properties of the material. Then regardless of the amount of prior plastic deformation, the rate equation (4.11) is also valid during elastic unloading since the terms in (4.11) do not involve the original reference configuration.

In most hydrocodes used for terminal ballistics simulations, the rate equation for deviatoric elastic response is $\dot{\mathbf{T}}_* = 2\mu_0 \mathbf{D}_* + \mathbf{W}\mathbf{T}_* - \mathbf{T}_*\mathbf{W}$; cf. [27, §11.1]. Clearly, this provides a good approximation only at low pressures or for materials with constant shear modulus, conditions which typically are not satisfied in such applications. Steinberg and Lund[28, eq. (4)] use a rate equation for $\mathbf{T}_*$ which reduces to $\dot{\mathbf{T}}_* = 2\mu \mathbf{D}_*$ when the response is elastic. While they account for the pressure dependence of μ via (4.4), their rate equation omits the other terms in (4.11). For the simulation of uniaxial strain plate impact tests, the rate equation $\dot{\mathbf{T}}_* = 2\mu \mathbf{D}_*$ is probably sufficient, since in this case $\mathbf{W} = \mathbf{0}$ and the $(\dot{\mu}/\mu)\mathbf{T}_*$ term in (4.11) is much smaller than the $2\mu \mathbf{D}_*$ term.

5 Exact Direct Formulas

In this section we indicate how the component formulas for $\mathbf{f}(\mathbf{U})^{\cdot}$ and $\mathbf{f}(\mathbf{V})^{\circ}$ in Section 2 can be used to derive exact direct formulas for these rates. For brevity we focus on

$\mathbf{f}(\mathbf{V})^{\circ}$, although a similar analysis applies to $\mathbf{f}(\mathbf{U})^{\cdot}$. For more details we refer the reader to the forthcoming paper [29]. Let $\mathbf{A}$ be any tensor coaxial with $\mathbf{V}$ and such that two principal values of $\mathbf{A}$ are equal iff the corresponding principal values of $\mathbf{V}$ are equal. By $(1.2)_2$, these conditions are equivalent to

$$\mathbf{A} = \sum_{i=1}^{3} a_i \, \mathbf{v}_i \otimes \mathbf{v}_i \qquad a_i = a_j \text{ iff } \lambda_i = \lambda_j \,, \tag{5.1}$$

where a_i are the principal values of $\mathbf{A}$. Then the Jaumann rate of $\mathbf{f}(\mathbf{V})$ can be expressed in terms $\mathbf{A}$ and $\mathbf{D}$ as follows:

$$\begin{aligned} \mathbf{f}(\mathbf{V})^{\circ} \;=\; & \alpha_{22}\mathbf{A}^2\mathbf{D}\mathbf{A}^2 + \alpha_{21}(\mathbf{A}^2\mathbf{D}\mathbf{A} + \mathbf{A}\mathbf{D}\mathbf{A}^2) + \alpha_{20}(\mathbf{A}^2\mathbf{D} + \mathbf{D}\mathbf{A}^2) \\ & \alpha_{11}\mathbf{A}\mathbf{D}\mathbf{A} + \alpha_{10}(\mathbf{A}\mathbf{D} + \mathbf{D}\mathbf{A}) + \alpha_{00}\mathbf{D} \,, \end{aligned} \tag{5.2}$$

where the coefficients α_{mn} depend on the strain measure f and the principal values of $\mathbf{A}$ and $\mathbf{V}$. Some useful choices for $\mathbf{A}$ are $\mathbf{V}$, $\mathbf{B}$, $\mathbf{f}(\mathbf{V})$, some other Eulerian strain tensor (e.g., $\ln \mathbf{V}$), or the deviatoric part of any of these tensors. Regardless of the choice for $\mathbf{A}$, the coefficients α_{mn} have the form

$$\alpha_{mn} = \sum_{\substack{i,j=1 \\ i \le j}}^{N} \beta_{mn}^{ij}(a_1, a_2, a_3)\, E_f(\lambda_i, \lambda_j) \,, \tag{5.3}$$

where N is the number of distinct principal stretches, $E_f(\lambda_i, \lambda_j)$ is given by (2.4), and β_{mn}^{ij} are rational functions whose form is independent of $\mathbf{A}$; various expressions for the β_{mn}^{ij} are given in [29]. If $N = 2$ we assume that $\lambda_1 \neq \lambda_2 = \lambda_3$; in this case $\alpha_{22} = \alpha_{21} = \alpha_{20} = 0$. If $N = 1$, i.e., if $\mathbf{V} = \lambda \mathbf{I}$, then the only nonzero coefficient in (5.2) is $\alpha_{00} = \lambda f'(\lambda)$.

There are three key steps in the derivation of (5.2)–(5.3). The first step is to show that (2.3) is equivalent to

$$\mathbf{f}(\mathbf{V})^{\circ} = \sum_{i,j=1}^{N} E_f(\lambda_i, \lambda_j)\, \mathbf{P}_i \mathbf{D} \mathbf{P}_j \,, \tag{5.4}$$

where $\mathbf{P}_i$ $(i = 1, \ldots, N)$ is the ith eigenprojection of $\mathbf{V}$, i.e., the perpendicular projection onto the eigenspace of $\mathbf{V}$ corresponding to the eigenvalue λ_i. The second step is to note that, in view of (5.1), $\mathbf{A}$ and $\mathbf{V}$ have the same eigenprojections. The third step is to employ the explicit formulas for the eigenprojections of a symmetric tensor $\mathbf{A}$; cf. [30, §79]. For example, if $N = 3$ then

$$\mathbf{P}_1 = \frac{\mathbf{A} - a_2\mathbf{I}}{a_1 - a_2} \frac{\mathbf{A} - a_3\mathbf{I}}{a_1 - a_3} \,, \tag{5.5}$$

with analogous formulas for $\mathbf{P}_2$ and $\mathbf{P}_3$. If $N = 2$ then

$$\mathbf{P}_1 = \frac{\mathbf{A} - a_2\mathbf{I}}{a_1 - a_2} \quad \text{and} \quad \mathbf{P}_2 = \frac{\mathbf{A} - a_1\mathbf{I}}{a_2 - a_1} \,. \tag{5.6}$$

If $N = 1$ then $\mathbf{P}_1 = \mathbf{I}$. Substitution of these formulas for the eigenprojections into (5.4) yields (5.2)–(5.3).

For the rates of the logarithmic strain tensors, results of the type (5.2)–(5.3), with $\mathbf{A} = \mathbf{V}$, were obtained by Hoger[14]. Hoger utilized her direct formula for $(\ln \mathbf{U})^{\cdot}$ to obtain the first rigorous proof (for $f = \ln$) of Hill's component formula (2.1)–(2.2) when the principal stretches are not distinct. In the derivation of her direct formulas, Hoger utilizes results from Carlson and Hoger[31] and Hoger and Carlson[32]. The approach outlined above appears to be more general and substantially simpler, and also yields more compact expressions for the coefficients α_{mn}.

6 Discussion

We have shown that the component formulas for the time-rates of generalized strain tensors provide a useful tool for deriving direct formulas (either exact or approximate) for these rates. In principle, one could also derive the approximate formulas in Section 3 from the exact formulas in Section 5. However, for the case of distinct principal stretches the complexity of the direct formulas makes such an approach impracticle.

Our formulas for the time-rate of change of Eulerian strain tensors have been expressed in terms of the Jaumann rate (1.16). Another corotational rate in common use is the one obtained by replacing $\mathbf{W}$ with $\mathbf{\Omega} \equiv \dot{\mathbf{R}}\mathbf{R}^{\mathrm{T}}$ in (1.16). It can be shown [20,21] that the approximate formulas (3.1), (3.8), (3.9) and (4.10) are valid for this corrotational rate as well. The remainder terms in these formulas are different, of course, but they satisfy the same bounds as before.

References

[1] C. Truesdell and R. Toupin. The Classical Field Theories. In *Encyclopedia of Physics*, volume III/1. Springer-Verlag, Berlin, 1960.

[2] C. Truesdell and W. Noll. The Non-Linear Field Theories of Mechanics. In *Encyclopedia of Physics*, volume III/3. Springer-Verlag, Berlin, 1965.

[3] C.-C. Wang and C. Truesdell. *Introduction to Rational Elasticity.* Noordhoff, Leyden, 1973.

[4] M. E. Gurtin. *An Intoduction to Continuum Mechanics.* Academic Press, New York, 1981.

[5] R. W. Ogden. *Non-Linear Elastic Deformations.* Ellis Horwood, Chichester, England, 1984.

[6] R. Hill. Aspects of invariance in solid mechanics. In C.-S. Yih, editor, *Advances in Applied Mechanics*, volume 18, pages 1–75. Academic Press, New York, 1978.

[7] R. Hill. Constitutive inequalities for isotropic elastic solids under finite strain. *Proc. R. Soc. London A*, 314:457–472, 1970.

[8] R. Hill. On constitutive inequalities for simple materials—I. *J. Mech. Phys. Solids*, 16:229–242, 1968.

[9] R. Hill. On constitutive inequalities for simple materials—II. *J. Mech. Phys. Solids*, 16:315–322, 1968.

[10] K. S. Havner. The theory of finite plastic deformation of crystalline solids. In H. G. Hopkins and M. J. Sewell, editors, *Mechanics of Solids*, pages 265–302. Pergamon Press, New York, 1982.

[11] S. Nemat-Nasser. On finite-deformation elasto-plasticity. *Int. J. Solids Struct.*, 18:857–872, 1982.

[12] S. Nemat-Nasser. On finite plastic flow of crystalline solids and geomaterials. *J. Appl. Mech.*, 50:1114–1126, 1983.

[13] Z.-H. Guo and R. N. Dubey. Basic aspect's of Hill's method in solid mechanics. *Solid Mech. Arch.*, 9:353–380, 1984.

[14] A. Hoger. The material time derivative of logarithmic strain. *Int. J. Solids Struct.*, 22:1019–1032, 1986.

[15] M. Scheidler. Time rates of generalized strain tensors. Part I: Component formulas. *Mech. Mat.*, 11:199–210, 1991.

[16] R. M. Bowen and C.-C. Wang. Acceleration waves in inhomogeneous isotropic elastic bodies. *Arch. Rational Mech. Anal.*, 38:13–45, 1970.

[17] P. Chadwick and R. W. Ogden. A theorem of tensor calculus and its application to isotropic elasticity. *Arch. Rational Mech. Anal.*, 44:54–68, 1971.

[18] J. M. Ball. Differentiability properties of symmetric and isotropic functions. *Duke Math. J.*, 51:699–728, 1984.

[19] P. M. Hummel and C. L. Seebeck. A generalization of Taylor's expansion. *Amer. Math. Monthly*, 56:243–247, 1949.

[20] M. Scheidler. Time rates of generalized strain tensors. Part II: Component formulas. *Mech. Mat.*, 11:211–219, 1991.

[21] M. Scheidler. Approximate formulas for the time rates of generalized strain tensors: Improved error bounds with applications to elasticity. In preparation.

[22] M. E. Gurtin and K. Spear. On the relationship between the logarithmic strain rate and the stretching tensor. *Int. J. Solids Struct.*, 19:437–444, 1983.

[23] M. W. Guinan and D. J. Steinberg. Pressure and temperature derivatives of the isotropic polycrystalline shear modulus for 65 elements. *J. Phys. Chem. Solids*, 35:1501–1512, 1974.

[24] D. J. Steinberg, S. G. Cochran, and M. W. Guinan. A constitutive model for metals applicable at high-strain rate. *J. Appl. Phys.*, 51:1498–1504, 1979.

[25] D. J. Steinberg. Computer studies of the dynamic strength of ceramics. Technical Report UCRL-ID-106004, Lawrence Livermore National Laboratory, 1990.

[26] D. J. Steinberg. Constitutive model used in computer simulation of time-resolved, shock-wave data. *Int. J. Impact Eng.*, 5:603, 1987.

[27] W. P. Walters and J. A. Zukas. *Fundamentals of Shaped Charges.* Wiley, New York, 1989.

[28] D. J. Steinberg and C. M. Lund. A constitutive model for strain rates from 10^{-4} to 10^{6} s^{-1}. *J. Appl. Phys.*, 65:1528–1533, 1989.

[29] M. Scheidler. Time rates of generalized strain tensors. Part III: Exact basis-free formulas. In preparation.

[30] P. R. Halmos. *Finite-Dimensional Vector Spaces.* Van Nostrand, Princeton, New Jersey, 1958.

[31] D. Carlson and A. Hoger. The derivative of a tensor-valued function of a tensor. *Quart. Appl. Math.*, 44:409–423, 1986.

[32] A. Hoger and D. E. Carlson. On the derivative of the square root of a tensor and Guo's rate theorems. *J. Elas.*, 14:329–336, 1984.

SESSION IIA: MICRO-MECHANICS

Session Chairman: *Dr. A. Mayer*

EXTREMAL MICROSTRUCTURES FOR COMPOSITE MATERIALS

Robert V. Kohn and Graeme W. Milton
Courant Institute of Mathematical Sciences,
251 Mercer Street, New York, NY 10012

1. Introduction

The macroscopic properties of a composite material depend in a subtle way on the geometry of the microstructure. One way to explore this dependence is through geometry-independent bounds on effective moduli. Composites with extremal behavior are of special interest. They arise naturally, from certain types of coherent phase transitions; and they arise synthetically, in problems of structural optimization.

Recent mathematical activity has led to new methods for bounding effective moduli and new classes of extremal microstructures. This progress has been achieved over a period of years, through the combined effort of many individuals. Here we survey selected aspects of this work.

2. Composite materials.

A composite is a mixture of distinct materials on a length scale small compared to that on which the loads and boundary conditions vary, but still large enough for continuum theory to apply. We consider exclusively linear models of material response, e.g. thermal conductivity, electrical resistivity, or linear elasticity. Material interfaces are considered to be perfectly bonded; thus in the elastic setting the displacement and the normal component of stress are continuous at material interfaces.

The effective moduli of a composite describe its macroscopic behavior. There is an extensive theory, in both the mechanics and mathematics literatures; see e.g. [1–5]. It makes little difference whether the microstructure is random, periodic, or of some other form. The effective conductivity α_*, for example, relates the macroscopic (i.e. locally averaged) current j to the voltage gradient $\nabla\phi$:

$$\langle j \rangle = \alpha_* \langle \nabla\phi \rangle \ . \tag{2.1}$$

Similarly, the effective Hooke's law C_* relates the macroscopic (locally averaged) stress σ to the strain $e(u) = \frac{1}{2}(\nabla u + \nabla u^T)$:

$$\langle \sigma \rangle = C_* \langle e(u) \rangle \ . \tag{2.2}$$

Here $\langle \cdot \rangle$ represents averaging — over an ensemble if the composite is random, over space if it is periodic, or interpreted via weak limits in a more general mathematical context. The effective conductivity α_* is a second-order tensor; the effective Hooke's law C_* is a fourth-order tensor. They can be anisotropic, even if the composite is made from isotropic materials, due to anisotropy of the microstructure.

3. New methods for bounding effective moduli.

The recent mathematical progress has been facilitated by a number of new methods for bounding effective moduli. One is a Fourier-space version of the well-known Hashin-Shtrikman variational principle, e.g. [6–10]. Another is the "translation method," which derives new variational principles from classical ones by the subtraction of a null-Lagrangian (or,

more generally, a quasiconvex quadratic form), e.g. [11–13]. A third uses the fact that the effective moduli depend analytically on the component properties, e.g. [14,15]. And a fourth uses linear fractional transformations to encode geometric information such as volume fractions into the definition of the effective tensor, e.g. [16,17]. (These references represent a mere sampling of the literature in each area.)

Much of the recent progress has focussed on bounds which are *optimal.* To show that a bound is optimal one must find a microstructure that achieves it. So it is important to have a sufficiently large class of microstructures with explicitly computable effective properties. This is provided by the construction known as *sequential lamination.* Its basis is the well-known fact that the effective moduli of a layered composite are explicitly computable. It is natural to iterate this, layering together materials which are themsevles composites. This idea goes back at least to Bruggeman [18]. It was rediscovered by various individuals and applied to prove the optimality of many different bounds. Two particular developments have been very important. One is an especially convenient formula for expressing the effective moduli of a sequentially laminated composite, introduced by Tartar for conductivity [11] and extended to elasticity by Francfort and Murat [19]. The other is a method for searching the class of sequentially laminated composites numerically to find a microstructure that is extremal for some particular purpose [20].

4. Examples of optimal bounds and extremal microstructures.

We now describe two specific successes of the theory.

4A. Mixtures of two elastic materials.

The following question arises naturally in structural optimization, see e.g. [21–23]. Suppose we are given two elastic materials with Hooke's laws A_1 and A_2 respectively. They are to be combined in specified volume fractions θ, $1-\theta$ to form a composite A_*. How should the microstructure be chosen so as to maximize the rigidity of the resulting composite? Of course, an elastic material which is rigid for one type of load may be soft for another one, so to specify the problem completely we must specify either the (macroscopic) stress σ or the (macroscopic) strain e. The goal is thus to find either

$$\max_{A_*} \langle A_* e, e \rangle = f_1(\theta, e) \tag{4.1}$$

or

$$\min_{A_*} \langle A_*^{-1} \sigma, \sigma \rangle = f_2(\theta, \sigma) \tag{4.2}$$

as A_* runs over all possible effective moduli attainable by mixing A_1 and A_2 in the specified value fractions. We emphasize that the symmetry of A_* is *not* restricted in (4.1)–(4.2). If e (respectively, σ) is not isotropic then there are preferred spatial directions, namely those of principal strain (stress), so the optimal A_* will not be isotropic.

The Hashin-Shtrikman variational principle applies if A_1 and A_2 are "well-ordered", i.e. if $A_2 - A_1$ is a positive definite Hooke's law. It yields a pair of explicit, concave optimizations for evaluating (4.1) and (4.2) [9]. The conditions of optimality determine examples of extremal sequential-

ly laminated microstructures. In general (for 3-dimensional composites, made of two anisotropic materials) the concave optimization will probably have to be solved numerically. It can be solved explicitly, however, in several interesting special cases; these include when A_1 and A_2 are isotropic and either (i) the spatial dimension is 2 [23–25], (ii) the spatial dimension is 3 and both materials are incompressible [7], or (iii) the spatial dimension is 3 and one material is degenerate or rigid [26].

When e and σ are isotropic, $\langle A_* e, e\rangle$ and $\langle A_*^{-1}\sigma, \sigma\rangle$ can be viewed as "generalized bulk moduli." In this case the optimal bounds (4.1)–(4.2) reduce to those established long ago by Hashin and Shtrikman [27]. However, unlike [27] our bounds do not assume that A_* is isotropic. Such generalized bulk modulus bounds can also be found in [6,14,19].

The examples (4.1)–(4.2) are merely special cases of a much more general theory [9]. It can handle upper as well as lower bounds, and sums of energies as well as a single energy.

Similar bounds can also be proved using the translation method [24–26]. That approach has the advantage of applying in some cases where A_1 and A_2 are not well-ordered. However, it has the disadvantage that we lack a direct connection between translation bounds and optimal microstructures.

A problem analogous to (4.1) arises in the modeling of coherent phase transitions. There energy minimization is due to thermodynamic considerations. The distinct phases have different stress-free strains as well as (possibly) different Hooke's laws. The special case of two phases with

identical Hooke's laws has been studied extensively in the metallurgical literature, e.g. [28–29]. A treatment from the present viewpoint is given in [30]. Not surprisingly, the Hashin-Shtrikman variational principle permits one to consider the case when both the stress-free strains and the Hooke's laws are distinct [31].

4B. Conducting polycrystals.

A polycrystalline composite is one consisting of a single, anisotropic material, mixed with itself in various orientations. We focus here on effective conductivity rather than elastic behavior. A natural question, analogous to (4.1)–(4.2), is to seek polycrystalline composites of maximal or minimal effective conductivity.

The problem may be formulated more precisely as follows. Consider an anisotropic material with conductivity tensor α. We may suppose that α is diagonal, so the basic material is completely determined by its three principal conductivities:

$$\alpha = \begin{pmatrix} \alpha_1 & 0 & 0 \\ 0 & \alpha_2 & 0 \\ 0 & 0 & \alpha_3 \end{pmatrix} .$$

Now consider a polycrystalline composite made from this material. We suppose for simplicity that it is macroscopically isotropic, i.e. that the effective conductivity has the form $\alpha_* I$. What are the smallest and largest possible values of α_*?

The optimal upper bound turns out to be

$$\alpha_* \leq \frac{1}{3}(\alpha_1 + \alpha_2 + \alpha_3) . \tag{4.3}$$

This bound is easily derived from classical variational principles; it was shown to be optimal by Schulgasser [32] using a version of sequential lamination.

The optimal lower bound is more interesting. It is

$$\alpha_* \geq \alpha_{\min} \ , \tag{4.4}$$

where $\alpha_{\min}$ is the unique positive root of the equation

$$\sum_{i=1}^{3} \frac{\alpha_i - \alpha_{\min}}{2\alpha_i + \alpha_{\min}} = 0 \ . \tag{4.5}$$

The only known proof of (4.5) makes use of the translation method [33]. The bound was shown to be optimal for a uniaxial basic crystal in [33], and for a general basic crystal in [20]. Interestingly, the construction used for the uniaxial case does not suffice for the general case. The optimal microstructures described in [20] have a sort of self-similar structure. They were discovered with the aid of a computer search for sequentially-laminated geometries of high resistivity.

The bound (4.4)–(4.5) is not in fact restricted to macroscopically isotropic composites. If α_{*i} are the principal conductivities of an anisotropic polycrystal then one can show that

$$\sum_{i=1}^{3} \frac{\alpha_{*i} - \alpha_{\min}}{2\alpha_{*i} + \alpha_{\min}} \geq 0 \ . \tag{4.6}$$

On the other hand, (4.6) is not always optimal in the anistropic setting [34].

There are also some analogous results for elastic polycrystals. These include bounds in the generalized bulk modulus of an anisotropic polycrystal in two or three space dimensions [35], and bounds on the effective

shear modulus of an isotropic elastic polycrystal in two space dimensions [36].

References

[1] R. Christensen, *Mechanics of Composite Materials*, Wiley Interscience, 1979.

[2] R. Hill, "Elastic properties of reinforced solids: some theoretical principles," *J. Mech. Phys. Solids* 11, 1963, 357.

[3] J. Willis, "Variational and related methods for the overall properties of composite materials, in *Advances in Applied Mechanics* 21, C. S. Yih, ed., 1981, 2–78.

[4] A. Bensoussan, J.-L. Lions, and G. Papanicolaou, *Asymptotic Analysis for Periodic Structures*, North-Holland, 1978.

[5] V. Zhikov, S. Kozlov, O. Oleinik, and K. Ngoan, "Averaging and G-convergence of differential operators", *Russian Math. Surveys* 34:5, 1979, 69–147.

[6] G. Milton and R. Kohn, "Variational bounds on the effective moduli of anisotropic composites," *J. Mech. Phys. Solids* 36, 1988, 597–629.

[7] R. Kohn and R. Lipton, "Optimal bounds for the effective energy of a mixture of isotropic, incompressible, elastic materials," *Arch. Rat. Mech. Anal.* 102, 1988, 331–350.

[8] M. Avellaneda, "Optimal bounds and microgeometries for elastic two-phase composites," *SIAM J. Appl. Math.* 47, 1987, 1216–1228.

[9] G. Allaire and R. Kohn, "Optimal bounds on the effective behavior of a mixture of two well-ordered elastic materials," submitted to *Q. Appl. Math.*

[10] C. Wu and R. McCullough, "Constitutive relationships for heterogeneous materials," in *Developments in Composite Materials*, Applied Science Pub., 1977, 119–187.

[11] L. Tartar, "Estimations fines des coefficients homogeneises," in *Ennio de Giorgi's Colloquium*, P. Kree, ed., Pitman Research Notes in Math. 125, 1985, 168–187.

[12] K. Lurie and A. Cherkaev, "Exact estimates of conductivity of composites formed by two isotropically conducting media taken in prescribed proportions," *Proc. Roy. Soc. Edinburgh* 99A, 1984, 71–87.

[13] G. Milton, "On characterizing the set of possible effective tensors of composites: the variational method and the translation method,"

Comm. Pure Appl. Math. 43, 1990, 63–125.

[14] Y. Kantor and D. Berman, "Improved rigorous bounds on the effective elastic moduli of a composite material," *J. Mech. Phys. Solids* 32, 1984, 41–62.

[15] G. Milton and K. Golden, "Thermal conduction in composites," in *Thermal Conductivity* 18, T. Ashworth and D. Smith, eds., Plenum Press, 1985, 571.

[16] G. Milton, "The field equation recursion method," in *Composite Media and Homogenization Theory*, G. Dal Maso and G. Dell'Antonio eds., Birkhauser, Boston, 1991, 223–245.

[17] L. Gibianski and A. Cherkaev, "The exact coupled bounds for effective tensors of electrical and magnetic properties of two-component two-dimensional composites," submitted to *Proc. Royal Soc. Edinburgh* Ser. A.

[18] D. Bruggeman, *Elastizität Konstanten von Kristallaggregaten*, Doctoral thesis, Utrecht, 1930.

[19] G. Francfort and F. Murat, "Homogeneization and optimal bounds in linear elasticity," *Arch. Rat. Mech. Anal.* 94, 1986, 307–334.

[20] G. Milton and V. Nesi, "Polycrystalline configurations that maximize electrical resistivity," *J. Mech. Phys. Solids*, to appear.

[21] R. Kohn and G. Strang, "Optimal design and relaxation of variational problems I–III," *Comm. Pure Appl. Math.* 39, 1986, 113–138, 139–182, 353–377.

[22] M. Bendsoe and N. Kikuchi, "Generating optimal topologies in structural design using a homogenization method," *Comp. Meth. Appl. Mech. Engrg.* 71, 1988, 197–224.

[23] G. Allaire and R. Kohn, "Optimal design for minimum compliance in plane stress using optimal microstructures," preprint.

[24] G. Allaire and R. Kohn, "Explicit optimal bounds on the elastic energy of a two-phase composite in two space dimensions," submitted to *Q. Appl. Math.*

[25] L. Gibiansky and A. Cherkaev, "Design of composite plates of extremal rigidity," Ioffe Physicotechnical Institute preprint 914, 1984 (in Russian).

[26] L. Gibianski and A. Cherkaev, "Microstructures of composites of extremal rigidity and exact estimates of the associated energy density," Ioffe Physicotechnical Institute preprint 1115, 1987 (in Russian).

[27] Z. Hashin and S. Shtrikman, "A variational approach to the theory of

the elastic behavior of multiphase materials," *J. Mech. Phys. Solids* 11, 1963, 127–140.

[28] A. Khatchaturyan, *Theory of Structural Transformations in Solids*, John Wiley & Sons, 1983.

[29] E. Kostlan and J. Morris, "The preferred habit of a coherent thin-plate inclusion in an anisotropic elastic solid," *Acta Metall.* 35, 1987, 2167–2175.

[30] R. Kohn, "Relaxation of a double-well energy," *Continuum Mechanics and Thermodynamics* 3, 1991, 193–236.

[31] R. Kohn, "Relaxation of the elastic energy for a system of two coherent phases with well-ordered elstic moduli," in preparation.

[32] K. Schulgasser, "Bounds on the conductivity of statistically isotropic polycrystals," *J. Physics C: Solid State Phys.* 10, 1977, 407–417.

[33] M. Avellaneda, A. Cherkaev, K. Lurie, and G. Milton, "On the effective conductivity of polycrystals and a three-dimensional phase-interchange inequality," *J. Appl. Phys.* 63, 1988, 4989–5003.

[34] G. Dell'Antonio and V. Nesi, "A scalar inequality which bounds the effective conductivity of composites," *Proc. Roy. Soc. Edinburgh Ser. A*, to appear.

[35] M. Avellaneda and G. Milton, "Optimal bounds on the bulk modulus of polycrystals, *SIAM J. Appl. Math.* 49, 1989, 824–837.

[36] M. Avellaneda, A. Cherkaev, L. Gibiansky, and G. Milton, in preparation.

MICROMECHANICS OF CRITICAL STATES

Dusan Krajcinovic*
Michal Basista**
Kaushik Mallick*

*Arizona State University, Tempe, AZ 85287-6106
**Institute of Fundamental Technological Research, Warsaw, Poland

INTRODUCTION

The mechanical response of a typical brittle elastic solid weakened by a diffuse distribution of microdefects can be divided into three distinctly disparate phases. During the initial phase, characterized by a rather dilute concentration of defects, the material hardens when subjected to quasistatically increasing mechanical forces or temperatures. As the defects multiply and grow, the specimen's stiffness (overall elastic moduli) decreases even though the tangent modulus remains positive. The subsequent phase occurs as a result of microdefect interaction. Phenomenologically, this phase is confined to a narrow neighborhood of the apex of the stress-strain (or, more accurately, force-displacement)curve, as the specimen's overall tangent stiffness approaches zero value. In the subsequent, or softening, phase the specimen's tangent modulus is negative.

The partition of the mechanical response into the above three phases is by no means formal. As the recent large scale numerical simulations [1, 2] clearly indicate, the succession of phases is directly related to the extent of the microcrack clustering within the solid. From the micromechanical viewpoint, these three phases (regimes) are characterized as follows:

(i) In a carefully manufactured material subjected to moderate external loads and temperatures the microdefect concentration is dilute during the initial

phase of a deformation process. The spatial fluctuations of stress and strain fields are confined to narrow neighborhoods of widely spaced defects. The probability that the stress concentrations may be enhanced by interaction of microdefects is rather remote. Consequently, the exact positions of the micro-defects within the specimen has little or no relevance to the macroresponse. As a result, during this phase the microdefects influence the macroresponse principally through their volume averages. The material is within this range macro-homogeneous, simple and local.

(ii) As the external loads are increased, new microdefects are nucleated and the already existing ones grow larger. The probability that the distance separating two growing microdefects becomes small enough to influence their further growth through interaction becomes more substantial. Thus, the distance between microdefects becomes an important parameter, defining not only the macroresponse of the solid but, more importantly, its propensity to failure. Non-locality becomes a significant feature of the macroresponse and the macro-fields become less homogeneous. In the neighborhood of the apex of the force-displacement curve, the deformation process is strongly influenced by the largest macrodefects. In general, a macrodefect (macrocrack or shear band) may form in two ways. Firstly, a macrodefect can form as a result of the loss of stability of a single microdefect of preferential geometry (brittle phenomena such as splitting). The second alternative emphasizes coalescence of a large number of interacting microdefects (localization or quasibrittle failure). A particular specimen may fail in either of these two modes depending on the temperature level, strain rate or the degree of lateral confinement. It is important to note that a material is not brittle or ductile per se. The degree of brittleness or ductility is a result of a set circumstances, i.e. loading and thermal environment to which the specimen is subjected.

(iii) During the softening regime (in strain controlled experiments) the deformation process is entirely dominated by the geometry of the largest cluster of defects spanning the entire specimen. The geometry of this defect is defined by the extreme statistical momenta of the initial distribution of micro-defects. Consequently, the response in the softening regime is essentially nondeterministic since it depends on the unlikely events (see the experiments on concrete specimens reported in [3]).

Analyses of the material behavior in these three regimes are substantially different. Hence, it is unlikely that a single method incorporating all possible alternatives can be made simple enough to be appealing in applications. The so called mean field theory (MFT) models are suitable for the analyses of systems in which the macro-response is primarily influenced by the volume averages of the micro-fields. In contrast, the percolation theory provides an eminently suitable and computationaly efficient framework for the consideration of systems near the percolation threshold (phase transition).

RELATIONS BETWEEN MACROFIELDS

One of the principal tasks in structural analyses of solids containing microdefects is to determine the expressions relating macrostresses and macrostrains. Assuming that the volume averaging is justified the incremental form relating volume average stresses $\sigma(\mathbf{x})$ and volume average strains $\varepsilon(\mathbf{x})$ is in the isothermal case

$$d\varepsilon = \mathbf{S} : d\sigma + d\mathbf{S} : \sigma + d\varepsilon^p \tag{1}$$

where $\mathbf{S}(\mathbf{x},H)$ is the fourth rank compliance tensor and $d\varepsilon^p$ the conventional plastic strain tensor. The components of the compliance tensor $\mathbf{S}$ depend on the concentration, shape, size and orientations of microdefects as defined by a set of parameters constituting the recorded history H, at each material point Thus, the total increment in strain $d\varepsilon$ is a sum of elastic and inelastic strain increments

$$d\varepsilon = d^e\varepsilon + d^i\varepsilon \tag{2}$$

The inelastic increment of the strain (as history is recorded $H \rightarrow H + dH$, implying dissipation of energy)

$$d^i\varepsilon = d\mathbf{S} : \sigma + d\varepsilon^p \tag{3}$$

incorporates both brittle and ductile components, i.e. changes in compliance (attributable to change in microcrack density) and plastic strain. The elastic strain increments are defined by the first term on the right-hand side of equation (1).

In conclusion, for given macrostress σ and its increment, the rate of change of the macrostrain $d\varepsilon$ can be computed from (1) provided that the effective compliance tensor $\mathbf{S}(H)$ and its rate of change $d\mathbf{S}$, along with change in the plastic strain, can be determined as a function of the change in the recorded history dH.

This presentation will focus on the first of these two tasks related to the formulation of the effective compliance tensor $\mathbf{S}(H)$ of an elastic matrix weakened by a distribution of microdefects. In contrast to most of the existing studies of this type the present one will not be limited to small-to-moderate concentration of defects.

MACROCOMPLIANCES - MEAN FIELD APPROXIMATIONS

The initial task in establishing the algorithms needed to compute the macrostrains and their rates of change from expression (1) consists of a rational, simple and reasonably accurate determination of the macro-compliance $\mathbf{S}(H)$ of a macro-homogeneous solid containing a large number N of inhomogeneities (voids, cracks and other microdefects). The problem is, obviously, associated with local fluctuations in stress and strain fields attributable to the microdefects. As shown in [4] these fluctuations can, at least in principle, be rigorously determined solving a system of N coupled integral equations. In cases of current interest N is, by definition, a very large number. Moreover, the kernels of the above mentioned integrals are complicated tensorial functions combining derivatives of the Green's function for displacements and tensors of elastic moduli. Consequently, a rigorous solution of the problem is feasible only when the matrix is homogeneous, isotropic and linearly elastic and when the defects are of simple geometry forming regular, periodic patterns.

In typical engineering materials neither of these conditions is satisfied. Even when the stress and defect fields are originally periodic (as in the case of plates joined by lines of rivets) the defect growth emphasizes increasing disorder. As shown by [5, 6] a self-similar growth of an initially periodic crack pattern represents a thermodynamically unstable path. Therefore, a physically appropriate model must emphasize the randomness of the microdefect pattern and pattern evolution.

In view of the extensive literature devoted to the determination of elastic parameters of materials containing defects (see, for example books [4, 7, 8, 9] and a long list of papers and state-of-art reviews) a comprehensive recital of all relevant details and existing models might, indeed, verge on being redundant. Nevertheless, a precis on main aspects of the theory, in the spirit of the recent [10] summary is needed to provide for a better understanding of the forthcoming arguments.

In general, most if not all of the existing models start from consideration of a homogeneous, linearly elastic material occupying a finite volume V which contains a statistically significant sample of microcracks and microvoids. Assuming that the defects are small in size in comparison to the characteristic length of the representative volume element V, it seems reasonable to assume that the macrofields can be computed simply by volume averaging of the corresponding microfields. In this case it can be shown [11, 12, etc.] that the expression for the overall compliance tensor allows for the additive decomposition

$$\mathbf{S}(\mathbf{x},H) = \mathbf{S}(\mathbf{x}) + \mathbf{S}^*(\mathbf{x},H) \qquad (4)$$

into the compliance tensor **S** of the virgin, elastic matrix and the compliance **S*** attributable to the presence of the microdefects. The compliance tensor **S*** can be determined in several different manners.

Derivation of expressions for the components of the compliance tensors **S*** and **S** (and/or elastic parameter tensors **C*** and **C**) is a matter of convenience and desired level of rigor. The expressions for the components of the tensor **S*** can be often derived using the already available formulas for the displacements in a point on the void perimeter. When formulas for the displacements are not available they can be, at least in principle, derived from the corresponding Green's function [4, 8]. More often than not these derivations are too arduous to be truly competitive with other methods. The other possibility is to apply the Eshelby inclusion method [8]. However, a direct connection exists [12] between the Eshelby inclusion method and the method based on the direct use of the expression for the displacements of the points on the void perimeter.

Within the space constraint of this paper an exhaustive appraisal of various mean-field models is obviously not possible. Instead it suffices to discuss in a rather superficial manner the three most frequently used models. The simplest model is the so-called dilute concentration (or Taylor's) model which entirely ignores the microdefect interaction. In the case of the self-consistent model each microdefect is influenced by the other microdefects only indirectly through the use of the overall effective compliance. The so-called differential method is based on essentially equipolent assumptions as the self consistent method. Generally speaking, common to all mean field (first order effective continua) theories are the following assumptions:

(a) the external stress field (far field) of each microdefect is assumed to be equal to the far field (macro) stresses,

(b) the external fields for each microdefect weakly depends on the exact positions of adjacent microdefects and is equal to the volume/area averaged microfields, and

(c) the characteristic length of the largest microdefect is small in comparison to the linear dimension of the volume over which the averaging is performed.

The first of these three assumptions eliminates the need for computing local stress fluctuations. The second assumption represents a major simplification by eliminating from considerations the exact position of each defect. Simultaneously, this assumption limits the application of mean field methods to low-to-moderate concentrations of microdefects. At higher concentrations the interaction becomes more important necessitating knowledge related to the statistics of distances separating the microdefects. The third assumption is intuitively obvious. Consequently, the mean field theories are inherently incapable of dealing with the critical states which are characterized either by the emergence of a large cluster of coalesced microdefects or by a macrodefect growing from a single microdefect of preferential geometry.

The mean field estimates for the elastic moduli are available in the existing literature for a host of defects of simple geometries. These derivations are especially simple when the overall response is macro-homogeneous. In a two dimensional, plane stress case of an elastic matrix weakened by randomly oriented rectilinear slits of equal length 2a it is possible to derive the requisite formulas in closed forms. Figure 1 depicts relative loss of elastic modulus as a function of the [13] damage variable Na^2 (where N is the number density, i.e. the number of slits per unit area). First order self-consistent and Taylor estimates are available in [14, 15, etc.]. The second order estimate [16] was determined after substantial computations. The same is true for the so-called replacement scheme [17].

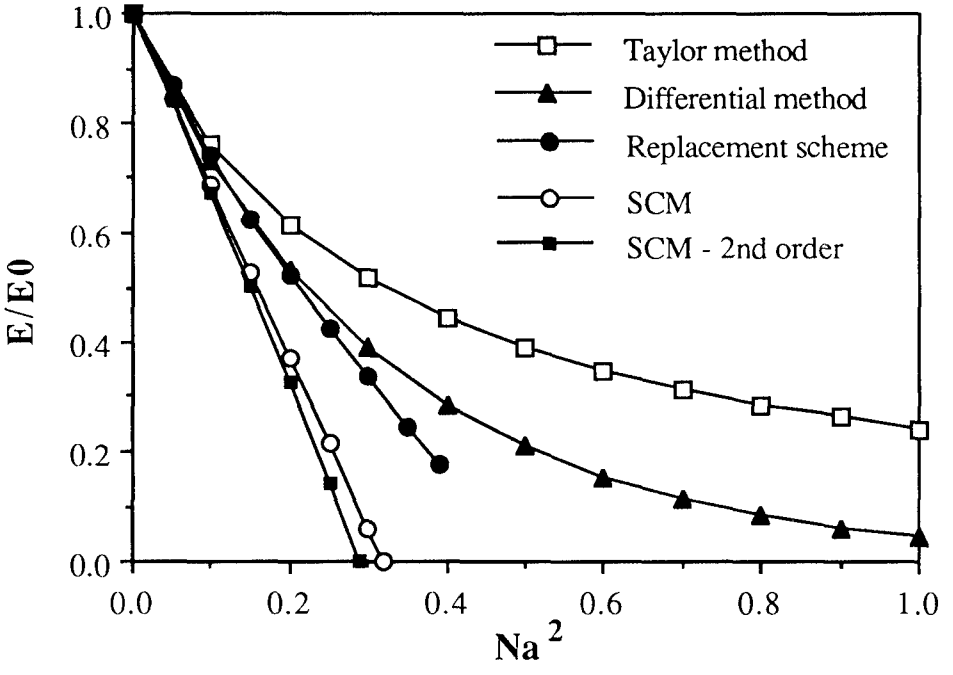

Fig.1. Reduction of elastic modulus as a function of slit concentration.

The analogous analyses are available for the elastic matrix in condition of plane strain perforated by a large number of circular voids of radius a. Figure 2 presents results summarized in [10] in addition to [18] computations and experimental data from [19]. In both cases it was the macrostress which was prescribed at the volume boundary.

Similar analyses are possible and available for rectangular and triangular voids. The derivation of self consistent estimates in cases of defect induced macro anisotropy [11, 12, 15, etc.] requires some computational effort and the results are not always available in a simple analytical form.

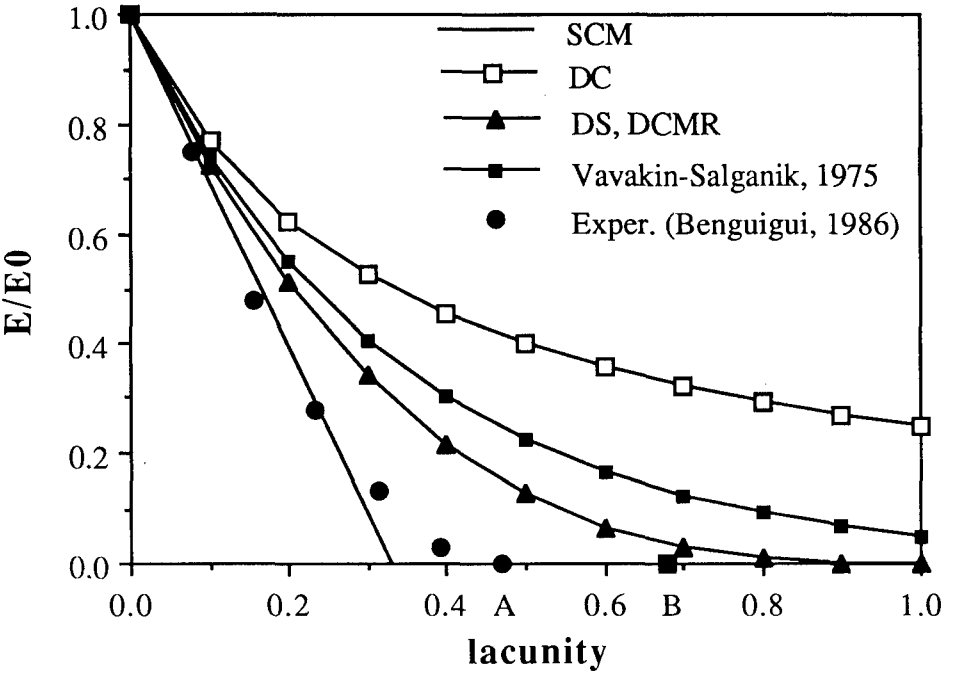

Fig.2. Reduction of elastic modulus as a function of concentration of circular voids (lacunity).

The advantages of the mean field theories are rather apparent from the discussion above and they, at least partially, explain their enduring popularity and omnipresence. The mean field models are obviously firmly based on the underlying physics and geometry of the the microstructure. Secondly, the mean field theory methods have an algorithmically appealing structure allowing for establishment of relatively efficient computational schemes. Nevertheless, these methods are not without shortcomings as pointed out in the literature. Some of the principal shortcomings and deficiencies of the mean field models, having a limiting effect on their applicability, are:

• Statement that the MFT are valid for low-to-moderate microdefect concentration densities is meaningless in absence of a physically justifiable quantitative criterion defining precisely the range of the concentration density within which these methods provide sufficiently accurate estimates.

• In absence of such a criterion and "exact" solutions it becomes impossible to select the most accurate model, i.e. with an exception of the dilute concentration model the choice of a particular approximation simply becomes a matter of preference.

• Eliminating from considerations the exact location of each defect, i.e. the distance between the defects and, thus, their direct interaction, the MFT become unsuitable for considerations of phenomena dominated by defect interaction (hot spots). For example, analyses of localization phenomena require introduction of a length scale absent in MFT models.

• Assumption that each defect is exposed to the average, in contrast to local, stresses becomes suspect for larger defect concentrations.

• The conclusion that macroparameters depends only on volume averages of microdefects is, at the very best, correct for overall moduli. It is intuitively obvious that the brittle rupture strength in most cases depend on the largest defect, i.e. on the extreme moments of the defect distribution (or unlikely events).

• Finally, it is seldom explicitly stated but nevertheless obvious that the largest defect must be much smaller than the linear dimension of the representative volume element (RVE). Otherwise, volume averaging makes little or no sense at all. This, naturally, means that the size of the RVE must be increased as the defects grow (assuming that one is actually appraised of the size of the largest defect). This process can be, at most, continued until the RVE becomes as large as the specimen itself unless in the meantime one of the defects, unbeknown to the analyst, exceeds its critical size.

All of these shortcomings and ensuing limitations are generally known if not always spelled out. Eliminating from considerations the position of defects and local stress fluctuations is exactly the reason for the superior computational efficiency of the MFT models. However, this efficiency is bought at the expense of the rigor and limitations in the range of its applicability. Unfortunately, the exact solutions of a very large system of coupled integral equations is computationaly prohibitive. In fact, since the defects themselves are typically of irregular geometry such a venture would make little sense as well.

Summing up all achievements and limitations of the mean field theories Cleary in [14] with a sense of foresight stated that "until some tractable probabilistic description has been achieved, it seems that a single isolated site model of heterogeneities will have to suffice".

MACROCOMPLIANCES, PERCOLATION MODEL

According to available evidence the mechanical response in the neighborhood of the apex of the force-displacement curve is characterized by increasing heterogeneity of the stress and strain fields as a result of the emergence of large clusters of coalesced defects. These clusters are typically of

random geometry and their sizes are commensurable in length to the smallest linear dimensions of the specimen itself. Once the volume averaging becomes suspect, analyses of topologically disordered microstructures by extensions, modifications and assorted reincarnations of the mean field, or similar deterministic models becomes a lost cause. In agreement with [14] the only rational strategy involves considerations based on the methods of statistical nature.

A class of methods, steadily gaining popularity in many fields of statistical physics dealing with critical phenomena, belongs to the general framework of the percolation theory. As already stated the percolation theory provides a powerful and efficient framework for the study of processes and systems in the close neighborhood of the critical state (or percolation threshold) defined as emergence of an infinite cluster. The principal objective of these studies is focused on the determination of certain universal laws and quantities which emerge from an otherwise random process and random geometry. All processes and systems having identical or nearly identical universal parameters form a universal class. These parameters are universal in the sense that they do not depend on the microstructure of the specimen, i.e. details of the distribution of defects, inhomogeneities, inclusions, etc..

Dilution of a homogeneous, elastic matrix by voids and/or crack-like defects constitutes one of these universal classes. The percolation studies of the problems and systems belonging to this class center on the determination of critical lacunity (i.e. critical volume/area defect density) f_{cc} and scaling law for the specimen stiffness $C \propto |f_{cc} - f|^r$ in the neighborhood of the percolation threshold $f \rightarrow f_{cc}$. The difference $|f_{cc} - f|$ is the proximity parameter and r (typically not an integer) is the universal exponent. It is notable that the percolation threshold f_{cc} depends to some extent on the microstructure of the material (i.e. distribution of bonds within the material microstructure). This is not only expected but also a physically justifiable consequence of the fact that the rupture depends on the crystalline structure of the material. In contrast, the scaling laws for the stiffness C and some other parameters are truly universal. In other words, the universal exponent r is for each of these parameters independent of the details of the microstructure. Indeed, as a defect cluster grows in size to a macrodefect (macrocrack, shear band, etc.) many times larger than a grain the dependence of the deformation process on the microstructural details becomes negligible. Naturally, the scaling laws in their simplest form $|f_{cc} - f|^r$ implicitly contain the assumption that in the close neighborhood of the percolation threshold all parameters depend only on the infinite cluster and not at all on the other defects and defect clusters. As a result, universal exponents can be obtained from simulations and/or experiments only approximately.

The distinction between the elastic percolation studies and more traditional inquires into conductivity (permeability) problems is readily appreciated from the following physical argument. In terms of conductivity, percolation takes place as soon as an infinite cluster at $f = f_c$ traverses a

specimen, connecting its opposite sides (i.e. forming a bore-hole). The loss of rigidity of the specimen will, however, occur only when the infinite cluster transects the specimen into two or more finite size fragments. The corresponding defect volume density $f = f_{ce}$ is in a three dimensional case larger than f_c. In two dimension the two percolation thresholds coincide with each other, since a cluster which traverses a specimen transects it at the same time.

In general, universality depends on the dimensionality of the problem, number of components of the order parameter exhibiting singular behavior and the site connectedness. An order parameter is a mechanical variable undetermined at the percolation threshold, i.e. a parameter which typically exists only on one side of the percolation threshold. In the case of elastic percolation problems, the specimen stiffness $\mathbf{C}(\mathbf{x})$ is a logical choice for the selection of the order parameter since some of its components vanish at the percolation threshold (critical lacunity). The number of the vanishing components of the fourth rank tensor defining the specimen stiffness $\mathbf{C}$ will depend on the defect shape and distribution (orientation).

The percolation thresholds f_{ce} and universal exponents are typically determined by large scale Monte Carlo numerical simulations. The magnitudes cited in the literature (and the subsequent text) refer to infinitely extended systems. Since the numerical simulations on infinite systems are not possible the theoretical values must be corrected using finite size scaling techniques.

Since the universality also depends on the connectedness range a distinction must be made between the cases of: (a) non-overlapping (impermeable or hard core) defects which may join into clusters only by sharing part of their perimeters without intersecting and (b) the overlapping (permeable or soft core) microdefects sharing part of their volume or surface.

The case of non-overlapping voids and/or cracks presents a much simpler problem. For numerical simplicity voids are generally assumed to be equal in size and shape. Void centers are assumed to occupy sites of either regular or random lattices with probability of $q = 1 - p$. At a given fraction of void occupied sites q, each void is, in average, connected to qz neighboring voids, where z is the coordination number or number of nearest neighboring sites. In other words, $q^b z$ is the average number of missing bonds per site of the lattice. The superscript b stands for the bond percolation.

Conversely, the lacunity (porosity) f of the solid may be determined as a product of the fraction of sites occupied by a void q^s and the packing (filling) factor v. Consequently, $q_c^s v$ is the critical lacunity or average number of sites occupied by voids at the percolation threshold. The shape of voids enters computations via their packing (filling) factor v. Superscript s stands for the site percolation model.

The critical lacunity (porosity) f_c of an infinite elastic plate containing critical concentration N_c (number of voids or slits per unit surface area) of voids (plotted in Fig. 2 as point A) can be then written as

$$f_c = v\, p_c^s = N_c\, A_{void} \approx 0.45 \pm 0.03 \qquad (5)$$

As an example consider plates perforated by circular voids with centers located on triangular and square lattices. According to the expression (5) the ability of the plate to transmit external loads will be exhausted at emergence of the infinite cluster, i.e. when the fraction of sites occupied by voids is $q_c^s = 1 - 0.5 = 0.5$ and $q_c^s = 1 - 0.593 = 0.407$, respectively for two considered lattice forms.

The above result contradicts the estimates of the critical lacunity computed on the basis of the cell method. Assuming that the periodicity of defects persists up to the failure leads to a nonconservative estimate of $q_c = 1.0$. Thus, the preservation of periodicity requires twice as much energy as it is needed in the actual process, emphasizing random distribution and growth of defects. The result (5), supported by experiments [19], contradicts the differential method estimates claiming that the macrofailure will occur only at infinite void density. It should be noted that the critical lacunity f_c is independent on the microstructure of the material (lattice). The dependence on the void shape is reflected through the packing (filling) factor v.

A much more complicated problem ensues if the void centers are allowed to form a truly random network and when the voids are allowed to overlap (intersect or permeate each other). The clusters shapes in this case may assume a large spectrum of irregular forms typically observed in micrographs of rupture surfaces.

A comprehensive recital of the requisite continuum percolation theory methods needed for these analyses would take much more space than accorded to this precis. For the present purposes it suffices to mention that the critical lacunity, i.e. fraction of plate surface occupied by randomly positioned circular voids is independent of loading and dilution sequence. Large scale Monte Carlo simulations [20, etc.] strongly corroborate this statement.

Using the so-called excluded area method [21] the total area of voids at the percolation threshold is for the case of overlapping circular voids equal to

$$f_c = (N\, A_{void})_c \approx 1.13 \qquad (6)$$

This result is somewhat deceiving since a large part of this critical area is in the case of overlapping voids counted more than once. The actual porosity can, in this case, be computed as being $f_c \approx 0.68$ (point B in Fig. 2).

Using similar methods [20, 22, etc.] the critical density of isotropically oriented rectilinear slits of length 2a (allowed to intersect) is again derived as a threshold value of the Budiansky, O'Connell damage parameter

$$\langle N\, a^2 \rangle \approx 1.40 \qquad (7)$$

The determination of the stiffness (or compliance) of an elastic specimen perforated by a dense and random distribution of voids is, at first glance, a formidable assignment offering little or no hope for analytical solution. However, if the objective is limited to the analyses of states at the incipient loss of stiffness, it suffices to focus on the consideration of weakest segments and their contribution to deformability. This problem, in relation to solids weakened by voids, is first addressed by [23] who mapped a perforated continuum on a discrete random lattice (network) known as "nodes-link-blob" (NLB) picture. In the case of circular (spherical) voids the NLB model is familiar under a picturesque sobriquet swiss-cheese model.

The initial step in mapping the perforated continuum on the node-link-blob model consists of constructing the Voronoi tesselation. Each edge of the Voronoi polyhedra is the line equidistant from the centers of the two voids it separates. If the two voids separated by the line do not touch or overlap, this link has a finite strength. The links separating centers of overlapping voids have zero strengths.

The entire structure is now approximated by macrolinks joined at nodes. The distance separating the nodes are proportional to the defect size, i.e. correlation length ξ. Each macrolink consist of microlinks (narrow stretches of segments separating the adjacent voids also known as cutting bonds) and thick parts (blobs) surrounding the nodes. The blobs and microlinks are connected in series. Taking a hint from the behavior of lattices near the percolation threshold, it seems reasonable to assume that the deformability of a macrolink is governed by its flexural stiffness as f tends to f_{ce}. Since the deformability of a link is proportional to the cube of its thickness of the segment ,it seems reasonable to assume that the contributions of blobs and thicker microlinks to the deformation of a macrolink are negligible. Thus, the actual deformability of a macrolink is dominated by the bending rigidity of thinnest microlinks. As the most flexible microlink deforms some of the load is transferred to the neighboring macrolinks. At the incipient loss of rigidity of the specimen every macrolink is loaded up to its capacity. The ultimate loss of rigidity (elastic percolation threshold) is, therefore, the result of a cascade-like sequential loss of bending rigidities of macrolinks. Thus, it is possible to assume that at the incipient loss of rigidity each macrolink has the same rigidity and carries identical load. Consequently, subject to all of these assumptions, the scaling law for the stiffness of the specimen at the percolation limit can be deduced from the flexibility of thinnest segments separating the adjacent voids.

After a long derivation , the scaling law for the axial macrostiffness for the elastic plate perforated by circular voids is obtained is obtained in [24] to be

$$K \sim (f_c - f)^{5.17} \qquad \text{as} \qquad f \rightarrow f_c \tag{7}$$

The extreme flatness of the stress-strain curve in the neighborhood of the percolation threshold makes experiments very difficult. Nevertheless, results measured by [19] are in close agreement with the analytical estimate (7).

SUMMARY AND CONCLUSIONS

In general, the mean field and percolation models are entirely complementary in the sense that they apply in different regimes. In matching, or coupling the estimates for the transport parameters (such as specimen stiffness, diffusivity, conductivity, etc.) computed using the mean field and percolation models a due caution must be exercised in interpretation of these estimates. From the standpoint of the mean field theories, the macro compliance and the average elastic moduli are entirely interchangeable. Knowing all components of the compliance tensor **S** (or tensor of elastic moduli **C**) it is always possible to compute unambiguously the overall (effective) elastic modulus E and Poisson's ratio ν. This is, of course, true as long as the correlation length ξ is much smaller than the linear dimension L_r of the representative volume element and the smallest linear dimension L_s of the specimen itself.

Percolation theory, in contradistinction, deals with systems near or at the incipient emergence of the infinite cluster $\xi \rightarrow \infty$. In the existing literature devoted to statistical physics, which is much more plentiful than the list of the herein referenced papers, the elastic percolation threshold is, somewhat less fortunately, defined as a void volume/surface density at which the elastic or bulk modulus vanishes. In fact, at this point the volume averages are meaningless since no volume exists which contains the largest defect as its characteristic (correlation) length ξ tends to infinity. For example, in a specimen transected into two large fragments averaging their elastic moduli makes absolutely no sense at all.

Thus a correct definition of the elastic percolation threshold would be that at $f = f_{cc}$ when one or, perhaps, more components of the specimen stiffness tensor **C**, defining its capability of transmitting forces in a given direction, vanish. It is in this light that the results of the mean field and percolation theories must be matched.

It is both notable and obvious that in absence of the percolation theory or exact solutions organizing statistics generated by many computations and experiments, the discussions related to the selection of the most accurate mean field theory are not entirely rational. Specifically, the self-consistent model

predicts that the elastic modulus of an elastic plate vanishes when the slit or void density is finite (Figs. 1 and 2). The differential method, based on the same fundamental assumptions, ascertains that the overall elastic modulus E approaches zero only as the slit and/or void density tends to infinity. The question of their relative accuracy, however, is not in their high defect concentration limit. In fact, neither of two is supposed to be valid near that limit. Even though the current percolation studies are suggestive in favoring the self-consistent method, comprehensive examination of the cross-over regime are necessary for more definitive conclusions with regard to relative merits of individual mean field models.

ACKNOWLEDGEMENT

The financial support for the research was rendered by research grants from the Army Research Office, Structural Mechanics Branch, Engineering Science Division and U.S. Department of Energy, Office of Basic Energy Sciences, Engineering Research Program to Arizona State University.

REFERENCES

1. Hansen, A., S. Roux and H. J. Herrmann, 1989, "Rupture of Central-Force Lattices", *J. Phys. France*, Vol. 50, pp. 733-744.
2. Krajcinovic, D. and M. Basista, 1991, "Rupture of Central-Force Lattices-Revisited", *J. Phys. France I*, Vol. 1, pp. 241-245.
3. Hegemier, G. A. and R. H. Read, 1985, "On Deformation and Failure of Brittle Solids: Some Outstanding Issues", *Mech. Mater.*, Vol. 4, pp. 215-229.
4. Kunin, I. A., 1983, Elastic Media with Microstructure II, Three-Dimensional Models, Springer Verlag, Berlin.
5. Bazant, Z. P., 1989, "Stable Stresses and Stable Paths of Propagation of Damage Zones and Interactive Fractures", *Cracking and Damage, Strain Localization and Size Effect,* J. Mazars and Z.P. Bazant, eds., Elsevier Appl. Sci., London, pp. 183-206.
6. Bazant, Z. P. and L. Cedolin, 1991, *Stability of Structures*, Oxford University Press, New York.
7. Shermergor, T. D., 1977, *Theory of Elasticity of Microheterogeneous Media*, Nauka, Moscow, 1977.
8. Mura, T., 1982, *Micromechanics of Defects in Solids*, M. Nijhoff Publ., The Hague.
9. Kreher, W. and W. Pompe, 1989, *Internal Stresses in Heterogeneous Solids*, Akademie-Verlag, Berlin.
10. Nemat-Nasser, S. and M. Horii, 1990, "Elastic Solids with Microdefects", *Micromechanics and Inhomogeneity - The Toshio Mura Anniversary Volume*, G.J. Weng, et al. eds., Springer-Verlag, New York, NY., pp. 297-320.
11. Horii, H. and S. Nemat-Nasser, 1983, "Overall Moduli of Solids with Microcracks: Load Induced Anisotropy", *J. Mech. Phys. Solids*, Vol. 31, pp. 155-171.

12. Krajcinovic, D., 1989, "Damage Mechanics", *Mech. Mater.*, Vol. 8, pp. 117-197.
13. Budiansky, B. and R. J. O'Connell, 1976, "Elastic Moduli of a Cracked Solid", *Int. J. Solids Structures*, Vol. 12, pp.81-97.
14. Cleary, M. P., Chen, I. W. and Lee, S. M., 1980, "Self-consistent Techniques for Heterogeneous Media", *J. Engg. Mech. Div. ASCE*, Vol. 106, EM5, pp. 861-887.
15. Sumarac, D. and D. Krajcinovic, 1989, "A Self-Consistent Model for Microcrack Weakened Solids", *Mech. Mater.*, Vol. 6, pp. 39-52.
16. Ju, J. W.and Chen. T. M. , 1991, "On Two-Dimensional Statistical Micromechanical Damage Models for Brittle Solids with Interacting Microcracks. Part II: Process Models", (to appear).
17. Aboudi, J. and Y. Benveniste, 1987, "The Effective Moduli of Cracked Bodies in Plane Deformations", *Engg.Fracture Mech.*, Vol.26, No.2, pp. 171-184.
18. Vavakin, A. S. and Salganik, R. L., 1975, "Effective Characteristics of Nonhomogeneous Media with Isolated Nonhomogeneities", *Izv, AN SSSR. Mekhanika Tverdogo Tela*, Vol. 10, pp 65-75.
19. Benguigui, L., 1986, "Lattice and Continuum Percolation Transport Exponents: Experiments in Two Dimensions", *Phys. Rev. B*, Vol. 34, pp. 8176-8178.
20. Pike, G. E. and C. H. Seager, 1974, "Percolation and Conductivity: A Computer Study", *Phys. Rev. B*, Vol. 10, pp.1421-1446.
21. Krajcinovic, D., M. Basista, D. Sumarac and K.Mallick, 1991, "Elastic Moduli of Perforated Plates in the Neighborhood of Critical State", submitted to *Int.J. Solids. Structures.*
22. Robinson, P. C., 1984, "Numerical Calculations of Critical Densities for Lines and Planes", *J. Phys. A: Math. Gen.*, Vol. 17, pp. 2823-2830.
23. Elam, W. T., A. R. Kerstein, and J. J. Rehr, 1984, "Critical Properties of the Void Percolation Problem for Spheres", *Phys. Rev. Lett.*, Vol. 52, pp. 1516-1519.
24. Halperin, B. I., Feng, S. and Sen, P. N.,1985, "Differences Between Lattice and Continuum Percolation Transport Exponents", *Phys. Rev. Lett.*, Vol. 54, pp. 2391-2394.

A STATISTICAL-MICROMECHANICS MODEL FOR PARTICULATE MATERIAL

Ching S. Chang

Department of Civil Engineering
University of Massachusetts, Amherst, MA. 01003

INTRODUCTION

Mechanical behavior of granular media is important in many fields of studies such as soil mechanics, powder mechanics, and ceramic mechanics. The mechanical behavior of granular media has been studied by borrowing the stress-strain models, such as elastic, elasto-plastic, or plastic models, developed for continuum materials. These continuum models consider neither the discrete nature nor the deformation mechanism of granular materials.

A more rational approach should be one that considers the granular system as an assemblage of particles. When subjected to loading, the deformation of the granular system results from particle deformation as well as slip between particles. Along this line, the constitutive behavior of granular assemblies is investigated using a micro-mechanics approach, taking into account the interactions between particles. Efforts in this direction can be found in references [1,2,3,4,5,6,7,8]. However, these work have been developed based on Ruess assumption of uniform strain. Thus, the developed stress-strain theories can only be applied to small deformation conditions. They are not suitable in the modelling of failure/damage of granular solid [9].

Effects of higher order strain including particle rotation has been investigated in references [10,11]. Non-uniform strain condition is a significant factor influencing the overall behavior of the granular material, especially in the condition of large deformation. Attempts of including the effect of heterogeneous strain on the constitutive modelling have been made in references [12.13].

Due to the complex nature of interactions among large number of particles, it is necessary to employ statistical methods to consider the non-local interaction within a heterogeneous material. Therefore micro-mechanics and its synergism with statistic theory is a viable way to model such type of material. In this paper, development of such synergism will be addressed and the derived constitutive relationship is illustrated by comparing the predicted

behavior with that measured from sand samples in experiments under various stress conditions.

GENERAL CONSIDERATION

For a granular material, it is possible to define a representative volume element which consists of a large number of particles. From a practical point of view, a necessary characteristic of a granular material is statistical homogeneity. A strict statistical definition of this concept must be expressed in terms of n-point probabilities and ensemble averages, see e.g. [14].

In such a representative volume, the space variation of the field variable such as stress and strain are statistical homogeneous, if the homogeneous boundary conditions are applied, given by either one of

$$u_i(S) = \varepsilon^{o}_{ij} x_j \quad \text{or} \quad T_i(S) = \sigma^{o}_{ij} n_j \tag{1}$$

where ε^{o}_{ij} and σ^{o}_{ij} are constant strain and stress respectively.

When strain ε^{o}_{ij} is prescribed on the boundary, it follows by Hill's principle [15], that the strain averaged over the representative volume $\bar{\varepsilon}_{ij}$ is equal to the strain ε^{o}_{ij}. Conversely, when stress σ^{o}_{ij} is prescribed on the boundary, the stress averaged over the representative volume $\bar{\sigma}_{ij}$ is equal to the stress σ^{o}_{ij}.

It is noted that the representative volume element is completely analogous the infinitesimal element in continuum mechanics. The infinitesimal element in continuum mechanics is in reality a representative element which is composed of a sufficiently large number of particles but has a size sufficiently small in relation to the size of engineering problem. This would imply that the classical field equations of continuum mechanics are assumed valid. And it is of interest to obtain the constitutive relationship between the averaged stress and strain:

THREE-LEVEL MICROMECHANICAL APPROACH

Granular material can be viewed at three levels, namely, 1) representative unit, 2) micro-element, and 3) contact. A

representative unit is defined as an assembly which contains large number of particles to be representative of the granular material. Each particle in the representative unit is in contact with several neighboring particles. These particles form a particle group, termed as micro-element, which is an elementary unit at microscopic level. Each contact within the micro-element between a pair of particles is regarded as the basic unit of granular material. A schematic representation of the three levels of granular material is shown in Fig. 1.

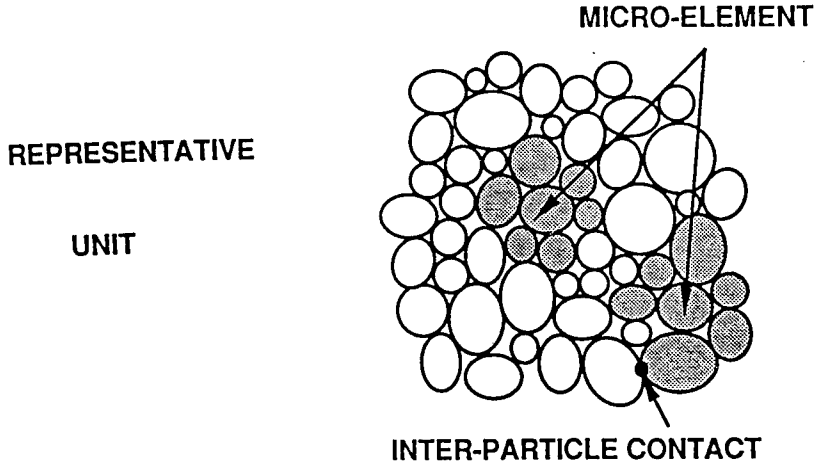

FIG. 1. Schematic figure for three levels of granular material

In the following, we first deal with the translation and rotation of discrete particles which cause the micro-scale discontinuity due to sliding and separation at contact level. At micro-element level, the continuum concepts of stress and strain are introduced accounting for the micro-discontinuity. At representative volume level, the overall behavior is obtained by averaging the behavior of micro-elements with a homogenizing process.

DISCRETE BEHAVIOR AT CONTACT LEVEL

Granular soil is envisioned to be rigid particles connected by imaginary elastic-plastic springs which allow sliding and separation of particles. There are two modes of movement for a particle: translation, u_i, and rotation, ω_i. Based on the kinematics of two rigid particles of convex

shape, the relative displacement $\Delta\delta_i^{nm}$ and relative rotation $\Delta\theta_i^{nm}$ between particle 'n' and particle 'm' at the contact point 'c'.

$$\Delta\delta_i^{nm} = \Delta u_i^m - \Delta u_i^n + e_{ijk}(\Delta\omega_j^m r_k^m - \Delta\omega_j^n r_k^n) \quad (2)$$

$$\Delta\theta_i^{nm} = \Delta\omega_i^m - \Delta\omega_i^n \quad (3)$$

where the quantity e_{ijk} = the permutation symbols used in tensor representation for cross product of vectors.

The relative angular rotation, $\Delta\theta_j^{nm}$, is related to the contact couple. For simplicity, we limit our discussion to particles with convex shape and neglect the effect of contact couples. The relative displacement representing spring-stretch at the contact point 'c', $\Delta\delta_j^{nm}$, is related to the contact force, Δf_i^{nm}, by a incremental expression as

$$\Delta f_i^{nm} = K_{ij}^{nm} \Delta\delta_j^{nm} - \Delta\hat{f}_i^{nm} \quad (4)$$

where K_{ij}^{nm} is the contact stiffness tensor and $\Delta\hat{f}_i^{nm}$ is the residual force in excess of the contact strength in the cases of particle sliding or separation. Shear contact stiffness vanishes after sliding occurs and normal contact stiffness vanishes after separation occurs.

EQUIVALENT CONTINUUM

Since the assembly consists of a large number of particles, it is expedient to treat translation and rotation of discrete particles as continuum fields. On this basis, the discrete system can be transformed into an equivalent continuum and its behavior can be described by the continuum concepts of stress and strain.

With the absence of couple stress of the micro-element, it has been shown [11] that an asymmetric deformation strain can be defined for granular soil in terms of the continuum variables $u_{i,j}^n$ and $\Delta\bar{\omega}^n$ in the following manner:

$$\Delta\varepsilon_{ij}^{n} = \Delta u_{i,j}^{n} + e_{ijk}\,\Delta\bar{\omega}_{k}^{n} \tag{5}$$

The symmetrical part of $\Delta\varepsilon_{ij}^{n}$ is equal to the symmetrical part of displacement gradient, representing the usual symmetric Cauchy strain of the micro-element. The skew symmetric part of $\Delta\varepsilon_{ij}^{n}$ represents the net spin of particles (i.e., the difference between rigid body rotation of the micro-element and the average rotation of particles).

The strain defined in this way not only is theoretically more generic but also furnishes a convenient kinematic relationship which relates strain to the spring stretch, $\Delta\delta_{i}^{nm}$, at the contact between the center particle 'n' and its neighbor particle 'm', given by

$$\Delta\delta_{i}^{nm} = \Delta\varepsilon_{ij}^{n}\, L_{j}^{nm} \tag{6}$$

where, L_{j}^{nm} is the branch vector joining the centroids of particle 'n' and particle 'm'. Note that $L_{j}^{nm} = r_{j}^{nc} - r_{j}^{mc}$, and r_{j}^{nc} = the vector measured from the centroid of the particle 'n' to the contact point 'c'.

The relationship between the contact forces and the stress of the micro-element can be defined by employing the theorem of stress mean [11, 16]. The local stress $\Delta\sigma_{ij}^{n}$ is expressed as the volume average of the dyadic product of contact force Δf_{j}^{nm} and branch vector L_{i}^{nm}

$$\Delta\sigma_{ij}^{n} = \frac{1}{2V^{n}} \sum_{m} L_{i}^{nm}\,\Delta f_{j}^{nm} \tag{7}$$

where V^{n} is the volume associated with the n-th micro-element. Summation of the volume V^{n} over all micro-elements is equal to the total volume of the representative unit, such that $V = \sum_{n} V^{n}$.

Based on the following relationships: (1) stress versus contact forces (Eq. 7), (2) force versus spring-stretch at contact (Eq. 4), and (3) strain versus spring-stretch at

contact (Eq. 4). The constitutive equation for the micro-element can thus be obtained in the following incremental form:

$$\Delta\sigma_{ij}^{n} = C_{ijkl}^{n} \Delta\varepsilon_{kl}^{n} + \Delta\hat{\sigma}_{ij}^{n} \tag{8}$$

where C_{ijkl}^{n} is the local stiffness tensor for the n-th micro-element given by

$$C_{ijkl}^{n} = \frac{1}{2V^{n}} \sum_{m} L_{i}^{nm} K_{jk}^{nm} L_{l}^{nm} \tag{9}$$

The stress $\Delta\hat{\sigma}_{ij}^{n}$ in Eq. 8 for the n-th micro-element, resulting from the residual forces due to sliding and separation, is given as follows;

$$\Delta\hat{\sigma}_{ij}^{n} = \frac{1}{2V^{n}} \sum_{m} L_{i}^{nm} \Delta\hat{f}_{i}^{nm} \tag{10}$$

HOMOGENIZATION PROCESS

Here, we consider a given volume to be representative of the granular solid such that the boundaries of the said volume are subject to displacements compatible with a uniform overall strain. Under such conditions, Hill [15] has shown that, for heterogeneous material, the overall stress and strain can be expressed as the volume averages of their corresponding quantities at local level.

Thus the overall stress and strain for the representative unit, denoted by $\Delta\sigma_{ij}$ and $\Delta\varepsilon_{ij}$, are regarded as volume averages of the local stress and local strain at the micro-element level, such that

$$\Delta\sigma_{ij} = \frac{1}{V} \sum_{n} V^{n} \Delta\sigma_{ij}^{n} \tag{11}$$

$$\Delta\varepsilon_{ij} = \frac{1}{V} \sum_{n} V^{n} \Delta\varepsilon_{ij}^{n} \tag{12}$$

Corresponding to the overall stress and strain, it is reasonable to define an overall stiffness tensor for the representative unit such that the overall stress-strain relationship can be expressed in the following form:

$$\Delta\sigma_{ij} = C_{ijkl}\,\Delta\varepsilon_{kl} \tag{13}$$

It is noted that the stiffness tensor C_{ijkl} is not the volume averaged stiffness tensor, $\bar{C}_{ijkl}$, defined by

$$\bar{C}_{ijkl} = \frac{1}{V}\sum_{n} V^{n}\, C^{n}_{ijkl} \tag{14}$$

In a heterogeneous material, the stiffness tensor at any given point can be decomposed into two parts: the average stiffness tensor of the volume and the fluctuation stiffness tensor at this point, given by

$$C_{ijkl} = \bar{C}_{ijkl} + \delta C_{ijkl} \tag{15}$$

At any point in a heterogeneous medium, force equilibrium must be satisfied, thus

$$\Delta\sigma_{ij,i} = (C_{ijkl}\Delta u_{k,l})_{,i} = 0 \tag{16}$$

The equilibrium condition at point 'p' can be expressed with an integral form in the following manner:

$$\int_{V} \Delta\sigma_{ij,i}(q)\; \Delta u^{*}_{jm}(p,q)\; dv(q) = 0 \tag{17}$$

where $\Delta u^{*}_{km}(p,q)$ is a weighted function. Here a function of Green's type is selected such that $\Delta u^{*}_{km}(p,q)$ represents the displacement Δu_{k} at point 'q' due to an unit force f_{m} at point 'p' in a homogeneous medium with $\bar{C}_{ijkl}$. The selected Green's function satisfies the following equation:

$$\bar{C}_{ijkl}\Delta u^{*}_{km,li}(p,q) + \delta_{mj}\delta(p,q) = 0 \tag{18}$$

where $\delta(p,q)$ is the dirac-delta function.

Integrating Eq. 17 by part, the equilibrium equation of integral form with Green's function can be expressed in terms of the displacement at any given point 'p' by

$$\Delta u_m(p) = \int_S t_j(q)\Delta u^*_{jm}(p,q)\ ds(q) - \int_S \Delta u_k(q)\ t^*_{km}(p,q)\ ds(q)$$

$$- \int_S \delta C_{ijkl}(q)\ \Delta\varepsilon_{kl}(q)\ \Delta u^*_{jm,i(q)}(p,q)\ dv(q) \qquad (19)$$

where

$$t_j(q) = C_{ijkl}(q)\ \Delta\varepsilon_{kl}(q)\ n_i \qquad (20)$$

$$t^*_{km}(p,q) = \bar{C}_{ijkl}(q)\ \Delta u^*_{jm,i(q)}(p,q)\ n_l \qquad (21)$$

The displacement at point 'p' is determined not only by the conditions on boundary surface but also by the fluctuation of stiffness and local strains in the heterogeneous material. It is evident from this equation that, for homogeneous material, the displacement at point 'p' can be determined solely by the conditions on boundary surface.

Taking derivative of Eq. 19 to express variables in terms of strain. Eq. 19 can be derived to obtain the strain at location 'p' in the heterogeneous body, given by

$$\Delta\varepsilon_{mn}(p) = \Delta\bar{\varepsilon}_{mn} - \int_V \delta C_{ijkl}(q)\Delta\varepsilon_{kl}(q)\Delta u^*_{jm,in}(p,q)\,dv(q) \qquad (22)$$

where

$$\Delta\bar{\varepsilon}_{mn} = \int_S t_j(q)\Delta u^*_{jm,n}(p,q)\,ds(q) - \int_S \Delta u_k(q)\,t^*_{km,n}(p,q)\,ds(q) \qquad (23)$$

Since the two surface integral terms in Eq. 23 are referring to a representative volume which is sufficiently large compared to the size of an individual particle, employing Hill's principle, the value of $\Delta\bar{\varepsilon}_{mn}$ is equal to the overall strain.

It is noted from Eq. 22 that the strain at point 'p' is affected by the strains at all other points in the volume, showing clearly a non-local effect. For simplicity, let the term of volume integral in Eq. 22 be expressed in reference to the mean strain tensor as:

$$\int_V \delta C_{ijkl}(q)\,\Delta\varepsilon_{kl}(q)\,\Delta u^{*}_{jm,in}(p,q)\,dv(q) = E_{mnkl}(p)\,\Delta\bar{\varepsilon}_{kl} \qquad (24)$$

Then we can relate the overall strain $\Delta\bar{\varepsilon}_{mn}$ to the local strain $\Delta\varepsilon^{n}_{mn}$ by,

$$\Delta\varepsilon^{n}_{ij} = G^{n}_{ijkl}\,\Delta\varepsilon_{kl} \qquad (25)$$

where the dimensionless tensor G^{n}_{ijkl}, associated with each micro-element, is given by

$$G^{n}_{mn} = I_{mnkl} - E^{n}_{mnkl} \qquad (26)$$

where I_{ijkl} is a fourth rank identity tensor defined in terms of Kronecker delta δ_{ij} as

$$I_{ijkl} = \frac{1}{2}\,(\delta_{ik}\delta_{jl} + \delta_{jl}\delta_{ik}) \qquad (27)$$

Since the representative unit consists of large number of randomly arranged particles, the heterogeneous system can be viewed as a statistical homogeneous system. The strain distribution tensor G^{n}_{ijkl} is approximated by,

$$G^{n}_{ijkl} = A_{ijmn}\,\mathrm{Exp}\,(-0.5\nu^{n}_{mnkl}) \qquad (28)$$

where ν^{n}_{ijkl} is a dimensionless tensor as the ratio of the variance of the micro-element stiffness C^{n}_{ijkl} with respect to the average stiffness of the packing $\bar{C}_{ijkl}$, defined as

$$\nu^{n}_{ijkl} = C^{-1}_{ijmn}(C^{n}_{mnkl} - \bar{C}_{mnkl}) \qquad (29)$$

The dimensionless tensor G^{n}_{ijkl}, associated with each micro-element, describes indirectly the degree of heterogeneity of the material. From Eq. 12, the following condition must be satisfied:

$$\sum_{n} G^{n}_{ijkl} = I_{ijkl} \tag{30}$$

Thus, mathematically, G_{ijkl} is a probability density function in tensorial form.

The constant tensor A_{ijkl} involved in the distribution function must satisfy the condition of identity (i.e., Eq. 30). Thus it can be obtained by

$$A^{-1}_{ijkl} = \frac{1}{V} \sum_{n} \mathrm{Exp}(-0.5 v^{n}_{ijkl}) V^{n} \tag{31}$$

With the fluctuation of strain (Eq. 25), using Eqs. 8, 11 and 13, the stiffness tensor C_{ijkl} can be written as a 'weighted' volume average of micro-element stiffness tensor C^{n}_{ijkl}, given by

$$C_{ijkl} = \sum_{n} C^{n}_{ijmn} G^{n}_{mnkl} \tag{32}$$

EXAMPLE

In the present theory, structure of the granular material is intended to be represented statistically by a set of micro-elements where each micro-element is defined by a specific arrangement of particle group. To illustrate the current model, the geometry of five micro-elements were randomly generated; each consists of eight spherical particles with 0.2mm radius. Each micro-element was rotated on the axes 6 times to create six micro-elements as shown in Fig. 2, resulting a total of 30 micro-elements. The idealized material, represented by these thirty micro-elements, has material symmetry along the directions of three axes. The idealized material has an average co-ordination number of 7 and void ratio 0.7, representing an uniformly graded medium dense sand with rounded particles.

To evaluate the capability of the constitutive model at large strain conditions, the stress-strain behavior of this idealized material is predicted for the following loading conditions: one dimensional test, and cubical triaxial tests. The normal and shear contact stiffness, $k_n = k_s = 105$ N/m, are used for the following predictions.

Prediction is made for one-dimensional compression behavior of granular material preceded by isotropic

compression. In this prediction, the inter-particle friction $\phi_\mu = 17^\circ$ is used. The predicted results in Fig. 3 shows that, during loading in the vertical direction, the value of K_o (i.e., the ratio of vertical stress to the horizontal stress) decrease from 1 to a value of 0.4 and remained to be nearly constant. The predicted trend is

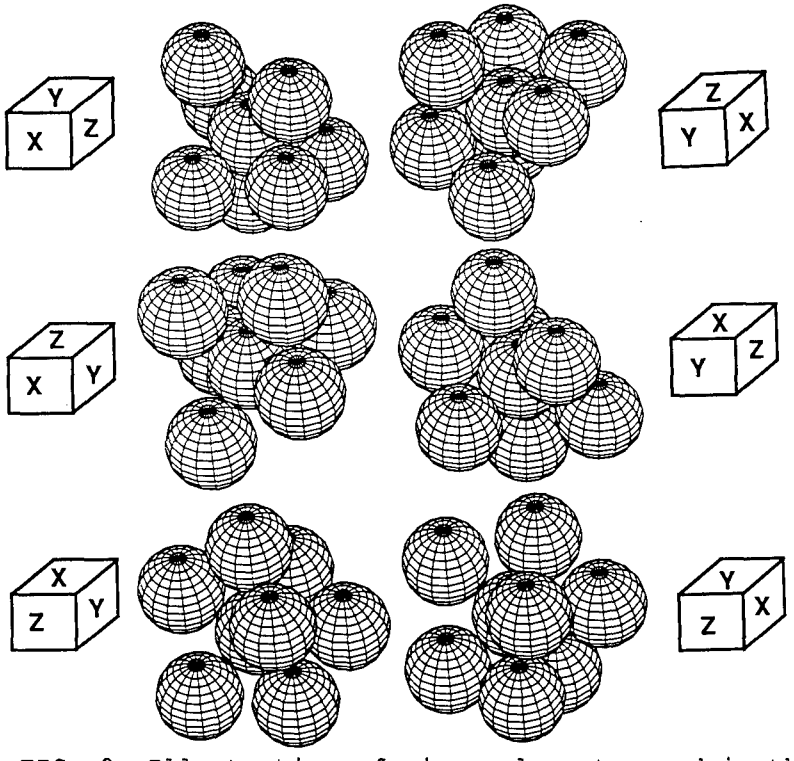

FIG. 2. Illustration of micro-elements used in the example

compared with the experimental results on medium dense Napa Basalt [17] shown in Fig. 3. The prediction gives excellent agreement with the experimental behavior even though the soil structure is hypothetical. It is noted that, at microscopic level, a substantial amount of sliding occurs despite the horizontal movement is constrained.

The constitutive model is used to predict stress-strain and volume change behavior of the idealized granular material under cubical triaxial loading conditions with different values of b, where $b = (\sigma_2-\sigma_3)/(\sigma_1-\sigma_3)$. Figure 4 shows the predicted stress-strain and volume change behavior using ϕ_μ equal to 25°.

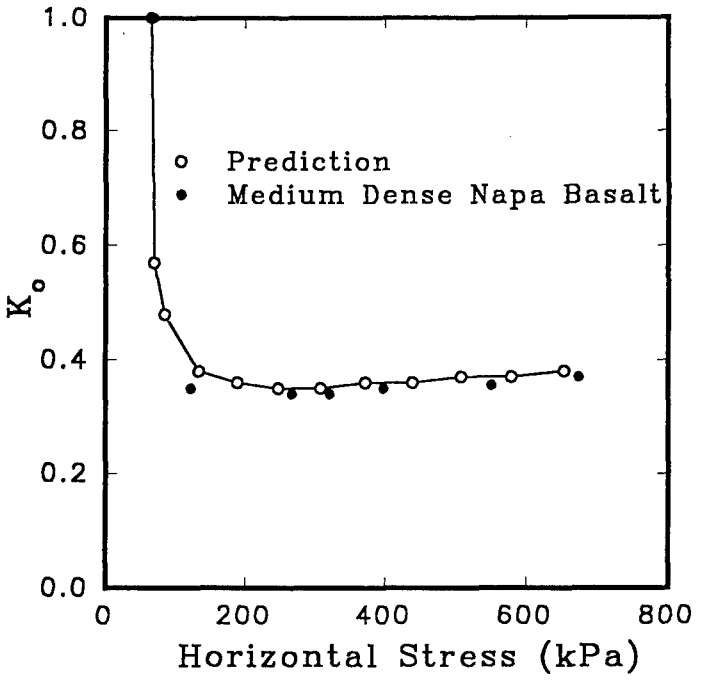

FIG. 3. Predicted one dimensional compression behavior

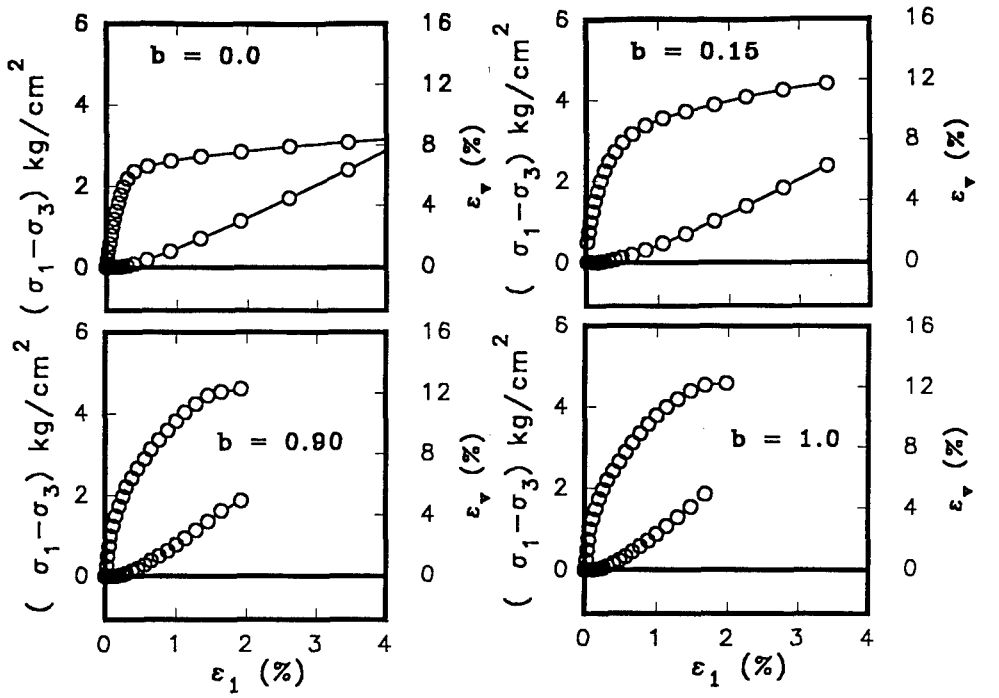

FIG. 4. Computed stress-strain curves for true triaxial condition.

Although the prediction is based on the idealized material represented by 30 micro-elements, the predicted trend of stress-strain and volumetric strain characteristics are remarkably similar to that of experimental values for Monterey sand [18]. The predicted peak frictional angle for various stress conditions are within the range of values experimentally obtained from various types of granular sand [18, 19].

The predicted failure surface on octahedral plane is compared with the failure surfaces empirically hypothesized by Mohr-Coulomb, Matsuoka [20] and Lade and Duncan [18], as shown in Fig. 5. It is the unique capability of the present theory which predicts the failure strength of granular material under complex loading conditions solely on the basis of inter-particle friction property.

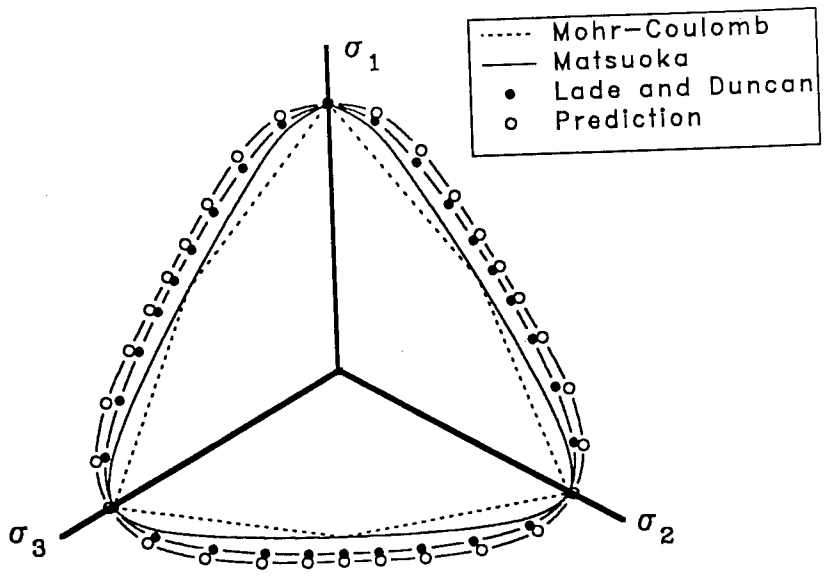

FIG. 5. Predicted failure surface on octahedral plane compared with other hypothesized failure surfaces.

SUMMARY

Perceiving granular material as a collection of particles, a constitutive law for granular material is derived based on micromechanics approach, taking into account the mechanisms of sliding and separation of

particles. The constitutive model explicitly accounts the effects of micro-structure and its evolution, thus is capable of modelling inelastic and failure behavior.

The predicted behavior for an idealized material represented by 30 randomly generated micro-elements, has shown remarkable similarity to the stress-strain behavior observed from experiments under various loading conditions. This agreement in the predicted and measured behavior indicates the potential applicability of this constitutive theory in comprehensive modelling of complex behavior for granular material.

REFERENCES

1. Deresiewicz, H. (1958), "Stress-Strain Relations for a Simple Model of a Granular Medium," Journal of Applied Mechanics, ASME, 402-406.
2. Duffy, J. (1959), "A Differential Stress-Strain Relation for the Hexagonal Close Packed Array," Journal of Applied Mechanics, Trans ASME, 88-94.
3. Duffy, J. and Mindlin, R.D. (1957), "Stress-Strain Relations and Vibrations of Granular Media," Journal of Applied Mechanics, ASME, 585-593.
4. Digby, P.J. (1981), "The Effective Elastic Moduli of Porous Granular Rock", Journal of Applied Mechanics, ASME, Vol. 48, No. 4, 803-808.
5. Jenkins, J.T. (1987), "Volume Chang in Small Strain Axisymmetric Deformations of a Granular Material", Micromechanics of Granular Materials, Eds. M. Satake, and J.T. Jenkins, Elsevier, Amsterdam, The Netherlands, 143-152.
6. Walton, K. (1987), "The Effective Elastic Moduli of a Random Packing of Spheres", Journal of Mechanics and Physics of Solids, Vol. 35, No. 3, 213-226.
7. Bathurst, R.J. and Rothenberg, L. (1988), "Micromechanical Aspects of Isotropic Granular Assemblies with Linear Contact Interactions", Journal of Applied Mechanics, ASME, Vol. 55, 17-23.
8. Chang, C.S. (1988), "Micromechanical Modelling of Constitutive Equation for Granular Material," Micromechanics of Granular Materials, Edited by J. T. Jenkins and M. Satake, Elsevier Science Publishers, 271-278.
9. Chang, C.S. and Misra, A. (1990b), "Application of Uniform Strain Theory to Heterogeneous Granular Solids," Journal of the Engineering Mechanics Division, ASCE. Vol. 116, No. 10, 2310-2328.
10. Chang, C.S. and Liao, C. (1990), "Constitutive Relations for Particulate Medium with the Effect of Particle

Rotation," International Journal of Solids and Structures, Vol. 26, No. 4, 437-453.
11. Chang, C.S. and Ma Lun (1990), "Modelling of Discrete Granulates as Micropolar Continuum," Journal of the Engineering Mechanics Division, ASCE. Vol. 116, No. 12, 2703-2721.
12. Misra, A. (1990), "Constitutive Relationships for Granular Solids with Particle Slidings and Fabric Changes," Ph.D. dissertation, University of Massachusetts.
13. Chang, C. S., and Misra, A. (1991), "Stress-Strain Modeling of Heterogeneous Granular Solid Based on Micromechanics," Proceedings of the Third International Conference on Constitutive Law for Engineering Materials, Tucson, Arizona, pp.501-504.
14. Beran, M. J. (1968), Statistical Continuum Theories, Wiley, New York.
15. Hill, R. (1967), "The Essential Structure of Constitutive Laws for Metal Composites and Polycryctals," Journal of Mechanics and Physics of Solids, Vol. 15, No. 2, 79-95.
16. Christoffersen, J., Mehrabadi, M.M. and Nemat-Nasser, S. (1981), "A Micromechanical Description of Granular Material Behavior", Journal of Applied Mechanics, Vol. 48, No. 2, 339-344.
17. Lade, P.V. (1975), "Elasto-Plastic Stress-Strain Theory for Cohesionless Soil with Curved Yield Surfaces," Report No. UCLA-ENG-7594, Soil Mechanics Laboratory, University of California at Los Angeles, 97.
18. Lade, P.V., and Duncan, J.M. (1973), "Cubical Triaxial Tests on Cohesionless Soil," Journal of the Soil Mechanics and Foundations Division, ASCE, Vol. 99, No. SM10, 793-812.
19. Reades, D.W., and Green, G.E. (1974), discussion, Journal of the Soil Mechanics and Foundations Division, ASCE, Vol. 100, No. GT9, 1065-1067.
20. Matsuoka, H. (1974), "Stress-Strain Relationships of Sands Based on the Mobilized Plane," Soils and Foundations, Vol. 14, No. 2, 47-61.

THE ROLE OF MICROSTRUCTURE IN THE DEFORMATION AND FAILURE OF TUNGSTEN HEAVY ALLOYS

J. Lankford
A. Bose
H. Couque
C. E. Anderson

Southwest Research Institute, San Antonio, Texas 78228-0510

Introduction

The application of tungsten heavy alloys (WHA) to the problem of kinetic energy penetration requires knowledge of the behavior of the material at high strain rates. Two issues are of particular concern, most obviously the ability of an alloy to resist dynamic tensile mode loading generated by projectile launch and subsequent flexure. In addition, it recently has been shown (1) that the penetration ability of depleted uranium (DU) appears to reside in its ability to undergo localized adiabatic shear failure and thereby self-sharpen. Tungsten-based penetrators have thus far not shown such behavior, and there is much interest in establishing a basis for changing this.

Unfortunately, while considerable past effort (2-10) has been devoted to generating stress-strain data for WHA subject to both static and dynamic tensile, compressive, and even torsional loading, relatively little light has been shed on the actual micromechanisms responsible for strain rate sensitive deformation and failure. In addition, most studies have involved minimal microstructural variation, so that the possible roles of grain size, prior deformation, and so forth have been difficult to assess. Accordingly, the authors have begun a systematic study of the influence of microstructural parameters in the development of damage in WHA. The objectives of this paper are to integrate both recent (11-14) and new results into a general picture of the critical microscale events involved in dynamic tensile and compressive (local shear) failure, and to assess the potential for controlling material response by microstructural alteration.

Materials

Four generic alloys were chosen for study, all based on 90-91 weight percent tungsten; their elemental makeup, corresponding designations, and tungsten grain sizes are given in Table I. As shown in Figure 1, these materials actually are composites composed of essentially pure, body-centered cubic tungsten dispersoids embedded within a tungsten-rich (typically 16-24 w/o) face-centered cubic matrix. All the alloys were prepared by liquid phase-sintering, and all of them were studied as-sintered. The Ni-Co alloy, however, also was prepared in a highly worked (swaged 25% and aged) condition. The latter is shown in Figure 1c, where the elongated W-grains are evident.

Table I. - Materials		
Designation	Composition (wt %)	Grain Size (μm)
8Ni-2Fe	90W-8Ni-2Fe	24
7Ni-3Fe	90W-7Ni-3Fe	16
Ni-Co	91W-6Ni-3Co	23
Ni-Mn	90-4Ni-6Mn	7

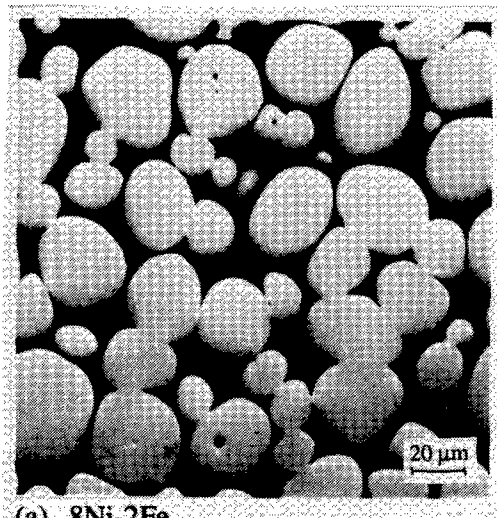

(a) 8Ni-2Fe

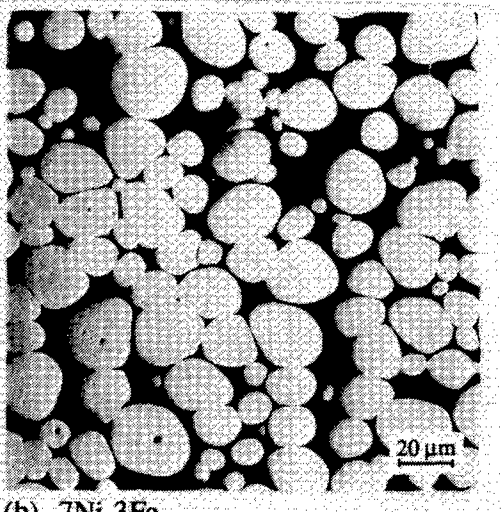

(b) 7Ni-3Fe

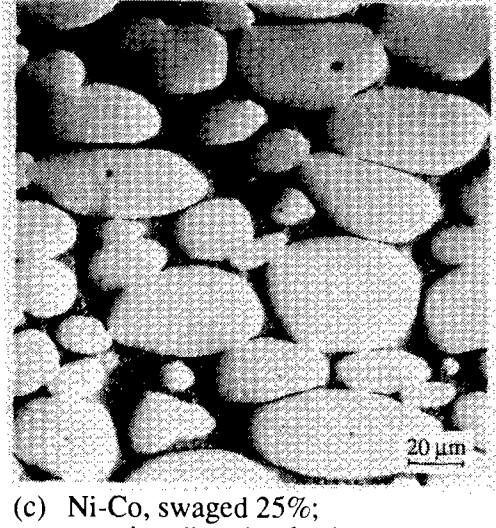

(c) Ni-Co, swaged 25%;
swaging direction horizontal

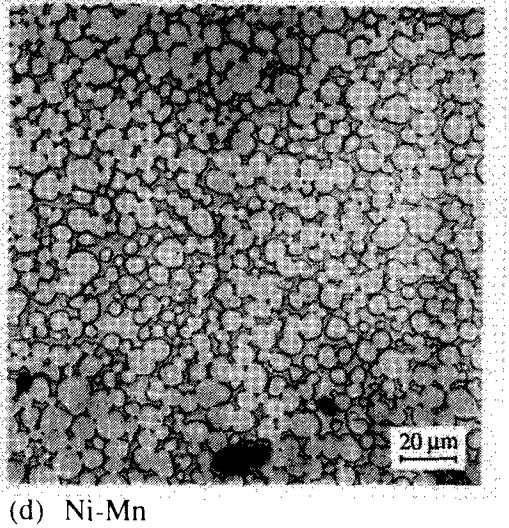

(d) Ni-Mn

Figure 1 - Alloy microstructures viewed at same magnification: tungsten grains (and precipitates) in relief due to preferential polishing of matrix.

Several other microstructural features are pertinent to the study. For example, the 8Ni-2Fe alloy was particularly "clean," i.e., homogeneous and pore-free, while the 7Ni-3Fe was characterized by a more inhomogeneous W-grain distribution and a significant pore population. Porosity also was present in the Ni-Mn (Figure 1d), an alloy whose matrix should, on the basis of these micromechanical considerations, be particularly prone to adiabatic shear. In the case of the Ni-Co alloy, the Co constituent reduced the ability of the matrix to maintain W in solution, resulting in a dispersion of fine tungsten precipitates throughout the matrix (Figure 1c). It should be noted that the Ni-Mn alloy turned out, because of its porosity, to be prone to premature, flaw-induced tensile failure.

Particularly important to the mechanical response of the alloys are the two distinct types of interface present in the microstructure. The first constitutes the two-phase boundary between W-grains and the matrix, while the second represents flat, roughly circular, direct single-phase contact between tungsten grains. To the extent that alloy constituents are able during processing to wet the latter surfaces, local bonding at W-W interfaces may be somewhat variable.

Experimental Procedures

Quasistatic compressive and tensile tests were performed at a strain rate of $10^{-4}s^{-1}$ using a servo-controlled hydraulic test machine under displacement control conditions. Dynamic tests, corresponding to strain rates of $600s^{-1}$ to $5500s^{-1}$, were run in a split Hopkinson pressure bar adapted for both compressive (15) and tensile (16) modes of loading. Compression specimens consisted of right circular cylinders 6.35 mm in diameter by 12.7 mm in length; tensile specimens were 3.18 mm in diameter, with 7.62 mm gage lengths. All compression tests were performed using unlubricated interfaces between samples and loading platens. The specimen barreling which resulted was desired, as it produced a state of stress within the specimen which tended to promote local shear.

In the following section, the results of "dynamic" tensile experiments performed at strain rates on the order of $1000s^{-1}$ are compared with compression tests run at $1000s^{-1}$ to $2000s^{-1}$. Another set of compression experiments was performed at a higher rate of loading, corresponding to a strain rate of approximately $5500s^{-1}$ and a strain of about 0.5, to afford maximum opportunity for the development of unstable shear bands.

After failure, tensile fracture surfaces were characterized by scanning electron microscopy (SEM), and some specimens were sectioned for evidence of early stages of damage. Compression specimens were likewise sectioned parallel to the load axis, polished, and examined by SEM.

Results

Shown in Figures 2, 3, and 4 are true stress (σ) - true strain (ε) curves for 8Ni-2Fe, 7Ni - 3Fe, and Ni-Co, all in the as-sintered state. It is evident that yield strengths,* flow stresses, and hardening rates for these materials are similar in both tension and compression at each strain rate. The principal difference between the data sets is the distinctly lower (tensile) ductility obtained for the 7Ni-3Fe material under quasistatic conditions, while the high strain rate elongations are virtually identical for all three materials. It appears that the primary effect of increasing the loading rate is to dramatically elevate the yield point, with a slight decrease of the hardening rate, while concurrently lowering the ductility. At both strain rates, tensile and compressive flow curves gradually deviate from one another with increasing strain, so that tensile failure occurs at a stress level significantly below the corresponding (equivalent strain) point in compression. However, beyond a certain strain, the tensile stress is nominal, in that necking occurs; similarly, the compression samples all bulge at their midsections with increasing strain, deviating from the ideal cylinder configuration assumed for the true stress computation. The combination of these two factors accounts for most of the apparent tension-compression stress differential shown in the figures.

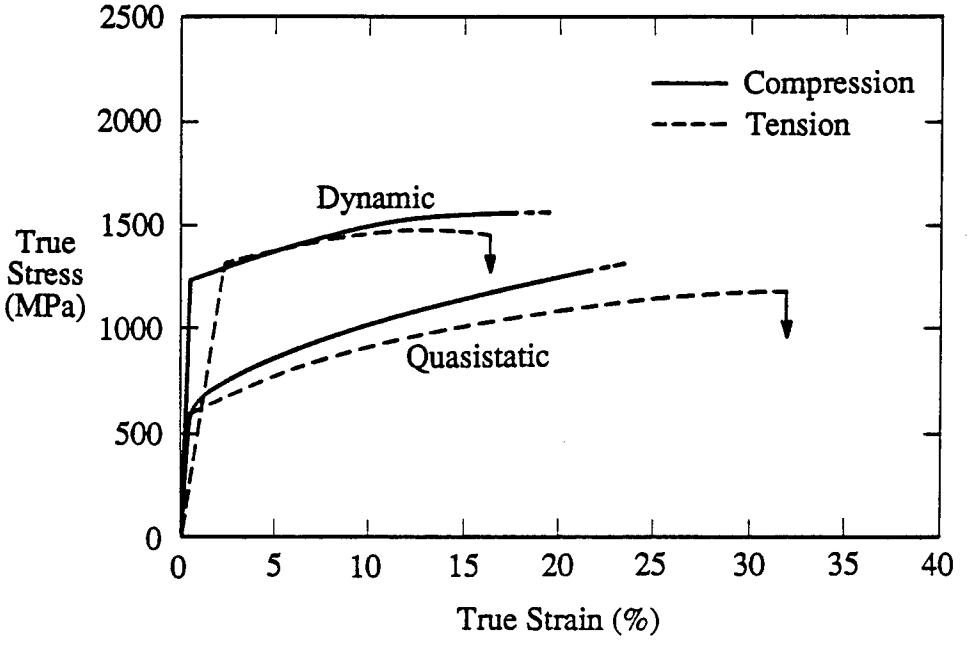

Figure 2 - Deformation behavior of as-sintered 8Ni-2Fe alloy.

* Approximate dynamic yield strengths result from extrapolation of the early Pochhammer-Chree oscillations in the sample, using a best-fit procedure and back-extrapolation of the unambiguous data for strains greater than a few percent.

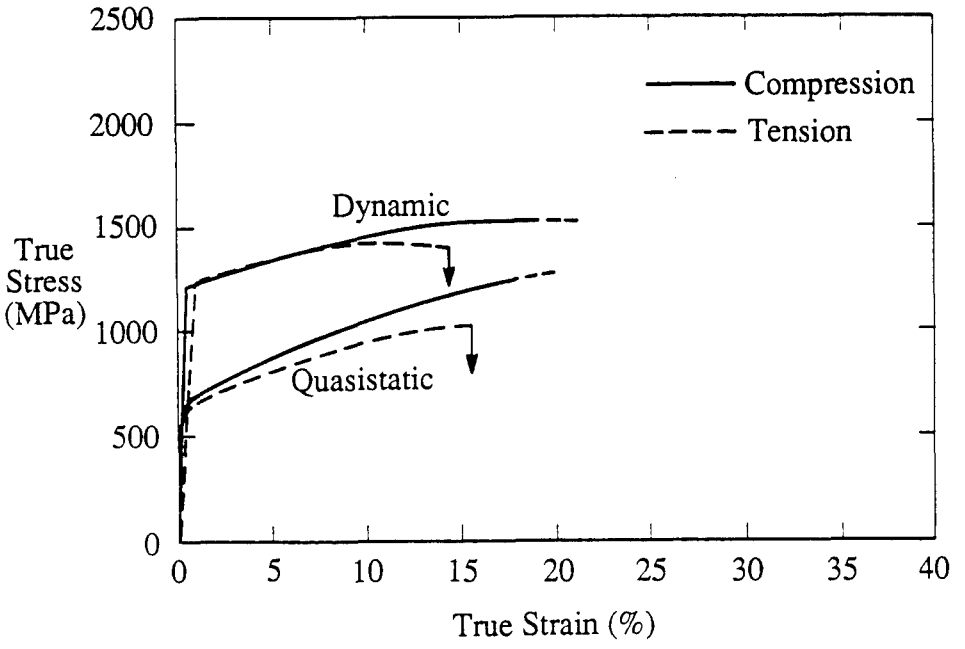

Figure 3 - Deformation behavior of as-sintered 7Ni-3Fe alloy.

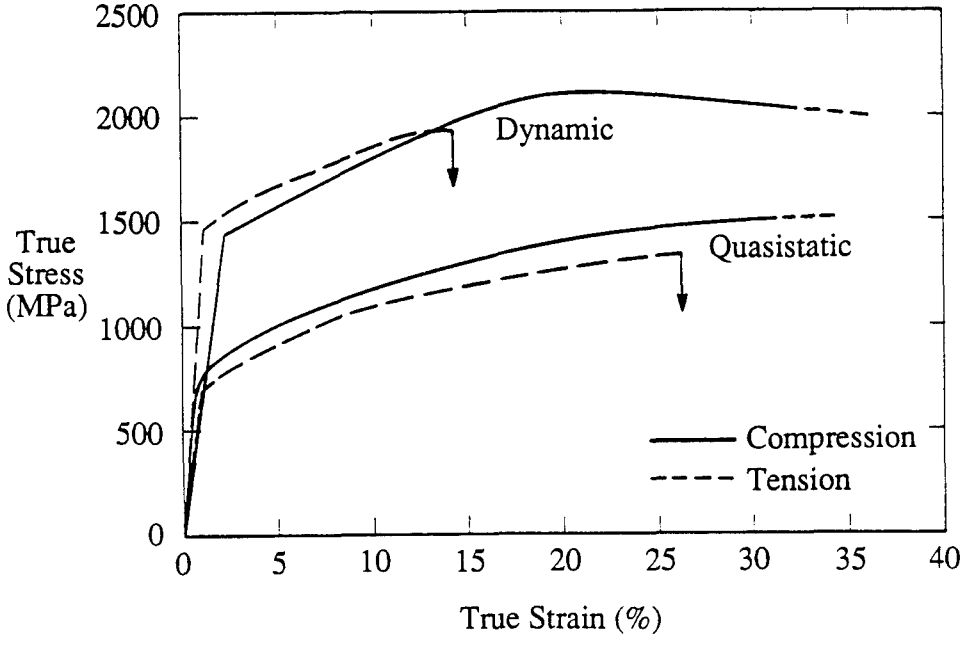

Figure 4 - Deformation behavior of as-sintered Ni-Co alloy.

Swaging alters the above picture dramatically. First (Figure 5), the average flow stress is increased, while the rate of strain hardening is greatly reduced. Under dynamic tension, in fact, the strain hardening coefficient now is negative. Yield points appear to be raised, with one exception; in the case of quasistatic compression, the deviation from elastic linearity occurs at approximately the same value of stress as for the unswaged material (Figure 4). Finally, both the quasistatic and dynamic ductilities of the swaged Ni-Co are drastically lowered, versus the corresponding values for all three of the as-sintered alloys.

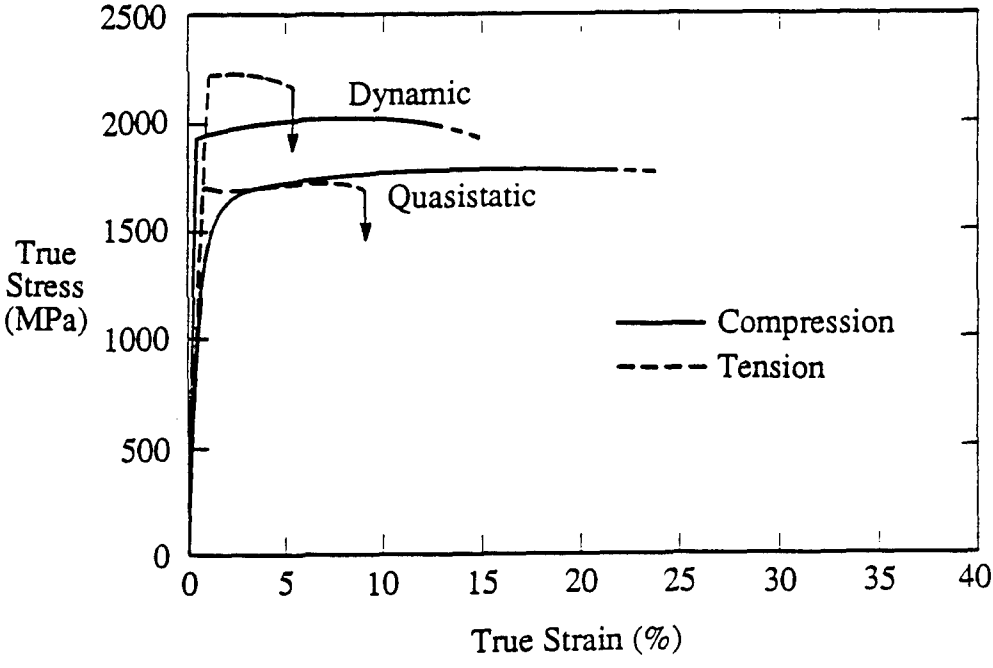

Figure 5 - Deformation behavior of 25% swaged Ni-Co alloy.

Characterization of tensile fracture surfaces by SEM shows that regardless of microstructure, the overall fracture at quasistatic loading rates is predominantly composed of cleared tungsten grains (Figure 6). Failed intergranular matrix zones also are observed, composed primarily of dimples; in the case of Ni-Co alloy, W-precipitates lie within the dimples. Under dynamic conditions, however, the most prominent fractographic features are W-W facets (Figure 7), surrounded by two variants of matrix failure. In the first case (8Ni-2Fe and 7Ni-3Fe), the facets generally lie at the centers of large dimples created by W-matrix decohesion (following W-W microfracture) to form contiguous ligaments. These eventually separate by void sheet nucleation and coalescence, or by tensile ligament shear failure (Figure 7a, b). In the second case, involving Ni-Co in both as-sintered and swaged conditions, there is little W-matrix decohesion following W-W fracture, and the latter facets are connected by extensive sheets of tungsten precipitate-nucleated microvoids (Figure 7c, d). Additionally, the overall fracture is more evenly divided between W-W cleavage and intragranular microfracture.

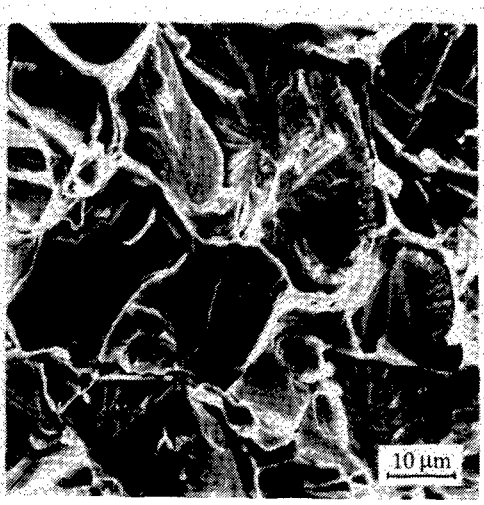

(a) 8Ni-2Fe

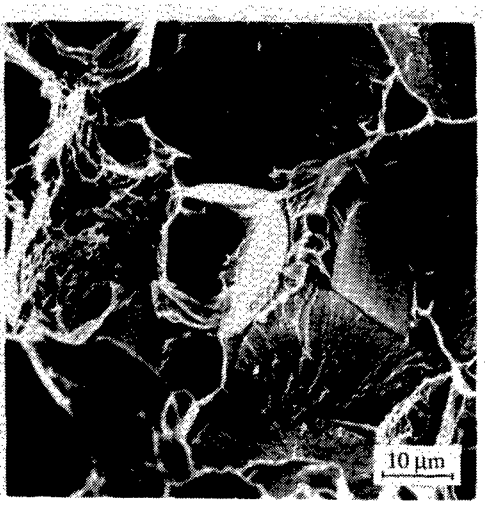

(b) 7Ni-3Fe

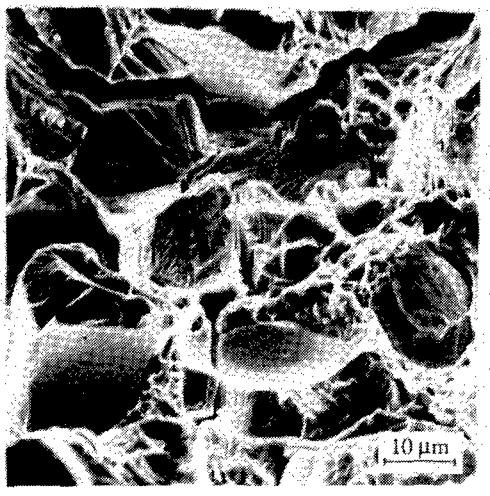

(c) Ni-Co, (as-sintered)

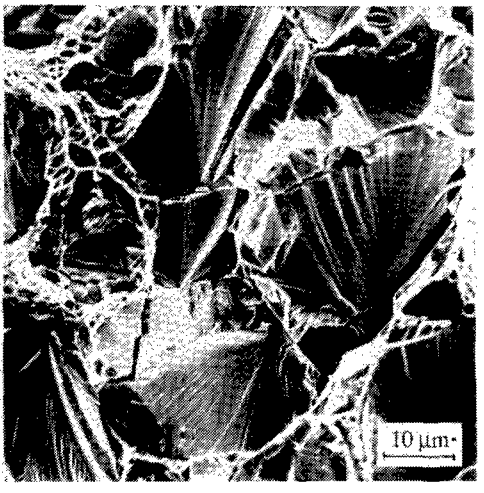

(d) Ni-Co (swaged 25%)

Figure 6 - Quasistatic fracture surfaces ($\dot{\varepsilon} = 10^{-4}s^{-1}$).

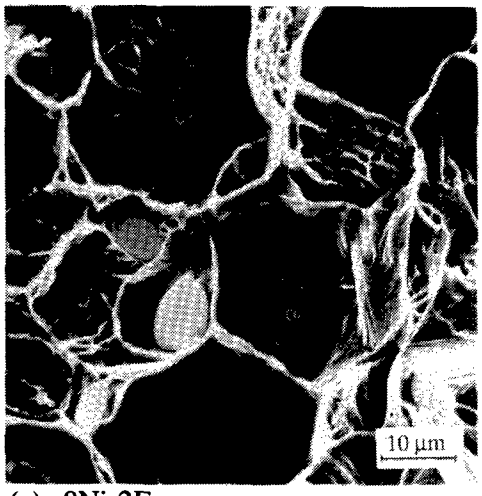

(a) 8Ni-2Fe

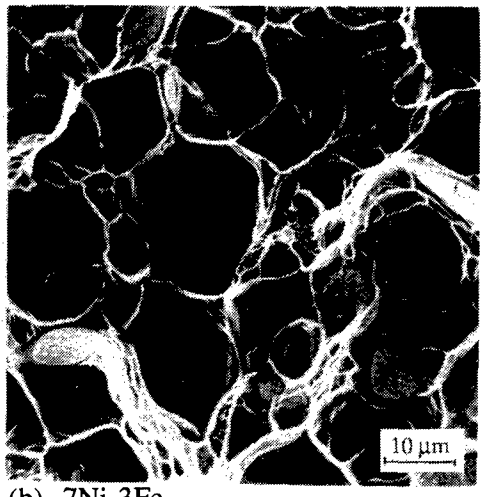

(b) 7Ni-3Fe

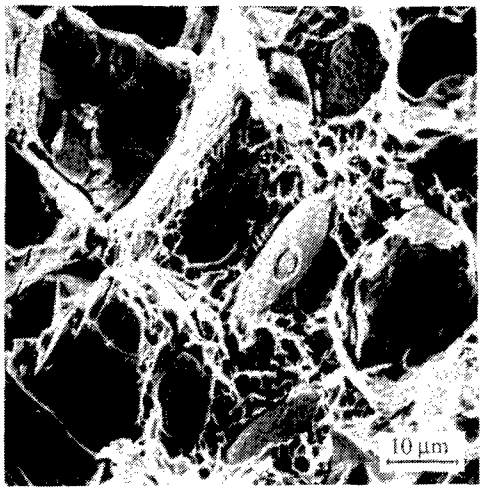

(c) Ni-Co, (as-sintered)

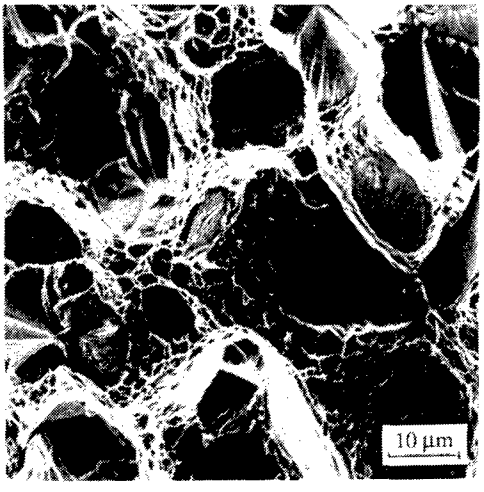

(d) Ni-Co (swaged 25%)

Figure 7 - Dynamic fracture surfaces ($\dot{\varepsilon} \cong 1000s^{-1}$).

Figure 8 represents a section through a 25% swaged Ni-Co tensile specimen failed dynamically at a strain rate of ~ $1000s^{-1}$. Within the neck indicated by the arrow in Figure 8a can be observed several modes of pre-failure damage, including W-W separation (Figure 8b) and W-cleavage cracks (Figure 8c). As indicated by the arrowed zone in Figure 8d, shear of tungsten grains appears to be involved in the formation of W-cleavage cracks.

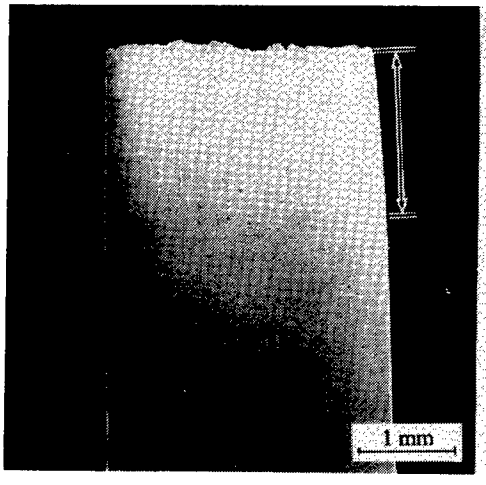

(a) Macroscopic view, showing necked region (arrow) containing damage.

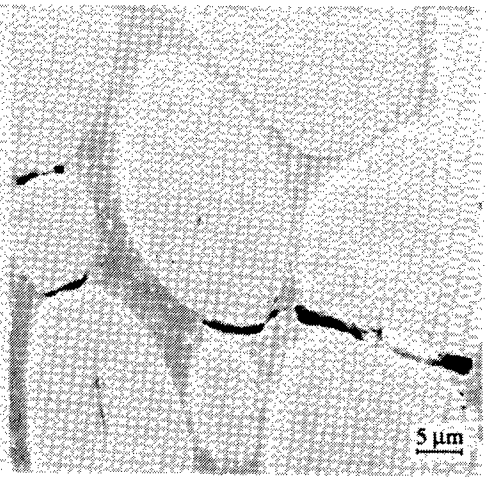

(b) W-W separation.

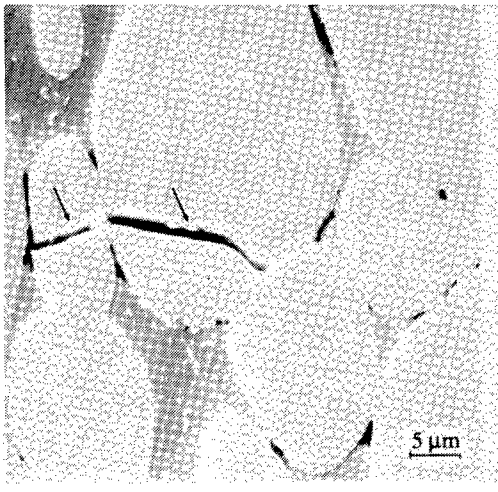

(c) Connected W-cleavage cracks (arrows).

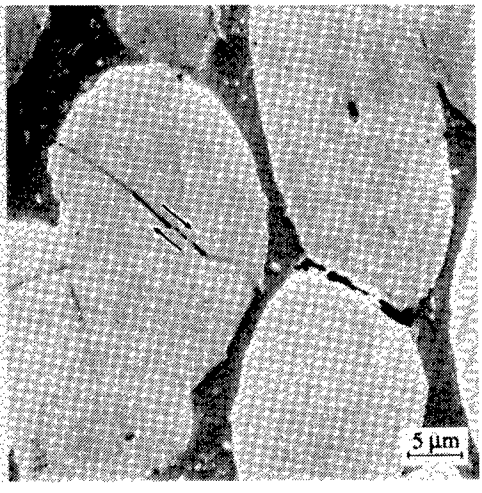

(d) Shear-nature of W-cleavage process.

Figure 8 - Section through dynamic tensile failure of Ni-Co (swaged 25%), showing sub-(fracture) surface damage mechanisms.

Compressive stress-strain curves obtained during high strain rate (~ 5500s^{-1}) deformation of all five materials (including Ni-Co in both the as-sintered and 25% swaged conditions) are shown in Figure 9. The qualitative similarities between the curves, i.e., initial hardening followed by subsequent softening, could be interpreted to imply that deformation mechanisms likewise are similar. Sectioning of specimens strained approximately 50% reveal that this definitely is not the case.

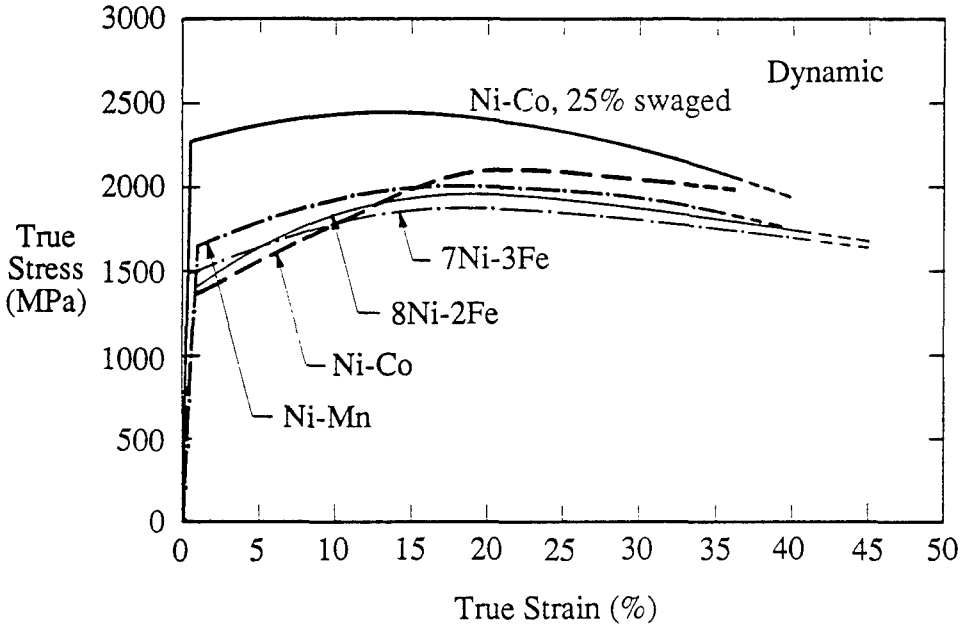

Figure 9 - Compressive deformation at dynamic strain rate of approximately 5500s^{-1}.

In particular, 7ni-3Fe, Ni-Mn, and swaged Ni-Co (Figures 10 - 12) all form narrow, unstable shear bands within broad, otherwise stable shear zones oriented at approximately 45° to the compression axis. These may crack over long distances (Ni-Mn, Figure 11) or on a localized basis (swaged Ni-Co, Figure 12). On the other hand, no such shear zones were produced in 8Ni-Fe (Figure 13) or in unswaged Ni-Co (not shown). The line in Figure 13 shows the locus of most intense strain within the broad general zone; no localized (unstable) deformation was evident. Study of cracked shear bands revealed evidence of melting, as shown for swaged Ni-Co in Figure 14. Energy dispersive spectroscopy indicated that the melted droplets along the crack interface consist of almost pure tungsten. The melting of tungsten (T_{MP} = 3410°C), strongly supports the attainment of an adiabatic state within local shear bands.

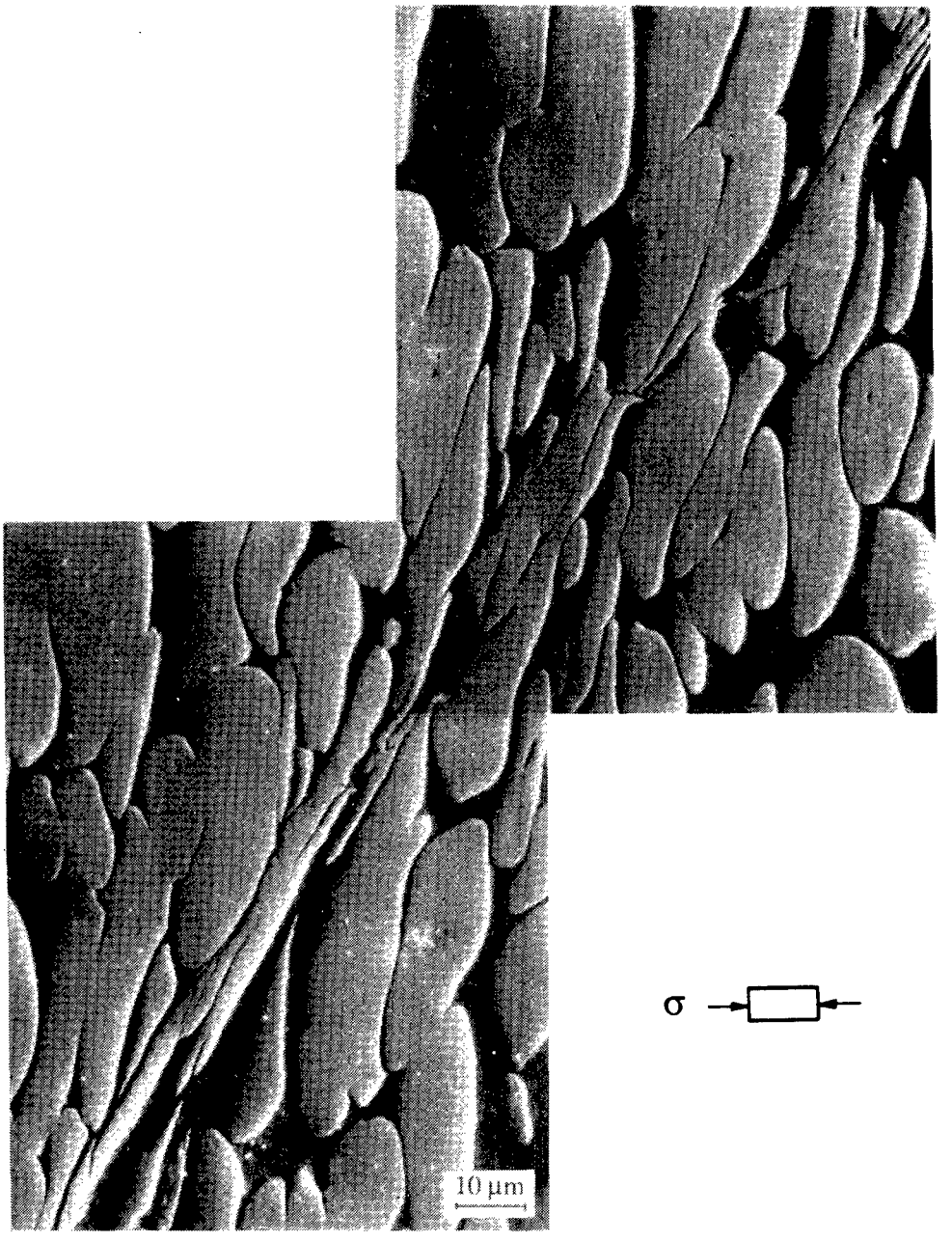

Figure 10 - Unstable compressive shear band in 7Ni-3Fe.

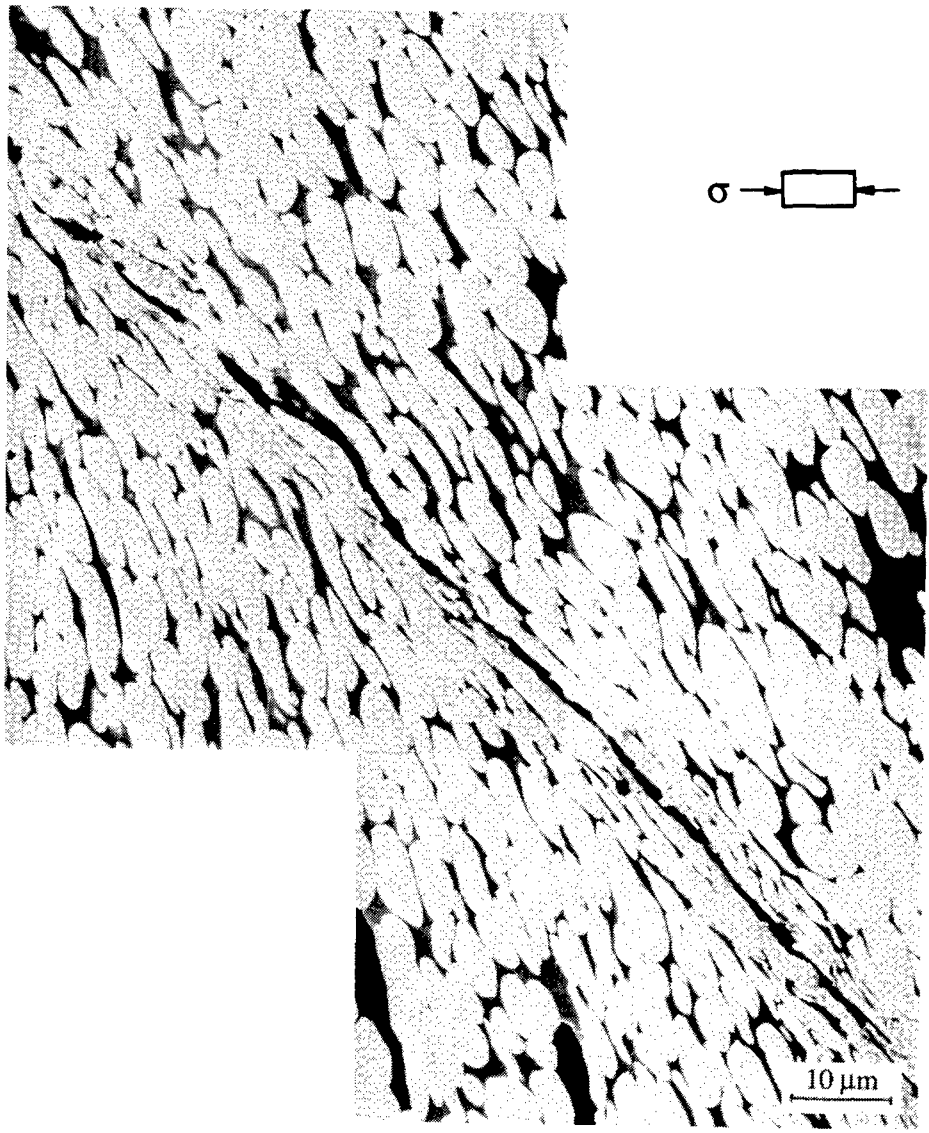

Figure 11 - Unstable compressive shear band and associated local microcracks in Ni-Mn.

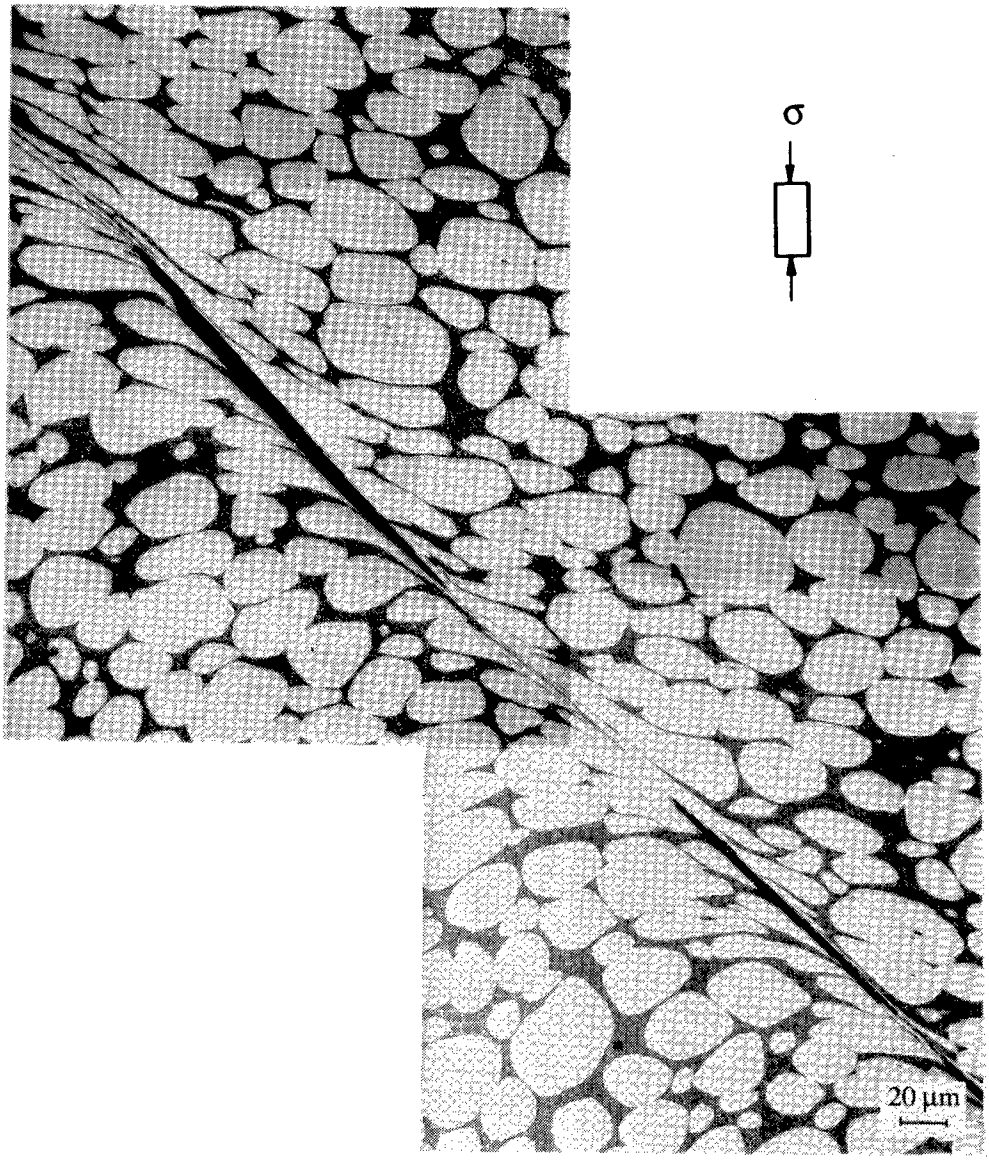

Figure 12 - Unstable compressive shear band and associated local microcracks in Ni-Co (25% swaged).

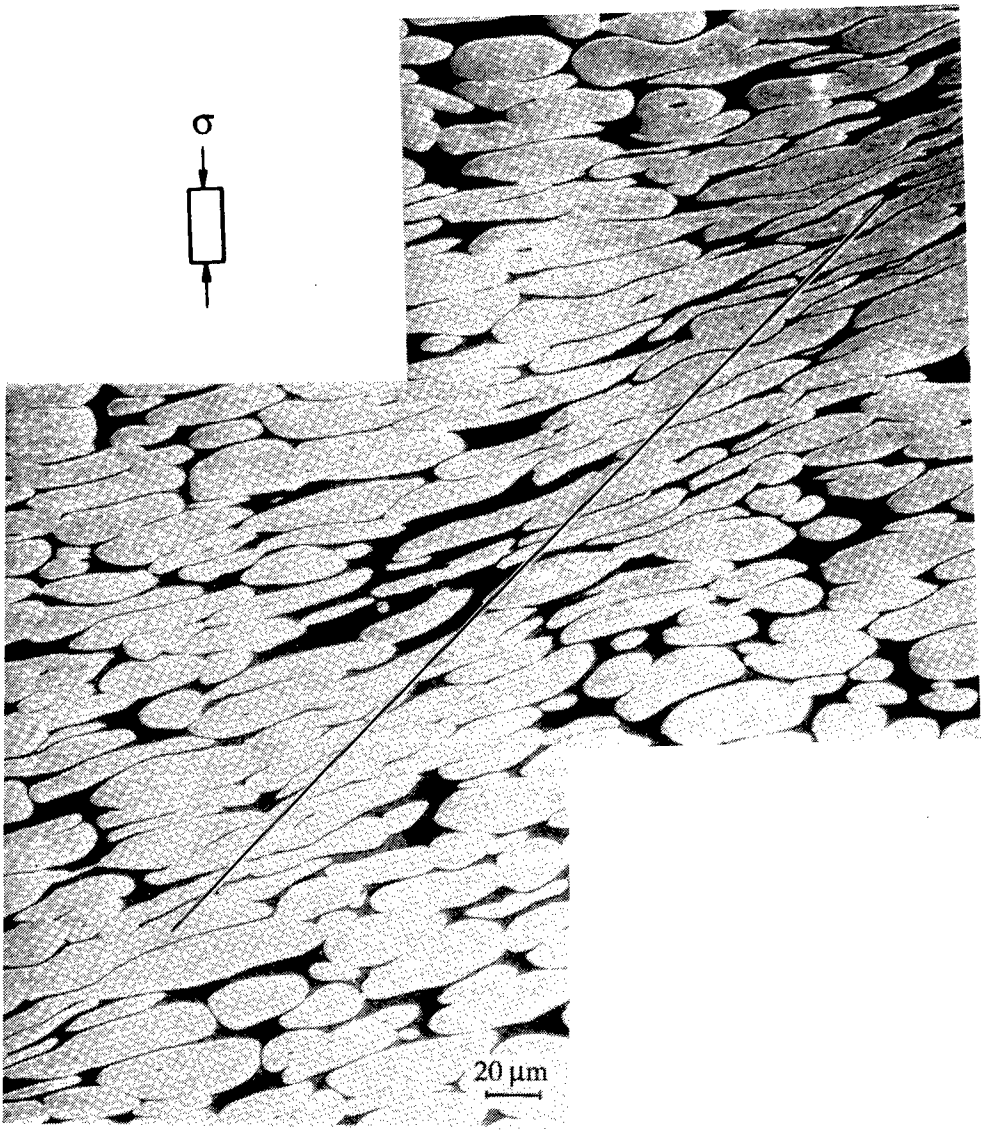

Figure 13 - Diffuse compressive shear band in 8Ni-2Fe. Line indicated approximate locus of maximum shear deformation.

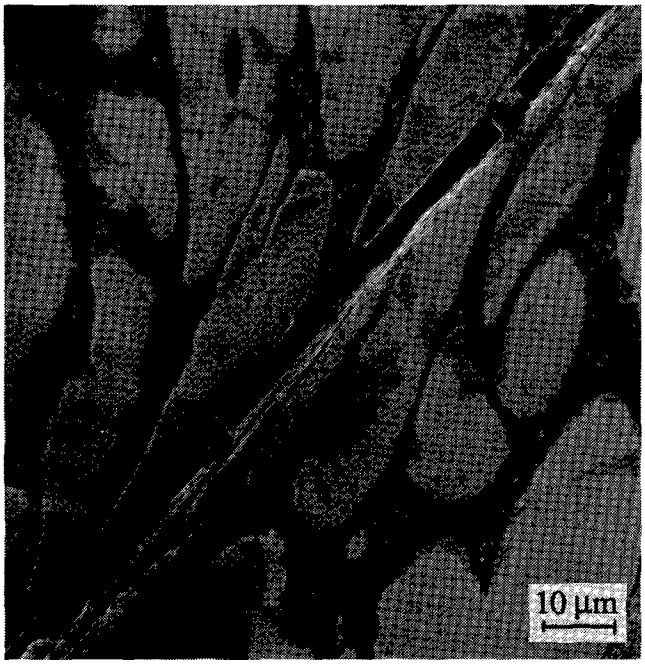

Figure 14 - High magnification view of apparent shear melt zone in Ni-Co (25% swaged); melted particles are pure tungsten.

Discussion

Recalling the stress-strain results and damage observations presented above, several questions present themselves:

1) What is responsible for the fact that the dynamic stress-strain curve is essentially simply the quasistatic curve offset by a higher yield point?
2) What is the origin of the quasistatic tensile ductility differential between the nominally similar 8Ni-2Fe and 7Ni-3Fe alloys, and why is it absent for dynamic loading?
3) What is responsible for the high strain rate decrease in tensile ductility versus that for quasistatic loading, and what (if anything) can be done to enhance the dynamic ductility?
4) What factors control the formation of adiabatic shear bands during rapid compressive loading?

In regard to the first question, it should be noted that BCC materials (like tungsten) are, as a class, extremely strain rate and temperature sensitive, as compared to FCC alloys (like the present WHA matrices). In particular, Argon and Maloof (7) have shown that for pure single crystal tungsten, the yield strength increases remarkably with decreasing temperature (hence, also with increasing strain rate, since the operative mechanism is thermally activated dislocation motion). Moreover, within a true strain of less than 0.04, the initial high rate of strain hardening, ~ 0.1, drops by more than an order of magnitude. This is true over a broad range in temperature, hence by analogy should hold for a wide strain rate regime as well. These tungsten-related trends are thus in excellent accord with the dynamic versus quasistatic results shown for the "composite" WHA alloys in Figures 2 - 5.

Further evidence of the dominant role of the W-phase is the fact that yield points in the 8Ni-2Fe, 7Ni-3Fe, and as-sintered Ni-Co alloys are nearly identical. The Ni-Co matrix is not only chemically different from those of the other two alloys, but it contains slip-impeding W-precipitates as well. On the other hand, the tungsten grain components are similar in all three alloys. On this basis, the higher quasistatic and dynamic yield strength measured for the swaged Ni-Co WHA presumably reflects the influence of the high dislocation content of the deformed W-grains.

The major difference between the two Ni-Fe alloys is the greater porosity of the 7Ni-3Fe variant. Thus, under quasistatic loading conditions, the two materials yield and flow within both phases at stress levels below that required to fail W-W interfaces. Within the W-grains, deformation is anisotropic (7), and dislocations will tend to pile up at grain boundaries without being able to relax by cross slip. If local voids are nearby, these stress raisers may trigger the early development of shear cleavage cracks and early failure, i.e., as in the 7Ni-3Fe alloy. On the other hand, failure in a void-free alloy like 8Ni-Fe (and as-sintered Ni-Co) will not occur until the overall stress level is sufficient to crack intragrain pile-ups. For this to occur, further strain and associated hardening will be required, and will therefore lead to extended ductility.

Under dynamic loading conditions, the applied stress is required to exceed the normal stress level for plastic flow, and the higher stress level is sufficient to fracture the microfacets joining contiguous W-grains. Coalescence of the resulting ensemble of microcracks produces failure at a lower value of strain than that measured for quasistatic conditions, which require a certain deformation level before the microcracks can occur. This difference in effect represents a critical strain (quasistatic case) versus critical stress (dynamic case) criterion for failure.

If this hypothesis is true, then it should be possible to demonstrate it by altering the nature of the W-W interface. Consequently, a dynamic tensile experiment was performed involving a conventional 8Ni-2Fe alloy that was sintered for an extended period of time (120 minutes versus conventional 30 minutes).

Results are shown in Figure 15, where it can be seen that while the overall flow stress is reduced, ductility is enhanced. In addition, the rate of strain hardening is increased.

The basis for this change can be understood by considering the fracture surface of the extended sinter alloy. As shown in Figure 16, the fracture morphology is similar to that produced by the normal sintering treatment, with one exception—many of the W-W facets are not "clean." Instead, they are covered with beads and filamentary strings composed of what energy dispersive spectroscopy prove is matrix material. Two basic types of wetting are observed.

In the first case, Figure 17a, it appears that while wetting (bonding) has occurred on the facet shown, there was no bond between the matrix material and the adjoining facet. To the extent that the wetting occurred, in this instance the apparent strength of the interface was lowered. In Figure 17b, however, it is clearly evident that wetting has occurred over most of both contiguous facets. Upon separating from one another, the interfacial alloy deforms in a ductile fashion. It is considered likely that this additional ductile deformation (rather than brittle microfracture) zone accounts for the enhanced overall ductility and enhanced strain hardening of the extended sinter alloy. Similarly, the partial wetting of other facets (Figure 17a) probably reduces the strength of these interfaces. Both effects are commensurate with the extended sinter results shown in Figure 15, i.e., enhanced strain hardening and ductility, but lower ultimate strength.

Recalling the high strain rate ($5500s^{-1}$) compressive stress-strain curves of Figure 9, it is evident that negative strain hardening in WHA is not a correlating factor for adiabatic shear. In fact, the one parameter which did seem to correlate with propensity to undergo unstable shear was the presence of some sort of defect structure. In particular, the stably-deforming 8Ni-2Fe and as-sintered Ni-Co alloys were structurally homogeneous and free of voids. Conversely, the 7Ni-3Fe alloy was characterized by pores and matrix inhomogeneity; Ni-Mn by porosity; and swaged Ni-Co by an apparent high initial population of mobile dislocations.

This is a surprising finding, since it is well known (17) that for non-composite (compared to WHA) materials such as steels, the development of adiabatic shear bands is controlled by material properties, rather than microstructural factors. For example, adiabatic shear bands form at a critical strain (18)

$$\gamma_c \cong \frac{n\rho_0 C_P (T_{MP} - T_0)}{\alpha(A + B)}$$

where n, A, and B are strain hardening parameters, ρ is the density, C_P is the specific heat, T_{MP} is the melting point, T_o is room temperature, and α is a constant. Thus, γ_c is a function of a collection of material properties. Similarly, the width of an adiabatic shear band should be (19)

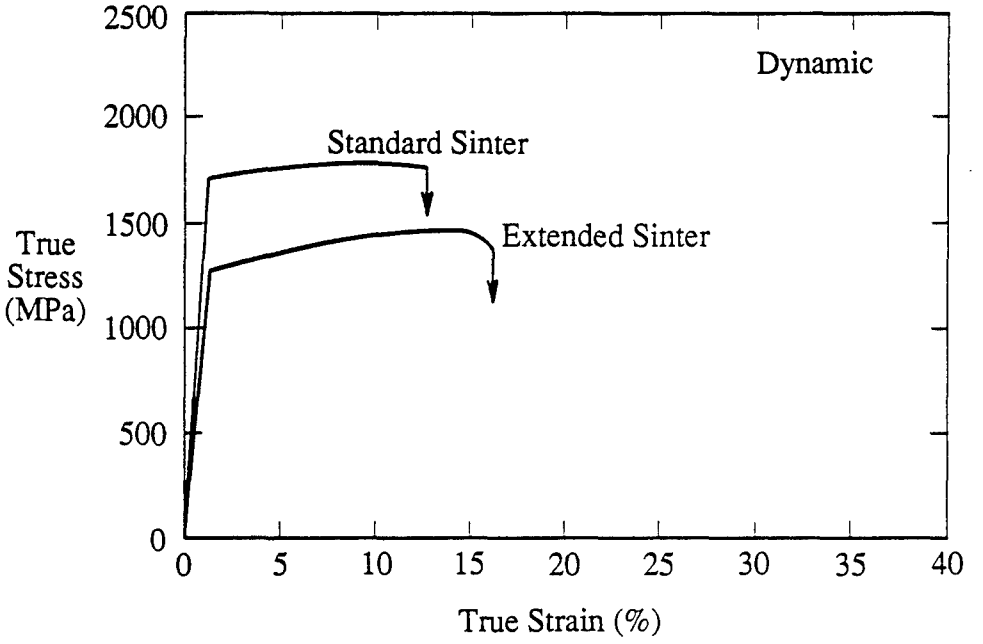

Figure 15 - Effect of sintering period on dynamic deformation of 8Ni-2Fe.

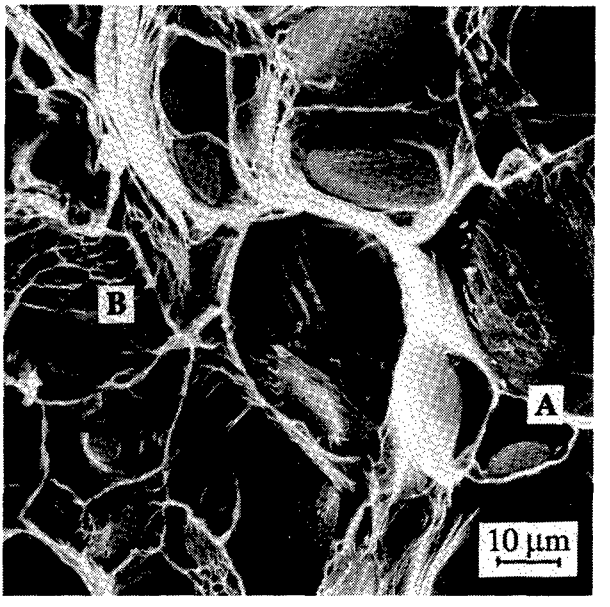

Figure 16 - Macroscopic view of fracture facets for extended-sinter 8Ni-2Fe alloy.

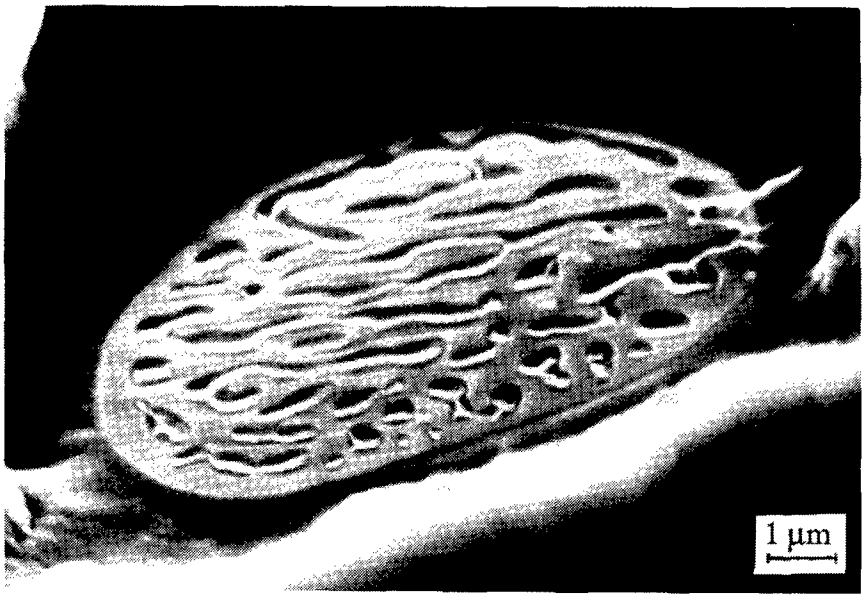

(a) Brittle failure of partially wet W-W facets (site A, Figure 16).

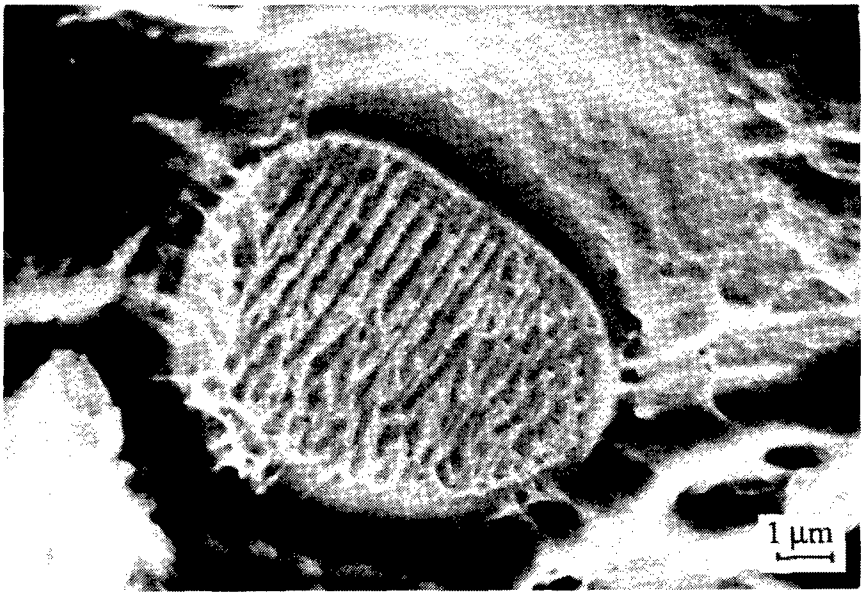

(b) Ductile failure of mutually we-W-W facets (site B, Figure 16).

Figure 17 - Details of fracture W-W facts in extended 8Ni-2Fe.

$$d \cong \left(\frac{\lambda T_*}{\tau_* \dot{\gamma}_*} \right)^{1/2} \quad (1)$$

where λ is the thermal conductivity, and T_*, τ_*, and $\dot{\gamma}_*$, are the temperature, shear stress, and strain rate, respectively, within the band. Again, the relationship is microstructure independent. Experiments on ferrous, Ti, Al, and Cu-based alloys have shown (18,19) the fundamental validity of these relationships.

Tungsten heavy alloys, however, may represent a more complex situation. Shown in Figure 18A is a plot of d (defined in Figure 18b) versus W-grain size (GS) for the three alloys which displayed adiabatic shear. It is clear that not only is $d \propto GS$, d is in fact approximately equal to GS. Moreover, since this is so, it suggests by similitude of deformation that γ_c must be about the same for each alloy—this despite the fact that their nominal thermophysical properties are sufficiently different (based on their matrix constituents) that widely varying γ_c appear possible. It is impossible to compute a theoretical value for γ_c due to the current unavailability of strain hardening data for the matrix alloys.

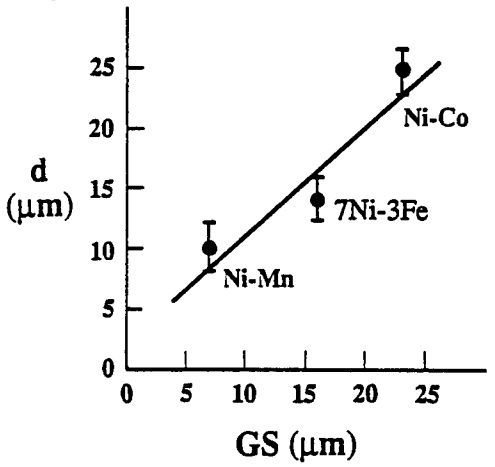

(a) Shear band width versus W-grain size

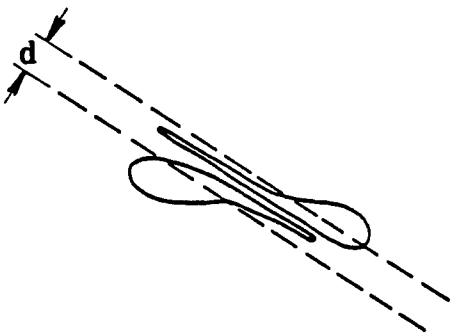

(b) Definition of shear band width

Figure 18 - Effect of W-grain size on formation of adiabatic shear bands.

Thus both γ_c and d seem to be related to the W-component, seemingly a contradiction, since calculations indicate that tungsten should not shear adiabatically. And, in fact, it almost certainly does not in the present context. Adiabatic shearing occurs in fact only in the matrix phase, *but* only when the W-grains have deformed sufficiently to reach a critical state such that an ade-

quate mean free path exists between a sufficient number of adjoining W-particles. This local instability event may be triggered by inhomogeneities such as voids or, especially, large pockets of matrix. Thus, the intrinsic shear instability threshold of the matrix may be significantly lower than that implied by the results of testing the composite. On the other hand, it is clear that the adiabatic shear criterion for the matrix alone, while important, is insufficient to predict the unstable shear resistance of a typical WHA. This is a key difference between this peculiar, essentially composite, class of material and a conventional structural alloy.

Acknowledgements

The authors gratefully acknowledge the support of the Defense Advanced Research Projects Agency through Army Research Office Contract DAAC03-88-K-0204.

References

1. L. Magness and T. Farrand, "Deformation Behavior and Its Relationship to the Penetration Performance of High-Density KE Penetrator Materials," Army Science Conference Proceedings, DTIC AD A230099, (1991).

2. R. L. Woodward, N. J. Baldwin, I. Burch, and B. J. Baxter, "Effect of Strain Rate on the Flow Stress of Three Liquid Phase Sintered Tungsten Alloys," Metallurgical Transactions, 16A (1985), 2031-2037.

3. S. J. Cimpoeru and R. L. Woodward, "High Strain Rate Properties of Three Liquid Phase Sintered Tungsten Alloys," Materials Science Letters, 9 (1990), 187-191.

4. A. Bose, D. Sims, R. M. German, "Test Temperature and Strain Rate Effects on the Properties of a Tungsten Heavy Alloy," Metallurgical Transactions A, 19A (1988), 487-494.

5. G. R. Johnson, J. M. Hoegfeldt, U. S. Lindholm, A. Nagy, "Response of Various Metals to Large Torsional Strains Over a Large Range of Strain Rates—Part 2: Less Ductile Metals," Journal of Engineering Materials and Technology, 105 (1983), 48-53.

6. R. S. Coates and K. T. Ramesh, "The Deformation of Tungsten Alloys at High Strain Rates," (Report JHU DIL-9002, Johns Hopkins University, 1990).

7. A. S. Argon and S. R. Maloof, "Plastic Deformation of Tungsten Single Crystals at Low Temperatures," Acta Metallurgica, 14 (1966), 1449-1462.

8. W. J. Bruchey, Jr. and D. M. Montiel, "Mechanical Property Evaluation of a Series of Commercial Tungsten Alloys," (Report BRL-MR-3606, US Army Ballistic Research Laboratory, Aberdeen Proving Ground, Maryland, 1987).

9. L. W. Meyer, H. D. Kunze, E. Staskewitsch, "Dynamic Strength and Ductility of a Tungsten Alloy for KE Penetrators in Swaged and Unswaged Condition Under Various Loading," Proc. 7th International Symposium on Ballistics, (1983), 289-293.

10. K. S. Churn and R. M. German, "Fracture Behavior of W-Ni-Fe Heavy Alloys," Metallurgical Transactions A, 15A (1984), 331-338.

11. J. Lankford, H. Couque, and A. Bose, "Dynamic Deformation and Failure of Tungsten Heavy Alloys," Tungsten and Tungsten Alloys - Recent Advances, ed. A. Crowson and E. S. Chen (New York, NY: The Minerals, Metals & Materials Society, 1991), 151-159.

12. J. Lankford, C. E. Anderson, S. R. Bodner, "Fracture of Tungsten Heavy Alloys Under Impulsive Loading Conditions," Jnl. of Materials Science Letters, 7 (1988), 1355-1358.

13. J. Lankford, H. Couque, A. Bose, and C. E. Anderson, "Microstructural Dependence of High Strain Rate Deformation and Damage Development in Tungsten Heavy Alloys," in Shock Waves and High-Strain-Rate Phenomena in Materials, (New York, NY: Marcel Dekker, Inc., 1991), in press.

14. H. Couque, J. Lankford, and A. Bose, "Tensile Fracture and Shear Localization Under High Loading Rate in Tungsten Alloys," Journal of Physique, (submitted).

15. U. S. Lindholm, "Some Experiments with the Split Hopkinson Pressure Bar," Journal of the Mechanics and Physics of Solids, 12 (1964), 317-335.

16. T. Nicholas, "Dynamic Tensile Testing of Structural Materials Using a Split Hopkinson Bar Apparatus," (Report AFWAL-TR-80-4053, 1980).

17. D. A. Shockey, "Materials Aspects of the Adiabatic Shear Phenomenon," Metallurgical Applications of Shock-Wave and High-Strain-Rate-Phenomena, ed. L. E. Murr, K. P. Stanhammer, and M. A. Meyers (New York, NY: Marcel Dekker, Inc., 1986), 633-656.

18. U. S. Lindholm and G. R. Johnson, "Strain-Rate Effects in Metals at Large Shear Strains," Material Behavior Under High Stress and Ultrahigh Loading Rates, ed. J. Mescall and V. Weiss (new York, NY: Plenum Publishing Corp., 1983), 61-79.

19. B. Dodd and Y. Bai, "Width of Adiabatic Shear Bands Formed Under Combined Stresses," Mat. Sci. Tech., 5 (1989), 557-559.

ON CONTINUUM CHARACTERIZATION OF CRACK ARRAYS AND CORRELATIONS BETWEEN FRACTURING AND CHANGE OF EFFECTIVE ELASTIC MODULI

Mark Kachanov

Department of Mechanical Engineering
Tufts University
Medford MA 02155

Abstract. Continuum characterization of crack arrays by vectorial and tensorial parameters (that are volume averages) and their use in analysis of physical properties of cracked solids (effective elastic moduli, effective conductivity) are briefly reviewed. Symmetry of the effective elastic properties of cracked solids is discussed.

It is argued that, whereas such a characterization provides a useful insight into the effective (i.e.volume average) properties, it may be less useful for characterization of the fracture-related properties (determined by local fluctuations of the defects' field geometry). Contrary to the spirit of many damage models, there seems to be no direct correlation between fracturing of a brittle microcracking body and change of its effective elastic moduli.

1. INTRODUCTION

A brief summary of continuum modelling of microcrack-related damage in brittle-elastic materials is presented below. Characterization of crack arrays by tensorial and vectorial (volume average) quantities is reviewed. In particular, the second order crack density tensor α (Kachanov et al [1-3]) is discussed.

Such tensor can be used for characterization of various effective (i.e. volume average) physical properties of cracked solids (effective elastic moduli, effective conductivity, etc.). The possibilities and limitations of such approaches are discussed.

It is argued that, whereas the use of α provides a useful insight into the *effective* properties, the use of α - type parameters in characterization of the *fracture-related* properties may not provide such an insight. The reason is that the fracture-related quantities (like stress intensity factors, SIFs) are governed by *local fluctuations* of the crack array geometry, to which the volume average quantities are not very sensitive. This also explains why no direct correlation between fracturing of a brittle microcracking body and the change of its effective elastic moduli seems to exist.

2. SOME REMARKS ON SCALAR CRACK DENSITY PARAMETER

A scalar crack density parameter conventionally used in various models for the effective elastic moduli is defined as follows:

$$\rho = (1/A) \sum l_i^2 = N\langle l^2\rangle/A \quad \text{in 2-D;} \tag{2.1a}$$

$$\rho = (1/V) \sum l_i^3 = N\langle l^3\rangle/A \quad \text{in 3-D} \tag{2.1b}$$

where N is a number of cracks in the representative area A (volume V) in 2-D (3-D) and l is a characteristic size of a crack which is half-length of a crack in 2-D and, in 3-D, radius of a circular crack (or a somewhat more complex parameter for cracks of other shapes: $l=(2S^2/\pi P)^{1/3}$ where S and P are the crack area and perimeter, see Budiansky and O'Connell [4]); note that some authors' definitions of ρ contain an extra multiplier π.

Below, we discuss certain implicit assumptions contained in the definition (2.1) that may limit the use of ρ as a parameter.

According to the definition (2.1), contribution of a given crack into the overall density ρ is proportional to l^2 in 2-D and to l^3 in 3-D. In fact, individual crack's contribution into the effective compliance is, as is well known, proportional to the product $\langle \mathbf{b} \rangle l$ in 2-D and to $\langle \mathbf{b} \rangle l^2$ in 3-D, where $\langle \mathbf{b} \rangle$ is the average displacement discontinuity across the crack.

Therefore, the proportionality assumed in (2.1) is rigorously correct for *non-interacting* cracks (when $\langle \mathbf{b} \rangle$ is proportional to l in 2-D and to l^2 in 3-D, with the coefficient of proportionality independent of crack translation, i.e. on the relative positions of cracks with respect to each other).

In general, however, this proportionality does not hold. For example, in the configurations where the dominant mode of crack interactions is stress "shielding" (parallel crack arrays), dependence of an individual crack's contribution on l will be weaker than l^2 in 2-D and than l^3 in 3-D, whereas in the configurations with stress "amplification" (collinear and coplanar arrays), it wil be stronger.

This reflects the basic feature of parameters that are simple volume averages (whether they are scalar or tensorial): they are *insensitive to mutual positions of cracks.*

In fact, however, even the *effective* properties - that are themselves volume averages - may be sensitive to mutual crack positions, i.e. to the statistics of crack centers. The following configuration provides a simple example of "infinitely high" such sensitivity. Let us consider an array of parallel cracks. In the first arrangement, they form rows of collinear cracks with vanishingly small ligaments between them; the distance between rows is sufficiently large (so that the overall density ρ is arbitrarily small). The effective stiffness in the direction normal to cracks then tends to zero (in spite of $\rho \to 0$). In the second arrangement, cracks are stacked in columns, with the distances between columns being sufficiently large but the spacings between stacked cracks within each column being vanishingly small, so that $\rho \to \infty$. The impact of this crack array on the effective modulus is vanishingly small.

(Note that the first arrangement also serves as an illustration that small crack density does not necessarily imply that the approximation of non-interacting cracks applies!).

If the *fracture*-related properties (that are determined by local fluctuations of the defects' field geometry rather than by the volume averages, see discussion below) are of interest, one should use ρ as a parameter characterizing the process with even more caution.

Another limitation of the use of ρ as a parameter is that it is defined by (2.1) with applications to the *elastic* properties in mind; therefore, the contribution of an individual crack into ρ is proportional to l^2 in 2-D and l^3 in 3-D. In the properties other than elastic, this contribution may be entirely different: for example, it will strongly depend on the crack opening in the problem of fluid filtration through a fissured medium.

Below, we discuss a *tensorial generalization* of ρ - second order crack density tensor - that accounts for *orientations* of cracks but, being a volume average quantity, retains the same limitations as ρ.

3. CRACK DENSITY TENSOR

Second order crack density tensor α was introduced by Vakulenko and Kachanov [1] and Kachanov et al [2,3] as a volume average damage parameter accounting fot crack orientations, as follows:

$$\alpha = (1/A) \sum l_i^2 \mathbf{n}_i \mathbf{n}_i \qquad \text{in 2-D} \qquad (3.1a)$$

$$\alpha = (1/V) \sum l_i^3 \mathbf{n}_i \mathbf{n}_i \qquad \text{in 3-D} \qquad (3.1b)$$

where **n** is a unit normal to a crack and **nn** is a dyadic product; summation may be substituted by integration over orientations.

Note that α is *symmetric* (as a sum of symmetric dyads) and *dimensionless* (so that the case of small crack density can be formulated in terms of smallness of α_{ij}).

Linear invariant of α

$$\rho \equiv \mathrm{tr}\,\alpha = (1/A)\sum l_i^2 \quad \text{in 2-D,} \quad \text{or} \quad (1/V)\sum l_i^3 \quad \text{in 3-D} \qquad (3.2)$$

coincides with the commonly used scalar crack density parameter. Thus, α is a natural tensorial generalization of the scalar crack density.

For an *isotropic* (random) crack orientation distribution

$$\alpha = \rho \mathbf{I}_2/2 \quad \text{(in 2-D)}, \qquad \text{or} \qquad \rho \mathbf{I}_3/3 \quad \text{(in 3-D)} \qquad (3.3)$$

where $\mathbf{I}_2$ and $\mathbf{I}_3$ are 2-D and 3-D unit tensors, correspondingly.

For a *parallel* crack array

$$\alpha = \rho \mathbf{nn} \qquad (3.4)$$

Generally, α , as any symmetric second order tensor, allows a principal representation:

$$\alpha = \rho_1 \mathbf{n}_1\mathbf{n}_1 + \rho_2 \mathbf{n}_2\mathbf{n}_2 + \rho_3 \mathbf{n}_3\mathbf{n}_3 \qquad (3.5)$$

where $\mathbf{n}_1, \mathbf{n}_2, \mathbf{n}_3$ are mutually orthogonal unit vectors (principal axes of α). Representation (3.5) means that, in the framework of characterization of a crack array by α, any crack array is equivalent to three mutually orthogonal families of parallel cracks, with densities ρ_1, ρ_2, ρ_3 .

Note that tensors identical or similar to α have been subsequently introduced by several authors (see, for example, Oda et al [5]).

4. USE OF CRACK DENSITY TENSOR IN THE PROBLEM OF EFFECTIVE ELASTIC MODULI

The effective elastic compliances M_{ijkl} can be derived from an elastic potential *f* (complementary energy density):

$$\varepsilon_{ij} = \partial f/\partial \sigma_{ij} = M_{ijkl}\,\sigma_{kl} \qquad (4.1)$$

so that the problem is reduced to finding $f = (1/2)\, M_{ijkl}\sigma_{ij}\,\sigma_{kl}$. We assume that, in addition to being a function of σ, f is also a function of α.

If the material is isotropic in absence of cracks, f will be an isotropic function of σ and α, i.e. will not change if both σ and α undergo the same orthogonal transformation. This implies that σ and α enter f through their invariants only (including the simultaneous ones). Since the stress-strain relations are linear at constant α, potential $f(\sigma,\alpha)$ must be quadratic in σ. Since the overall strain can be represented as a sum of the matrix contribution $M^{o}_{ijkl}\sigma_{kl}$ and the contribution $\Delta M_{ijkl}\sigma_{kl}$ from cracks, similar representation holds for f:

$$f(\sigma\,,\,\alpha) = f_o(\sigma) + \Delta f(\sigma\,,\,\alpha) \qquad (4.2)$$

where $f_o = (1/2)\, M^{o}_{ijkl}\sigma_{ij}\,\sigma_{kl}$. The expression for $\Delta f(\sigma\,,\,\alpha)$ comprises seven terms representing all independent combinations of the invariants:

$$\Delta f(\sigma\,,\,\alpha) = \eta_1 \mathrm{tr}\,\sigma\;\mathrm{tr}(\sigma\cdot\alpha) + \eta_2\,\mathrm{tr}(\sigma\cdot\sigma\cdot\alpha) + \text{five more terms} \qquad (4.2a)$$

where dot indicates one index contraction and the scalar coefficients η_i are, generally, functions of invariants of α.

Since α is a second order symmetric tensor, effective elastic properties are always *orthotropic*, i.e. a *material with any arbitrary orientation srtatistics of cracks possesses a rectangular symmetry* (the axes of orthotropy being co-axial with the principal axes of α).

The following question arises: to what extent is the conclusion on orthotropy of the effective properties rigorous, i.e., to what extent is the representation of elastic potential in the form $f = f(\sigma\,,\,\alpha)$ justified ?

As shown in [2], such representation is rigorously correct in the 2-D case of non-interacting cracks and is approximately correct (with good accuracy) in the 3-D case of non-interacting cracks.

For *interacting* cracks, computer experiments based on the recently developed method of analysis of interacting cracks [6] show that, even at high crack densities, when the effective moduli are significantly altered by interactions, the effective properties remain orthotropic with a good accuracy: the terms in the matrix of elastic moduli that would have been zeros for an orthotropic material, remain one-two orders of magnitude smaller that the other, orthotropic terms.

This fact implies that there exists a *"natural" coordinate system* for calculation of the efffective elastic moduli - it coincides with the principal axes of the crack density tensor α - such that the matrix of efffective moduli looks "almost orthotropic" in this system.

The results outlined above can be generalized for the case when the *matrix is anisotropic in absence of cracks*. Then, tensors σ and α enter the potential $f(\sigma,\alpha)$ through their *invariants with respect to the group of symmetry of the matrix* (rather than with respect to all orthogonal transformations). Such a generalization was outlined by Vakulenko and Kachanov [1] and Kachanov [2] and explored in detail by Talreja [7] (with the difference that instead of a damage tensor, a vectorial parameter was used; see section 8 for discussion of vectorial parameters). Anisotropy of the overall properties will depend on mutual orientation of the axes of symmetry of the matrix and of the crack array. The material will not be orthotropic, except for the cases when the crack orientations are aligned with the symmetry axes of rhe matrix. The expression for $f(\sigma,\alpha)$ will be much lengthier than (4.2) and will contain a large (to very large) number of coefficients at the invariants. They can be expected to be approximately constant when the crack density is small (data of Talreja seem to imply their constancy). Experimental determination of a large number of these coefficients seems to be a challenging task, however.

5. FURTHER APPLICATIONS OF CRACK DENSITY TENSOR IN THE PROBLEM OF EFFECTIVE ELASTIC PROPERTIES

One can use representation of potential $f(\sigma,\alpha)$ in the form (4.2) as a convenient and simple tool for extension the results of either the *self-consistent* or *differential* schemes (in the differential scheme, crack density is increased in small increments and the reference matrix is recalculated at each step) obtained for the *random* and *parallel* crack orientation statistics to the case of *arbitrary* orientation statistics.

Note that direct application of these schemes to the case of arbitrary crack orientation statistics is difficult; the conceptual difficulty arises from the necessity to specify *a priori* the *type* of anisotropy and its *orientation*, since solution of the problem of a single crack in an *anisotropic* effective matrix will be required. (Note that another difficulty, of a more technical nature, arises from the fact that such solutions may not be readily available, if crack's orientation with respect to the axes of matrix' anisotropy is arbitrary). Therefore, applications of these methods have been limited to the cases of random or parallel cracks, or cracks with normals lying in one plane (Hoenig [8]) when the type and orientation of anisotropy are obvious. In the general case, however, they may not be obvious.

One can use the results obtained in either the self-consistent or differential schemes for the random and parallel crack orientation statistics as an "input" and then use the representations of the type of (4.2) to tensorially transform these results, through the use of α, to the *arbitrary* orientation statistics. As demonstrated in [3], such an extension is done by quite simple means.

We also note that for the *differential scheme*, such an extension to the arbitrary orientation statistics corrects a significant defect of this scheme - its "path-dependence" (sensitivity of the results to the *sequence* in which cracks of different orientations are introduced). Indeed, let us consider a 2-D configuration of two families of cracks forming an arbitrary angle between them and restrict ourselves to the simplest case of small crack density (non-interacting approximation applies). As discussed in section 3, the material is *rigorously* orthotropic in this case. However, if the differential scheme is used and one family of parallel cracks is introduced first and then the second one is added into the newly recalculated (transversely isotropic) reference matrix then the material is *not* orthotropic. This "path-dependence" is eliminated if the above described procedure is used.

6. OTHER APPLICATIONS OF CRACK DENSITY TENSOR

Crack density tensor α can be used in characterization of the effective (i.e.,volume average) physical properties other than elastic: electro- and heat conductivity, fluid filtration. The use of α is based on representation of the tensor that characterizes the state physical property in terms of α. For example, in the problem of (anisotropic) electric conductivity of a medium that, in addition to a certain isotropic "background" conductivity, contains crack-like cavities filled with conducting material, the tensor $\mathbf{K}$ relating the vector of electric current $\mathbf{j}$ to the gradient of electric potential ($\mathbf{j} = \mathbf{K}\cdot\nabla\Phi$) can be expressed as

$$\mathbf{K} - k\mathbf{I} = f(\alpha) \qquad (6.1)$$

where the term $k\mathbf{I}$ characterizes the isotropic "background" conductivity and $f(\alpha)$ is a function of invariants of α. Unlike the fourth order tensor M_{ijkl} of elastic moduli, tensor $\mathbf{K}$ is a second order tensor; this makes representation (6.1) much simpler than the one for the elastic properties. Similar representations can be constructed for the heat conductivity and fluid filtration, see [2] for details.

An important observation is that, although all the mentioned physical properties possess the same orthotropic symmetry, the *orientation* of their orthotropy axes is *different* from the one of the *elastic* properties.

Indeed, if α is used for characterization of the physical properties other than elastic, *it should be modified,* as follows. According to the definition (2.1), contribution of a given crack into the overall density α is proportional to l^2 in 2-D and to l^2 in 3-D. This relative weight of an individual crack is appropriate fort the *elastic* properties, but may have to be modified when other physical properties are considered (for example, in the problem of electric conductivity it seems that this weight should be proportional to l and l^2, in 2-D an 3-D; for fluid filtration in a fissured medium it should also include crack opening).

For each of the mentioned physical properties, the axes of orthotropy are oriented along the principal axes of the appropriate modification of α; therefore, these orientations are, generally, different. This implies, for example, that the data on anisotropy of electric conductivity *cannot* be used to predict the anisotropy of wavespeeds, etc.

Note, also, that the appropriately averaged dyadics of the **nn** - type were used in mechanics of granular materials for characterization of the average orientations of grain contacts (for a brief review of such uses, see Mehrabadi and Nemat-Nasser[10]).

7. HIGHER ORDER DAMAGE PARAMETERS

Crack density tensor α provides the simplest tensorial generalization of the scalar crack density. As discussed above, in spite of its simplicity, this tensor provides useful insights into the effective properties of cracked media and into the anisotropy of these properties (for example, the orthotropy of the effective elastic properties, verified by more precise calculations of the method of [6], holds with surprising accuracy). The use of α in combination with the self-consistent or differential schemes provides a convenient tool to transform the predictions of these schemes for the random and parallel cracks to the general case of arbitrary crack orientation statistics.

If one wishes to use more "refined" damage parameters, then the refinements can be made along the following two lines:

(A) Remaining in the framework of *volume average parameters*, one can introduce more refined characterization of the crtack orientation distribution, by adding to the **nn** - type dyads tensors of the higher (even) orders, of the **nnnn**, **nnnnnn**, etc. types. Such refinements were considered in literature from several points of view (see, for example, Kanatani [11]).

This, however, may not necessary in the problem of effective elastic properties, since, as discussed above, orthotropy of these properties (coaxial with the *second order* crack density tensor) holds with good accuracy. As far as other effective properties (conductivity, filtration) are concerned, they are characterised by *symmetric second order* tensors (like tensor **K** of electric conductivity, see section 6) and therefore possess the symmetry of an ellipsoid; it seems that characterization of these properties by higher order tensors may not be necessary.

(B) Using quantities that are not simple volume averages, but depend on *mutual positions* of cracks.

Refinements of this kind appear to be more important than the ones of (A), not only for the fracture-related problems (where the importance of mutual positions of cracks is obvious) but even in the problem of effective elastic moduli - two configurations of parallel cracks considered in section 2 provide an illustration.

It seems that a physically reasonable way to construct a continuum description of a crack array that goes beyond volume averages can be based on the approach to many cracks' problems developed in [6]: it will have to use statistical averaging of the transmission Λ– factors (that incorporate the essential information on crack array geometry that determines crack interactions).

8. ON CHARACTERIZATION OF CRACK ARRAYS BY VECTORS

Several authors (see, for example, Talreja [7] and Krajcinovic [9]) used *vectors* (rather than second order tensors) as damage variables. We remark that inadequacy of the *odd* order tensors as parameters of state was discussed, from the point of view of general restrictions on constitutive equations, by Leckie and Onat [12]. We note, also, that two other difficulties arise when one tries to to actually use such variables:

(1) In the simplest case of *random* (isotropic) crack orientation statistics, it is not clear what the vector of damage is;

(2) If one tries to construct the elastic potential as a function of σ and a vector of damage ω: $f = f(\sigma,\omega)$, then it appears *impossible to linearize f* with respect to ω; in other words, *the simplest case of small crack density (non-interacting cracks) cannot be recovered.* This follows from the fact that, in order to form a simultaneous invariant of the vector ω and the second order tensor σ, one has to contract ω with σ twice, i.e. to form terms of the type $\sigma_{ij}\omega_i\omega_j$ or $\sigma_{ij}\sigma_{jk}\omega_i\omega_k$ that are homogeneous quadratic functions of ω and cannot be linearized in ω.

9. ON CORRELATION BETWEEN FRACTURING OF A BRITTLE MICROCRACKING SOLID AND CHANGE OF ITS EFFECTIVE ELASTIC MODULI : GENERAL COMMENTS

In the sections above, we outlined the possibilities of characterization of crack arrays by volume average quantities (like crack density tensor) and demonstrated that this may provide useful insights into various *volume average physical properties* (effective moduli, effective conductivities, etc.).

However, the use of such volume average parameters may not be adequate in the *fracture-related* problems, like estimates of proximity of a given configuration to the failure point, estimates of lifetime, etc. The basic difficulty is that the fracture-related quantities (like stress intensity factors, SIFs) are governed by *local fluctuations* of the crack array geometry, to which the volume average quantities are not very sensitive.

This observation is relevant for a number of damage models which are aimed at description of *fracturing* of a brittle microcracking solid but in fact deal with its *elastic constants*. This substitution is done either explicitly, by using the effective constants as a damage parameter, or implicitly, by constructing the elastic potential f containing a certain damage parameter D; aside from the statement that the derivative $\partial f/\partial D$ can be interpreted as an energy release rate associated with damage, such a construction is simply a model for the effective moduli.

The underlying idea - that progression towards failure is uniquely correlated with the change of effective elastic moduli - may seem reasonable; it appears particularly attractive because the effective moduli can be easily measured.

An objection can be raised that, as is well known, a small crack in a brittle material has a very small impact on the effective elastic constants but drastically reduces tensile strength. One may argue, however, that, after a certain initial set of cracks has been nucleated and started to grow, the progression towards failure *is* uniquely correlated with the change of effective elastic constants.

These issues are discussed below from several points of view. Computer experiments that were used in the course of analysis (solving crack interaction problems for a number of crack arrays) utilized the method of analysis of many cracks' problems of [6].

10. "PARADOXICAL" EXAMPLE

The configuration shown below present an example when introduction of new cracks results in

(1) *reduction of elastic stiffness* (in the direction normal to cracks); a

(2) *reduction of the SIFs* (due to increased shielding), i.e., strengthening the material

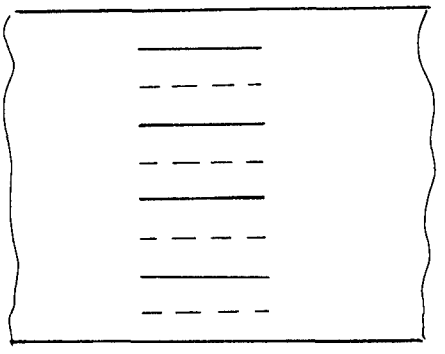

Fig.1. Introduction of new cracks as shown (dashed lines) reduces the SIFs and, at the same time, "softens" the material (since it produces additional displacements at the boundaries).

11. RANDOM CRACK ARRAYS. CLUSTERING OF CRACKS

The example above indicates that the relation between fracture-related and effective elastic properties is not straightforward. This configuration may not, however, represent realistic microcrack statistics (although such crack patterns do occur in rocks and certain composites).

We considered *randomly oriented* cracks, and did the following computer experiments. A number of 2-D randomly oriented crack arrays were generated; statistics of crack centers was also random (subject to the restriction that cracks were not allowed to intersect; this was achieved by generating cracks successively and discarding a newly generated crack if it intersects the already existing ones). For each sample array, we calculated:

(1) the effective Young's modulus E_{eff} ;

(2) maximal, among all crack tips, value of $K_I^2+K_{II}^2$ induced by a uniaxial loading.(Strictly speaking, the value of $K_I^2+K_{II}^2$ determines the initiation of crack propagation only in the case of rectilinear crack extension; if both K_I and K_{II} are present, a certain other combination of K_I and K_{II} is a relevant parameter. Typically, however, this combination does not differ much (numerically) from $K_I^2+K_{II}^2$ so that the latter quantity can be used for an approximate estimate of proximity of a crack to the onset of propagation).

We found that the value of E_{eff} was quite stable from one statistical sample to another, whereas the value of Max $(K_I^2 + K_{II}^2)$ fluctuated significantly (reaching high values in the samples containing two closely spaced crack tips). Moreover, Max $(K_I^2 + K_{II}^2)$ tends to increase with the size of the sample, at the same (or even decreasing!) crack density reflecting a higher probability of occurrence of closely spaced cracks, i.e. at the same (or even increasing!) effective stiffness E_{eff}. Thus, the fracture-related parameter Max $(K_I^2+K_{II}^2)$ is statistically unstable, depends on specimen's size and does not appear to be correlated with the statistically stable effective stiffness E_{eff}.

A closely related issue is that the SIFs are sensitive to *clustering* of cracks: Max$(K_I^2+K_{II}^2)$ is, typically, substantially higher in the configurations of the type 2b as compared with configurations of the type 2a, whereas the difference between the moduli M_{ijkl} for these configurations is generally insignificant (provided the overall crack density is the same).

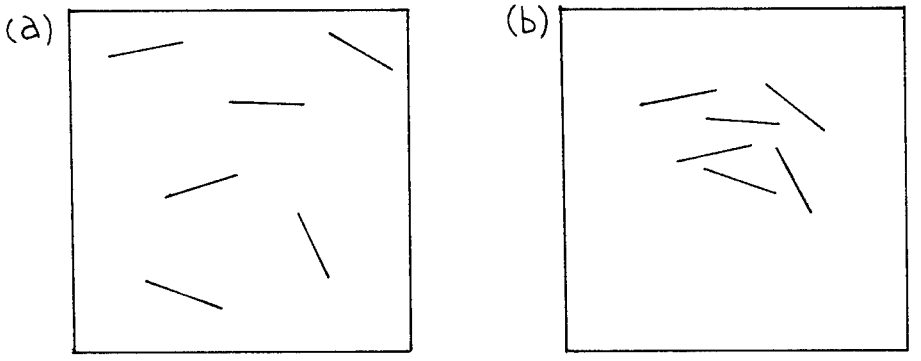

Fig.2. Clustering of cracks. SIFs are quite sensitive to clustering whereas the sensitivity of effective elastic moduli is very low.

At the same time, the effective elastic moduli's sensitivity to clustering is quite low, i.e. the difference between the values of M_{ijkl} for the configurations 2a and 2b is generally insignificant (provided the overall crack density is the same).

Thus, *monitoring the change in effective elastic constants may not necessarily detect the onset of strong crack interactions and clustering of defects* - events that are crucially important from the point of view of progression towards failure.

12. CRACK - MICROCRACK INTERACTION PROBLEM

Fracture propagation in brittle micro-inhomogeneous materials is often accompanied by microcracking (see, for example, observations of Han and Suresh [13] on high temperature fracture of ceramics).

Microcracking may affect the resistance to fracture through several physically different mechanisms (among them: toughening due to "energy sink"- expenditure of energy on nucleation of microcracks). Here, we discuss the mechanism of *elastic interactions* of the main crack with microcracks (see [14] for details). Such interactions result in either decrease or increase of SIF at the main crack tip, thus producing either toughening or enhancing effect on fracture propagation.

In the analysis of this mechanism, the absense of correlation between the effective elastic constants and the fracture-related properties is particularly apparent. Indeed, if the microcracked zone is modelled by an elastic material of reduced stiffness, the impact of this zone on the main crack tip is the one of shielding. In reality, however, the interaction effect is dominated by the several microcracks closest to the main crack tip, and is highly *sensitive to the exact positions of these closest neighbours.*

Therefore, if locations of the microcrack centers are more or less random, the impact of microcracks on SIFs fluctuates significantly and even qualitatively (from shielding to amplification) from one sample of the microcrack statistics to another. Thus, in the 2-D case, there is no statistically stable effect of either shielding or amplification. In the 3-D case (crack front interacting with arrays of microcracks), presence of *local peaks* of SIFs along the crack front (where local crack advances will take place) makes the overall effect of interactions the one of amplification [15] - contrary to the predictions obtained by replacing the microcracked zone by an "effective" material of reduced stiffness.

(This does not exclude, of course, the possibility of stress shielding due to interactions with some *special* microcrack arrangements, like an extremely dense array of microcracks parallel to the main crack [16] or when locations of the microcrack centers are not random but "biased" towards shielding configurations, as seems to be the case in some experimental observations [13]).

Note, also, that stochastic asymmetries in the microcrack array produce *mode II* SIF on the main crack under mode I loading. This effects - physically significant since it causes crack kinking - is missed if the damage zone is modelled by an effective material of reduced stifness.

13. CASES WHEN FRACTURING CAN BE MONITORED BY CHANGE OF EFFECTIVE ELASTIC STIFFNESS

The basic reason for the absense of direct correlation between progression towards fracture and change of the effective elastic moduli is that the fracture-related quantities (like SIFs) are determined by *local fluctuations* of the microdefect field geometry whereas the effective elastic properties are *volume average* quantities, relatively insensitive to such fluctuations.

Therefore, in the cases when evolution of the defects' population follows more or less *deterministic* pattern, the progression towards fracture may indeed be monitored by reduction of the effective elastic stiffness. Such situations occur in certain laminated composites: for a *fixed arrangement of layers*, formation of microcracks may follow well established patterns; see [17] where these patterns were called "characteristic damage states".

(We note, however, that, even in these cases, the correlation is not straightforward: as fig.7 of [17] shows, for two (out of three) arrangements of layers, the E-T curve is almost flat during most of the specimen's lifetime).

14. CONCLUSIONS

We discussed the continuum characterization of crack fields by tensorial volume average quantities, and the limitations of such approaches.

It appears that the continuum characterization may provide useful insights into various *effective* properties of cracked solids, like effective elastic moduli, effective conductivity, etc. At the same time, it may not be adequate for the *fracture-related* properties. The basic underlying reason is that the fracture-related quantities (like stress intensity factors) are sensitive to *local fluctuations* of the crack array geometry (like defects' clustering) to which the volume averages are not very sensitive.

ACKNOWLEDGEMENT. Support of the U.S.Army Research Office (Grant DAAL02-88-K-0027) and of the U.S.Department of Energy (Grant DE-FG02-86ER3607) is acknowledged.

REFERENCES

1. Vakulenko, A. and Kachanov, M. (1971), "Continuum theory of medium with cracks", *Mechanics of Solids*, v.6, no.4, pp.145-151, Plenum Press (English transl. of Izvestia AN SSSR, Mekhanika Tverdogo Tela).

2. Kachanov, M. (1980), "Continuum model of medium with cracks", *Journal of the Engineering Mechanics Division*, v.106, no.EM5, pp.1039-1051.

3. Sayers, C. and Kachanov, M. (1991), " A simple technique for finding effective elastic constants of cracked solids for arbitrary crack orientation statistics", *International Journal of Solids and Structures*, v.27, no.6, pp.671-680.

4. Budiansky, B. and O'Connell (1976),"Elastic moduli of a cracked solid", *International Journal of Solids and Structures*, v.12, pp.81-97

5. Oda, M.,Yamabe,T. and Kamemura, K. (1986), " A crack tensor and its relation to wave velocity anisotropy in jointed rocks", *International journal of rock mechanics and mining sciences*, v. 23, no.6, pp.387-397.

6. Kachanov, M. (1987), "Elastic solids with many cracks: a simple method of analysis", *International Journal of Solids and Structures*,v.23, pp.23-43.

7. Talreja, R. (1985), " A continuum mechanics characterization of damage in composite materials", *Proceedings of the Royal Society of London*, A399, pp. 195-216.

8. Hoenig, A. (1979), " Elastic moduli of a non-randomly cracked body", *International Journal of Solids and Structures*, v.15, pp.137-154.

9. Krajcinovic, D. (1983), "Constitutive equations for damaging materials", *Journal of Applied Mechanics*, v. 50, pp. 355-360.

10.Mehrabadi,M.M. and Nemat-Nasser,S.(1983),"Stress, dilatancy and fabric in granular materials", *Mechanics of Materials*, v.2,pp.155-161.

11.Kanatani,[illegible]K.,"Stereological determination of structural anisotropy", *International Journal of Engineering Sciences*, v.22,pp.531-546.

12. Leckie, F. and Onat, T. (1981), "Tensorial nature of damage measuring internal variables", in *Physical non-linearities in Structural Analysis*, Springer, Berlin, pp.140-155.

13. Han, L.X. and Suresh, S. (1989), "High temperature failure of an alumina-silicon composite under cyclic loads", *Journal of the American Ceramic Society*, v.72, pp.1233-1238.

14. Kachanov,M.,Montagut,E. and Laures,J.P.(1990), "Mechanics of crack-microcrack interactions", *Mechanics of Materials*, v.10,pp.59-71.

15. Laures, J.-P. and Kachanov, M.(1991), "Three-dimensional interactions of a crack front with arrays of penny-shaped microcracks", *International Journal of Fracture*, v. 48, pp.255-279.

16.Chudnovsky, A. and Wu,S.(1990), "Effect of crack-microcrack interactions on energy release rates",*International Journal of Fracture*,v.44, pp.43-566

17. Reifsnider,K. and Stinchcomb(1983),"Stiffness change as a fatigue damage parameter for composite laminates",*Advances in Aerospace Structures, Materials and Dynamics*, ed.U.Yuceoglu et al,ASME,N.Y,pp.1-6

SESSION IIB: APPLICATION

Session Chairman: *Dr. D. Tracey*

ESTIMATION OF RESIDUAL STRESSES IN RAILROAD RAILS

A.B. Perlman[1]
J.E. Gordon[2]
M. Zamora[3]
O. Orringer[2]
J. Orkisz[4]

[1] Professor, Department of Mechanical Engineering
Tufts University, Medford, MA 02155

[2] Mechanical Engineer, Volpe National Transportation Systems Center
U.S. Department of Transportation, Cambridge, MA 02142

[3] Technical Analyst, E.G.&G. Dynatrend, Cambridge, MA 02142

[4] Professor, Cracow Institute of Technology
Cracow, Republic of Poland

Introduction

One of the contemporary challenges in solid mechanics is the prediction of residual stresses in bodies subjected to plastic deformation under rolling contact. In particular, it is of great practical interest to estimate the actual shakedown residual stresses when such bodies are subjected to repeated loading which can be described in terms of an envelope. Bearings, rail vehicle wheels, and railroad rails are examples of such bodies.

The problem of calculating residual stress in railroad rails has motivated implementation of the scheme for practical applications. Recent studies have demonstrated that residual stresses play a significant role in the formation and propagation of fatigue cracks in rails [1 - 4]. Figure 1 illustrates the concern with this issue [5]. The thin lines are contours of measured values of the axial residual stress, σ^r_{zz}, in a rail, superposed on a schematic representation of the growth of a detail fracture (DF). This rail was involved in a controlled crack growth experiment which was conducted at the Facility for Accelerated Service Testing (FAST) at the Transportation Test Center in Pueblo, Colorado. The DF began as a shell in the rail head propagating longitudinally just below the running surface. At some point in service, this shell turned down into the head and began to grow in the plane of the rail cross-section. In this figure, the three heavy lines denote the course of the crack front during the experiment. They represent crack front positions during slow growth. The positions shown correspond to crack

sizes, in terms of respective percent of the rail head area: 12%, 30% and finally 80%, at which the rail fractured. A section of rail adjacent to the fracture was removed following the test and subjected to a destructive procedure for estimating residual stress states [6]. The shaded area identifies the region of tension for the axial component determined by the measurements. The rail was also subjected to thermal stress (axial tension) during the test, since it was installed in a string of continuous welded rail similar to the construction found in modern railroad track. When the effect of the thermal stress is considered, the figure suggests that most of the observed crack growth occurred in a zone of moderate tension on the plane containing the crack. Clearly such stresses will tend to accelerate the crack growth rate for this type of rail defect, a potentially serious safety problem for railroads in the United States and Europe.

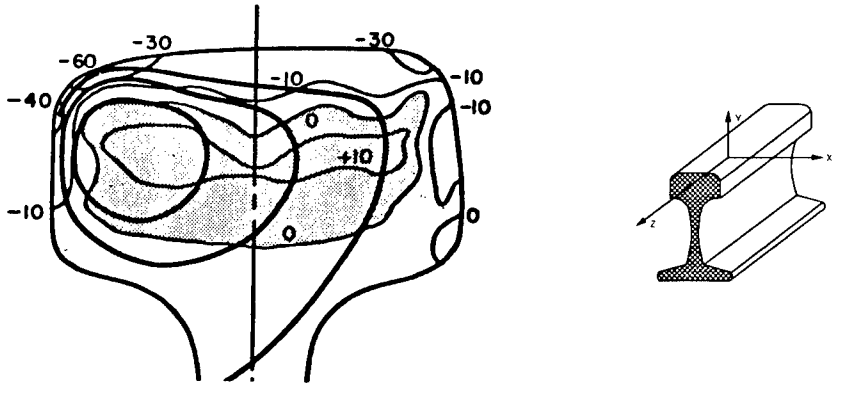

Figure 1. Experimental contours of axial residual stress with fatigue crack profile superposed. Contour levels in ksi (1 ksi = 6.895 MPa).

Background

Classical shakedown analysis, based on Melan's and Koiter's theorems [7, 8], yields the residual stress or strain distribution for the maximum load at which a shakedown state exists. Conversely, this type of analysis cannot be used to find the residual stress or strain distribution corresponding to actual maximum loads which are smaller than the maximum shakedown load.

As part of the Federal Railroad Administration's rail integrity research program, a new approach has been developed to estimate the residual stress distribution corresponding to actual loads, under certain simplifying assumptions [9, 10]. The mathematical basis for the model is a formulation of the problem proposed and developed by Orkisz [9]. The problem is treated as quasi-static,

and the loading program is assumed to be cyclic with specified bounds. Also, the material is assumed to behave as an elastic - perfectly plastic medium with a flow stress independent of both load amplitude and number of cycles, and the actual residual stresses are assumed to be time-independent. An additional convenient assumption, which also has some experimental support, is that the residual stresses may be characterized by a field $\sigma_{ij}^r(x, y)$, independent of the axial coordinate z along the rail.

Under the foregoing assumptions, an estimate of the residual stress distribution $\sigma_{ij}^r(x_k)$ is obtained by means of a nonlinear optimization to find the minimum of the total complementary energy:

$$W(\sigma_{ij}^r - \sigma_{ij}^{Ro}) = \frac{1}{2}\int_V C_{ijkl}(\sigma_{ij}^r - \sigma_{ij}^{Ro})(\sigma_{kl}^r - \sigma_{kl}^{Ro})dV \tag{1}$$

subject to the constraints:

$$\frac{\partial \sigma_{ij}^r}{\partial x_j} = 0 \text{ in V (equilibrium equations)} \tag{2}$$

$$\sigma_{ij}^r \nu_j = 0 \text{ on } S_\sigma \quad \text{(static boundary conditions)} \tag{3}$$

$$\Phi(\sigma_{ij}^r + \sigma_{ij}^E) \leq 0 \text{ in V (yield conditions)} \tag{4}$$

where C_{ijkl} are the elastic compliance moduli, ν_j are the components of the unit outward normal vector to S_σ, $\sigma_{ij}^{Ro}(x_k)$ are the actual initial residual stresses in the body, and $\sigma_{ij}^E(x_k, t)$ is the stress distribution obtained from a solution of a purely elastic boundary value problem for the body under the given maximum applied loads. The nonlinear inequality constraint (4) used in the present work is the Mises - Hencky criterion:

$$\Phi(\sigma_{ij}) = (\sigma_{11} - \sigma_{22})^2 + (\sigma_{22} - \sigma_{33})^2 + (\sigma_{33} - \sigma_{11})^2 + 6(\sigma_{12}^2 + \sigma_{23}^2 + \sigma_{31}^2) - 2\sigma_Y^2 \tag{5}$$

where $\sigma_{ij} = \sigma_{ij}^r + \sigma_{ij}^E$ and σ_Y is the material flow stress. For analysis of a rail, the flow stress is assumed to be equal to the specified yield strength of new rail. This assumption has been made to avoid the bias in the comparison of results for different grades of steel. Also, it is well known that rail steel which has worked thoroughly under the contact stress levels found in service tends to exhibit

reduced yield strength coupled with kinematic hardening to plastic stress levels above the original yield strength. Thus the present model may be viewed as a compromise for the actual stress-strain diagram. The method presented here can, in principle, accommodate more complicated material models, e.g., different yield strengths as a function of location in the rail cross-section, representing the in-situ properties after work-hardening in service. The residual stress estimate σ_{ij}^{r} thus obtained corresponds to an upper bound in the sense that $W(\sigma_{ij}^{r} - \sigma_{ij}^{Ro}) \geq W(\sigma_{ij}^{R} - \sigma_{ij}^{Ro})$.

Alternative models based on the finite element method (FEM), boundary element method (BEM), and finite difference method (FDM) have been formulated to discretize $\sigma_{ij}^{r}(x_k)$ in the complementary energy objective function [11]. Most of the numerical implementation work completed to date has been based on the original finite element formulation, which has advanced to the initial stage of practical application.

The calculation procedure takes place in three distinct phases. First, the elastic solution, which comprises the input to the nonlinear optimization, is obtained by applying a contact pressure distribution (which simulates a railroad wheel in contact with the rail head). The equations of bending for a beam on an elastic foundation are used in conjunction with some assumptions which describe the contact stress distribution to result in a complete description of the elastic stresses induced in the rail cross-section under consideration.

Next, with substructuring elimination techniques, the objective function is reduced to an expression in terms of the essential decision variables, namely: those coefficients which determine $\sigma_{ij}^{r}(x_k)$ at a set of discrete locations in the region of the body which is assumed to have experienced plastic yielding and flow before shakedown (the "assumed plastic zone"). The search for these coefficients comprises the final phase of the calculation procedure.

A software package for generalized nonlinear optimization [12] was modified for the present work by taking advantage of the convex quadratic form of the Mises - Hencky yield condition. The new procedure has recently been enhanced by the addition of two new algorithms. The first guides the adjustment of the assumed plastic zone as the optimization progresses; the second determines the degree of satisfaction of the Kuhn - Tucker optimality conditions [13]. In combination, these additions to the optimization procedure have significantly increased the level of automation possible in conducting these analyses.

The nonlinear optimization scheme performed well in numerical experiments on simple problems with independently known exact solutions. The first group of test problems was based on a model of a beam with a rectangular cross section. Cases of pure bending and combined bending/tension were examined. In the second group of experiments, the optimization scheme results were compared with independent solutions of the problem of a thick-walled cylinder subjected to internal pressure, axial load, and torsion singly and in combination [11, 14 - 16]. All cases produced results of good quality, i.e., the solutions obtained by means of the optimization scheme converged rapidly to the independent solutions within a few iterations and with modest spatial grid refinement.

These test cases are the basis for an analysis of the rail problem, since the discretization can be carried out on a two-dimensional grid in the rail cross section. Figure 2(a) illustrates a typical result for the axial residual stress σ'_{zz} computed for the AREA 132 lb/yd rail section. The figure shows only the rail head, and stress contours are shown only in the regions where the stress is tensile. This result, obtained in an earlier calculation [11], is in reasonable qualitative agreement with measurements of axial residual stress in rails which have been subjected to rail vehicle wheel loads, such as the example shown in Figure 2(b) [17].

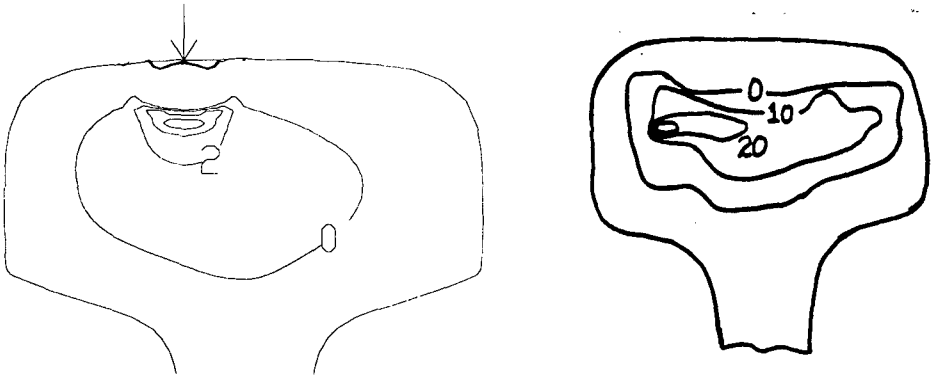

(a) Typical residual stress prediction for 33-kip (147 kN) vertical wheel load. Contours plotted at 2 ksi intervals.

(b) Experimental stress measurements on AREA 132 rail section exposed to service loading.

Figure 2. Comparison of predicted and measured residual stresses. (Axial tensile stress contours shown.)

However, it has not been possible to make a direct quantitative comparison between the idealized analyses and measurements of rail stress caused by train traffic because of five factors which complicate the numerical modeling task.

First, unlike the idealized single-line-of-travel assumption, railroad vehicle wheels actually tend to wander laterally about an average center-of-contact position on the rail, sometimes also producing two distinct contact regions. This tends to laterally diffuse the residual stress as well (see Figure 2(b)). Second, the magnitudes of traffic loads can only be described in terms of probability distributions because vehicle gross weights vary and the wheel loads are further influenced by vehicle dynamics. Thus, the maximum applied load required as input to the analysis cannot be specified with absolute certainty. Third, the wheel/rail contact force usually has lateral and axial components in the running surface tangent plane, as well as the normal component presently modeled. The tangent force components can be included in principle, but one must first have reliable values for their magnitudes and reliable solutions for the corresponding elastic stress distributions. Fourth, the elastic stress distributions corresponding to the normal contact force and rail bending are based on engineering approximations, since the precise distributions are not known. Fifth, rail steel exhibits considerable plastic strain hardening, unlike the elastic - perfectly plastic material model presently assumed in the analysis. A sixth factor, the stiffness of the track foundation, also defies precise modeling but appears to have little effect on rail residual stress.

While residual stress predictions thus cannot be directly compared with measurements on rails taken from service, they can be compared with the results of well controlled full scale laboratory experiments. Such experiments are now in progress at the Central Research Institute of the Polish State Railways [18]. A special-purpose fixture applies repeated rolling contact loads to samples of unused rail of UIC-60 section, with the load magnitude and line of travel precisely controlled. In the initial experiments, the wheel travels along the rail crown in pure rolling motion (no tangent forces), and the rail base rests directly on a heavy steel bed to suppress foundation flexibility effects. After the loading program is completed, these samples will be destructively sectioned following a procedure similar to that described in [6] in order to measured the residual stress distribution.

Of the five factors described above which complicate this modeling task, the first three are precisely controlled in the experiment, and can be adequately duplicated in the analytical approach. Thus, the only aspects of the experiment not precisely modeled in the present analysis are the contact pressure and stress distributions and the strain hardening property of the rail steel. The effects of foundation flexibility, eccentric line of travel, and loading with tangent components are to be introduced in later experiments.

Results and Discussion

A model used to calculate residual stress fields must account for these same factors. In addition, selection of a mesh and representation of the elastic stress field are extra considerations that influence the accuracy of the estimate when a numerical procedure is implemented.

Control of load position, magnitude and direction equal to that in a laboratory experiment is routine for the numerical model. Matching the material properties and contact patch that exist in a test is more challenging. It was mentioned earlier that a flow stress equal to the yield strength of new rail is assumed to obtain an elastic - perfectly plastic model which is a rough compromise for the actual cyclic stress-strain diagram for rail steel. No such rationalization is possible to account for the uncertainties in estimating the geometry of the contact zone. A calibration of the analytical solution to the results of the experiments must be made to properly adjust the assumed dimensions of the patch.

The goal of this study is to examine the unique factors introduced by the implementation of the numerical calculation so that a procedure can be defined to compare the analytical estimates with strain gauge readings taken during the experiments.

The elastic stress distribution used in this work is obtained by superposition of a beam on elastic foundation representation of the rail in bending [3] and the stress resulting from contact. Questions have been raised about the validity of the beam representation, particularly in a situation where the foundation is very stiff, the circumstance of the current experiments. To investigate the validity of the numerical approach used to compute the elastic field which serves as input to the nonlinear optimization problem, a quarter-symmetric three-dimensional finite element model of the UIC-60 rail section was developed from the two-dimensional model used in the residual stress analysis shown in Figure 2(a). The three-dimensional model was constructed by extruding the two-dimensional grid to a length of approximately eighteen inches in the z-direction, resulting in a model consisting of 1645 elements and 1850 nodes. The calculation was performed using the NIKE3D code. The experiments in Warsaw take place on an extremely stiff foundation which eliminates the beam on elastic foundation effects, thus permitting the comparison with this simple finite element model since three-dimensional wave effects at relatively long distances from the load application point do not exist.

The results of this comparison indicate that the empirical estimates appear reasonable. It is also suggested by these results that the softer foundation which

exists beneath rails in service should not have a strong effect on the predictions of residual stress, since the stress distribution in the railhead is dominated by contact stresses.

Previous experience has identified difficulties in characterizing these analytical predictions in terms of a single scalar indicator, such as the maximum axial residual stress predicted at a single nodal location [11]. Two issues are of interest here. First, a measure of the maximum axial residual stress in the tensile zone is desired because of its importance in fatigue crack growth calculations (see Figure 1). Second, selection of nodal locations that are coincident with the maximum value of any stress component *a priori* is nearly impossible. The dependency of the predictions of the analytical model on the mesh used in the analysis is evident in Figure 3, which shows contour plots of the distribution of axial residual stress in the plane of the cross-section and a composite plot of the distributions along the vertical centerline of the rail for three different meshes. All results in Figure 3 are for a 33.12-kip vertical wheel load which is the load level to be used in the first series of experiments at the Railway Institute in Warsaw.

From the point of view of railroad operations, the most interesting effect on residual stress is the magnitude of the wheel load imposed. Empty cars (low wheel loads) cause very little plasticity and low levels of residual stress, while increased wheel loads show a substantial rise in the amount of residual stress imparted to the rail head. In the analytical procedure used here, increasing the wheel load results in an increased number of elements in the assumed plastic zone, and a proportionate number of decision variables in the nonlinear optimization problem. Higher loads used with meshes with many elements are likely to pose computational challenges.

The meshes depicted in Figure 3 were used in calculations with several different loads as listed in Table 1. As can be seen in the table, calculations were made at load levels from 10 to 50 kips, with at least two meshes for each load. Peak vertical wheel loads in excess of 50 kips are not uncommon in North American railroad operations. Dynamic amplification factors up to 3.3 have been recorded in experiments on the Northeast Corridor. Mesh C (the finest of the three under consideration) has been used at each load level except for the 50-kip case in which Meshes A and B were used in the calculation. Computational difficulties associated with large numbers of decision variables, were experienced during the course of the 50-kip calculation with Mesh C. Generally, the finest mesh used predicted the maximum value of axial residual stress.

As seen in Figure 3(d), the single nodal value representing the maximum (or minimum) will be extremely sensitive to the strong gradient of axial residual stress as well as the location of the extreme value. This leads to the conclusion that any given mesh may not be capable of capturing the true peak magnitude of a stress component. The proximity of a node to the peak stress location is thus as important as the mesh density. Therefore, we have chosen to operate with a fixed mesh, in spite of the fact that it may not produce a consistent maximum. To compensate for this weakness, we have also chosen to use an averaged measure as explained below.

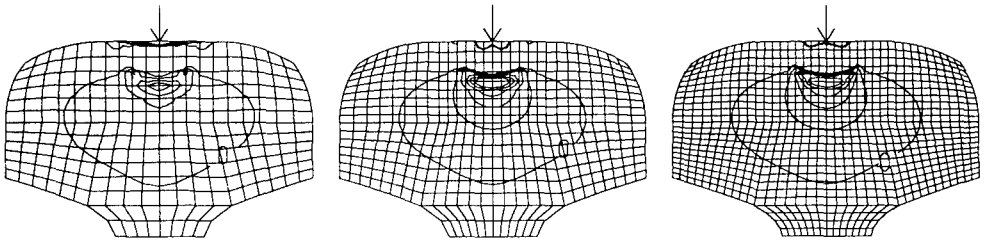

Contours plotted at 1 ksi intervals.

(a) Mesh A: 412 elements; 474 nodes. Nodal maximum: 4.1 ksi.

(b) Mesh B: 768 elements; 849 nodes. Nodal maximum: 8.1 ksi.

(c) Mesh C: 1248 elements; 1351 nodes. Nodal maximum: 7.7 ksi.

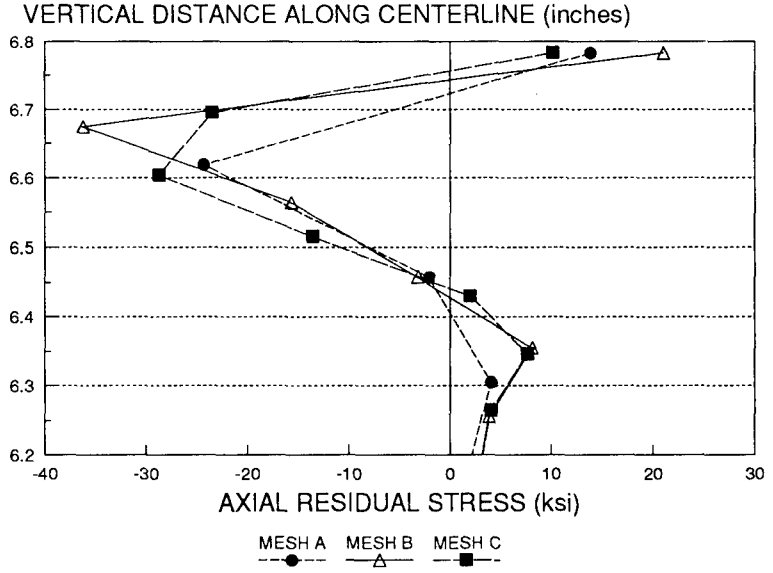

(d) Distributions of axial residual stress along vertical centerline.

Figure 3. Distributions of axial residual stress in UIC-60 rail head for three mesh densities.

Table 1. Load levels and meshes used in current study.

VERTICAL LOAD (kips)	MESHES USED
10	B, C
20	A, B, C
27	B, C
30	A, B, C
33.12	A, B, C
38	B, C
40	A, B, C
44	B, C
50	A, B

Since coordination of these predictions with experimental measurements is a primary objective of this study, averaging of nodal numerical values over a defined area is a sensible means to address this dependency on mesh construction. Actual occurrences of highly localized peaks predicted by the analytical method would be suppressed by the averaging inherent in measurements made over a finite physical length of a transducer such as a strain gauge. This consideration is the basis for adopting a 0.175-inch by 0.090-inch area, equal to that of the gauges used in the experiments, as the averaging region. Nine points, one at the node located at the local maximum, the others at the corners and mid-sides of the rectangular area superposed on the finite element mesh (as shown in Figure 4), are used in the calculation. The values at these locations are linearly interpolated from the stresses calculated at the four adjacent mesh nodes. The weighted sum of the point values is the average stress over the area occupied by this fictitious "gauge."

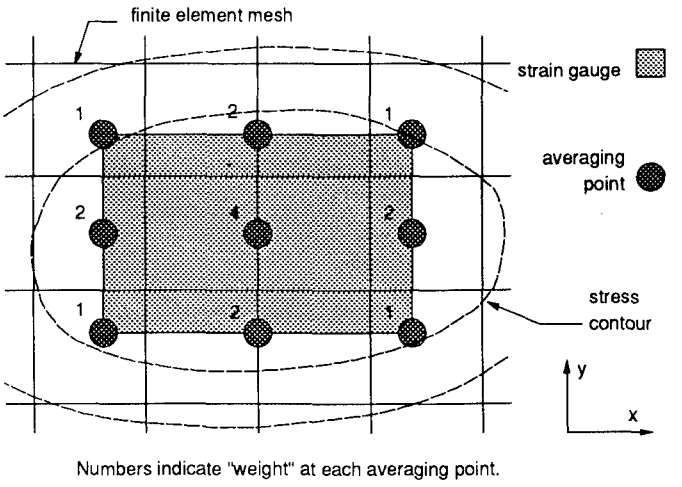

Figure 4. Schematic of strain gauge averaging procedure.

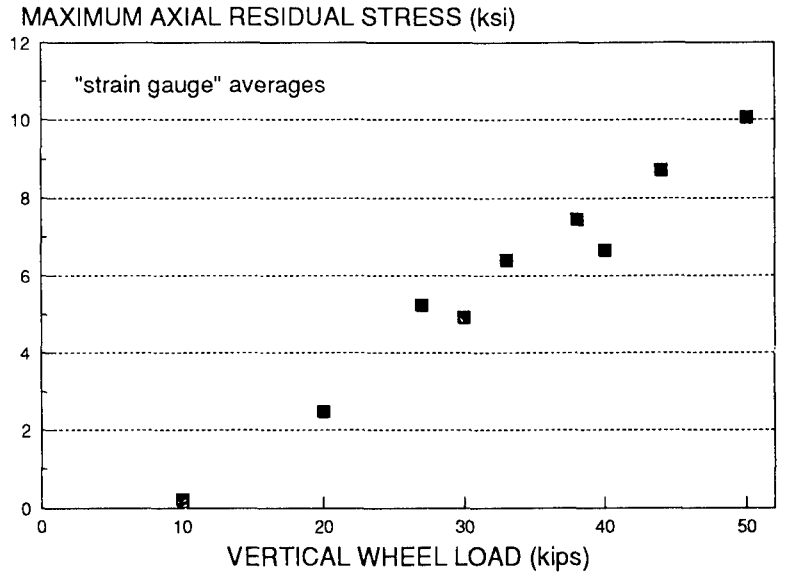

Figure 5. Strain gauge averaging procedure applied to analytical results.

Figure 5 illustrates the results for the cases listed in Table 1, after application of the averaging procedure. Each point in the Figure represents the highest nodal average computed for calculations performed with Mesh B or C at each load level. The trend displayed in the figure does not clearly indicate either saturation (leveling off) or a continued increase. However, it is clear from this data that

wheel load magnitude has a significant effect on the axial residual stress present in the rail, whose value increases from approximately 0.2 ksi at 10 kips to over 10 ksi at 50 kips. The area of residual tension remaining in the rail head at 50 kips has grown as well. (Note that the 2-ksi contour for the 50-kip load in Figure 6(a) encloses an area larger than any of the areas enclosed by the 1-ksi contours in Figure 3(a, b, c) for 33.12 kips.)

Figure 6(b) is a plot of the axial residual stress distribution along the vertical centerline for the 50-kip case. Comparison of this plot with Figure 3(d) suggests that artificial strain gauge average must be interpreted with some care. In particular, it appears that the average is depressed by the strong stress gradient in those cases for which the applied load is less than 40 kips. Conversely, the nodal maximum and the area average may be nearly equal at higher loads.

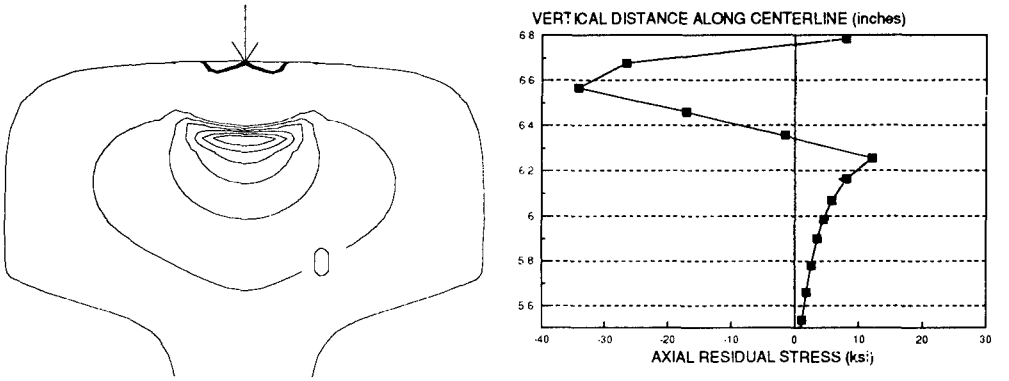

(a) Axial residual stress distribution. Contours plotted at 2 ksi intervals.

(b) Vertical distribution of axial residual stress along centerline.

Figure 6. Results for 50-kip load on UIC-60 rail section.

The actual pressure distribution to which the rail is subjected is dependent on a variety of location-specific variables. Variations in wheel tread profile and rail head geometry caused by wear can significantly alter the shape and position of the contact zone. Previous studies of wheel/rail contact have provided sufficient data to support the premise that many distributions are possible [19].

The most common estimate of the contact area and pressure distribution used in wheel/rail interaction models is elastic Hertz contact, idealized as an elliptic contact patch created by imposing a vertical load on a pair of crossed cylinders as shown in Figure 7(a). This approximation cannot possibly account for all details of field conditions, since there is no provision for transmission of

tangential loads. Also, experimental evidence [19] indicates that the actual contact area is more nearly rectangular than elliptic and that the maximum contact pressure is often lower than the Hertzian prediction.

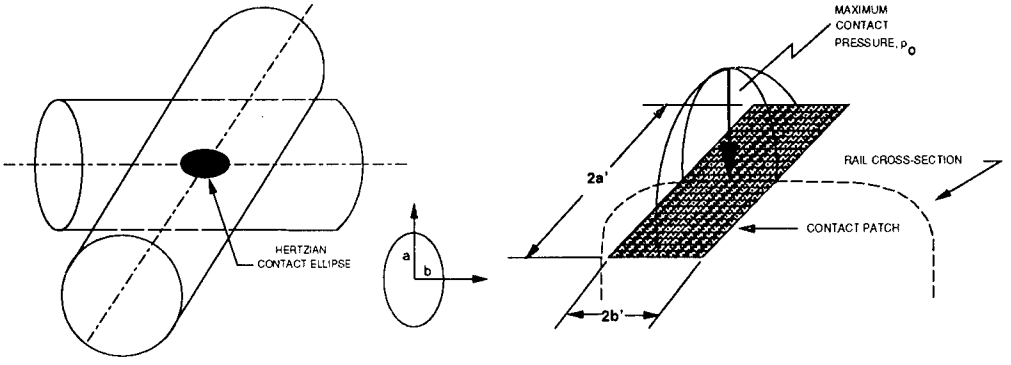

(a) Schematic of elastic Hertz contact. *(b) Translation to wheel/rail contact.*

Figure 7. Contact pressure distribution characterization.

The analytical representation of contact stresses in the elastic solution used in the present work is based on a Green's function approach which uses a Boussinesq point load that allows adaptation of the solution to an arbitrarily selected patch. For simplicity, a bi-parabolic pressure distribution applied to a rectangular area of the rail surface was assumed to simulate wheel/rail contact as depicted in Figure 7(b). For each wheel load considered, a Hertz crossed-cylinder calculation was performed to determine a maximum pressure, p_{max}, and the dimensions of the contact ellipse, a and b, as shown in Figure 7(a). The size of the corresponding rectangular patch, $2a' \times 2b'$, was set by scaling the dimensions of the calculated ellipse to make the maximum pressure in the bi-parabolic distribution, p_o, equal to p_{max}.

It is interesting to observe the effect on the residual stress predictions of variations in the dimensions of the contact rectangle. Figure 8 illustrates three results obtained by applying the static 33.12-kip wheel load over contact patches of varying size. The simplest measure of the resulting load intensity is found by normalizing the maximum pressure at the center of contact (p_o) by the material yield strength in shear (k). For rail steel, the parameter k is approximately 40.5 ksi. The residual stress value at each of these points is that obtained after averaging as described above. The sensitivity of the maximum axial residual stress prediction is clearly seen from this plot. The value of p_o / k was varied from a minimum of 4.5 to a maximum of 5.84 by adjusting the dimensions of

the contact patch. It is also interesting to note that these extremes are comparable to those for the minimum and maximum loads used in this study. (For a 20-kip wheel load, p_o / k is 4.24; at 50 kips, p_o / k is 5.77.)

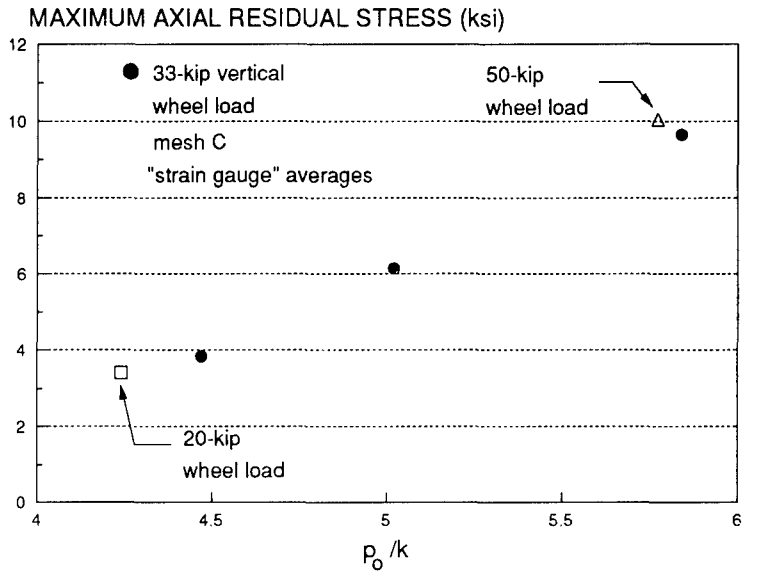

Figure 8. Axial residual stress predictions for 33-kip vertical wheel load distributed over contact zones of varying size.

Concluding remarks

If our calculation procedure is truly capable of replicating the experimental results, then it should be possible to match a data point from Figure 8 to the maximum axial residual stress measured in the experiments conducted at the same load, which will indicate the apparent value of p_o/k which was imposed during the programmed loading. One possible means of checking this hypothesis would be to estimate the contact zone size by measuring its apparent width on a sample of rail in the loading fixture. As it becomes available, this information will permit modifications to the procedure used to model the size of the contact patch.

These results have substantially increased our confidence in quantitative predictions of residual stress in bodies as complicated as loaded rails. It is obvious that further work is needed to establish criteria for relating mesh characteristics to the accuracy of a solution. However, the current approach of checking results with multiple meshes is adequate to proceed with a systematic investigation of

the influence of operational factors on residual stress levels. Sensitivity to assumed values of flow stress and to variation of the point of load application are logical candidates for the next investigation.

By coordinating the use of the nonlinear optimization scheme in parallel with a series of increasingly complex experiments, we hope to establish quantitative confidence in the software in an orderly manner, refining one or two aspects of the model at each stage, as needed. The completed model will then be a valuable tool for interpreting the results of measurements on rails taken from service and for evaluating the extent to which rail vehicle weights can be increased to improve railroad productivity.

References

[1] D.Y. Jeong, A.B. Perlman, R.C. Rice, and O. Orringer, "Beam theory predictions of shell nucleation life", in *Contact Mechanics and Wear of Rail/Wheel Systems II* (G.M.L. Gladwell, H. Ghonem, and J. Kalousek, ed.), University of Waterloo Press, Waterloo, Ontario, Canada, addendum, 1987.

[2] D.D. Davis, M.J. Joerms, O. Orringer, and R.K. Steele, "The economic consequences of rail integrity", Association of American Railroads, Chicago Technical Center, Chicago, IL, R-656, 1987.

[3] O. Orringer, Y.H. Tang, J.E. Gordon, D.Y. Jeong, J.M. Morris, and A.B. Perlman, "Crack propagation life of detail fractures in rails", DOT Transportation Systems Center, Cambridge, MA, DOT/FRA/ORD-88/13, 1988.

[4] O. Orringer, "Rail testing: strategies for safe and economical rail quality assurance", *Transportation Research Record 1174: Rail Replacement and Maintenance Management*, Transportation Research Board, National Research Council, Washington, DC, 28-42 (1988).

[5] O. Orringer, J.M. Morris, and D.Y. Jeong, "Detail fracture growth in rails: test results", *Theoretical and Applied Fracture Mechanics, 5(2)*, 63-95 (1986).

[6] J.J. Groom, "Determination of residual stresses in rails", Battelle Columbus Laboratories, Columbus, OH, FRA/ORD-83/05, 1983.

[7] W.T. Koiter, "General theorems for elastic-plastic solids", in *Progress in Solid Mechanics* (R. Hill and I. N. Sneddon, ed.), North Holland Publishing Company, Amsterdam, 1960.

[8] G. Martin, *Plasticity: Fundamentals and General Results*, MIT Press, Cambridge, MA, 1975.

[9] J. Orkisz and A. Harris, "Analysis of residual stresses at shakedown: a hybrid approach", *Theoretical and Applied Fracture Mechanics 9*, 109-128 (1988).

[10] J. Orkisz, O. Orringer, M. Holowinski, M. Pazdanowski, and W. Cecot, "Discrete analysis of actual residual stresses resulting from cyclic loadings", *Computers & Structures 35(4)*, 397-412 (1990).

[11] O. Orringer, J. Orkisz, and Z. Swiderski (ed.), *Residual Stress in Rails: Effects on Rail Integrity and Railroad Economics. Vol. II: Theoretical and Numerical Analyses*, Kluwer Academic Publishers, Dordrecht, The Netherlands, in press.

[12] G.N. Vanderplaats, "ADS - a FORTRAN program for automated design synthesis, Version 1.10", Engineering Design Optimization, Inc., Santa Barbara, CA, 1985.

[13] D.A. Wismer and R. Chattergy, *Introduction to Nonlinear Optimization*, North Holland Publishing Company, Amsterdam, 1978.

[14] R. Hill, E. Lee, and S.J. Tupper, "The theory of combined plastic and elastic deformation with particular reference to a thick tube under internal pressure", *Proc. Royal Soc. 191*, 278-303 (1947).

[15] P.G. Hodge, Jr. and G.N. White, "Quantitative comparison of flow and deformation theories of plasticity", *J. Applied Mechanics 17(2)*, 180-184 (1950).

[16] M. Zyczkowski, *Combined Loadings in the Theory of Plasticity*, PWN - Polish Scientific Publishers, Warsaw, 1981.

[17] C.H. Cundiff and R.C. Rice, "Comparative evaluation of several alternative methods for measuring rail residual stress", *Residual Stress in Rails: Effects on Rail Integrity and Railroad Economics Vol. I: Field Experience and Test Results*, (O. Orringer, J. Orkisz, and Z. Swiderski, ed.), Kluwer Academic Publishers, The Netherlands, in press.

[18] Z. Swiderski and A. Wójtowicz, "Plans and progress of controlled experiments on rail residual stresses using the EMS-60", *Residual Stress in Rails: Effects on Rail Integrity and Railroad Economics Vol. I: Field Experience and Test Results*, op.cit.

[19] Andrews, H.I., "The Creep of Locomotive Driving Wheels", *Rail Engineering International 5(1)*, 1975.

COMPARISON OF FATIGUE AND DAMAGE-TOLERANT LIFE ESTIMATES FOR A LIGHT WEIGHT TWIN ENGINE AIRPLANE

Y. H. Tang
M. G. Violette
O. Orringer

Volpe National Transportation Systems Center
US Department of Transportation
Cambridge, MA 02142

Introduction

In the past, the commuter aircraft were designed in accordance with safe-life fatigue calculations as a life estimation method. A group of experts in the aircraft industries has recently suggested that commuter airplanes should be inspected based on damage tolerance criteria. The commuter aircraft manufacturers, however, lack funding and resources to perform detailed damage tolerance assessments. As part of the Federal Aviation Administration's (FAA's) Continued Airworthiness Research Program, the Volpe National Transportation Systems Center (VNTSC) is developing simplified damage tolerance estimation methods applicable to commuter airplanes. One of the tasks was to perform life calculations for the wing spar of a light weight twin engine airplane.

In November 1990, VNTSC presented the method being developed, together with preliminary results. Table 1 lists life estimates for the twin engine airplane wing spar, and the method of calculation used. The first four entries in the table are based on "safe life" fatigue calculations. The values for the Australian CAA and the British CAA have been established as life limits for the same model of airplane operating in those countries. The factored lives are listed in Table 1, but the scatter factors and unfactored lives are unavailable. The last entry in the table was based on the present damage tolerance approach, described in Section 4.

At the November meeting, the industry experts raised two concerns about the damage tolerance calculations. The first concern was the validity of the crack growth rate (da/dN) data used, which was taken from the 1975 Battelle Damage Tolerant Design Handbook [1]. The group considered the 1975 data inaccurate because it was reduced using the

secant method rather than the currently accepted incremental polynomial method. The second concern was the accuracy of the analytical method, compared with a block spectrum computation method.

Table 1. Summary of life calculations for the light weight twin engine wing spar.

		Unfactored life (hours)	Scatter factor	Factored life (hours)
Australian CAA	safe life	-	-	13,000
British CAA	safe life	-	-	8,500
Manufacturer's aircraft report	safe life	65,000	5	13,000
VNTSC	safe life	31,000 to 40,000	3	10,300 to 13,000
VNTSC damage tolerance	slow crack growth life	22,850	2	11,425

Fatigue (safe-life) calculations

The fatigue calculations are based on the method given in [2] and on the example presented by Nauert and Campbell [3] for safe-life evaluation of general aviation airplanes. The analysis was performed assuming a 1-g stress level of 7288 psi, which was obtained from a report produced by the manufacturer of the airplane. The material was assumed to be aluminum 2024-T3 sheet.

The typical mission for the airplane was assumed to have a cruise velocity of 175 mph, and flights of 80 minutes each, or 0.75 flights per hour. As specified in the Federal Aviation Regulations [4], the incremental limit load factor, a_{nLLF} is 2.5 for gust and +2.8 and -2.52 for maneuvers. The incremental limit load factor represents a normal acceleration (in g's); steady level flight, or "1-g flight", is represented by a_{nLLF} of zero.

The fatigue life was calculated using Miner's Rule. The fatigue damage per hour is due to gusts, maneuvers, and the Ground-Air-Ground (GAG) cycle. Damage due to landing and taxiing were assumed to be negligible. The inverse of the total damage per hour is the fatigue life, in hours.

The procedure for calculating fatigue damage is the same for gusts and maneuvers, but the two load exceedance curves are different. The exceedance curves were taken from reference [2], for general-usage twin-engine aircraft, and are reproduced in Figure 1. These curves give cumulative exceedances per nautical mile, as a function of acceleration fraction, a_n/a_{nLLF}. Each curve was converted to a table of exceedances per hour. The lowest load in the table is approximately equivalent to the stress amplitude for $N = 3 \times 10^7$ cycles, the lowest stress amplitude for which results are plotted on the 2024-T3 S-N curves in MIL-HDBK-5E [5]. The load increments are somewhat arbitrary, but following the example calculation by Nauert and Campbell [3], increments of 0.06 in a_n/a_{nLLF} were used. The positive and negative load exceedances which occur with the same frequency were combined to obtain stress levels (S_{min}, S_{max}).

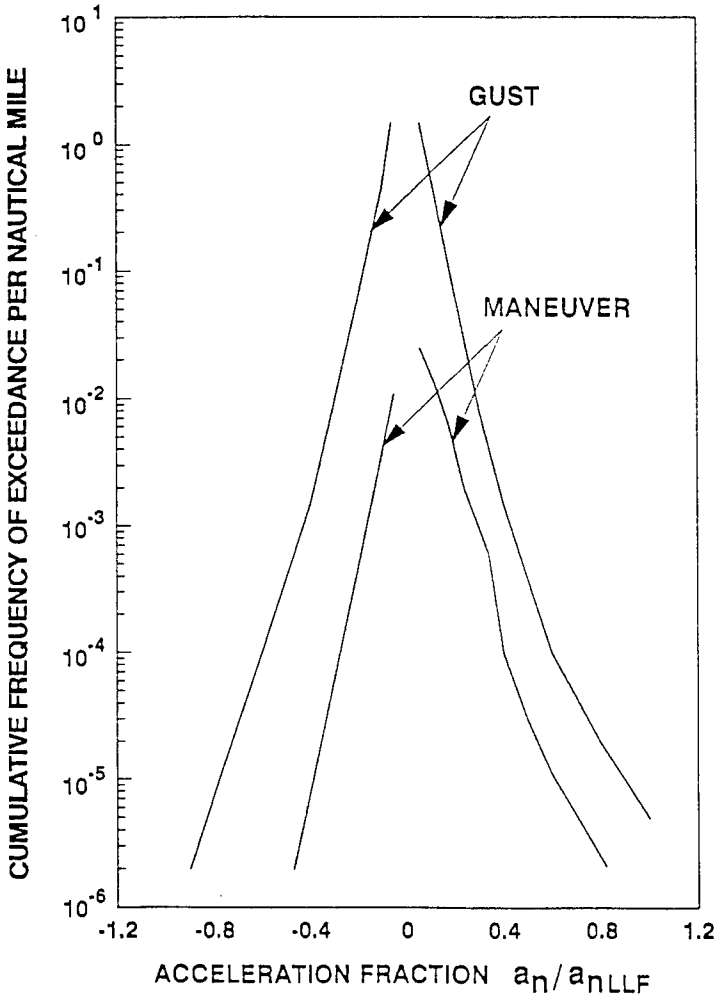

Figure 1. Exceedance curves for general-usage twin-engine aircraft.

For each stress level, the fatigue life in cycles, N, was found from the S-N curves for 2024-T3 sheet. A stress concentration factor of $K_t = 5.0$ was assumed, as being a fatigue quality typical in small airplane construction. Finally, the damage per hour for gusts and for maneuvers were calculated using Miner's Rule:

$$D = \Sigma\left(\frac{n_i}{N_i}\right) \tag{1}$$

where: D = Fatigue damage per hour
n_i = Occurrences per hour of stress level i
N_i = Fatigue life (cycles) for stress level i

The maximum stress in the GAG cycle is the maximum stress with a total frequency of once per flight. The total frequency for a given stress level is its frequency of occurring in the gust spectrum, plus its frequency of occurring in the maneuver spectrum. The minimum stress in the GAG cycle was taken to be zero, since landing and taxiing loads were neglected. The fatigue life in cycles, N, for the GAG cycle was read from the S-N curves. The GAG damage is 1/N, converted to damage per hour by multiplying by 0.75 flights per hour.

The total fatigue damage per hour was obtained by summing the damage due to gusts, maneuver, and the GAG cycle. The unfactored fatigue life is the inverse of the total fatigue damage:

$$D_{total} = D_G + D_M + D_{GAG} \tag{2}$$

$$\text{Unfactored Life} = \frac{1}{D_{total}} \tag{3}$$

$$\text{Factored Life} = \frac{\text{Unfactored Life}}{\text{Scatter Factor}} \tag{4}$$

where: D_{total} = total fatigue damage per hour
D_G = damage per hour due to gusts
D_M = damage per hour due to maneuvers
D_{GAG} = damage per hour due to GAG cycle

Reference [2] states that a scatter factor between 3 and 8 should be applied to the unfactored life. For the present analysis, a scatter factor of 3.0 was chosen, since using the fatigue data for $K_t = 5.0$ was conservative. The factored fatigue life is 10,300 hours to 13,000 hours, depending on the accuracy of reading the S-N curves.

Crack growth rate data

The primary sources of publicly available crack growth rate data are the 1975 Battelle Damage Tolerant Design Handbook [1], and the 1983 Battelle Damage Tolerant Design Handbook [6]. Two additional sets of data were considered: data obtained by private communication with Mr. Thomas Swift of the FAA, and data obtained from Prof. Regis Pelloux of MIT as part of the Continued Airworthiness Research Program. In all cases, the data were for 2024-T3 aluminum alloy, which is a material commonly used in airplanes.

A line corresponding to a Walker type equation was fitted to each set of data:

$$\frac{da}{dN} = C\frac{(\Delta K)^m}{(1-R)} \tag{5}$$

where C = Crack growth rate constant
m = Crack growth rate exponent
K = Stress intensity factor
R = Stress ratio

A crack growth rate exponent of four was used for all cases, which is common practice for aluminum alloys. Since the data are plotted on a logarithmic scale, this equation becomes a straight line with slope of 4, the position of the line determined by R and C. For the data from Mr. Swift, MIT, and the 1983 Handbook, a constant of $C = 4 \times 10^{-10}$ $in./cyc(ksi\sqrt{in.})^4$ provided a reasonable fit. However, the constant C for the data from the 1975 handbook ranged from 0.625×10^{-10} to 4.02×10^{-10}, as shown in Table 2. For calculations using the 1975 handbook, a constant of $C = 2.5 \times 10^{-10}$ was chosen as a representative, somewhat conservative, value. This value is lower than the value for the other three sources by a factor of 1.6.

The data from the 1975 handbook were assembled from a large number of tests performed independently by different researchers. The 1983 handbook contains a much smaller sample size; for alclad 2024-T3, it contains only two of the 12 graphs from the 1975 handbook. It is unclear on what basis those particular graphs were selected for inclusion in the updated handbook, while the other graphs were omitted.

Table 2. Summary of crack growth rate constants from 1975 handbook for 2024-T3 clad aluminum.

Stress ratio, R	10^{10} C t = 0.90 "	10^{10} C t = 0.125 "
-1.0	0.625	
0.0	2.5 1.9	1.56
0.05		1.9
0.1	1.095	
0.33	4.02 2.615	
0.5	2.5	
0.7	2.315	

Several possible explanations exist for the range of crack growth rate constants in the 1975 Handbook. First, specimens that are nominally the same alloy, but were produced in different batches or by different manufacturers, may exhibit different crack growth behavior. Also, the improvements in metal production and processing that have been made over time may mean that a batch of metal produced one year would have somewhat different characteristics from a batch produced several years later.

Another possible source of apparent differences in crack growth rates is the method used to reduce the crack growth data (a vs. N) to rate data (da/dN vs. ΔK). Most of the data in the 1975 Handbook were reduced using the secant method, which approximates the crack growth curve by a series of straight lines connecting the data points. The crack growth rate is the slope of the line connecting two adjacent points, determined by dividing the change in crack length by the number of cycles it took to grow that distance. The stress intensity factor is computed using the average crack length. Thus, if the crack length is a_1 at N_1 cycles, and subsequently grows to a_2 at N_2 cycles:

$$\frac{da}{dN} = \frac{\Delta a}{\Delta N} = \frac{a_2 - a_1}{N_2 - N_1} \qquad (6)$$

$$a_{avg} = \frac{a_1 + a_2}{2} \qquad (7)$$

$$K = K(a_{avg}) \qquad (8)$$

Using the secant method can lead to scatter in the rate data. The n-point incremental polynomial method [7] of data reduction tends to minimize scatter in the computed rate data. This method uses the least square error technique to fit a parabola to sets of n successive data points, where n is 3, 5, 7, or 9. The crack growth rate is taken as the derivative of the parabolic function, computed at the data point in the middle of the set.

To evaluate the difference between the data reduction methods, the crack growth data obtained from MIT was reduced using both the secant method and the 7-point incremental polynomial method. The data were from center-cracked panels, tested in constant-amplitude loading at different stress ratios. The secant method does lead to more scatter in the rate data than the seven-point method. However, the reduction method does not significantly change the position of the curve. This is illustrated in Figure 2, in which the Walker equation with a constant C = 4.0×10^{-10} is fitted to curves generated by the two methods. In this case, the test specimens were from the same batch of aluminum, so data scatter due to material variability is at a minimum.

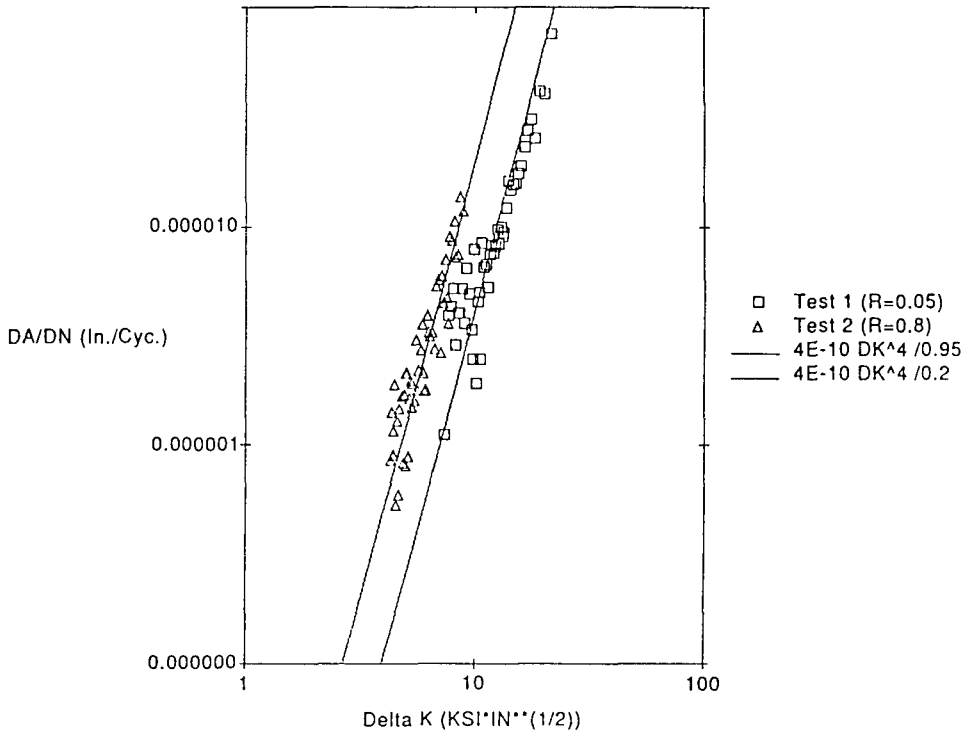

Figure 2a. Test data for secant method with Walker equation.

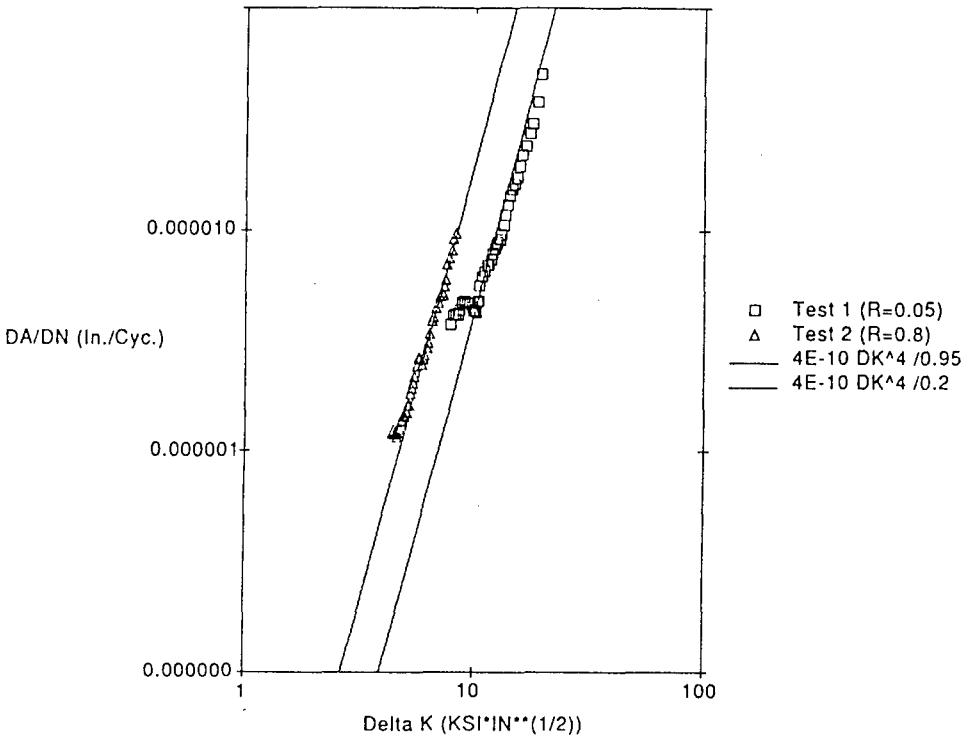

Figure 2b. Test data for seven-point method with Walker equation.

As can be seen from Figure 2, the chosen rate equation fits the average of the secant method data as well as it fits the polynomial method data. Therefore, one can conclude that the secant method yields the same average da/dN as the polynomial method, i.e., a difference in data reduction method alone can not explain the wide range of crack growth rate constants in the 1975 Handbook. Since the data sample size in the 1983 Handbook is limited, and appears to be a subset of the data from the 1975 Handbook, there is no way to determine which set of data (and hence which crack growth rate constant) is most applicable to the materials used in older airplanes.

Damage tolerance calculations

Damage tolerance calculations for the light weight twin engine wing spar were made for the assumed crack growth sequence shown in Figure 3. Two initial cracks are located at a non-load-bearing fastener hole in the spar cap. The .05 inch crack is a standard assumed "rogue" man-

ufacturing defect size for a corner crack. The .005 inch crack represents an average quality defect. The first stage of crack growth life, where the .05 inch crack grows through the wing spar thickness and at the same time the .005 inch crack grows to a .015 inch crack, is calculated with the stress intensity factor for corner cracks at hole [8]. The second stage, where the through crack is growing toward one edge of the cap and the .015 inch crack grows to a .018 inch crack, is calculated with stress intensity factor for a crack emanating from a hole in rectangular plate [9]. The third stage, where the .018 inch crack grows to a through crack, is calculated with the stress intensity factor for corner cracks at hole, with the applied stress increased by a net section magnification factor to account for the reduced load-carrying area. The final stage, where the through crack grows to failure of the cap, is calculated with the stress intensity factor for a single edge crack [9].

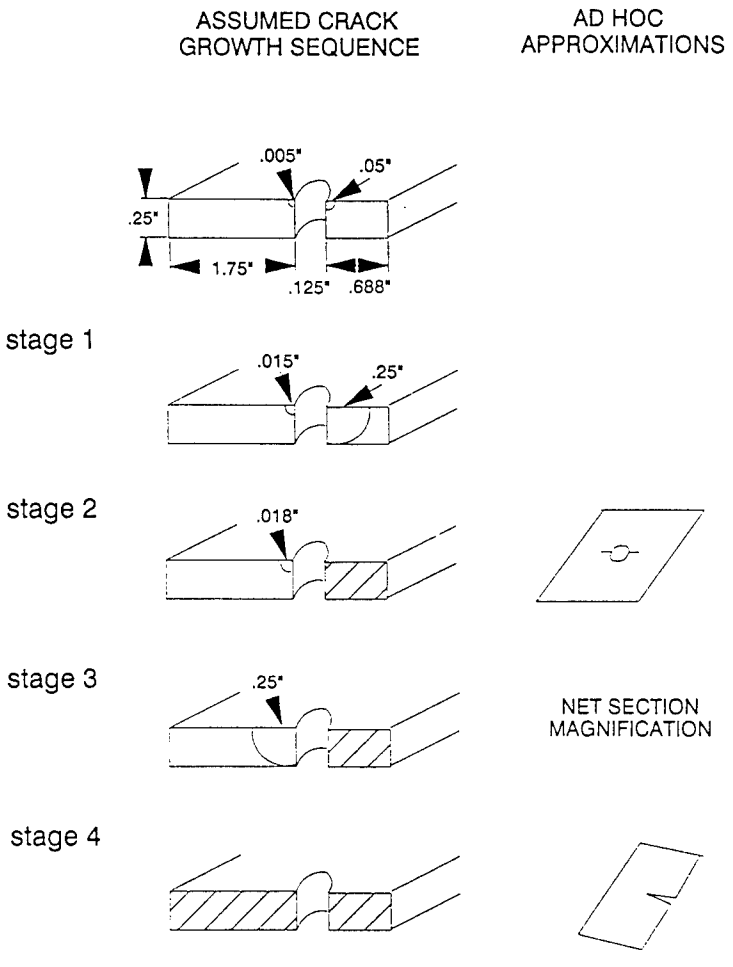

Figure 3. Stages of assumed crack growth sequence.

One of the questions raised by the industry group concerned the treatment of the basic crack growth rate data for life calculation. It was suggested that the accuracy of the calculation would be improved if data reduced by the polynomial method were used in tabular form, with rates interpolated for intermediate ΔK and R values.

This question was studied by using Mr. Swift's data, which was available in tabular form, and by comparing with calculations based on the curve-fitted equation (5), with $C = 4 \times 10^{-10}$ and $m = 4$. The da/dN values calculated with the crack growth rate equation for the corner crack at the hole geometry were compared to the da/dN values interpolated from the tabular data for each stress range of the spectrum. The comparisons were made for crack sizes of .02, .05, .15, and .25 inch, load with and without net section magnification factor as described above, and stresses with and without R-truncation. (R-truncation means that the crack growth rate is calculated with $S_{min} = 0$ for any cycle in which $R \leq 0$.) Typical comparisons for crack size of .05 inch are shown in Figure 4.

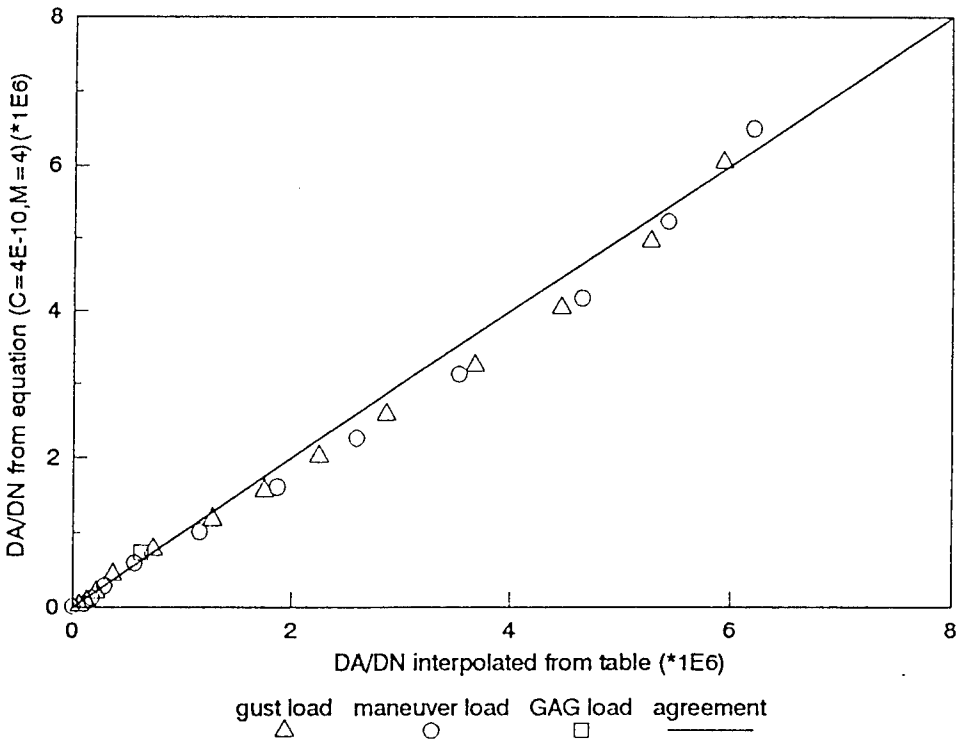

Figure 4a. Comparison of DA/DN values, (a_0 =.05, without net section magnification, with R-truncation).

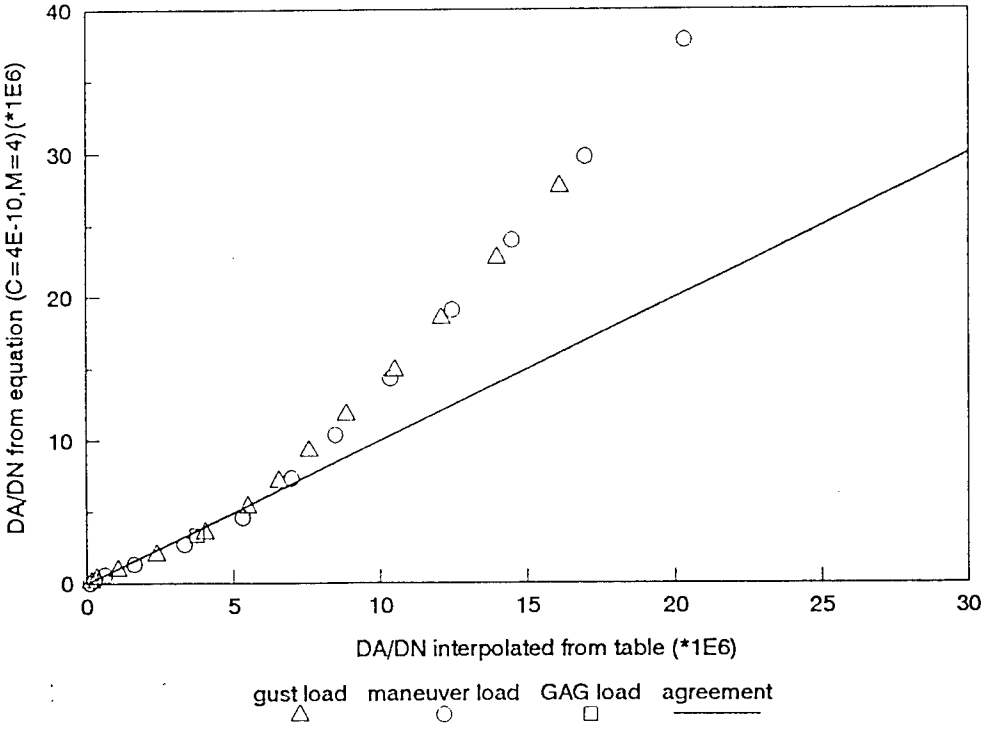

Figure 4b. Comparison of DA/DN values, (a_O=.05, with net section magnification, with R-truncation).

Figure 4a corresponds to the most frequently occurring loads in the spectrum and indicates agreement between the two methods for calculating the crack growth rates. Figure 4b indicates that the curve-fit estimates exceed the interpolated values at high growth rates, but these points correspond to infrequently occurring loads and should thus have little effect on the spectrum life estimate. The crack growth rates computed from the da/dN equation were also found to be more conservative for the larger crack sizes, but again, this should have only a small effect on the life estimate.

A comparative life calculation for the wing spar was done by using the block-spectrum computation method and interpolating the da/dN values from Mr. Swift's tables. All cycles per flight were "blocked" into groups of common range and ratio. The rate table was then used to project the increment and updated crack length per block. Due to the time-consuming nature of the block-spectrum calculation, only the first stage of the assumed crack growth sequence was treated. (However, this

stage is more than two thirds of the entire crack growth life.) Two block-spectrum calculations were made, giving unfactored lives of 9,986 hours with R-truncation and 9,906 hours without R-truncation.

The rapid analysis method used in the present study is based on an application of Miner's rule to cases in which load interaction effects can be neglected [10]. The original rapid analysis presented in 1990, was based on the Walker equation with $C = 2.5 \times 10^{-10}$ rather than 4×10^{-10} and gave 16,082 hours as the unfactored life for the first stage shown in Figure 3. To put this analysis on the same basis as the block-spectrum computation method requires only division of the result by the factor of 1.6, which is the factor between the two crack growth rate constants. This leads to a rapid estimate (no R-truncation) of 10,051 hours, i.e., only 145 hours (1 percent) more than the block-spectrum computation method.

The rapid estimate for total damage tolerance life with a crack growth rate constant of 4.0×10^{-10}, corresponding to the recent material data, is also obtained by means of scaling. Table 3 includes this result in the comparison with the other life estimates. The revised damage tolerance life is shorter than the fatigue safe lives, although it is comparable to the most conservatively estimated safe life.

Table 3. Updated summary of life calculations for the light weight twin engine wing spar.

		Unfactored life (hours)	Scatter factor	Factored life (hours)
Australian CAA	safe life	-	-	13,000
British CAA	safe life	-	-	8,500
Manufacturer's aircraft report	safe life	65,000	5	13,000
VNTSC	safe life	31,000 to 40,000	3	10,300 to 13,000
VNTSC damage tolerance 1 $C = 2.5 \times 10^{-10}$	slow crack growth life	22,850	2	11,425
VNTSC damage tolerance 2 $C = 4.0 \times 10^{-10}$	slow crack growth life	14,281	2	7,140

Conclusions

Damage tolerance life is lower than fatigue life when the more conservative crack growth rate is assumed, but is still comparable to the most conservative fatigue life estimate. Fitting crack growth rate data carefully with a Walker equation and then using the rapid calculation method is suitably accurate, compared with interpolation of tabular rate data and with block spectrum computation.

The choice of crack growth rate constant in the Walker equation greatly affects the calculated life. The data presented in the 1975 Handbook contain a wide range of growth rate constants. However, this variation cannot be attributed to the use of the secant method to reduce the data. The data in the 1983 Handbook is more consistent with other recent but unpublished data. However, the sample size is much smaller than for the 1975 data. Therefore, there is no basis for judging whether the old or new published data better represents the older material which would be found in aging commuter aircraft.

References

[1] Metals and Ceramics Information Center, Air Force Materials Laboratory and Air Force Flight Dynamics Laboratory, "Damage Tolerant Design Handbook", January 1975, Part 2, pp. 8.1-14(12/72) to 8.1-21(9/73).

[2] Anon., "Fatigue Evaluation of Wing Associated Structure on Small Airplanes", Report no. AFS-120-73-2, May 1973.

[3] Nauert, H. and Campbell, D., "Sample Calculations Showing Use of Method in AFS-120-73-2 Fatigue Report," unpublished.

[4] Code of Federal Regulations, Title 49, Aeronautics and Space, Part 23.337.

[5] Department of Defence, "Military Standardization Handbook, Metallic Materials and Elements for Aerospace Vehicle Structures", MIL-HDBK-5E, June 1987.

[6] Metals and Ceramics Information Center and Air Force Materials Laboratory, "Damage Tolerant Design Handbook", December 1983, Volume 3, pp. 7.6-13.

[7] "Standard Test Method for Measurement of Fatigue Crack Growth Rates", ASTM Standard E647-88, American Society for Testing and Materials, June, 1988.

[8] D. Broek, *Elementary Engineering Fracture Mechanics*, Noordhoff International Publishing, Leyden, the Netherlands, 1974, pp. 322-326.

[9] Y. Murakami, *Stress Intensity Factors Handbook*, Pergamon Press, New York, 1987, Volume 1.

[10] O. Orringer, "Rapid estimation of spectrum crack-growth life based on the Palmgren-Miner rule", *Computers & Structures 19*, pp. 149-153 (1984).

DEVELOPMENT OF A FATIGUE LIFE INDICATION SYSTEM

Gopal Samavedam
Douglas Thomson
Foster-Miller, Inc., Waltham, Massachusetts 02154

Brian Hornbeck
USA Belvoir, RD&E Center, Fort Belvoir, VA 22060-5606

A new fatigue monitoring device which is suitable for use on mobile Army bridges has been developed by Foster-Miller, Inc. and is being evaluated by the Belvoir RD&E Center. This device is comprised of two thin metal "pre-cracked" coupons made from different materials which are directly attached to the bridge tension member. The crack growth in the twin coupons is used to resolve the *bridge loading histogram.* This definition of the stress levels and cycles experienced by the bridge permits calculation of the useful fatigue life consumed. As mobile military bridges typically experience varied and undefined loading, this indicator has the potential to provide service life information not currently available.

Several existing fatigue indicators are not suitable for application on mobile Army bridges. Electronic strain gauge type devices, while they should inherently be the most accurate, are expensive, require constant power, and often suffer from long-term stability problems. Mechanical recording devices are also expensive and complex and most require specialized machinery and personnel for readings. Plain or notched coupons are dependent on the phenomenon of crack initiation which is well documented to display high scatter. This scatter results in unacceptable margins of error for this low cycle fatigue application. Single pre-cracked coupons, while based on the same stable crack growth concept as the FLI, cannot indicate the loading histogram. Their life calculations are based on a laboratory developed empirical relationship which is only valid at the coupon attachment area. While each of these indicating systems may have useful applications, the FLI is clearly the best suited for use on mobile bridges.

Theoretical Basis

Crack propagation in metals can be defined by the Paris Crack Law:

$$da/dN = C\Delta K^n \tag{1}$$

where:

$$\Delta K = \beta\Delta\sigma(\pi a)^{1/2} \tag{2}$$

where:

a is the half crack length, $\Delta\sigma$ is the applied stress cycle, da/dN is the half crack growth rate per number of cycles (N), β is a shape factor to account for finite geometry, and C and n are material constants. Initial tests were conducted to define the material constants for the two coupon materials. The Paris Crack Law for a infinite plate ($\beta = 1$), was found to fit well to the laboratory crack propagation data. The material constants (C,n) were defined for each of the coupon materials by this fit. The 6061-T6 coupon required a bi-linear fit. This characteristic is consistent with the published data.

Since the cracks in the two dissimilar coupons will grow at different rates due to their different material constants (C,n), the two crack lengths can be compared and the loading histograms deduced. Integration of the Paris Crack Law yields the following equation.

$$N = \frac{a_f^{1-n/2} - a_i^{1-n/2}}{c\Delta\sigma^n \pi^{n/2} (1-n/2)} \tag{3}$$

Since the two coupons are attached such that they experience the same number of cycles (N) and the same magnitude of stress cycle ($\Delta\sigma$), this equation can be rearranged to deduce the stress cycle from the final crack lengths (a_f) while knowing the initial crack lengths (a_i) for the two coupons (1 and 2). The following equation defines the stress cycle.

$$\Delta\sigma = \left\{ \frac{c_2 \pi^{\frac{n_2}{2}} \left(1 - \frac{n_2}{2}\right) \left[a_1^{1-\frac{n_1}{2}} - a_{1_i}^{1-\frac{n_1}{2}} \right]}{c_1 \pi^{\frac{n_1}{2}} \left(1 - \frac{n_1}{2}\right) \left[a_2^{1-\frac{n_2}{2}} - a_{2_i}^{1-\frac{n_2}{2}} \right]} \right\}^{\frac{1}{n_1 - n_2}} \tag{4}$$

This equation demonstrates the need for two coupons of different materials as n_1 and n_2 must not be equal.

A basic computer program was written to deduce the loading history based on the two crack lengths. The program written uses the initial and final crack lengths to calculate the stress cycle using Equation 4. Due to the bi-linear fit of the 6061-T6 data, an iterative program was required to determine the transition point of the fit. This point was defined when the calculated stresses were equal for the two linear regions. The total number of cycles at this stress level is then calculated using Equation 3. The stress cycle and number of cycles are the output of this program.

Laboratory Proof-of-Concept

The Fatigue Life Indicator (FLI) system was developed and demonstrated in numerous laboratory tests. A method was developed for fabrication of the coupons which included precracking of the coupons at a low stress level of 15 Ksi to avoid crack retardation at the operational levels of the AVLB. Optical crack measurement was found to have sufficient resolution under laboratory conditions.

A test assembly was designed with the two FLI coupons attached to a representative bridge structure using a bolted attachment, as shown in Figure 1. Tests were first conducted to define the Paris Crack Law constants C and n. Four assemblies were then tested to verify the operation of the system in the laboratory. As shown in Table 1 and Figure 2, the agreement of the applied test loads and cycles with the computer prediction is very good. The one problem that did surface in Assemblies H and I was that precracking at a higher stress level can cause retardation of crack growth. This problem was corrected for Assemblies J and K. Some growth retardation was still observed in the multiple stress level histogram of Assembly K. However, in an actual FLI application, the structure being monitored may experience similar damage retardation due to spectrum loading. Also, further laboratory and field testing of this system may allow development of data corrections for these phenomena. Based on the data from these tests, the system was considered to be functional in the laboratory with need of further laboratory development and field proof-of-concept.

Field Proof-of-Concept

Two sets of Fatigue Life Indicator coupons were attached to each of two Armored Vehicle Launched Bridges (AVLB) at Ft. Belvoir, VA. Two sets were prepared for a standard useful life of 10,000 cycles. Two sets were cycled to longer initial crack lengths for a target useful life of 2000 cycles to provide greater accuracy during the planned field tests. One set of each type was attached to each of the bridges.

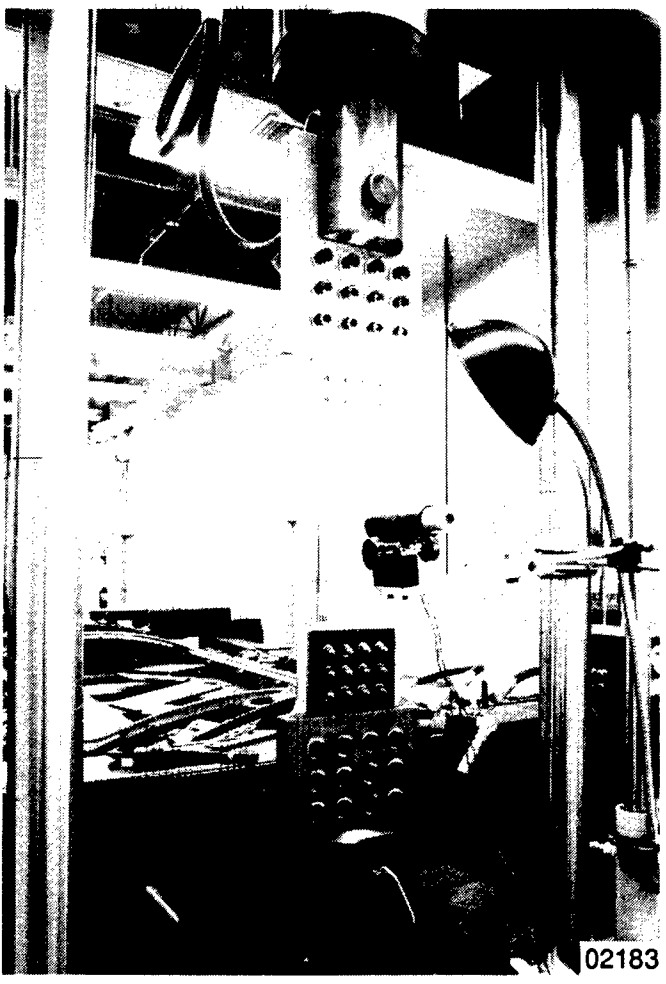

Figure 1. FLI Test Facility

The coupon sets were mounted to the AVLBs using the bolted doubler plate attachment method. Individual coupons of a set were mounted to the bottom flange of the bridge tension chord on opposite sides of the center hinge at an end location 41 in. from the center pin. The coupons were then sealed with silicone to prevent moisture and dirt penetration.

The two ALVBs were transported to Aberdeen Proving Ground (APG) and tested for a total of 2000 crossings under several loading conditions. Table 2 summarizes the three intervals for which data was collected and analyzed. For these intervals,

Table 1. Test Results versus Predictions

	Test Results		Predictions	
Assembly	Cycles	Stress (Ksi)	Cycles	Stress (Ksi)
H	0	20.0		
	2,000	20.0		
	4,000	20.0	400	37.1
	6,000	20.0	900	31.9
	0	25.0		
	500	25.0	500	29.5
	1,000	25.0	1,200	26.3
	1,500	25.0	2,300	24.3
	2,000	25.0	2,700	24.8
	2,500	25.0	3,500	24.7
	3,000	25.0	3,800	25.5
I	0	20.0		
	2,000	20.0		
	4,000	20.0	300	38.0
	6,000	20.0	1,300	29.2
	0	25.0		
	1,000	25.0	1,200	23.6
	1,500	25.0	1,700	23.7
	2,000	25.0	2,400	23.1
	2,500	25.0	3,100	23.2
	3,000	25.0	4,000	22.6
	3,500	25.0	5,900	21.5
	4,000	25.0	6,500	21.9
	4,500	25.0	7,300	22.5
J	0	17.0		
	2,000	17.0	1,500	18.4
	4,000	17.0	3,300	17.8
	5,200	17.0	4,300	17.9
	6,000	17.0	4,700	18.1
	7,000	17.0	5,700	17.9
	8,000	17.0	6,800	17.7
	9,065	17.0	7,900	17.6
	10,000	17.0	8,900	17.4
	11,000	17.0	9,800	17.5
	12,000	17.0	11,000	17.3
	13,000	17.0	12,000	17.3
	14,000	17.0	13,100	17.3
	15,000	17.0	14,400	17.4
K	0	20.0		
	2,000	20.0	2,220	20.4
	4,000	20.0	4,000	20.0
	6,000	20.0	7,000	18.9
	6,500	25.0	7,500	26.4
	7,000	25.0	8,300	24.7
	7,500	25.0	9,900	22.7

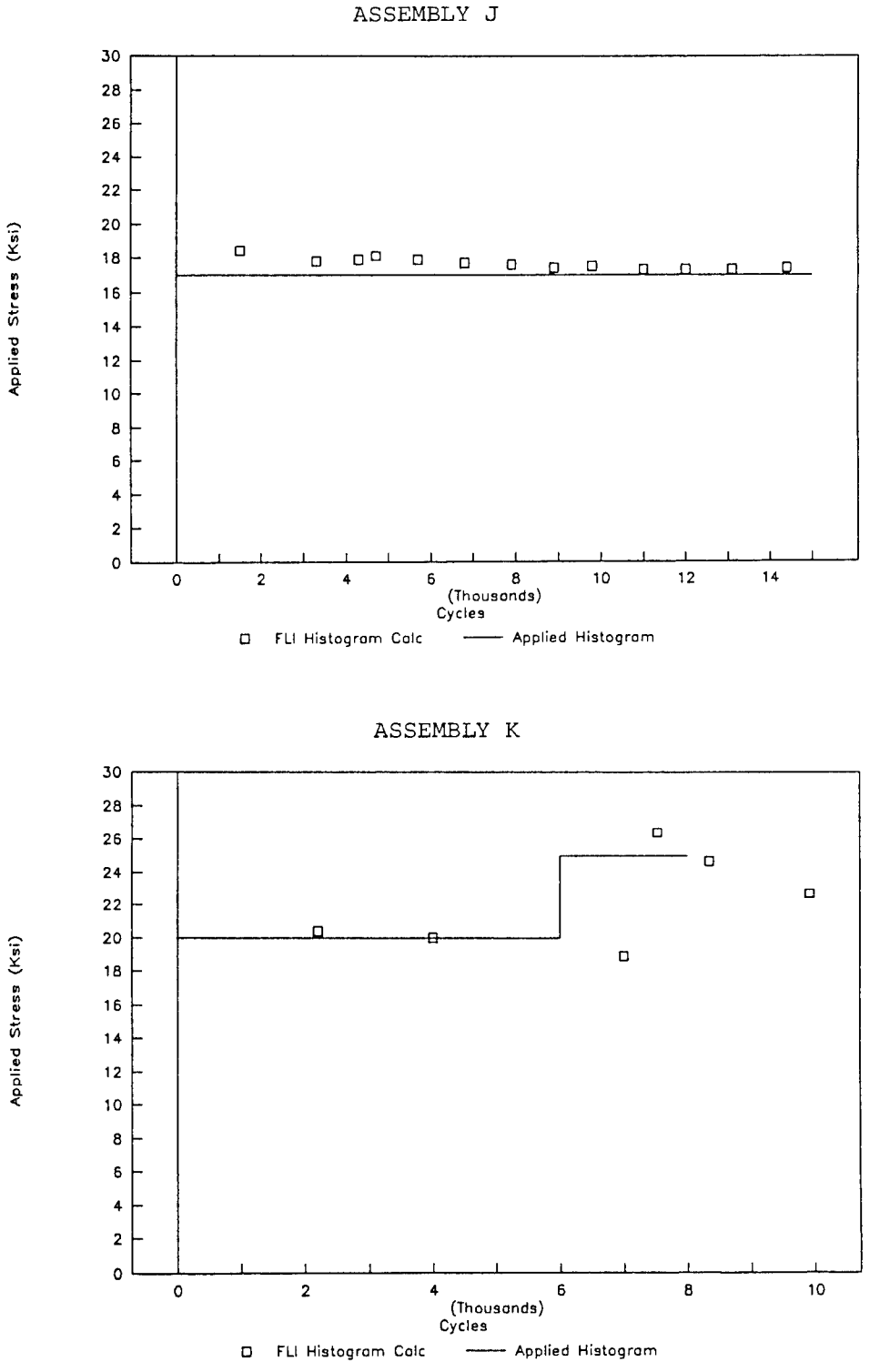

Figure 2. Laboratory Test Results

Table 2. Field Proof-of-Concept Tests

Data	Coupon Material	Initial Half Crack Length (in.)	Final Half Crack Length (in.)	Calculated		Actual	
				Cycles	Stress (Ksi)	Cycles	Stress (Ksi)
1	2024-T3 6061-T6	0.400 0.450	0.455 1.000	420	23.2	426	23.9
2	2024-T3 6061-T6	0.40 0.450	0.455 1.000	420	23.2	406	23.9
3	2024-T3 6061-T6	0.280 0.290	0.300 0.310	720	19.1	740	18.1

agreement with the actual crossings was excellent. However, coupon slippage occurred and the bolted attachments needed repairs and readjustment. Thus, the system has been successfully demonstrated in the field but further development is required.

Laboratory System Development

Numerous development tests were conducted concurrent with the field tests to improve system performance. The three target aspects for refinement were coupon attachment, crack measurement and coupon size.

Coupon Attachment

The bolted attachment method requires damage to the bridge structure and also risks coupon slippage. The development of an improved bonded attachment method was the focus of this work. Five candidate adhesives were used to fabricate small-scale test assemblies. More than 20 of these assemblies were mechanically and thermally cycled to evaluate their strain transfer characteristics and degradation as it applied to the FLI. Based on these tests, Tra-Bond 2143D was selected for full-scale testing.

Full-scale FLI assemblies, shown in Figure 3, were fabricated to develop the bonded attachment method and to evaluate alternative crack measurement techniques. As shown by the results in Table 3 for one assembly, the FLI with a

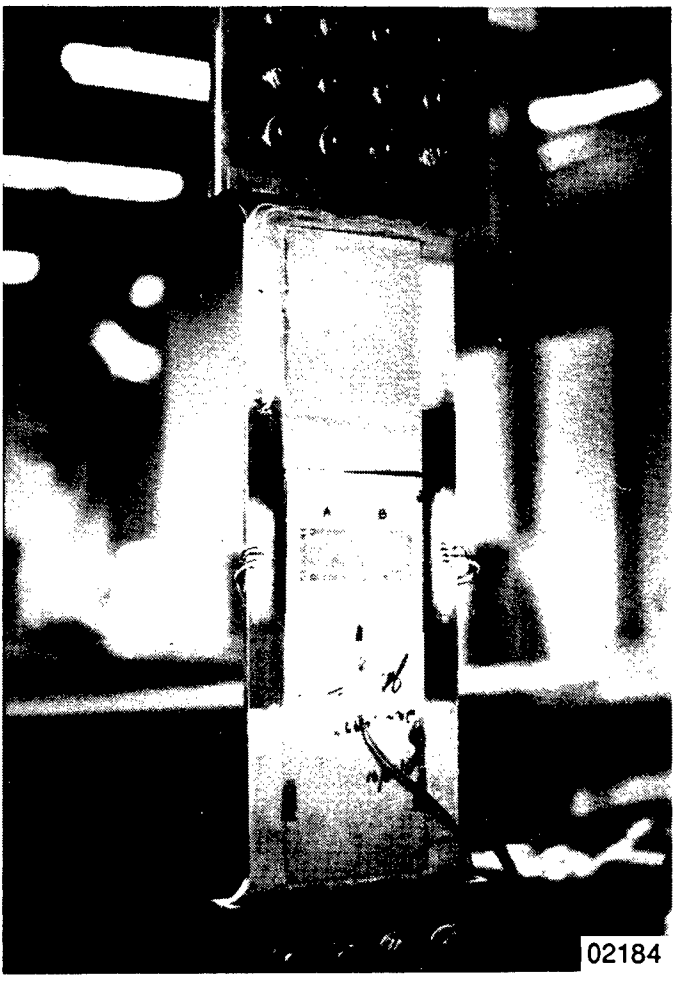

Figure 3. FLI Assembly with Bonded Attachment

bonded attachment properly indicates the cycles and a stress level equal to 80 percent of the applied stress. This reduction is consistent and results from the lower modulus of the adhesive. Testing also indicated that complete bonding of the coupon reduced the stress intensity factor at the crack tip and thus crack growth was unacceptably retarded. These tests demonstrated that while bonding is a preferable alternative to bolting, further development of the technique is required.

Crack Measurement

Three electronic crack measurement systems were considered to allow automated, remote measurement. Extensive literature was reviewed on the AC Potential Drop (ACPD) method. While it has been successfully utilized under controlled laboratory conditions, the literature indicated that this method is too involved for field use.

Table 3. Results for FLI Assembly with Bonded Attachment

Applied		Calculated	
Cycles	Stress	Cycles	Stress
0			
1,300	20.0	1,000	16.4
3,000	20.0	2,400	17.3
4,000	20.0	4,100	17.0
5,000	20.0	5,550	16.2
6,600	20.0	6,500	16.5
8,000	20.0	7,800	16.5
9,000	20.0	9,100	16.1
10,000	20.0	9,700	16.1
12,000	20.0	11,700	15.8
13,000	20.0	12,400	15.7
14,000	20.0	13,700	15.4
15,000	20.0	14,700	15.3
16,000	20.0	15,200	15.3

Ladder gauges provide electronic crack growth measurement using microwires which break as the crack propagates. Several of these gauges were tested in the laboratory and compared to optical crack measurements. The results indicated that some problems exist due to crack closure and stability during system disconnect.

Additionally, although these problems may be surmountable, these gauges have, by design, a fairly low resolution due to their discreet measurement points.

The Krak Gage system provides crack growth measurement electronically using an indirect DC potential drop method. A thin foil Krak-Gage is bonded directly to the test specimen and the crack propagates through the gauge as it propagates through the test specimen.

The change in the resistance of the gauge is precisely measured by a Fractomat data acquisition device. This two-channel instrument contains precision constant current sources for excitation as well as signal conditioners and amplifiers to process the input. The two calculated crack lengths are displayed on the instrument front panel. This system, which is in wide use in fatigue laboratories, provides several significant advantages over the other crack measurement devices which were tested.

During the full-scale laboratory bonding tests, Krak Gages were applied for testing of this measurement system. Two gauges were applied to each FLI coupon in order to measure the total tip-to-tip crack length, as shown in Figure 4. The gauges provided adequate data for system evaluation.

The Krak Gage tests successfully demonstrated several key aspects of system performance. A comparison of the Krak Gage readout to precision optical measurements made with a graduated microscope is presented as Figure 5. Agreement was excellent with any error likely due to some difficulty in correctly identifying the crack tip during optical measurement. Since the gauge itself is an analog indicator, its resolution is dependent on the recording device. For the 30 mm gauges typically used in these tests, the minimum displayed resolution of the Fractomat is 0.01 mm (0.0004 in.). The Fractomat also can display the peak readout of the gauge to eliminate any error due to crack closure during cyclic loading. Also, unlike the ladder gauges, which sometimes disbonded near the crack tip, all of the Krak Gages tested remained fully bonded to the FLI coupons through the duration of testing.

Four gauges of different crack lengths were tested statically to quantify the effects of crack closure. The applied stress required to overcome closure was proportional to the crack length. The error associated with crack closure may be

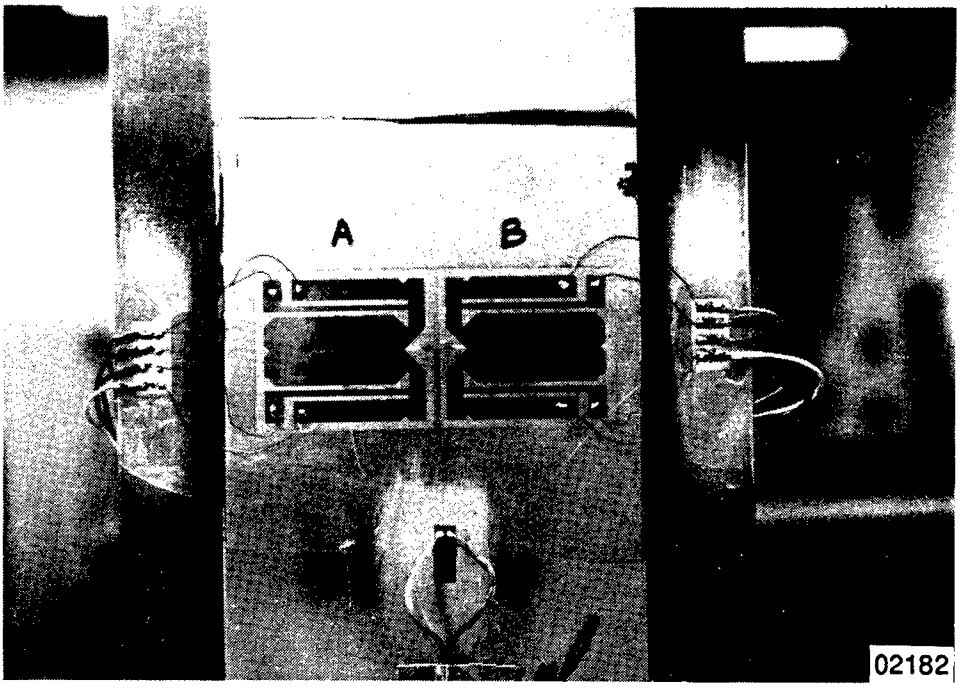

Figure 4. Krak Gages

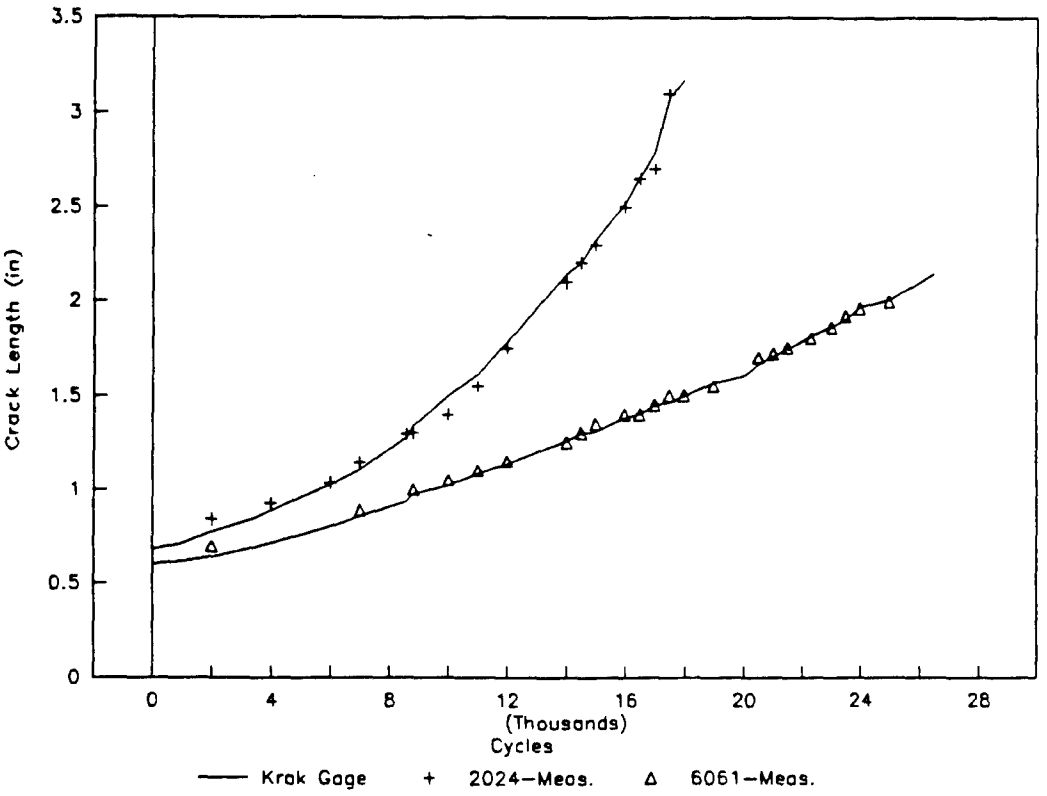

Figure 5. Krak Gage Comparison to Optical Measure

significant with extremely small crack lengths. However, the stress due to the dead weight of the bridge was sufficient to overcome closure effects in all but the smallest cracks.

Throughout all testing, the Fractomat was connected to the gauges through standard cannon plugs. These plugs were disconnected and reconnected at numerous times throughout the testing. No errors were recorded due to these actions. Since the system maintains a pre-set, constant current, changes in system resistance were automatically compensated for and the output was not adversely affected.

The system does have some disadvantages. The initial cost of the Fractomat data acquisition system is relatively high (≈ $7,000). Standard 110 VAC power must be available to operate the system when a reading is to be made. Also, the coupon will be completely sealed from visual inspection of the cracks. However, this system demonstrated superior performance among those evaluated.

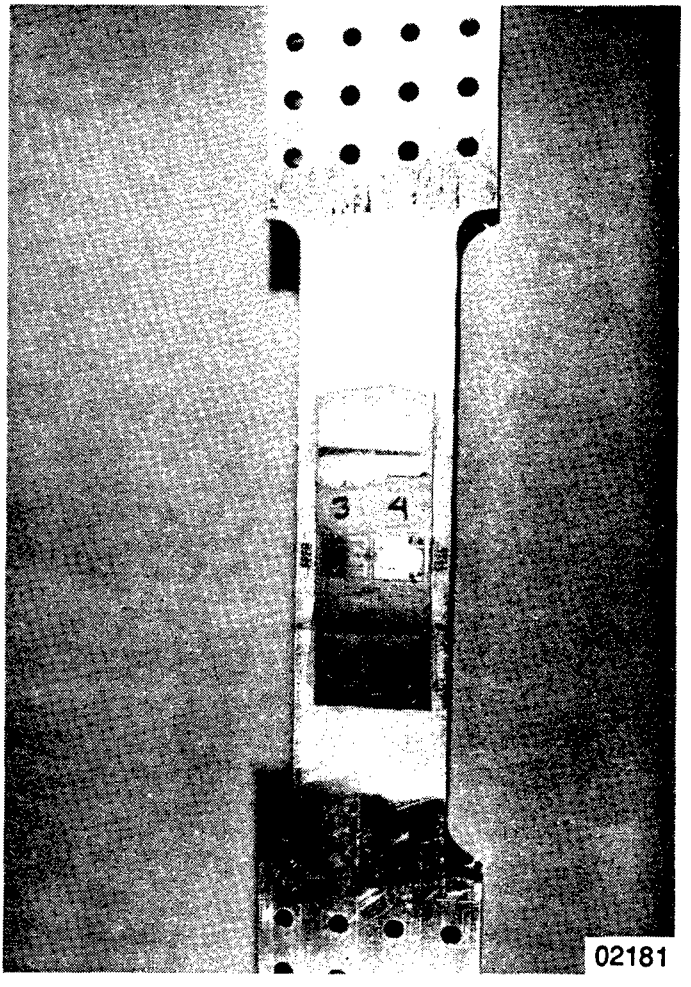

Figure 6. Reduced Size FLI Coupon

Coupon Size

Reduction of the FLI coupon size was the third goal of this program. One assembly, shown in Figure 6, was tested using a substantially reduced coupon. Smaller coupon size will permit application of the FLI to many other bridges and structures. While this assembly test demonstrated that sufficient stable crack growth can be achieved in the smaller coupons, additional testing is required to quantify the effects of reduced coupon width on the crack growth rates.

Concluding Remarks

The Twin Coupon Fatigue Life Indicator system has been successfully demonstrated in numerous laboratory tests and the vehicle crossing tests on the AVLB. The test results provided proof of the Twin Coupon concept.

The laboratory proof-of-concept tests defined a coupon manufacturing method and the crack growth law constants. Further testing demonstrated that the computer program will consistently indicate the loading history based solely on the two measured crack lengths.

The computer software to resolve the loading history from the coupon crack lengths, developed on the basis of laboratory test data, can be reliably applied for field conditions. The bridge crossing histories were accurately resolved from the crack length data recorded at these tests. Typical predicted results were within 5 percent of the measured stress. The calculated number of cycles was typically within 5 percent of actual.

Bonded assembly laboratory tests also demonstrated that the stress histogram can be accurately resolved from the two crack lengths. Typical data indicated numbers of cycles and stress levels within 10 percent of actual. The latter took into account the 20 percent reduction in strain transfer consistently observed in the bonded attachment.

Laboratory tests showed that remote crack length measurement can be accomplished automatically with either the Krak Gage system or the ladder gauges. The Krak Gage system, which demonstrated an error of less than ± 0.001 in., was significantly superior in all performance aspects and can be expected to perform well in the field.

Significant coupon size reduction potential was demonstrated in the laboratory. This was possible due to the success of the bonded attachment method and the improved resolution of a remote crack measurement system.

This passive, fatigue life monitoring system has demonstrated the capability to record the bridge loading history. It is relatively inexpensive and does not require the constant power and electronics of strain gauge type devices. This system has the potential to assist safe and timely removal of bridges from service.

STATIC AEROELASTIC AND DYNAMIC ANALYSIS OF T-38 WING

Jong-Ho Woo

US Army Ballistic Research Laboratory, APG, Maryland 21005-5066

ABSTRACT

This report documents the investigation of a 3-dimensional finite element model for predicting static displacement and dynamic analysis of a T-38 wing and comparison of the results with T-38 wing experimental data from Northrop Aircraft, Inc.

The T-38 wing structure was modeled by rod and bar(beam), membrane and shear panel finite elements. The general structural analysis programs MSC/NASTRAN and/or MSC/PAL2 were used to calculate deflection and mode shape.

A finite element model of the wing consisting of quadrilateral plate, triangular plate, shear panel, and rod/bar(beam) elements was found that yielded excellent agreement between calculated and test results for the 8 loading conditions studied. The methodology developed in this study is expected to provide a valuable tool for static aeroelastic and dynamic analysis of damaged T-38 wings.

I. INTRODUCTION

This work represents the first step in an overall task to predict the response of an aircraft wing damaged by weapons fire in combat. In this work, an attempt was made to find an adequate structural model for a wing that could subsequently be used to accurately calculate static and dynamic aeroelastic effects of combat damage.

The first step in such an effort involved the following tasks:

a) Develop modeling techniques for efficiency and accuracy
b) Compare calculated deflections with experimental data
c) Calculate natural frequencies and mode shapes

The overall purpose of this work was to:

a) Select a finite element model for the prediction of failure loads for a damaged wing structure.
b) Develop an aerodynamic model based on a finite element model for static aeroelasticity, flutter analysis, and dynamic aeroelasticity.

The experimental wing deflection data was obtained from Northrop Corporation Norair Division from tests conducted in 1960. See Reference [1]. During the wing test, the aircraft was supported at the fuselage forward and aft hoist points by two steel jigs which

were tied to the steel erectile structure. Loading was accomplished by means of hydraulic hand pumps and pressure gages, Northrop electrically-operated load maintainers, and Edison hydraulic proportioning units. Point loading was applied symmetrically to both wings at each of the loading points.

General Approach to the Problem

The MSC/NASTRAN and/or MSC/PAL2 analytical program has been used in this analysis for structural design. It has special conventional tools for the analysis of thin-skinned aircraft structures.

For the undamaged T-38 wing case, the MSC/PAL2 Finite Element Analysis program was used on a 486/25 microcomputer. Following this current effort, MSC/NASTRAN will be used for damaged wing, static aeroelasticity and dynamic cases.

The finite element model named Model 1 was the basis for the entire problem and was used in each of the analyses. These analyses and the associated MSC/NASTRAN and/or MSC/PAL2 solutions are described in general in the following.

1. The finite element model of the structure was confirmed with respect to membrane stiffness and bending stiffness using influence coefficients. A static solution was used for static analysis.
2. Natural frequencies and mode shapes were used for the flutter analysis. Therefore, the eigenvalue problem for the wing was solved using the dynamic analysis.

To perform static and dynamic aeroelasticity and flutter analysis of the T-38 wing, a structural model was developed as shown in Figure 1. To calculate undamaged T-38 wing deflection, four variations of finite element models were developed and evaluated.

The first is the simplest model describing the wing geometry. See Figure 2. The nodes in this first model were located on the top and bottom surfaces of the wing at the intersection of two or more of the spar caps, rib flanges, or stringers. See Figure 4, Model 1. The second model has an increased number of elements between two major ribs. For example, in Figure 2, the elements between ws 125.0 and ws 101.0 have increased numbers of elements. The same applies between ws 101.0 and ws 64.8. See Figure 4, Model 2. The third model has an even greater number of elements defined between the wing tip and wing root shown as Model 3, Figure 4. The fourth model was further modified to include triangular plates and quadrilateral plates. See Figure 4, Model 4. All the models used rod(beam), membrane plate, and shear panel finite elements. These 4 models are shown in Figure 4 and defined in Table 1. Of these 4 models, the one that compares best to test results will be used in future analyses using the MSC/NASTRAN static and dynamic aeroelasticity and flutter solutions.

For all of the models, the same analytical solution approach was used: MSC/PAL2 and/or MSC/NASTRAN. Different types of wing skin elements were used for all of the models. For the spar and rib webs, shear panel elements only were used. Rod and bar(beam) elements were used for the spar and rib chords, To verify these finite element models, Rattinger's wing, Reference [2], was modeled and shown to have very good agreement with test results.

II. WING FINITE ELEMENT MODEL ANALYSIS

Development of the Finite Element Model

Wing Description

The T-38 wing is a structure with aluminum panels(upper and lower surfaces) that are riveted to the root rib, main spar, auxiliary spar, and tip rib. The data necessary to describe the physical characteristics of the wing for MSC/PAL2 and/or MSC/NASTRAN were generated from blue prints. There were two missing parts of the drawing. One was the leading edge spar chord and web and the other was the minor rib chord and web. These two webs were reconstructed by knowledge of the dimensions of connecting rib webs and edge views of themselves.

Structural Element

The files follow the format XYZi.DAT, where X represents the wing skin elements, Y the spar and rib webs elements, Z the truss elements and i represents the wing model number. X denotes Q for quadrilateral plate elements, T the triangular plate elements, Y denotes S for the shear panel elements, Z denotes R for rod elements and B for beam elements. For instance, TSR1.DAT means the triangular plate element is used for the wing skins, shear panel elements are used for the spar and rib webs, and rod elements are used for spar and rib caps for Model 1. See Table 1.

A three-dimensional finite element model of the T-38 wing structure was used to compare with Northrop test results. As mentioned earlier, 4 models were used for the static analysis. Each model has a different application. The element substructures that were used to model the wing skins were triangular membranes and bending elements and quadrilateral membranes and bending elements. As shown in Figure 4 and Table 1, models QTSR4.DAT and QTSB4.DAT were composed of triangular and quadrilateral plate elements for wing skins. Several quadrilateral elements were divided into triangular elements for geometrical reasons or to change mesh spacing between assemblies of quadrilateral plates. For models 1, 2 and 3, only triangular or quadrilateral plates were used for the wing skins as shown by Figure 4. Model 1 has plate elements with large aspect ratios. To avoid large aspect ratios, model 2 and 3 have been utilized. MSC/NASTRAN and MSC/PAL2 have special rod and shear panel model tools for the analysis of thin-skinned aircraft structures. The shear panel element does not represent membrane and bending stiffnesses. Consequently, SSR1.DAT was used for this treatment and represents the shear panel elements that were used for the wing skins and the spar and rib webs, while rod elements were used for the spar and rib chords.

Boundary Conditions

The finite element model boundary conditions were based on the experimental conditions. As shown in Figure 5, the y-z(z-y) plane was assumed to be a plane of symmetry and therefore x-displacements in this plane were assigned zero values. The finite-element models used in this report were constrained in the x-directions at the aircraft centerline and in the z-directions at the wing roots.

Static Analysis

For static analysis of the T-38 wing, the static solution (SOL 24 in MSC/NASTRAN and STAT2 in MSC/PAL2) was used. The mathematical formulation of the solution process is based on the linear theory of elasticity. The stiffness matrix was formulated and then partitioned with respect to the constrained degrees of freedom and unconstrained degrees of freedom to be solved.

The finite element model developed allowed load(force) to be concentrated at a grid point for the static analysis. The set of forces is reduced to 1-set for nodal forces from the constraint partitioning resulting from satisying the equilibrium equations for stiffness versus force. The resulting equation can be expressed as

$$\{P\} = [S]\{D\}$$

The vectors {P} and {D} represent the nodal forces and displacements, respectively, and the matrix [S] represents the FEM stiffness matrix. For solution of the equations, MSC/PAL2 or MSC/NASTRAN reduces the stiffness matrix into its upper and lower triangular factors. Then forward-backward substitution is performed for all the load cases having the same constraints, which is the case here. The displacement solution for each load case contains three translational values for each grid point(except those displacements which are constrained). In this manner, transverse displacements were calculated for 9 grid points(A-I) shown in Figure 2. These displacements were plotted and compared with experimental data. Figures 6 through 13 present these comparisons for load applications from 200 lb to 5000 lb. Each figure has 6 plots a, b, c, d, e, and f. Plots a, b, c, d, and e represent comparison of displacements from models 1-3 and test data and plot f represents a comparison of displacements from model 4 and test data. Each plot has 3 stations. The top station shows deflections of grid point A, B, and C(See Figure 2), the middle station shows grid points D, E, and F, and the lower station shows deflections of grid point G, H, and I. In other words, the top station represents 3 grid points on wing station 125.0, the middle station represents on wing station 101.0 and the lower station represents on wing station 64.8. The 3 grid points at each station correspond to chord positions of 15.0%, 44.0%, and 66.6% chord.

Dynamic Analysis

Normal mode shapes and resonant frequencies were computed with the natural frequency analysis option in the DYNA2(dynamic analysis solution in MSC/PAL2) program. In this report, due to the limitation of active degrees of freedom for normal modes using MSC/PAL2, the command ELIMINATE was used to reduce the number of degrees of freedom. This command was added to QTSB4.DAT and renamed T38.DYN for the dynamic analysis. This reduction was used primarily in the dynamic analysis, particularly to reduce model size to one solvable in MSC/PAL2. Though this reduction is not exact for the dynamic analysis, it is accurate enough that the lowest one-third of the computed resonant frequencies are accurate. The first 10 natural frequencies are shown in Table 2 and the first 4 mode shapes are in Figure 14. The x and y translation and z rotation are zeroed out to calculate the bending vibration.

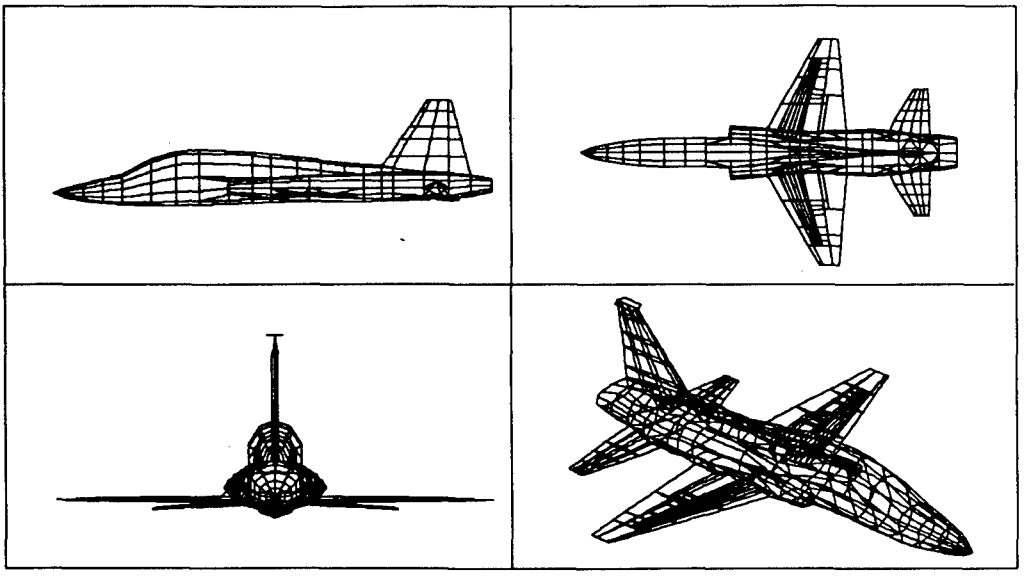

Figure 1. T-38 Structural Finite Element Model

Table 1. Designation of Finite Element Model

Model 1					
FILE.NAME	QSB1.DAT	QSR1.DAT	TSB1.DAT	TSR1.DAT	SSR1.DAT
WING SKIN	CQUAD4	CQUAD4	CTRIA3	CTRIA3	CSHEAR
SPAR & RIB WEB	CSHEAR	CSHEAR	CSHEAR	CSHEAR	CSHEAR
SPAR & RIB CHORD	CBEAM	CONROD	CBEAM	CONROD	CONROD

Model 2				
FILE.NAME	QSB2.DAT	QSR2.DAT	TSB2.DAT	TSR2.DAT
WING SKIN	CQUAD4	CQUAD4	CTRIA3	CTRIA3
SPAR & RIB WEB	CSHEAR	CSHEAR	CSHEAR	CSHEAR
SPAR & RIB CHORD	CBEAM	CONROD	CBEAM	CONROD

Model 3				
FILE.NAME	QSB3.DAT	QSR3.DAT	TSB3.DAT	TSR3.DAT
WING SKIN	CQUAD4	CQUAD4	CTRIA3	CTRIA3
SPAR & RIB WEB	CSHEAR	CSHEAR	CSHEAR	CSHEAR
SPAR & RIB CHORD	CBEAM	CONROD	CBEAM	CONROD

Model 4		
FILE.NAME	QTSB4.DAT	QTSR4.DAT
WING SKIN	CQUAD4 & CTRIA3	CQUAD4 & CTRIA3
SPAR & RIB WEB	CSHEAR	CSHEAR
SPAR & RIB CHORD	CBEAM	CONROD

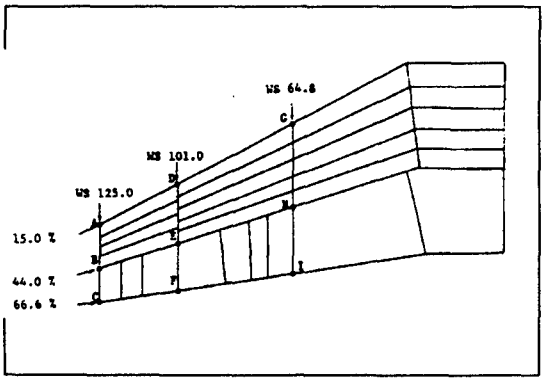

Figure 2. Location of Loading Grid Points

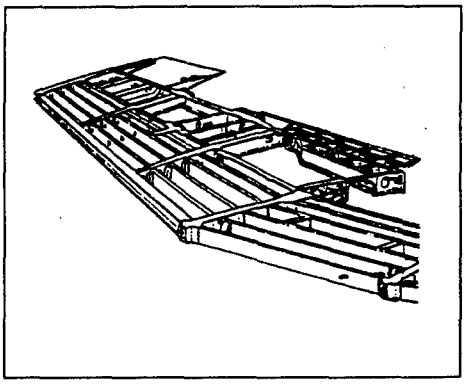

Figure 3. Real T-38 Wing Structure

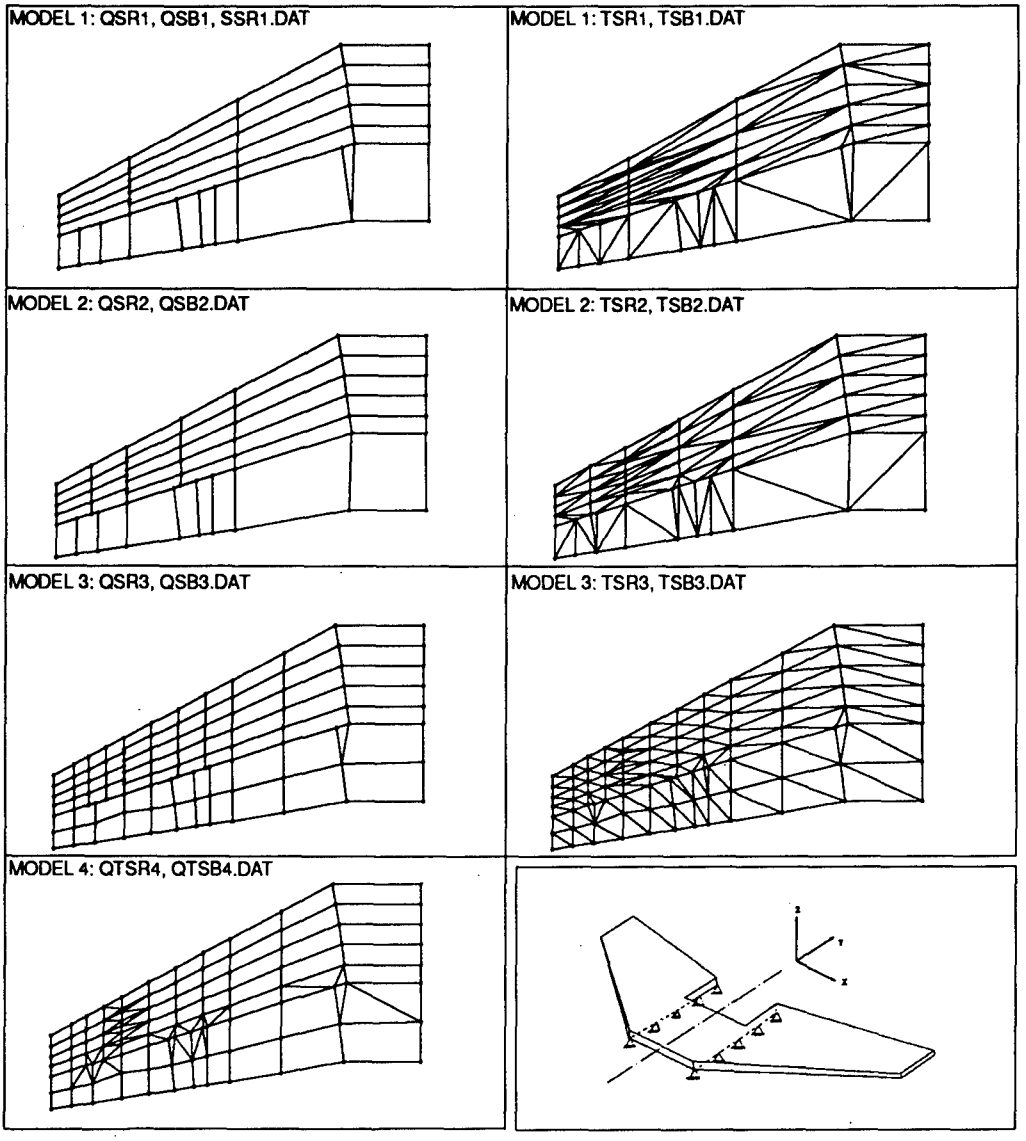

Figure 4. T-38 Wing Finite Element Model

Figure 5. Boundary Condition

III. DISCUSSION OF RESULTS

The results calculated by MSC/NASTRAN and/or MSC/PAL2 are in very good agreement with the test results. In a few loading cases the finite element results are slightly different from the test results, especially for 3,000 lb and 5,000 lb loading cases. In this report many different finite element models are used to obtain deflections. The results from TSRi.DAT and TSBi.DAT agree very well with test. The QSRi.DAT and QSBi.DAT agreement is good, but not as good as the results of TSRi.DAT and TSBi.DAT. The T-38 wing skin has a slight curvature and some portions of the structure require better meshing. As a result, triangular elements were chosen to obtain better aggrement. The combination of quadrilateral and triangular plate were evaluated in this report. The corresponding two data files(Model 4 in Table 1) are QTSB4.DAT and QTSR4.DAT and were actually modified from QSB4.DAT and QSR4.DAT. The results from QSRi.DAT and QSBi.DAT are still not good enough because of impractical quadrilateral plates. Consequently, 102 triangular plate elements were used instead of 34 quadrilateral plate elements from QSB4.DAT and QSR4.DAT, and very good results were produced. All results are shown in Figures 6-13.

Choice of the type of spar and rib chords depends on the structural model. For the current work, the spar and rib chords of the T-38 wing were modeled as beam(bar) and rod elements in separate wing models. The method of sizing the rod elements of the spar and rib of a wing explained in Reference [3] was used in this effort. According to Reference [3], one way to treat the effective area of the rod element is a summation of its own area, plus the additional term comprised of the skin thickness between the two rods times one half the distance between the rods. There is assumed to be no bending and membrane stiffness in the top and bottom skins(as compared to a real wing structure and boxbeam). Because of this assumption the rod element stiffness is increased. It is the author's experiences that a typical difficulty exists in calculation of the effective area of rod. For example, from equation $\mathbf{A}_{eff} = A_f + bt/2$, (b is the distance between two spar or rib chords, t is the thickness of wing skins, and, A_f is the physical cross section area of spar and rib chords) the value of b should be defined. In the case of the T-38 wing, it has a general quadrilateral shape, so an average value of b is taken. This procedure was used in the model SSR1.DAT. SSR1.DAT has the shear panel option for top and bottom skins and spar and rib webs: The weakness in using this procedure is shown in Figures 6(e)-13(e). Otherwise, for the case of the Rattinger's wing(boxbeam with a symmetric planform and the same geometric parameter), good results were obtained. From the author's experience, it has been found that this is a good procedure for simple box-beam type wing structures.

Figure 14 shows four flap bending modes and the associated natural frequencies. The natural frequencies for the higher modes appear in Table 2. At this time test data is not available for correlation purposes.

The following are some recommendations based on this work.

1. Improved results can be expected with more nodes and elements than model 1, 2, 3, and 4 and running MSC/NASTRAN on the CRAY computer.

2. The T-38 wing skin has variable thicknesses so it is recommended with MSC/NASTRAN to choose the CQUAD8 card which defines a curved quadrilateral shell element with eight grid points. For the triangular plate, CTRIA6 will be used in the follow-on effort.

Table 2. Natural Frequencies of T-38 Wing

Mode No.	Natural Frequencies (cps)
1	4.643
2	6.745
3	7.092
4	7.105
5	7.799
6	7.944
7	8.269
8	10.681
9	11.542
10	12.655

IV CONCLUSION

In view of the agreement between test and analytical results, Model 4(QTSR4.DAT and QTSB4.DAT) that were used quadrilateral and triangular plate elements for wing skins , shear panel elements for spar/rib webs and rod or bar(beam) elements for spar/rib chords is adequate for determining deflections of complex wings such as the T-38 wing. This model 4, which was used to reduce the problem size is efficient and accurate as shown in Figures 6(f)-13(f). It will be selected as the T-38 wing model for static and dynamic aeroelasticity and flutter solutions because accurate determination of influence coefficients is needed in such analyses.

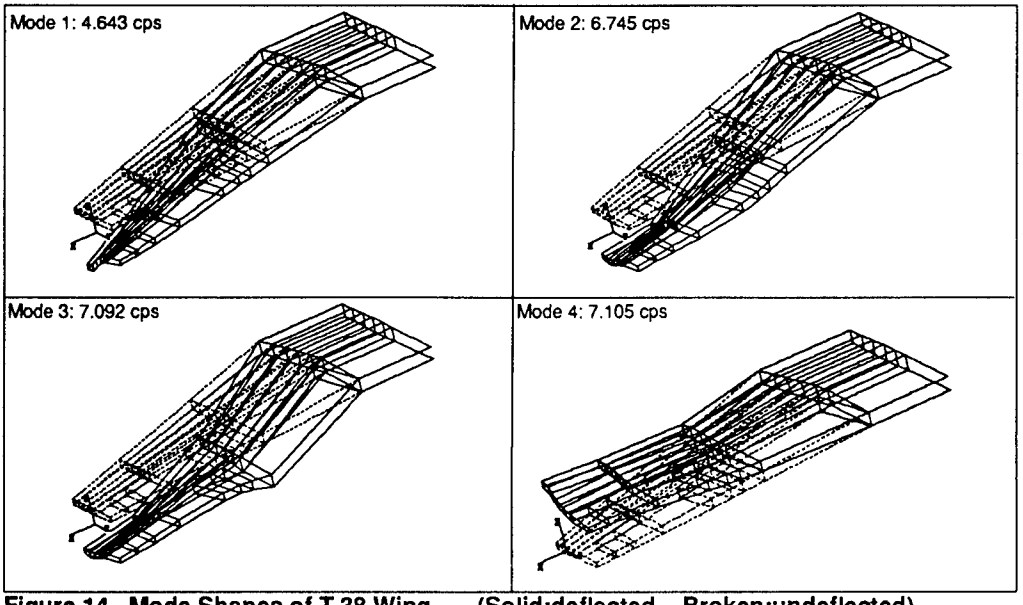

Figure 14. Mode Shapes of T-38 Wing (Solid:deflected Broken:undeflected)

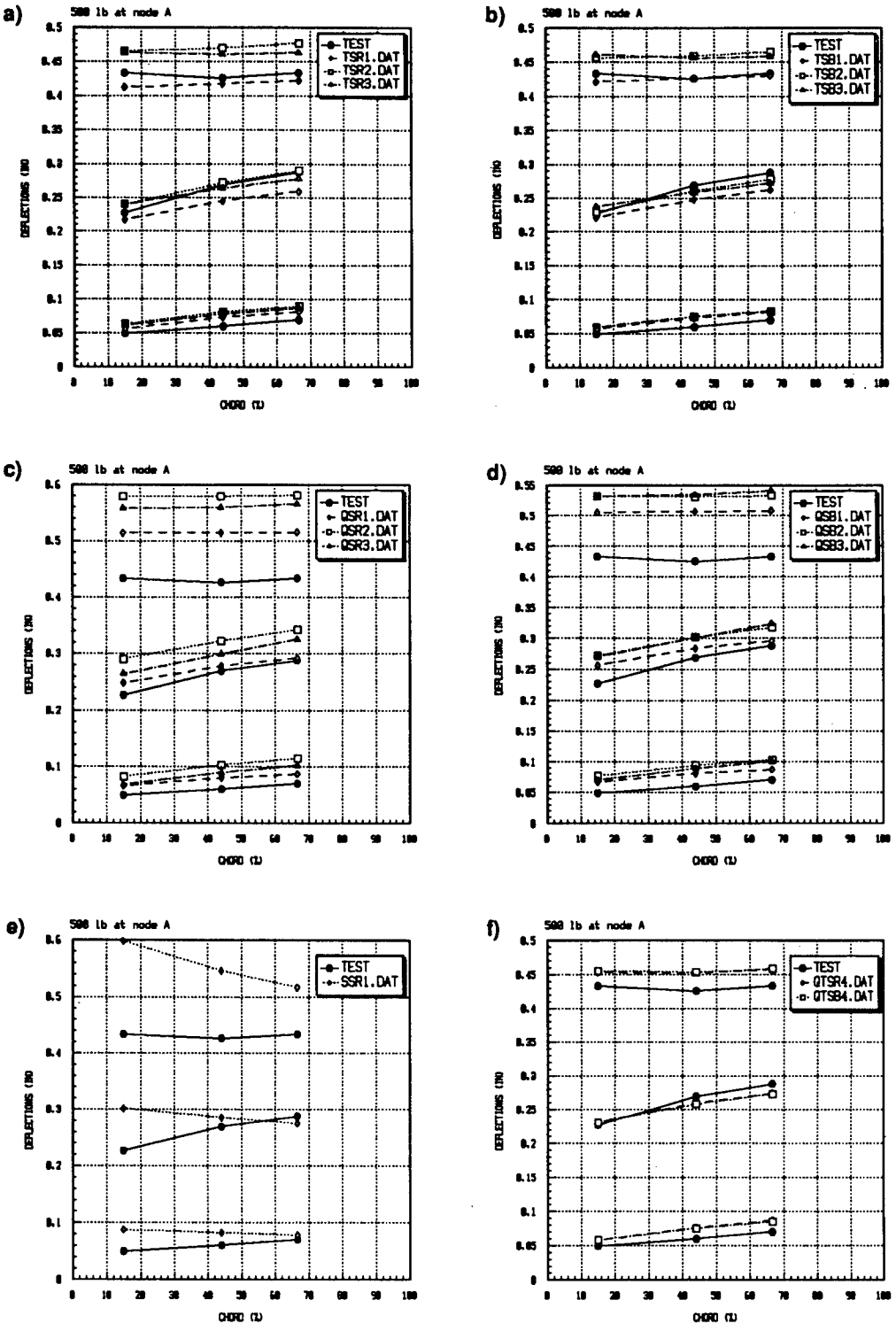

Figure 6. Comparison of Displacements from FEM and TEST - 500 lb Load at Node A

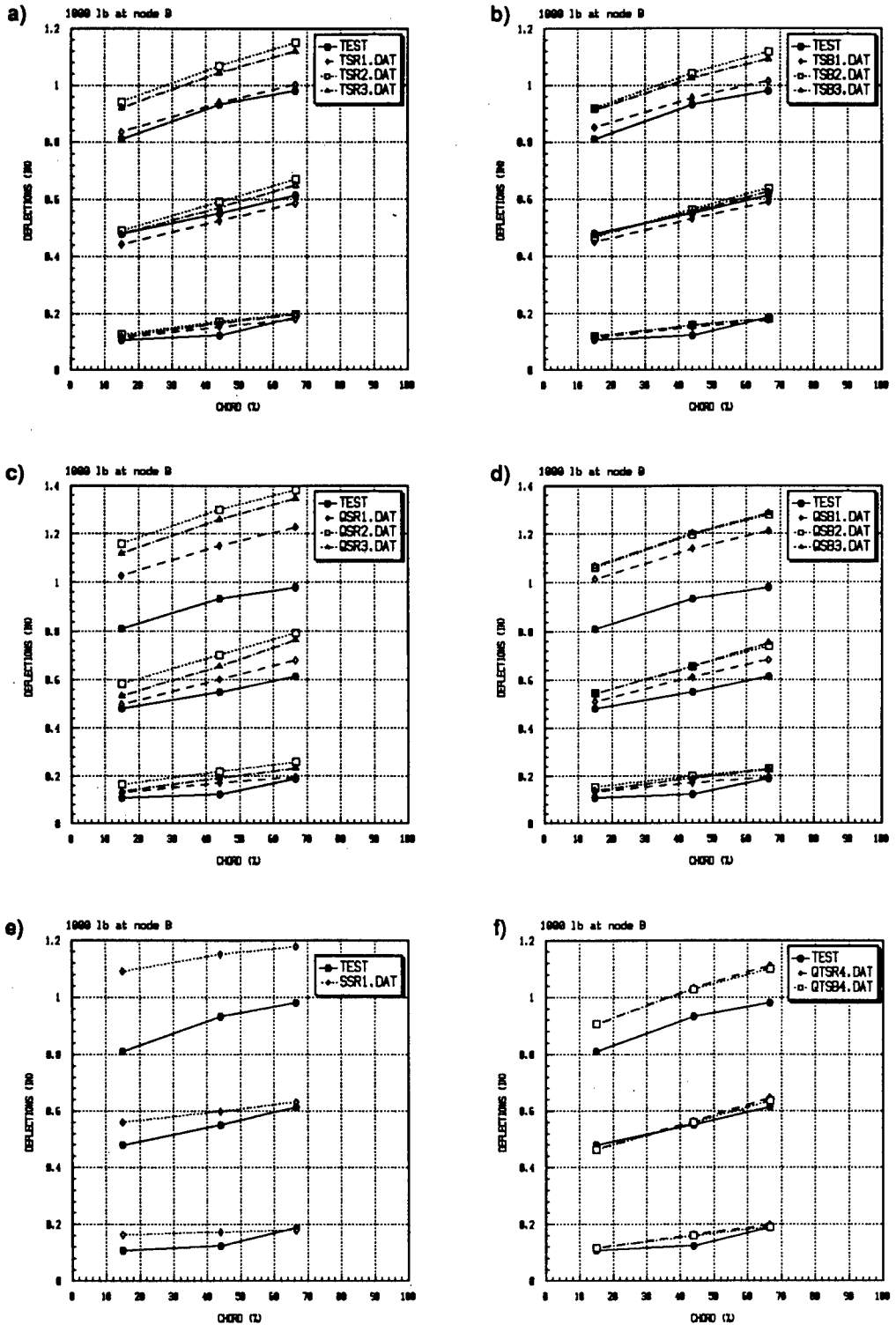

Figure 7. Comparison of Displacements from FEM and TEST - 1000 lb Load at Node B

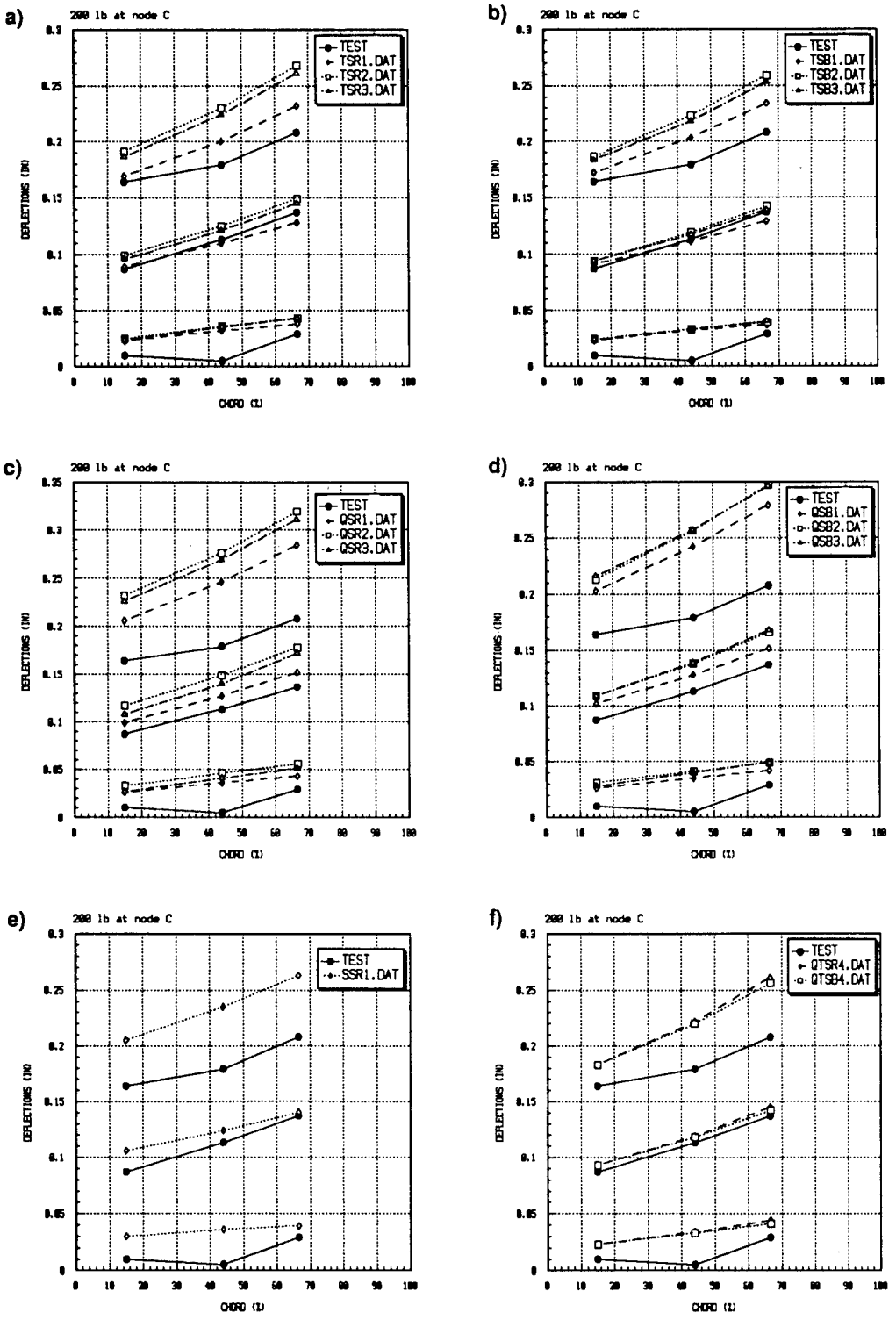

Figure 8. Comparison of Displacements from FEM and TEST - 200 lb Load at Node C

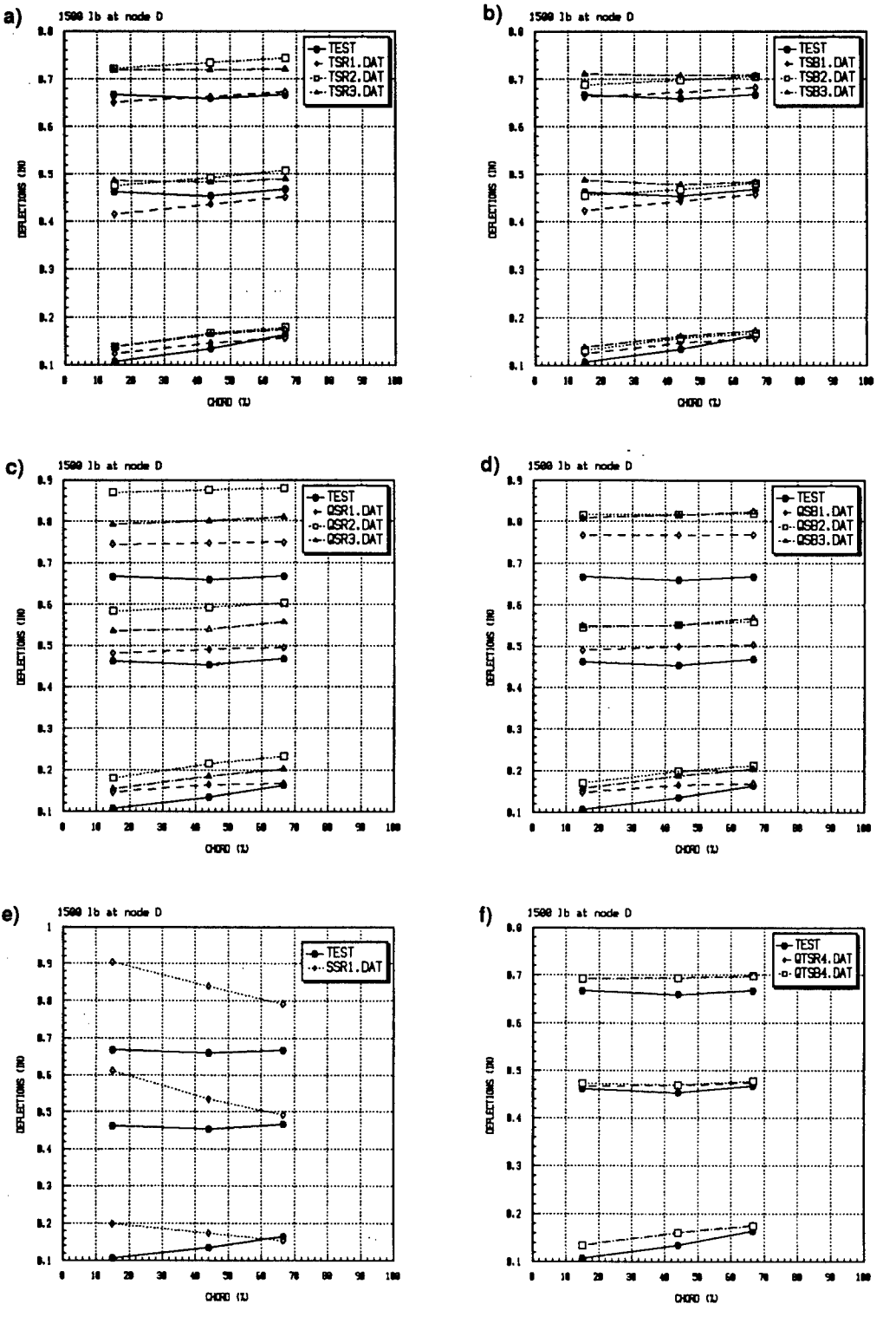

Figure 9. Comparison of Displacements from FEM and TEST - 1500 lb Load at Node D

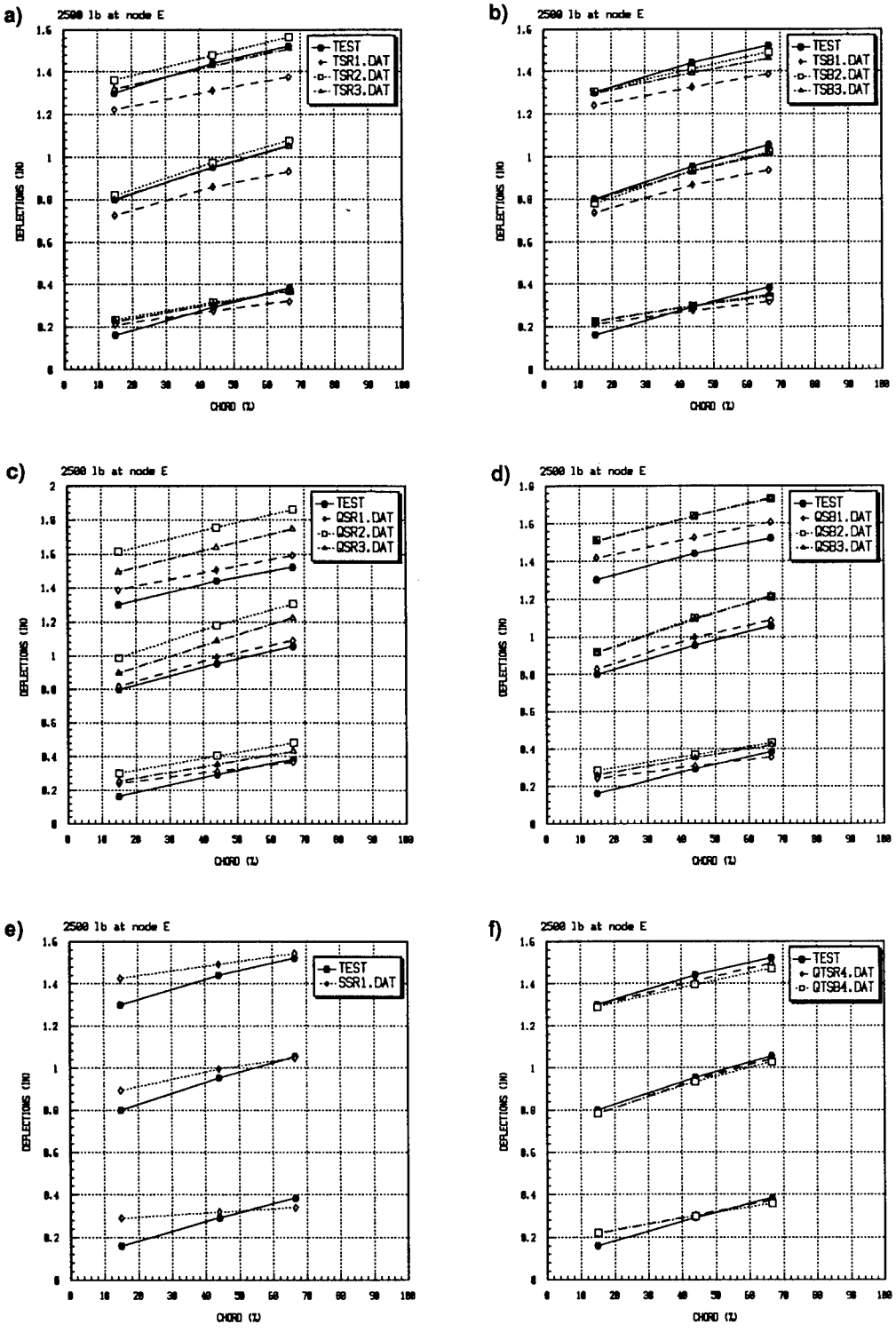

Figure 10. Comparison of Displacements from FEM and TEST - 2500 lb Load at Node E

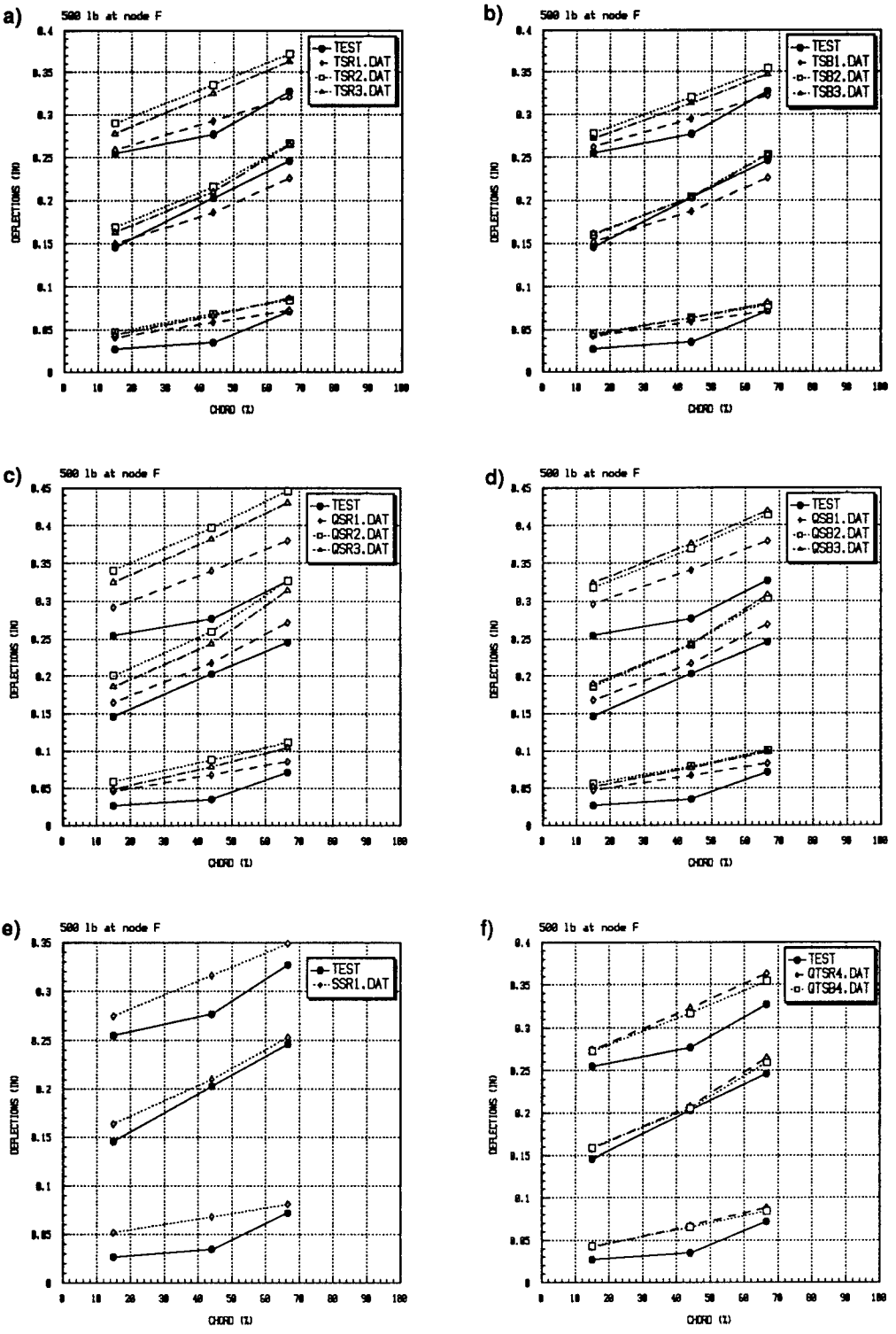

Figure 11. Comparison of Displacements from FEM and TEST - 500 lb Load at Node F

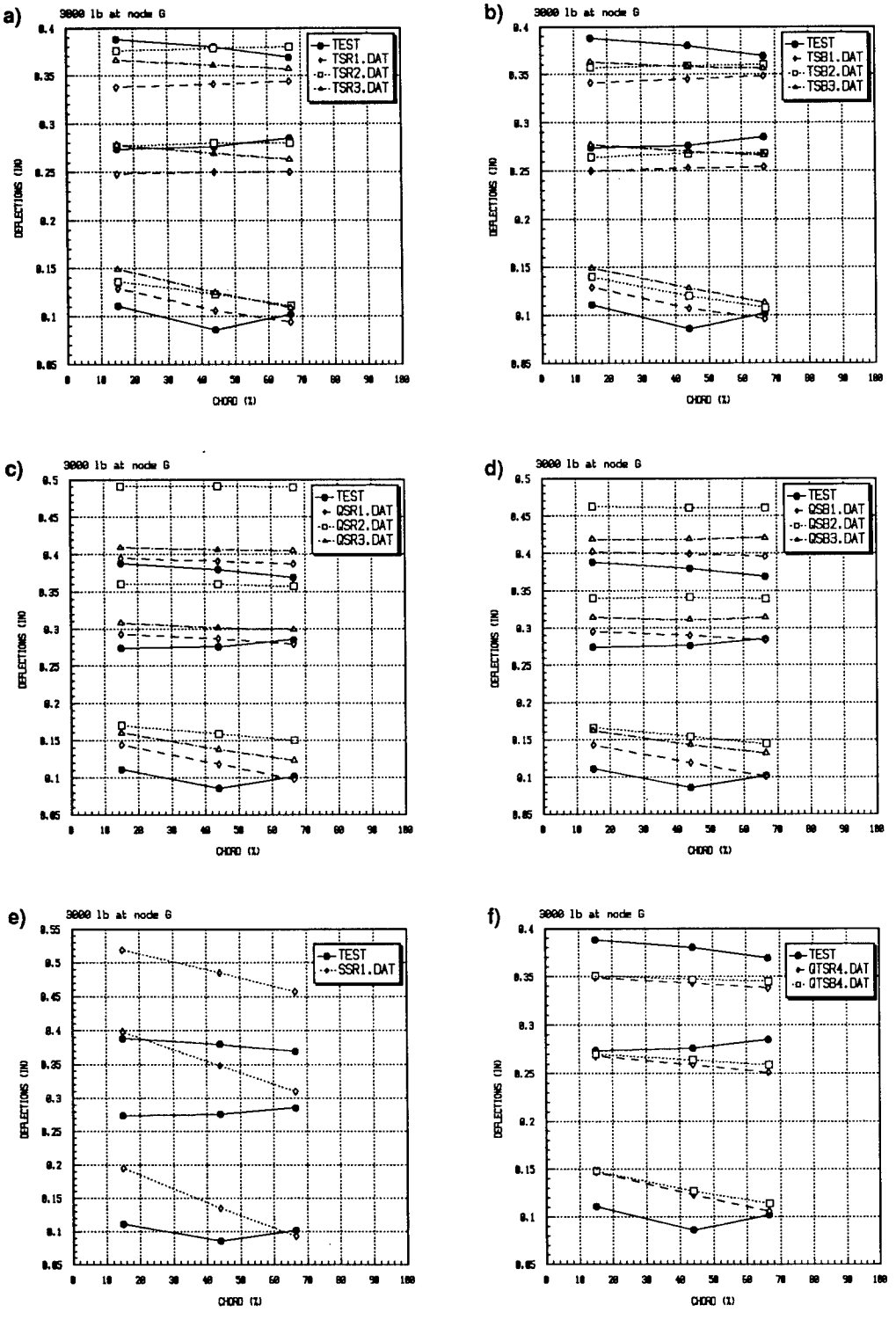

Figure 12. Comparison of Displacements from FEM and TEST - 3000 lb Load at Node G

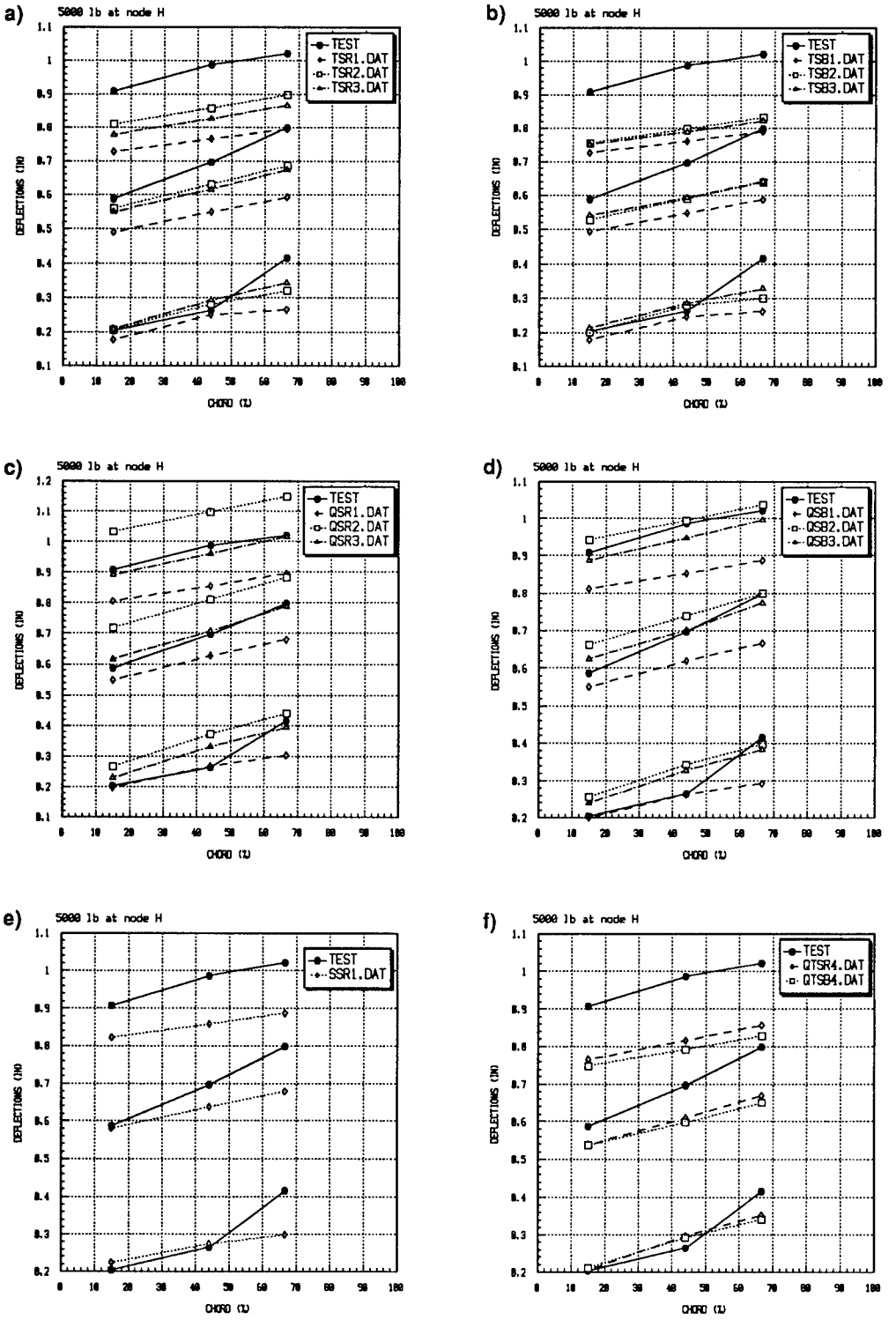

Figure 13. Comparison of Displacements from FEM and TEST - 5000 lb Load at Node H

REFERENCES

1. NOR-60-6. Static Test of Complete Airframe for the T-38A Airplane. Hawthorne, California: Northrop Aircraft, Inc., March 1960.

2. Rattinger, I., Dickenson, H., Cole, C.D., "Preliminary Report Comparison with Test of Analytically Derived Influence Coefficients for a Straight Low-Aspect Ratio Model Wing," Bell Aircraft Report No. 9001-914001, 1957.

3. An Experimental and Analytical Study of the Static Response of an Undamaged and Damaged F-84 Wing, Vols. I and II. 61 JTCG/ME-76-11-1 and -2. Eglin AFB, Fla.: Joint Technical Coordinateing Group for Munitions Effectiveness, Aug. 24, 1976.

4. Bruhn, E. F. Analysis and Design of Flight Vehicle Structures. Cincinnati: Tri-State Offset Company, 1973.

5. Stronge, W.J. Failure Prediction for Damaged Aircraft Wings. Proceedings of the Fifth Navy-NASTRAN Colloquium, NSRDC, 1974.Stronge, W.J. Modeling damaged Wings - Element Selection and Constraint Specification. Naval Weapons Center.

6. Stronge, W.J. Modeling damaged Wings - Element Selection and Constraint Specification. Naval Weapons Center.

A HIGH PURITY ALUMINA WITH EXCEPTIONAL COMPRESSIVE AND FLEXURE STRENGTH BEHAVIOR
OR
ALUMINA REVISITED - BUT MUCH BETTER THAN EVER

James M. Staehler*
William W. Predebon*
Bruce J. Pletka**

***Department of Mechanical Engineering-Engineering Mechanics**
****Department of Metallurgical and Materials Engineering**
Michigan Technological University
1400 Townsend Drive
Houghton, MI 49931-1295

INTRODUCTION

Aluminum oxide has traditionally been considered a purely brittle material at room temperature. However, its compressive fracture stress has been shown to exhibit some strain rate dependance [1]. This strain rate dependance suggests that either some dislocation or twinning activity is occurring or that microcracking is taking place throughout the volume of the material at room temperature. Munson and Lawrence [2] speculated that the deformation of alumina at room temperature was the result of microcracks being activated throughout the sample and that this was accompanied by either dislocation motion or twinning. Indeed plastic deformation has been observed [1],[3],[4], particularly in the form of twinning. Lankford [1] suggested that the twinning nucleates the microcracks, generally at grain boundary-twin intersections. In addition, the degree to which a ceramic material exhibits a strain rate dependance of its compressive strength (fracture strength) will be governed by its microstructure. The microstructural factors of importance include purity, grain size, porosity, as well as flaw size distribution.

A considerable amount of data exists on the mechanical properties of alumina. Unfortunately it is difficult sometimes to draw conclusions about the dependance of these properties on microstructural factors because very few commercially available alumina's are similar in composition. In order to obtain a more fundamental understanding of the rate dependance of the fracture strength we have fabricated our own alumina using a high purity

alumina powder. This allowed us to control the microstructure of the alumina produced, namely the grain size and porosity level. Testing has been conducted over the strain rate range of 10^{-4} to $10^{3}s^{-1}$. Therefore, the purpose of this paper was to present preliminary results of the strain rate dependence of this ultra pure, high strength alumina.

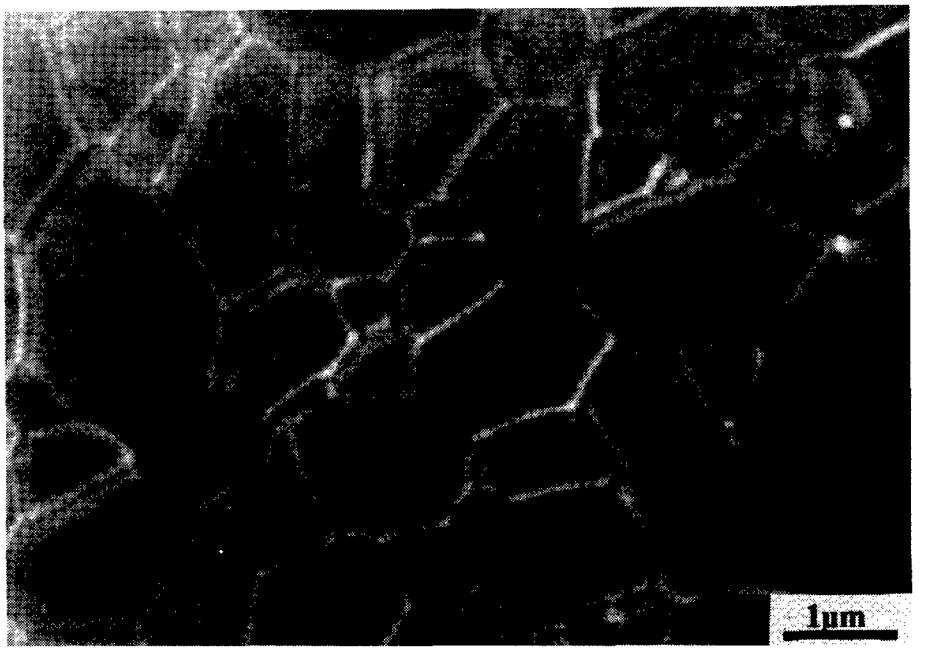

Figure 1. SEM micrograph showing grain structure of MTU JS-I alumina.

MATERIAL PREPARATION

The starting powder, CR6-2[1], was a 99.99% pure alumina with a median particle size of 0.52 μm. No additions of any kind were made to the powder, thereby minimizing the formation of any second phases during processing. To remove any organic impurities, the powder was calcined at 650°C in high purity alumina crucibles for 1 hour. Following the calcining the powder was pulverized using a mortar and pestle to eliminate any large agglomerates which may have formed during calcining. Primary consolidation of the powder was performed using a vacuum hot press (VHP) with graphite dies. The hot pressing conditions were 1400°C for 2.5 hours at 34.5 Mpa (5000 psi). This was then followed by a 172.4 Mpa (25 ksi) hot isostatic press (HIP) cycle at 1300°C for 2 hours. The material thus produced will be called

[1]Baikowski Int. Corp., Charlotte, NC, USA.

MTU JS-I. By using different heat treatments on JS-I it was possible to produce materials with different microstructures. Material MTU JS-II was produced by heat treating JS-I in air for 50 hrs at 1475°C followed by a 2 hr HIP at 1300°C and 172.4 Mpa.

Figure 1 is an SEM micrograph of a representative sample of JS-I that was polished and then thermally etched at 1500°C for 5 minutes. Using an image analysis system, the mean grain diameter was determined to be 0.95 μm. The two dimensional representation of the grains in the micrographs were corrected by multiplying by 1.56 yielding a mean grain size of 1.48 μm [5]. In addition to obtaining a mean grain size, the grain size distribution was determined and is shown in Figure 2.

Alumina has a tendency to form plate-like grains when subjected to high temperatures. In order to characterize the degree of grain shape anisotropy, the digitized information was also used to calculate a form factor for each grain. This form factor, ff, represents the extent to which each grain deviates from a perfect circle. It is based on the area and perimeter of the grain using the following relationship

$$ff = \frac{4\pi A}{P^2}$$

where P is the perimeter and A the area. For comparison, a circle would have a form factor of 1.0. However, a dense high purity ceramic would not be expected to have circular or spherical grains. An ideal, high density, equiaxed grained ceramic in two dimensions could be expected to have six neighboring grains. The form factor of such a structure using the above relationship would be 0.91. The distribution of form factors for JS-I are shown in Figure 3. The median form factor was found to be 0.86 with an average of 0.84.

The density of JS-I was nearly 100%. Figure 4 is a TEM micrograph of the material. The existing porosity was predominantly transgranular. Because the pores are isolated from the grain boundaries, further densification would be very difficult. Densities measured by immersion in distilled water indicate the material to have a density greater than 99.5% of theoretical.

One consequence of processing an alumina in a vacuum hot press with graphite dies is the tendency for void formation when the material is heated in air [6]. This void formation or bloating is believed to be the result of CO and CO_2 forming at grain boundaries when oxygen in the air combines with carbon trapped along grain boundaries. Due to this bloating, the porosity of JS-II has increased relative to JS-I and this increased porosity tends to be distributed at the grain boundaries. Using immersion techniques the density

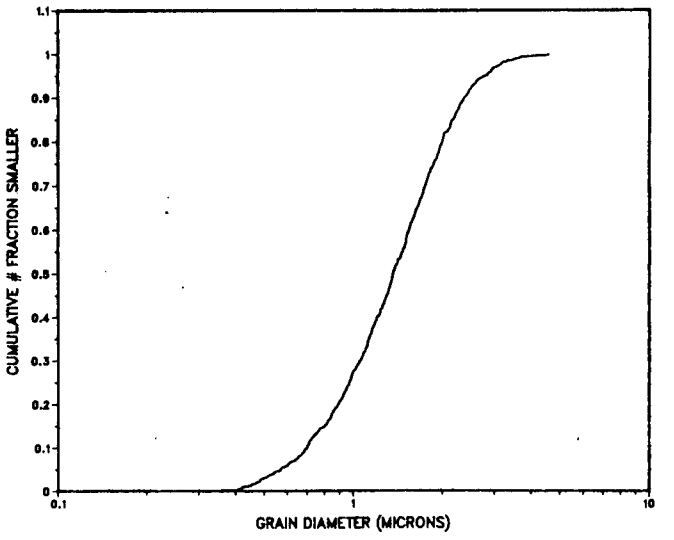

Figure 2. Grain size distribution of MTU JS-I.

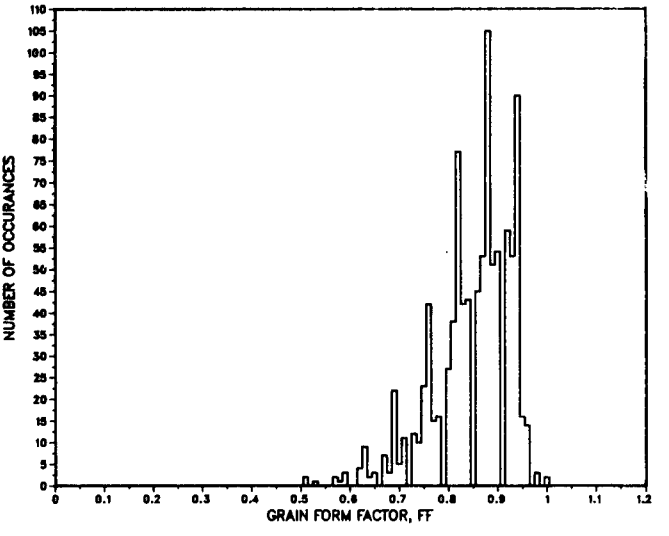

Figure 3. Form factor distribution of MTU JS-I.

of JS-II was found to be approximately 99.3%. An additional consequence of the grain growth in JS-II is that the shape of its grains are slightly less equiaxed than those of JS-I. At this time the microstructure of JS-II has not been characterized with the digitization technique used for JS-I. However the grain size of JS-II is approximately 10 μm.

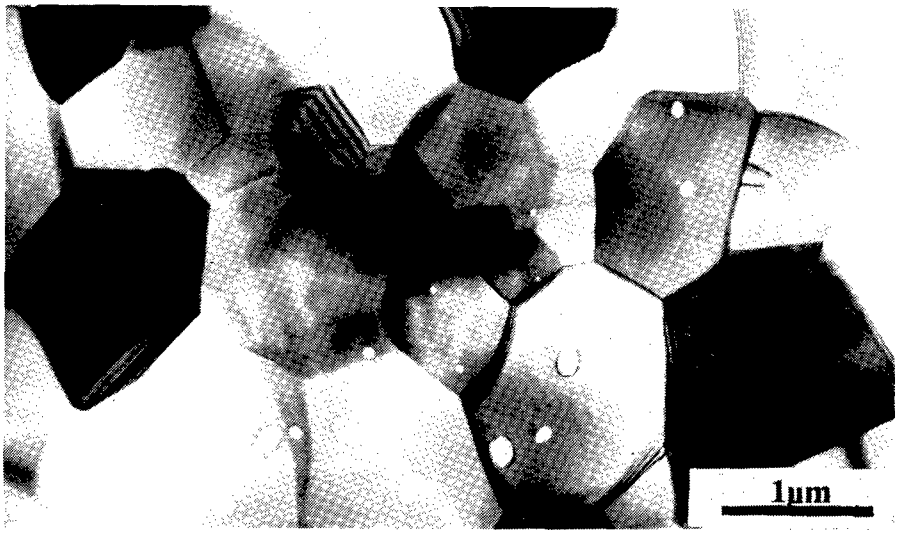

Figure 4. TEM micrograph of JS-I showing porosity.

In addition to the MTU JS alumina's, a commercially available alumina was tested as well. The material, brand name Ceraver, is a 92 percent alumina with a mean grain size of 3.73 microns. Figure 5 is a TEM micrograph showing the extensive presence of a glass phase in the microstructure of the Ceraver. The primary reason for testing this material was to provide a check of our experimental technique with published data for the Ceraver [7].

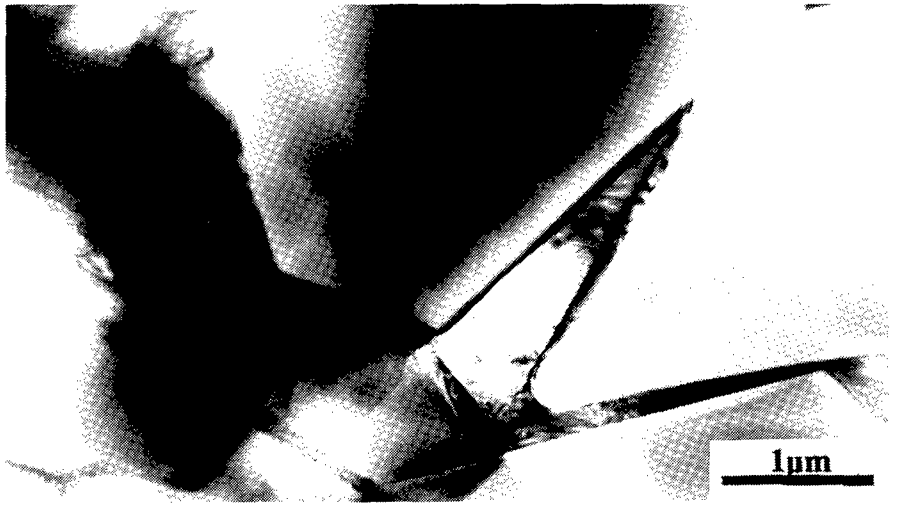

Figure 5. TEM micrograph of Ceraver with glass phases.

Compression samples of the MTU alumina were machined to

4.76 mm dia. x 9.52 mm in length. The dimensional tolerances and surface finishes are summarized in Table 1. They are similar to those used by Lankford [1]. The Ceraver samples were machined to 6.35 mm dia. x 12.7 mm in length. These were the original dimensions recommended by Lankford for the Hopkinson bar tests (which are discussed later). The reason for the reduction in size of the MTU alumina samples was because the Hopkinson bar test set-up would not have been able to attain the stresses necessary to fracture the MTU alumina without risking permanent damage to the apparatus itself. The surface finish of the Ceraver samples were typically poorer than those of the MTU alumina. This can be attributed to the pull-out of grains in the Ceraver due to the high glassy phase content.

TABLE 1. Machining Tolerances for Compression Samples and Anvils.

Diameters: to within 0.05 mm
Dimensions: x.xx ± 0.02 mm
x.xxx ± 0.002 mm
Parallelism: end faces to within 0.0005 mm
Perpendicularity: end faces to sample centerline within 0.002 mm
Flatness: end faces to within 0.0125 mm
Surface finish: end faces to 1 micron or better

The cylindrical surfaces of the MTU alumina samples, with the exception of a few of the JS-I samples, were polished through ¼ μm diamond paste. This was carried out to minimize the effect of surface damage due to machining on the fracture strength and also to allow for SEM or optical analyses of the surfaces of deformed samples. This procedure was not performed on the Ceraver due to grain pullout problems during polishing. Despite the polishing, no significant difference in compressive fracture strength was observed between JS-I samples with their cylindrical surfaces polished and those tested in the as machined condition.

EXPERIMENTAL PROCEDURE

A die set was used during the quasi-static compression tests to insure the sample and series of anvils were always parallel and in line. Two D2 tool steel platens heat treated to a R_c of ≈60 were bolted to the upper and lower cross members of the die set. Between these tool steel platens and the sample

were either AD999[2] alumina anvils or KF306[3] tungsten carbide anvils. The anvils were 12.7 mm dia. x 9.52 mm in length with the end facing the sample polished to the same surface finish as that specified for the sample faces (See Table 1). The use of the AD999 anvils was discontinued because they typically failed during the test. The WC anvils were chosen as an alternative to the AD999 anvils to avoid anvil failure. As an additional precaution, the WC anvils were placed in steel rings which clamp tightly to the anvil and add radial confinement. Although surface damage was apparent in the WC anvils following testing of the MTU material, they did not fail catastrophically as did the AD999 anvils. Each anvil was used only once. Teflon tape was used at the sample anvil interfaces and at the interfaces between the anvils and the D2 tool steel platens.

In order to obtain accurate strain measurements, strain gages were attached to the samples. In most cases both axially and circumferentially positioned gages were used. This allowed for measurements of stiffness, strain rate, and Poisson's ratio. Using this approach the effect of machine stiffness was minimized. Strains and strain rates are measured directly off of the sample.

An MTS servo-hydraulic testing machine was used for all the tests completed at 10^{-4} to $10^{0}s^{-1}$ strain rates. Load, axial strain, and circumferential strain data were recorded with an IBM Model 50SX. The software and interfacing board were from Labtech Notebook.

The high strain rate tests (10^{3} sec^{-1}) were performed at Southwest Research Institute (SwRI) using their split Hopkinson pressure bar (SHPB) apparatus. Axial and in most cases circumferential strain gages were mounted on the tested samples in order to obtain the actual strain profiles in the samples. Rogers and Nemat-Nasser [8] indicated that the traditional method of obtaining the strain profile in a ceramic using the reflected strain signal in the incident bar was insufficient. In testing Mg-PSZ samples with the Hopkinson bar they used strain gages to measure axial and transverse strains. Anderson et al [9] reached the same conclusion and attributed the discrepancy to the small amplitude of the reflected pulse which occurs because of the similar elastic impedances between the steel bars of the SHPB and the ceramic. However, we have also observed that the stress profile in the sample inferred from the transmitter bar signal can differ significantly from that measured using the sample strain gages. This will be shown later. The

[2]Coors Porcelain Co., Golden, CO, USA.

[3]Kennametal Inc., Raleigh, NC, USA.

transmitter bar signal requires more than the normal correction for the change in area between the sample and bars. While it was possible to observe trends based on the signals recorded off the transmitter and incident bars, it was not possible to determine actual stress magnitudes. All of these problems were eliminated by using strain gages mounted directly on the alumina samples.

As with the quasi-static testing, it was necessary to use WC anvils for the Hopkinson bar tests. The AD999 anvils failed prematurely. The WC anvils used in the Hopkinson bar were 12.7 mm Dia. x 12.7 mm in length. Both faces were machined and polished to the specifications used for the samples. Despite the switch to the WC anvils, anvil failure still occurred. Consequently the fracture stresses of the samples at the strain rate of 10^3 s^{-1} may be underestimated, but are still very high compared with other alumina.

In addition to the compression tests, a limited number of four-point bend tests were also performed on the MTU JS-I alumina. This testing was conducted in accordance with sample style B of MIL-STD-1942. The tensile surface of each sample was polished using 15, 6, 3, 1, and ¼ μm diamond paste on either Tex Met or nylon cloth. The nominal dimensions of the samples were 45 mm x 4 mm x 3 mm.

RESULTS

Typical stress-strain curves for JS-I alumina and a Ceraver sample for a strain rate of 10^{-4} s^{-1} are shown in Figure 6. Table 2 summarizes the elastic properties of the two materials obtained during compression testing. Young's modulus for the Ceraver was the same as that reported for this material by ALCOA [7]. The higher purity, slightly finer grain sized MTU JS-I alumina has a significantly higher compressive strength than the Ceraver. It also exhibited a 25% greater stiffness. The axial strain history of the samples given in Figure 6 are shown in Figure 7. Due to slack in the machine which is taken up during loading, the strain is not linear in time initially. The strain rate characterizing a test was taken as the slope of the linear portion of the curve.

TABLE 2. Elastic Properties

Material	Young's Modulus	Poisson's Ratio
MTU JS-I	414 Gpa	0.25 ± 0.02
MTU JS-II	348 Gpa	0.25 ± 0.02
Ceraver	310 Gpa (307 GPA)*	0.25 ± 0.02

*Manufacturer's value [7]

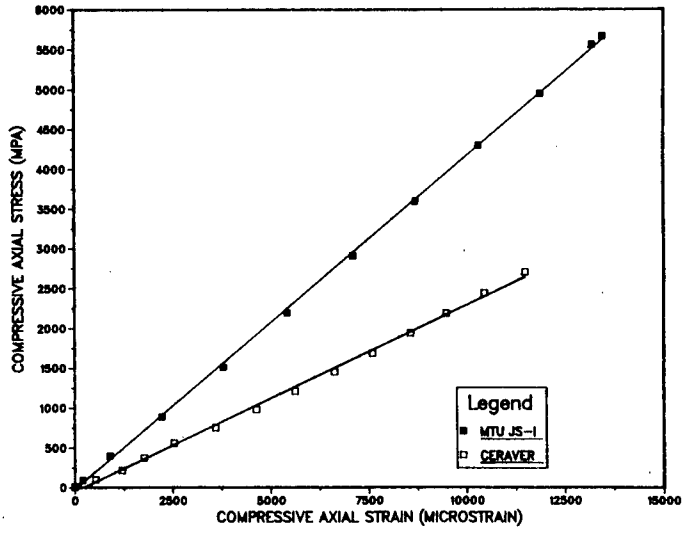

Figure 6. Stress-strain behavior of MTU JS-I and Ceraver at a strain rate of $10^{-4}s^{-1}$.

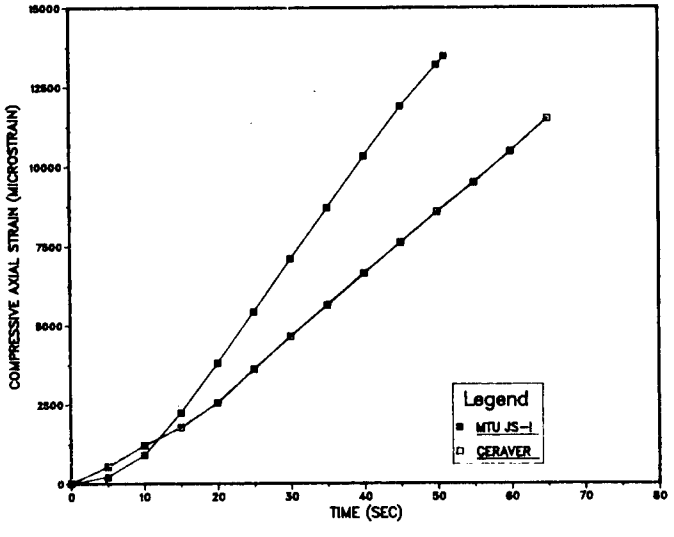

Figure 7. Typical strain histories of MTU JS-1 and Ceraver in the $10^{-4}s^{-1}$ range.

The MTU JS-I and the Ceraver were each tested at strain rates ranging from 10^{-4} s^{-1} to 10^{3} s^{-1}. The compressive strength as a function of strain rate is shown in Figure 8 for these materials as well as data collected by Lankford

on Lucalox [1]. The figure shows that the compressive strengths of the Lucalox and Ceraver are quite similar at the low and intermediate strain rates. This is true even though their grain sizes are quite different; 25 μm for the Lucalox versus 3.73 μm for the Ceraver. The JS-I alumina exhibits a significantly higher strength than the other two aluminas at all strain rates tested. Surprisingly JS-II had the lowest fracture strength at the lowest strain rate. As an independent verification of the quasi-static compressive strength of the MTU JS-I alumina obtained in our laboratory, one sample was tested at SwRI with a strain rate of 10^{-4} s^{-1}. They obtained a similar compressive strength.

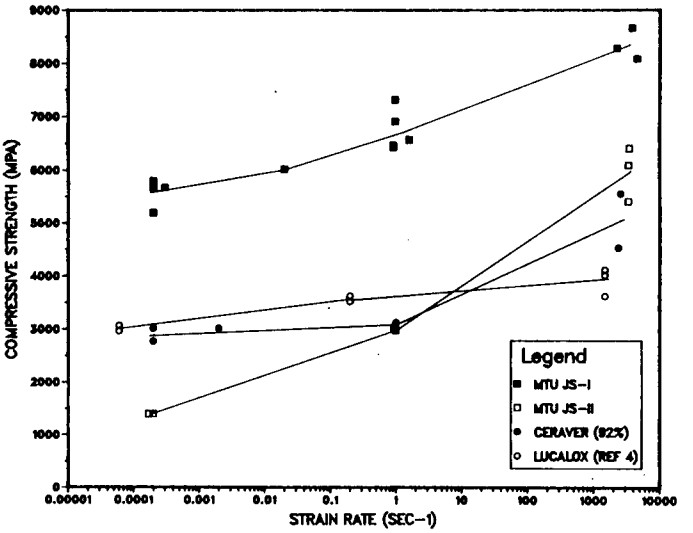

Figure 8. Compressive strength as a function of strain rate for JS-I, JS-II, Ceraver and Lucolux.

A typical axial strain history for a MTU JS-I alumina sample tested with the Hopkinson bar are shown in Figure 9. The axial strain rate is again the slope of the best fit line through the data and in Figure 9 this was about 4560 s^{-1}. The peak axial strain in the sample was approximately 1.95%. Using the strain signal from the strain gages mounted directly to the sample along with the Young's modulus obtained from the quasi-static tests, the peak stress is 8073 Mpa. Figure 10 shows the stress pulse taken from the transmitter bar. The magnitude of the stress has already been corrected for the change in cross sectional area between the bar and the sample. The peak stress in the sample indicated from this figure however is only 3850 Mpa, 52.3% lower than that obtained from the sample strain gage data. For the three tests of JS-I at $10^3 s^{-1}$ the stress inferred from the transmitter bar signal was always less than the

stress obtained from the sample strain gage signal. The results are summarized in Table 3. This emphasizes the problems associated with using the transmitter bar strain gage data to infer the stress state in a ceramic material. All the Hopkinson bar fracture stresses presented here are derived from the strain signal and Young's modulus.

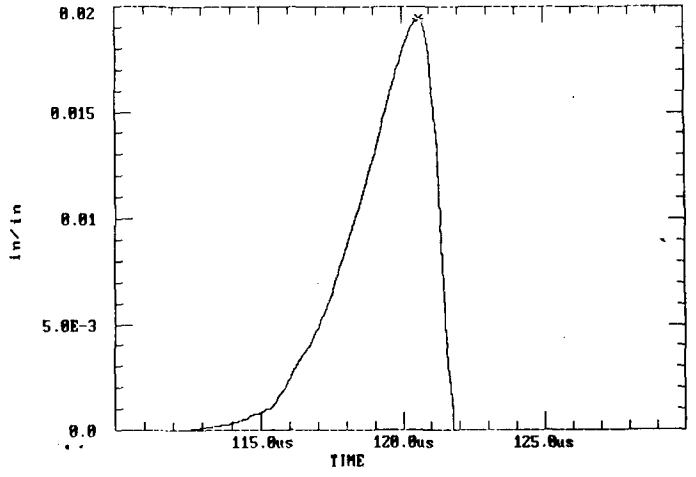

Figure 9. Strain history of JS-I sample from specimen gage.

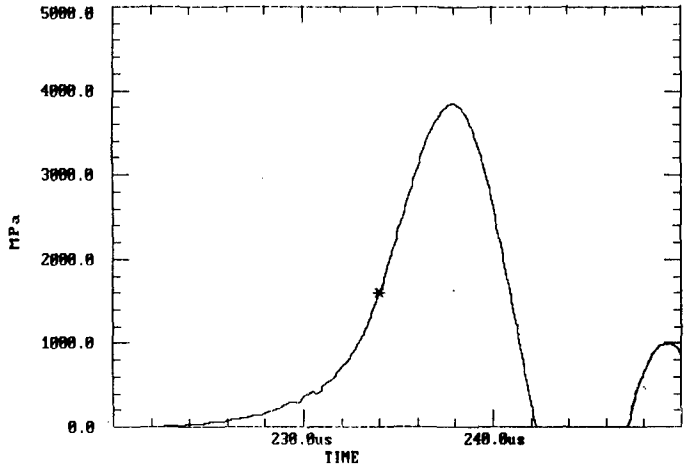

Figure 10. Stress history in a JS-I sample using transmitter bar signal.

TABLE 3. Comparison of Transmitter Bar signal and sample gage signal.

Sample	Anvil	Transmitter Bar Signal (Mpa)	Sample gage Signal (Mpa)	% Difference
B18C1	WC	5350	8400	36.3
B19C1	JS-I	3850	8070	52.3
B18B1	WC	3820	8650	55.8

The mean flexural strength of the JS-I material from four-point bend tests was approximately 909 Mpa. This is approximately 40% greater than the manufacturers listed strength for AD999 [10]. In each of the tests to date, failure has occurred under one of the center supports of the test fixture. Additional testing is in progress to obtain the Weibull distribution for the material. Strain gages were mounted to the compression surface of the four-point bend test pieces to check the actual strain rate and stress state to failure. The fracture strengths calculated using the strain gage data and the materials Young's modulus agreed with the elementary solution from strength of materials to within 2.5%. However, it was found that the strain rate was slightly less then the 10^{-4} s^{-1} specified by MIL-STD-1942 even though the required crosshead velocity was used.[4]

DISCUSSION

One of the concerns in using the Hopkinson bar with our small sample geometry is that a uniaxial state of stress may not exist in the sample during the test. The longitudinal sound speed of the JS-I alumina is about 10.9 to 11.0 km/s. It therefore takes the leading edge of the stress wave approximately 0.87 μs for it to travel the length of the JS-I sample. The total time of the pulse to failure in the sample is typically around 7.5 μs. Therefore the wave has travelled the length of the sample approximately 8.6 times before sample failure. The time for a wave to travel from the center of the sample to its outer radius and then back is approximately 0.43 μs. This should ensure sufficient time for relief waves from the outer edge of the sample to unload any inertial confinement and result in a state of uniaxial stress (a

[4]The actual strain rate was approximately $7x10^{-5}$ s^{-1}. The difference is due to the stiffness of the machine. However, this slight difference in strain rate is not believed to be significant.

condition necessary for valid split Hopkinson bar results) when failure occurs. This same argument has been used by Anderson et al [9] to verify a state of uniaxial stress. They also obtained computer simulations which verified this result.

A ceramic, which generally shows little plastic deformation before failure, will typically fracture during the rise portion of the incident wave in the Hopkinson bar [1],[9]. However, the rise time of the strain signal in Figure 9 approaches the rise time of the pulse in the incident bar shown in Figure 11. If the rise times are nearly the same, the sample may not fracture during the rise but instead at or after the peak of the incident pulse. This was unexpected and may indicate that the fracture strengths thus obtained are underestimated. More analysis is needed to verify this.

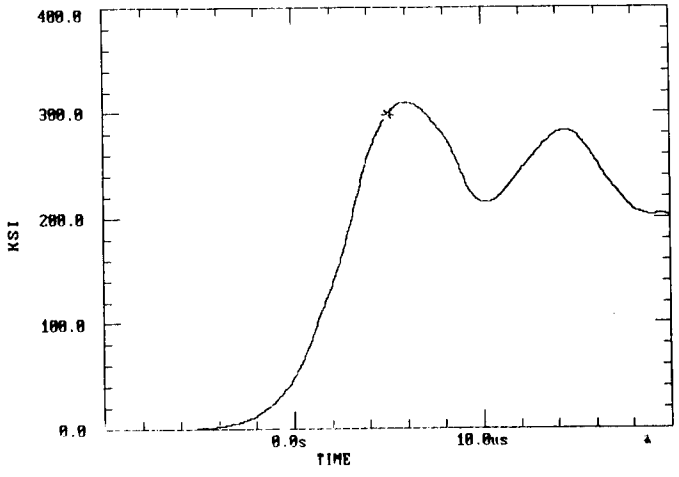

Figure 11. Stress wave off of incident bar.

There is an appreciable difference between the compressive strengths of the JS-I and JS-II alumina. This is not surprising since JS-I has a finer grain size and higher density. However, an interesting observation from Figure 8 is that the slope of the line through the JS-I and JS-II data from 10^{-4} to $10^{0}s^{-1}$ strain rates are approximately parallel, but then deviate beyond $10^{0}s^{-1}$ strain rate. Since the main difference between JS-I and JS-II is grain size one would have expected a similar strain rate dependence. Although more data is needed on JS-II at the lower strain rates, it is the authors belief that the fracture strength of JS-I at $10^{3}s^{-1}$ may be due to anvil failure and thus underestimated. In this regard when the anvil material was changed from AD999 to WC there was a significant increase in the strength of the JS-I material. A similar rise occurred with the Ceraver at 10^{3} s^{-1} when AD999 anvils were substituted with WC anvils.

Figures 12 and 13 show the fracture surfaces recovered from JS-I and JS-II samples loaded in compression. In comparing these fracture surfaces it can be seen that they are distinct. JS-I has a mixture of both intergranular and transgranular fracture whereas JS-II is dominated by transgranular failure. However, the analysis of the fracture surfaces indicated that no transition from one dominant type of fracture to another occurred with strain rate. The lower density and coarser grain size of the JS-II material had a significant effect on both its strength and fracture behavior. The increased porosity of JS-II due to bloating was distributed mainly along grain boundaries. One might have expected cracks to propagate along grain boundaries because of these additional voids. This does not appear to be the case.

The Ceraver and Lucalox do not show the same rate dependence as JS-I and JS-II. This may be due to a combination of factors including flaw and grain sizes as well as nonequiaxed grains and purity. Figure 8 suggests that the Ceraver is much more rate dependent than the Lucalox at the high strain rates. This is difficult to explain based on microstructural differences alone, but it may change if the Lucalox was tested using WC anvils and sample mounted strain gages.

Despite some of the uncertainties in the Hopkinson bar results, the compressive strengths of the MTU JS-I alumina is impressive. The fact that such high strengths can be achieved with a polycrystal alumina demonstrates the importance of purity level and control of the microstructure in order to obtain the true material properties of a ceramic such as alumina.

Acknowledgements: This research was supported by Alliant Techsystems Inc. (formerly Honeywell), ALCOA Foundation and the College of Engineering of Michigan Technological University.

REFERENCES

[1] J. Lankford, J. Material Science, 12 (1977) 791.

[2] D. E. Munson and R. J. Lawrence, J. Appl. Phys., v50, n10 (1979) 6272.

[3] R. L. Cable and N. M. Parikh, Fracture, An Advanced Treatise, edited by H. L. Liebowitz (Academic, New York, 1972), Vol VIII, p. 243.

[4] J. A. Brusso, D. E. Mikkola, J. E. Flinn, and P. V. Kelsey, Scripta Met., v22, (1988), 47.

[5] M. I. Mendelson, J. Am. Cer. Soc., v52, n8, (1969), 443.

[6] S. J. Bennison and M. P. Harmer, J. Am. Cer. Soc., v68, n11, (1985), 591.

[7] J. A. Derkacy, ALCOA Technical Center, private communication, (1988).
[8] W. P. Rogers and S. Nemat-Nasser, presented at 91st Annual Meeting of American Ceramic Society, Indianapolis, IN, paper No. 139-B-89, (1989).
[9] C. E. Anderson, Jr., P. E. O'Donoghue, J. Lankford, and J. D. Walker, to be published in Int. J. of Fracture.
[10] Material properties brochure, Coors Ceramics Co., Golden, CO.

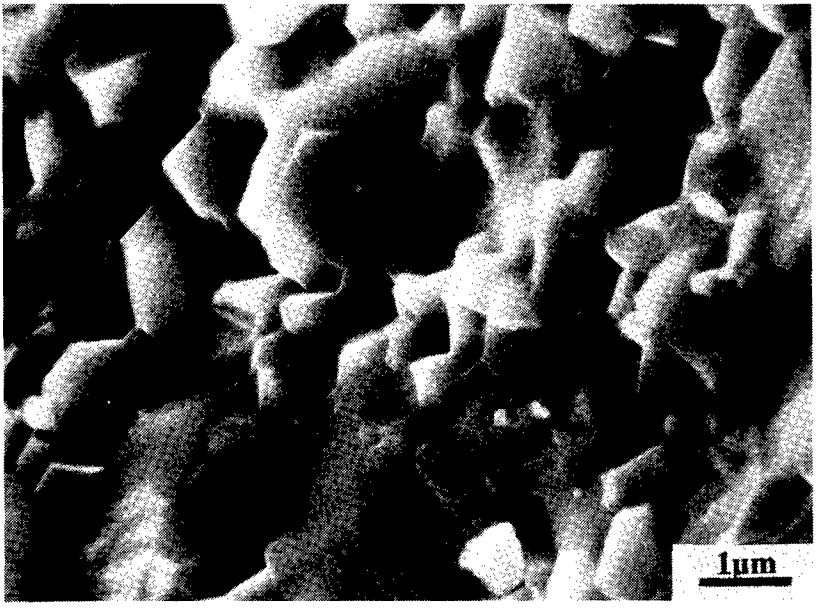

Figure 12. SEM micrograph of JS-I fracture surface.

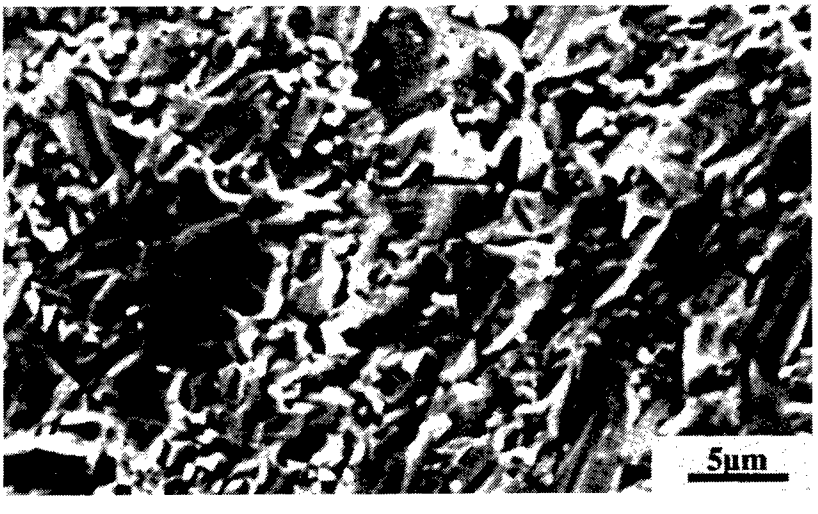

Figure 13. SEM micrograph of JS-II fracture surface.

NONLINEAR DYNAMIC RESPONSE ANALYSIS OF COMMUNICATION SHELTER SUBJECTED TO BLAST LOADS

Luka Serdar Jr.
and
Raffi Yeghiayan
KAMAN SCIENCES CORPORATION
Burlington, MA

and

Ellice Patnaik
HARRY DIAMOND LABORATORIES,
Adelphi, MD

ABSTRACT

A new conceptual design was developed to enhance the hardness of a 7 psi hardened shelter to a 10 psi performance level. The design consists of low cost, low weight, and easy to install/remove structural enhancement devices (SED) that strengthen the structural capability of the shelter with the use of diagonal truss members without significantly reducing the useful interior volume. To validate the design concept, a nonlinear dynamic structural response analysis of the shelter subjected to blast loading was performed using the finite element method. After the analysis predicted adequate response, the shelter was tested at the Gramat shock tube test facility shown in Figure 1. The shelter/truck test setup within the shock tube is shown in Figure 2.

Once the new conceptual design was established, finite element (ADINA) models were developed and nonlinear dynamic structural response analyses were performed. Shelter 3-D models of the sidewall and endwall orientations respectively were then developed. Based on the calculated response predictions, the design was recycled and the models updated. The final set of analytical computer runs predicted the successful performance of the shelter with the installed structural enhancements. The predicted response data included accelerations, velocities, and displacements, internal loads, stresses and strains for the entire shelter as a function of time. These data sets, one for sidewall blast and one for endwall blast orientation, also served to develop the test instrumentation plan. Accelerometers, strain gages and displacement "break sticks" locations and response ranges were developed from post-processing the ADINA time history output for specific locations and global direction of interest.

INTRODUCTION

Kaman AviDyne has previously performed numerous finite element dynamic analyses of shelters subjected to blast loadings as described in References 1 and 2. Based on this experience it was expected that shelter wall-panel deflections would approach or even exceed the sandwich thickness and therefore, as expected, a large deflection or geometrically nonlinear analysis was required. The finite element code ADINA (Reference 3) was chosen for the analysis due to the fact that a baseline ADINA shelter model was already developed and verified by Kaman AviDyne in a previous shelter design and analysis program (Reference 1).

The I-shelter is a nuclear (blast/thermal/fragment) hardened, field shelter designed for transport by military transport vehicles. The shelter is 138. in. long, 81.5 in. wide, and 77. in. high. The walls, roof, and floor are single multilayered composite panels consisting of a 0.063 in. thick inner and outer aluminum skins sandwiching a light urethane foam core of 2.5 in. thickness. A 0.05 in. thick Kevlar applique bonded to the outer aluminum skin provides both fragmentation and nuclear thermal pulse protection. Glass fiber reinforced plastic (FRP) box stiffeners with 3.0 x 2.5 in. cross section of 0.14 in. thickness, unidirectionally spaced at 22.0 in., provide shear carrying support within each panel. FRP channels of 0.10 in. thickness provide stiffness at panel edges. Aluminum joint doublers/stiffeners of 0.05 in. thickness and edge covers of 0.10 in. thickness, are used together with FRP edge caps to form the panel joint assembly. A 0.020 in. thick layer coating of Chartek gives edge covers nuclear/thermal protection, while four types of adhesives bond the respective shelter components. The entire shelter is supported on three elastic skids and secured to a truck's cargo bed with four steel cables running from the lifting eyes located at the upper shelter corners to the cargo-bed side wall. Detailed drawings of the shelter components as well as a complete description of the structure may be found in References 1 and 4.

ANALYSIS

The ADINA analysis involved a full detailed 3-D model of the entire shelter. An existing baseline model (Reference 1) of the sidewall encounter was updated to include the SEDs as shown in Figure 3. They were represented with 2 node beam elements. It should be noted that when the baseline shelter model was developed (Reference 1) a major simplifying assumption was necessary to keep the model size within

acceptable bounds. A vertical plane of symmetry was assumed dividing the shelter into front and rear halves. This allowed for modeling one half of the shelter, but excluded modeling the air conditioners and door, which are asymmetrical features. Since the enhanced shelter was to be tested for door-end wall shock encounter, response predictions for this orientation were also of interest in this test program. A new 3-D shelter model was developed for this case. A vertical plane of symmetry was also assumed and it divided the shelter into roadside and curbside halves. In this model the entry/exit door and framing was modeled explicitly. Three SEDs were again represented with 2 node beam elements (see Figure 4). The shelter walls were represented with 3D sandwich elements and edge members with 3D solid elements.

Thus final dynamic shelter response predictions were determined by performing ADINA runs with two separate 3-D shelter models; one for curbside/roadside blast encounter (see Figure 5) and one for door-end orientation (see Figure 6). The sidewall blast model consisted of 906 nodes and 47 pressure load functions. The newly developed door-end blast model had 1938 nodes and 76 pressure load functions.

The full I-shelter (with SEDs) finite element analyses were performed for blast loads. Pressure loading was applied to all external element surfaces in the 3-D ADINA I-shelter model, except on the floor, which was shielded from the blast by the truck cargo-bed and support skids. Each external sandwich element loading was input as a uniformly loaded shell surface pressure and each external 2-D element loading was input as a uniformly loaded 3-D surface pressure. A pressure time-history representing the instantaneous average pressure was input for each pressure surface. For the blast-side wall and leeward side wall the pressure at the centroidal of the element was used. For the roof and side walls parallel to the blast, the centroidal pressure was adjusted for the engulfment of the shock from the leading edge to the trailing edge. This was accomplished by giving the pressure time history a finite rise time.

An analytical approach was used to define the 10 psi nuclear blast pressure loading for the I-shelter. Predictions were obtained using the BLOCK code. BLOCK is a digital computer program developed by Kaman AviDyne for calculating the blast loading on box like structures (Reference 5). The program computes the overpressures due to a shock wave traveling parallel to the ground and impinging on a closed, rectangular parallelepiped from any angle. Both the

diffractive and drag phrases of the loading are predicted on the surfaces of the structure.

The standard 60 W? HOB, sea level model was selected using a 100-KT nuclear yield. The range was specified such that 10.0 psi peak incident overpressure resulted. A total of 76 pressure load time histories were generated for the various loading surfaces on the shelter model for the endwall blast direction. For the sidewall blast orientation 47 pressure load time histories were generated. In the ADINA input, each curve is represented by multiple linear segments derived using a process of curve fitting the generally smooth pressure histories produced by BLOCK.

The nonlinear dynamic, elastic-plastic response of the I-shelter was calculated using the two half models subjected to the aerodynamic loadings as described above. Each model represented a symmetric half of the shelter with the vertical plane of symmetry at shelter centerline and parallel to the blast direction. This final design verification analysis involved calculating the model displacements with time using more than 2,500 equations of equilibrium. To obtain a solution for this large set of coupled nonlinear equations, the Newmark beta numerical integration procedure was selected. The analysis was carried out to 12 milliseconds with a time step of 0.10 milliseconds. Solving the equilibrium equations at each time increment (ΔT) requires that the mass and stiffness matrices be formed, and then inverted. With nonlinear response, the stiffness matrix changes with every time step, and frequent stiffness reformations are necessary. The stiffness matrix updating was specified to be performed at every solution time step ($t + \Delta t$).

A consistent mass matrix formulation was used for the dynamic response calculations. This mass matrix is calculated by using the same special interpolation functions for velocity and acceleration as for displacements. Consequently, the mass matrix, stiffness matrix, and applied loads are consistent with each other.

The BFGS (Broyden-Fletcher-Goldfarb-Shanno) matrix updating method was used to restore equilibrium to the solution at every step ($t + ?t$). Based on Kaman AviDyne's past experience, this iterative procedure is considered best in ADINA because of its excellent convergence characteristics.

TEST/ANALYSIS RESULTS

The ADINA computed peak deformed shapes for the sidewall blast and the endwall blast orientations are shown in Figures 7 and 8. The voluminous output data contained the predicted accelerations, velocities, and displacements, internal loads, stresses and strains for the entire shelter as a function of time. During the shock tube test more than forty channels of response data were collected. Still photography and real time video were also taken. Time history measurements of strains and accelerations at selected locations were recorded. Displacement measurements were obtained by so-called break sticks. These thin balsa wood sticks were attached to the internal electronic racks pointing toward sidewalls and roof at locations of interest.

A complete correlation study was performed on the sidewall and endwall blast test and analysis results (see Reference 6). Several key comparisons are included in this discussion to show the levels of response measured as compared to the analytical predictions.

The displacement response test data was obtained with the break stick system as described above. This meant that only maximum displacements were known with no information available on the time response. Thus, when comparing the analysis displacement time history to test results, only the peak displacement response may be checked. The sidewall blast displacements for the blast sidewall at about 1/3 horizontal span and half way up vertically compared to test peak level is shown in Figure 9. There is good agreement in the magnitude of displacements, not only on the blast sidewall, but on the roof and the leeward sidewall as well. Figure 10 shows a similar comparison for the endwall blast orientation. This time the location is on the blast endwall 2/3 up and next to the centered door frame. Excellent displacement response agreement was found also on other shelter walls for this test.

Strain time history data was collected at selected points for which finite element locations were coincident and which described the structural response of the shelter. A typical blast sidewall strain in the inner skin of the sandwich is shown in Figure 11. The strain time history correlation was generally good at center regions of the walls and roof. A somewhat worse correlation was found at locations near edges of walls where the disparity was typically on the order of 50%. This was mostly due to the mechanical joints between walls which were not explicity modeled. Figure 12 shows the strain results for the endwall blast case. In this case the strains

are not in excellent agreement due to the endwall doorway and its framing/gasket connections. The effects of this local hardware were not modeled explicitly and thus only an approximate endwall stress/strain distribution was predicted. Other sidewalls and the roof showed a much better correlation as in the sidewall blast case.

Numerous accelerometers were installed in both tests. Figure 13 shows a very typical excellent agreement between the finite element prediction and the test data for a location on the blast sidewall. The blast endwall comparison is presented in Figure 14. In both tests the acceleration correlation was excellent at all locations except for points on the endwall near the door. This was again primarily due to the approximations used in the modeling of this localized region.

The ADINA finite element analysis predicted a satisfactory performance of the shelter when subjected to the specified blast wave. The tests results confirmed this and also verified the predicted response levels throughout the shelter structure.

REFERENCES

1. R. Bartelmann, "I-Shelter ADINA Structural Analysis", Kaman AviDyne, July 1986, HDL-CR-86-057-1.

2. G. Zartarian, R.P. Yeghiayan, A.M. Lush, "Nuclear Blast Simulation Tests on HATS Type A Shelters in Event MILL RACE and in the CEG Shock Tube-Response Results and Correlation with Analysis", Kaman AviDyne, December 1985, HDL-CR-85-013-1.

3. K.J. Bathe, "ADINA, A Finite Element Program for Automatic Dynamic Incremental Nonlinear Analysis", Report AE81-1, ADINA Engineering, September 1981.

4. I-Shelter Development Specification HD-(D)-S-0032, 1 November 1984.

5. W.N. Lee, and G. Zartarian, "BLOCK - A Digital Computer Program for Calculating the Blast Loading on Box-Like Structures", Kaman AviDyne, Technical Report KA TR-156, January 1979, Unpublished.

6. R.P. Yeghiayan, L. Serdar, D.C. Coyne, "Design and Analysis of Structural Enhancement Devices (SED) for the I-Shelter, Enhanced (ISE) Configuration," Kaman AviDyne, Technical Report KA TR-300, May 1991.

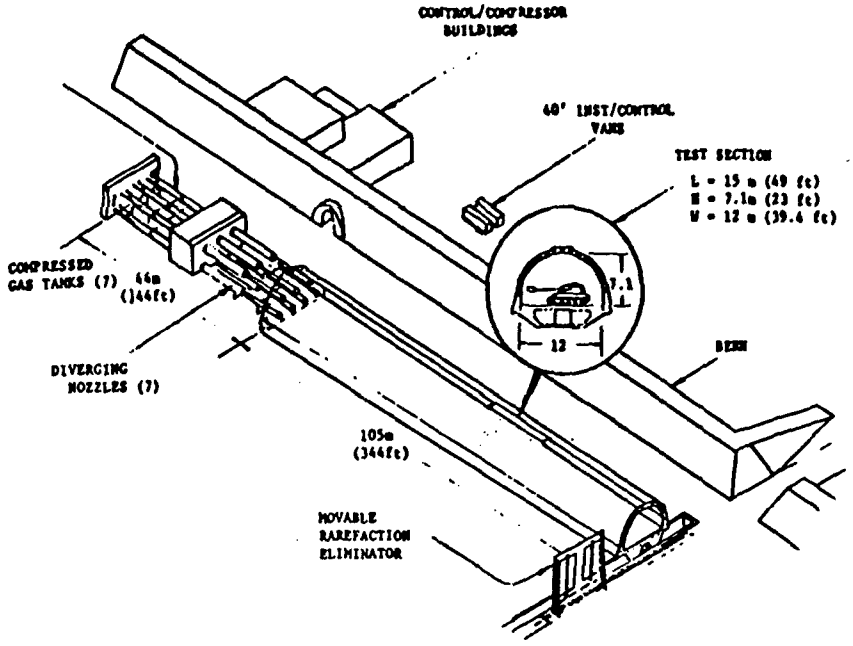

Figure 1. Centre d'Etudes de Gramat (CEG) shock tube facility.

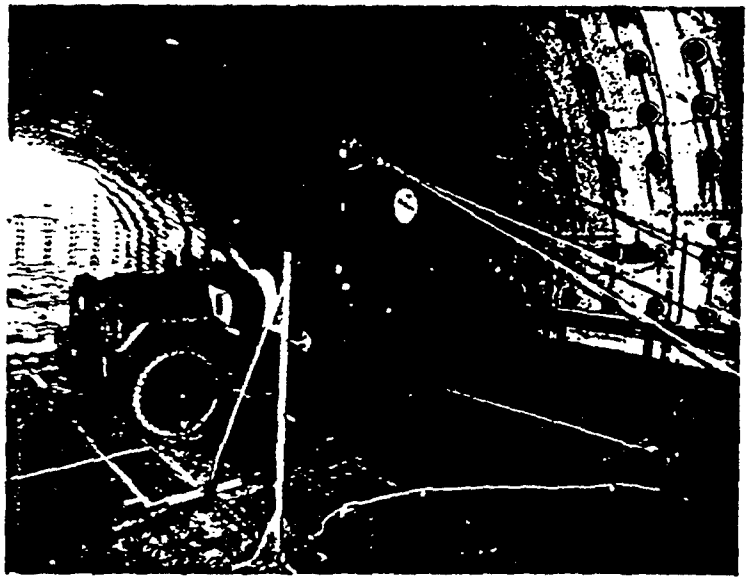

Figure 2. A4 shelter in CEG shock tube, positioned before experiment CEG-2.

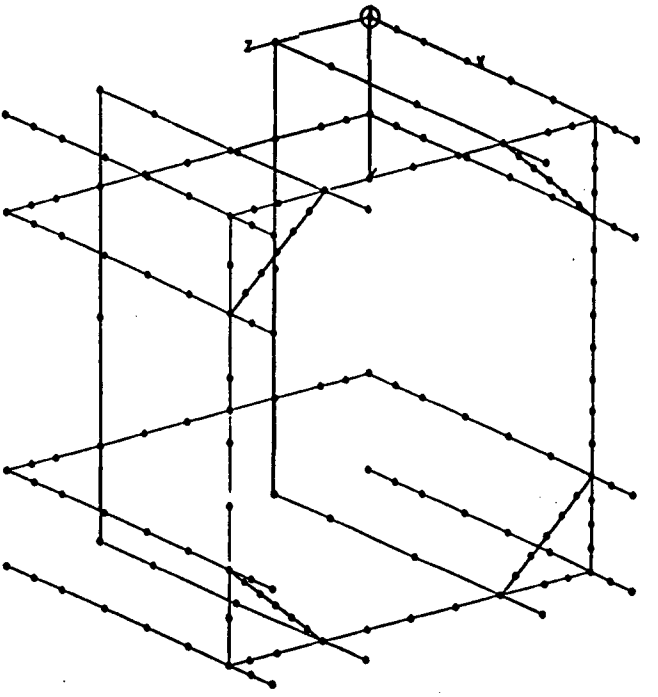

Figure 3. SEDs side wall blast model.

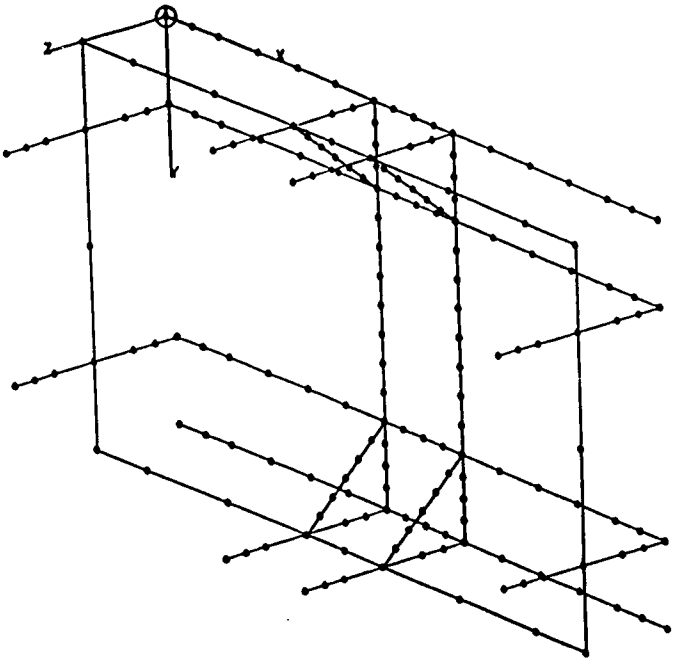

Figure 4. SEDs end wall blast model.

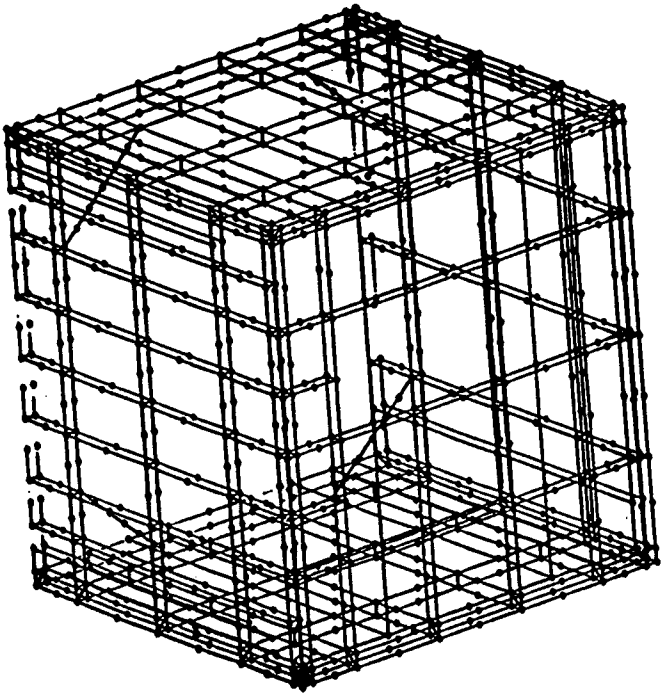

Figure 5. Side wall blast model.

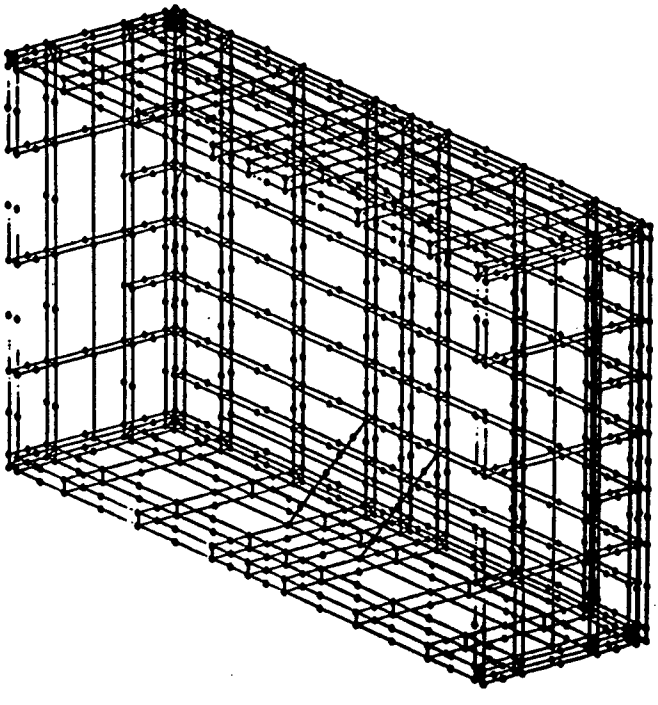

Figure 6. End wall blast model.

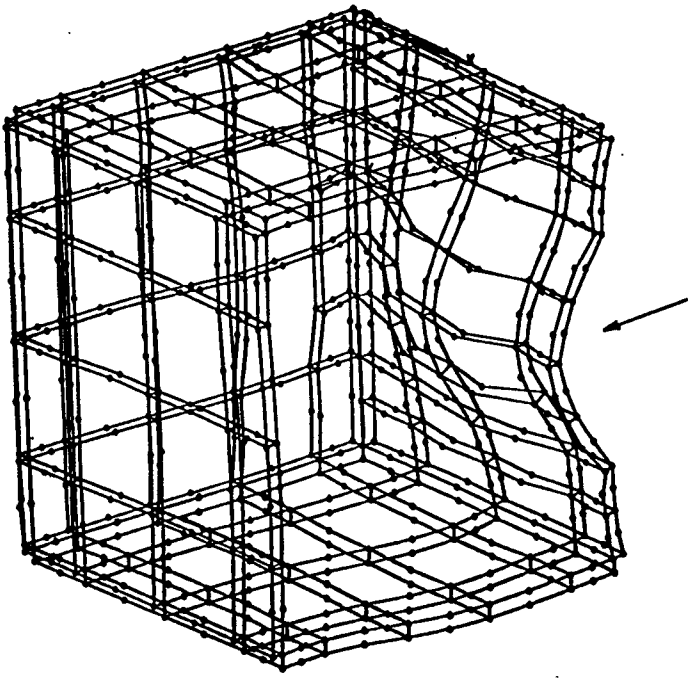

Figure 7. Side wall blast at 10 psi T = 4.1 msec MAG = 10.

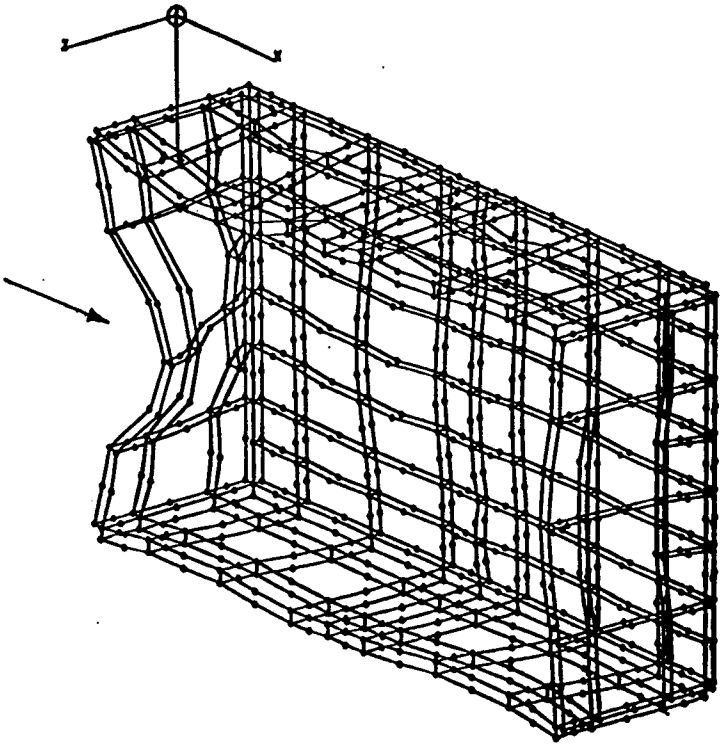

Figure 8. End wall blast at 10 psi T = 6.7 msec.

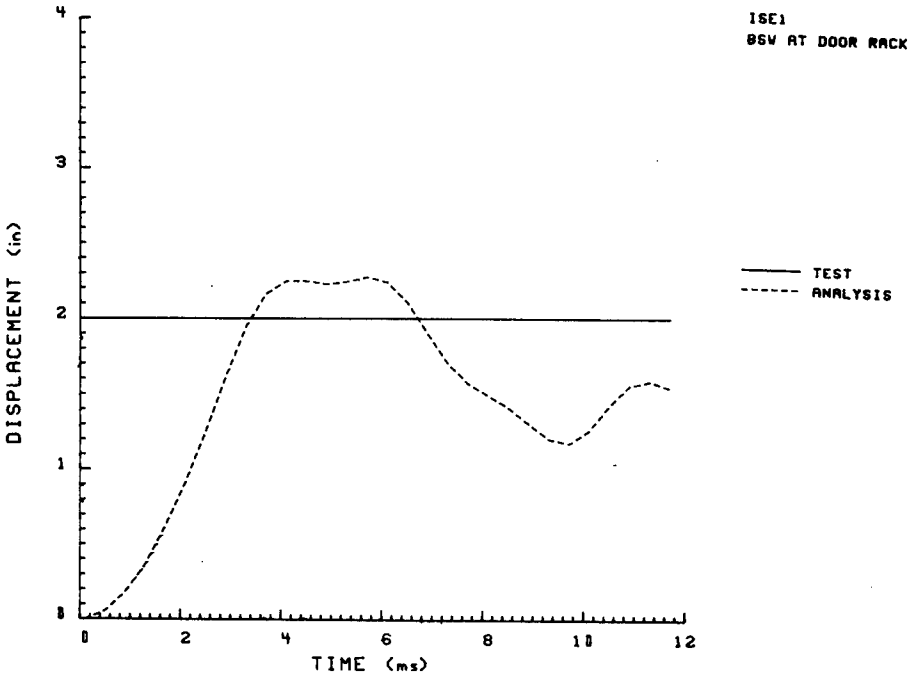

Figure 9. Blast sidewall displacement.

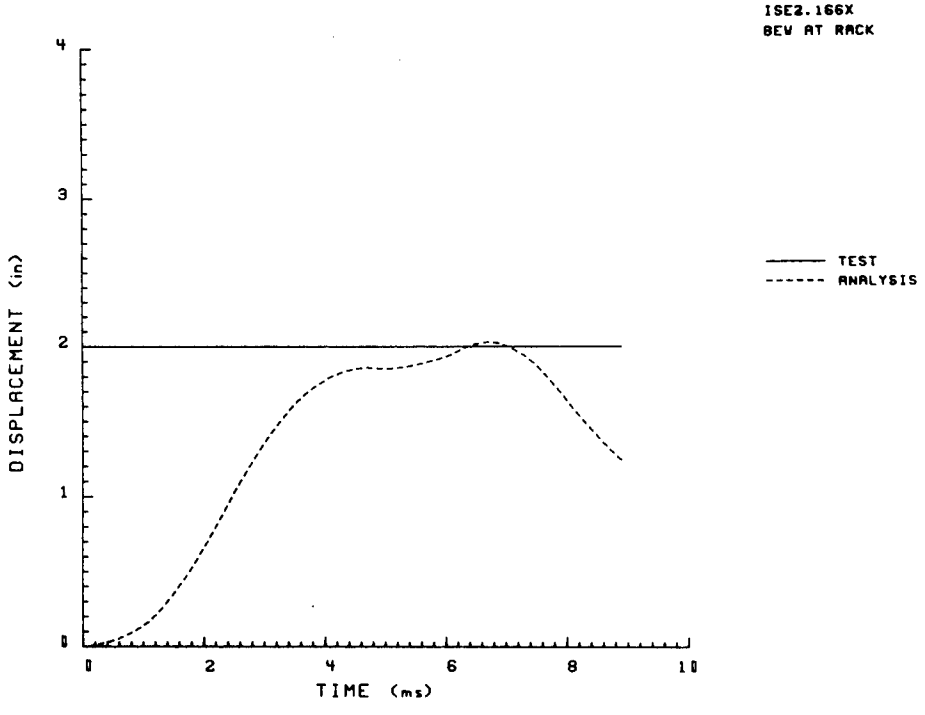

Figure 10. Blast endwall displacement.

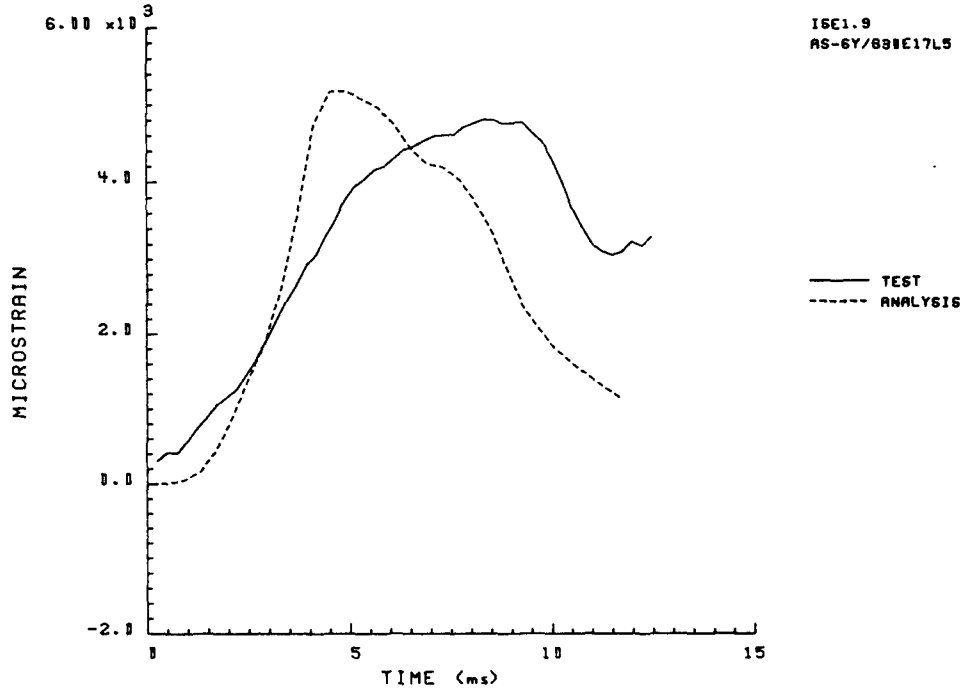

Figure 11. Blast sidewall sandwich skin strain.

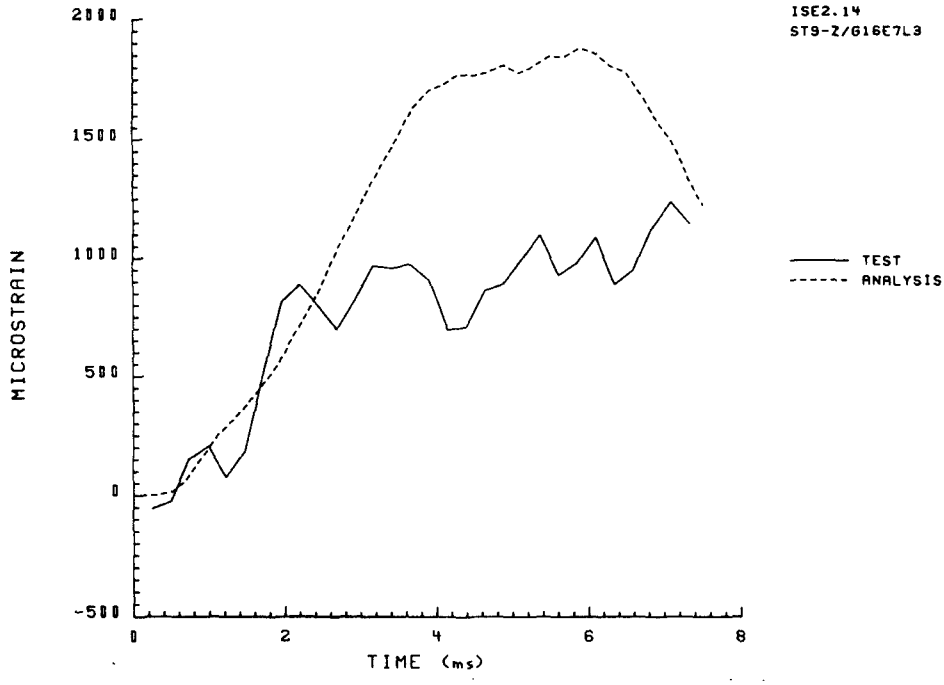

Figure 12. Blast endwall sandwich skin strain.

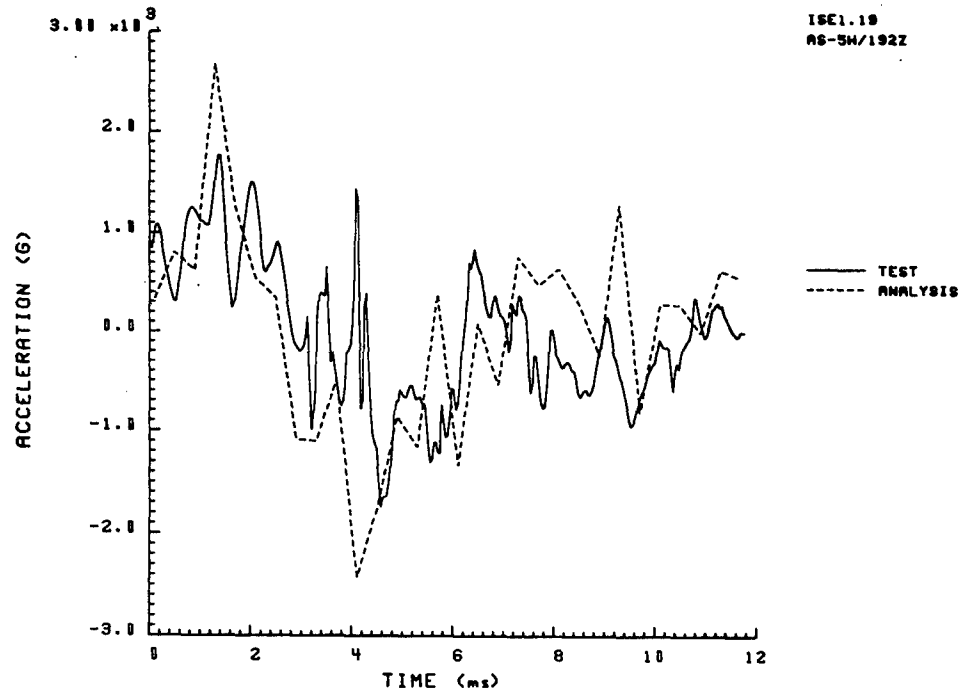

Figure 13. Blast sidewall acceleration.

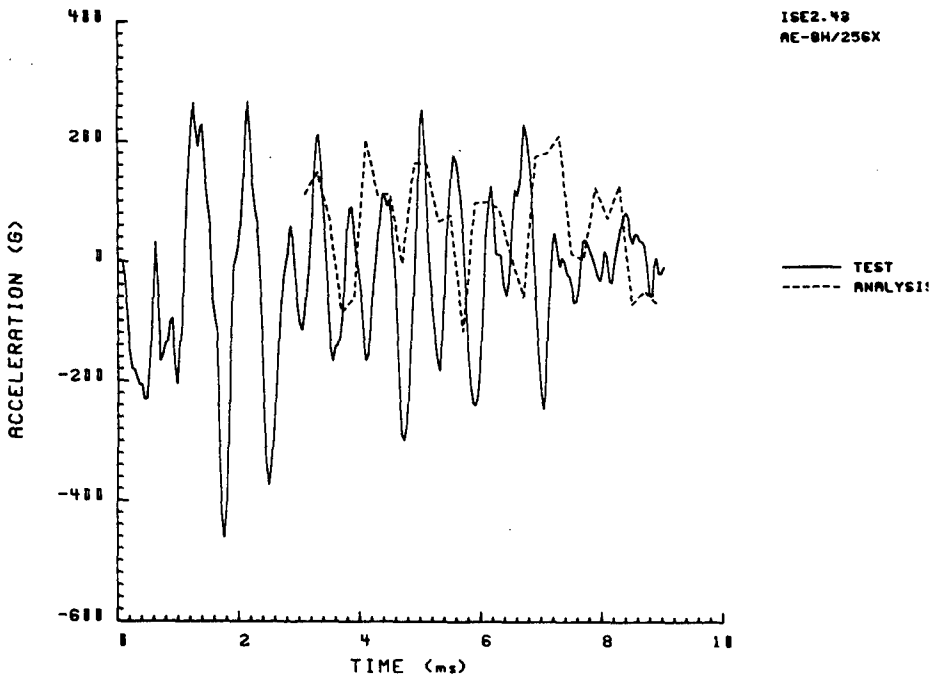

Figure 14. Blast endwall acceleration.

STRUCTURAL ANALYSIS OF PERSHING 1A OVERPACK SHIPPING CONTAINER

David L. Gray

Kaman Sciences Corporation
Colorado Springs, Colorado 80907

INTRODUCTION

The Pershing 1A (P1A) overpack shipping container was designed in 1990 as a low cost, easily produced container for transporting the Pershing 1A nuclear warhead. It was a design modification of the H838 hand truck intended to provide improved protection to the warhead payload. Recently, much attention has been given to the safety of nuclear munitions transportation and the design requirements have become much more stringent. As a result, the overpack design has been revisited to make some simple modifications to the existing design in an effort to meet these more stringent requirements.

The design requirements for the present work involve a crash scenario from an airplane or helicopter crash. Although the likelihood of such an event ever occurring is very small, the potential hazard of radioactive contamination is sufficient to warrant a rigorous analysis of the ability of the shipping container to withstand the severe loading environment of an airplane or helicopter accident. In addition to the energy of the crash itself, the container must be able to withstand an engulfing fuel fire for a certain length of time, presumably until fire fighting equipment could reach the crash scene to extinguish the fire.

A nominal design requirement of 90 ft/sec end-on impact followed by a 45 minute fuel fire was originally proposed by the Project Manager for nuclear munitions (PM/NUC) - United States Army. The current design goal is a 150 ft/sec end-on impact followed by a 60 minute fuel fire. The synergism between the two environments (impact and fire) is of critical importance. Also of concern is the possibility of an edge impact.

The P1A overpack shipping container is shown in Figure 1. It consists of a warhead payload surrounded by foam inside an aluminum container (H838 hand truck with wheels cut off). The inner aluminum container is surrounded by additional foam which is covered by 3/4 inch plywood. For thermal reasons, it is important that the inner container maintain its structural integrity to provide a

thermal barrier to heat. It is also necessary that the outer (plywood) container remain basically intact since the outer foam provides thermal protection to the payload, as well.

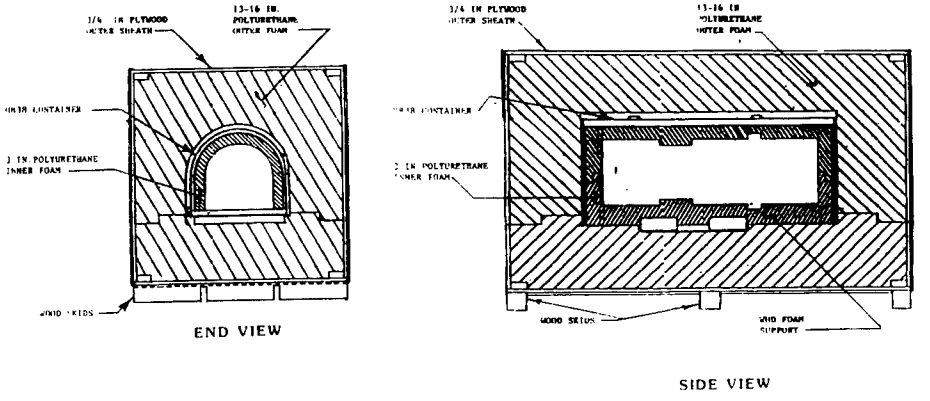

FIGURE 1. PERSHING 1A OVERPACK SHIPPING CONTAINER

DISCUSSION

In keeping with the original design requirement, a full scale end-on drop test was conducted at Sandia National Laboratory in August of 1990. The velocity at impact onto a concrete pad was 96 ft/sec. The inner container ruptured at the impact end due to the excursion of the warhead inside the container. Figure 2 shows the damage to the end of the inner container. As can be seen the end plate ruptured approximately 270 degrees around but did not completely perforate. It would appear that a threshold energy level was achieved in that the container tore but did not fully perforate. Nevertheless, sufficient damage did occur to raise doubts about the containers ability to withstand a fuel fire after impact with the inner container structural integrity compromised.

A finite element analysis has been done using ABAQUS [1] to correlate the results of the full scale drop test using an axisymmetric model. Figure 3a shows the initial model that was used. Axisymmetry was employed to minimize computer cost and because the response of the structure appears to have been reasonably axisymmetric, even though the container itself is not. ABAQUS was chosen for its ability to do nonlinear large deformation plasticity calculations and for its ability to model crushable foam materials.

The inner container is made of 5083-H113 aluminum and is 0.060 inches thick. The foam was modeled as General Plastics FR-

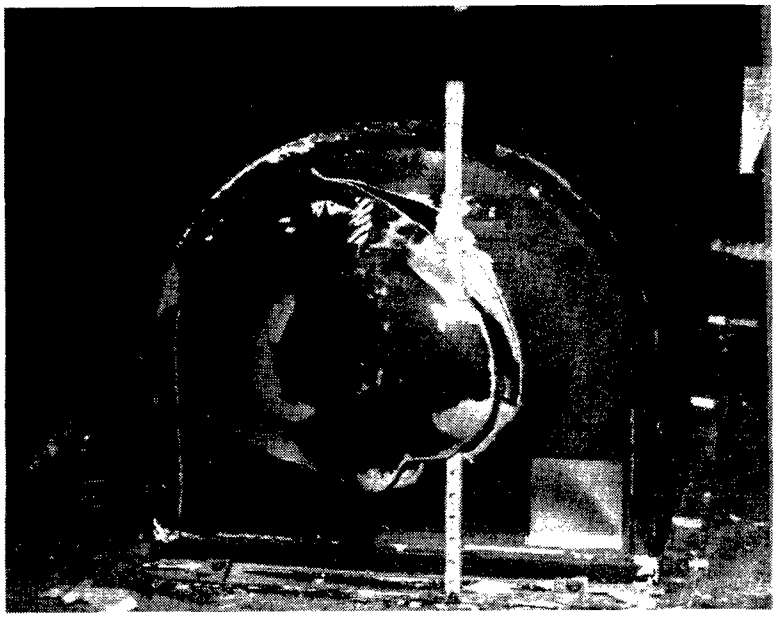

FIGURE 2. POST TEST DAMAGE OF INNER CONTAINER

3710 crushable polyurethane foam. The payload was modeled as a mass and frontal area mockup of the actual warhead. No attempt was made to simulate the response of the warhead itself. The material properties that were used are shown in Table 1.

The ABAQUS *FOAM [2] model was not suitable for the foam in this analysis. The *FOAM model requires a monotonic increase in the stress-strain curve whereas the actual stress-strain curve for the General Plastics foam is not monotonic. Figure 4 shows the actual stress-strain curve compared to three *FOAM calibration curves forced to match at 60 percent, 70 percent and 80 percent strain. As can be seen none of the *FOAM curves accurately represent the real foam. As a result, an elastic-plastic material was used for the foam material model with the actual stress-strain data as input. The disadvantage in doing this is that the model will not simulate the crushing behavior of the real foam. Rather than remaining crushed, as with the real foam, the elastic-plastic model will come back down the stress-strain curve and restore energy to the system. This problem can be overlooked as long as the material remains in compression. The analysis in the present work is considered to be complete when the warhead has bottomed out, and up until then the foam material in front of the warhead has been under compression the entire time. Therefore, it is believed that the

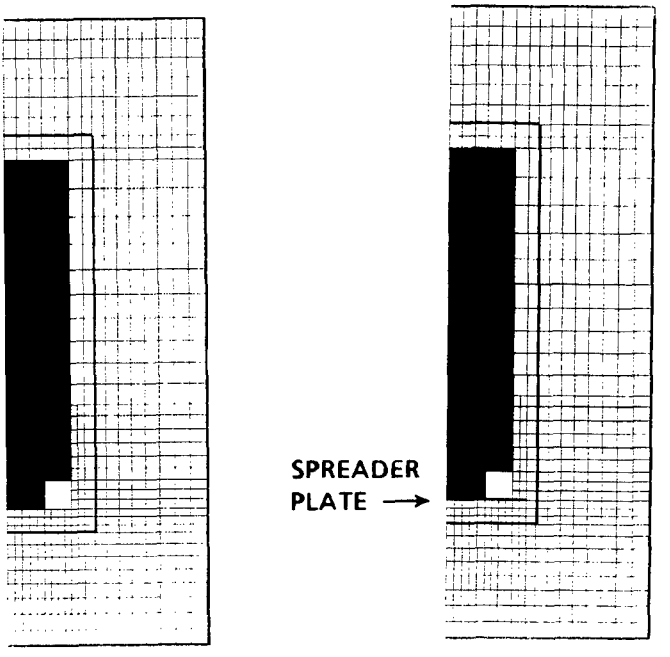

FIGURE 3. ABAQUS AXISYMMETRIC FINITE ELEMENT MODEL

TABLE 1. MATERIAL PROPERTIES

Material	Young's Modulus (psi)	Poisson's Ratio	Density (lb/in^3)	Yield Strength (psi)	Tensile Strength (psi)	Failure Strain (in/in)
5083-H113 Al	10.3E + 06	0.331	0.098	33.0E + 03	46.0E + 03	0.160
1020 St	30.0E + 06	0.300	0.283	30.0E + 03	55.0E + 03	0.250
G. P. Foam	10.8E + 03	0.000	0.00579 (10.0 pcf)	532.0		
Payload	30.0E + 06	0.300	0.04442			
3/4 Plywood	1.6E + 06	0.100	0.01534 (25.5 pcf)			

model yields accurate results and can be used for an end-on impact analysis.

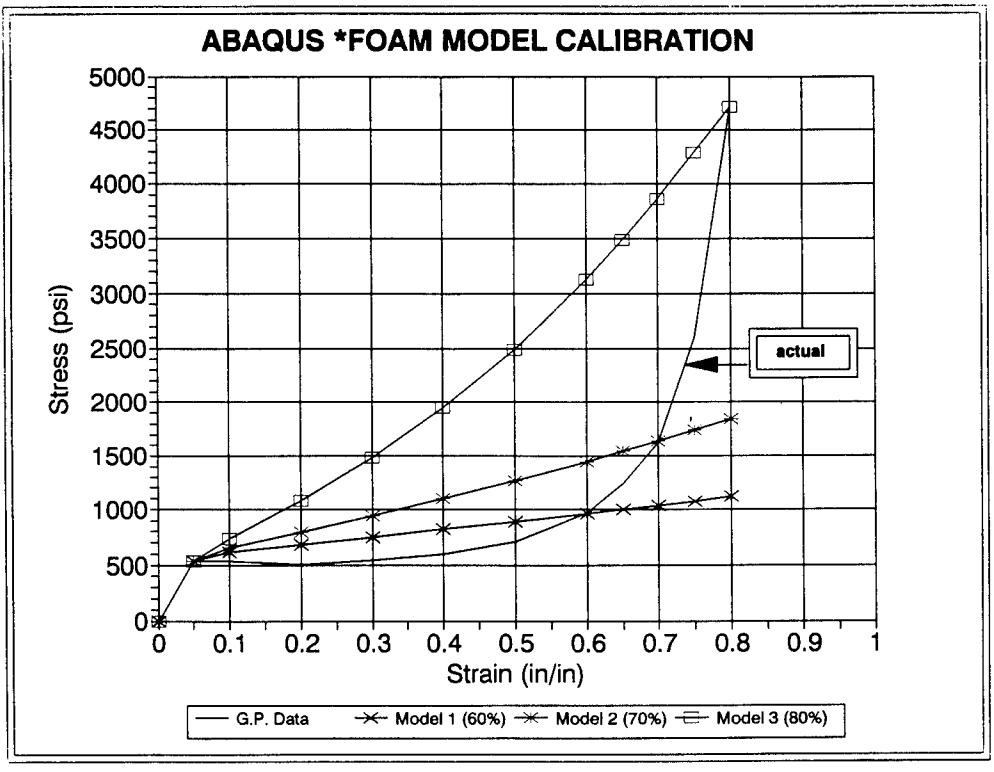

FIGURE 4. GP FOAM (FR-3710) STRESS-STRAIN CURVE

Excellent correlation with the full scale drop test was achieved in the analysis with an end-on impact velocity of 96 ft/sec. The ABAQUS finite element model accurately predicted the failure location (radially) of the aluminum container and the overall deformation of the inner and outer containers. The payload traveled approximately 5.0 inches and bottomed out at approximately 7.0 milliseconds after impact. Figure 5a shows the overall deformed geometry of the shipping container. As can be seen, the payload has shifted forward significantly and has pushed the end of the inner container forward. Figure 5b shows the deformation and equivalent plastic strain of the inner container after impact. Using a strain to failure of 16.0 percent for the aluminum, it can be seen that the inner container end plate has ruptured. The location of the failure point is at approximately R = 5.6 inches. This corresponds very well to the rupture location shown in Figure 2.

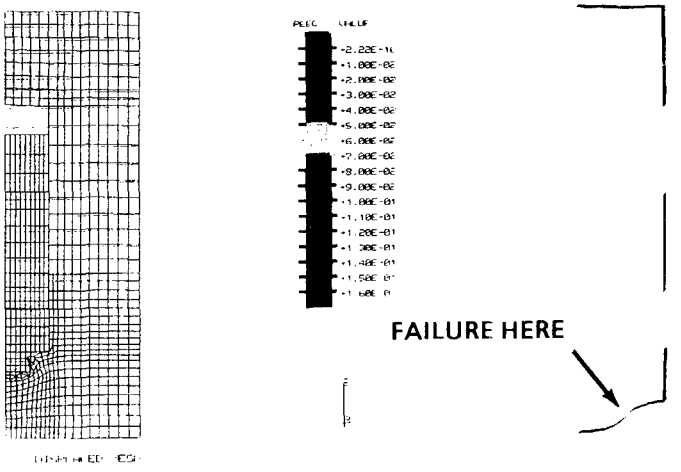

a b

FIGURE 5. ABAQUS DROP TEST CORRELATION RESULTS

In addition to the finite element analysis, a subscale testing program was conducted to give further insight into the failure modes and damage mechanisms of the inner container and to provide a low cost alternative testing method to assess the efficacy of the suggested design modifications at higher velocity impacts.

The Kaman light gas gun facility was used to shoot one-sixth scale models of the inner container with a scale mass simulation payload at the original impact velocity of 96 ft/sec. Figure 6 shows a drawing of the subscale test article. The test article was fired into the outer foam which was backed by concrete and fixed to ground.

The threshold energy level was accurately established with the subscale models. Figure 7 shows a photograph of three test articles fired at 100, 84, and 92 ft/sec. As can be seen, total perforation (punch-out) occurred at 100 ft/sec, no rupturing occurred at 84 ft/sec, and tearing without perforation occurred at 92 ft/sec, approximately 100 degrees around. This result corresponds very well with the full scale drop test as shown in Figure 2.

Having correlated the finite element model and subscale tests with the full scale drop test, the next step was to analyze simple design modifications and their effectiveness at higher velocity impacts. The design modifications must be simple retroactive fits to

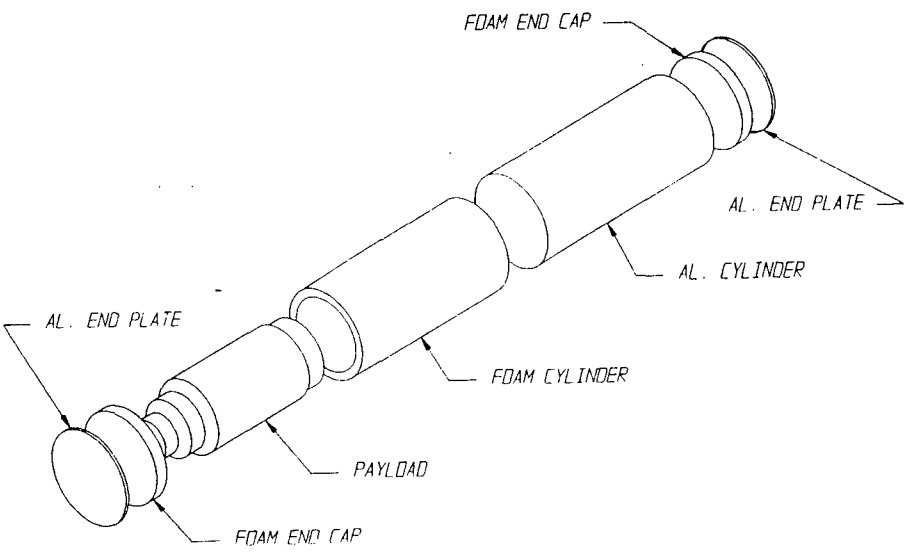

FIGURE 6. SUBSCALE TEST ARTICLE - EXPLODED VIEW

the existing design and weight is a consideration. The two primary design modifications under consideration were:

- Change the inner container from 0.060 inches aluminum to 0.090 inches steel.
- Add a load spreader plate between the ends of the warhead and the inner foam inside the inner container.

The load spreader plate, as the name implies, distributes the load of the warhead out over a larger area and provides additional resistance to warhead excursion by the spreader plate deforming and thus absorbing kinetic energy. Changing the inner container material and thickness will obviously increase its strength and thus provide greater resistance to rupturing.

Figure 3b shows the finite element model that was used to model the spreader plate. The changes of material and thickness of the inner container were also made. The spreader plate material is steel and the thickness varied from 0.250 inches to 0.375 inches. The analysis was done for an end-on impact at 150 ft/sec.

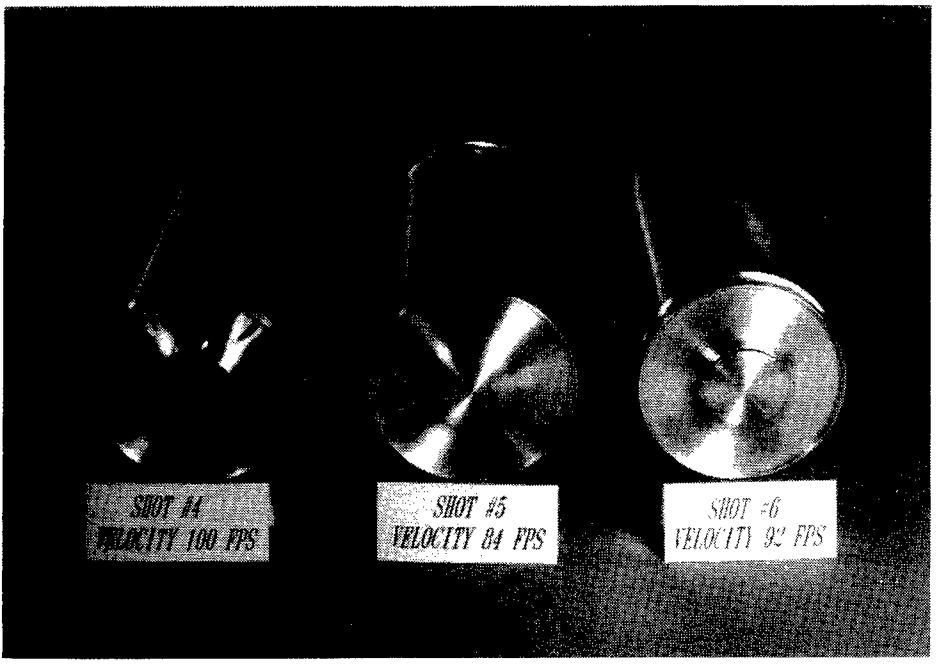

FIGURE 7. SUBSCALE TEST DROP TEST CORRELATION RESULTS

For a spreader plate thickness of 0.250 inches, the payload traveled approximately 7.7 inches and bottomed out at approximately 7.0 milliseconds after impact. Figure 8a shows the overall deformed geometry of the shipping container. Figure 8b shows the deformation and equivalent plastic strain of the inner container end plate and spreader plate. Using a failure criterion of an equivalent plastic strain of 25.0 percent for mild steel, the outer container appears to have failed.

For a spreader plate thickness of 0.375 inches, the payload traveled approximately 7.4 inches and bottomed out at approximately 7.0 milliseconds after impact. Figure 9a shows the overall deformed geometry of the shipping container. Figure 9b shows the deformation and equivalent plastic strain of the inner container end plate and spreader plate. As can be seen, both the spreader plate and inner container end plate equivalent plastic strains are less than 25.0 percent. The maximum strain in the spreader plate is 19.0 percent and the maximum strain in the inner container end plate is 21.0 percent.

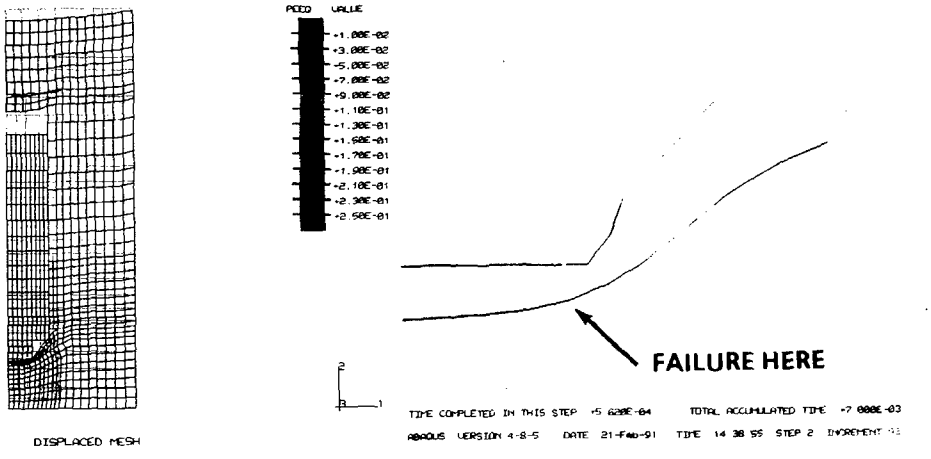

a b

FIGURE 8. ABAQUS PREDICTION ($T_{spreader}$ = 0.250 in)

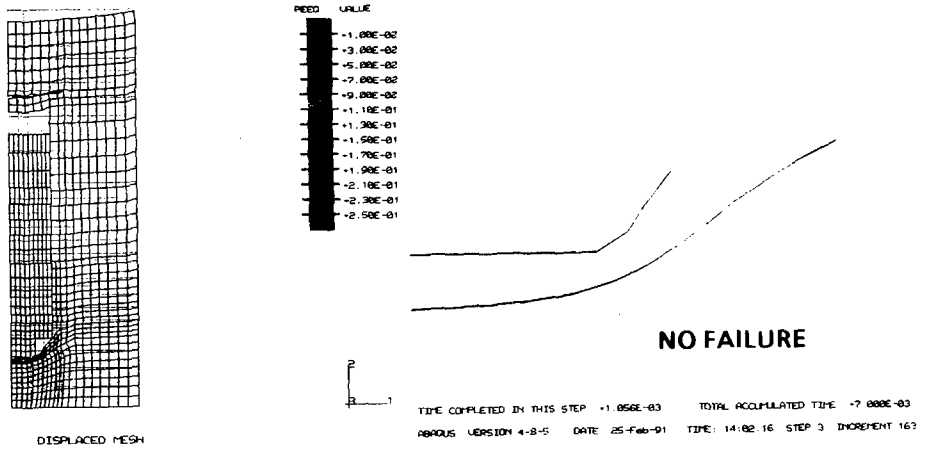

a b

FIGURE 9. ABAQUS PREDICTION ($T_{spreader}$ = 0.375 in)

As a result of this analysis, it is believed that for an end-on impact of 150 ft/sec and with the suggested design modifications (spreader thickness = 0.375 inches), the inner container will

withstand the impact without rupturing. The outer container also remains basically intact for this impact velocity and it is believed that the overpack will meet the current design goal from a structural standpoint.

Some subscale testing was done at the higher velocities with the design modifications. The effect of removing the inner container from the overpack and firing it at the outer foam became an issue at the higher velocities and with the greater mass of the modified inner container design. The boundary condition along the side of the inner container was no longer being properly simulated and as a result the test results were not valid. A new test facility has been proposed and is being built, which will allow larger scale testing of the overpack and inner container as a single projectile.

CONCLUSIONS AND RECOMMENDATIONS

The ABAQUS finite element model accurately predicted the failure location and overall geometry of the inner container for the existing P1A design. The subscale testing also correlated very well with the full scale drop test. The finite element model was then used to determine the design modifications necessary in order to meet the current design goals.

As a result of the structural analysis, it is believed that the following two design modifications will enable the P1A overpack shipping container with a W50 payload to withstand an end-on impact of 150 ft/sec without rupturing the inner container:

- Inner container made of 0.090 inches steel.
- Steel spreader plate (0.375 inches thick) between the W50 payload end and the inner container inner foam.

No effort has been made to date to determine the effect of an edge impact on the response of the modified design. A new vacuum launch test facility currently under development at Kaman Sciences will enable testing of one-fifth scale models (overpack and inner container combined) for both edge as well as end impacts at velocities in the 150 to 200 ft/sec regime. No thermal analysis has been done to date. Testing has been done to determine the ablation rate and thermal conductivity of the actual foam that was used.

ACKNOWLEDGEMENTS

The author acknowledges the support of Messrs. John Wander and Frank Shuler of the Project Managers Office for Nuclear Munitions - United States Army. Credit goes to Mr. Dick Keeffe for

the idea of subscale testing and for overall technical supervision of this work. Special thanks to Messrs. Scott Doane, Ken Newborn and Dave Crosby for their work in conducting the subscale tests and to Messrs. Ted Tetman and Daryl Koldenhoven for their manufacturing support of the subscale tests.

REFERENCES

1. ABAQUS Finite Element Code, Hibbitt, Karlsson & Sorensen, Inc., Providence, RI.
2. ABAQUS *Foam, Foam Plasticity Model, HKS, Inc., Providence, RI.

SESSION III:
FAILURE AND DAMAGE

Session Chairman: *Dr. U. Lindholm*

DYNAMIC RESPONSE AND FAILURE MODES OF CERAMICS AND CERAMIC COMPOSITES

Sia Nemat-Nasser

Center of Excellence for Advanced Materials
Department of Applied Mechanics and Engineering Sciences
University of California, San Diego
La Jolla, California 92093-0411

ABSTRACT

Dynamic response and failure modes of ceramics, ceramic composites, and generally brittle materials under high-velocity impact, involve a complex sequence of microcracking, crack coalescence and fragmentation, pulverization, and subsequent granular flow. A fundamental understanding for physically-based micromechanical modeling which may lead to computational constitutive algorithms with reliable predictive capabilities, requires synergistic basic research to integrate theoretical and experimental mechanics, mathematical analysis in computational modeling, and material characterization.

The dynamic experiments require *recovery* techniques, where specimens are subjected to pre-assigned stress pulse histories and are then *recovered* for microscopic analysis to relate the history of loading to the microstructural evolution. The experiments must be controlled to yield reliable time-resolved data over a broad range of strain rates from quasi-static to greater than 10^6/s. The theoretical modeling must include possible crack initiation under compression during the initial compressive loads, crack interaction and crack coalescence, pulverization, and finally, modeling of flow of pulverized materials in full confinement, which includes nonclassical effects such as friction, dilatancy/densification, and possible melting. The computational algorithm must be accurate, stable, and broad enough to be able to accommodate fracturing, fragmentation, and frictional effects, as well as intense pressure, high temperature, and volumetric changes.

The results of model experiments, mathematical and computational analysis, and dynamic recovery experiments, are used to discuss the micromechanics of compression failure of brittle materials in general, and under high-velocity impact conditions in particular. Attention is focused on the mechanics of microcracking in compression; the influence of confinement on the failure process by microcracking, including brittle-ductile transition; stiffness degradation due to high-density interacting microcracks; the possible mechanics of pulverization in compression; and the flow of confined pulverized materials.

1. INTRODUCTION

Dynamic response and failure modes of ceramics, ceramic composites, and generally brittle materials under high-velocity impact and penetration, involve many events which include initial compression-induced fracturing, fracturing through wave reflection, crack growth and coalescence, and fragmentation and pulverization, leading to complex interaction between an impactor or a projectile and a ceramic target. For a fundamental understanding with the aim of capturing the physics of the process through simple but effective micromechanical models, essential features of each event need to be identified through *recovery* experiments with time-resolved data, involving a broad range of strain rates, from quasi-static to greater than $10^6/s$. This is then followed by quantitative estimates of stiffness degradation by dynamic fracturing; modeling of crack growth, coalescence, and shock-induced metastable states which may result in pulverization; as well as the development of physically-based constitutive relations for rapid granular flow of densely packed (containing essentially no voids) pulverized ceramics and the associated intense boundary layer which may form adjacent to the penetrator. Figure 1.1a is a schematic representation of these processes when a penetrator pierces into a confined ceramic; Viechnicki *et al.* (1991) [1]. Various possible damage regions are identified in this Figure. They include: (1) comminuted and plastically deformed high pressure/shear region; (2) granular flow region of pulverized ceramic involving an intense boundary layer; (3) radial cracks; and (4) crack induced by wave reflection. Figure 1.1b shows damage produced by the impact of a tungsten projectile against a confined alumina sample. Similar results are reported by Shockey *et al.* (1990) [2].

This very complex nonlinear response and failure process may therefore be broken into the following four essential components:

- Initial fracturing and crack growth
- Crack interaction and coalescence: fragmentation

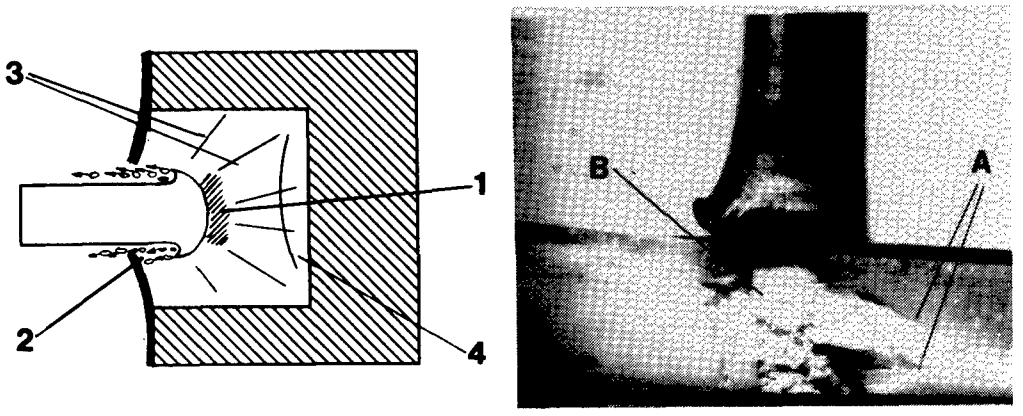

(a) (b)

Figure 1.1a,b (a) Projectile impacting a confined ceramic at high velocity; Viechnicki *et al.* (1991) [1]; and (b) Damage produced by impact of tungsten projectile against confined ceramic target: (A) radial cracks; and (B) comminuted zone (Experiment at UCSD)

- Metastable states: pulverization
- Flow of pulverized (granular) media
- Generation of intense boundary layer adjacent to a penetrator and its effect on the overall response

It is clear that the composition and microstructure of the ceramic or any other brittle material, as well as the configuration, geometry, and component properties of the composite structure, of which the ceramic is a constituent, have profound effects on the sequence of events outlined above. A basic understanding of these processes require synergistic research to integrate theoretical and experimental mechanics, mathematical analysis in computational modeling, and material characterization by microscopy.

This paper reviews some of the recent progress towards addressing the above issues. The necessary recovery experimental techniques are discussed elsewhere[1] and, therefore, will not be detailed in this work; specific results obtained by exploiting these novel experimental techniques, will be used to illustrate microcracking in compression. In Section 2, compression-induced fracturing and brittle-ductile transition phenomena are discussed. In Section 3, a model for estimating stiffness degradation due to closely packed highly interacting

[1] See Rogers and Nemat-Nasser (1990) [3], Nemat-Nasser (1991) [4], Nemat-Nasser *et al.* (1991) [5], and CEAM Facilities Report (1990) [6].

microcracks, is outlined. Section 4 deals with the flow of pulverized granules under confinement.

2. COMPRESSION-INDUCED FRACTURING

Experimentally observed tensile cracking of brittle materials under overall pressures (even hydrostatic pressures) has intrigued scientists and, indeed, led Bridgman (1931) [7] to a number of experiments, whose results came to be known as *Bridgman paradoxes.* These paradoxes involve *tensile cracking of brittle materials under all-around hydrostatic pressure.* Based on the results of these experiments, which seemed to defy intuition, Bridgman concluded (pp. 91-93) [7]:

> "For myself, I am exceedingly skeptical as to whether there is any such thing as a genuine criterion of rupture."

A number of Bridgman's paradoxes were merely hydraulic fracturing (because the hydrostatic pressure was introduced through pressurized fluids), and have since been resolved; see Jaeger and Cook (1963) [8], Scholz *et al.* (1986) [9], and Nemat-Nasser (1989) [10]. Two of Bridgman's paradoxes do not relate to hydraulic fracturing and, in fact, bear directly on the fundamental question of *whether or not tensile cracks are produced -- either quasi-statically or dynamically -- in brittle materials such as ceramics and glasses, under overall compressive loads.*

Here, we briefly explain one of these paradoxes, called *the ring paradox.* The experiment has been recently repeated by Scholz *et al.* (1986) [9], using a pyrex glass tube, tightly fitted on a steel rod with a tolerance better than 3μm; Figure 2.1a. (The tube's thickness is slightly over 1mm, and its length and radius are about 1cm.) The tube is sealed (Figure 2.1b) and the entire construction is enclosed in a rubber jacket (Figure 2.1c), before submerging in the fluid which is then pressurized. By direct measurement, through strain gauges placed on the glass tube and by calculations, it is established that *all three principal stresses everywhere within the glass tube are compressive.* Nevertheless, 2 to 6 axial *tension* cracks are seen to form from the interior surface of the glass tube, growing radially and axially, without reaching the exterior surface.

This paradox has been addressed by Scholz *et al.* (1986) [9] in terms of model calculations of Nemat-Nasser and Horii (1982) [11]. Scholz *et al.* [9] consider a preexisting flaw and estimate the required flaw size to produce tension cracks under the prevailing compressive stress state, using the "sliding crack model" proposed initially by Brace and Bombolakis (1963) [12], and later quantified rigorously, as well as confirmed experimentally, by Nemat-Nasser and Horii (1982) [11]; Figure 2.1d.

Calculations show that a preexisting flaw of 10μm is sufficient to produce such axial tension cracks, under overall hydrostatic pressures of 3 to 7kb. SEM observations showed these axial cracks emanate from preexisting flaws of about

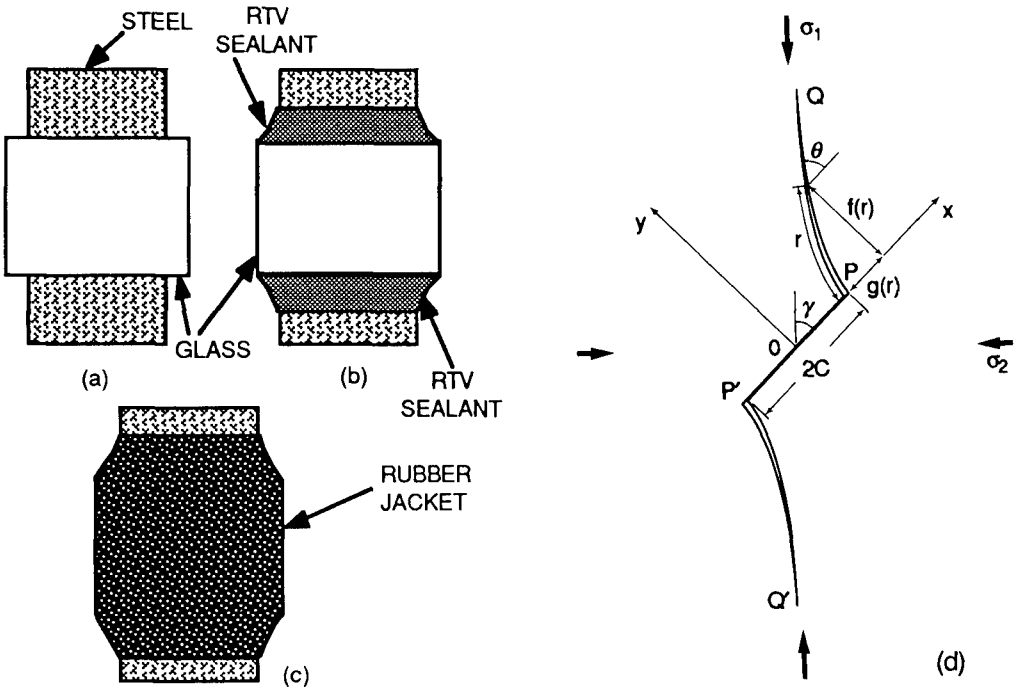

Figure 2.1a-d: Bridgman's ring paradox: (a) a glass tube tightly fitted on a steel bar; (b) its ends are sealed; (c) the entire construction is enclosed by a rubber jacket before submerging into a fluid which is then pressurized; and (d) pre-existing flaw PP′ and curved cracks PQ and P′Q′

20μm, and that each consists of several cracks initiated from different preexisting flaws; see Figures 2.2a-d. This laboratory experiment not only resolves the Bridgman paradox, but also shows the role of preexisting flaws (essentially any micro-inhomogeneities) in generating tensile cracks in brittle solids under all-around quasi-static compression.

Compression-induced microcracking in ceramics has been clearly established in *uniaxial stress* at UCSD, using novel recovery Hopkinson bar techniques. *These cracks are seen to emanate from microdefects and extend in the direction of compression*, as predicted by the theory of Nemat-Nasser and Horii (1982) [11], Horii and Nemat-Nasser (1985, 1986), [13,14] Ashby and Hallam (1986), [15] and Nemat-Nasser (1989) [16]. A vivid example is shown in Figures 2.3a and b, which are micrographs of a sample of Mg-PSZ, subjected to uniaxial stress *in two separate sequences of loading:* Figure 2.3a shows the microcracks extending

horizontally in the direction of axial compression (first loading). Then the cubic sample was loaded in compression in a direction normal to the first loading direction, producing a second set of microcracks, essentially normal to the first set of cracks,

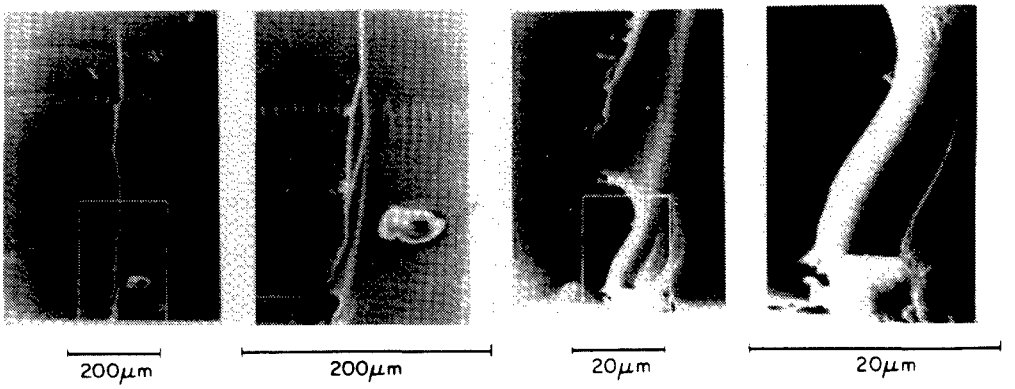

Figure 2.2a-d: Scanning electron photomicrographs of axial crack in jacketed ring experiment, at successively greater magnifications, a, b, c, and d. This was a cycled experiment, and several successive positions of the crack front can be seen. The view is perpendicular to the fracture plane, with the inside surface of the Pyrex ring appearing at the bottom of each photograph. The crack starts at a complex flaw at the center, and an abrupt jog in the crack plane extends from the flaw. Arrest lines from repeated pressurizations are visible in a and b; Scholz *et al.* (1986) [9]

extending in the direction of the second compressive stress; Figure 2.3b. For this class of ceramics, microcracking is accompanied by phase transformation which introduces local compressive stresses, arresting the cracks and, therefore, preventing *axial splitting* which may take place in uniaxial stress if the applied stress pulse contains sufficient energy. The phase transformation from tetragonal to monoclinic crystal structure also involves twinning which introduces additional microcracking, as shown by the TEM micrograph of Figure 2.3c; Subhash and Nemat-Nasser (1992) [17].

Similar results have been obtained in other ceramics. For example, Figures 2.4a and b show micrographs illustrating dynamic cracking in a silicon nitride specimen with crystalline boundary phase, subjected to repeated uniaxial compressive pulses; Sharma *et al.* (1991) [18]. In this experiment, each sample is subjected to a *single* compressive pulse of pre-assigned shape and magnitude using UCSD's Hopkinson bar technique Nemat-Nasser *et al.* (1991) [5], and then

recovered for nondestructive characterization, after which the sample is subjected to exactly the same stress history. Figures 2.4a and b are for a sample that has been repeatedly loaded 42 times. The sample has split axially into two parts in the loading direction (axial splitting). Figure 2.4a shows the striations on the fracture surface, and Figure 2.4b shows dislocations within grains.

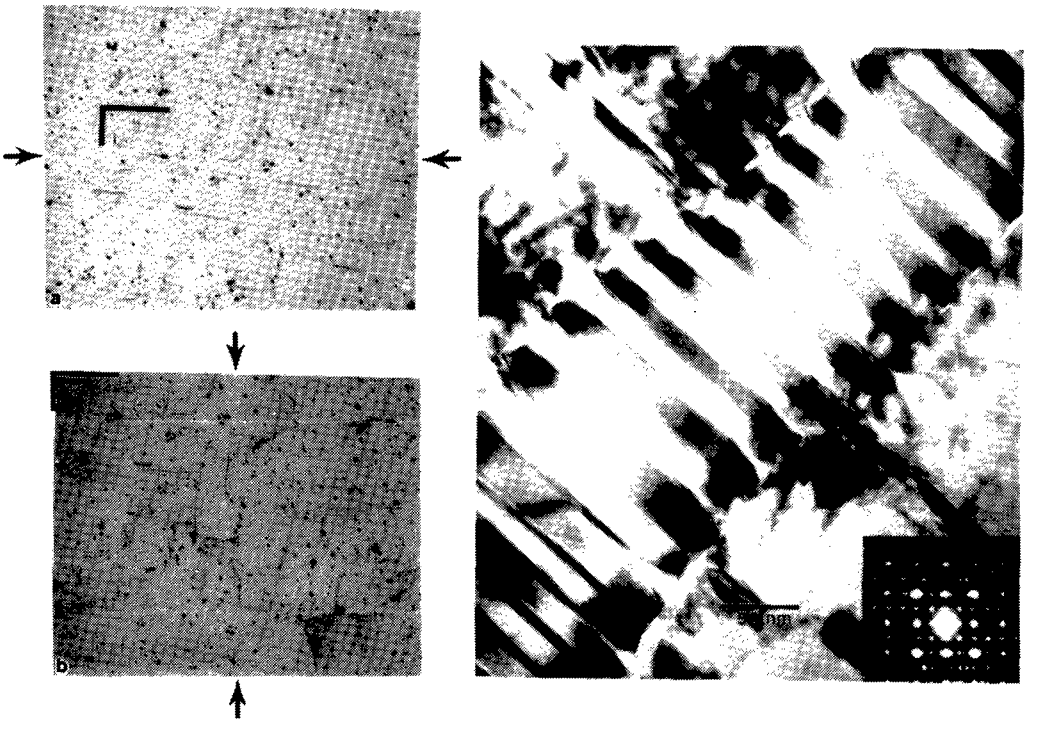

(c)

Figure 2.3a,b,c: (a) Axial cracks in Mg-PSZ subjected to uniaxial compression in the direction of arrows (first loading); (b) the same sample after second loading applied normal to the first loading. (Note vertical cracks are produced normal to the horizontal cracks of the first loading); and (c) high magnification TEM picture of transversely twinned precipitate and the corresponding selected area diffraction pattern along <100> axis; Subhash and Nemat-Nasser (1992) [17]

When lateral confinement accompanies axial compression, a dramatic change in the overall response of brittle materials, especially rocks and concrete, is often observed. Microscopic observation shows that, in this case also, microcracks are nucleated at various micro-inhomogeneities, and these cracks grow essentially in the direction of maximum compression. However, the presence of confinement seems to arrest further growth of cracks of this kind. Indeed, electron microscopy, as well as optical microscopy, seem to suggest a more or less uniform

distribution of microcracks within the sample, up to axial loads rather close to the peak stress; see, for example, Hallbauer, Wagner, and Cook (1973) [19], Olsson and Peng (1976) [20], and Wong (1982) [21]. Close to the peak stress, a region of high density microcracks begins to emerge, which eventually becomes the final failure plane. The sample fails by faulting at an angle somewhere between 10 and 30 degrees with respect to the axial compression.

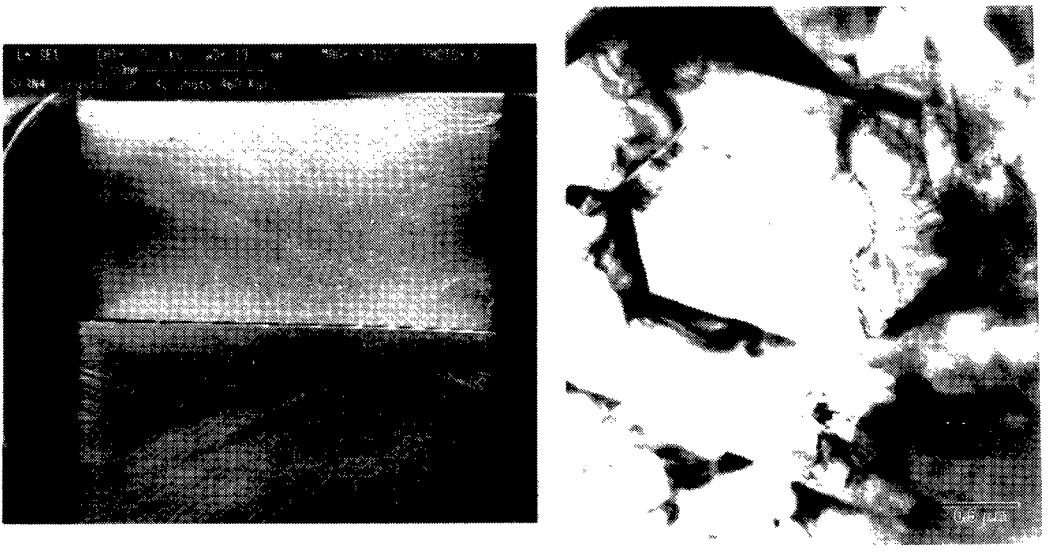

(a) (b)

Figure 2.4a,b: Silicon nitride sample with crystalline boundary phase subjected to repeated axial compressive pulses: (a) striation upon axial splitting; and (b) dislocations within grains; Sharma *et al.* (1991) [18]

Horii and Nemat-Nasser (1985, 1986) [13,14] have suggested that such faulting may be the result of the interactive unstable growth of tension cracks emanating from suitably oriented sets of microflaws. To verify this, a series of model experiments are made on plates which contain sets of small flaws and a number of large flaws; a flaw here is a thin slit (0.4mm thick) containing two thin brass sheets (0.2mm each). Two identical specimens are tested, one without confining pressure, the other with some confinement; see Figures 2.5a,b,c. In the absence of confinement, cracks emanate from the tips of the larger flaws, grow in the direction of axial compression, and lead to axial splitting, while many of the smaller flaws have not even nucleated any cracks, Figure 2.5b. On the other hand, when some confinement accompanies axial compression, cracks emanating from the larger flaws are soon arrested. Then, at a certain stage of loading, suddenly, cracks emanating from many small flaws grow in an unstable manner, leading to eventual faulting; Figure 2.5c.

When the confining pressure is large enough, e.g., exceeding 25-30% of the peak stress, then a transition from brittle failure by faulting to the ductile response by overall plastic flow takes place. Microscopic observation shows a rather general distribution of microcracks accompanying extensive plastic deformation. (These are at suitably low temperatures, where creep effects can be regarded insignificant.) The sample may fail by either localized plastic shearing or by barreling. Horii and Nemat-Nasser (1986) [14] suggest a model which seems to capture the involved mechanism.

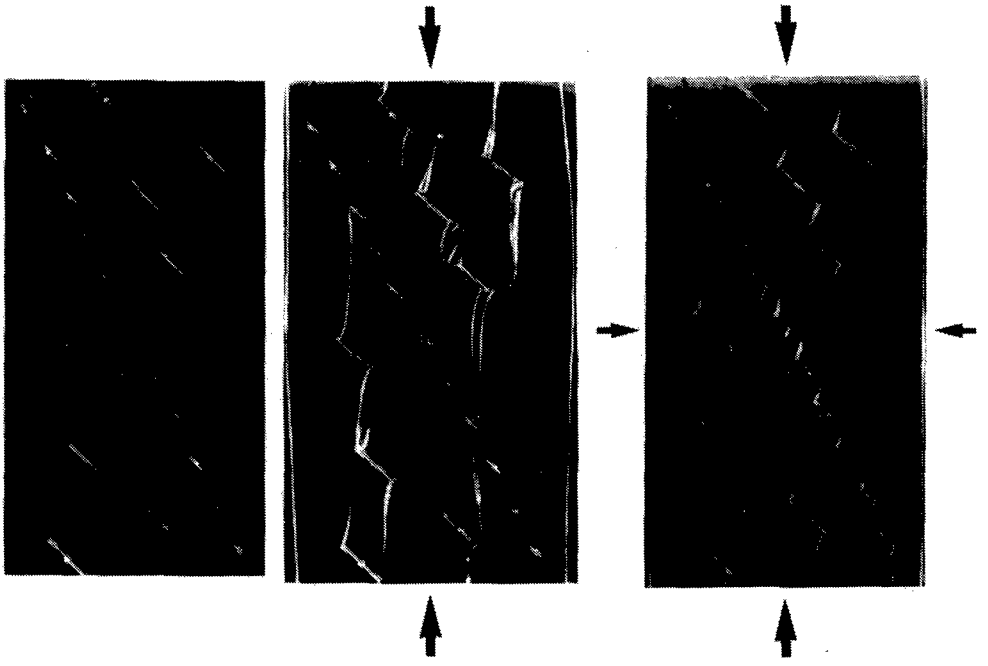

(a) (b) (c)

Figure 2.5a,b,c: (a) Specimen containing a row of small flaws and several larger flaws. (b) Axial splitting under axial compression *without* lateral confinement; (c) shear failure under axial compression *with* lateral confinement; Horii & Nemat-Nasser (1985) [13]

Normal plate-impact recovery experiments on boron-carbide aluminum cermets at stress levels below HEL (Hugoniot Elastic Limit), suggest compression-induced microcracking in *uniaxial strain;* see, Ramesh *et al.* (1989) [22]. Similar results have been reported for alumina by Louro and Meyers (1989) [23], Yeshurun *et al.* (1988) [24], and Clifton *et al.* (1990) [25]. *These results, however, are by no means conclusive, and the question of microcracking in*

compression and in the presence of inertial confinement requires a definitive experimental resolution. Indeed, the brittle-ductile transition model of Horii and Nemat-Nasser (1986) [14] suggests that increasing confining pressure suppresses microcracking, leading to ductile flow of nominally brittle rocks. This transition is shown to depend on the size of the micro-inhomogeneities and, hence, the grain size, a fact which is supported by the recent study of Cagnoux and Cosculluela (1991) [26], in plate-impact experiments on alumina. These authors find that small-grained alumina specimens (2-7μm) show clear indication of ductile behavior by plastic deformation of the grains, with no indication of microcracking, at shock stresses exceeding HEL by 50%. In contrast, coarse-grained alumina (20-70μm grain size) showed a high density of microcracks at 20% below HEL. This observation correlates well with the *ductility parameter* Δ which emerges in the model of Horii and Nemat-Nasser (1986) [14],

$$\Delta = \frac{K_c}{\tau_Y \sqrt{\pi c}}, \tag{2.1}$$

where K_c is the fracture toughness, τ_Y is the yield stress in shear, and 2c is the flaw size. The ductility parameter Δ for fine-grained alumina is more than three times that of coarse-grained alumina. Hence, *the fine-grained ceramic has inherently a greater tendency towards ductile flow than the coarse-grained one.*

Indirect evidence for compressive damage in alumina has been provided by Louro and Meyers (1990) [27], who have studied the effect of stress pulses consisting of compression followed by tension and the variation in the tensile pulse due to compression-induced damage. The tension is produced by encapsulating the sample in a lower shock-impedance material. The tensile stress amplitude is shown to be altered by damage due to initial compression pulses of suitable magnitudes. Their analysis suggests that compressive damage precedes and preconditions the material, possibly by microcracking.

As final evidence which seems to suggest the formation of microcracks during pre-Hugoniot (pre-HEL) compression waves, we cite work by Rosenberg *et al.* (1988) [28] and Yeshurun *et al.* (1988) [24], who report a significant decrease in spall strength and an increase in microcrack density with increasing compression amplitude, especially beyond 30-40kb. This decrease in spall strength has been interpreted to stem from prior compression-induced microcracking.

The inelastic response of ceramics in shock experiments seems to depend strongly on the microstructure and physico-chemistry of the material. Inelasticity in this loading regime may stem from dislocation generation and pile-ups at grain boundaries and other obstacles, mechanical twinning, phase transformation, and possibly more importantly, continued microcracking, crack coalescence, fragmentation, and comminution. An important mechanism of pulverization under high

amplitude shock pressures, may be *a sudden and complete disintegration of the ceramic which is deformed to a metastable state.* The interaction energy associated with microheterogeneities and shock-induced uniaxial straining at extreme rates, may take the material to a metastable state where the stored energy density is far beyond what the material is able to accommodate. After a short incubation time period, the inertially confined, highly pressurized region may simply disintegrate all at once (i.e., over a very short time period), with little or no net change in its volume.

The exact micromechanisms responsible for such varied inelastic behavior, have not been established, and the process itself is not well understood; see Kipp and Grady (1990) [29] for some new experimental observations. No systematic characterization by detailed microscopy has been done at various post-HEL deformation states. There is no question that a systematic and scientific inquiry of this kind is essential for a fundamental understanding of the relation among physicochemistry and the microstructure of the ceramic, and the corresponding inelastic dynamic response and failure process.

3. DYNAMIC MICROCRACKING AND STIFFNESS DEGRADATION

In an impact situation, the state of stress, in general, is *triaxial.* As pointed out before, the stress differential (i.e., the difference between the principal stresses) in the presence of microflaws, can produce tensile microcracks. The sequence, inception and formation of these cracks, is an interesting problem, yet to be fully understood.

Depending on the microstructure, the rate of loading, and the resulting stress state, cracks may initiate from dominant flaws and grow dynamically with increasing loads, or, alternatively, damage may accumulate within individual sub-grains by dislocation pile-ups, phase transformation, twinning, and other mechanisms, storing elastic energy and suddenly generating microcracks which may result in disintegration of the grains and hence, the ceramic. This latter mechanism is an observation worthy of experimental verification.

This dichotomy in the failure process has been observed in the uniaxial, repeated dynamic loading of silicon nitride by Sharma *et al.* (1991) [18]. Silicon nitride of fully crystalline microstructure develops microcracks which grow continuously in each cycle of loading; see Figures 2.4.a,b. On the other hand, *repeated dynamic loading of silicon nitride with an amorphous phase present between grains, accumulates dislocations within the grains (the amorphous phase traps dislocations), and once a level of damage due to dislocation pile-up is attained, the grains simply disintegrate*; Sharma *et al.* (1991) [18]. This is shown in Figure 3.1a,b, which should be contrasted with Figure 2.4a,b. It should be noted that the overall state in this case is uniaxial *stress*, whereas in high-velocity impact, it is uniaxial strain.

In general, it is possible that both fracturing modes occur under an impact condition, see Figures 1.1a,b. In the experiment of Figure 1.1b, the comminuted region may be the result of the initial intense microdamage precipitated under initial shock, whereas the larger cracks are the result of both compression- and tension-induced cracking which may have occurred subsequently.

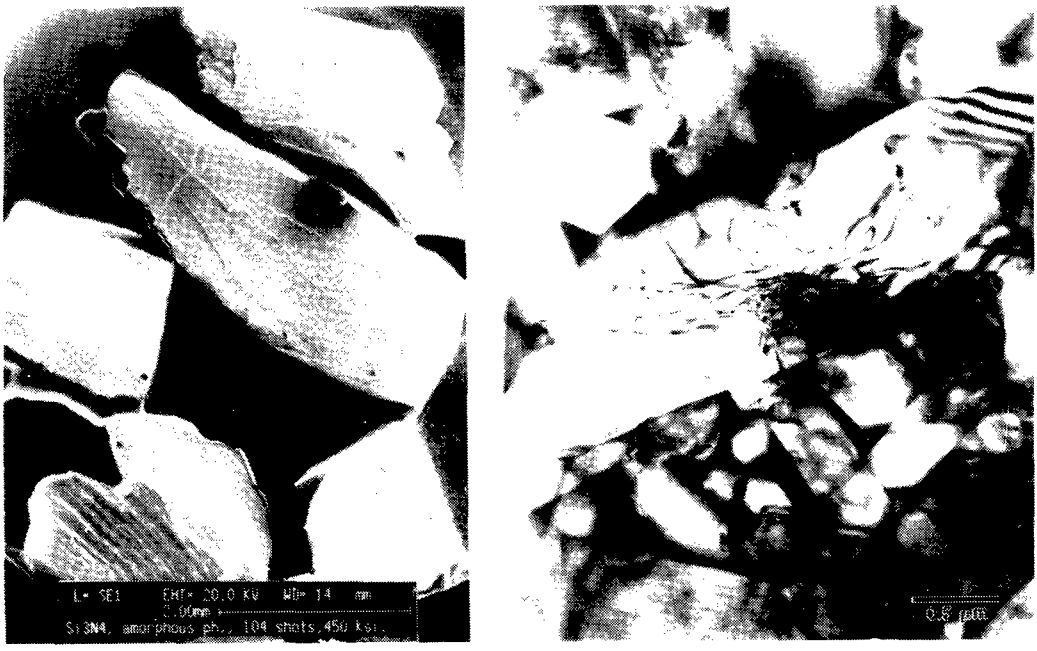

(a) (b)

Figure 3.1a,b: Silicon nitride sample with glassy phase subjected to repeated axial compressive pulses: (a) fragmentation of the sample; and (b) dislocation pile-up in grains; Sharma *et al.* (1991) [18]

3.1. Model of Noninteracting Microcracks

The simplest model of damage due to microcracks is obtained when cracks are assumed to be so far apart that their interaction can be neglected. For problems of interest here, this is hardly ever a valid assumption. Nevertheless, the model serves as a starting point, providing some information on strength loss due to microcracking. Furthermore, it is possible to include the effect of *dynamic* crack growth in this model. For this reason, the model is briefly outlined in the following:

At each instant the total strain in a given continuum material element of a damaged ceramic consists of the following contributions: elastic strain, inelastic strain due to deformation of flaws (e.g., sliding of cracks), crack opening displacement (dilatancy), formation of new tensile microcracks, and deformation due to overall farfield stresses; see, Nemat-Nasser and Obata (1988) [30]. The model hence reflects the inelastic deformation of the flaw, in terms of its mechanical properties and the load history, and the dynamic growth of tension cracks, on the basis of a suitable dynamic fracture criterion. Once the contributions to the total strain rate from each flaw and the associated tension cracks are formulated, the result are averaged over a representative volume element, using a weighting function which may take into account the *anisotropic distribution of the microcracks* caused by stress triaxiality.

Preliminary calculations by Deng and Nemat-Nasser (1991) [31] show promise. As an illustration, Figure 3.2 is a numerical simulation of stress attenuation by such microcracking in uniaxial stress conditions. Each profile corresponds to the stress sensed at a point further along a bar which is subjected to an initially rectangular pulse.

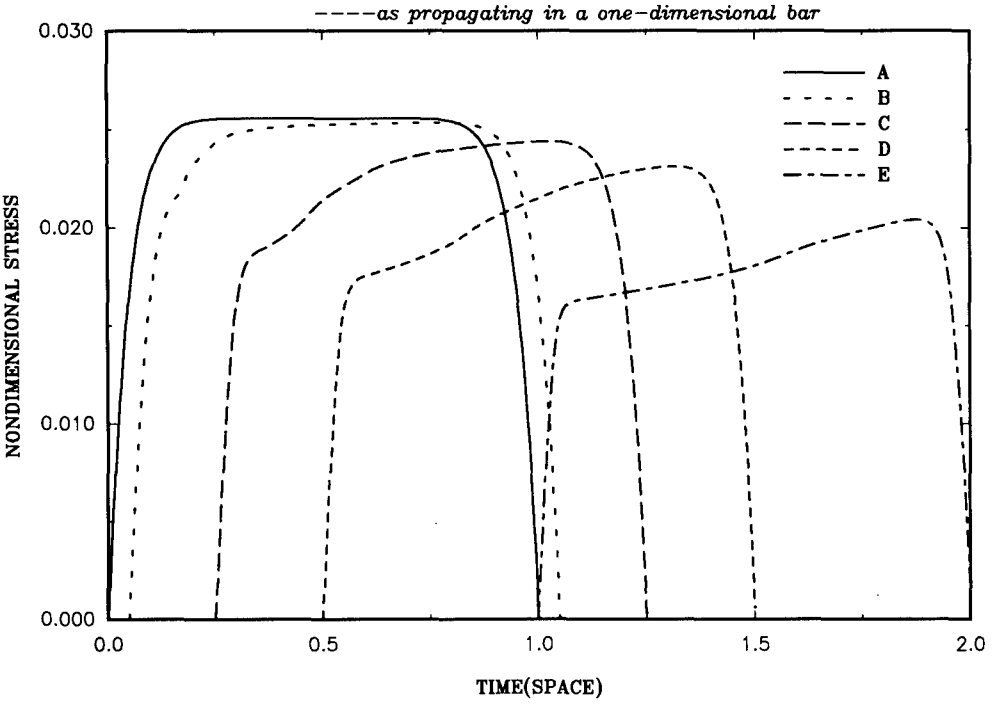

Figure 3.2: Stress-pulse attenuation due to dynamic micro-cracking under uniaxial stress; Deng and Nemat-Nasser (1991) [31]

3.2. Model of Interacting Microcracks

An alternative mode of comminution is by microcrack interaction and coalescence, which may be a preferred failure regime for certain ceramics with suitable micro-physico-chemistry. This and the preceding overall stiffness degradation may be modeled by considering a *representative unit cell* which interacts with its neighboring cells; its dimensions are defined by the grain size and the mean spacing of the dominant defects. Using the concept of *eigenstrain* to homogenize a periodic microstructure, crack growth and its effect on stiffness degradation can be modeled, taking full account of interactions at the microlevel. This follows the work of Nemat-Nasser and Taya (1981, 1985) [32,33], Nemat-Nasser *et al.* (1982) [34], Iwakuma and Nemat-Nasser (1983) [35], Accorsi and Nemat-Nasser (1986) [36], and more recently, Hashin (1988) [37], and Nemat-Nasser, and Hori (1989) [38] Figure 3.3 is a typical result for penny-shaped microcracks periodically distributed in an elastic solid; Nemat-Nasser, Yu, and Hori (1991) [39]. *The formulation allows for including several cracks within each cell, which may curve, grow toward the boundaries, and coalesce with a neighboring crack.*

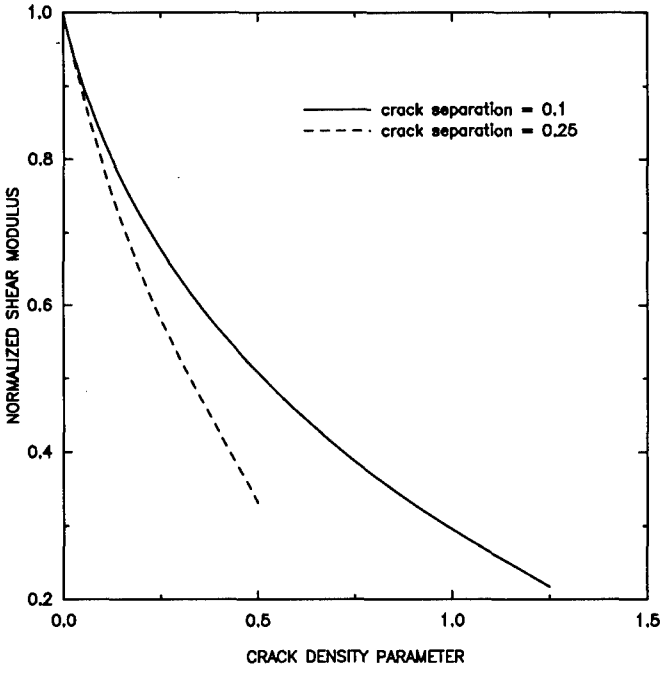

Figure 3.3: Stiffness degradation of solid by formation of densely packed, penny-shaped cracks; Nemat-Nasser *et al.* (1991) [39]

4. DYNAMIC GRANULAR FLOW

The mechanism of dilatancy accompanying shearing under inertial confinement, is perhaps one of the most important features of the dynamic flow of pulverized ceramics.

Based on the micromechanical model of Nemat-Nasser and co-workers (1980, 1981, 1986) [40,41,42], Balendran and Nemat-Nasser (1992) [43] recently have developed a simple constitutive model for granular flow, which seems to capture some essential features of the deformation process. The kinematics is based on the sliding of layers of granules over each other, through rolling and frictional sliding of individual granules, which results in overall dilatant shearing of the granular medium. The dilatation is related to the effective frictional resistance (flow stress), as well as the void ratio which itself is affected by the local mean compression; void ratio e is the volume of the void divided by the volume of the solid. The theory is capable of modeling both rate-independent frictional flow, as well as rate-dependent inelastic deformation. For a two-dimensional model, the final rate-constitutive equations are quite simple, and encompass the most essential physical features of the deformation process. These equations are:

$$\overset{\circ}{\sigma}_{kk} = 2K(D_{kk} \mp \dot{\gamma}B), \tag{3.1a}$$

$$\overset{\circ}{\boldsymbol{\sigma}}' = 2G\left[\boldsymbol{D}' \pm \beta(\mathbf{1} - \boldsymbol{\mu}\otimes\boldsymbol{\mu}):\boldsymbol{D}' \mp \dot{\gamma}\frac{\boldsymbol{\mu}}{\sqrt{2}}\right], \tag{3.1b}$$

$$\dot{\gamma} = H(\pm\sqrt{2}G\,\boldsymbol{\mu}:\boldsymbol{D}' + M\,K\,D_{kk}), \tag{3.1c}$$

$$\boldsymbol{\mu} = \frac{\boldsymbol{\sigma}'}{\sqrt{2}q}, \qquad q = (\tfrac{1}{2}\boldsymbol{\sigma}':\boldsymbol{\sigma}')^{1/2}, \tag{3.2a,b}$$

$$B = \pm\frac{\sin\delta}{\cos(\phi_1 - \delta)}, \quad \beta = \frac{G\alpha}{q \mp G\alpha}, \quad \alpha = \frac{\sin(\phi_1 - \delta)}{\cos\delta}, \tag{3.3a-c}$$

$$H = (h\,p + G \pm M\,K\,B)^{-1}, \qquad h = \frac{\partial M}{\partial\gamma}. \tag{3.4a,b}$$

where $\boldsymbol{\sigma}$ is the Cauchy stress tensor, $\boldsymbol{D}$ is the symmetric part of the velocity gradient, $\boldsymbol{\mu}$ is the unit deviatoric tensor, q is the effective shear stress, B is the dilatancy parameter, α is the noncoaxiality coefficient, and M is the effective frictional resistance. The upper signs of the symbols $\pm$ and $\mp$ correspond to continued loading while the lower signs correspond to reverse loading. The model is based on frictional sliding of layers of granules over each other. The sliding criterion is,

$$-M^U p \le q \le M^L p\,,$$

$$M^L = \sin(\phi_1^L + \phi_2)/\cos\phi_2, \quad M^U = \sin(\phi_1^U + \phi_2)/\cos\phi_2. \tag{3.5a-c}$$

The angles, ϕ_1^L and ϕ_1^U, represent the effective frictional resistance to sliding by interparticle friction as well as the fabric structure, while the angle ϕ_2 represents the resistance due to isotropic interaction of particles. The angle ϕ_1^L is for

continued loading, whereas ϕ_1^U corresponds to unloading and reverse loading. The *dilatancy* of the granular mass is governed by,

$$\delta = \phi_1^L + \phi_2 - \phi_\mu \quad \text{for } \textit{loading}\,,$$

$$\delta = \phi_1^U + \phi_2 - \phi_\mu \quad \text{for } \textit{unloading}\,, \qquad (3.6a,b)$$

where ϕ_μ is the angle of interparticle friction. Equations (3.6a,b) are obtained from a general balance of energy which ensures overall consistency of the formulation. Details are given by Balendran and Nemat-Nasser (1991) [43]. It is necessary to define a hardening rule based on the physics of the problem.

To illustrate the effectiveness of this model, Figures 4.1a,b show the response under monotonic, and Figures 4.2a,b for cyclic shearing under *constant confining pressure* for indicated initial void ratios.

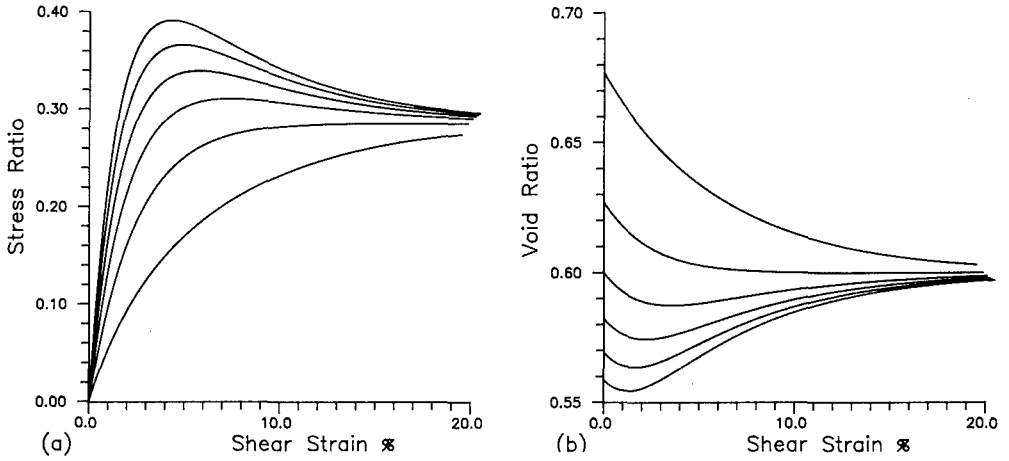

Figure 4.1a,b: Physically-based model of monotonic granular flow: (a) stress-strain relation in simple shearing; and (b) the corresponding dilantancy; Balendran and Nemat-Nasser (1991) [43]

More germane to the flow of pulverized ceramics is the result shown in Figures 4.3a,b for pure shearing with *no* volume change. As is seen, the pressure quickly builds up to four times its initial value, depending on the value of void ratio e, for only 10% shear straining. Observe that for a void ratio of e = 0.08 the shear stress (flow stress) is twice that for e = 0.2%. Note also that this flow stress is *normalized by pressure* which is also twice as large for e = 0.08, as compared with that for e = 0.20.

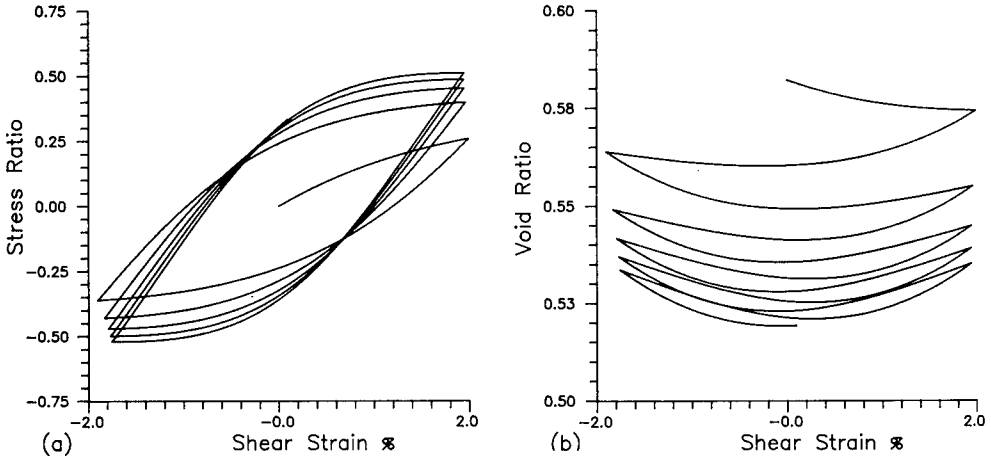

Figure 4.2a,b: Physically-based model of granular flow in cyclic shearing: (a) stress-strain relation; and (b) volumetric strain; Balendran and Nemat-Nasser (1991) [43]

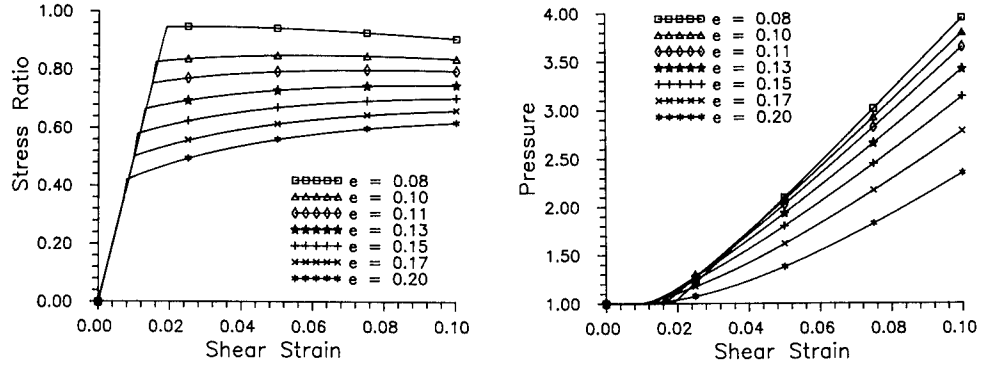

(a) (b)

Figure 4.3a,b: Pure shearing of granular medium with full confinement: (a) stress-strain relation; and (b) pressure buildup due to shearing (Note: even 10% shear strain results in manyfold pressure increase); Balendran and Nemat-Nasser (1991) [43]

Acknowledgment

This work has been supported by the U.S. Army Research Office under Contract No. DAAL-03-86-K-0169 to the University of California, San Diego.

5. REFERENCES

1. Viechnicki, D., M.J. Slavin, M.I. Kliman, J. Amer. Cer. Soc. Bull., Vol. 70 (1991), p. 1035.
2. Shockey, D.A., A.H. Marchand, S.R. Skaggs, G.E. Cort, M.W. Burkett and R. Parker, Int'l. J. Impact Eng., Vol. 9, No. 3 (1990), p. 263.
3. Rogers, W.P. and S. Nemat-Nasser, J. Amer. Cer. Soc., Vol. 73, No. 1 (1990), p. 136.
4. Nemat-Nasser, S., J. Mech. Phys. Solids, Ser. 1, Vol. 34, No. 1 (1991), p. 111.
5. Nemat-Nasser, S., J.B. Isaacs and J. Starrett, Proc. R. Soc. Lond., Vol. 435 (1991), p. 371.
6. CEAM Facilities Report, Univ. of Calif., San Diego (1990).
7. Bridgman, P.W., Phys. of High Pressure, Bell, London (1931).
8. Jaeger, J.C. and N.G.W. Cook, J. Geophys. Res., Vol. 68 (1963), p. 1759.
9. Scholz, C.H., G. Boitnott and S. Nemat-Nasser, Pure Appl. Geophysics, Vol. 124 (1986), p. 587.
10. Nemat-Nasser, S., Proc. Seventh International Conference on Fracture (ICF7), Houston, Texas, March 20-24, *Advances in Fracture Research*, Vol. 1 (1989), p. 423.
11. Nemat-Nasser, S. and H. Horii, J. Geophys. Res., Vol 87 (1982), p. 6805.
12. Brace, W.F. and E.G. Bombolakis, J. Geophys. Res., Vol. 68 (1963), p. 3709.
13. Horii, H. and S. Nemat-Nasser, J. Geophys. Res., Vol. 90 (1985), p. 3105
14. Horii, H. and S. Nemat-Nasser, Phil. Trans. R. Soc. Lond., Vol. A319 (1986), p. 337.
15. Ashby, M.F. and S.D. Hallam, Acta Metall., Vol. 34 (1986), p. 497.
16. Nemat-Nasser, S., Proc. Seventh International Conference on Fracture (ICF7), Houston, Texas, March 20-24, *Advances in Fracture Research*, Vol. 1 (1989), p. 423.

17. Subhash, G. and S. Nemat-Nasser, "Dynamic Stress-Induced Transformation and Texture Formation in Uniaxial Compression of Zirconia Ceramics", J. Amer. Cer. Soc. (1992) to appear.

18. Sharma, V., K.S. Vecchio and S. Nemat-Nasser, unpublished research (1991).

19. Hallbauer, D.K., H. Wagner and N.G.W. Cook, Int. J. Rock Mech. Min. Sci. Geomech. Abst., Vol. 10 (1973), p. 713.

20. Olsson, W.A. and S.S. Peng, Int. J. Rock Mech. Min. Sci. Geomech. Abstr., Vol. 13 (1976), p. 53.

21. Wong, T.F., Int. J. Rock Mech. Min. Sci. Geomech. Abstr., Vol. 19 (1982), p. 49.

22. Ramesh, K.T., B. Altman, G. Ravichandran, and S. Nemat-Nasser, Proc. Seventh International Conference on Fracture, ICF7, Houston, Texas, March 20-24, *Advances in Fracture Research*, Vol. 1 (1989), p. 811.

23. Louro, L.H.L. and M.A. Meyers, J. Matls. Sci., Vol. 24 (1989), p. 2516.

24. Yeshurun, Y., D.G. Brandon and Z. Rosenberg, *Impact Loading and Dynamic Behavior of Materials*, (eds) C.Y. Chiem, H.-D. Kunze and L.W. Meyer, DGM, Germany (1988), p. 399.

25. Clifton, R.J., G. Raiser, M. Ortiz and H. Espinosa, Proc. APS Conference on "Shock Waves in Condensed Matter - 1989" ed. by S.C. Schmidt, J.N. Johnson and L.W. Davison, Elsevier (1990) p. 437.

26. Cagnoux, J. and A. Cosculluela, "Influence of Grain Size on Triaxial Dynamic Behavior of Alumina", presented at "International Seminar on Dynamic Failure of Materials", Jan. 2-4, 1991, Vienna, Austria (1991).

27. Louro, L.H.L. and M.A. Meyers, *Shock Compression of Condensed Matter*, S.C. Schmidt, J.N. Johnson and L.W. Davidson, (eds), Elsevier (1990), p. 465.

28. Rosenberg, Z., N.S. Brar and S.J. Bless, J. de Physique, Vol. 49, Colloq. C3, (1988), p. 707.

29. Kipp, M.E. and D.E. Grady, *Shock Compression of Condensed Matter*, S.C. Schmidt, J.N. Johnson and L.W. Davidson, (eds), Elsevier (1990), p. 377.

30. Nemat-Nasser, S. and M. Obata, J. Appl. Mech., Vol. 55 (1988), p. 24.

31. Deng, H. and S. Nemat-Nasser, "Stress-Pulse Attenuation in Brittle Solids", Proc. of Symposium on Recent Advances in Damage Mechanics and Plasticity, ASME Applied Mechanics Summer Conference, April 29 - May 1, 1992 (1992).

32. Nemat-Nasser, S. and M. Taya, Q. Appl. Math., Vol. 39 (1981), p. 43.

33. Nemat-Nasser, S. and M. Taya, Q. Appl. Math., Vol. 43 (1985), p. 187.

34. Nemat-Nasser, S., T. Iwakuma and M. Hejazi, Mech. of Mat., Vol. 1 (1982), p. 239.

35. Iwakuma, T., and S. Nemat-Nasser, Computers and Structures, Vol. 16, Nos. 1-4 (1983), p. 13.

36. Accorsi, M.L. and S. Nemat-Nasser, Mech. of Mat., Vol. 5, No. 3 (1986), p. 209.

37. Hashin, Z. J. Mech. Phys. Solids, Vol. 36 (1988), p. 719.

38. Nemat-Nasser, S. and M. Hori, The Toshio Mura Anniversary Volume (1989), p. 297.

39. Nemat-Nasser, S., N. Yu and M. Hori, "Damage in Solids Due to Periodically Distributed Cracks of Arbitrary Geometry", Proc. Ninth Engineering Mechanics ASCE Conference, College Station, Texas, May, 1992 (1992),

40. Nemat-Nasser, S., Japanese Soc. of Soil Mech. and Foundation Eng., Vol. 20, No. 3 (1980), p. 59.

41. Christoffersen, J., M.M. Mehrabadi and S. Nemat-Nasser, J. Appl. Mech., Vol. 48 (1981), p. 339.

42. Nemat-Nasser, S. and G. Lance, Mech. of Mat., Vol. 5, No. 1 (1986), p. 1.

43. Balendran, B. and S. Nemat-Nasser, "Double Sliding Elastoplastic Model for Cyclic Deformation of Granular Materials", J. Mech. Phys. Solids (1992) to appear. (1991), p. 1035.

Effect of Grain Size on Deformation Stability of Copper under Quasi-Static and Dynamic Tensile Loading

David H. Lassila and William H. Gourdin

University of California
Lawrence Livermore National Laboratory
Livermore, CA 94551

Abstract

The effects of grain size on the deformation stability of copper deformed in tension under quasi-static and dynamic conditions have been studied experimentally and analitically. Oxygen Free Electronic (OFE) copper samples with grain sizes of 15 μm and 120 μm were tested. Results of the tests indicated that an increase in grain size resulted in greater extents of elongation prior to deformation instability and eventual failure under both quasi-static and dynamic loading. We have applied the deformation stability condition of Considére to both a simple power law modified to include a Hall-Petch grain size dependence and the more descriptive mechanical threshold stress (MTS) model. Calculations of the stress-strain behavior in uniaxial tension and the instability strain under quasi-static loading are compared with experiment. Both models predict an increase in the instability strain with increasing grain size, but the power law, included as a heuristic, yields a poor overall fit to both the stress-strain and the instability strain data. In contrast, the MTS model agrees well with stress-strain data and measured quasi-static instability strains. Under dynamic loading comparison of the experimental results with analitical predictions were diffucult due to inherent inacuracy in the dynamic stress-strain data.

* Work performed under the auspices of the U. S. Department of Energy by the Lawrence Livermore National Laboratory under contract No. W-7405-ENG-48.

INTRODUCTION

The constitutive behavior of a ductile metal has long been known to control its deformation stability under tensile loading assuming that the deforming body is homogeneous and isotropic [1,2,3]. A straightforward analysis shows that plastic deformation under uniaxial tensile loading is unstable when

$$\frac{d\sigma}{d\varepsilon} \leq \sigma, \tag{1}$$

where σ is true stress and ε is true strain. Equality in Equation (1), which we will refer to as the instability criterion, represents the point during deformation at which geometric softening due to reduction of the cross sectional area of the sample (assuming constant volume deformation) occurs at a greater rate than work hardening of the deforming material. This instability corresponds to the maximum tensile load and is a necessary condition for plastic instability, but by itself it does not predict localization of deformation such as a neck. Gross localized deformation and ensuing failure generally occurs at some value of strain greater than that predicted by Equation (1) [4]. The amount of post uniform strain and the rate of growth of a neck has been shown to be a function of the work hardening behavior and strain rate sensitivity [5,6,7]. In this work we do not address the formation and growth of localized necking from an annalitical standpoint, although we observe the necking phenomenon experimentally. Our purpose is to assess the effect of grain size, manifested as an effect on constitutive behavior, on deformation stability as described by Equation (1).

Numerous studies have shown that the flow stress of copper increases with decreasing grain size according to an expression of the Hall-Petch type [8,9]:

$$\sigma\,(T,\dot{\varepsilon}...) = \sigma_t\,(T,\dot{\varepsilon}...) + kd^{-1/2}, \tag{2}$$

where $\sigma(T,\dot{\varepsilon}..)$ is the true flow stress, $\sigma_t(T,\dot{\varepsilon}..)$ is the "frictional stress", k is the Hall-Petch parameter and d is the average grain diameter. Recent studies [10,11,12] indicate that k is independent of strain and strain-rate in the absence of dynamic recrystallization. As indicated by the parentheses, $\sigma_t(T,\dot{\varepsilon}..)$ and hence $\sigma(T,\dot{\varepsilon}..)$ are functions of the temperature, strain-rate, and the internal state variables that describe the evolution of the dislocation structure during deformation[1]. Experiments demonstrate that the work hardening of copper is independent of grain size when deformed at fixed

[1] We note that the strain is not a proper internal state variable, and that the flow stress at a given strain depends on the deformation conditions (e.g. strain-rate, temperature).

strain-rate and temperature [12] and further imply that $\sigma_t(T,\dot{\varepsilon}...)$ is independent of d. When these conditions prevail, application of Equation (1) to a simple monotonically increasing flow stress leads immediately to the conclusion that the instability strain must increase with increasing grain size. A quantitative description, however, depends on the detailed behavior of $\sigma_t(T,\dot{\varepsilon}...)$.

In this paper, we first examine, experimentally, the effects of grain size on the stress-strain behavior, deformation stability and necking behavior of copper deformed in tension under quasi-static and dynamic conditions. The experimentally determined instability strains are then compared to the instability strains predictioned by both a simple heuristic (and non-physical) expression for $\sigma_t(T,\dot{\varepsilon}...)$ and a realistic description provided by the mechanical threshold stress (MTS) model [12,13].

EXPERIMENTAL AND RESULTS

Test samples were machined from cold rolled OFE copper bar stock, nominally 99.98 Cu. The test samples were annealed at 375° C and 800° C for one hour in an argon atmosphere to produce nominal grain sizes of 15 μm and 120 μm respectively. Optical micrographs illustrating the recrystallized equiaxed microstructures are shown in Figure 1.

Dynamic and quasi-static testing was performed using 1.00 mm thick tensile samples with a width of 2.54 mm and a gage length of 5.08 mm. This sample geometry was chosen to minimize inertia effects in the dynamic test while still providing a sufficient cross sectional area so that anisotropy due to single crystal effects in the large grain size materials were not appreciable [14].

Quasi-static tensile tests were performed at a nominal strain rate of 10^{-3} s^{-1} using a screw driven test machine. Loading of the sample was recorded using a standard strain gage load cell and displacement of the gage section was measured using extensometers attached directly to the gage section. These data were used to construct engineering stress-strain curves shown in Figure 2. The strain at which deformation instability occurs is termed "instability strain" (ε_i) and is taken to be the value of true strain at the point of maximum load on the engineering stress-strain curves. The instability strains for all tests are given in Table 1. The data shown in Figure 2 clearly indicate that the large grain size material has a larger instability strain than the small grain size material. Although the determination of the onset of localized deformation is somewhat subjective and also dependent on the measurement technique, direct observations indicated that gross necking occurred at values of strain 5% to 10% beyond the instability strain, which is consistent with other work [4].

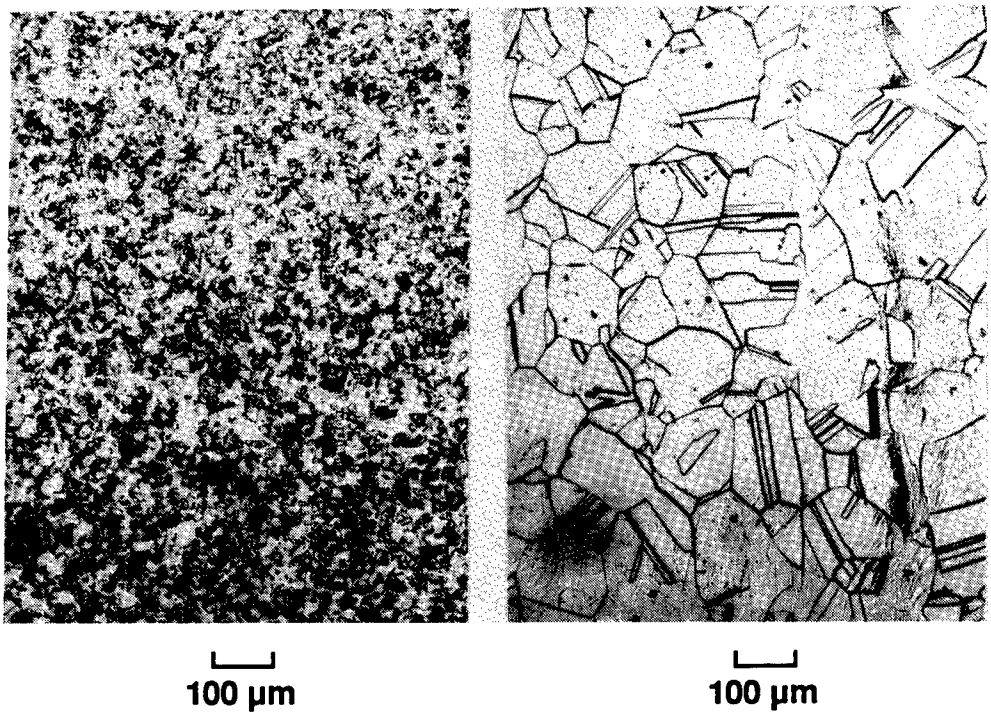

Figure 1. Optical light micrographs showing the recrystallized equiaxed microstructures of the 15 µm and 120 µm grain size test materials.

Table 1
Instability Strain

Strain Rate	Grain Size (µm)	Instability Strain (true strain)
10^{-3}	15	.30
5×10^{3}	15	.40
10^{-3}	120	.35
5×10^{3}	120	.47

Dynamic testing was performed at nominal strain rates of about 5000 s^{-1} using the split Hopkinson pressure bar technique. Detailed descriptions of the test hardware and data reduction techniques used in this work will be given elsewhere [15]. Engineering stress in the sample was measured

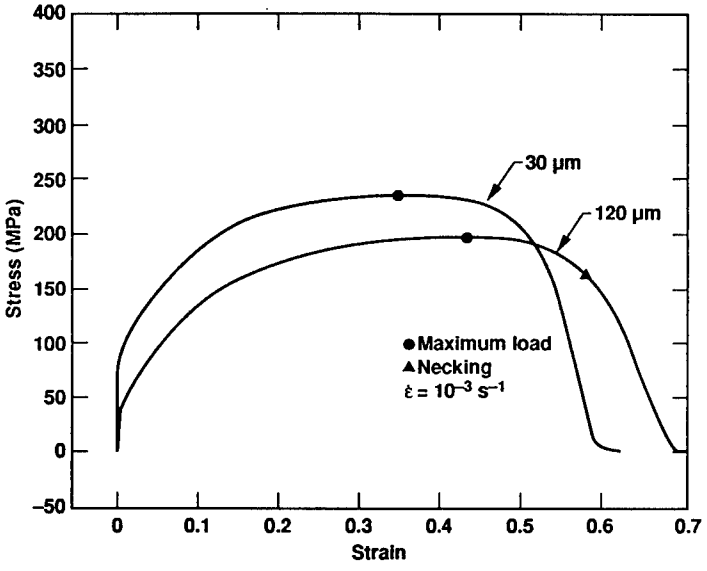

Figure 2. Engineering stress strain behavior of the test materials under quasi-static loading $\left(\dot{\varepsilon} = 10^{-3}s^{-1}\right)$ The instability strains are 0.30 (true strain) and 0.35 (true strain) for the 15 μm and 120 μm test materials respectively. Visible necking occurred at strains considerably greater than the instability points.

dynamically by a transmitter bar. A high-speed framing camera, which produces approximately 80 back-lit images, was used to record the deformation of the sample. Selected framing camera images are shown in Figure 3. Engineering strain in the sample as a function of time was calculated using values of relative displacement of the gage marks on the sample taken off the framing camera record. The engineering stress and engineering strain records as functions of time are phased to construct an engineering stress-strain plot as shown in Figure 4 for the 15 μm and 120 μm materials. The instability strains, as defined above, are taken to be 0.40 and 0.47 for the large and small grain size materials respectively .

The strain at which necking initiates in the dynamic tests was determined visually using the framing camera record. As was the case in the quasi-static test results, the large grain size material produced a greater extent of uniform elongation prior to necking than the small grain size material. As expected, necking occurred at values of strain significantly beyond the instability strain as shown in Figure 4.

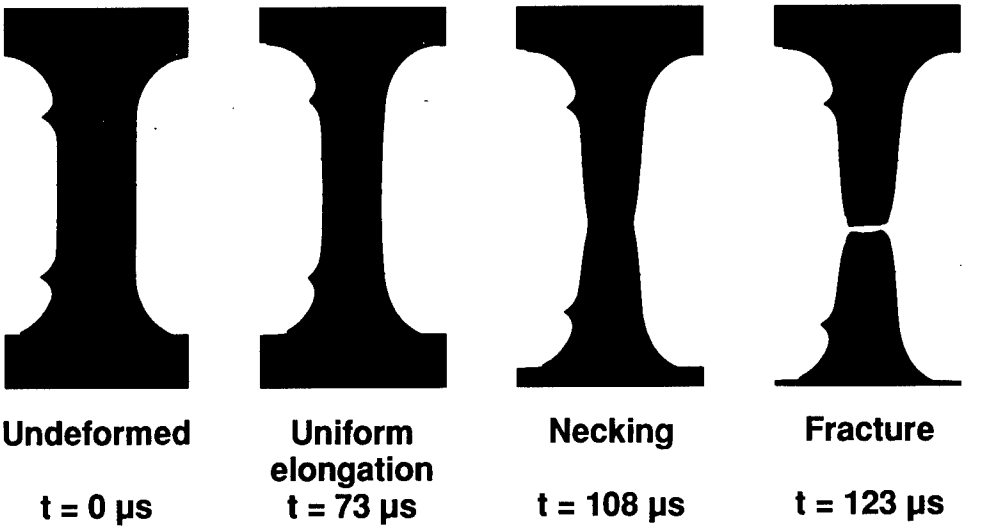

Figure 3. Framing camera record pictures of a 15 μm grain size test sample under dynamic loading showing uniform elongation, necking and fracture.

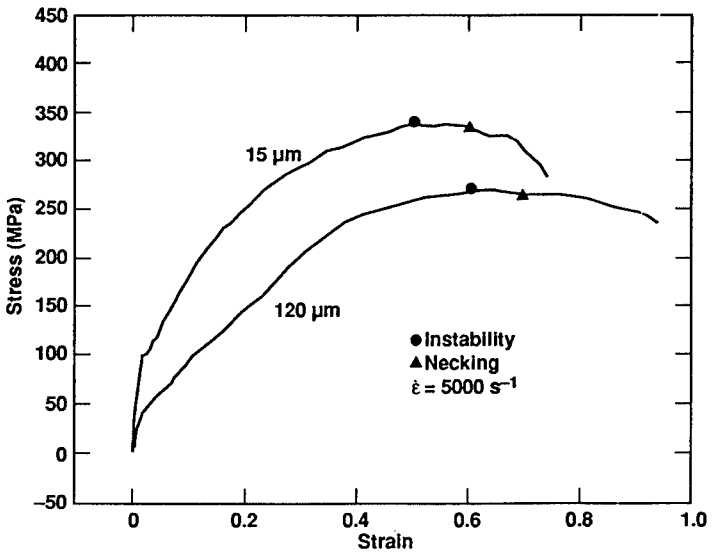

Figure 4. Engineering stress-strain behavior under dynamic tensile loading determined using the split Hopkinson pressure bar technique. The instability strains are 0.40 (true strain) and 0.47 (true strain) for the 15 μm and 120 μm grain size materials. The occurrence of necking indicated on the stress strain curves was determined visually using framing camera records.

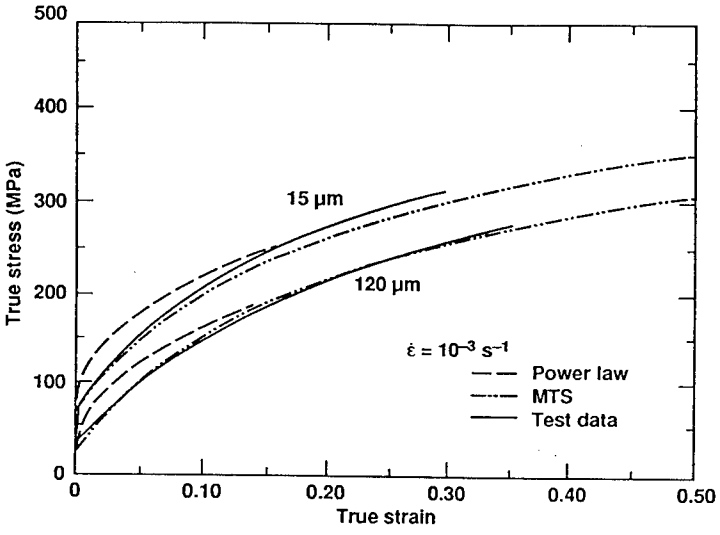

Figure 5. True-stress true-strain behavior of 15 μm and 120 μm grain size copper at a strain rate of $10^{-3}s^{-1}$. The power law hardening and MTS material model fits are shown.

ANALYSIS AND DISCUSSION

The true stress-true strain behavior of the test materials under quasi-static loading, shown in Figure 5, was determined from the engineering stress-strain data given in Figure 3 using the standard conversions. A heuristic material model was derived by modifying a power law hardening model to include the Hall-Petch relationship;

$$\sigma(\varepsilon) = K\varepsilon^n + kd^{-1/2} \qquad (3)$$

Although the strain is not a proper state variable and Equation (3) is too simple to properly describe the known deformation behavior of copper, it nevertheless serves as a convenient means of illustrating, in closed form, the effect of grain size (manifested as an effect on constitutive behavior) on deformation stability. The value of k was taken to be 2.78 x 10^{-4} MPa - $m^{1/2}$ which has been reported to described the behavior of OFE copper over a wide range of strains and strain rates (Table 2) [12]. Parameters K and n were determined to be 430 MPa and 0.48 respectively by averaging values

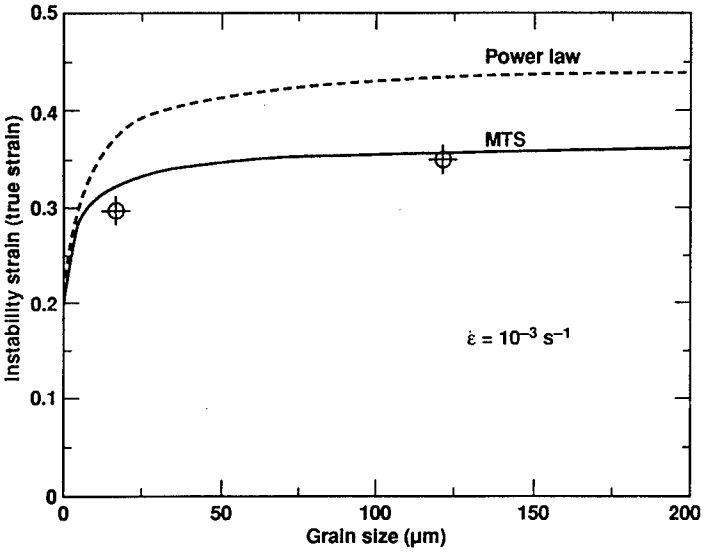

Figure 6. The instability strain calculated using the power law hardening and MTS material model plotted against grain size indicating an increase in deformation stability with increase in grain size. The test data is in good agreement with the MTS model prediction.

obtained from a least squares fit to data for 15 μm and 120 μm grain size specimens for strains between 0.2 and 0.3. Application of Equation (1) to Equation (3) yields

$$nK\varepsilon_i^{n-1} = K\varepsilon_i^n + kd^{-1/2}, \qquad (4)$$

which was solved for the instability strain ε_i using a Newton-Raphson iteration. The instability strain (ε_i) is plotted versus grain size in Figure 6, along with values of ε_i determined experimentally at a strain-rate of $10^{-3}\ s^{-1}$. The instability strain decreases with grain size, dropping rapidly for grain sizes below about 20 μm. Quantitative agreement with the test data is poor. The following analysis using the more descriptive MTS material model suggests this is because the power law material model provides a poor description of stress-strain behavior of the specimens (Figure 5).

The MTS model, described in detail in references 12 and 13, is a physically-based internal state variable model that provides a realistic description of OFE copper over a wide range of deformation conditions. Within this model, the true flow stress is given by

$$\sigma = \hat{\sigma}_a M(T) + \hat{\sigma}_t M(T)\left\{1 - \left[\frac{kT}{G_0}\ln\left(\frac{\dot{\varepsilon}_0}{\dot{\varepsilon}}\right)\right]^{1/q}\right\}^{1/p} , \qquad (5)$$

where $M(T)$ is the ratio of the shear modulus μ at temperature T to its value at $T = 295$ K [12], the activation energy $G_0 = g_0\mu b^3$, and $\dot{\varepsilon}$ is the true strain rate. The mechanical threshold stress [2],

$$\hat{\sigma} = \hat{\sigma}_a + \hat{\sigma}_t , \qquad (6)$$

characterizes the influence of structure on the flow stress through Eq. (5). The "athermal" portion $\hat{\sigma}_a$ is independent of both temperature and deformation and varies with grain size according to [12]

$$\hat{\sigma}_a = \frac{2.78 \times 10^{-4}}{\sqrt{d}} \text{(GPa)} \qquad (7)$$

where d is the grain size in meters. The "thermal" portion $\hat{\sigma}_t$ is independent of the grain size but changes with deformation as specified by the rate of change of the threshold stress with strain, $d\hat{\sigma}_t/d\varepsilon = d\hat{\sigma}/d\varepsilon = \theta(\hat{\sigma}_t, T, \dot{\varepsilon})$. For simple experiments in uniaxial tension or compression [12,13], θ is described well by the following empirical relationship:

$$\theta = \theta_0\left[1 - \frac{\tanh\left(\frac{2\hat{\sigma}_t}{\hat{\sigma}_{ts}}\right)}{\tanh(2)}\right] , \qquad (8)$$

where $\hat{\sigma}_{ts}$ is a saturation value of the thermal component of the threshold stress, achieved at very large strains, and θ_0 is the rate of change of the threshold stress with strain at zero strain, given by

---

[2] The mechanical threshold stress is formally defined to be the flow stress at 0 K. For reasons explained in Ref. 12, it is here referred to 295 K.

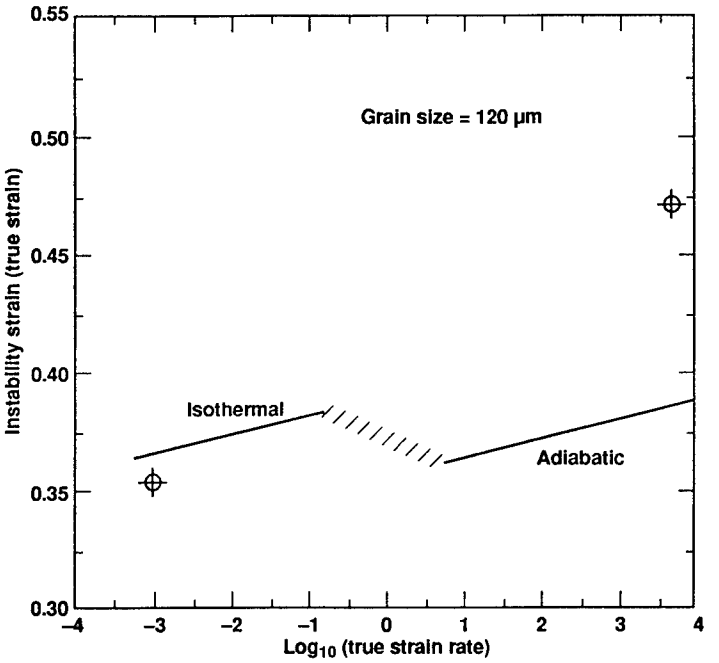

Figure 7. The instability strain for 120 μm copper as a function of true strain rate calculated using the MTS material model. The dynamic test result is not in good agreement with the predicted instability strain, possibly due to the problems associated with measuring load in the test sample under dynamic conditions.

$$\theta_0 = C_1 + C_3 \dot{\varepsilon} \ . \tag{9}$$

The saturation stress $\hat{\sigma}_{ts}$ changes with temperature and strain rate according to

$$\frac{\hat{\sigma}_{ts}}{\hat{\sigma}_{ts0}} = \left(\frac{\dot{\varepsilon}}{\dot{\varepsilon}_{s0}} \right)^{1/n} , \tag{10}$$

Table 2.
Physical constants and non-adjustable model parameters.

Quantity	Description	Value/units
μ	Temperature-dependent shear modulus: $\mu = \mu_0[1 + W_\mu(T - 300)]$	GPa
μ_0	Shear modulus at 300 K	42 GPa
W_μ	$d\mu/\mu dT$ at 300 K	-3.8×10^{-4}
c_p	Temperature-dependent specific heat $c_p = (4.1868/w)(A + 10^{-3}BT)$	J/kg/K
w	Molecular weight	63.546×10^{-3} kg/mol
A	c_p coefficient	5.41 cal/mole
B	c_p coefficient	1.40 cal/mole/K
b	Burger's vector	2.56×10^{-10} m
k/b^3	Boltzmann's constant divided by b^3	8.23×10^{-4} GPa/K
p	Activation energy exponent	2/3
q	Activation energy exponent	1
$\dot{\varepsilon}_0$	Strain rate pre-exponential	10^7 s^{-1}
g_0	Dimensionless activation energy $g_0 = G_0/\mu b^3$	1.6
$\hat{\sigma}_a$	Athermal threshold stress	See Eq. (3)
C_1	θ parameter	2.15 GPa
C_3	θ parameter	3.4×10^{-5} GPa-s
$\hat{\sigma}_{ts0}$	Saturation stress	1.11 GPa
$\dot{\varepsilon}_{s0}$	Saturation strain rate	5.66×10^{10} s^{-1}
A	Saturation activation	0.235

where $n = \mu b^3 A/kT$ and A is a dimensionless activation energy. Values of the various parameters are summarized in Table 2 [12].

The MTS model provides a good fit to the quasi-static test data as shown in Figure 5. The instability strain as a function of grain size was determined numerically using the true strain rate history of the quasi-static tests and assuming isothermal deformation (T = 25°C). The results, shown in Figure Table 2. indicate the experimental and predicted values of the instability strain are in very good agreement.

Using the MTS model the instability strain was calculated for 120 μm copper as a function of (constant) strain rate. For strain rates less than 10^{-1} s^{-1} the deformation was assumed to be isothermal, while for strain rates greater than 10 s^{-1} deformation was assumed to be adiabatic. In the case of adiabatic deformation it was assumed that all of the mechanical work was manifested as an increase in temperature of the deforming material, calculated using a temperature dependent constant pressure heat capacity. A plot of the instability strain versus strain rate is shown in Figure 7. In both the isothermal and adiabatic regimes the calculations predict a linear increase in the instability strain with increasing strain rate, with the adiabatic data displaced to somewhat lower levels of strain. The experimentally determined instability strain under quasi-static loading ($\dot{\varepsilon} = 10^{-3} s^{-1}$) is in good agreement with the predicted value (see also Figure 6). However, the dynamic value ($\dot{\varepsilon} = 5000\ s^{-1}$) is considerably greater than what is predicted. The primary reason for this poor agreement is the uncertainty in the experimentally determined engineering stress-strain curves from which the values of ε_i were determined. Recent work [15] documents the inherent inaccuracy of this stress-strain response and suggests it is due to stress wave reflections in the grips. We are currently working on a 3-D computer model of the tensile Hopkinson bar test to evaluate the dynamic loading of the test sample and accuracy of the engineering stress-strain extracted from the test.

SUMMARY

1. Experimental results clearly indicate an increase in the extent of deformation prior to instability in large grain size material (120 μm) compared with that in small grain size material (15 μm) under quasi-static loading conditions. We do not believe we have a valid experimental determination of the instability strain under dynamic loading due to inherent inaccuracy in the tensile SHPB stress-strain information. However, under dynamic loading the large grain size material exhibited greater extents of deformation prior to the observation of necking and fracture.

2. Under fixed deformation conditions, the instability strain calculated using constitutive descriptions which included a Hall-Petch grain size parameter indicated a decrease in the instability strain with decreasing grain size.

3. Instability strains calculated using the MTS model are in excellent agreement with quasi-static test results. Lack of agreement under dynamic loading is believed to be due to inaccuracy in the experimentally determined values of instability strain.

ACKNOWLEDGMENTS

The authors would like to acknowledge Mary LeBlanc who performed all of the experimental work. This work was performed under the auspices of the U.S. Department of Energy by the Lawrence Livermore National Laboratory under Contract No. W-7405-Eng-48.

REFERENCES

1. E. W. Hart, *Acta Met.* 15, 351 (1967).
2. J. D. Campbell, *J. Mech. Phys. Solids* 15, (1967) p 359.
3. A. Considére, Ann. Ponts Chaussees 9, (1885), p 574.
4. A. K. Gosh, J. Eng. Mat. Tech. ASME. 99, (1977), p 264.
5. J. W. Hutchinson and K. W. Neal, *Acta Met.* 25, (1977), p 839.
6. A. K. Ghosh, Acta Met. 25, (1977), p 1413.
7. N. Christodoulou and J. J. Jonas, Acta Met. 33, 719 (1985).
8. R. W. Armstrong, I. Codd, R. M. Douthwaite and N. J. Petch, *Phil. Mag.* Vol 7, Vol. No. 72, p 45 (1962).
9. N. Hansen and B. Ralph, Acta Met. 30, (1982), p 411.
10. D. H. Lassila, Inst. Phys. Conf. Ser. No. 102, (1989), p 323.
11. D. J. Parry and A. G. Walker, Inst. Phys. Conf. Ser. No. 102, (1989), p 329.
12. W. H. Gourdin and D. H. Lassila, *Acta Met. et Mater,* 39 [10] (1991) 2337-2348.
13. P. S. Follansbee and U. F. Kocks, Acta Met., 36, (1988), p 81.
14. R. W. Armstrong, *J. Mech. Phys. Solids*, 9, (1961), p 196.
15. M. LeBlanc and D. H. Lassila, University of California, Lawrence Livermore National Laboratory, Doc in Prep. (1991).

ADIABATIC SHEAR BANDS IN AISI 4340 STEEL : MICROSTRUCTURAL OBSERVATIONS

C.O. Mgbokwere
S.R. Nutt
J. Duffy

Division of Engineering, Brown University, Providence, RI 02912

Introduction

The phenomenon of strain localization in metals often occurs in situations where the strain rate is high, as in high-speed machining and forming operations, and in ballistic impact. Under these circumstances, metals often develop narrow zones of highly localized deformation known as adiabatic shear bands. Material within the shear band undergoes large plastic strain at a high strain rate, thus causing localized heating and softening. The development of a shear band often initiates failure, and is thus an important practical problem. However, the phenomenon is not well understood, particularly the microstructural events involved in the evolution of shear bands, the possibility of a phase transformation within the shear band because of the heat generated, and the microstructural features that contribute to shear band development. The objective of the present study is to observe the microstructure of shear bands formed during dynamic torsion experiments on AISI 4340 VAR steel (HRC 44), and to determine from these observations the micromechanical processes involved in shear band formation. The approach is to employ transmission electron microscopy to observe microstructures within and adjacent to shear bands, and to correlate these observations with measurements of local temperature, local strain, strain rate, and stress.

Previous studies of shear banding in steels have employed different approaches ranging from experimental observations to mechanical modeling. Thermomechanical instability mechanisms have been invoked to explain the formation of shear bands, and numerical solutions have been developed to model the process. These have been reviewed by Rogers and Shastry [1], Hutchison [2], Shawki and Clifton [3], and LeMonds *et al* [4]. In addition, analytic modeling of shear localization has been performed by Molinari and Clifton [5], Wright and Walter [6], and Anand *et al* [7]. Experimental studies have determined that it might be possible to classify shear bands according to whether or not a phase transformation had occurred [8]. This distinction was

based on the observations of etching behavior, and it was proposed that a phase transformation to untempered martensite (via austenite) occurred within the shear band [9]. Wittman *et al* used TEM observations to investigate the shear band microstructure in AISI 4340 steel subjected to ballistic loading, but found no conclusive evidence of phase transformation [10]. They reported a gradual transition form microcrystalline material at the shear band center to heavily deformed martensite away from the band. Recently Beatty *et al* reported similar observations on AISI 4340 steel deformed by impact of hat-shaped specimens [11]. Extremely small grains were observed within the shear bands, but diffraction patterns revealed an absence of austenite and carbide reflections. It was concluded that no transformation had occurred, and that the shear band material was simply highly deformed martensite.

In the studies described above, the dynamic experiments employed loading configurations that involved compressive and/or tensile stresses in addition to shear. Furthermore, the microscopy observations were often complicated by extremely small grain sizes, as well as the inevitable difficulties of preparing high-quality specimens in which shear bands intersected the transparent regions. In experiments described here, a torsional Kolsky bar is used to impose a dynamic shear strain on a thin-walled tube specimen. The experiment allows for measurement of local shear strain, local strain rate, local temperature, and shear stress. Thin foil TEM specimens are prepared from the tested samples after shear band formation. Comparisons between results from the present study with those of previous studies provide insight into the process of shear band formation and the effects of experimental parameters on shear band microstructures.

Experimental Procedure

The material selected for this investigation was AISI 4340 VAR steel tempered to a hardness of 44 HRC (see Table I). A short thin-walled tubular specimen was machined with a pair of flanges for mounting in a torsional Kolsky bar, as shown in Figure 1 and described in references [12,13]. The bar is made of 6061-T6 aluminum supported along its length by Teflon bearings. High strain rates are achieved by the sudden release of a stored torque at one end of the bar. A torsional loading pulse propagates down the bar toward the specimen while an unloading pulse propagates from the clamp toward the pulley. The pulse transmitted through the specimen provides a measure of the shear stress in the specimen as a function of time, while the reflected pulse provides a measure of the shear strain rate. The stress-strain curve is obtained by integrating the reflected pulse to give shear strain as a function of time.

The same loading apparatus and specimen geometry is employed to obtain quasi-static stress-strain curves.

The torsional Kolsky bar provides an attractive framework for the study of adiabatic shear bands because torsional loading does not involve the problems of necking or barreling associated with tensile and compressive loading. Strain rates of 10^{-4}/sec and up to 5 x 10^{3}/s can be achieved, and large, well-defined strains can be imposed at known stress levels. Furthermore, the geometry makes the specimen accessible to high-speed photography and infrared radiation sensors used for measuring local strain and temperature during dynamic loading. To facilitate the measurement of strain, a grid is deposited on the surface of the specimen prior to loading, as shown in Figure 1a. Displacement of the grid lines gives a direct measure of the local shear strain [14]. Measurement of temperature is accomplished using an array of infrared-sensitive photodiodes with submicrosecond response times. The infrared emission from the specimen is focused on the diode array by an optical system consisting of two spherical concentric mirrors [12,13]. By proper calibration, the infrared output is interpreted as a temperature, and the spatial resolution of the system is approximately 17 μm.

In the present study, tubular specimens were loaded at shear strain rates sufficient to cause shear bands without complete fracture. Disk-shaped samples were cored from the thin-walled tube by electro-discharge machining (EDM) such that the disks were bisected by the shear band. Disks were mechanically polished and lightly etched with a 3% nital solution to reveal the shear band. This procedure rendered the shear band clearly visible and allowed the disk to be positioned on a dimpler stub such that the shear band was centered under the dimpler tool. Final thinning was accomplished by one of two methods. Some samples were dimple polished to a thickness of 15 μm and ion thinned to perforation. Other samples were dimple-polished to 40 μm and electropolished to perforation in a 20°C solution of 10% perchloric acid and 90% acetic acid. Because the perforation generally occurred outside the shear band, the jet-polished samples were ion-milled briefly to extend the perforation to the shear band. Specimens were examined in a Philips EM420T equipped with a double-tilt holder and operated at 120 kV.

Results

Shear Experiments

The typical dynamic stress-strain behavior in shear of AISI 4340 steel deformed at room temperature is shown in Figure 2. The general trend is for

the plastic flow stress to reach a maximum, followed by a slight decrease with further straining. The material then deforms at a nearly constant stress, and finally the stress drops rapidly prior to fracture as shown in reference [14]. The stress-strain response can be divided into three stages, as illustrated by high-speed photography of the grid lines deposited onto the sample by a photoresist technique (Figure 2b). In the first stage, the grid lines are inclined but essentially straight, implying that plastic deformation is homogeneous. A second stage follows in which the grid lines are slightly curved, indicating inhomogeneous deformation (the slope of the grid lines is a direct measure of the shear strain). Finally, in the third stage, the grid lines are discontinuous, implying the formation of a shear band or possibly fracture. During this stage, the local shear strain increases dramatically to several thousand percent, while the nominal shear strain is only about 35%, and the local strain rate in the shear band can exceed 10^5/sec.

One important difference between stages 2 and 3 is not apparent from the results in Figure 2. In stage 3, the strain distribution is strongly dependent on circumferential coordinate, while the distribution in stage 2 depends only on the axial position. It is common to have shear localization in one part of the tubular specimen and not in another, a fact that can be made apparent by photographing a larger region of the specimen. Another interesting aspect of the response that merits comment is the small drop in the stress that occurs during stage 1 at the peak stress. This phenomenon is commonly observed in dynamic torsion experiments on a wide variety of steels and other metals that exhibit shear localization, and it appears to be analogous to a yield point phenomenon. The mobilization of pinned dislocations is one possible explanation for this observation.

The discrete localization that occurs during stage 3 coincides with a sharp drop in the load-carrying capacity of the material and a large increase in local temperature. Using the 17 μm spot size of the optical system, the maximum temperature detected in the sample was 460°C, which occurred at the shear band. Figure 3 shows the detector outputs for a typical experiment on AISI 4340 steel HRC 44. In this test, a shear band formed in the neighborhood of detector 9, which provided the highest output at 155 μsec. The width of the shear band is only approximately half the width of the observed spot size of 17 μm, and thus the recorded output represents an average over the shear band area and adjoining regions that experience less deformation and less heating. Consequently, the detector output corresponds to temperatures lower than the peak temperature in the shear band, and it is calculated that the average temperature inside the shear band is 770°C [15].

Comparisons of results obtained in dynamic deformation ($\gamma \sim 10^3/s$) with quasi-static deformation ($\gamma \sim 10^{-4}/s$) carried out to large strains reveal two significant differences. First, localization of strain occurs only in dynamic deformation, and while the final strain distribution resulting from quasi-static deformation is not entirely homogeneous, the deviations from homogeneous strain are not large. In contrast, dynamic deformation produces initial localization that is relatively wide and then becomes concentrated in a narrow band 5-10 μm in width. Secondly, the final strain at fracture is much smaller for dynamic deformation, an aspect that is undoubtedly related to the localization of shear deformation that occurs. One final distinction between the two types of deformation is the small drop in stress that occurs at the onset of stage 2, which resembles a yield point phenomenon. No explanation is presently available for this observation.

Microstructural Observations

The heat treatment employed for the AISI 4340 VAR steel produced an average prior austenite grain size of 10 to 20 microns and a martensitic microstructure. Figure 4a shows that the heat-treated microstructure prior to testing consisted of packets of martensite laths approximately 1 μm in diameter and fine carbides. Selected area diffraction patterns from prior austenite grains showed a secondary spot pattern superimposed on a primary pattern from the austenite phase (Fig. 4b). The martensite laths within a single packet generally had a single orientation that was related in a specific way to the parent austenite grain. Additional reflections from the small Fe_3C carbide phases of various orientations were also present. These carbides tended to be rod-shaped and nucleated preferentially on the interlath boundaries. Carbides at the lath boundaries had an average length of 630 nm, while those within the laths were ~150 nm in length.

The microstructure within the shear band was characterized by highly elongated grains, as shown in Figure 5a. The grains were approximately 35-90 nm in width and 500-800 nm in length, corresponding to aspect ratios of ~10, and were also aligned parallel to the shear direction, indicated by the double arrow. Grain boundaries were generally sharp and well-defined, and the configurations were typically straight, with only small occasional curvatures, as shown in Figures 5a-b. The grain morphologies bore little resemblance to the lenticular martensite laths shown in Figure 4, which were conspicuously absent in the shear band, and the misorientations across the boundaries were usually large (>10°). The grains were highly dislocated, causing grains in diffracting orientations to appear mottled, a consequence of partial overlap of strain fields of closely spaced dislocations. Extremely fine equiaxed carbides

appeared as faint "speckles" within the elongated grains, as shown in Figure 5b (upper left region), although the rod-like carbide morphologies noted in Figure 4 were no longer present.

Some regions of the shear band showed evidence of dislocation cells within the elongated grains, as shown in Figure 6 (arrow). The cells were 30-90 nm in diameter and approximately equiaxed, and cell interiors were relatively free of dislocations. Microdiffraction experiments revealed misorientations that ranged from $< 5°$ in some cases and $>10°$ in others. Whether the cell structure precedes or follows the development of elongated grains is presently unclear.

Structural analysis of the shear band region was performed by selected area diffraction (SAD). A typical SAD pattern from the shear band is shown in Figure 7. The sharp bright rings, indexed as α-Fe (bcc), exhibited slightly non-uniform intensities, although there was no clear evidence of a deformation texture. The appearance of the rings implies large misorientations between the elongated grains, which is in accord with results of microdiffraction measurements of misorientations between adjacent grains. Faint diffuse rings were also present in the pattern, indicating the presence of small grains of an additional phase. These rings were assumed to correspond to a carbide phase, although efforts to match these rings and the corresponding spacings to a common carbide phase were unsuccessful, and a definitive phase identification was not possible.

Discussion

Torsional shear experiments at high strain rates on AISI 4340 VAR steel (HRC 44) resulted in the formation of shear bands accompanied by a localized increase in temperature. The microstructure within the shear bands was characterized by narrow elongated grains of α-Fe with a fine dispersion of equiaxed carbides. These observations differ substantially from the observations reported by Wittman *et al* and by Beatty *et al* who also performed studies of dynamic deformation of AISI 4340 steel [10,11]. In their work, a stepped specimen geometry was used to produce shear bands, and loading conditions were varied to control the extent of the shear localization. In both studies, the shear band was characterized by a microcrystalline structure that gradually changed to highly deformed martensite outside the shear band. Within the shear band, the local strain was 500% or greater, and equiaxed crystallites were 8-20 nm across. Interpretation of diffraction patterns led to the conclusion that the shear band was highly deformed martensite [10,11]. The authors proposed that carbide dissolution had occurred within the band,

leaving residual carbon in solution that also contributed to local hardening. There was no evidence of transformation to austenite, and the peculiar etching behavior of the shear band was attributed instead to the microcrystalline nature of the band.

In the present study, the shear band microstructure contained narrow elongated grains of α-Fe, but showed no evidence of martensite or austenite. The α-Fe grains were considerably larger and different in shape than those reported by Wittman et al and Beatty et al, despite similar strain rates and materials [10,11]. However, there are several important differences between the present experiments and those reported previously. First, the heat treatments employed were different, resulting in different microstructures and hardnesses of the samples. A second important distinction involves the loading geometry employed, which in the present case resulted in a simple shear stress state, as opposed to a superposition of compressive and shear stresses. Furthermore, the local strain was only ~250%, as opposed to 500-800% in the work reported by Beatty et al. These differences should have strong effects on the process of shear localization and may account for the dissimilar microstructures observed within the shear bands. Interesting issues to explore in the future include the effects of combining compressive stress with shear loading on shear band microstructures, as well as the effects of heat treatments and alloy composition on shear band development.

None of the microstructural investigations reported to date have produced sufficient evidence to support the occurrence of a phase transformation to austenite within the shear band, and it appears unlikely that such a transformation occurs. Nevertheless, there are dramatic changes in the microstructure that require explanation and may help to understand the process by which shear bands form. First of all, the martensitic structure is virtually erased within the shear band and replaced by narrow elongated grains of α-Fe which contain a fine dispersion of second-phase particles, ostensibly carbides. The local strain in the band can be several thousand percent and the local temperature can reach as high as 770°C. This maximum temperature is reached for only a few microseconds before the band is quenched and heat is dissipated to the adjoining material. These conditions appear to be sufficient to form new grains with orientations that are different from and bear little resemblance to the parent martensite packets. The new grains acquire elongated shapes because of the large strains imposed, and have large misorientations relative to adjacent grains. The processes occurring in the shear band involve both large strain and high temperature, conditions that might enable dynamic recovery and/or dynamic recrystallization. The driving force for dynamic recrystallization is the difference in energy stored in two adjacent grains, while the driving force for dynamic recovery is simply the

stored energy of dislocations resulting from plastic flow [16,17]. The first process should result in new strain-free grains, while the latter should result in subgrain formation. Dynamic recovery occurs concurrently with strain and tends to promote structural uniformity, thereby inhibiting the necessary microstructural configurations needed for recrystallization [18]. Dynamic recrystallization on the other hand is inhibited by concurrent strain which creates substructure in grains and thus reduces the requisite differential driving force [18]. These arguments favor the contention that dynamic recovery is the dominant process occurring within the shear bands. However, because the local straining and heating occur simultaneously, the effects of each on the microstructure tend to be convoluted, making unambiguous interpretations difficult. For example, grains that might recrystallize might also be subsequently deformed. Further microscopy study is intended to resolve this issue.

To what extent carbide dissolution occurs within the shear band, as suggested in previous reports [10,11], remains an open question. The additional reflections present in the SAD pattern shown in Figure 7 correspond to a second phase with spacings of 2.63, 1.61, and 1.22 Å, which cannot be associated with any of the common carbide phases such as χ, ε, or Fe_3C. Further diffraction experiments are required to identify this phase, and to resolve the issue of carbide dissolution within the shear band.

Acknowledgments

The research support of the Army Research Office under Grant DAAL03-91-G-0025 and the NSF Materials Research Group at Brown University is gratefully acknowledged. Technical assistance of G.J. Labonte, Jr., is also appreciated.

References

1. H.C. Rogers and C.V. Shastry, "Materials Factors in Adiabatic Shearing in Steels," Ch. 18 in Shock Waves and High-Strain-Rate Phenomena in Metals, ed. by M.A. Meyers and L.E. Murr (1981) 285-298.

2. J.W. Hutchinson, "Viewpoint Set on Shear Bands," *Scripta Metall.* **18** (1984) 421-459.

3. T.G. Shawki and R.J. Clifton, *Mech. of Mater.* **8** (1989) 13-43.

4. J. LeMonds and A. Needleman, *J. Mech. of Mater.* **5** (1986) 339-361.

5. A. Molinari and R.J. Clifton, *J. Appl. Mech.* **5** (1987) 806-812.

6. T.W. Wright and J.W. Walter, *J. Mech. Phys. Solids*, **35** (1987) 701-720.

7. L. Anand, K.H. Kim, and T.G. Shawki, *ibid.*, **35** (1987) 407-429.

8. M.E. Backman and S.A. Finnegan, in Metallurgical Effects at High Strain Rates, R.W. Rohde, B.M. Butcher, J.R. Holland, and C.H. Karnes, eds., Plenum Press, NY (1973) 531-543.

9. C. Zener and H.H. Hollomon, *J. App. Phys.* **15** (1944) 22-32.

10. C.L. Wittman, M.A. Meyers, and H.-R. Pak, *Metall. Trans.* **21A** (1990) 707-715.

11. J.H. Beatty, L.W. Meyer, M.A. Meyers, and S. Nemat-Nasser, US Army Materials Technology Laboratory Technical Report, MTL TR 90-54, Nov. 1991.

12. Y.C. Chi and J. Duffy, Brown University Technical Report, September 1989.

13. K. Cho, Y.C. Chi, and J. Duffy, *Metall. Trans.* **21A** (1990) 1162-1175.

14. A. Marchand and J. Duffy, *J. Mech. Phys. Solids* **36** (1988) 251-283.

15. E.E. Crisman, J. Duffy, and Y.C. Chi, "A Short Rise-Time Probe for Temperature Measurements During the Formation of Adiabatic Shear Bands," *AMD* **102**, Micromechanics: Experimental Techniques, ed. by W.N. Sharpe, Jr., Amer. Soc. Mech. Engrs., 163-178.

16. B. Derby and M.F. Ashby, *Scripta Metall.* **21** (1987) 879-884.

17. A. Korbel and K. Swiatkowski, *J. Metal Sci.* **6** (1972) 60-63.

18. H.J. McQueen, *Mater. Sci. & Engr.* **101** (1988) 149-160.

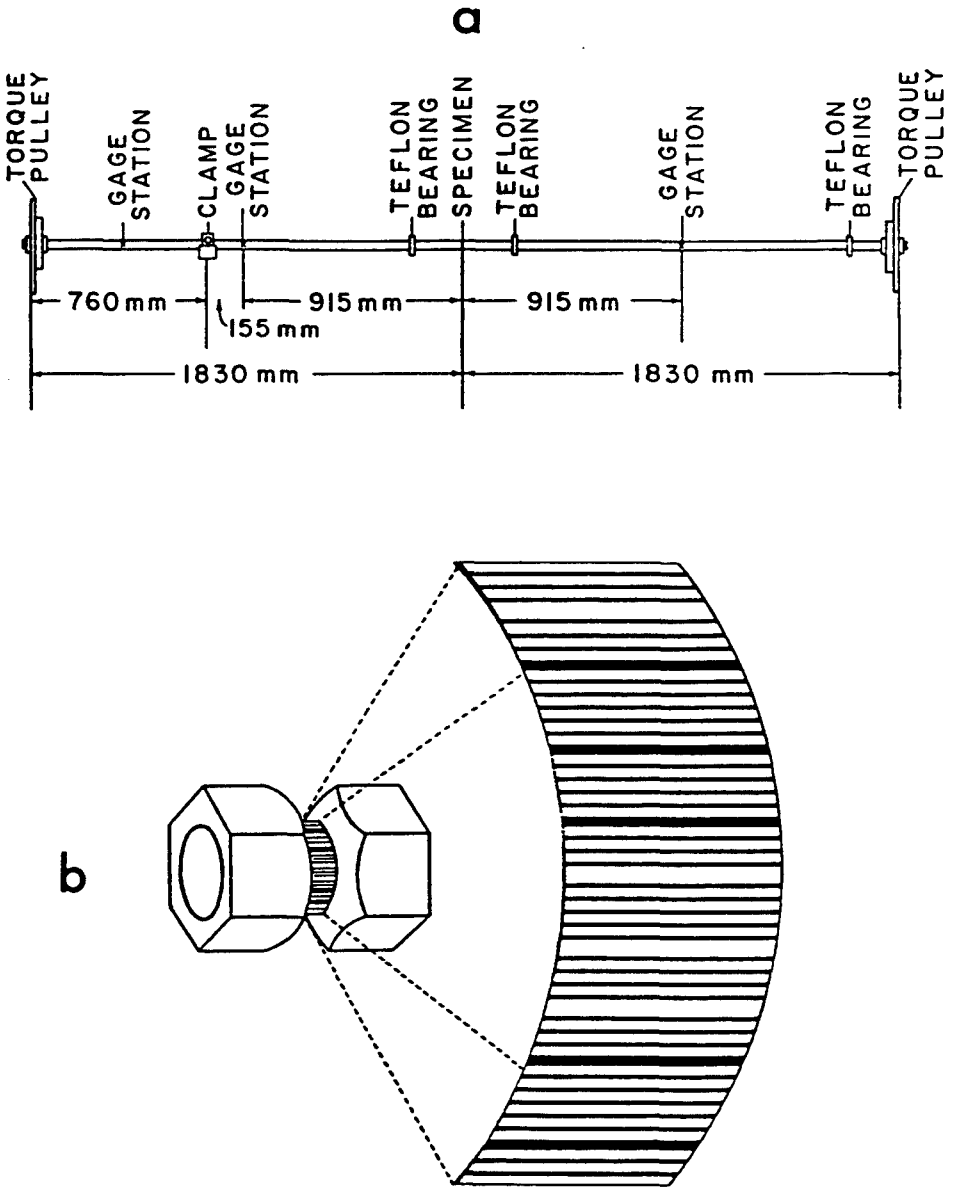

Figure 1. Experimental apparatus and specimen configuration. (a) Schematic of the torsional Kolsky bar. (b) Sketch of the thin-walled tubular specimen with enlargement showing photoresist gridlines deposited on the specimen surface to facilitate high-speed photography measurements of the strain localization.

TABLE 1.

AISI 4340 VAR Steel

(a) Chemical Composition

C	Mn	P	S	Si	Cu	Ni	Cr	Mo	Al	N	O	Hppm
.42	.46	.009	.001	.28	.19	1.74	.89	.21	.031	.005	.001	1.0

(b) Heat Treatment for the 4340 VAR steel (HRC = 44)

	Temperature (°C)	(°F)	Time (hours)	Cooling
Normalize	900	1652	1/2	Air Cool
Austenitize	845	1553	1/2	Oil Quench
Temper	425	797	1/2	Oil Quench

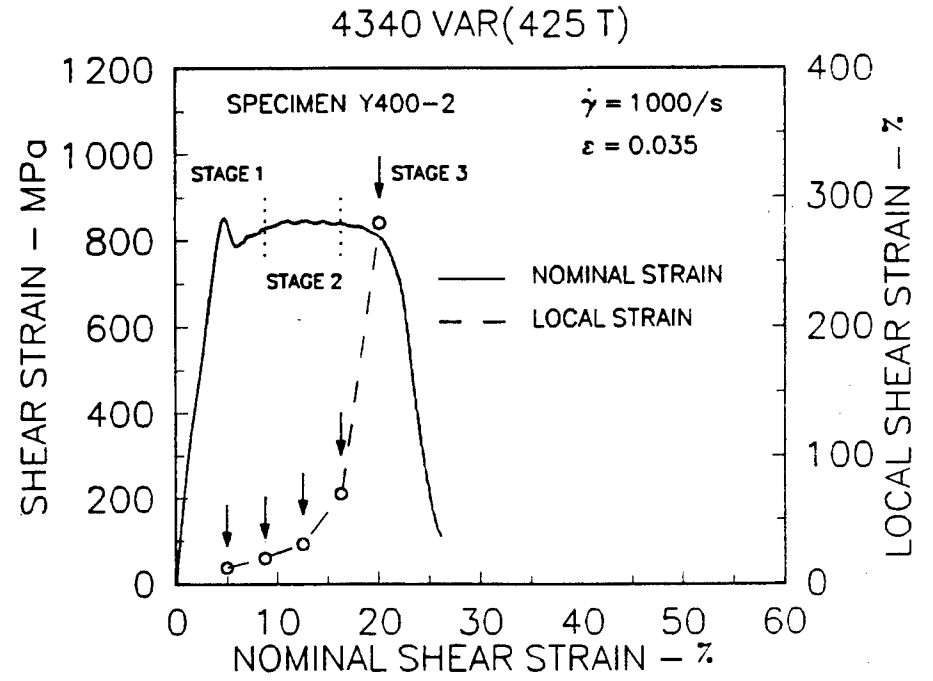

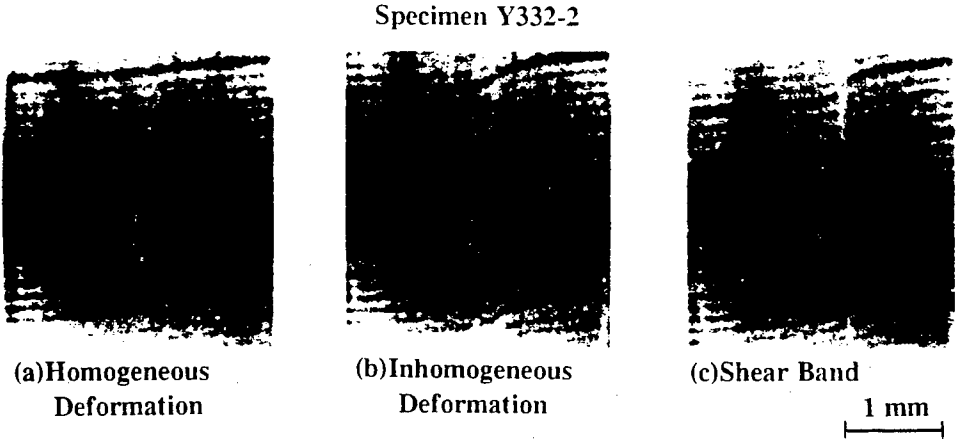

Figure 2. (a) Typical stress-strain curves of 425 temper of AISI 4340 VAR steel, HRC = 44 for dynamic deformation. Local shear strain values are measured from the deformed gridlines using high-speed photography. (b) High-speed photographs of the grid pattern during shear band formation, corresponding to the three stages of dynamic shear localization.

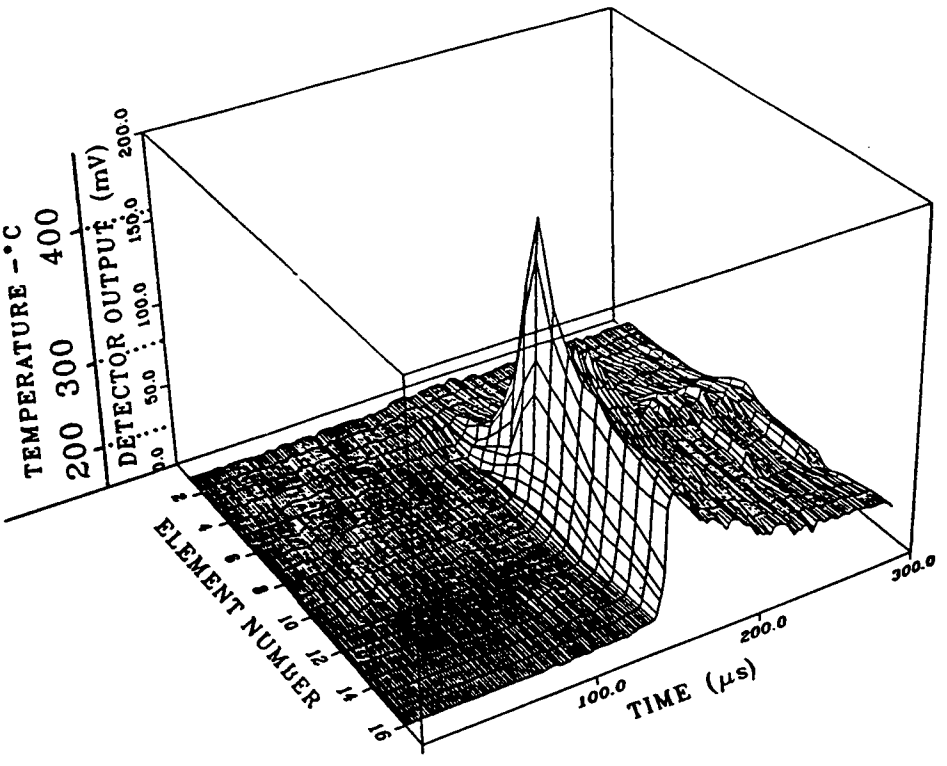

Figure 3. Typical output of infrared detectors during the formation of a shear band in 4340 VAR steel, HRC=44. The 16 elements cover ~0.3 mm or 1/8 of the gage length.

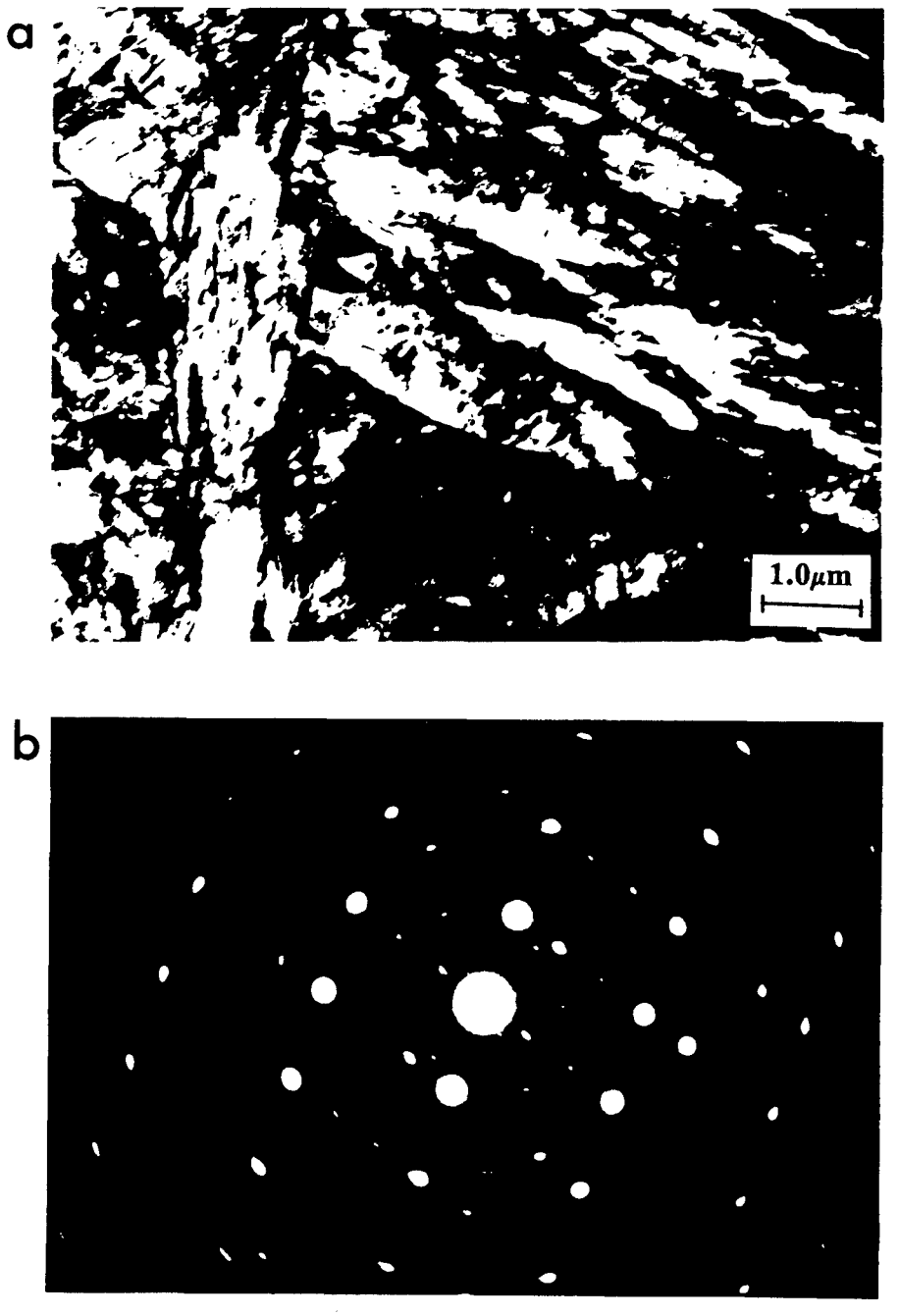

Figure 4 Microstructure of 4340 VAR steel, HRC=44. (a) Bright field image of martensitic lath packets. (b) SAD pattern showing martensite pattern superimposed on primary spot pattern from matrix (B=[113]).

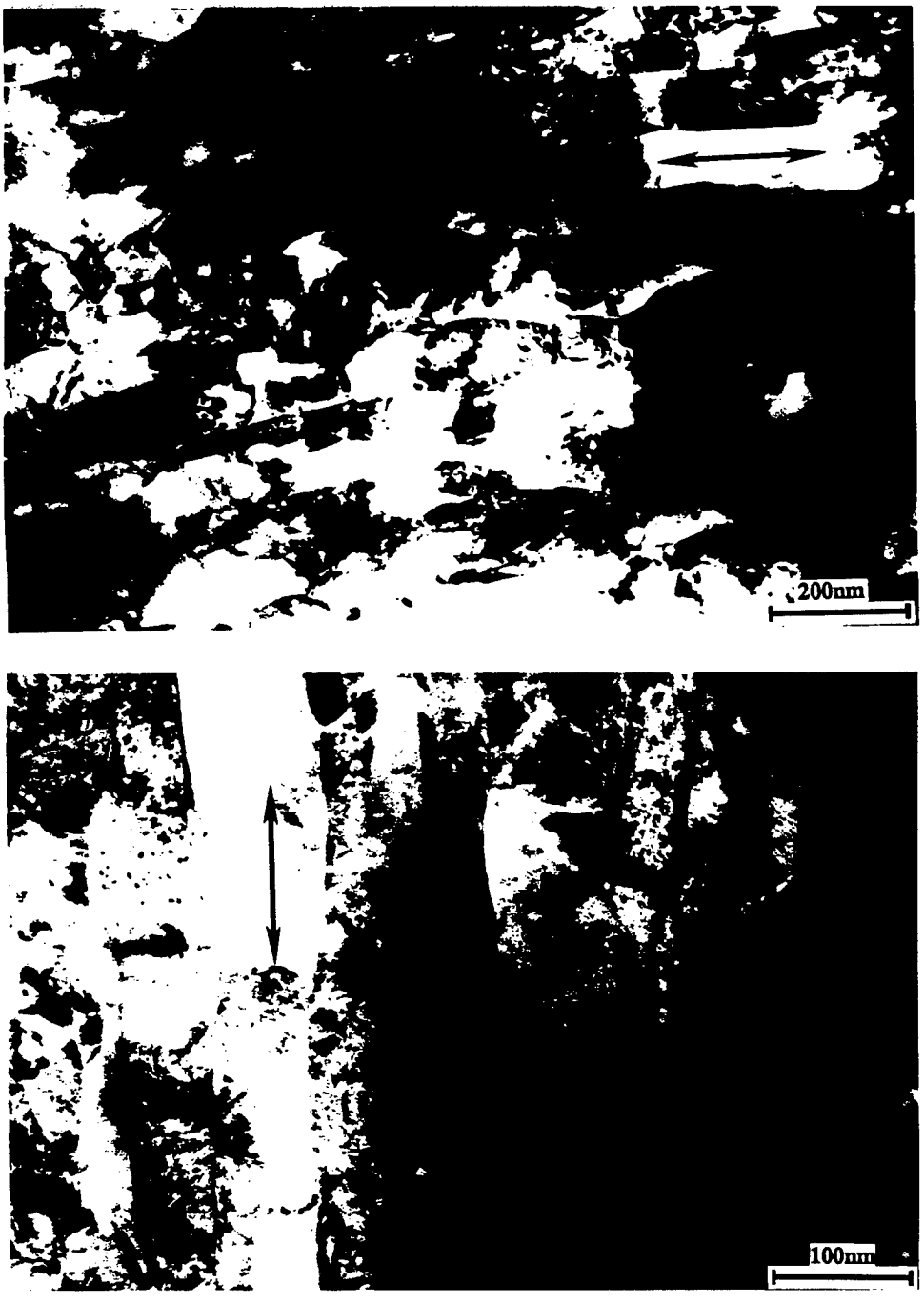

Figure 5. Shear band microstructure. (a) Elongated grains extending in the shear direction (arrow). (b) Enlarged view of elongated grains within the shear band showing finely dispersed second-phase particles, possibly carbides.

Figure 6. Dislocation cell structure within the elongated grains of the shear band. Cell walls are designated CW, while grain boundaries are marked GB.

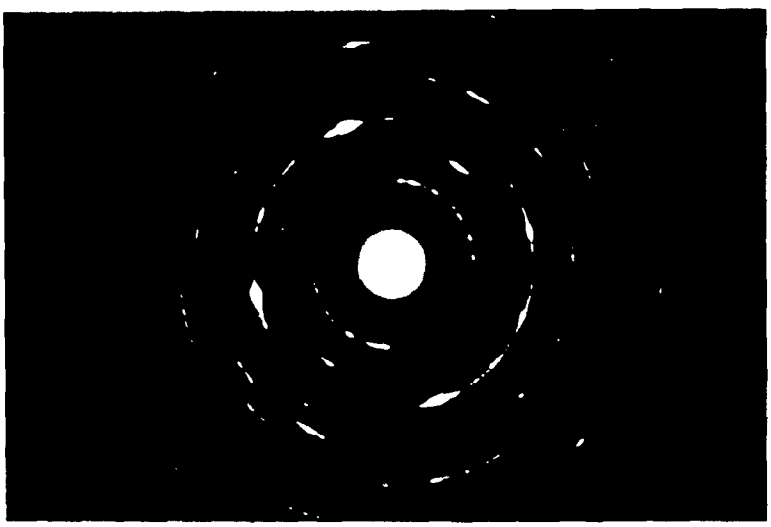

Figure 7. Selected area diffraction pattern from the center of the shear band showing sharp rings corresponding to α-Fe and faint diffuse rings from unidentified microphase particles.

THERMOMECHANICAL SIMULATION OF ADIABATIC SHEAR BAND IN HIGH SPEED FORMING

A. A. Tseng
P. C. Chou
J. Hashemi

Department of Mechanical Engineering and Mechanics
Drexel University
Philadelphia, Pennsylvania 19104
U.S.A.

SUMMARY

The thermomechanical behavior of metallic materials under high speed forming has been simulated with the goal of studying high strain rate deformation phenomena. It has been observed that the adiabatic shear banding is the major deformation mode in high speed forming processes. The micro scale nature of the shear band and the plastic instability associated with it, have made the numerical simulation of this phenomenon extremely difficult. In this paper, a Lagrangian finite element code has been successfully used to simulate the adiabatic shear banding phenomenon for high speed indentation forming conditions. The simulation has shown that when strain hardening together with thermal softening effects are considered, a distinct shear band is formed. Without these thermal softening effects, the generated deformation is continuous with no evidence of localization or shear banding. The thermal effects are simulated by solving the unsteady-state heat conduction equations. An attempt has also been made to use this numerical code to study the high speed machining process. Chip formation in high-speed machining has been simulated to be associated with the formation of a segmented or shear-localized chip and adiabatic shearing is believed to be the principal mechanism controlling the formation of this segmented chip.

Submitted to Army Symposium on Solid Mechanics, November 4-7, 1991, Plymouth, Massachusetts

INTRODUCTION

Adiabatic shear banding is a localized plastic instability phenomenon under high strain rate (impact) or other high speed loading process. During plastic deformation, most of the plastic work is converted to heat. If the strain rate is high, or the material has poor thermal conductivity, there is not enough time for this heat to dissipate to the surrounding material, and the temperature will rise locally. This local rise in temperature will then cause thermal softening. If the thermal softening effect is greater than the strain hardening effect, an unstable localized material flow will occur, where a narrow band is formed within which shear deformation is very large. Adiabatic shear banding phenomenon has been identified as the major deformation mode in high strain rate forming or in high speed machining of metals. It should be noted that a truly adiabatic deformation does not exist, since there is always some heat transfer to the surrounding material. The term "adiabatic" is used mainly due to the fact that a large part of the generated heat remains within the band [1].

The adiabatic shear banding phenomenon was first recognized by Zener and Hollomon [2] in the early forties. Since then, a number of theoretical formulations have appeared in the literature. One of these was performed by Recht [3] who derived an expression for critical strain corresponding to the onset localization, and further determined the value of this critical strain for many materials. Dormeval [4] presented an extensive review of the existing analytical work on adiabatic shear bands. The influence of heat conduction on the onset of shear band formation has been studied by Olsen, Mescall, and Azrin [5]. They concluded that heat dissipation due to conduction does not affect the initiation of the shear band and becomes important only after the band is fully developed.

In recent years, there have been many efforts to simulate shear band formation in forming type deformations using finite element techniques. Ringer [6], using a Lagrangian finite element code, generated shear cracks in plates under impact or high strain rate loading by prearranging the path of crack initiation. Mescall [7] simulated the formation of shear bands under an idealized pure shear loading. Nasser [8] has modeled formation of shear bands in simple tension and compression by introducing an artificial defect and a special hardening coefficient. Needleman [9] used a similar approach to Nasser's to simulate shear band formation in plane strain compression. More recently, Batra and Liu [10] studied shear band formation in plane strain compression by introducing a temperature defect, as opposed to a strength defect as used by Needleman and also by developing a constitutive relationship with strain rate and temperature dependent viscosity.

In machining, earlier theoretical efforts were limited to the low speed orthogonal cutting process. In the forties, Merchant [11] developed the classical shear angle solution. In early fifties, Lee and Shaffer [12] obtained the well-known slip-line solution. Recently, many attempts have been made to simulate the process of machining by finite element techniques [13]. However, none of these simulations has studied machining in the high speed range where the shear band is formed. In fact, the shear band failure mechanism is still not completely understood, especially in its relation to machining. Therefore, study of the high speed machining process with its associated localized shearing phenomena is a logical extension of the current endeavor.

In the present research, the shear band phenomenon in both the high speed

forming and machining of metals is studied. A single material constitutive relationship is imposed in the whole domain and the coupled thermomechanical effect is used directly to simulate the unstable localized softening behavior without introducing any artificial defect or a special material hardening parameter. A Lagrangian finite element code is used in modeling a high speed indentation forming process. Effort is also made to use this code to study the high speed machining process. Chip formation in high-speed machining has been studied by simulating the formation of a segmented chip. The effects of the mesh sensitivity and the heat conduction effects in relation to prediction of shear band width and the onset of instability are also discussed. Additional results of this research may be found in Chou, et al. [14].

ADIABATIC SHEAR BAND

As mentioned earlier, adiabatic shear, also known as catastrophic shear, occurs when the local rate of change of temperature has a negative effect on strength which is equal to or greater than the positive effect of strain hardening. It usually occurs at very high deformation rates where the heat generated by the localized deformation is large enough to upset the flow stress increase and a flow stress decrease results [2]. A number of theoretical formulations have appeared in the literature to describe the critical strain corresponding to the onset localization. Most of the theoretical formulations are based on the flow stress, τ,

$$\tau=\tau(\gamma,\dot{\gamma},\theta) \tag{1}$$

where τ is a function of the shear strain, γ, shear strain rate, $\dot{\gamma}$, and temperature, θ. The differential of the shear stress is then given by,

$$d\tau=\left[\left(\frac{\partial\tau}{\partial\gamma}\right)_{\dot{\gamma},\theta} d\gamma+\left(\frac{\partial\tau}{\partial\dot{\gamma}}\right)_{\gamma,\theta} d\dot{\gamma}+\left(\frac{\partial\tau}{\partial\theta}\right)_{\gamma,\dot{\gamma}} d\theta\right] \tag{2}$$

It is believed that plastic instability will occur when

$$d\tau=0. \tag{3}$$

Equations (2) and (3), together with an appropriate material model, Eq. (1), will provide a critical strain, or strain rate, at which instability will be initiated.

Various experimental techniques have been developed to study the shear banding effect in different materials. A comprehensive survey of those experimental procedures and the materials studied has also been presented by Dormeval [4].

There have been numerous attempts to model the formation of adiabatic shear bands in metals. Chou, et al. [14] recently presented a survey on the numerical work towards simulation of adiabatic shear banding. Ringer [6], using EPIC-2 code, simulated target plugging in plates under impact. A node

splitting technique was used to simulate shear cracks. The results obtained by Ringer, presented a jagged splitting pattern along the plugged surface. Mescall [7] simulated the formation of shear bands under an idealized pure shear loading using HEMP code. They showed that shear bands could occur in materials whose constitutive description included a plastic instability (a maximum in its true stress- true strain curve) as opposed to those without such instability. Nasser [8], Needleman [9], and Batra and Liu [10] have all simulated shear band formation under simple compression and tension conditions. The common assumption in all of the above simulations has been the preexistence of a defect in the workpiece. In all cases, an artificial defect was introduced to the geometry of the simulation and in all cases simulated shear bands originated from the point of inhomogeneity. The nature of the defect, based on material hardness, strength, or temperature differs from one analysis to the other.

The general nature of plastic instability has been well demonstrated by these finite element simulations. But simulations of more complicated geometries, those other than simple tension and compression, and without artificial defects, have not appeared in the literature.

NUMERICAL MODELING

Results of DEFEL code calculation are presented in this paper. DEFEL [16] is a two-dimensional finite element program originally designed for dynamic analysis of impact and explosive detonation problems in a continuum body. The program is based on a Lagrangian finite element formulation, where the equations of motion are integrated directly and explicitly.

In the present research, a modified version with the heat transfer capability has been used to study the thermomechanical behavior of shear band formation. In this version, a slide-line algorithm has also been implemented to simulate crack initiation and propagation in metals. The latter option has been utilized together with a simplified fracture criterion based on ultimate strain to simulate segmented chip formation in high speed machining. Originally, non linear material behavior was included in the program to account for elastic-plastic behavior, work hardening, and strain rate effects. Recently, a more complete material model which includes thermal softening effects (the Johnson-Cook model) has been included in the code with the proper material constitutive equations to simulate shear band formation. In the next section, the basic formulation of the code, the heat transfer computation, the slide-line algorithm, and the constitutive relationship will be discussed.

Formulation

The DEFEL is based on the hydro-code formulation similar to that used in EPIC code [15]. The program uses a sliding surface algorithm to simulate contact between tool and work-piece and any number of surfaces that come in contact [16]. Complex geometrical shapes can be represented simply by providing an adequate assemblage of elements. The basic element used in DEFEL code is the triangular constant strain element. This makes DEFEL well suited to simulate severe deformation which often occurs in metal forming

problems and shear banding. Following standard finite element procedures [17], the equations of motion for the finite element model can be written as

$$M\ddot{q} = f - p \tag{4}$$

where **M** is the mass matrix, **q** is the nodal displacement vector, **f** is the external force vector, and **P** is the equivalent nodal force vector calculated from the element stresses. The superposed dots denote differentiation with respect to time. In general, the vector **P** is a function of the current nodal displacements and velocities for non-linear problems, and can be expressed in terms of the current element stress vector **s** by

$$p = \sum \int_{V_e} B^T \sigma \, dV \tag{5}$$

where **B** is the strain-displacement matrix. The advantage of this formulation is that the process of assembling global stiffness matrix can be bypassed if an explicit integration scheme and a lumped mass matrix are used. In that event, the system of Equations (5) are uncoupled into

$$m_i \ddot{q}_i = f_i - p_i \tag{6}$$

in which the subscript i corresponds to the ith component of the nodal displacement vector **q**. An explicit integration scheme with central difference quadrature is used in the DEFEL code to integrate the differential equations in time. For this purpose, Equation (4) is rewritten in the following form

$$m_i \ddot{q}^t = f_i^t - p_i^{t-\Delta t} \tag{7}$$

where Δt is the time increment, and the left superscript t refers to the time instant t. The velocity and displacement of the ith node are then given by

$$\dot{q}_i^{t+0.5\Delta t} = \dot{q}_i^{t-0.5\Delta t} + \Delta t \, \ddot{q}_i^t = \dot{q}_i^{t-0.5\Delta t} + \Delta t \left[\frac{f_i^t - p_i^{t-\Delta t}}{m_i} \right] \tag{8}$$

and

$$q_i^{t+\Delta t} = q_i^t + \Delta t \, \dot{q}_i^{t+0.5\Delta t} \tag{9}$$

respectively. Combining Equations (7), (8) and (9), the displacement of node i at time instant $t+\Delta t$ can be obtained as

$$q_i^{t+\Delta t} = \frac{(\Delta t)^2}{m_i} \left[f_i^t - p_i^{t-\Delta t} \right] - 2q_i^t - \Delta t \, q_i^{t-\Delta t} \tag{10}$$

Due to the conditionally stable nature of the explicit integration scheme, the

time increment, Δt, may need to be readjusted at each time step to ensure numerical stability. In DEFEL code, the following stability criterion is used [16]

$$\Delta t_{new} = \frac{0.7\, H_{min}}{\sqrt{\frac{\lambda + 2\mu}{\rho}}} \tag{11}$$

In equation (11), H_{min} is the minimum height of the element, ρ is the density, and λ and μ are the Lame constants of the material.

The spherical and deviatoric strain rates are computed from the nodal velocities, the stress increments and total stress components are then computed. Proportional unloading technique is used to pull the over-estimated stress components back to the current yield surface, and various work hardening and softening models [16] can then be used to establish a new yield surface. This process is repeated at each time increment.

Heat Transfer Calculations

Capability has been modified to account for heat conduction. Due to the nature of the formulation of the code, the mechanical and thermal equations were uncoupled and integrated independently. It was assumed that temperature varies linearly within the element. The heat flow was obtained from,

$$q_r = -k \frac{\partial T}{\partial r}$$
$$q_z = -k \frac{\partial T}{\partial z} \tag{12}$$

where k is the thermal conductivity of the material. These equations represent the rate per unit area at which heat is flowing through the element. The incremental increase in thermal energy at the nodes, or nodal heat forces, are obtained by integrating the heat flow with respect to area and time, Equation (13).

$$\Delta Q_i = \pi \bar{r} (q_r b_i + q_z c_i) \Delta t + \Delta Q^p \beta .0 \tag{13}$$

where r is the average elemental radii and Δt is the integration time increment. ΔQ^p is the plastic work generated within the element during the previous integration cycle. The updated temperatures of the nodes are then calculated by,

$$T_i^{t+\Delta t} = T_i^t + \sum Q_i / M_i C_{pi} \tag{14}$$

where, $T_i{}^{t+\Delta t}$ and $T_i{}^t$, are the temperatures of node i at time $t+\Delta t$, and t, respectively. ΣQ_i is the sum of the heat contributed by all elements which

contain node i, M_i is the mass of node i, and c_{pi} is the specific heat of node i. The integration time increment based on the heat conduction portion of the computations requires that

$$\Delta t < \rho c_p h_{min}^2 / 4k \tag{15}$$

where ρ is the density, c_p is the specific heat, and h_{min} is the minimum altitude of the element. However, since the time increment governed by the mechanical portion is much smaller than the thermal portion, it is selected as the controlling increment.

Johnson-Cook Material Constitutive Model

The Johnson-Cook model [18] presents a constitutive equation for material subjected to large strains, high strain rates, and high temperatures. This constitutive equation is used for simulations of high speed indentation forming and machining. The basic form of the model is well suited for numerical computations since the variables used in the model are calculated in most dynamic codes. For this model, the flow stress, σ, is determined by the equation

$$\sigma = [\, A + B\, \varepsilon^{n} \,] \, [1 + C \ln \varepsilon^{*} \,] \, [1 - T^{*m} \,] \tag{16}$$

where ε is the equivalent plastic strain; ε^* is the normalized plastic strain rate; and T^* is the homologous temperature, $(T - T_{room})/(T_{melt} - T_{room})$. The expression in the first bracket gives the stress as a function of strain with strain hardening coefficient B and strain hardening exponent n. The expression in the second bracket gives strain rate effects and the third bracket gives thermal softening effects. Here C is the strain rate coefficient and m is the thermal softening constant.

Material data for this model are available for OFHC copper, Cartridge Brass, Nickel 200, Armco iron, Tungsten alloy and DU-.75 Ti [18]. These data have been obtained from tension tests with varying strain rates, static tension tests, dynamic Hopkinson bar tensile tests and Hopkinson bar tests at elevated temperatures. An evaluation of the model was made by performing cylinder impact tests and comparing the results of the computer simulation to results of those tests using the Johnson-Cook model. The results showed good agreement for Armco iron and 4340 steel and reasonable agreement with OFHC copper.

HIGH SPEED INDENTATION FORMING

A finite element modeling of the high speed indentation forming process was performed, as shown in Figure 1. More details of the modeling results may be found in [14]. In this set-up the impactor, penetrator, and stopper were modeled as rigid material. The work-piece material was tool steel and the corresponding material constants of tool steel based on the Johnson-Cook

constitutive equation are listed in Table 1.

MATERIAL	$\sigma = (A+B\varepsilon^{n})(1+\ln \dot{\varepsilon}^{*})(1-T^{*})^{m}$					Thermal Cond.	Specific Heat
	A	B	n	C	m	k	C_p
	Gpa	Gpa	---	---	---	J/m.sec. C	J/kg. C
S-7 TOOL STEEL	1.538	0.475	0.180	0.012	1.0	45.0	486.0

TABLE 1. Material properties of S-7 tool steel based on Johnson-Cook equation.

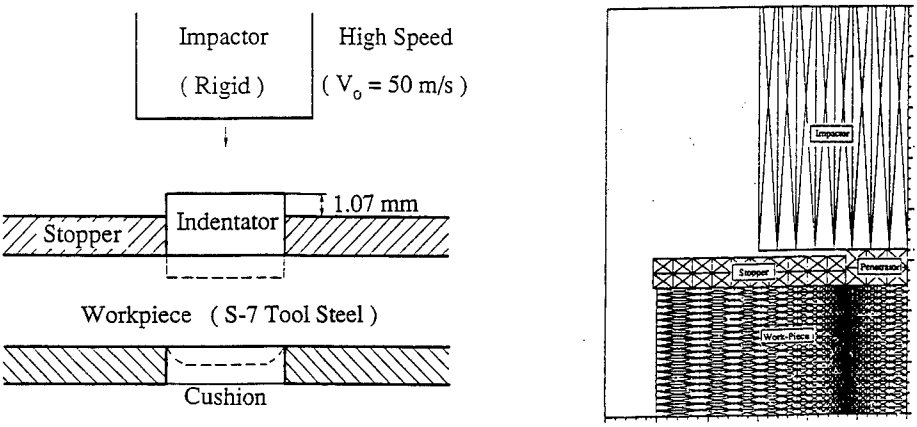

(a) Controlled depth-of-indentation apparatus

(b) Finite-element representation

FIGURE 1. Initial geometry and mesh assembly of the high speed forming process

An initial velocity of 50 m/s was assigned to the impactor together with a specified depth of penetration of 1.07 mm. Initially, a distribution of mesh was used such that through a gradual decrease in mesh size, the smallest column of mesh would be situated directly below the edge of the impactor.

Adiabatic shear banding was successfully simulated, Figure 2, and comparison with experimental results were encouraging. In this simulation, the effects of heat conduction were neglected and the process was assumed to be fully adiabatic. It was assumed that 95% of the work done due to plastic deformation would be converted to heat.

The examination of the calculated results indicated that the temperature rise within the shear band is close to the melting temperature of the workpiece material, and it drops sharply to the materials' initial temperature at the neighboring elements of the shear band region. The same is also true about the effective plastic strain of the elements.

In order to verify that the formation of the shear band was the result of the thermal softening effect, an identical simulation was performed by removing the

thermal softening portion of the equation. The results did not show any strong evidence of shear banding and the deformation was spread to a larger region within the workpiece near the edge of impact, Figure 3.

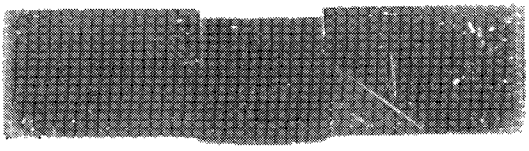

(a) Experimental observation of shear bands in forming process

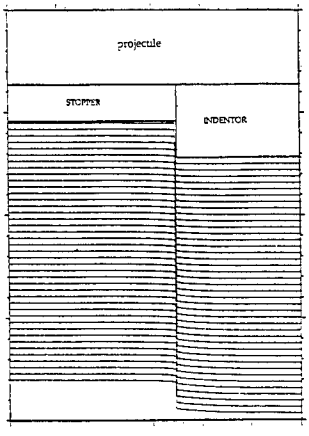

(b) Computer simulation of shear band with thermal softening effect, horizontal mesh lines are plotted only

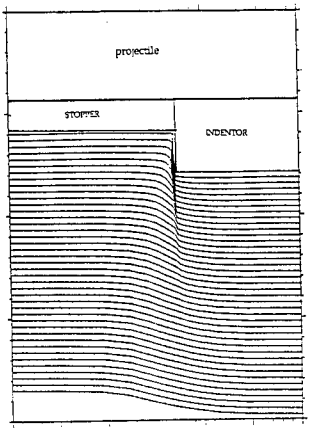

(c) Computer simulation of shear band without thermal softening effect, horizontal mesh lines are plotted only

FIGURE 2. Adiabatic shear band formation.

Further simulations were performed to determine the effect of mesh size and shape on the outcome of the simulation. It was observed that the height to base ratio, or aspect ratio, of the triangular elements used in this simulation, plays an important role in determination of the direction of the shear band propagation. For an aspect ratio of greater than 1.5, the shear band was observed to tilt towards the center of the workpiece. This is clearly not physical and it indicates that for proper simulation, not only should the mesh size be small, but the aspect ratio should be less than 1.5.

In the second round of simulations, a region of uniform fine mesh was placed below the edge of the impactor and the simulation was performed under identical conditions, Figure 4. The objective was to simulate the shear band formation without any bias due to uneven mesh size. The results did not show any significant difference between the two simulations.

Another study was performed to investigate the effect of the magnitude of

the mesh size. It was not clear whether a smaller mesh size would yield different shape and width of the shear band. As a result, three different mesh sizes were selected, $d_1 = 0.0100$ mm, $d_2 = 0.0050$ mm, and $d_3 = 0.0025$ mm. Figure 5 shows the results for the case where smallest mesh size was 0.005 mm. The shapes of the shear band from the two smaller meshes, d_2 and d_3 were very similar, indicating that any further reduction of mesh size could not alter the shape.

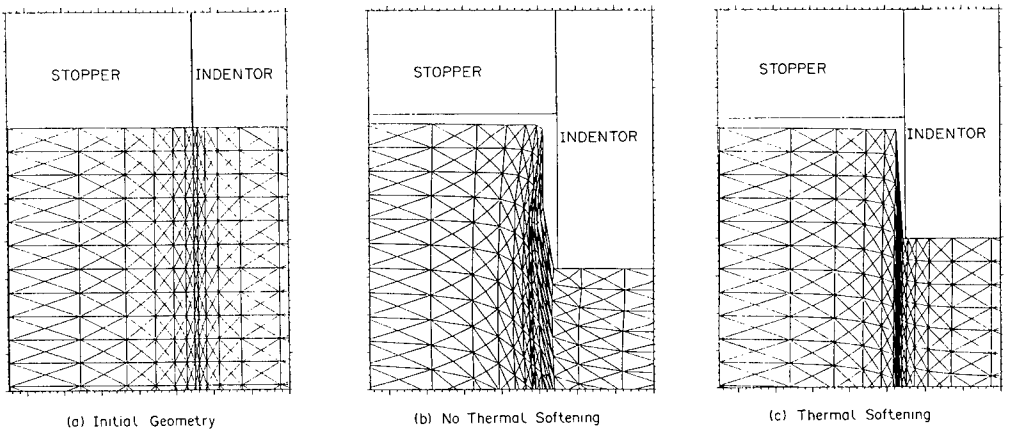

FIGURE 3. Simulation of high speed forming disregarding the thermal softening effect.

Also, the corresponding temperature distribution of those simulations, revealed that no significant differences between the two temperature fields would be observed by further reduction of the mesh size (Figure 6).

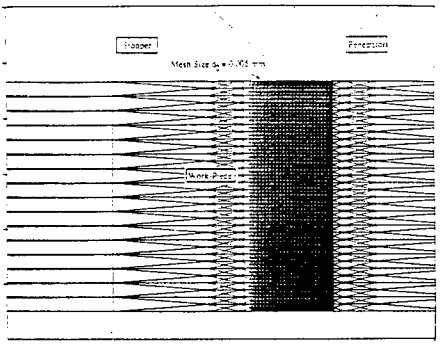

FIGURE 4. Initial geometry of forming with uniform mesh in the shear band region.

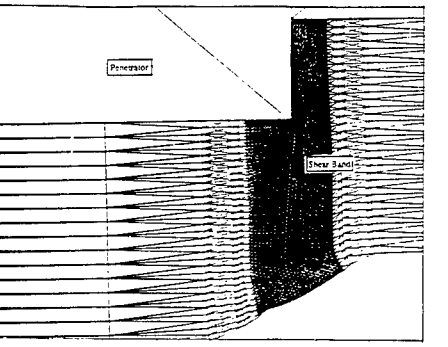

FIGURE 5.Shear band simulation using uniform mesh size of 0.005 mm

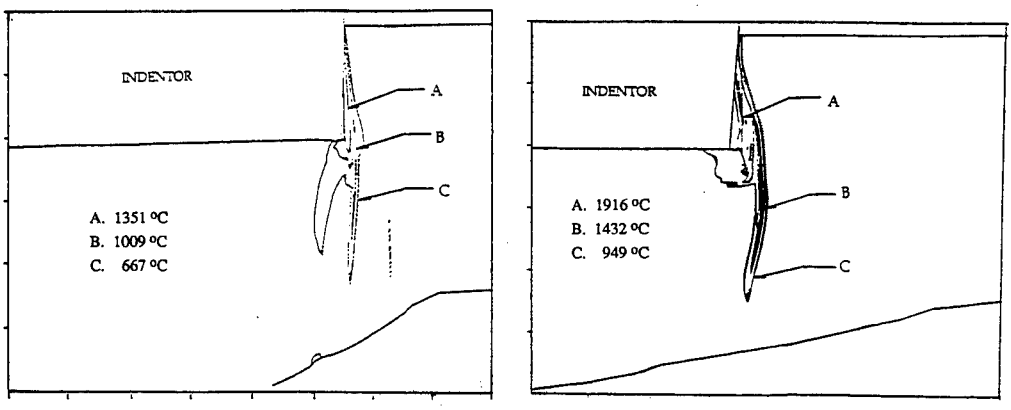

(a) $d_2 = 0.005$ mm

(b) $d_3 = 0.0025$ mm

FIGURE 6. Temperature distribution in the shear band region.

However, the width of the shear band, in all cases, is always controlled by the width of one column of mesh directly below the edge of impactor. Therefore it is not clear that the simulated width is due to the finite size of the mesh, or is the true behavior of the mechanics. The computing time of the smallest mesh size, d_3, was close to 3.5 hours on CRAY-YMP computer. This long calculation time, which is mostly due to severe deformation of the elements, makes further reduction of mesh size impractical.

Another factor that could affect the formation of the shear band was the heat transfer effect. A thermomechanical version of DEFEL code was utilized to simulate this phenomenon. The thermal properties used, were those of tool steel, k = 45 J/m-s-^{o}C , and Cp = 486 J/kg-^{o}C. Figure 7 shows the comparison between the temperature fields of the fully adiabatic, (k = 0), and the non-adiabatic cases.

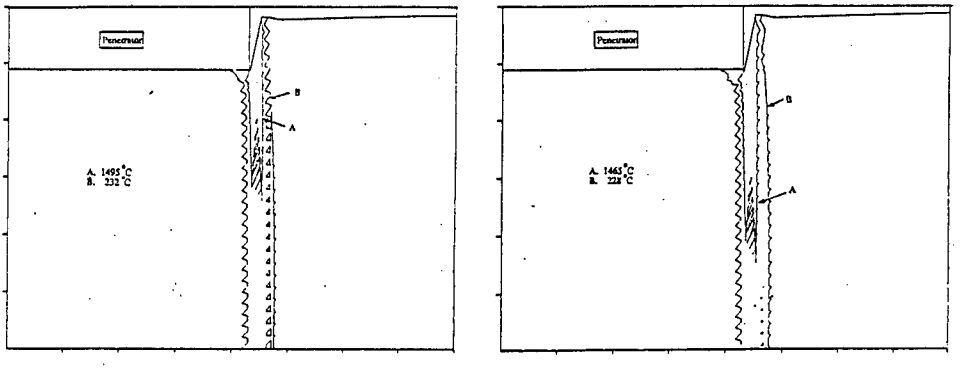

(a) Temperature field for a fully adiabatic case, k = 0.

(b) Temperature field for a non-adiabatic case, k = 45 J/m-s-°C.

FIGURE 7. Thermomechanical simulation of shear bands.

In both simulations shear bands were formed at the same stage of the

forming process and no significant difference between the two cases was observed. This is consistent with the general belief that in high strain rate processes heat dissipation prior to onset of instability is small and does not affect shear banding significantly. It should be mentioned that Figure 7 shows a very small region close to the surface of the contact and the minor differences in the temperature field are extremely local.

To assure the proper execution of the thermomechanical code, a simple heat transfer calculation with the material constants of tool steel was performed and compared with the existing analytical solutions. The analytical solution of transient heat flow in a semi-infinite solid was used to solve the problem of a semi-infinite axisymmetric body undergoing a sudden jump in temperature at the surface. The calculations showed that at a distance of 0.3 microns away from the surface, the temperature changed by only 2% after 5 ms. The above problem was also solved by DEFEL code and excellent agreement was achieved. In current forming problem, the shear band was formed within the first 5 ms. This indicates that in the deformation stage of the shear band, heat conduction plays a minor role.

HIGH SPEED MACHINING

In this section, the DEFEL code is applied in simulation of high speed machining processes with fragmented chips. A plane strain simulation of orthogonal metal cutting processes at high speeds was performed. Figure 8, shows the initial geometry of that simulation, in which a coarse mesh is used to keep the geometry as simple as possible. For more details, please see [19].

An elastic-perfectly plastic material constitutive equation was used to simulate the work-piece material and the cutting tool was assumed to be rigid. A cutting velocity of 25 m/s was assigned to the cutter. The simulation was primarily intended to provide numerical results to model continuous and segmented chip formation in high speed machining of metals. Fracture elements together with the sliding surface algorithm were implemented to achieve the simulation objectives. Cracks would initiate at nodal points where the fracture criterion was exceeded, and then extend in a direction normal to the principal stress direction at that point. The fracture criteria used for this simulation was based on the ultimate plastic strain of the material. The material used was an aluminum alloy with the material constants listed in Table 2.

MATERIAL	Shear Modulus	Yield Strength	Bulk Modulus
	G	Y_o	K
	Gpa	Mpa	Gpa
ALUMINUM	27.6	517	76.6

TABLE 2. Material constants used in machining simulation

The analysis of the results, in the case of continuous chip generation,

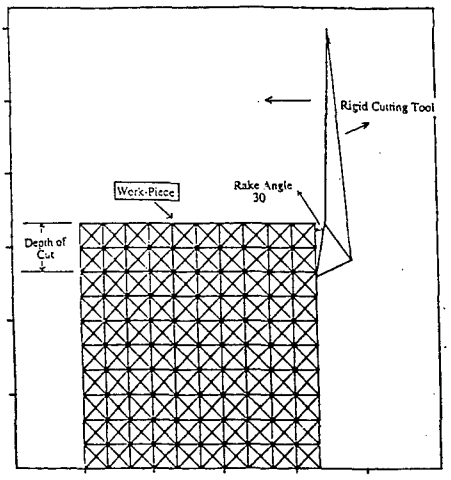

FIGURE 8. Initial mesh for the plane strain simulation of high speed metal cutting.

Figure 9(a), showed that the material separating from the workpiece and in contact with the cutting tool undergoes severe shearing strain. The corresponding experimental results of continuous chip formation is presented in Figure 9(b).

Through the application of a simplified fracture criterion based on ultimate plastic strain, segmented chip formation was simulated as shown in figure 10(a). The corresponding experimental observation of the segmented chip formation is presented in figure 10(b). The shearing strain is large along the shear plane which extends from the cutting edge to the free surface of the workpiece. These results indicate that through the use of a more accurate material model, such as that of Johnson-Cook, advances could be made towards proper simulation of segmented chip formation due to adiabatic shear banding and the corresponding localization of strain and temperature.

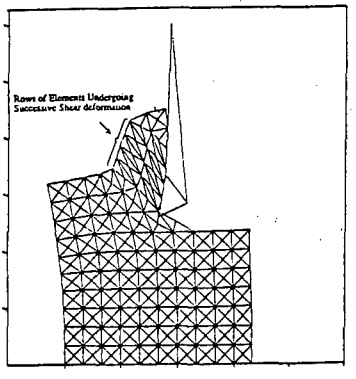

(a) Computer simulation of continuous chips

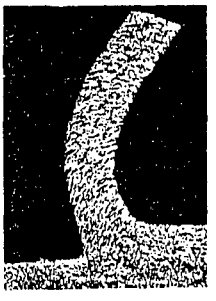

(b) Corresponding experimental result

FIGURE 9. Experimental and computer simulation of continuous chip formation.

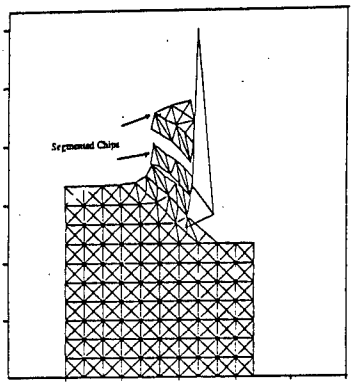

(a) Computer simulation

(b) Experimental observation

FIGURE 10. Simulation of segmented chip formation in high speed cutting of metals.

CONCLUSION

Adiabatic shear bands, as a mode of dynamic failure in high speed forming, were successfully simulated by finite element code. The simulation under both adiabatic and non-adiabatic cases indicated that heat conduction effects were minimal at the early stages of localization. There is simply not enough time for the heat to diffuse to other regions of the material. One could conclude that the above fact is the basis for shear band formation. The width of the formed band was not accurately predicted in these simulations and it was always constrained to one column of mesh regardless of the size of the mesh. The heat conduction simulation did not show any influence on the width of the shear band, however more investigation is necessary to determine the factors controlling the width of a formed shear band.

The initial simulations of the high speed machining process indicated that the numerical scheme is capable of simulating this complex process. However, for realistic results more accurate constitutive equations that include temperature and strain rate effects should be utilized. The effectiveness of the Johnson-Cook equation as a viable candidate for high strain rate processes is well demonstrated in this paper. The application of this equation together with a reasonable mesh density could make the simulation of metal cutting operations possible.

The formation of shear bands depends on the work-hardening and thermal softening properties of the workpiece. Although some of these properties have been documented as mentioned in the section on the Johnson-Cook Model [18], for most metals the thermal softening behavior under high strain rate loading are not available. The split Hopkinson bar tests for the selected materials will be conducted to obtain the needed information for the numerical simulation.

ACKNOWLEDGEMENT

The authors wish to express their sincere appreciation to Prof. K. P. Jen of Villanova University for his helpful discussions. Thanks also to Mr. S. D. Li for his finite element programming assistance and Mr. D. J. Li for his help in shear band testing.

REFERENCES

1. Rogers, H.C., "Adiabatic Plastic Deformation," Ann. Rev. Mater. Sci., Vol. 9, pp. 283-311, 1979.
2. Zener, C.and Hollomon, J. H., "Effect of Strain Rate on Plastic Flow of Steel," ASME J. Applied Mech., Vol. 15, pp. 22-32, 1944.
3. Recht, R.F., "Catastrophic Thermoplastic Shear," ASME J. Applied Mech., Vol. 18, pp. 189-193, 1964.
4. Dormeval, R., "The Adiabatic Shear Phenomenon," in Materials at High Strain Rate, pp. 47-67, Elsevier, London, 1987.
5. Olson, G. B., Mescall, J. F., and Azrin, M., "Adiabatic Deformation and Strain Localization," in Shock Waves and High-Strain-Rate Phenomena in Metals, pp. 221-247, Plenum, New York, NY, 1981.
6. Ringers, B. E., "Modeling Adiabatic Shear," Tec. Rep. BRL-TR-2662, US Army Ballisitc Research Laboratory, Aberdeen, MD, 1985.
7. Mescall, J., "Stress and Deformation States Associated With Upset Tests in Metals," in Computational Aspects of Penetration Mechanics, pp. 47-62, Springer-Verlag, Berlin, 1983.
8. Nasser, N. S., "Micromechanics of Failure at High Strain Rates: Theory, Experiments, and Computations," Tec. Rep. BRL-TR- 2662, US Army Ballistic Research Laboratory, Aberdeen, MD, 1985.
9. Needleman, A., "Dynamic Shear Band Development in Plane Strain," ASME J. Applied Mech., Vol. 56, pp. 1-99, 1989.
10. Batra, R. C.and Liu, D., "Adiabatic Shear Banding in Plane Strain Problems," ASME J. Applied Mech., Vol. 56, pp. 527-534, 1989.
11. Merchant, M. E., "Mechanics of the Metal Cutting Process,"J. Appl. Phys., Vol. 16, pp. 267-318, 1945.
12. Lee, E. H. and Shaffer, B. W., "The Theory of Plasticity Applied to a Problem of Machining," ASME J. Applied Mech., Vol. 18, pp. 405-413, 1951.
13. Wang, B. P., Sadat, A. B., and Twu, M. J., "Finite Element Simulation of Orthogonal Cutting," in Materials in Manufacturing Processes, MD-Vol. 8, pp. 87-91, American Society of Mechanical Engineers, 1988.
14. Chou, P. C., Hashemi, J., Chou, A. and Rogers, H. C., "Experimental and Finite-Element Simulation of Adiabatic Shear Bands in Controlled Penetration Imapct," Int. J. Impact Engng, Vol. 11, No. 3, pp. 305-321, 1991.
15. Johnson, G. R., "Analysis of Elasto-plastic Impact Involving Severe Distortion," ASME J. Applied Mech., Vol. 98, pp. 439-444, 1976.
16. Chou, P. C. and Wu, L., "A Dynamic Relaxation Finite Element Method For Metal Forming Processes," Int. J. Mech. Sci., Vol. 28, pp. 231-250, 1986.

17. Bathe, K.-J., Finite Element Procedures in Engineering Analysis, Prentice-Hall, Englewood Cliffs, NJ, 1982.
18. Johnson, G. W. and Cook, W. H., "A Constitutive Model and Data For Metals Subjected to Large Strain Rates and High Temperatures," in Proc. of 7th Int. Sym. on Ballistics, pp. 541-548, 1983.
19 Meir, G., Hashemi, J., and Chou, P. C., "Finite-element Simulation of Segmented Chipping in High-speed Machining," Advanced Machining Tech. Conf., Paper No. MR 88-120, Society of Manufacturing Engineers, 1988.

ADIABATIC SHEAR-BANDING IN HIGH-STRENGTH ALLOYS

John H. Beatty †
Yeou-Fong Li ††
Marc A. Meyers ††
Sia Nemat-Nasser ††

† US Army Materials Technology Laboratory, Watertown MA 02172
†† University of California-San Diego, La Jolla CA 92093

ABSTRACT

A special experimental technique has been developed by which adiabatic shear bands can be generated under controlled conditions to allow for an experimental and theoretical study of adiabatic shear-banding in high-strength alloys. This allows the systematic examination of the shear-band microstructure at various stages of its evolution. The technique has been used to develop shear bands in AISI 4340 steel for a variety of quenched and tempered microstructures. Both the strain and strain rate were controlled. The shear-band microstructure has been analyzed using optical, scanning electron, and transmission electron microscopy. Parallel with this work, Hopkinson bar techniques were used to develop high-strain, high-strain-rate constitutive properties of the material. These properties were then embedded in a viscoplastic constitutive model and used in the explicit finite element computer code PRONTO 2D to study the deformation of the specimen, leading to initiation and growth of shear bands.

This paper presents observations of the microstructure of shear bands, results of the high-strain, high-strain-rate constitutive relations of the material used, and a set of finite-element simulations of the experiment.

INTRODUCTION

During high-strain-rate deformation, a localized region (the shear band) is sheared at a sufficiently high strain rate to preclude significant heat transfer away from the deforming zone. Many processes such as turning, reaming, punching, projectile deformation, and armor penetration can create adiabatic shear bands in a variety of ductile materials. Material within the band undergoes both a large accumulated strain and a significant increase in temperature.

This study aimed at developing a thorough understanding of microstructural influences on shear-band initiation. "Hat"-shaped specimens were tested using a split-Hopkinson compression bar {following Meyer [1,2]}. Previously, we tested several microstructures of a VAR 4340 steel to compare resistance to shear-band formation. These preliminary results showed the technique was sensitive to microstructural changes and allowed for metallographic examination of the band at various stages of its formation[3]. Thus this "hat" test has proved very useful for qualitative comparisons.

To complement the microstructural study, the hat test itself has been examined using a phenomenological viscoplastic constitutive model. The high-strain-rate properties are determined by a series of standard split Hopkinson compression tests at different strain rates. These relations are then used in the explicit finite-element code PRONTO 2D to study the deformation of the specimen and the initiation and growth of the shear bands. Thus we have simultaneously examined both the hat test as well as the predictive capabilities of the model itself.

EXPERIMENTAL PROCEDURE

A VAR 4340 steel alloy was used in the current study. Four microstructures were examined, all of which have a hardness of Rockwell C 52. The size and distribution of the grain-refining carbides was varied by using a two-step austenitizing treatment. The first austenitization was carried out at either 845°C, 925°C, 1010°C, or 1090°C for two hours. At each austenitizing temperature, a unique distribution of grain-refining carbides is produced by the differences in dissolution and/or coarsening rates. The second short austenitizing treatment at 845°C for 15 minutes was too short to significantly alter the carbide distribution, but restored a uniform

austenite grain size. These microstructures have been previously characterized by Cowie [4,5] and examined in our earlier paper[3].

The specimen configuration used is shown in Figure 1. Under uniaxial compression, the hat-shaped, cylindrically symmetric specimen undergoes intense shearing in the regions indicated in the side cutaway portion of the figure. To limit this shear deformation, precision machined "stop rings" are placed around the upper portion of the hat, to halt the shearing process at selected stages of shear-band formation. From these interrupted samples, metallographic, SEM, and TEM specimens are produced to observe microstructure-deformation interactions.

The samples are loaded in compression using a compression split-Hopkinson bar. The profile of the compression pulse impinging on the sample through the incident bar is controlled by placing a copper cushion at the striker end of the incident(input) bar; see Nemat- Nasser [6] for details.

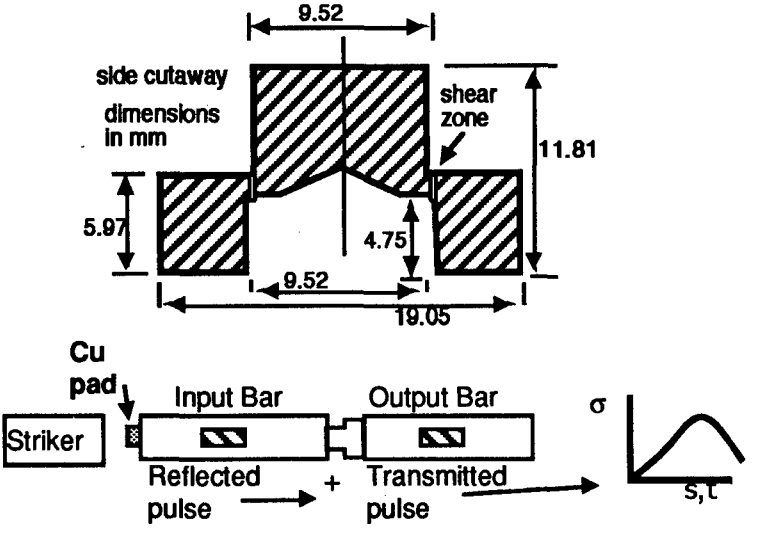

Figure 1. Hat specimen dimensions and split Hopkinson apparatus.

TEM samples of the sheared regions were made by mechanically thinning the material to a thickness of less than 0.125mm. Discs 3 mm in diameter were abrasively cut from the thinned material using a slurry disc cutter. The foils were electropolished in a 5% perchloric 95% methanol solution at -20°C and 50 volts. The shear-band region polished preferentially, but produced insufficient electron transparent regions. Ion milling at 15 degrees impact angle and 4 kV was used to further thin the specimens for TEM

examination. Both a 300kV Philips CM-30 and a JEOL 200 CX electron microscope were used.

NUMERICAL SIMULATION

Quasi-static and high-strain-rate simple compression tests were performed on samples of a single microstructure (austenitized at 845°C). The results were used for constitutive modelling and were subsequently integrated into the finite-element simulation of the hat-shaped tests. For this purpose, strain rates from 8×10^{-4} to 4×10^{3} / s were used.

An elastoviscoplastic constitutive model is used, in which the deviatoric deformation rate tensor $\underset{\sim}{D}'$ is decomposed into an elastic and a viscoplastic part,

$$\underset{\sim}{D}' = \underset{\sim}{D}'^{el} + \underset{\sim}{D}'^{pl} \qquad (1)$$

where

$$\underset{\sim}{D}'^{el} = \frac{1}{2G}\overset{\circ}{\underset{\sim}{\tau}}' \quad , \qquad (2)$$

$$\underset{\sim}{D}'^{pl} = \dot{\gamma}\frac{\underset{\sim}{\tau}'}{\sqrt{2}\tau}, \quad \tau = \sqrt{\frac{1}{2}\underset{\sim}{\tau}':\underset{\sim}{\tau}'} \quad . \qquad (3,4)$$

Above, $\underset{\sim}{\tau}'$ is the deviatoric portion of the Cauchy stress, and $\overset{\circ}{\underset{\sim}{\tau}}'$ is an objective stress rate; in the computer code PRONTO 2D[7], the stress rate is calculated in the Lagrangian triad and hence, the objective stress rate is defined, using the spin of the Eulerian triad relative to the Lagrangian triad; see Nemat-Nasser[8].

In the elastoviscoplastic model used here, the plastic shear strain rate, $\dot{\gamma}$, is assumed to relate to the rate-dependent flow stress in shear of the material, τ_y, in the following manner:

$$\tau_y = \tau_o\left(\frac{\dot{\gamma}}{\dot{\gamma}_o}\right)^{\left(\frac{1}{m}\right)}\left(1+\frac{\gamma}{\gamma_o}\right)^{N} e^{-\lambda(\Delta T)} \quad , \qquad (5)$$

where τ_0 and γ_0 are the initial flow stress and flow strain, respectively, at some reference strain rate $\dot{\gamma}_0$, and N, m, and λ are material parameters. In eqn. (5),

$$\Delta T = \int_0^t \chi\xi\tau\dot{\gamma}dt \quad , \quad 0<\chi\leq 1 \quad , \qquad (6)$$

where χ represents the fraction of plastic work which is converted to heat, and ξ is a dimensional parameter which relates the rate of plastic work to the change in the temperature, ΔT, of the material; $\xi = 2.7455 \times 10^{-7} m^3 °C/J$, for this case.

To fix the material parameters N and m, as well as the reference quantities τ_o and γ_o, simple quasi-static and Hopkinson bar compression tests were used. For the quasi-static experiments, the temperature effects in (5) can be neglected. At increasing strain-rates, however, some of the heat generated remains within the deforming sample, causing thermal softening. For our final simulation of the hat specimen, the plastic deformation was localized over a very small region, and since the test duration was suitably short, one can assume the process was completely adiabatic with good accuracy. Therefore, we first determined τ_o, γ_o, m, and N, using a least-squares scheme. This produced $\tau_o = 1030$ MPa ($\sigma_{o\ eff} = 1790$ MPa) , $\gamma_o = 0.015$, m = 90, and N = 0.0875. For different strain rates the parameters λ and χ change, and had to be fitted to the experimental data. A simple procedure is to set λ equal to a constant, and then change χ for different strain rates. For example, we obtained $\lambda = 0.0019$ and $\chi = 1.0, 0.8, 0.72$ for strain rates of 4000, 2000, and 1200 sec^{-1}, respectively. Figure 2 shows the true

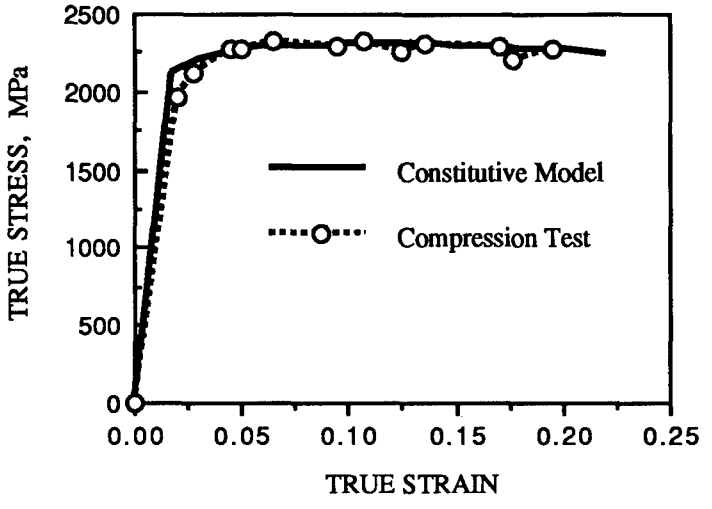

Figure 2. True stress vs. true strain curve from constitutive model and experimental data (o) from split Hopkinson compression tests. $\dot{\varepsilon}$ = 2000/s.

stress vs. true strain obtained in this manner for a strain rate of 2000 sec^{-1}, along with the experimental data. Similar good fits were achieved for the other strain rates. For the adiabatic case, $\chi = 1$.

EXPERIMENTAL RESULTS AND DISCUSSION

From the stress-time and velocity-time curves obtained during the hat test, a stress displacement plot is generated by integrating the velocity-time curve. A typical shear stress vs. displacement curve for this steel is shown in Figure 3. For these microstructures, the samples showed a large linear region, and the stresses fell smoothly after instability. Instability is defined as the point where the shear stress reaches its maximum value. The shear strain rate is estimated from combining the measured width of the deforming zone (from optical cross sections prior to shear-band formation) and the displacement rate, giving $\dot{\gamma} \approx 1.01 \times 10^5 s^{-1}$. This shear strain rate and resulting strain are not entirely uniform, as the geometry of the sample creates some localization at the outset of the test.

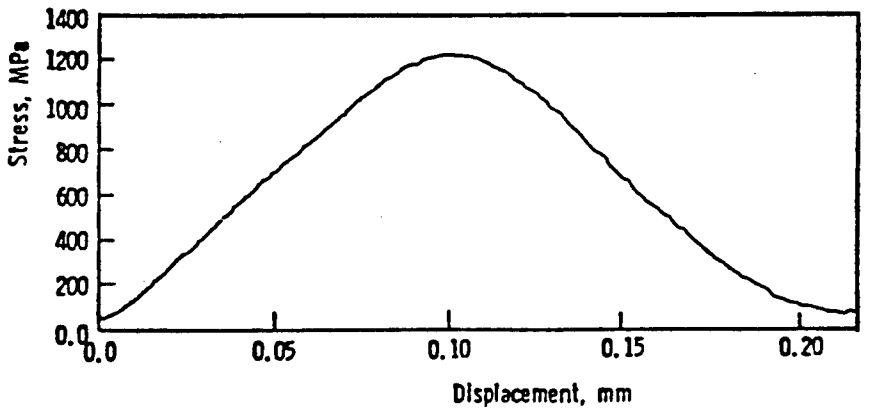

Figure 3. Typical shear stress-displacement curve of VAR4340 steel at a hardness of Rc52. This sample was given its first austenitization treatment at 1090°C.

Figure 4 shows shear band development using optical(4a) and scanning electron microscopy(4b,c) in typical samples. The shear bands etch white in nital, typical of the so-called "transformed" band type. Figure 4b,c are SEM micrographs of a shear band formed in the microstructure normalized at 925°C. Figure 4c shows this band near its tip. Note the alignment of the martensite laths with the shearing direction along the band edges and the absence of any resolvable grain structure within the band at this magnification.

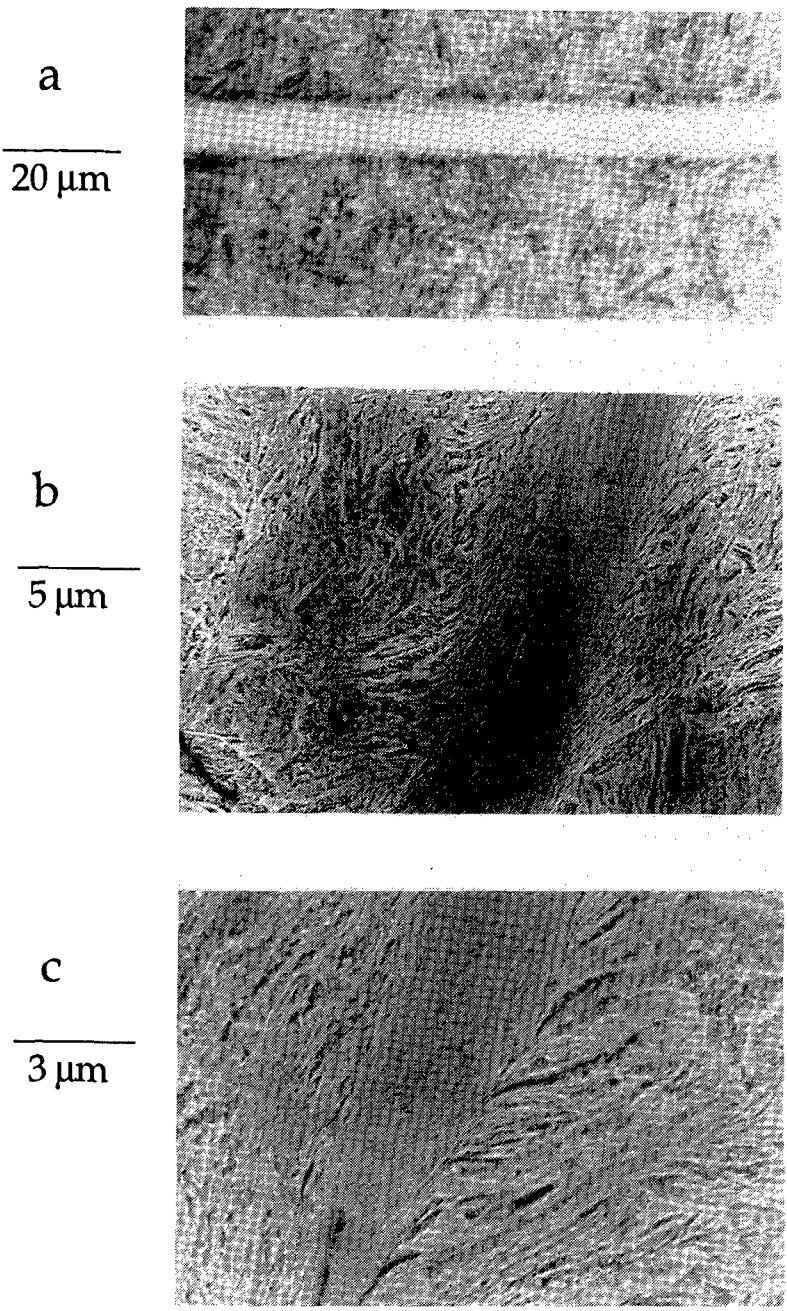

Figure 4. Micrographs of shear bands produced using the "hat" specimen developed by Meyer[1,2]. a) Optical micrograph of the shear band. b) Scanning electron micrograph showing lath realignment and "flow" regions near the edge of the band. c) Propagating shear band at the tip.

"Flow" lines (martensite lath realignment) can be detected parallel to the shear direction within the band.

The maximum shear stress attained was virtually independent of the four microstructures tested. The same microstructures were previously studied[4,5] at low strain rates in pure shear, and here too, no effect on the instability stress was found. However, significant differences between the microstructures were noted when energy absorption was considered. Figure 5 plots the energy absorbed before instability (E_i) vs. austenitizing temperature relationship for a strain rate of $\dot{\gamma} \approx 10^5 s^{-1}$; note the energy peak for the 925°C austenitizing temperature. Recent work also suggests that resistance to ballistic failure by plugging in thin plate follows the same trend[9].

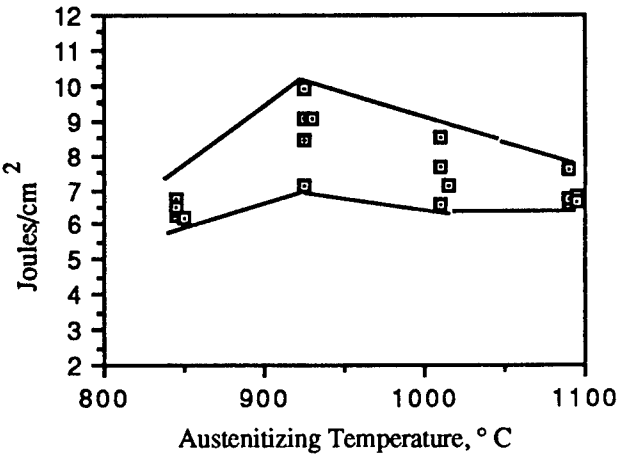

Figure 5. Energy absorbed to the point of instability per unit area sheared, Ei, versus austenitizing temperature.

Dark-field transmission electron microscopy was used to examine a region near the center of the shear band. By centering the first bright ring along the optical axis, the microcrystals can be individually illuminated. Figure 6 is such a dark-field micrograph where the crystallite size can be determined to range from 8 to 20nm. This size is an order of magnitude smaller than previously assumed[10], but otherwise the structure is in general agreement with earlier TEM evaluations of shear bands[3,10-14]. The change from a true microcrystalline structure to "normal" heavily deformed martensite away from the band was gradual, as verified previously[3] using Selected Area Diffraction Patterns (SADPs) as a function of distance away from the center of the band.

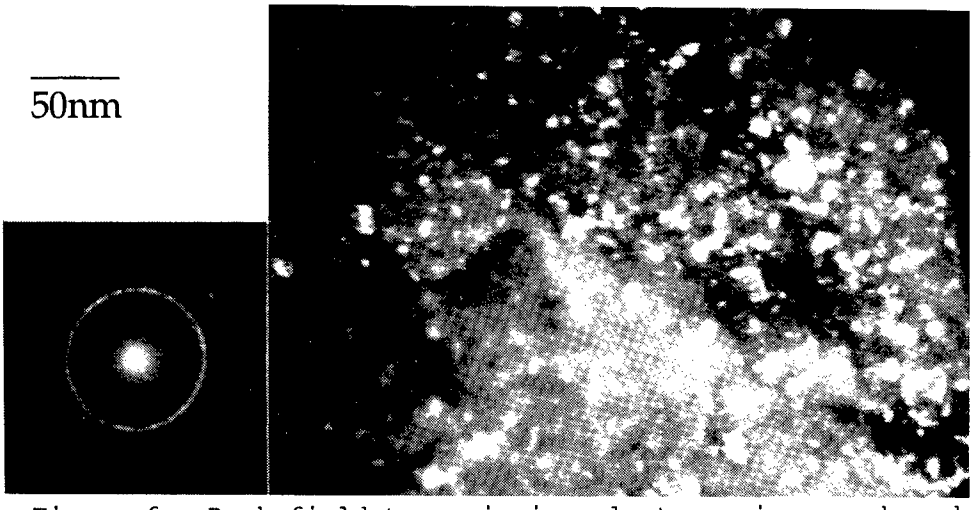

Figure 6. Dark-field transmission electron micrograph and selected area diffraction pattern taken from the center of a shear band. Microcrystals range from 8 to 20nm in diameter.

No carbide spots or austenite reflections could be found near the center of the band. The extremely fine grain size and rapid quench rate should increase levels of retained austenite, if any martensite transformed while shearing. The absence of any austenite reflection near the center of the band therefore suggests that no transformation has occurred for this particular case, and that the increased hardness and white etching characteristics are caused by the ultra-fine grain size and the breakup/dissolution of carbides.

NUMERICAL SIMULATION RESULTS

The results from the finite-element calculations are given in Figures 7-10. Figure 7 shows the undeformed and deformed meshes. The initial transverse element width in the concentrated shear region is 18 μm, which compares to the observed shear band width of 9-15 μm in the microstructures studied (compare to Figure 4a). The intense shearing occurs within one single column of elements, which shows that shear band width will vary with choice of element size, no matter how small of a mesh size is selected. Previously Olson, Mescall and Azrin demonstrated this limitation[15], but it is not within the scope of this work to address this important problem. The total shear strain profile from point A

a)

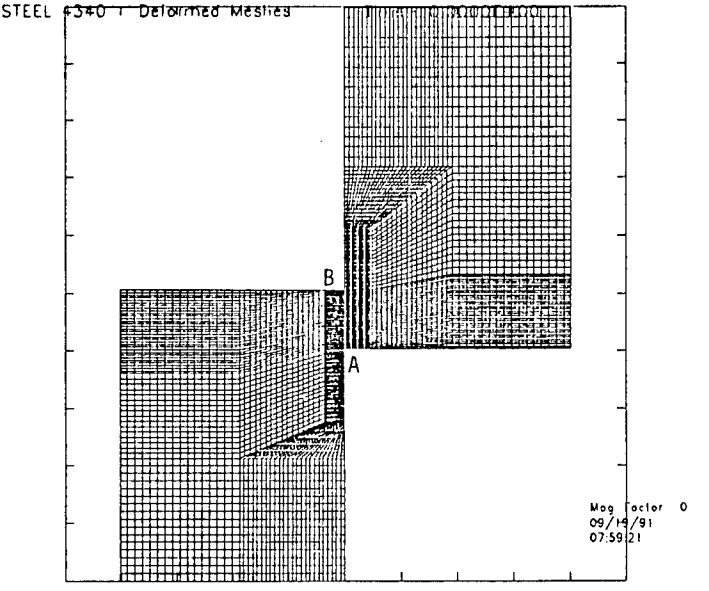

b)

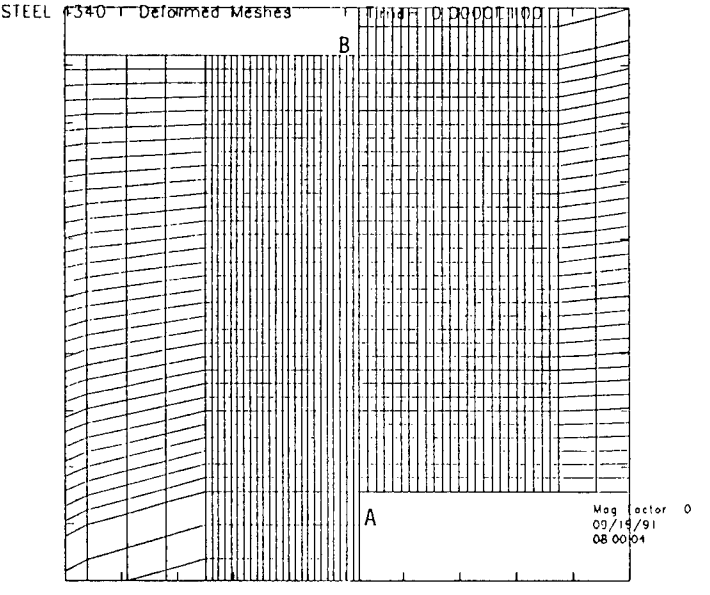

Figure 7. Finite-element meshes. Undeformed finite- element meshes used to simulate the hat test. a) Entire specimen. b) Concentrated shear region. Width of elements is 18 μm in the shear zone.

c)

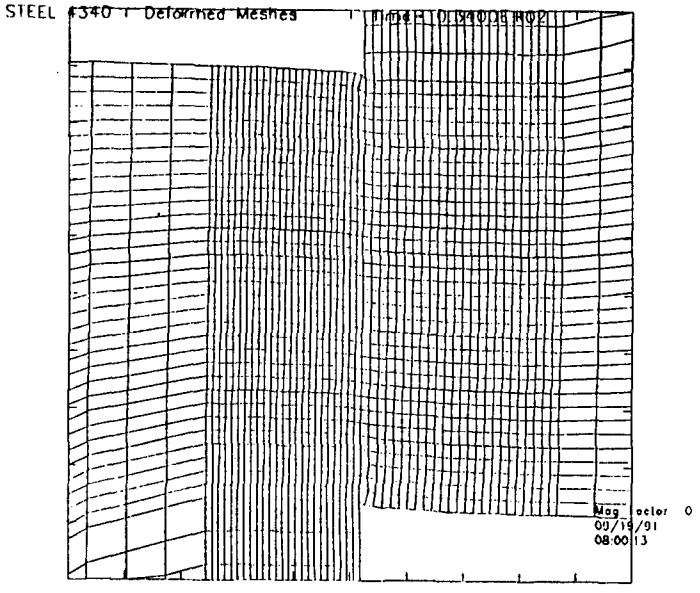

d)

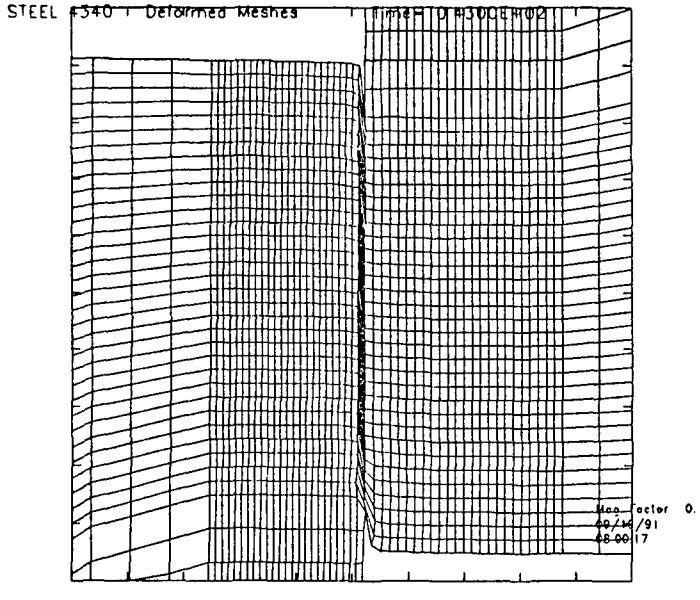

Figure 7, continued. c) Deformed mesh at the instability point (33μsecs). d) Deformed mesh at end of simulation (43μsecs).

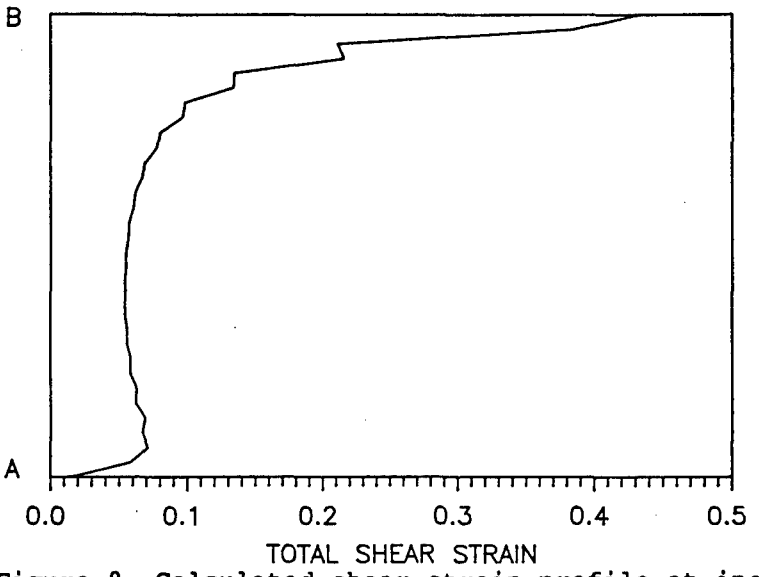

Figure 8. Calculated shear strain profile at instability. (A-B as denoted in Figure 7.)

to point B (see Figure 7) calculated at the instability point is given in Figure 8. Shear strains range from about 0.1 in much of the band to 0.45 near point B.

Of further interest is the temperature range predicted near the point of instability. Figure 9 gives the predicted temperature profile from point A to point B in the concentrated shear region, just before thermal instability is reached. The temperatures predicted just before instability, at 34 μsecs, are fairly low, with the highest temperature reaching only 160°C at point B. Just after instability, at 35μsecs, the predicted profiles suddenly jump to extremely high levels - above 2000°C- and we do not consider the solution to be valid close to this state (Figure 10). Though the model does predict thermal destabilization near the appropriate point of the stress-time curve, the degree of destabilization predicted is too great, and is largely dependent on the value of λ in eqn(5); clearly, λ cannot remain constant over such broad ranges of strain rates and temperatures. Further work is needed to adapt the constitutive model to work in this extreme regime of high-temperature, large-strain, and high-strain-rate deformation, where the shear band may be regarded as a discontinuity.

The simulation also produces stress-time curves, analogous to the data obtained in the split Hopkinson hat test. Therefore we can compare the experimental results from the hat test to the model predictions. This comparison is shown in Figure 11. Thus, the

finite-element model based on constitutive relations derived from simple compression tests gives reasonable results when used to predict a much more complex experiment, at least to the point of destabilization. Although some potentially important aspects are ignored (for example, the effect of confining pressure), the simulation does closely reproduce the observed experimental behavior. This suggests that equations of the form of equation (5) can be used in a variety of complex high-strain, high-strain-rate approximations after the parameters are fitted to a series of simpler high-strain-rate tests.

CONCLUSIONS: The hat specimen technique utilized in this study allows for the systematic examination of shear band microstructures at various stages of its evolution, and gives a qualitative comparison of shear band initiation resistance. A constitutive model and finite-element simulation based on simpler compression tests at various strain rates is in good agreement with the experiment up to and including the onset of thermal destabilization. However, the degree of destabilization predicted by the simulation is too extreme because of the assumed constant value of the parameter λ. Further refinement of the constitutive model is possible through a more realistic representation of the thermal softening effect.

ACKNOWLEDGEMENTS This work has been partially supported by the Army Research Office under contracts DAAL-03-86-K-0169 and DAAL-03-88-K-0118 awarded to the University of California, San Diego. The authors express their gratitude to Dr. Lothar Meyer, IFAM, Germany, for his advice and to Mr. John Isaacs for his technical contributions.

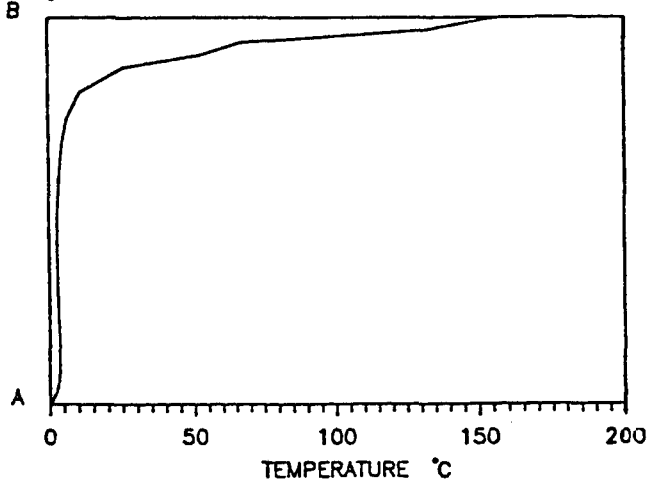

Figure 9. Simulated temperature profile of shear region at 34μsecs, just before instability (A-B as in Figure 7).

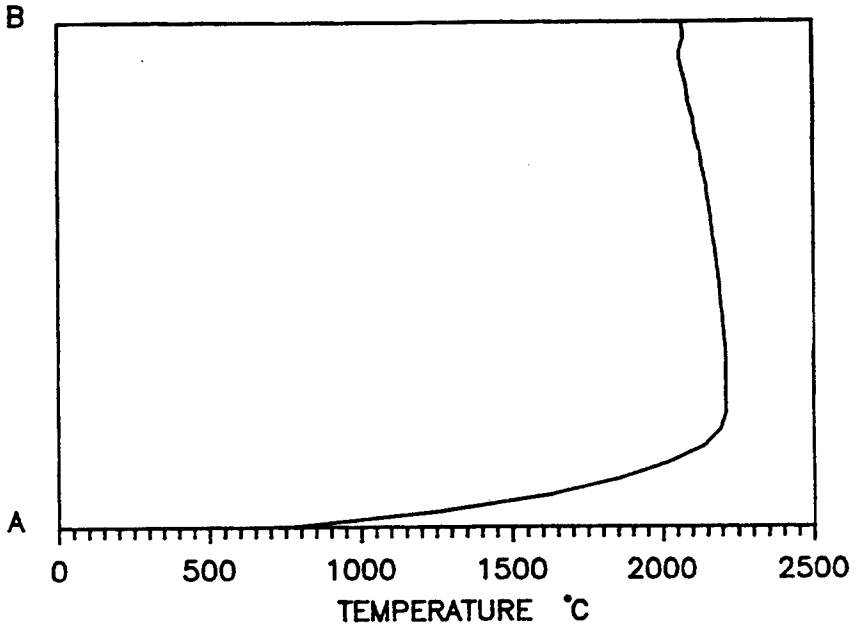

Figure 10. Simulated temperature profile of the concentrated shear region at 35μsecs, after instability. The solution is of questionable validity for this state (A-B as in Figure 7).

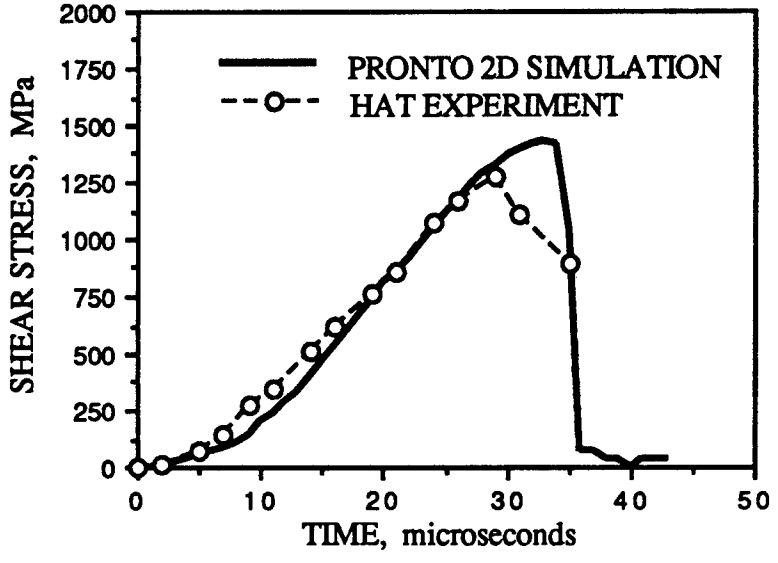

Figure 11. Stress-time curves. 1) Predicted by the finite-element model (solid line) and 2) Measured during the hat test (open circles).

REFERENCES

1. K-H Hartman, H.D. Kunze, and L.W. Meyer, "Metallurgical Effects on Impact Loaded Materials," in Shock Waves and High-Strain-Rate Phenomena in Metals, M.A. Meyers and L.E. Murr, eds, pub Plenum Press, New York, 1981.

2. L.W. Meyer, and S. Manwaring, "Critical Adiabatic Shear Strength of Low Alloyed Steel Under Compressive Loading,"in Metallurgical Applications of Shock-Wave and High-Strain-Rate Phenomena, L.E. Murr, K.P. Staudhammer, and M.A. Meyers, eds., pub Marcel Dekker, Inc, New York,1986.

3. J.H. Beatty, L.W. Meyer, M.A. Meyers, and S. Nemat-Nasser, "Formation of Controlled Adiabatic Shear Bands in AISI 4340 High Strength Steels," in Shock Waves and High Strain-Rate Phenomena in Materials, eds. Meyers, Murr, Staudhammer, published by Marcel Dekker, 1991.

4. J.G. Cowie, "The Influence of Second Phase Dispersions on Shear Instability and Fracture Toughness of Ultrahigh Strength 4340 Steel," US Government Report MTL TR 89-20, March 1989.

5. M. Azrin, J.G. Cowie, and G.B. Olson, "Shear Instability Mechanisms in High Hardness Steel," US Government Report MTL-TR 87-2, January 1987.

6. S. Nemat-Nasser, J.B. Issacs, and J.E. Starrett, "Hopkinson Techniques for Dynamic Recovery Experiments," Technical report of the University of California, San Diego, Center of Excellence for Adv. Materials, Feb. 1991.

7. L.M. Taylor and D.P. Flanagan, "PRONTO 2D: A Two-Dimensional Transient Solid Dynamics Program," Sandia Report, SAND86-0594, 1987.

8. S. Nemat-Nasser, "Certain Basic Issues in Finite-Deformation Continuum Plasticity," *Mechanica*, **25**, p.223-229 , 1990.

9. J.H. Beatty and M. Azrin , 1991 (to be published).

10. Y. Meunier, L. Sangoy, and G. Pont, "Metallurgical Aspects of Adiabatic Shear Phenomenon in Armor Steels with Perforation," in Impact Loading and Dynamic Behaviour of Materials, C.Y. Chiem, H.-D. Kunze, L.W. Meyer, eds, DGM Informations gesellschatt, Oberursel/Frankfurt, Vol 2:711, 1988.

11. R.C. Glenn and W.C. Leslie, Met Trans 1971 v2, p2954.

12. A.L. Wingrove," A Note on the Structure of Adiabatic Shear Bands in Steel", Australian Defense Standard Laboratories, Technical Memo., 33 1971.

13. C.L. Wittman and M.A. Meyers, "Effects of Metallurgical Parameters on Shear Band Formation in a Low Carbon Steels," submitted to Metall. Trans.

14. C.L. Wittman, M.A. Meyers, and H.-r Pak, "Observation of an Adiabatic Shear Band in AISI 4340 Steel by High Voltage Electron Microscopy," Metall. Trans., V 21 A, March 1990.

15. G.B. Olson, J.F. Mescall, and M. Azrin, "Adiabatic Deformation and Strain Localization'" in Shock Waves and High-Strain-Rate Phenomena in Metals, eds. Meyers, Murr, pub. Plenum, 1981.

STRAIN ENERGY DENSITY APPROACH TO STABLE CRACK EXTENSION UNDER NET SECTION YIELDING

D.Y. Jeong and O. Orringer
U.S. Department of Transportation
Volpe National Transportation Systems Center
Cambridge, MA 02142

G.C. Sih
Institute of Fracture and Solid Mechanics
Lehigh University
Bethlehem, PA 18015

Introduction

Fail-safe airframe designs are expected to arrest certain isolated large fractures which may initiate, in some circumstances, under normal flight loads. For the pressurized fuselage structure in commercial transport airplanes, this crack arrest capability must be demonstrated in order for the design to comply with U.S. certification standards (14 CFR 25.571). This requirement was originally established in the 1950s, in response to accidents involving uncontained fuselage skin fractures initiated by propeller failures in some of the medium-altitude piston-engine transports of that era (Figure 1) [1].

Accepted practice for demonstrating compliance with the standard is a full-scale ground test, in which an explosive charge drives a blade into the fuselage, creating a longitudinal skin crack approximately one frame bay in length. The blade is positioned to create the crack midway between longerons and centered on a frame, which is also cut by the penetrating blade (Figure 2). This configuration maximizes the local flexibility of the failing structure and thus provides a conservative test of the ability of the surrounding structure to arrest a large fracture initiated by foreign object damage.

Today's high-altitude transports are equipped with much more reliable turbojet engines, and containment structure is included to deflect rotor fragments away from the fuselage in the event of an engine failure. The certification requirement has been retained, but it is now interpreted more broadly to apply to fractures that might initiate from fatigue as well as foreign object damage.

Figure 1. DC-6 fuselage failure.

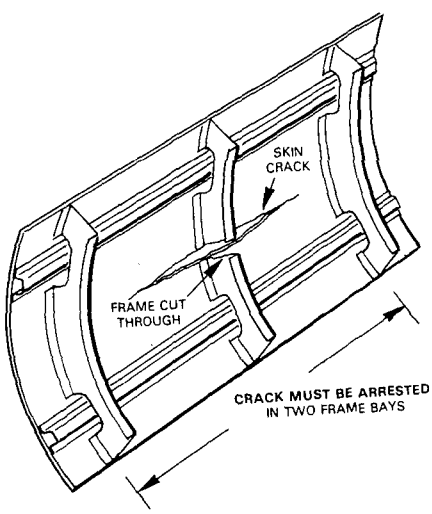

Figure 2. Demonstration of fuselage crack arrest capability.

Design of damage-tolerant fuselage structure is based on thin-skin fracture resistance, as characterized by the K_R curve [2,3]. For design purposes it is implicitly assumed that the fracture resistance for a given skin thickness, as expressed in terms of stress intensity K_R, is an unique function of crack extension independent of initial crack length. Estimation of a critical crack length for fracture initiation then requires only calculation of the applied stress intensity factor, K_A, and a graphical construction like the one shown in Figure 3. Such estimates are needed to specify the blade length for a crack arrest test and also to specify schedules for fatigue crack inspections in service.

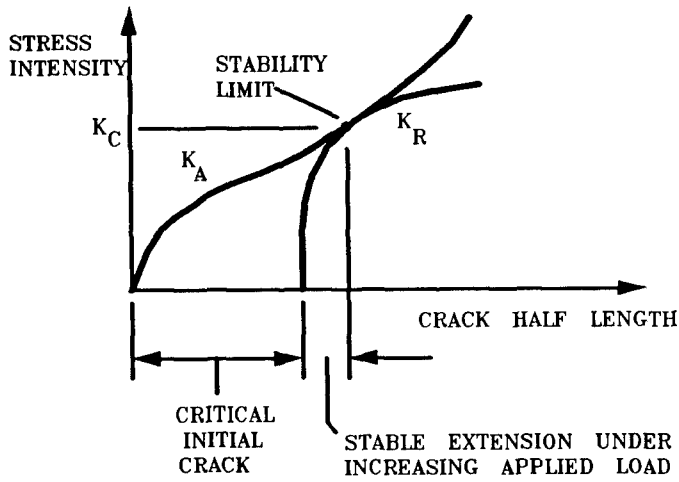

Figure 3. R-Curve estimation of critical crack length.

For the aluminum skin alloys and design stress levels found in typical civil aircraft fuselage structure, the critical crack length is on the order of 20 inches, and tests to obtain the K_R curve are typically conducted with 10-inch initial cracks in center-cracked panels 20 to 40 inches wide. Thus, the conditions in both the R-curve test and the airframe are such that most of the remaining ligaments along the crack line behave elastically during the stable extension phase.

Conversely, the critical crack length is much smaller, and the remaining ligaments undergo plastic yielding, when fatigue cracks form at multiple sites along a fastener row. The in-flight failure of a jet transport fuselage in 1988 (Figure 4) [4] is believed to have been caused by the linking of such multiple site cracks and the associated degradation of the structure's crack arrest capability in adjacent bays.

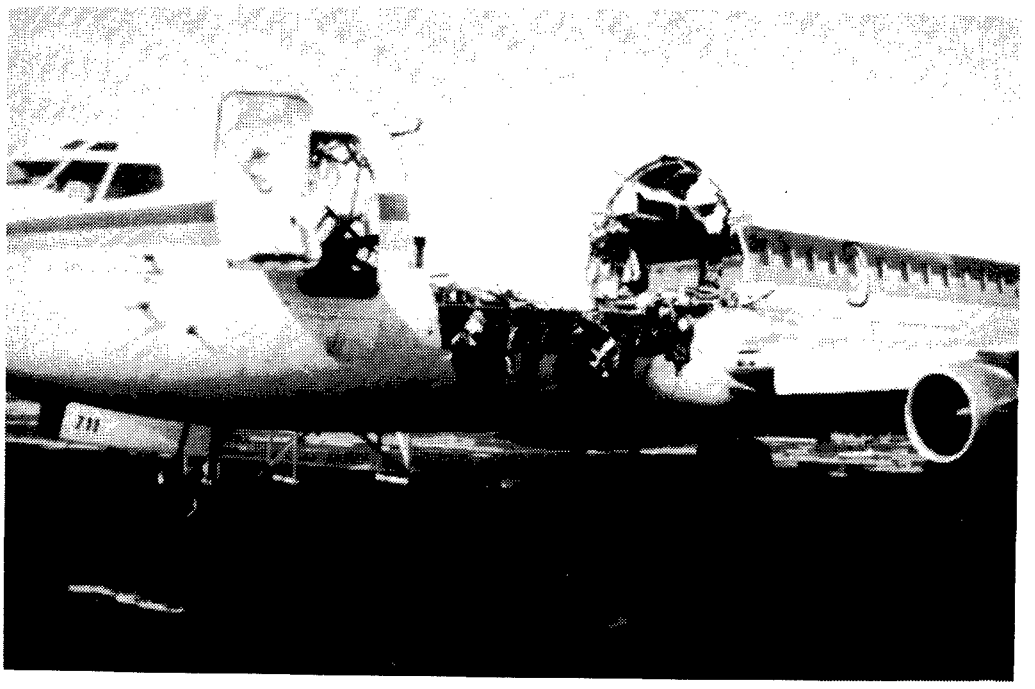

Figure 4. N73711 fuselage failure.

It would obviously be useful to have estimates of the critical crack lengths both for the initial linking in one bay and for overload-induced linking in adjacent bays (following the first bay failure). Rough estimates can be made by means of plastic collapse models. These models, which range from simple net-section failure criteria to numerical analyses with implicit elastic-plastic boundaries, are based on classical plasticity theories which do not account for stable crack extension.

Recent experiments on open-hole tensile coupons with hole diameter and spacing similar to typical aircraft construction details have shown that stable crack extension does occur under these conditions [5]. Therefore, it would be useful to have a material mechanics model which could account for stable crack extension when the remaining ligaments have already entered the plastic deformation regime.

Strain energy density criterion

The strain energy density criterion was developed in the 1970s by Sih [6] as a rational approach to linear elastic fracture mechanics (LEFM) under mixed mode conditions. The criterion was later found to be

applicable to ductile fracture as well [7], and is thus a logical candidate for correlation of stable crack extension phenomena under plastic ligament conditions.

Mechanical and physical interpretation

The criterion is based on a property of the strain energy density function for a linearly elastic isotropic body (Young's modulus E, Poisson's ratio ν). Sih observed that, under plane strain conditions, maxima of the ratio of dilatational to distortional strain energy density U''/U' coincide with minima of the total strain energy density:

$$U = U' + U'' \tag{1}$$

where

$$U' = \frac{1+\nu}{3E}[\sigma_1 + \sigma_2 + \nu(\sigma_1 + \sigma_2)]^2 - \frac{1+\nu}{E}[\sigma_1\sigma_2 + \nu(\sigma_1 + \sigma_2)^2] \tag{2}$$

$$U'' = \frac{1-2\nu}{6E}[\sigma_1 + \sigma_2 + \nu(\sigma_1 + \sigma_2)]^2 \tag{3}$$

and σ_1, σ_2 are the in-plane principal stresses.

If Irwin's asymptotic solution [8] for the stress field near the tip of a macrocrack is substituted into the strain energy density function, then U is expressed in terms of polar coordinates (r, θ) with origin at the crack tip. Let $S \doteq rU$ be defined as the strain energy density factor, a quantity independent of r for the asymptotic solution. One can then find extreme values of U as a function of θ by finding the angles θ which extremize S. For example,

$$S = \frac{1+\nu}{8E}(3 - 4\nu - \cos\theta)(1 + \cos\theta)\sigma^2 a \tag{4}$$

corresponds to Mode I uniform remote stress σ applied to a crack of length $2a$ in an unbounded sheet. In this case, the minimum S is defined by $\theta = 0$, which is also the direction of crack extension. In the

general case, which includes combined Mode I and Mode II loads, the minimum S corresponds some other angle θ, which can be interpreted as the expected trajectory for crack extension. The physical argument in support of this interpretation is that the maximum of U''/U' fosters void formation, growth, and coalescence along the trajectory.

The extension to ductile fracture is founded on another property of the strain energy density function and the results of numerical experiments. It is well known that, inside the plastic zone surrounding a crack tip, the asymptotic stress and strain fields deviate from the $1/\sqrt{r}$ singularity which characterizes the elastic stress distributions. However, the strain energy density function retains its characteristic behavior, $U = S/r$, independent of the constitutive equation. Therefore, the strain energy density factor S can still be used to search for minimum U trajectories.

Of course, the Irwin asymptotic solutions cannot be used in the plastic zone, and a numerical stress or strain analysis must be carried out instead. Numerical results for $U(r, \theta)$ at several radii can be used to estimate $S(\theta)$ on discrete rays, and $\min[S(\theta)]$ can then be interpolated from these estimates. The technique is compatible with standard numerical stress analysis procedures, e.g., the finite element method. Reasonable trajectory analyses can be carried out, in principle, by means of grid refinement in models of plastically deformed structures approaching collapse. (In practice, of course, the accuracy of the numerical results will be degraded by ill-conditioning in the finite element model before the collapse state is closely approached.)

Analyses such as just described have been carried out, together with auxiliary calculations to determine the dilatational and distortional energy components. The numerical results have shown that the ratio U''/U' tends to a maximum near the ray on which U is a minimum [9]. Therefore, one can argue heuristically that in the plastic case, just as in the elastic case, the ray defined by $\min[S(\theta)]$ can be interpreted as the expected crack extension trajectory.

Crack extension and stability limit

The strain energy density criterion includes hypotheses for crack extension and a stability limit based on two physical parameters: the critical strain energy density U_c, and the critical strain energy density

factor S_c. The first parameter is obtained from basic material properties, while the second depends on structure geometry, crack size, and load at the point of fracture instability.

The critical strain energy density is defined as the maximum energy density that a material can absorb before the onset of local plastic failure (microligament necking and void coalescence). For elastic bodies, the hypothesis is that a macrocrack will extend radially, along the expected trajectory, as far as there exist material points at which the applied-load strain energy density exceeds U_c. The value of U_c is estimated as the area under the tensile stress-strain curve, based on the conventional hypothesis that this curve also represents the relation between equivalent plastic stress and strain. For elastic-plastic bodies, the consumption of energy at points inside the plastic zone, before crack extension, must be accounted for. Figure 5 illustrates an example, in which the state at a given material point in the plastic zone is represented by the point P on the equivalent stress - equivalent strain diagram. The energy $U(P)$ has already been consumed, and thus, the crack extends to the radius:[1]

$$r = \frac{S}{U_c - U(P)} \tag{5}$$

where S is the strain energy density factor corresponding to the applied load.

---

1 Interpretation of the extension radius is straightforward in pure Mode I cases, where the crack extends along its own line. In mixed mode cases, one can take small load steps and interpret the incremental results as a piecewise linear approximation of a curved trajectory. Incremental analysis requires the tracking of strain energy in the volume ahead of the extending crack, so that the energy accumulated up to the last increment can be subtracted from U_c before the next extension increment is calculated.

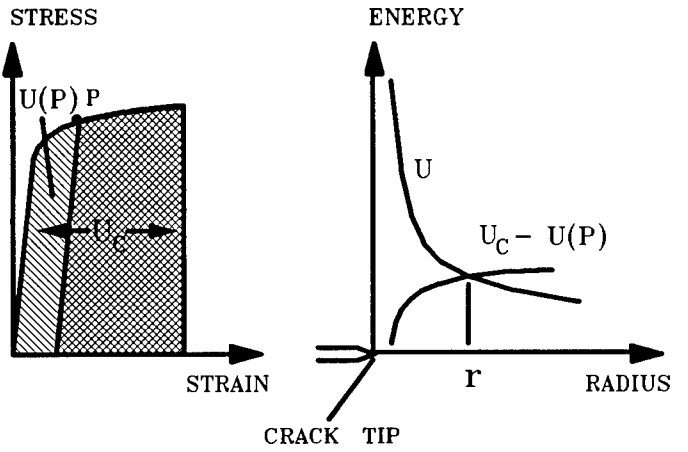

Figure 5. Strain energy density criterion for stable crack extension.

The extension is presumed to be stable as long as the critical strain energy density factor S_C is not attained. In the Mode I case, where the crack extends along its own line, the stability criterion can be expressed equivalently as $r < r_C$, where $r_C \doteq S_C / U_C$. The value of S_C must be derived from the results of a fracture test under conditions similar to those of the intended application. Under LEFM conditions, for example, the plane strain fracture toughness is simply substituted in the Irwin asymptotic solution to find:

$$S_C = \frac{(1+\nu)(1-2\nu)}{2\pi E}(K_{IC})^2 \qquad (6)$$

However, cases of practical interest involving ductile fracture require a numerical analysis of the test specimen, with the critical crack subjected to the critical applied load, as experimentally determined.

The conventional approach for isolated long cracks is to characterize the behavior by means of an experimentally determined R curve. The strain energy density criterion can be considered as an alternate approach in which the stable segment of the R curve is estimated from the critical state data.[2] The R-curve method is not valid when plastic collapse

---

2 One can also employ three dimensional stress analysis to make rational extrapolations of thickness effects, whereas the R-curve method requires interpolation between tested thicknesses.

controls the stability limit, e.g., under multiple site damage conditions like those mentioned in the introduction. However, it is still possible to apply the crack extension part of the strain energy density criterion to such cases, using only the U_c parameter, as illustrated in the following section.

Example application

The tensile coupon experiments mentioned in the introduction [5] were chosen as a test case. The coupons were designed to produce crack extension under conditions similar to multiple site damage along an aircraft skin splice, except that the critical nominal stress was approximately twice the typical maximum design stress for aircraft fuselage skins.

Coupon configuration and test procedure

The coupons consisted of clad 2024-T3 aluminum sheet, 4 inches (100 mm) wide × 0.04 inch (1 mm) thick, with one row of three drilled holes 3/16 inch (4.8 mm) in diameter and 1.0 inch (25 mm) on center. The central hole was symmetrically notched, and fatigue loads were applied to produce sharpened cracks. The inner edges of the outside holes were then notched to produce a final configuration for the experiment, such that the cracks and notches all had approximately the same initial length a_0 in a given coupon (Figure 6). Coupons with a_0 = 0.15, 0.22, and 0.26 inch (3.8, 5.6, and 6.6 mm) were tested.

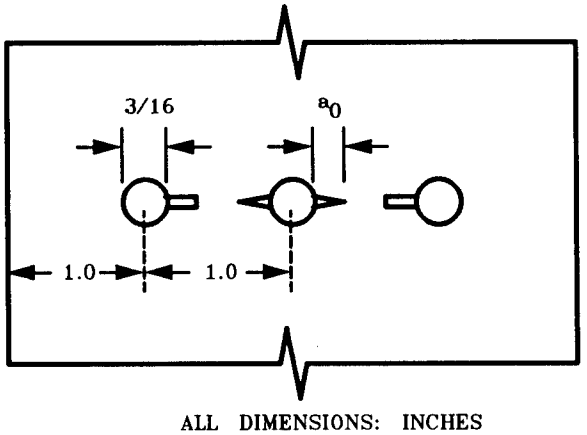

Figure 6. Initial configuration of test coupons.

The objective of the experiment was to measure crack extension resistance curves analogous to the R curves which characterize long crack behavior. Each coupon was loaded under quasi-static conditions while the extensions of the central cracks were visually monitored through a 20X measuring microscope. Extensions less than approximately 0.005 inch (0.1 mm) could not be resolved, but enough data for larger extensions was collected to define the asymptote regions of the resistance curves. Individual extensions Δa_L and Δa_R were recorded for the left and right cracks, but the average extension:

$$\Delta a = \frac{1}{2}(\Delta a_L + \Delta a_R) \tag{7}$$

is used here for comparison with the strain energy density analysis.

Analysis assumptions, model, and procedure

The stress-strain curve for the coupon material was also measured as a part of the test program [5]. Figure 7 illustrates the curve, and Table 1 summarizes the material properties. The experimental data were fitted with a Ramberg-Osgood equation:

$$\epsilon = \frac{\sigma}{E} + \left(\frac{\sigma}{B}\right)^n \tag{8}$$

with the values of E, B, n as given in Table 1. Equation (8) is considered to define the relation between equivalent stress σ and equivalent strain ϵ. The value of U_C was obtained by integrating the Ramberg-Osgood equation up to the material ultimate strength.

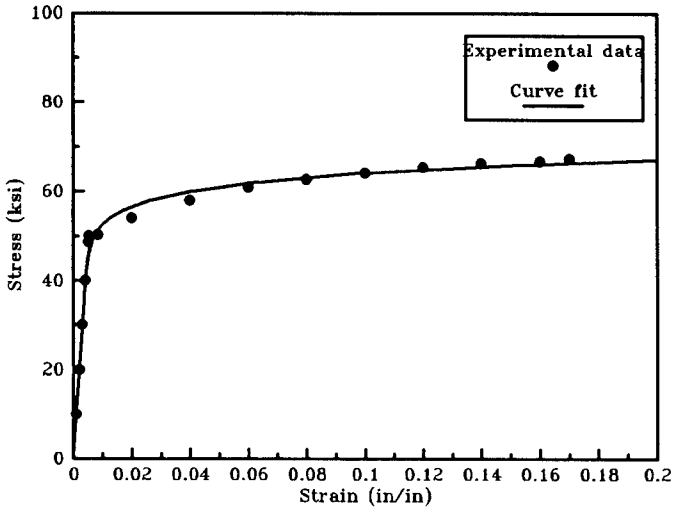

Figure 7. Stress-strain diagram for 2024-T3 coupon material.

Table 1. Material Properties Assumed for Analysis.

Yield strength f_{ty} ksi (MPa)	Ultimate strength f_{tu} ksi (MPa)	U_c ksi (MPa)	Ramberg-Osgood constants	
			E msi (GPa) B ksi (MPa)	n
49.8 (343)	67.2 (463)	12.5 (86.2)	10.00 (69.00) 74.81 (515.8)	15.26

Elastic-plastic finite element analysis was carried out on a plane-stress quarter symmetric model of the coupon, using bi-cubic isoparametric displacement elements in the grid shown in Figure 8, in accordance with the following approximate procedure. The finite element grid was configured to match the initial crack length a_o, and was loaded by a total nominal stress corresponding to the first experimental data point. The elements surrounding the crack tip were configured with mid-edge nodes at the 1/9 and 4/9 points to represent the crack-tip singularity in the assumed displacement fields. The strain energy density factor $S(\theta = 0)$ was estimated from the numerical results for $U(r, 0)$, and the corresponding cumulative crack extension was calculated from:

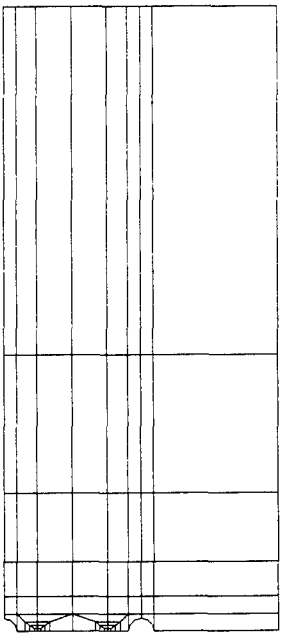

(a) full model

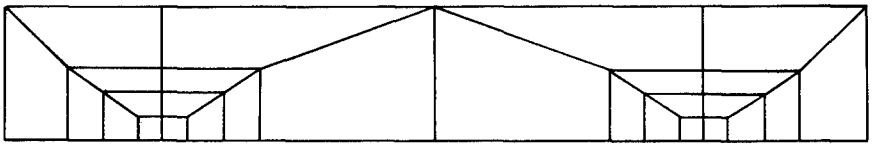

(b) detail of region between holes

Figure 8. Quarter-symmetric model of test coupon.

$$\Delta a = r = \frac{S(0)}{U_c - U(r)} \tag{9}$$

The applied stress was then increased, the mesh updated to the new crack length, and the procedure was repeated until ill-conditioning error intervened.

Results

The results of the strain energy density analysis are compared with the experimental results in Figure 9. Solid and open symbols represent the analytical and experimental data points, respectively. Lines between data points have been included for visual guidance but have no physical or numerical meaning. The calculated crack extensions appear to be in reasonable agreement with the experimental observations. The calculations indicate the level of the resistance curve asymptotes but are not able to precisely track the asymptotes as the plastic collapse state is approached.

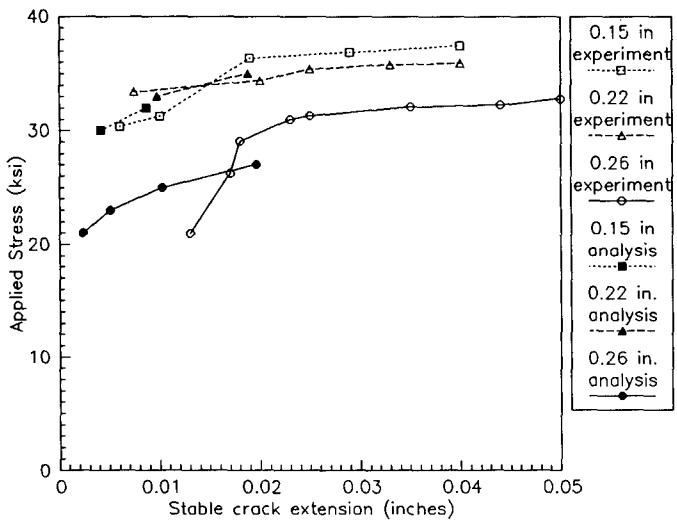

Figure 9. Comparison of results.

Discussion

The agreement between the analytical and experimental crack extension resistance curves was found to be reasonable but not precise. One obvious reason for the lack of better agreement is the approximate procedure used in the elastic-plastic finite element analysis. Although the complications of an incremental analysis were avoided, the approximate procedure must be expected to produce increasing error as the magnitude of the finite crack extension increases.

Another reason is the presence of some experimental error in the crack extension measurements. The microscope resolution limit mentioned earlier represents a band of uncertainty amounting to 25 to 50 percent of the measured extensions for which calculations could be made (see Figure 9).[3] Therefore, no final judgement about the accuracy of the strain energy density analysis can be made from the present comparison of results.

At first glance, it may appear inconsistent to use a global plane stress analysis for application of a fracture theory which is supposed to account for thin-section effects. In fact, however, there is no difficulty in reconciling the two contrasting modes of failure because one (crack extension) is local and the other (plastic collapse) is global. In other words, both crack extension and plastic deformation can contribute to the reduction of structural stiffness until the critical state of global instability is reached. The stationary property of the strain energy density function automatically accounts for the apportionment of energy between the two modes. The prediction of ductile crack extension leading up to global instability of the structure by plastic collapse has been made [11] where the collapse load estimated from limit analysis is a special case of the strain energy density theory.

The examples considered here involve failures totally controlled by plastic collapse. If the theory were to be applied instead to cases on the borderline between plastic collapse and ductile fracture, numerical analysis of the critical load/crack configuration could be carried out, and the thickness effect would be accounted for via the empirically determined critical strain energy density factor S_c.

Another perspective on the strain energy density analysis is gained by comparison with net section theory. The net section failure criterion

3 The visual resolution problem led to a later investigation of AC potential drop techniques as a means for obtaining continuous crack extension versus load data [10].

is a widely accepted conventional method for estimating the strength of mechanical joints under plastic collapse conditions. The critical nominal stress is calculated as:

$$\sigma_{CR} = \frac{A_{NET}}{A} f_{tf} \qquad (10)$$

where A is the nominal cross-section area, A_{NET} is the net section area (nominal area less the area occupied by holes, cracks, and notches), and f_{tf} is an assumed material property called the flow stress.

Equation (10) represents the physical hypothesis that the stress distribution is uniform tension across the net section at the collapse state. The hypothesis is justified by the known tendency of plastic deformation to smooth out uneven stress distributions along fastener rows in skins. There is no universally accepted rule for defining the flow stress, which is generally assumed to lie somewhere between the yield strength f_{ty} and the ultimate strength f_{tu}.

Values of f_{ty} and f_{tu} for the coupon material were given in Table 1. The net section strength estimates for the original and modified coupons with α_0 = 0.15 inch (3.8 mm) are summarized in Table 2. Comparison with Figure 10 shows that the strain energy density analysis produces essentially the same strength estimates as the net section criterion with $f_{tf} = f_{ty}$.

Table 2. Net Section Strength Estimates.

Quantity	$\frac{A_{NET}}{A}$	σ_{CR} ksi (MPa)	
		Based on f_{ty}	Based on f_{tu}
Value	0.71	35 (241)	48 (331)

On one hand, the preceding comparison is encouraging because the strain energy density analysis produces results in good agreement with a widely accepted conventional analysis method. On the other hand, why make the extra effort to carry out a strain energy density analysis? The answer is that multiple site damage in actual structures often propagates under mixed mode conditions. The net section criterion cannot be applied to such cases because there is no obvious way to define the net section.

The jet transport fuselage failure mentioned in the introduction provides a good example. This failure occurred along a splice at mid-fuselage height (Figure 4), where the skin is subjected to combined biaxial pressurization stress and transverse shear due to body bending. Multiple site cracks still in the slow propagation stage found at similar locations elsewhere on this fuselage were oriented at about 20^{o} from the splice line (Figure 10). Inspections of other aircraft following this accident revealed some multiple site cracks, at a later point in the slow growth stage, with curved trajectories like the schematic in Figure 11.

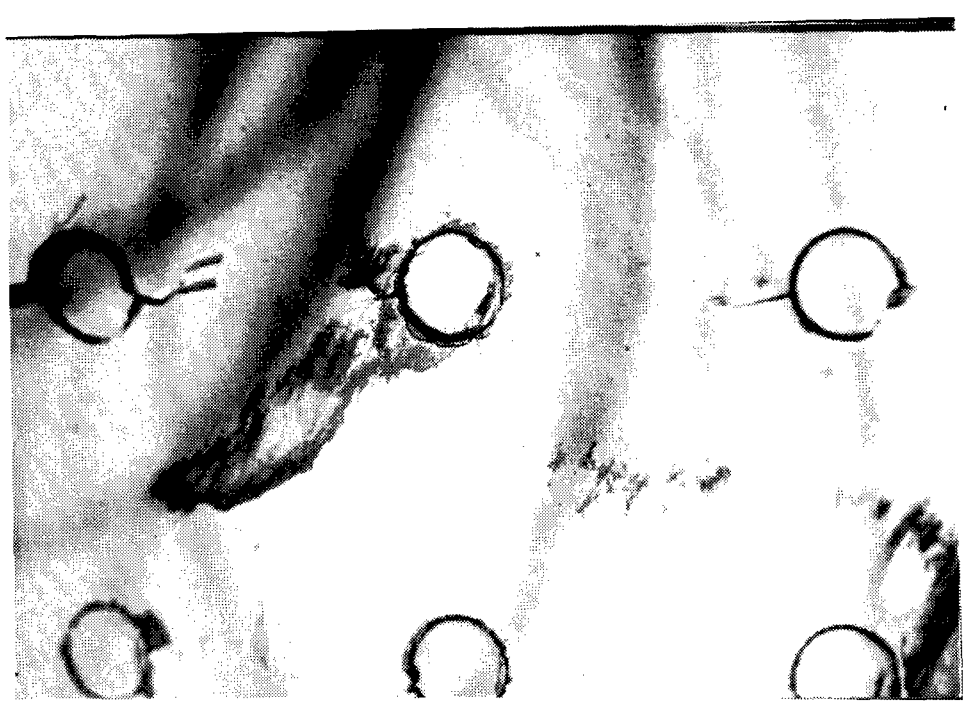

Figure 10. Inclined multiple site fatigue cracks in N73711 fuselage.

Figure 11 . Typical curved trajectories of multiple site fatigue cracks.

Conclusions

The strain energy density criterion was evaluated as a method for determining the critical length of multiple site cracks, which can suddenly link to form a long crack when the stability limit is attained. The stability limit in such cases is known to be controlled by a plastic collapse mechanism, for which conventional R-curve analysis is not valid. The evaluation was performed by comparing the strain energy density analysis with the results of a tensile coupon experiment in which multiple site crack linking was simulated under Mode I conditions. The accuracy of the criterion could not be precisely evaluated because of experimental error in the visual measurement of crack extension, and because of approximations made in the numerical stress analysis from which the strain energy density was calculated. However, the following preliminary conclusions can be drawn from the results.

Within the limits of experimental and numerical error, the strain energy density analysis appears to provide reasonable predictions of the stable extension observed in Mode I cracks similar to multiple site cracks.

The predictions of crack extension are limited by capability of the numerical stress analysis. In the present case, the numerical analysis could not provide valid results for crack extensions which closely approached the stability limit. Nevertheless, the crack extension which was predicted was sufficient to allow estimates of the critical applied stress asymptote.

The stress asymptote estimates were found to be in good agreement with estimates made from the net section failure criterion when the material yield strength was used to represent the net section flow stress.

Strain energy density analysis is thus a logical and credible approach to damage tolerance evaluation of multiple site cracking in actual structures, where mixed mode conditions prevail, and where the stability limit may be either controlled by plastic collapse or on the borderline between plastic collapse and ductile fracture.

References

[1] T. Swift, "Damage Tolerance in Pressurized Fuselages," *14th ICAF Symposium, New Materials and Fatigue Resistant Aircraft Design*, International Committee on Aeronautical Fatigue, Ottawa, Canada, 1987.

[2] D.E. McCabe (ed.), *Fracture Toughness Evaluation by R-Curve Methods, ASTM STP 527,* American Society for Testing and Materials, Philadelphia, PA, 1973.

[3] ASTM Standard E-561-86, "Standard Practice for R-Curve Determination," American Society for Testing and Materials, Philadelphia, PA, 1986.

[4] Anon., "Aircraft Accident Report -- Aloha Airlines, Flight 243, Boeing 737-200, N73711, near Maui, Hawaii, April 28, 1988," National Transportation Safety Board, Washington, DC, June 1989.

[5] G. Samavedam and D. Hoadley, "Fatigue and Fracture Strength Evaluation of Multiple Site Damage Aircraft Fuselages - Curved Panel Testing and Analysis," Foster-Miller, Inc., Waltham, MA, final report to Volpe National Transportation Systems Center, contract DTRS57-89-D-00009 (in press).

[6] G.C. Sih, "Strain-Energy-Density Factor Applied to Mixed Mode Crack Problems," *Int J Fracture 10*, 305-321 (1973).

[7] G.C. Sih and E. Madenci, "Fracture Initiation Under Gross Yielding, Strain Energy Density Criterion," *Eng Fract Mech 18*, 667-677 (1983).

[8] G.R. Irwin, "Analysis of Stresses and Strains Near the End of a Crack Traversing a Plate," *Trans. ASME, J Appl. Mech. E24*, 361 (1957).

[9] G.C. Sih and E. Madenci, "Crack Growth Resistance Characterized by the Strain Energy Density Function," *Eng Fract Mech 18*, 1159-1171 (1983).

[10] D.A. Jablonski, "Development of ACPD Procedures for Crack Detection in Aluminum Aircraft Panels," Instron Corporation, Canton, MA 02021, final report to Volpe National Transportation Systems Center, contract DTRS57-89-D-00007, project VA9011 (in press).

[11] A. Carpinteri and G.C. Sih, "Damage accumulation and crack growth in bi-linear materials with softening: application of strain energy density theory," *Theoretical and Applied Fracture Mechanics 1*, 149-159 (1984).

A CAVITATION LOCUS SURROUNDING A MODE I PLANE STRAIN CRACK IN A NEO-HOOKEAN MATERIAL

Claudia J. Quigley †
David M. Parks ‡

† U.S. Army Materials Technology Laboratory, Watertown, MA 02172
‡ Massachusetts Institute of Technology, Cambridge, MA 02139

Abstract

To better understand the relationship between cavitation and crack growth in elastomers, a local cavitation surface surrounding a Mode I plane strain crack was identified. A finite element analysis of this crack in a NeoHookean material was performed under the assumptions of small-scale nonlinearity, and the resulting crack tip field quantities were compared to the theoretical asymptotic solution for this problem. Far from the crack tip, the linear elastic asymptotic solution was found, while the nonlinear elastic asymptotic solution was identified in a small region surrounding the crack tip. All load parameters in the nonlinear elastic asymptotic solution were determined either analytically or from the computational results. The computed in-plane stress field showed close agreement with the theoretical solution for this problem. After verifying the accuracy of the numerical crack tip stress fields, a local cavitation surface enclosing the crack tip was identified. The cavitation surface predicted that the locus of potential cavitation extends to 0.015 $J_{\text{applied}}/\mu L$ in front of the deformed crack tip.

1 Introduction

Crack growth in thick elastomers is often preceded by cavitation near the crack tip [1, 2, 3]. The relationship between cavitation and the onset of crack growth is not well understood and was explored in this investigation by examining the cavitation locus surrounding a Mode I plane strain crack. A new theory developed by Hou [4], which defines a local cavitation surface under nonsymmetric loading, was applied to the finite element results for a plane strain Mode I crack in a NeoHookean material under small-scale

nonlinearity, in which a dominant linear elastic crack tip field surrounds a nonlinear crack tip region. The resulting cavitation locus is discussed.

Ball [5] analytically modelled cavitation under radially symmetric loads in the context of finite elasticity. He assumed that cavitation was a consequence of material instability. A solid sphere was subjected to a radially symmetric load across its outer radius. As the load was increased, a bifurcation analysis showed that, at a critical stress level, it became energetically more favorable for a cavity at the origin to nucleate and grow. This stress level, a critical value of the hydrostatic tension, $\tau_{ii}/3$, where τ_{ij} denotes the Cauchy stress components, predicts the onset of void formation and its growth. In the general case of a large body containing a void whose initial radius is infinitesimally small(bounded), the void will remain small until the applied load reaches some critical value, at which the void will grow without bound. Ball thus demonstrated that a critical value of the hydrostatic tension can predict either the onset of cavitation or the unbounded growth of a pre-existing microvoid. For a NeoHookean material, the critical value of the hydrostatic tension is 2.5 times the infinitesimal shear modulus, μ.

Hou and Abeyaratne[4] extended Ball's work by considering a finite body containing a pre-existing spherical void under uniform remote loading. A deformation field was constructed which characterizes a broad field of kinematically possible deformations of a cavity in a large body. Using this specific family of deformation fields, the principle of virtual work was then invoked to approximately solve for a cavitation surface in terms of the remote principal stresses, τ_i. For a NeoHookean material, they describe a cavitation surface by

$$(4\tau_3 - \tau_1 - \tau_2)(4\tau_2 - \tau_1 - \tau_3)(4\tau_1 - \tau_3 - \tau_2) - 125\mu^3 = 0. \qquad (1)$$

As the stress field approaches that of hydrostatic tension, the cavitation surface reduces to Ball's criterion, where the hydrostatic stress equals 2.5μ at the site of cavitation. Hydrostatic tension represents the minimum value along a cavitation surface for a NeoHookean material so that, under non-hydrostatic loading, the cavitation surface is found along principal stress states of greater magnitude: $\tau_1 \geq 2.5\mu$.

In this analysis, the cavitation surface defined by equation (1) was applied to a plane strain Mode I crack. This condition was selected because cavities have been found in vulcanized rubber cylinders [3] and in elastomer cubes [6]. Stress analyses of both test specimens indicated that cavities were located at sites of maximum hydrostatic tension, as predicted both by Ball [5] and Hou [4]. The cylindrical test specimens have been extensively studied to define the site of cavitation. Gent and Lindley [3]

performed an approximate stress analysis based on linear elasticity to show that the stress state was hydrostatic and that cavitation occurred at sites of maximum hydrostatic tension. Finite element analyses by Stringfellow and Abeyaratne [7], and Hou and Abeyaratne[4] confirmed that the stress state is only approximately hydrostatic and that when both cavitation criteria discussed above were applied to the finite element results, a cavitation surface could be accurately correlated with the locus of cavity nucleation obtained from experimental evidence. It can be concluded that these cavitation theories have been successfully applied to experiments on rubber materials under axisymmetric loading conditions.

If cavitation does precede crack growth in elastomer materials, then the local cavitation surface surrounding the crack tip region may provide insight into potential sites of void growth. The mechanical crack tip field was obtained through finite element analysis under the assumptions of small-scale nonlinearity. The cavitation surface in equation (1) was then applied to the mechanical crack tip stress field.

2 Problem Description

Consider a stationary plane strain Mode I through-thickness crack of length L, in a thick body of NeoHookean material as shown in Figure (1-a). A NeoHookean material is incompressible and its strain energy, W, is expressed as

$$W = \mu/2(I-3) \tag{2}$$

where $I = \lambda_1^2 + \lambda_2^2 + \lambda_3^2$, the first strain invariant, and λ_i are the stretch ratios.

A small tensile stress, σ, is applied normal to the plane of the crack and thermal and body forces are absent. The surfaces of the crack are traction free. A Cartesian coordinate system x_i is introduced at the tip of the crack, representing the undeformed coordinate system, where polar coordinates can be defined by

$$x_1 = r\cos(\theta), \qquad x_2 = r\sin(\theta). \tag{3}$$

A deformed coordinate system, Figure (1-b), y_i is also introduced at the crack tip, and

$$y_i = x_i + u_i, \qquad \text{or} \qquad \frac{\partial y_i}{\partial x_i} = F_{ij}, \tag{4}$$

given the displacement field, u_i and the deformation gradient field F_{ij}.

Under the assumptions of small-scale nonlinearity, the linear elastic asymptotic field is confined to a small region, compared to the crack length

and the geometry of the body, around the crack tip where small geometry changes and linear elastic material behavior are present providing the applied loads are sufficiently small. As $r \to 0$, these conditions are physically violated and the small region containing the linear asymptotic solution encloses a smaller region where large geometry changes and nonlinear material behavior are present. It is in this smaller region where the nonlinear elastic asymptotic solution is found.

In this problem, the linear elastic asymptotic field [8],

$$\begin{aligned}
\sigma_{11} &= \frac{K_I}{\sqrt{2\pi r}} \cos\frac{\theta}{2}\left(1 - \sin\frac{\theta}{2}\sin\frac{3\theta}{2}\right) + o\left(r^{1/2}\right) \ , \\
\sigma_{22} &= \frac{K_I}{\sqrt{2\pi r}} \cos\frac{\theta}{2}\left(1 + \sin\frac{\theta}{2}\sin\frac{3\theta}{2}\right) + o\left(r^{1/2}\right) \ , \\
\sigma_{12} &= \frac{K_I}{\sqrt{2\pi r}} \cos\frac{\theta}{2}\cos\frac{3\theta}{2}\sin\frac{\theta}{2} + o\left(r^{1/2}\right) \ ,
\end{aligned} \tag{5}$$

where σ_{ij} are the nominal stresses and K_I is the stress intensity factor, was applied as consistent nodal point forces by integrating the stress field along the outer radius R of a semicircular crack tip region. The linear elastic asymptotic solution will dominate the stress field at large radii. However, close to the crack tip, as $r \to 0$, the nonlinear elastic mechanical crack tip field [9, 10],

$$\begin{aligned}
\tau_{11} &\sim \frac{\mu}{2} b^2 (1 - \cos\theta) \ , \\
\tau_{22} &\sim \frac{\mu}{4} a^2 r^{-1} \ , \\
\tau_{12} &\sim \frac{\mu}{2} a b r^{-1/2} \sin\frac{\theta}{2} \ , \\
y_1 &\sim b r \sin^2\frac{\theta}{2} + \frac{1}{a} r^{3/2}\left(2\cos\frac{\theta}{2} - \frac{2}{3}\cos\frac{3\theta}{2}\right) \ , \\
y_2 &\sim a r^{1/2}\sin\frac{\theta}{2} + r^{3/2}\left(d\sin\frac{3\theta}{2} - \frac{b^2}{2a}\sin\frac{\theta}{2}\right) \ ,
\end{aligned} \tag{6}$$

referenced to the polar undeformed coordinate system (r, θ), will be present, where τ_{ij} denote the Cauchy stresses, and a, b, and d are independent load amplitude constants. When the nonlinear asymptotic field is applied to a particular energy conservation integral, the J-integral [11], an analytical solution [9, 10, 13] for the load amplitude parameter, a, can be found in the limit as $r \to 0$. Consequently, only the two remaining load amplitude parameters, b and d, need to be determined from the finite element analysis, to be shown below. A comparison of the linear and the nonlinear

asymptotic fields in equations (5) and (6) shows that, while the order of the singularity, $\sqrt{r}$, is the same for each in-plane stress component in the linear elastic solution, the order of the singularity differs for each stress component in the nonlinear elastic crack tip field. The τ_{22} stress component has the strongest singularity, $1/r$, and is independent of θ. Component τ_{11} is a function of theta only and is independent of r. Only τ_{12} is a function of both r and θ and the order of its singularity, $\sqrt{r}$, is the same as the linear elastic solution.

For a crack extending in the x_1 direction, the J-integral can be expressed as

$$J = \int_{\Gamma} [W n_1 - s_i u_{i,1}] dS \tag{7}$$

where W represents the strain energy, n_1 is the unit normal in the x_1 direction, and s_i is the nominal traction vector. The J-integral is path independent when evaluated along any suitable contour Γ which encompasses the crack tip, as shown in Figure (1-a), while dS is an element of arc length along Γ.

The load amplitude constant, a, in the nonlinear asymptotic solution equation (6), is determined by the direct evaluation of the J-integral, equation (7), along a circular contour of radius r. Noting that the J-integral and the energy release rate are equivalent under small-scale nonlinearity [12],

$$J = {K_I}^2 (1 - \nu)/2\mu, \tag{8}$$

where the Poisson ratio ν equals $1/2$ for incompressible materials. The load amplitude constant, a, can now be expressed in terms of the stress intensity factor as $r \to 0$ by

$$a = \frac{K_I}{\mu\sqrt{\pi}}. \tag{9}$$

3 Finite Element Model

Only the top half of the crack tip region was modelled in the finite element analysis because this problem possesses reflective symmetry about the x_1-axis. The finite element model was a semicircle whose outer radius, R, is equivalent to the crack length. The finite element mesh, Figure (2), consisted of two regions, a refined mesh, where accurate crack tip field quantities can be found, and, inside the refined mesh region, a coarse mesh close to the crack tip. Both the refined and the coarse mesh regions were composed of rings of eight-noded pressure hybrid isoparametric quadrilateral elements[14]. Within each ring, all elements had equal angular extent

and the same radial length. For background information on this mesh design, the reader is referred to reference [13].

The coarse mesh extended radially to $10^{-6}R$ and had four rings. The first ring was composed of three elements of length $10^{-9}R$. In each subsequent ring, the number of elements was doubled so that the fourth ring contained twenty-four elements. Element radii in the remaining three rings of the coarse mesh were biased such that, along a radius extending from the crack tip, the elements were equally spaced on a logarithmic scale from $10^{-9}R$ to $10^{-6}R$. Nodal displacements were constrained along each ring to enforce compatibility. Surrounding the coarse mesh was the refined mesh, composed of thirty-six rings, each containing twenty-four elements. As in the coarse mesh region, the element radii increased with distance from the crack tip with reference to a logarithmic scale. Six rings of elements, equally spaced on a logarithmic scale, were contained within a decade unit of crack length, $10^{-m+1}R$ to $10^{-m}R$, where m ranges from 5 to 0. The refined mesh extended from $10^{-6}R$ to R. The entire mesh contained 2850 nodes, each possessing two kinematic degrees of freedom, and an additional pressure degree of freedom at each corner node. The coarse mesh was constructed from 45 elements while the refined mesh had 864 elements, so that there was a total of 909 elements.

The finite element analysis was performed using ABAQUS [15] on an Alliant FX-8 computer. The J-integral was calculated using the domain integral method [16].

The finite element solution was obtained by applying consistent nodal point forces, obtained through the integration of the linear elastic stress field, equation (5), along the outer radius R of the finite element mesh. At sufficiently small values of K_I, the linear elastic asymptotic crack tip field was accurately found throughout the mesh. The numerically calculated value of the J-integral was within one per cent of the applied value, equation (8), where the error in the J-integral was determined from

$$\% \text{ error} = \frac{J_{\text{numerical}} - J_{\text{applied}}}{J_{\text{applied}}}. \tag{10}$$

As the magnitude of K_I increased, the nonlinear asymptotic solution began to evolve at the crack tip and grow in size and intensity.

4 Results

Before applying the cavitation surface, equation (1), to the finite results, it was necessary to verify the accuracy of the finite element solution by

checking the assumptions of small-scale nonlinearity and by comparing the finite element results to the theoretical asymptotic solution. Under small-scale nonlinearity, the J-integral must be path-independent and must equal the energy release rate, equation (8). Previously [13], it had been shown that, when the calculated value of the path independent J-integral is within five per cent of its applied value, equation (10), the numerical solution is independent of the boundary condition type. That is, the finite element results are the same whether the boundary conditions are applied as displacements or as consistent nodal point forces.

In this computational analysis, the J-integral was within one per cent of its mean value along all contours from $r = 10^{-6}R$ to $3.0\text{x}10^{-6}R$, the largest radius at which the J-integral was evaluated, demonstrating that path independence was maintained. In addition, the calculated value of the J-integral was within two per cent of its applied value for all load levels. Thus, the small-scale nonlinearity condition was met.

Before examining the crack tip field quantities, it was necessary to identify and locate the region of nonlinearity surrounding the crack tip. The region of geometric nonlinearity can be arbitrarily defined in terms of the deformation gradient, where

$$F_{ij} = \delta_{ij} + \frac{\partial u_i}{\partial x_j} \quad \text{and} \quad \left| \frac{\partial u_i}{\partial x_j} \right| < 0.1. \tag{11}$$

Inside the region of nonlinearity, the nonlinear asymptotic solution should be present, while ouside of this region, the linear elastic asymptotic field should dominate. The region of nonlinearity in the finite element mesh extended outside the first decade of elements in the refined mesh region to a radial distance of $0.11\ J_{\text{applied}}/\mu$ in the undeformed configuration.

There are three load amplitude constants associated with the nonlinear asymptotic solution: a, b and d. From the deformation fields y_i, equation (6), the accuracy of the deformation field can be examined and the load amplitude constants b and d can be determined. Along $\theta = 0$, the deformation field y_1 , minus a rigid body displacement, becomes

$$y_1 = 4/3ar^{3/2}. \tag{12}$$

In the nonlinear crack tip region, for the first decade of elements in the refined mesh region, y_1 can be predicted from equations (9) and (12) along $\theta = 0$. The deformation field obtained from the finite element analysis agreed within four per cent to the predicted value at all load levels. The load amplitude constant b was found directly from y_1, where, as $r \to 0$ in the refined mesh region,

$$b \sim -1.6, \tag{13}$$

when $J_{\text{applied}} = 0.065$ MPa-m. Similarly, now that a value for b has been determined, the load amplitude constant d in the y_2 deformation field can be evaluated and, as $r \rightarrow 0$ in the refined mesh region,

$$d \sim 1.1 \frac{\mu}{K_I}. \tag{14}$$

A comparison of the stress field determined by the finite element analysis demonstrates good agreement with the theoretical asymptotic solutions, equations (5) and (6), refer to Figures (3) - (5) which show the in-plane stress field evaluated along $\theta = 71.25$ degrees. Far from the crack tip, the linear asymptotic solution can be found for all three in-plane stresses; however, as $r \rightarrow 0$, these in-plane stresses transition to the nonlinear asymptotic crack tip stress field. In Figure (3), the change in the order of the singularity for τ_{22}, from $1/\sqrt{r}$ to $1/r$ is readily apparent as $r \rightarrow 0$. The order of the singularity for both the linear and the nonlinear asymptotic solution is the same, $1/\sqrt{r}$, for τ_{12}, but the angular function differs, as shown in Figure (4). Figure (5) demonstrates how τ_{11} transitions to its nonlinear asymptotic value which is independent of r and is constant for $\theta =$ constant . The components τ_{22} and τ_{12} possess the closest agreement with the nonlinear asymptotic field, and it is noted that $\tau_{22} > \tau_{12} \gg \tau_{11}$. In this analysis, the largest stress quantities appear to approximated more accurately.

Having verified the accuracy of the finite element mechanical crack tip stress fields, the cavitation criterion in equation (1) can now be applied to the computational results. The cavitation surface surrounding the crack tip in the deformed configuration is shown in Figure (6). The cavitation surface closely follows the crack face up to a height of $0.24\ J_{\text{applied}}/\mu$. This surface indicates that the locus of extensive void growth should extend in the nonlinear elastic region, no further than approximately $0.015\ J_{\text{applied}}/\mu$ in front of the deformed crack tip.

5 Discussion and Conclusions

The relationship between a Mode I plane strain crack in a NeoHookean material under the assumptions of small-scale nonlinearity and a local cavitation criterion [4] was examined using finite element analysis. The computational results demonstrate that the region of nonlinearity, where the nonlinear asymptotic crack tip solution can be found, is small under the assumptions of small-scale nonlinearity, extending to $0.11\ J_{\text{applied}}/\mu$ in the undeformed coordinate system. However, within this region, the finite

element results compare favorably with the theoretical asymptotic solution for this problem, and all load amplitude parameters in the theoretical solution were determined either analytically or numerically. Outside of the nonlinear region, the linear elastic asymptotic solution was accurately found.

A local cavitation surface was then identified in the nonlinear crack tip region, and predicted that cavitation could occur ahead of the crack tip, up to approximately 0.015 J_{applied}/μ in the deformed configuration.

References

[1] Kinloch, A. J. and Young, R. J., Fracture behavior of polymers. *Elsevier Applied Science Pub.* New York (1983).

[2] Kausch, H., Polymer fracture. *Springer-Verlag*, New York (1987).

[3] Gent, A. N. and Lindley, P. B., Internal rupture of bonded rubber cylinders in tension. *Proc. Roy. Soc.* **A249** (1958) 195-205.

[4] Hou, H. and Abeyaratne, R., Cavitation in elastic and elastic-plastic solids, to be published in *J. Mech. Phys. Solids.*

[5] Ball, J. M., Discontinuous equilibrium solutions and cavitation in non-linear elasticity, *Phil. Trans. Roy. Soc.* **A306** (1982) 189.

[6] Singh, S., Deformation behavior and thermomechanical failure of carbon black filled elastomers, Ph.D. Thesis, Massachusetts Institute of Technology (1987).

[7] Stringfellow, R. and Abeyaratne, R., Cavitation in an elastomer: comparison of theory with experiment. *Mat. Sci. Eng.* **A112** (1989) 127-131.

[8] Williams, M. L., On the stress distribution at the base of a stationary crack. *J. App. Mech.*, **24** (1957) 109-114.

[9] Knowles, J. K., Finite elastostatic fields with unbounded deformation gradients. In: *Finite Elasticity*, Applied Mechanics Division, ASME **27** (1977) 23-40.

[10] Stephenson, R., The equilibrium field near the tip of a crack for finite plane strain of incompressible elastic materials. *J. Elasticity* **12** (1982) 65-99.

[11] Rice, J.R., A path independent integral and the approximate analysis of strain concentration by notches and cracks. *Journal of Applied Mechanics*, **35** (1968) 379-386.

[12] Hutchinson, J.W., Nonlinear fracture mechanics, The Technical University of Denmark (1979).

[13] Quigley, C.J., A computational and experimental investigation of a Mode I crack in an elastomer, S.M. Thesis, Massachussetts Institute of Technology (1990).

[14] Nagtegaal, J.C., Parks, D.M., and Rice, J.R., On numerically accurate finite element solutions in the fully plastic range. *Computer Methods in Applied Mechanics and Engineering* **4**, (1974) 153-177.

[15] ABAQUS, Version 4.7, Hibbitt, Karlsson, and Sorensen, Inc., Providence, R.I.

[16] Moran, B., and Shih, C.F., Crack tip integrals and associated domain integrals from momentum and energy balance. *Engineering Fracture Mechanics*, **27** (1987) 615-642.

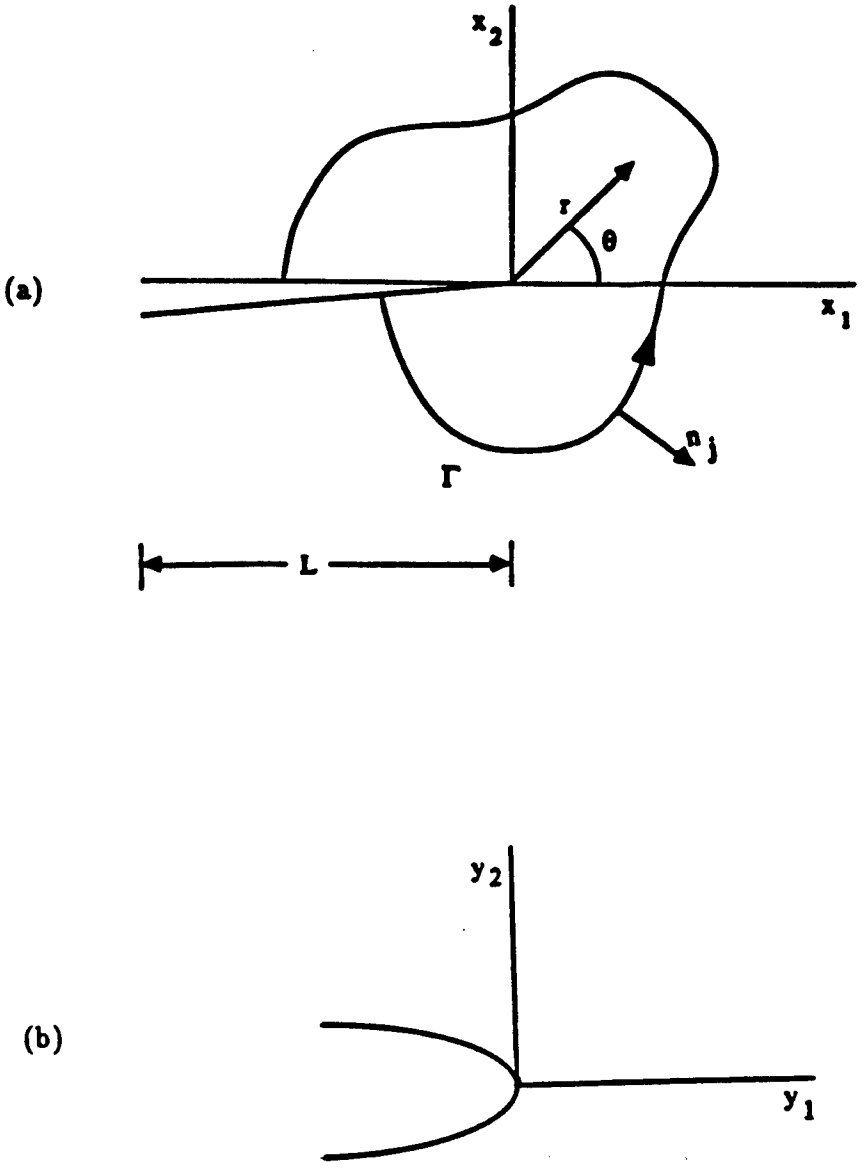

Figure 1: Undeformed(a) and deformed(b) coordinate systems in a stationary crack.

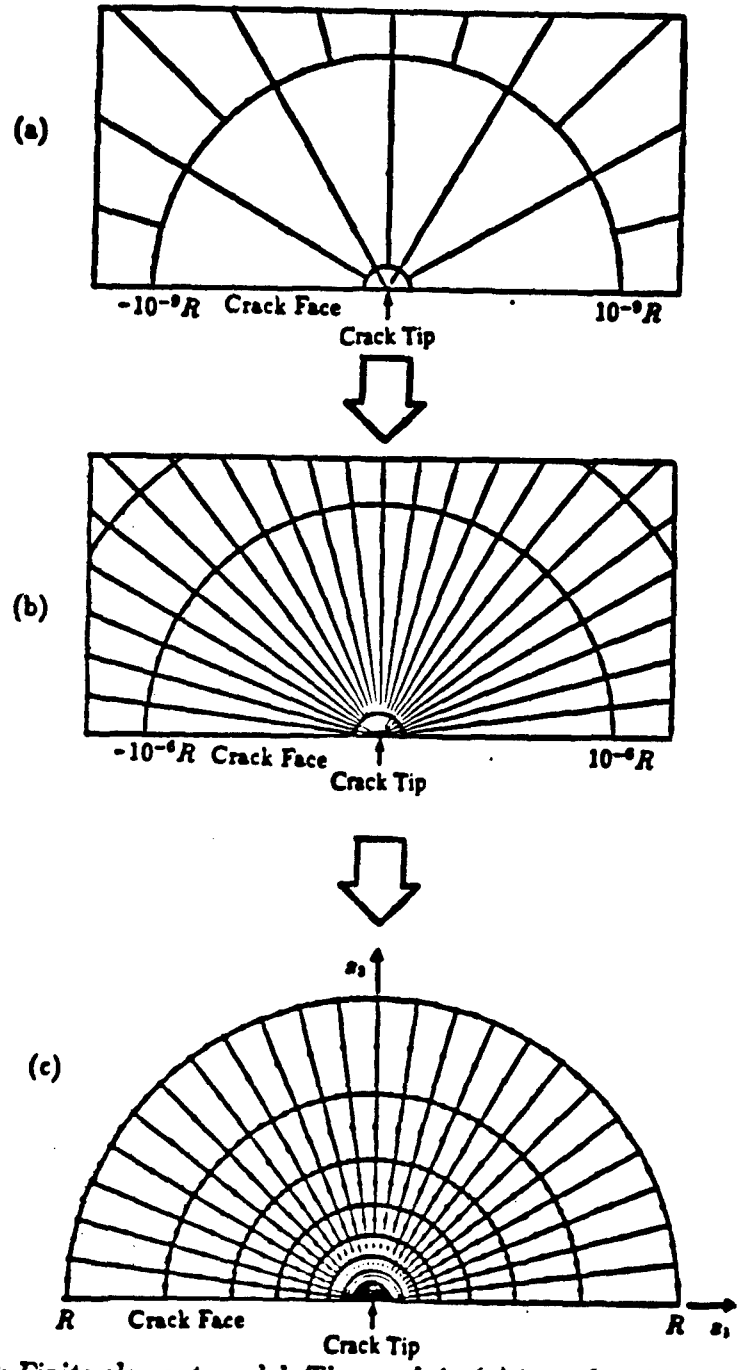

Figure 2: Finite element model. The mesh in (a) is enclosed by the mesh in (b). Similarly, the mesh in (b) is enclosed by the mesh in (c).

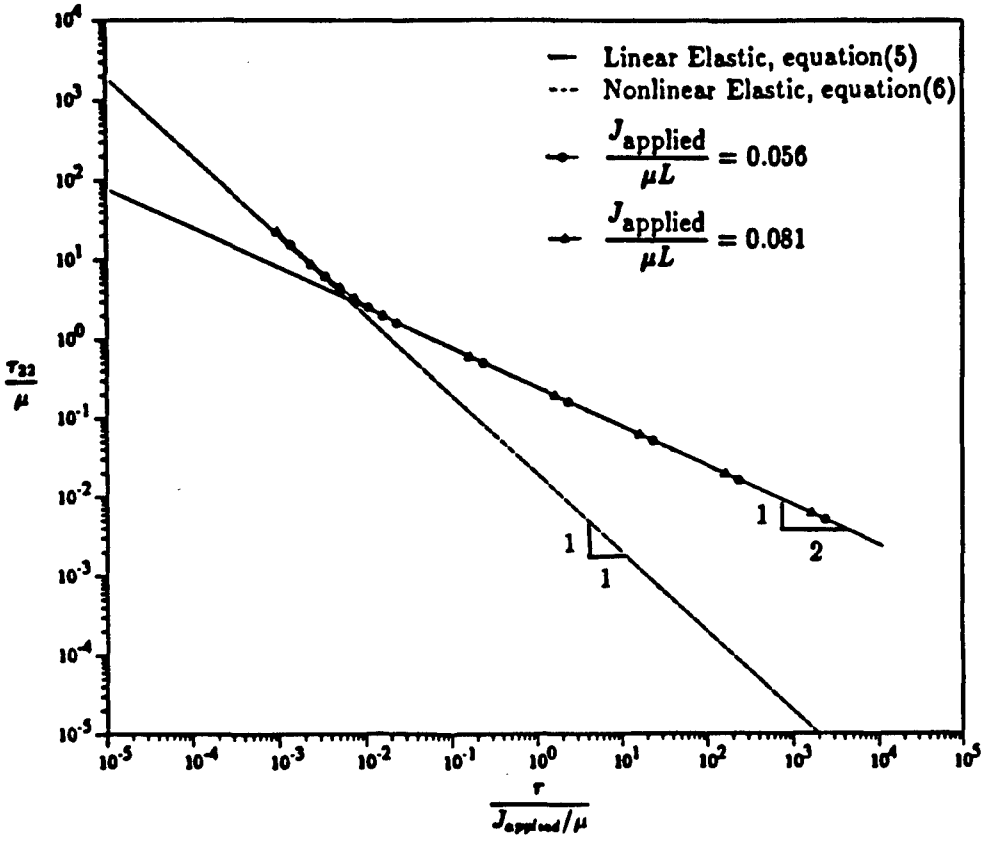

Figure 3: τ_{22} along $\theta = 71.25$ degrees.

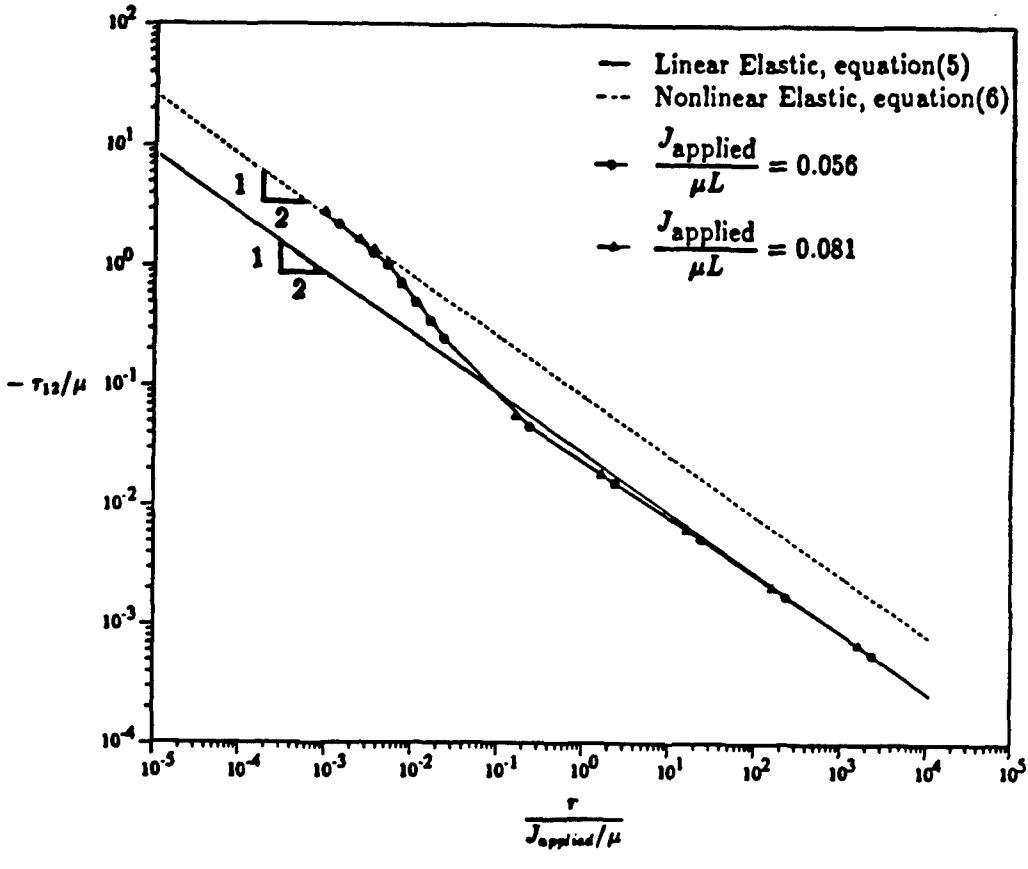

Figure 4: τ_{12} along $\theta = 71.25$ degrees.

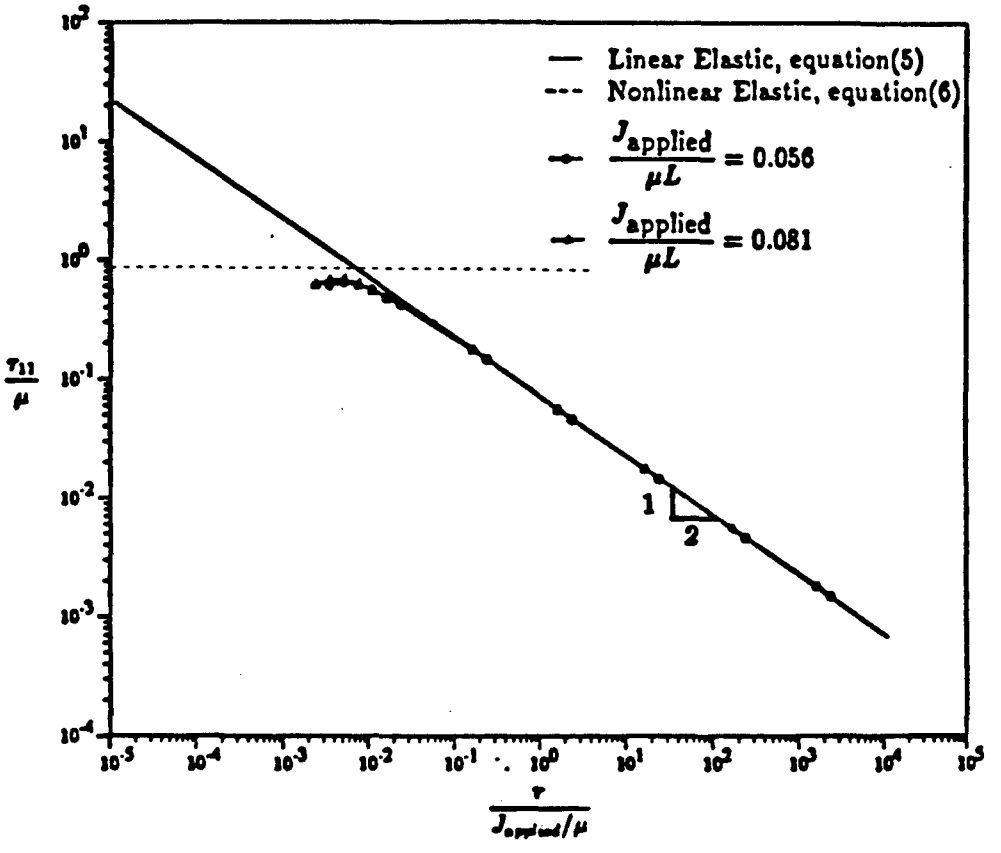

Figure 5: τ_{11} along $\theta = 71.25$ degrees.

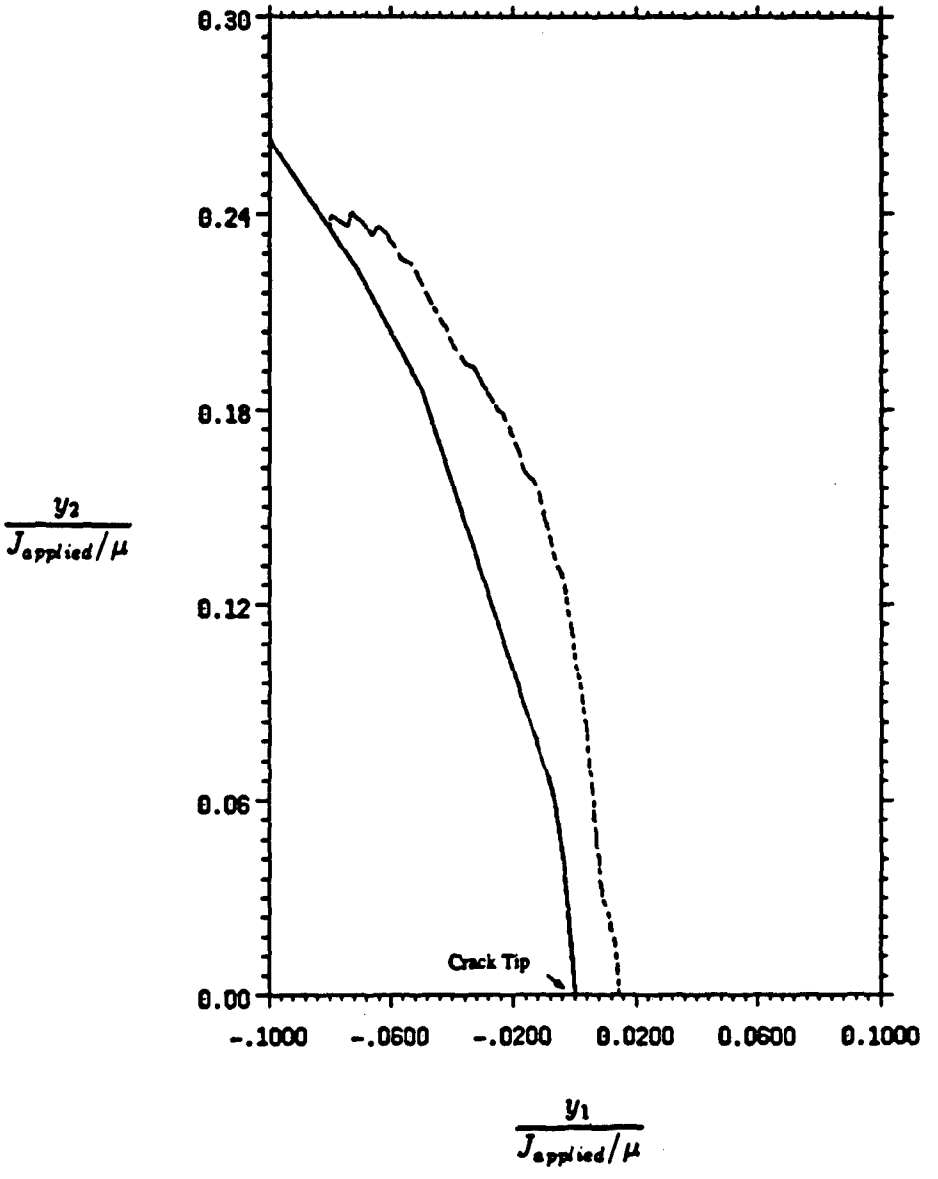

Figure 6: A local cavitation surface surrounding the crack tip in the deformed configuration.

SESSION IV: PENETRATION MECHANICS

Session Chairman: *Dr. K. Iyer*

EFFECT OF MATERIAL ELASTICITY AND FRICTIONAL FORCES ON THE STEADY STATE AXISYMMETRIC DEFORMATIONS OF A THICK TARGET

R. C. Batra
X. Chen
R. Jayachandran

Department of Mechanical and Aerospace
Engineering and Engineering Mechanics
University of Missouri - Rolla
Rolla, MO 65401-0249

ABSTRACT

Steady state axisymmetric deformations of a thick target being penetrated by a fast moving rigid cylindrical rod have been analyzed. Two different problems, namely, one in which the target material is modeled as elastic perfectly plastic and the target/penetrator interface smooth, and the other involving a viscoplastic target and rough target/penetrator interface are studied. The frictional force at the contact surface is assumed to depend upon the normal traction and the relative velocity of sliding between the two surfaces. Computed results show that the consideration of elastic effects reduces the hydrostatic pressure at the target/penetrator interface and the consideration of frictional forces affects minimally the distribution of normal tractions on the target/penetrator interface.

INTRODUCTION

An outstanding problem in penetration mechanics is to find, within reasonable resources, whether or not for the given penetrator and target geometries, materials, target support conditions, penetrator speed, and the angle of attack, the target will be perforated. If the target is perforated, the speed of the penetrator when it ejects out of the target is of interest. If the target is not perforated, one would like to know the shape and size of the hole made in the target. This problem has defied a complete solution for many years. We refer the reader to review articles by Backman and Goldsmith [1], Wright and Frank [2], Wright [3], and

Anderson and Bodner [4] for a review and discussion of most of the work done on ballistic penetration. Different engineering models have been proposed by Awerbuch [5], Awerbuch and Bodner [6], Ravid and Bodner [7], Ravid *et al.* [8], Forrestal *et al.* [9], and Batra and Chen [10]. For impact velocities in the range of 0.5 km/s to 10 km/s, Birkhoff *et al.* [11], Pack and Evans [12], Allen and Rogers [13], Alekseevskii [14], and Tate [15] have proposed using the Bernoulli equation or its modification to analyze the penetration process. The last three references introduced a resistive pressure, dependent upon the material strength, in the Bernoulli equation. Tate [16,17], Pidsley [18], Batra and Gobinath [19], Batra and Chen [10], and Jayachandran and Batra [20] have estimated the value of the resistive pressure. Whereas Tate used a solenoid fluid flow model of the steady state penetration process, other investigations used a numerical solution of the problem. Both Pidsley [18] and Wright [3] have pointed out that the transverse gradients of the shear stress evaluated on the axial line make noticeable contributions to the resistive pressure terms in the modified Bernoulli equation.

For a rigid/perfectly plastic target, it is very likely that the hydrostatic pressure at target points adjoining the penetrator/target interface is increased due to the rigidity of the surrounding target material. Also, the assumption used heretofore by Batra and co-workers [20-27] that the target/penetrator interface is smooth is not very realistic. The distribution of the frictional force on this surface is not known *a priori*. Chen and Batra [28] have recently proposed that the frictional force at a point on this interface be assumed to be a function of the normal traction and the relative velocity there between the adjoining target and penetrator particles. Jayachandran and Batra [20] have studied the effect of the elasticity of the target material on its deformations. We summarize below some of the results from these two investigations.

FORMULATION OF THE PROBLEM

With respect to a cylindrical coordinate system with origin at the center of the penetrator nose and positive z-axis pointing into the target, equations governing the target deformations are:

Balance of mass: $$\text{div } \underset{\sim}{v} = 0, \tag{1}$$

Balance of linear momentum: $$\text{div } \underset{\sim}{\sigma} = \rho \, (\underset{\sim}{v} \cdot \text{grad}) \, \underset{\sim}{v}, \tag{2}$$

Constitutive relations:

$$\underset{\sim}{\sigma} = -p\underset{\sim}{1} + \underset{\sim}{s}, \tag{3}$$

$$\overset{0}{\underset{\sim}{s}} = 2G\,(\underset{\sim}{D} - \underset{\sim}{D}^{p}), \tag{4}$$

$$\underset{\sim}{s} = 2\mu\,(I)\,\underset{\sim}{D}^{p}, \tag{5}$$

where

$$2\mu = \frac{\sigma_0}{\sqrt{3I}}(1 + bI)^m, \qquad 2I^2 = \mathrm{tr}\,(\underset{\sim}{D}^{p2}), \tag{6}$$

$$\overset{0}{\underset{\sim}{s}} = (\underset{\sim}{v}\cdot \mathrm{grad})\,\underset{\sim}{s} + \underset{\sim}{s}\,\underset{\sim}{W} - \underset{\sim}{W}\,\underset{\sim}{s}, \tag{7}$$

$$2\underset{\sim}{D} = \mathrm{grad}\,\underset{\sim}{v} + (\mathrm{grad}\,\underset{\sim}{v})^{T}, \quad 2\,\underset{\sim}{W} = \mathrm{grad}\,\underset{\sim}{v} - (\mathrm{grad}\,\underset{\sim}{v})^{T}. \tag{8}$$

Equations (1) and (2) are written in the Eulerian description of motion. The operators grad and div denote the gradient and divergence operators on fields defined in the present configuration. In equations (1) - (8), $\underset{\sim}{v}$ is the velocity of a target particle relative to the penetrator, $\underset{\sim}{\sigma}$ the Cauchy stress tensor, $\underset{\sim}{s}$ its deviatoric part, p the hydrostatic pressure not determined by the deformation history, and an open circle on $\underset{\sim}{s}$ indicates the Jaumann derivative defined by eqn. (7) for the steady stress field. Furthermore, G is the shear modulus, $\underset{\sim}{D}^{p}$ the plastic strain-rate, μ defined by eqn. $(6)_1$ may be interpreted as the shear viscosity of the target material, σ_0 is the yield stress in a quasistatic simple compression test, $\underset{\sim}{D}$ the strain-rate tensor, $\underset{\sim}{W}$ is the spin tensor, and parameters b and m characterize the strain-rate sensitivity of the material. Equation (4) expresses Hooke's law written in the rate form, and is based on the tacit assumption that the strain-rate has additive decomposition into elastic and plastic parts. In eqns. (3) - (5) we have assumed that a material particle is undergoing elastic and plastic deformations simultaneously. Substitution

from eqns. (5) and (7) into eqn. (4) gives the following differential equation for $\underset{\sim}{s}$.

$$(\underset{\sim}{v} \cdot \text{grad})\, \underset{\sim}{s} + \underset{\sim}{s}\, \underset{\sim}{W} - \underset{\sim}{W}\, \underset{\sim}{s} + (G/\mu)\, \underset{\sim}{s} = 2G\, \underset{\sim}{D}. \tag{9}$$

On the target/penetrator interface, we impose

$$\underset{\sim}{t} \cdot (\underset{\sim}{\sigma}\, \underset{\sim}{n}) = -\nu\, (v/v_0)^{\beta}\, \underset{\sim}{n} \cdot (\underset{\sim}{\sigma}\, \underset{\sim}{n})\, (\underset{\sim}{v}/v), \tag{10}$$

$$\underset{\sim}{v} \cdot \underset{\sim}{n} = 0, \tag{11}$$

where $v = |\underset{\sim}{v}| = (v_r^2 + v_z^2)^{1/2}$, $\underset{\sim}{n}$ and $\underset{\sim}{t}$ are, respectively, a unit normal and a unit tangent vector to the surface, and β and ν are constants. Thus, the frictional force at the contact surface is assumed to depend upon the relative speed between the penetrator and the target. Prior to discussing boundary conditions on other surfaces, we note that the governing equations are highly nonlinear, and we intend to seek their approximate solution by the finite element method, which necessitates that we consider a finite region. The bounded region R of the target whose deformations are analyzed is depicted in Figure 1, which also shows the discretization of the domain into finite elements. The boundary conditions imposed on the bounding surfaces of this finite region are:

$$v_r = 0, \quad v_z = -1.0 \quad \text{on the bounding surface EFA,} \tag{12}$$
$$\sigma_{rz} = 0, \quad v_r = 0 \quad \text{on the axis of symmetry DE,} \tag{13}$$
$$\sigma_{zz} = 0, \quad v_r = 0 \quad \text{on the surface AB.} \tag{14}$$

Conditions (13) follow from the assumed axisymmetric nature of deformations. We note that eqn. (9) can not be solved for $\underset{\sim}{s}$, but is to be solved simultaneously with eqns. (1) and (2). Accordingly, we need to specify the state of stress of the material entering the region R [29]. We set

$$p = 0, \quad s_{rr} = 0, \quad s_{\theta\theta} = 0, \quad \text{and} \quad s_{rz} = 0 \quad \text{on the bounding surface EFA.} \tag{15}$$

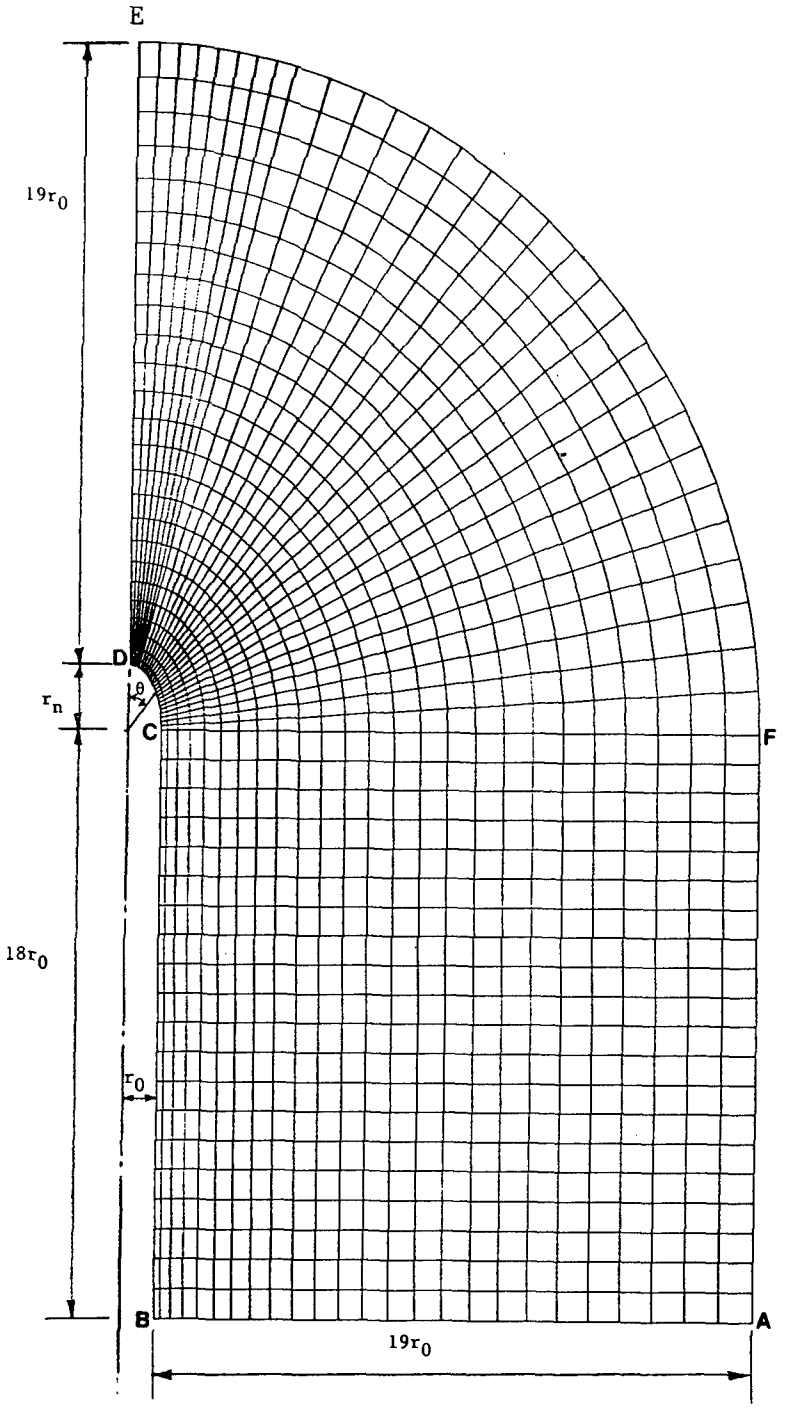

Figure 1. The finite region studied and its discretization

COMPUTATIONAL CONSIDERATIONS

An approximate solution of the aforestated problem has been obtained by the finite element method. The region R is divided into quadrilateral elements, and within each element $\underset{\sim}{v}$ and $\underset{\sim}{s}$ are approximated by bilinear functions defined in terms of their values at the corner nodes and the pressure p is assumed to be constant. Thus, $\underset{\sim}{v}$ and $\underset{\sim}{s}$ are continuous across interelement boundaries, but p is discontinuous. The pressure field is smoothened by using

$$\sum_{j=1}^{M} \left(\int N_i \, N_j \, dV\right) p_j = \int N_i \, \bar{p} \, dV, \quad i = 1, 2, \ldots, M \tag{16}$$

where M equals the number of nodes, $\bar{p}$ is the discontinuous pressure field computed above, and N_1 and N_2, ... are the piecewise bilinear finite element basis functions. We used the Petrov-Galerkin [30] formulation of eqn. (9), but the Galerkin [30] formulation of eqns. (1) and (2). The iterative process used to solve the resulting nonlinear algebraic equations was stopped when

$$\left(\sum \|\underset{\sim}{\phi}^{m} - \underset{\sim}{\phi}^{m-1}\|^2\right)^{1/2} \leq 0.01 \left(\sum \|\underset{\sim}{\phi}^{m-1}\|^2\right)^{1/2} \tag{17}$$

where $\|\underset{\sim}{\phi}\|^2 = \phi_r^2 + \phi_z^2$ when $\underset{\sim}{\phi}$ is a vector, $\|\underset{\sim}{\phi}\|^2 = \text{tr}\,(\underset{\sim}{\phi}\,\underset{\sim}{\phi}^{T})$ when $\underset{\sim}{\phi}$ is a second order tensor and $\|\underset{\sim}{\phi}\| = |\phi|$ for a scalar ϕ. The summation sign in eqn. (17) implies the sum of the indicated quantity evaluated at all nodes, and the convergence criterion (17) is applied to the fields of the velocity, the deviatoric stress tensor, and the pressure.

RESULTS AND DISCUSSIONS

In order to investigate the effect of material elasticity, we set b = 0.0 in eqn. $(6)_1$ and $\upsilon = 0.0$ in eqn. (10). Thus, the target/penetrator interface is now taken to be smooth, and the target material to be elastic/perfectly plastic. The distribution of the non-dimensional normal

tractions, normalized with respect to the yield stress σ_0 in a quasistatic simple compression test, on the nose surface of a hemispherical nosed penetrator for $\alpha = \rho v_0^2/\sigma_0 = 10$, and $\gamma = \sigma_0/G = 10^{-2}, 10^{-3}, 10^{-5}$, and 10^{-8} is shown in Figure 2. Note that $\gamma = 0$ for a rigid/perfectly plastic material. The curves for $\gamma = 10^{-5}$ and 10^{-8} overlap each other. These plots reveal that the consideration of elastic effects reduces the normal traction on the penetrator nose surface. This reduction is due to the lower value of the hydrostatic pressure for the elastic/plastic problem as compared to that when the target material is modeled as rigid/perfectly plastic.

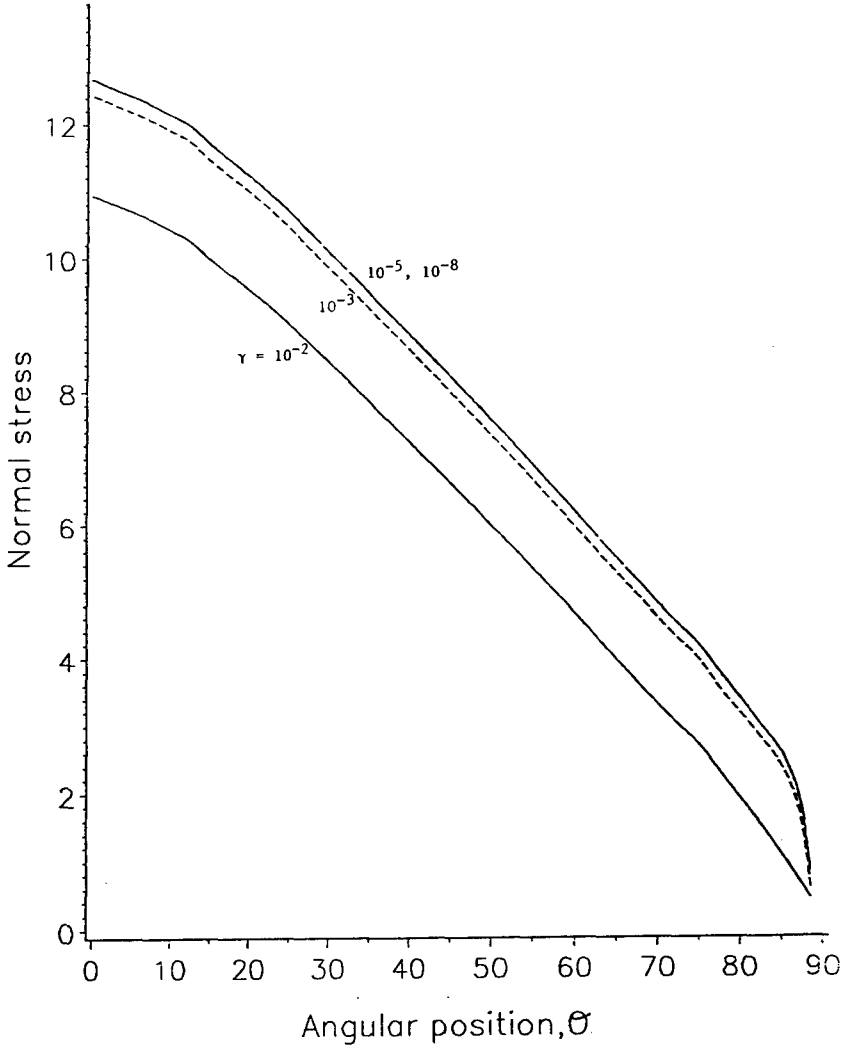

Figure 2. Distribution of the compressive normal stress divided by σ_0 on the penetrator nose surface for different values of $\gamma = \sigma_0/G$ when the target material is modeled as elastic perfectly plastic.

The least squares fit to the computed values of the maximum hydrostatic pressure p_{max} and the axial resisting force F experienced by the penetrator for different values of α gives

$$p_{max} = 7.20 + 0.48\,\alpha, \quad F = 7.67 + 0.042\,\alpha$$

for a rigid/perfectly plastic target, and

$$p_{max} = 5.29 + 0.47\,\alpha, \quad F = 5.90 + 0.038\,\alpha$$

when the target material is modeled as elastic perfectly plastic. It is clear that F depends upon α very weakly. The corresponding values for the target resistance parameter R_t appearing in the modified Bernoulli equation are

$$R_t = 7.86 - 0.0186\,\alpha, \quad \text{for a rigid/perfectly plastic target,}$$
$$R_t = 5.96 - 0.027\,\alpha, \quad \text{for an elastic/perfectly plastic target.}$$

We note that p_{max} and R_t are scaled by σ_0, and F by $\pi\, r_0^2\, \sigma_0$. The value of R_t computed from Tate's formula [17] is 5.734 which matches well with our value for an elastic/plastic target.

Figure 3 depicts the contours of the nondimensional hydrostatic pressure (i.e., p/σ_0) in the deforming target region for $\alpha = 10$. These show that the pressure drops off to zero along any radial line, the rate of drop being high near the nose surface and quite low as one moves away from the target/penetrator interface. The contour of the zero hydrostatic pressure near the bounding surface is not plotted.

We refer the reader to [20] for a detailed discussion of results for other nose shapes and some other results for the hemispherical nosed penetrator.

When studying the effect of frictional forces at the contact surface, we disregard elastic deformations, and accordingly omit eqns. (4) and (9). Equation (1) and that obtained by substituting from (5) and (3) into (2) together with boundary conditions (10) - (14) are solved for $\underset{\sim}{v}$ and p. The

distribution of the non-dimensional normal tractions on the nose surface of a hemispherical nosed penetrator for $\alpha = 6.15$, $\beta = 1.5$, $b = 10^6$ sec, $m = 0.09$, and the coefficient of friction $\upsilon = 0$, 0.1, 0.2, 0.3, and 0.4 is plotted in Figure 4. These plots vividly demonstrate that the coefficient

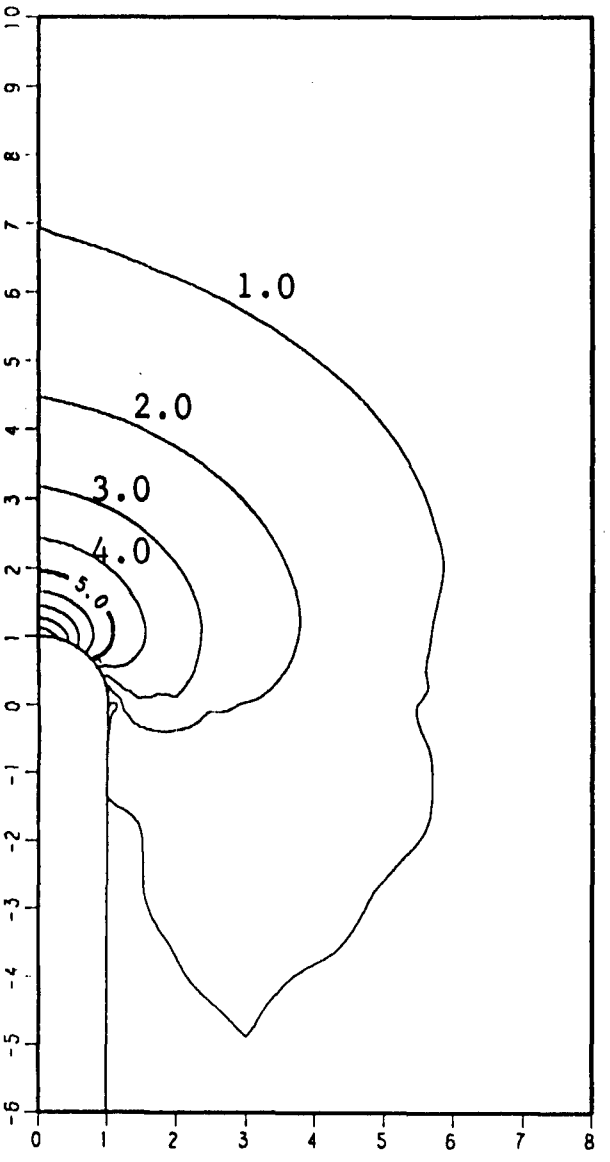

Figure 3. Contours of the hydrostatic pressure divided by σ_0 in the deforming target region.

of friction affects little the normal traction on the penetrator nose surface. However, the distributions of the tangential speed and the second invariant I of the strain-rate tensor on the target/penetrator interface are quite different for different values of υ. These results and the motivation for the expression (10) for the frictional force are given in Ref. [28].

Acknowledgement: This work was supported by the U. S. Army Research Office Contract DAAL89-K-0050 to the University of Missouri - Rolla.

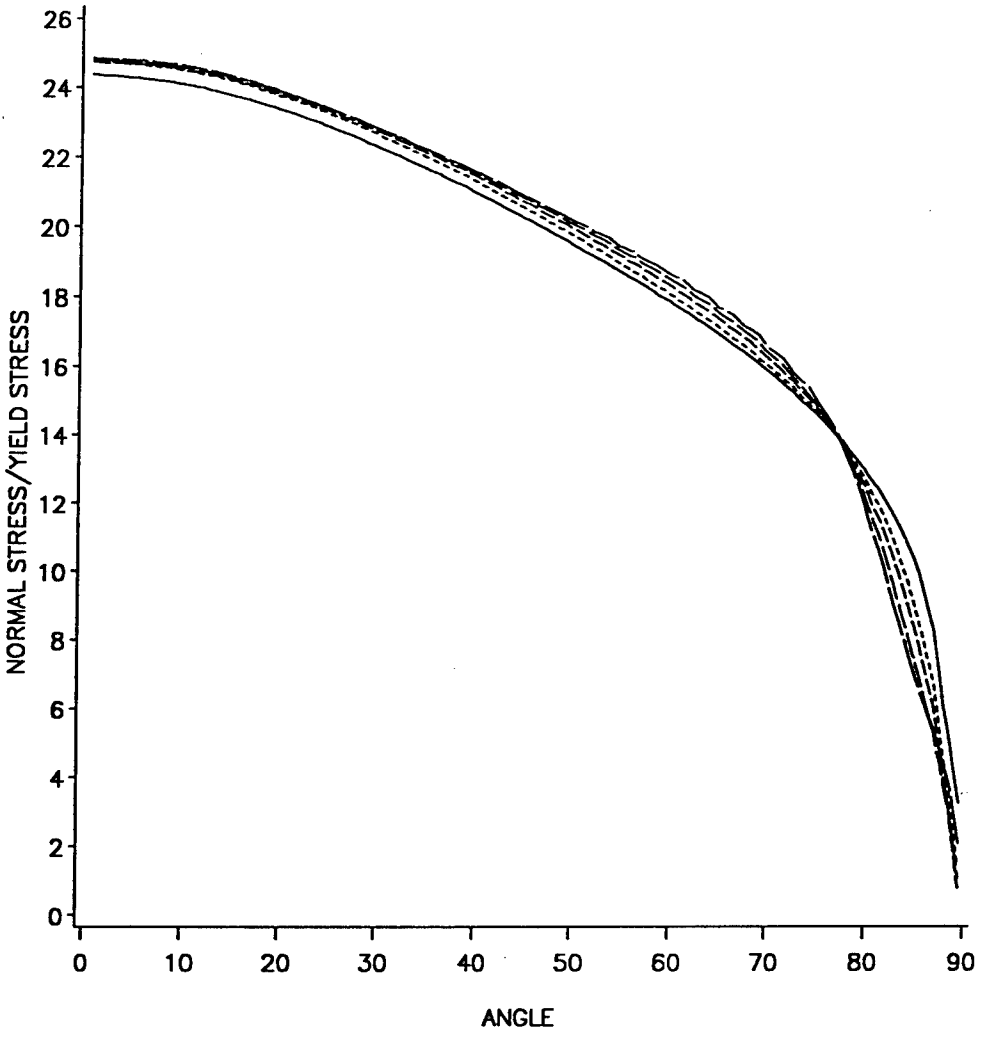

Fig. 4. Distribution of the normal traction on the hemispherical nose of the penetrator for different values of the coefficient of friction. (——— μ = 0.0, ----- μ = 0.1, – – – – μ = 0.20, — — — μ = 0.3, (—— —— —— μ = 0.4)

REFERENCES

1. M. E. Backman and W. Goldsmith, *Int. J. Engr. Sci., 16*, 1-99 (1978).
2. T. W. Wright and K. Frank, Approaches to Penetration Problems, SMIRT Symposium, No. 14, Impact, Lausanne, Switzerland (1987).
3. T. W. Wright, A Survey of Penetration Mechanics for Long Rods. In *Lecture Notes in Engineering*, Vol. 3, Computational Aspects of Penetration Mechanics (Eds. J. Chandra and J. Flaherty), Springer-Verlag, New York (1983).
4. C. E. Anderson and S. R. Bodner, *Int. J. Impact Engr., 7*, 9-35 (1988).
5. J. Awerbuch, Technion-Israel Institute of Technology, MED Report No. 28 (1970).
6. J. Awerbuch and S. R. Bodner, *Int. J. Solids and Structures, 10*, 671-684 (1974).
7. M. Ravid and S. R. Bodner, *Int. J. Engr. Sci., 21*, 577-591 (1983).
8. M. Ravid, S. R. Bodner, and I. Holcman, *Int. J. Engr. Sci., 25*, 473-482 (1987).
9. M. J. Forrestal, K. Okajima, and V. K. Luk, *J. of Appl. Mechs., 55*, 755-760 (1988).
10. R. C. Batra and Xingju Chen, *Int. J. Engr. Sci., 28*, 1347-1358 (1990).
11. G. Birkhoff, D. P. McDougall, E. M. Pugh, and G. Taylor, *Proc. Phys. Soc. Lond., 57*, 147 (1945).
12. D. C. Pack and W. M. Evans, *Proc. Phys. Soc. Lond., B64*, 298-303 (1951).
13. W. A. Allen and J. W. Rogers, *J. Franklin Inst., 272*, 275 (1961).
14. V. P. Alekseevskii, *Comb. Expl. and Shock Waves, 2*, 63-66 (1966). (Translation from Russian, Faraday Press, New York.)
15. A. Tate, *J. Mech. Phys. Solids, 15*, 387-399 (1967).
16. A. Tate, *J. Mech. Phys. Solids, 17*, 141-150 (1969).

17a. A. Tate, *Int. J. Mech. Sci., 28*, 535-548 (1986).

17b. A. Tate, *Int. J. Mech. Sci., 28*, 599-612 (1986).

17c. A. Tate, *Int. J. Engr. Sci., 16*, 845-858 (1978).

18. P. H. Pidsley, *J. Mech. Phys. Solids, 32*, 315-333 (1984).
19. R. C. Batra and T. Gobinath, *Int. J. Impact Engr., 11*, 1-31 (1991).
20. R. Jayachandran and R. C. Batra, Steady State Penetration of Elastic Perfectly Plastic Targets, *Acta Mechanica* (in press).
21. R. C. Batra and T. W. Wright, *Int. J. Engr. Sci., 24*, 41-54 (1986).

22. R. C. Batra, *Int. J. Engr. Sci., 25*, 1131-1141 (1987).
23. R. C. Batra, *Comp. Mech., 3*, 1-12 (1988).
24. R. C. Batra and Pei-Rong Lin, *Int. J. Engr. Sci., 26*, 183-192 (1988).
25. R. C. Batra and P. R. Lin, *Int. J. Impact Engr., 8*, 99-113 (1989).
26. R. C. Batra and P. R. Lin, *Int. J. Engr. Sci., 28*, 93-98 (1990).
27. P. R. Lin and R. C. Batra, *Int. J. Engr. Sci., 27*, 1155-1165 (1989).
28. X. Chen and R. C. Batra, Effect of Frictional Forces on Steady State Axisymmetric Deformations of a Thick Viscoplastic Target (submitted for publication).
29. Y. Shimazaki and E. G. Thompson, Elasto Visco-Plastic Flow with Special Attention to Boundary Conditions, *Int. J. Num. Meth. Engr., 17*, 97-112 (1981).
30. T. J. R. Hughes, The Finite Element Method. Linear Static and Dynamic Problems, Prentice-Hall, Englewood Cliffs (1987).

EXPERIMENTAL INVESTIGATION OF RHA PLATE PERFORATION BY A SHAPED-CHARGE JET

Martin N. Raftenberg

U.S. Army Ballistic Research Laboratory, Aberdeen Proving Ground, MD 21005

Abstract
In each of a series of experiments, a shaped charge warhead is fired into an RHA plate. The parameters varied are target plate thickness and standoff. Data are presented for pre-impact jet geometry, behind-armor-debris patterns, perforation hole throat radius, ejecta ring radius, spall ring radius and total mass lost by the target plate.

1. INTRODUCTION

A series of ten experiments is performed in each of which a shaped charge warhead is fired at normal incidence into a plate of rolled homogeneous armor (RHA). The experimental setup is sketched in Figure 1. The warhead contains a conical OFHC copper liner with a vertex angle of 42° and a base diameter of 81.3 mm (≡ 1 charge diameter, or 1 C.D.) Three X-ray tubes are employed to produce flash radiographs. The two parameters varied in the series are the standoff S, or distance between charge base and the target plate, and target plate thickness d. The values of d and S in each experiment are listed in Table 1. Most combinations of d and S values are repeated to assess round-to-round variability and to allow for six flash radiographs for a given set of values. Also listed in Table 1 are the target plate's cross-sectional dimensions and a Brinell hardness measurement for the entrance and exit surfaces.

Results to be presented in this paper include (i) flash radiographs, both of the jet prior to impact and of the behind-armor-debris pattern at specific times following perforation, (ii) measurements pertaining to the final geometry of the target plate hole, and (iii) measurements of the total mass lost by the target plate. The intention is to provide a set of benchmarks to modelers and thereby lead to a deeper understanding of phenomena associated with RHA plate perforation by a shaped-charge jet.

2. DISCUSSION

2.1. The Pre-Impact Jet

Figure 2 shows a radiograph at 5 μs before impact from a test involving the short standoff of 3.00 C.D. The stretching jet is still intact. The diameter of the

jet's wide tip region is 7.8 mm, while the "stalk" behind this region has a fairly uniform diameter of about 4.0 mm. The jet tip speed is known from previous experience with this warhead to be 7.7 mm/μs.

Figure 3 shows a radiograph at 4 μs before impact from a test involving a 12.00 C.D. standoff. By now the jet has broken up into particles. The leading particle has a foremost "bulb" with a 6.2 mm diameter, followed by a "stalk" with a 4.8 mm diameter. The total length of this leading particle is 26 mm. It is therefore expected on the basis of hydrodynamic theory [1] to be able to perforate a 13- or a 25-mm-thick target plate without assistance from subsequent particles. The speed of this leading particle is known from a previous experiment to be 7.7 mm/μs [2].

2.2 Post-Perforation Radiographs of Behind-Armor-Debris

Each of Figures 4 through 7 shows a series of six radiographs for the respective cases of d = 13 mm and S = 3.00 C.D., d = 25 mm and S = 3.00 C.D., d = 51 mm and S = 3.00 C.D., and d = 13 mm and S = 12.00 C.D. The six views apply at the approximate times of 5 μs before impact and 15, 30, 70, 140 and 210 μs after perforation. (These times are computed from times after initial impact given in the figures based on an assumed penetration speed of 4.0 mm/μs.) The views at 5 μs before impact and at 70 μs after perforation have a magnification factor of 0.8 times that of the others. The first experiment listed pertains to the three earliest views, and the second to the three latest.

RHA fragments in the radiographs are called "ejecta" if located between the plate's entrance surface and the original warhead location and "debris" if positioned on the opposite side of the exit surface as was the original warhead. At 15 μs after perforation, Figures 4 through 7 each shows a debris cloud composed of small fragments, presumably created by reflection of the initial shock. The foremost fragments of this cloud are at about the same elevation as the jet tip (Figures 4, 5 and 6) or the tip of the leading jet particle (Figure 7).

In each of Figures 4 through 7, the largest visible debris fragments become larger as time increases. New fragments appear to be forming long after perforation is complete. In Figure 6, which corresponds to the case of d = 51 mm and S = 3.00 C.D., highly-deformed exit surface material seems to separate from the plate between 70 and 140 μs. This separation forms the "spall ring", to be discussed in Section 2.3. At S = 3.00 C.D., as d is successively increased from 13 to 25 to 51 mm, the size of the largest late-time debris fragments increases. The largest late-time debris fragments in the 12.00 C.D. case of Figure 7 are smaller than those in Figure 6, and perhaps intermediate between those in Figures 4 and 5.

The largest late-time ejecta fragments are larger than the largest debris fragments in Figures 4 and 7, which both pertain to 13-mm-thick plates. No late-time ejecta fragments are visible in Figures 5 and 6 due to restricted field of view.

2.3. Target Plate's Final Hole Geometry

An axisymmetric idealization of the final hole geometry for a given test is sketched in Figure 8. The hole's "throat" is its most narrow cross-section, corresponding to a particular elevation. The "ejecta ring" is the interface between entrance surface material that has remained on the plate and that that has separated to form (presumably mostly ejecta) fragments. Similarly, the "spall ring" is the interface between exit surface material that has remained on the plate and that that has separated to form debris fragments.

Following each shot, an entrance and an exit view photograph of the perforated target plate are obtained. As an example, an exit view of the 51 mm plate is presented in Figure 9. The roughly circular interfaces identified with the throat and the spall ring are indicated. These interfaces are digitized. The entrance view yields a second digitization of the hole throat and one of the ejecta ring. Numerical integrations of these digitized coordinates produce two results for throat area A_t for each plate and one for each of ejecta ring area A_{er} and spall ring area A_{sr}. Throat, ejecta ring, and spall ring radii, r_t, r_{er}, and r_{sr}, respectively, are defined by

$$r_t = \left[\frac{A_t}{\pi}\right]^{1/2}, \qquad r_{er} = \left[\frac{A_{er}}{\pi}\right]^{1/2}, \qquad r_{sr} = \left[\frac{A_{sr}}{\pi}\right]^{1/2} \tag{1}$$

The results for r_t are plotted as a function of plate thickness d with standoff S a parameter in Figure 10. At S = 3.00 C.D., r_t shows little change as d is increased from 13 to 25 mm, then decreases substantially as d is further increased to 51 mm. At S = 12.00 C.D., r_t decreases as d is increased from 13 to 25 mm. At both d = 13 mm and d = 25 mm, r_t increases as S is increased from 3.00 C.D. to 12.00 C.D. This last result may be due to enlargement by subsequent particles of the hole created by the leading jet particle at S = 12.00 C.D. A least-squares-error fit of r_t data as a function of d and S is

$$r_t(d,S) = \left[14.16\ \text{mm} - 0.02043d - (0.001022\ \text{mm}^{-1})d^2\right](1 + 0.01435S) \tag{2}$$

In this and in all equations that follow, d is measured in millimeters and S in charge diameters. Equation (2) evaluated at S = 3.00 C.D. and at S = 12.00 C.D. are included in Figure 10.

r_{er} data are plotted as a function of d with S a parameter in Figure 11. At S = 3.00 C.D., r_{er} decreases as d is increased from 13 to 25 mm, then increases as d is further increased to 51 mm. At S = 12.00 C.D., r_{er} decreases as d is increased from 13 to 25 mm. At both d = 13 mm and d = 25 mm, r_{er} seems to increase as S is increased from 3.00 C.D. to 12.00 C.D. (This last statement has been worded cautiously because of the overlap at d = 13 mm.) A least-squares-error fit to the data in Figure 11 is

$$r_{er}(d,S) = \left[24.28\ \text{mm} - 0.3065d - (0.004578\ \text{mm}^{-1})d^2\right](1 + 0.006286S) \tag{3}$$

Equation (3) is shown evaluated at S = 3.00 C.D. and at S = 12.00 C.D. in Figure 11.

Finally, r_{sr} data are plotted as a function of d with S a parameter in Figure 12. At S = 3.00 C.D., r_{sr} increases as d is increased from 13 mm to 25 mm and from 25 mm to 51 mm. r_{sr} shows wide scatter at d = 51 mm, S = 3.00 C.D. At S = 12.00 C.D., r_{sr} increases as d is increased from 13 to 25 mm. r_{sr} shows a weak dependence on S at both d = 13 mm and at d = 25 mm. r_{sr} will therefore be represented as a function of d only. A quadratic least-squares-error fit is

$$r_{sr}(d) = 14.25 \text{ mm} + 0.7051d - (0.005724 \text{ mm}^{-1})d^2 \quad (4)$$

Equation (4) is included in Figure 12.

2.4. Total Mass Lost By Target Plates

Each RHA plate is weighed before and after the experiment to determine its total mass loss, ΔM. Results for ΔM are plotted in Figure 13 as a function of d with S a parameter. Only eight data points are included, since ΔM was not measured to sufficient accuracy in Rds. 4142 and 4189. This is because the four hooks welded onto each plate to enable its support separated from the plates in these two rounds.

Figure 13 shows that at S = 3.00 C.D., ΔM increases as d is increased from 13 to 25 mm and from 25 to 51 mm. Less scatter is evident at d = 51 mm, S = 3.00 C.D. in Figure 13 than in Figure 12 because no ΔM measurement is obtained for Rd. 4142. At S = 12.00 C.D., ΔM increases as d is increased from 13 to 25 mm. At both d = 13 mm and at d = 25 mm, ΔM shows little dependence on S, so ΔM is represented by a function of d only. A quadratic least-squares-error fit is

$$\Delta M(d) = 108.7 \text{ gm} - (0.5852 \text{ gm mm}^{-1})d + (0.1323 \text{ gm mm}^{-2})d^2 \quad (5)$$

which is plotted in Figure 13.

REFERENCES

1. Birkhoff, G., MacDougall, D.P., Pugh, E.M., and Taylor, G.I., "Explosives with Lined Cavities", *J. Appl. Phys.*, 19, 1948, pp. 563-582.

2. Raftenberg, M.N. and Krause, C.D., "RHA Plate Perforation by a Shaped-Charge Jet; Experiment and Hydrocode Simulation", to appear in *Proceedings from the International Conference on Shock-Wave and High-Strain-Rate Phenomena in Materials*, Marcel Dekker, New York, 1992.

Table 1. Experiment Descriptions

Rd.	d (mm)	$BHN_{ent.}$	BHN_{exit}	X-sect. (mm^2)	S (C.D.)
4099	12.5	364	340	251x252	3.00
4186	12.5	340	340	251x254	3.00
4098	25.5	364	364	254x256	3.00
4187	25.1	364	364	252x253	3.00
4097	51.1	321	321	250x255	3.00
4142	51.4	332	302	255x255	3.00
4188	51.3	302	321	255x256	3.00
4190	12.8	340	364	253x253	12.00
4189	12.6	340	364	250x254	12.00
4100	25.6	364	340	251x252	12.00

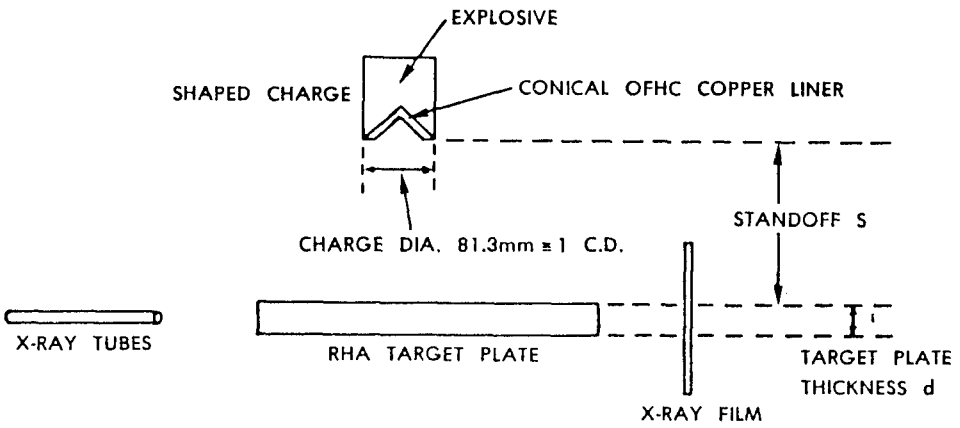

Figure 1. Experimental Setup.

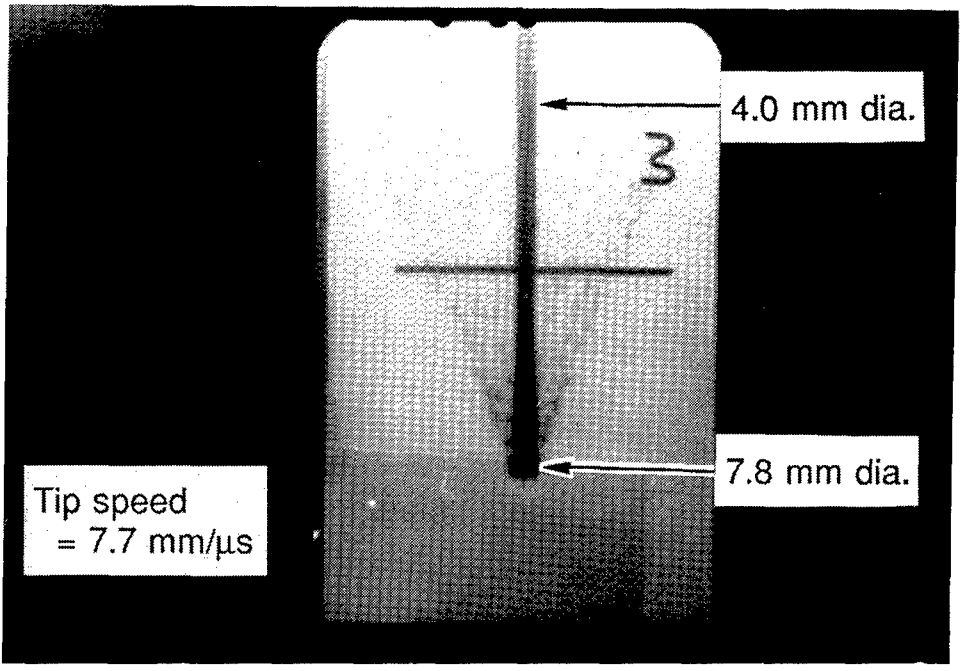

Figure 2. Radiograph at 5 μs Before Impact for Rd. 4097, for Which S = 3.00 C.D.

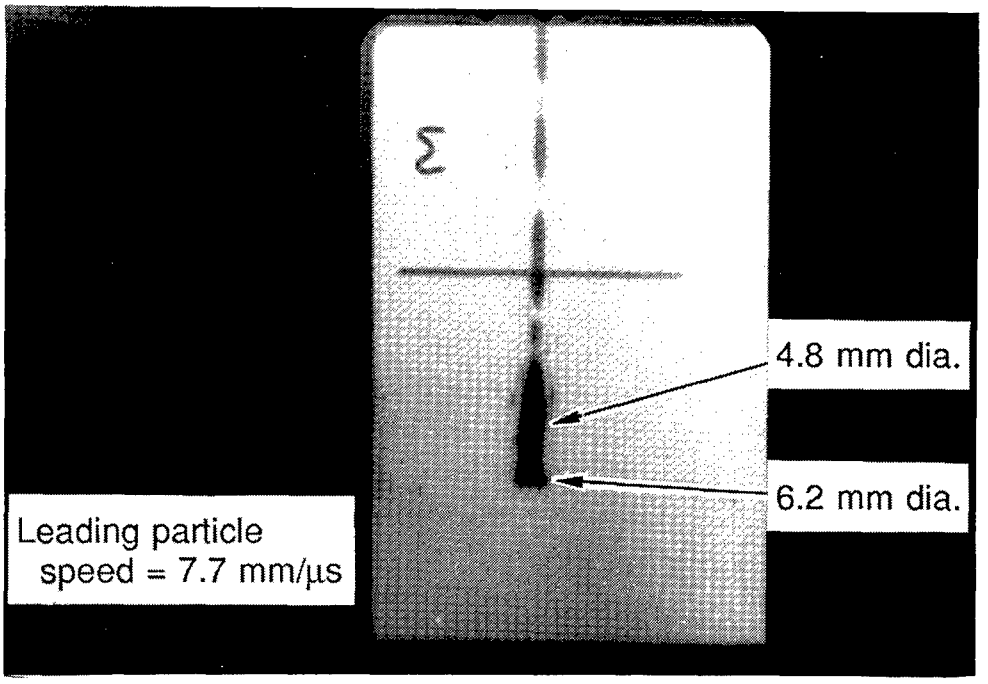

Figure 3. Radiograph at 4 μs Before Impact for Rd. 4100, for Which S = 12.00 C.D.

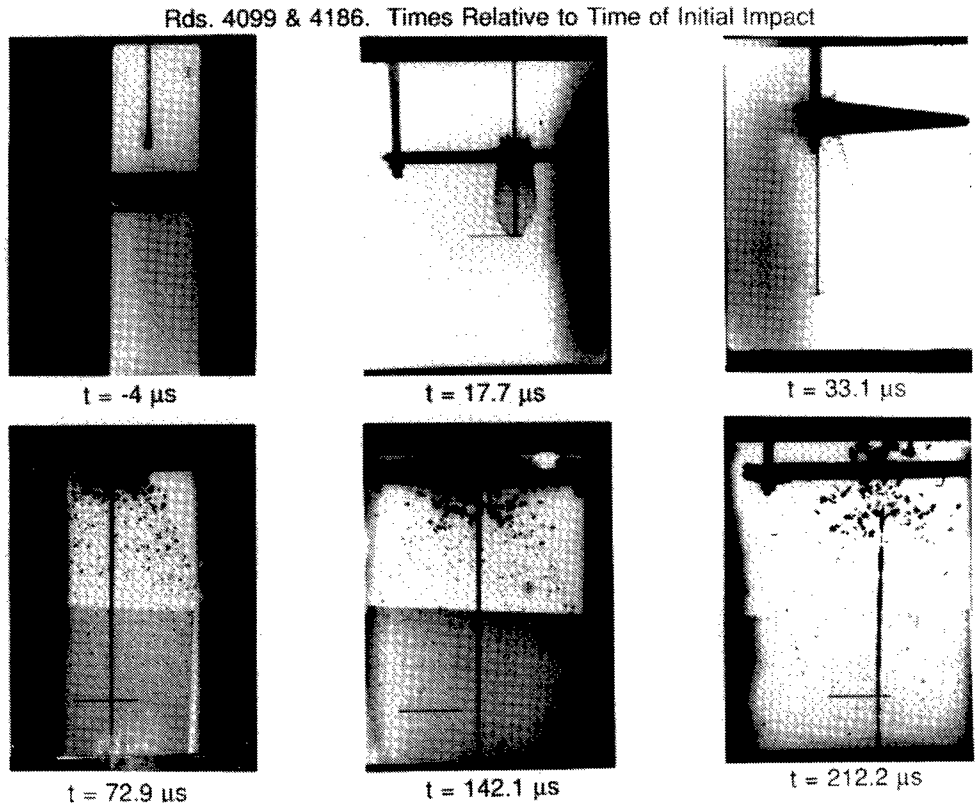

Figure 4. Radiograph Series for d = 13 mm, S = 3.00 C.D.

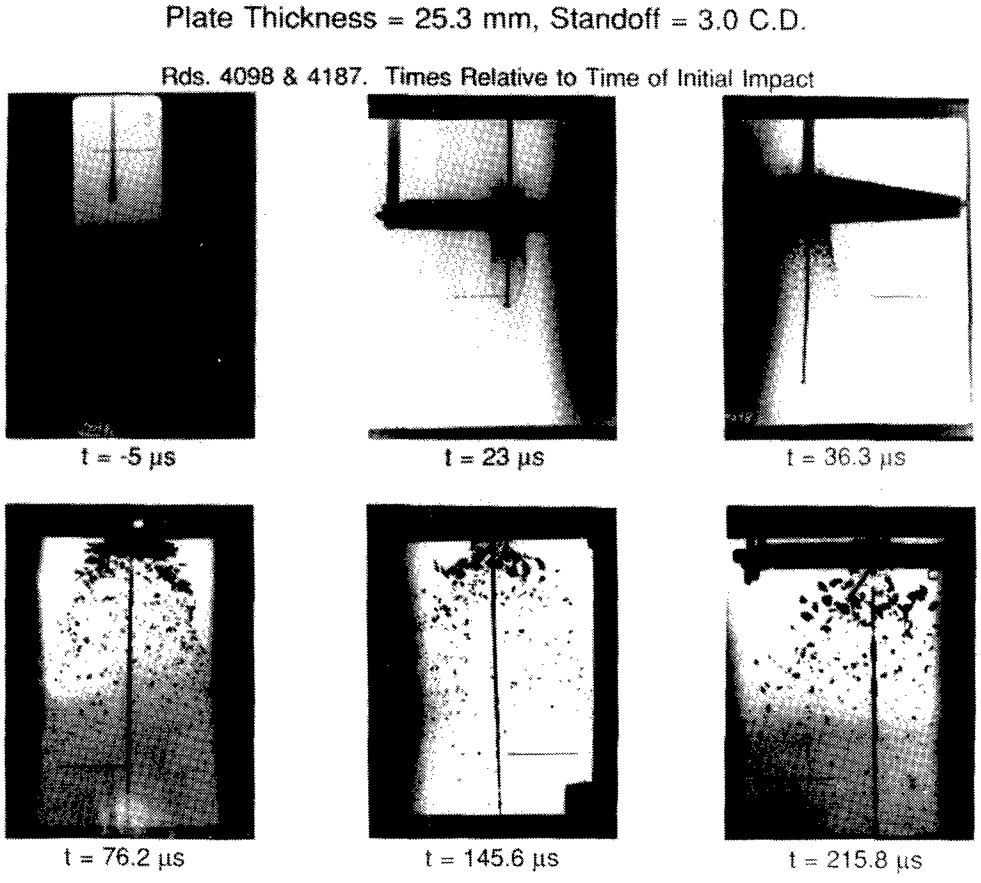

Figure 5. Radiograph Series for d = 25 mm, S = 3.00 C.D.

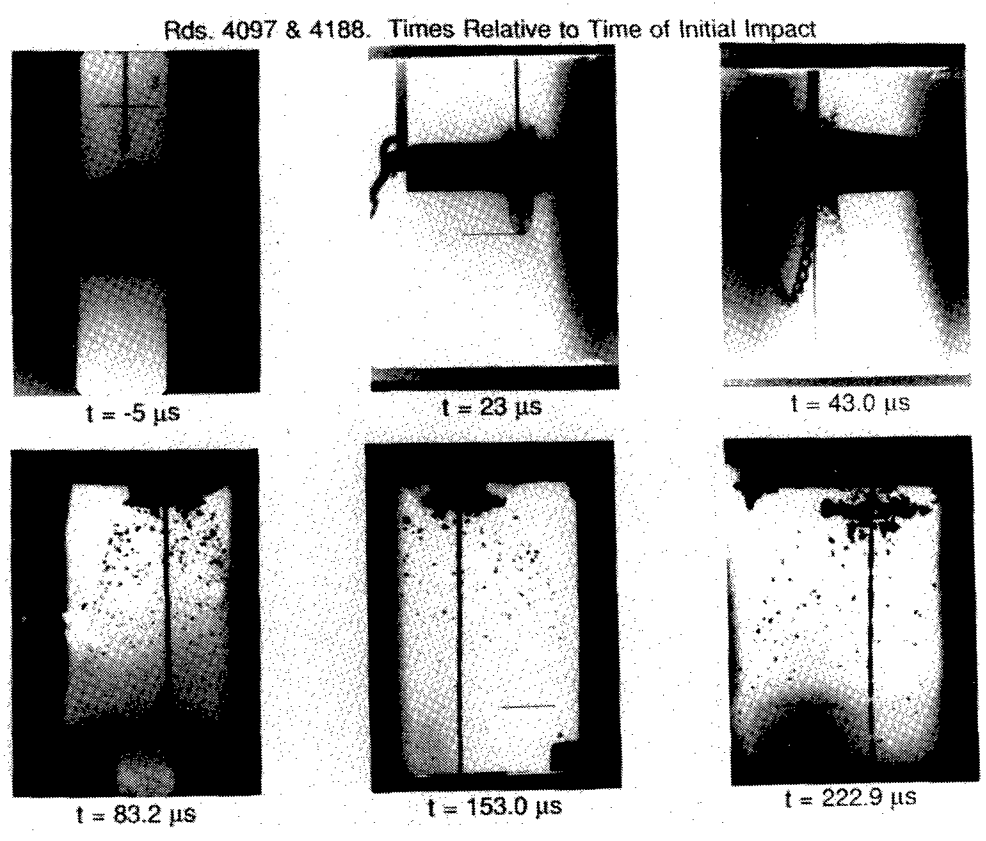

Figure 6. Radiograph Series for $d =$ 51 mm, $S =$ 3.00 C.D.

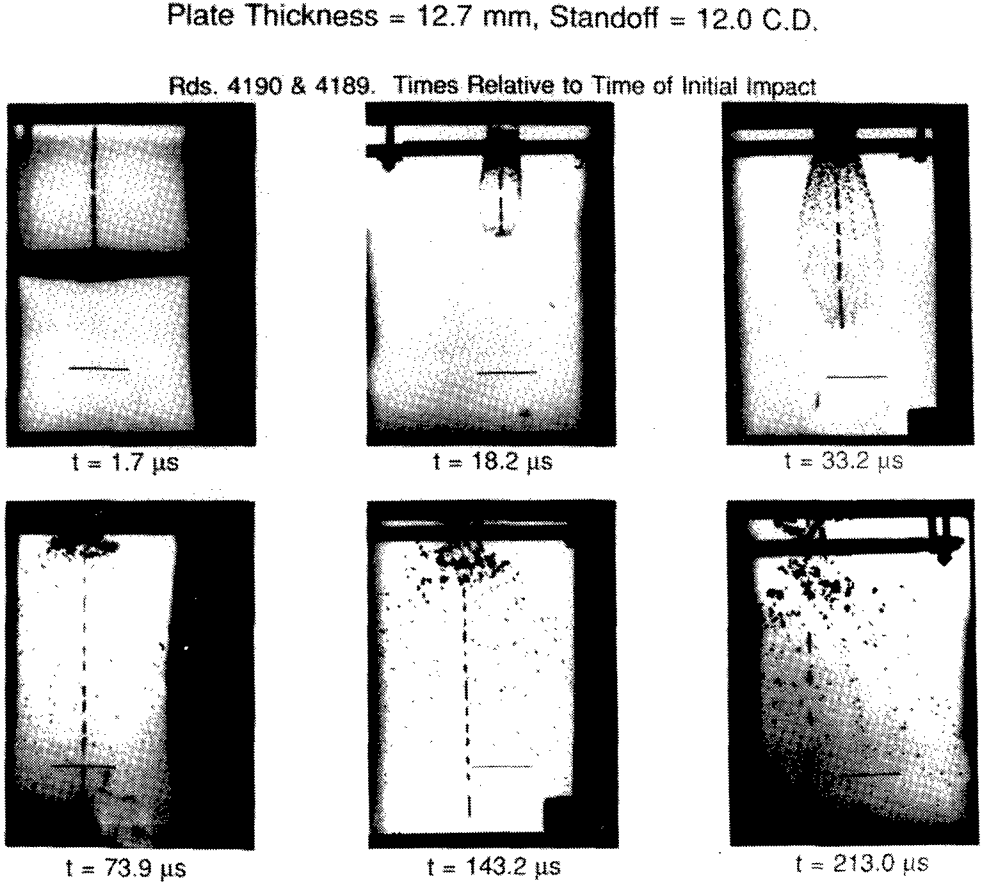

Figure 7. Radiograph Series for d = 13 mm, S = 12.00 C.D.

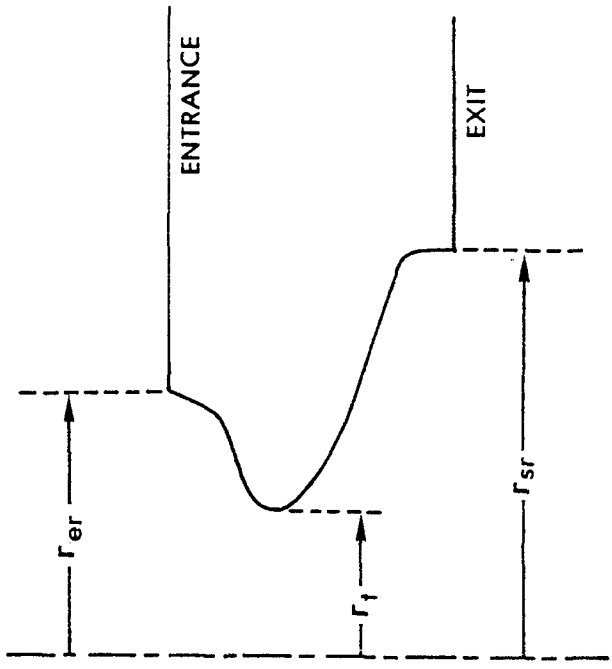

r_t = THROAT RADIUS

r_{sr} = SPALL RING RADIUS

r_{er} = EJECTA RING RADIUS

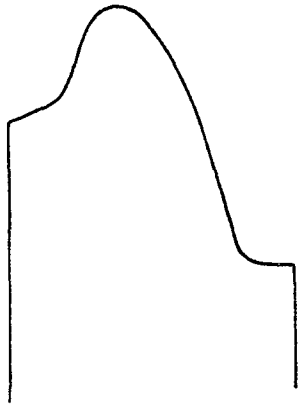

Figure 8. Idealized Perforation Hole Geometry.

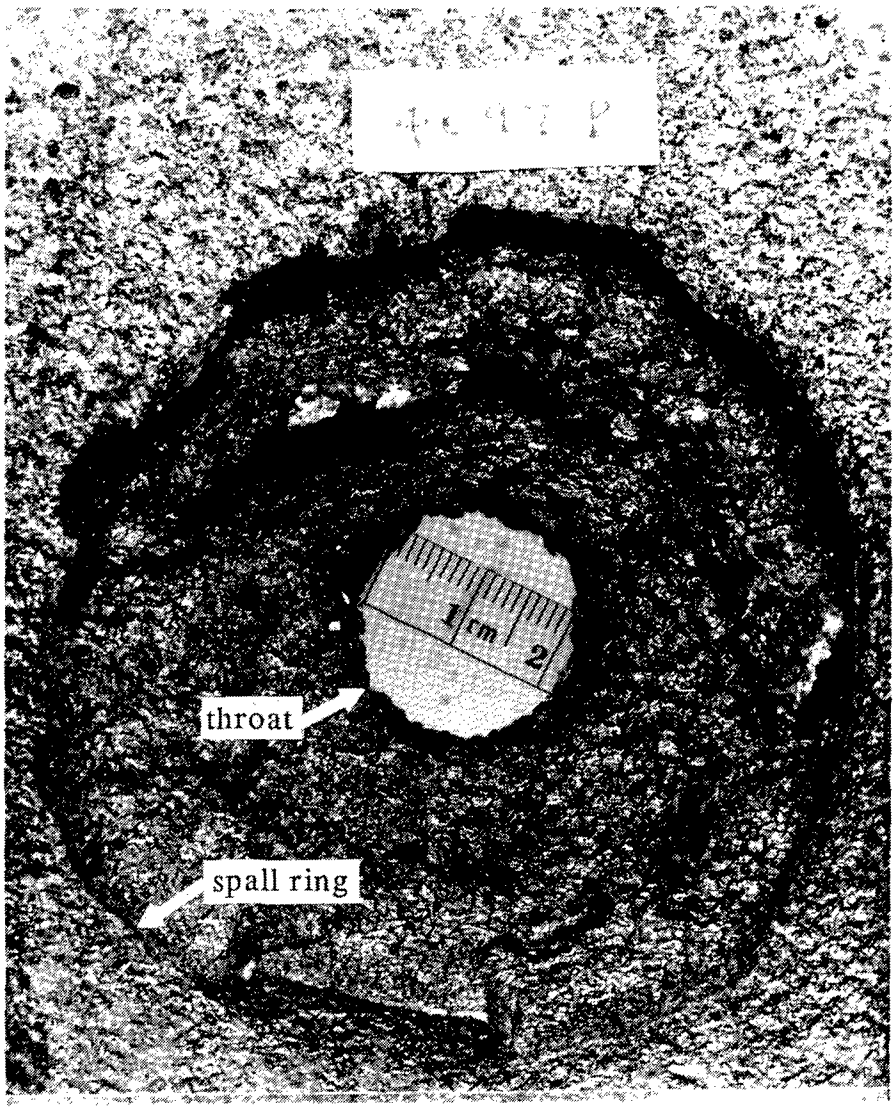

Figure 9. Exit View of Perforated Target Plate From Rd. 4097.

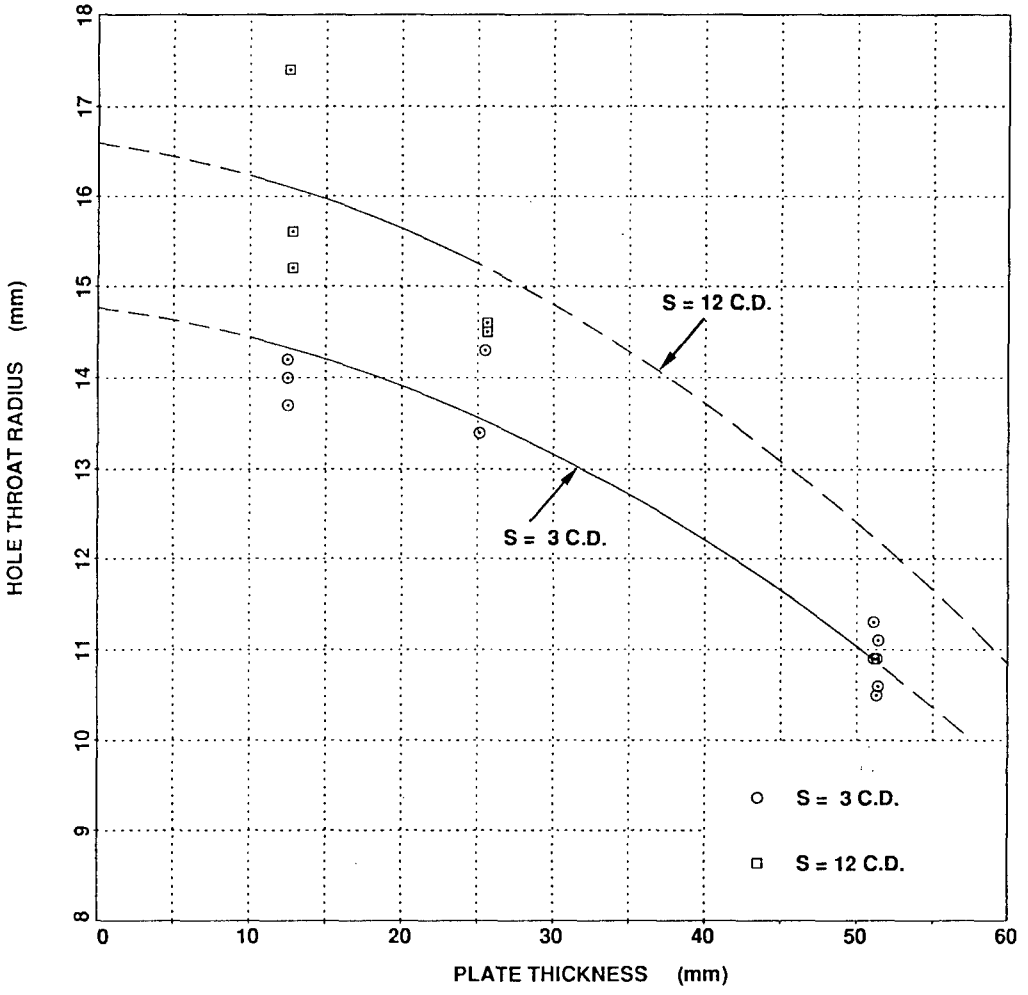

Figure 10. Throat Radius r_t vs. Plate Thickness d with Standoff S a Parameter, Plus Least-Squares-Error Fit of Equation (2).

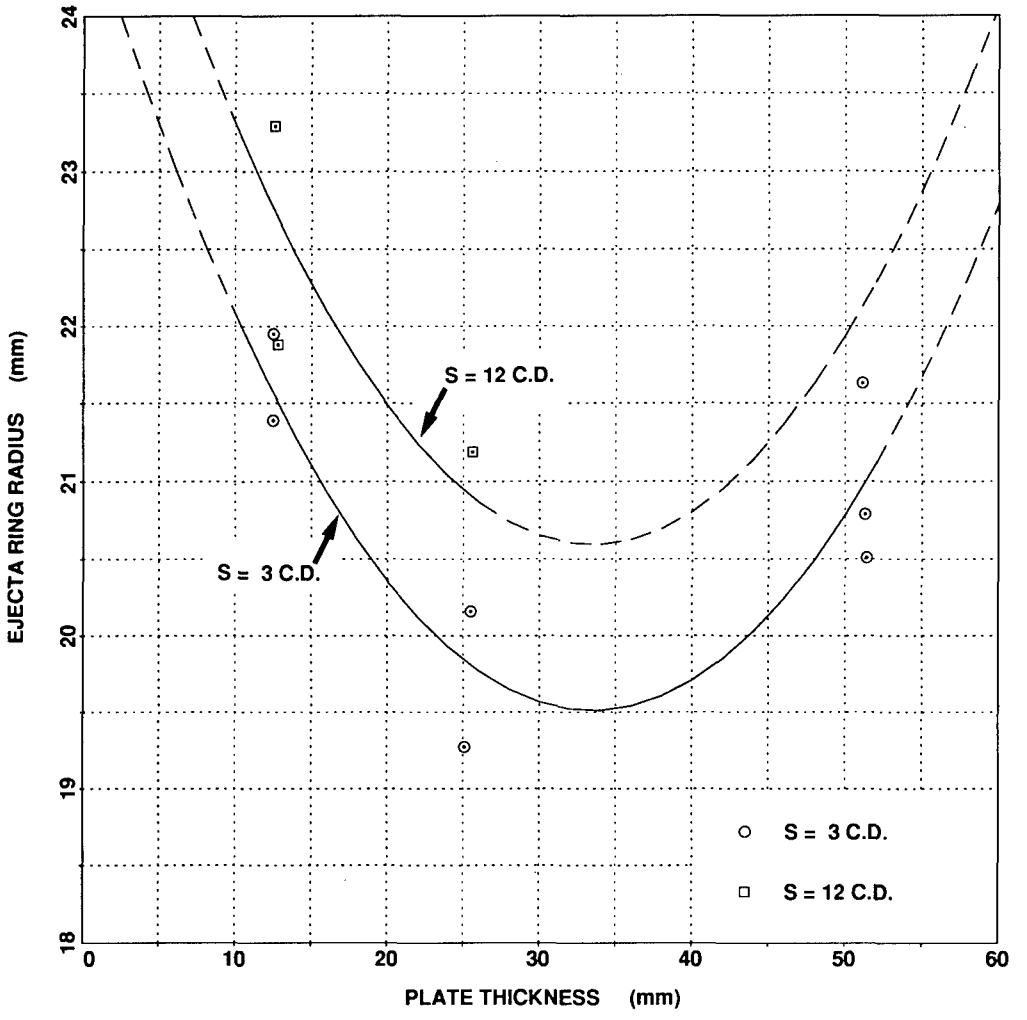

Figure 11. Ejecta Ring Radius r_{er} vs. Plate Thickness d with Standoff S a Parameter, Plus Least-Squares-Error Fit of Equation (3).

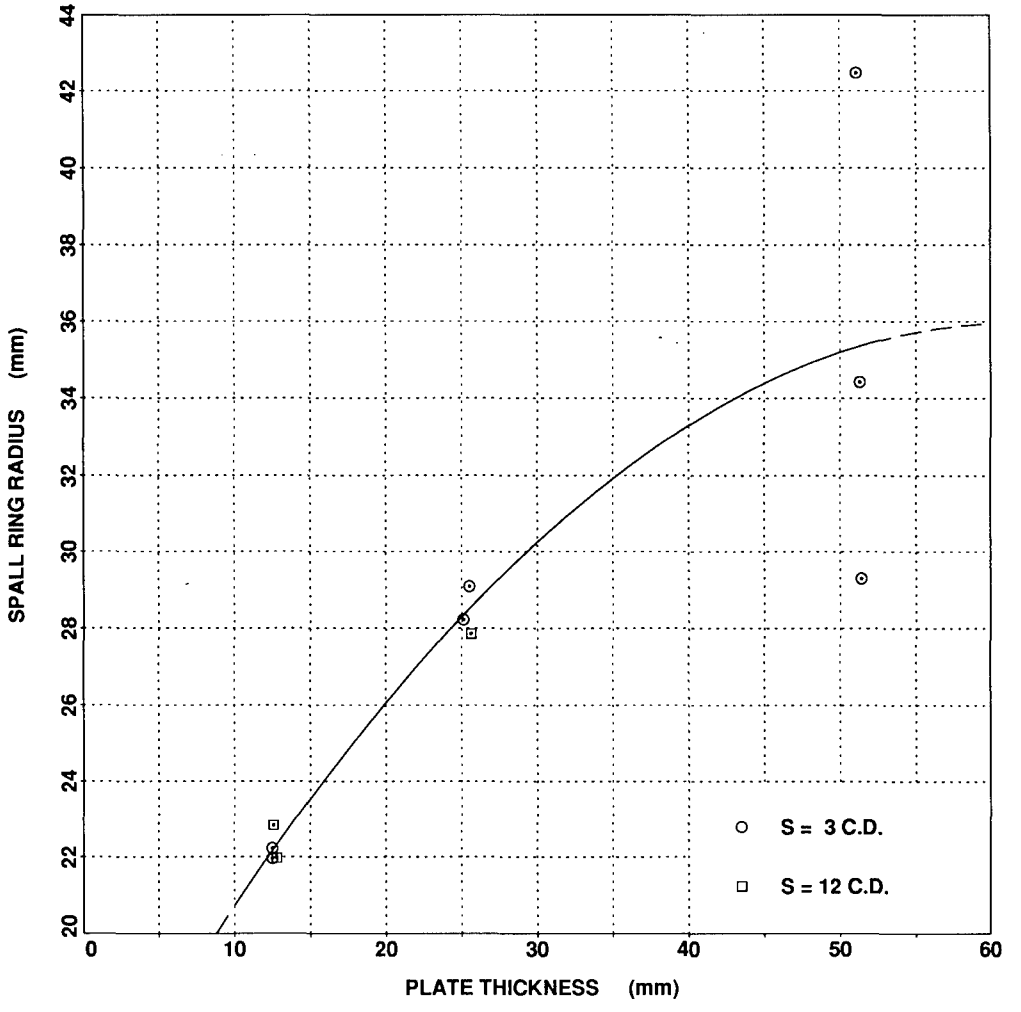

Figure 12. Spall Ring Radius r_{sr} vs. Plate Thickness d with Standoff S a Parameter, Plus Least-Squares-Error Fit of Equation (4).

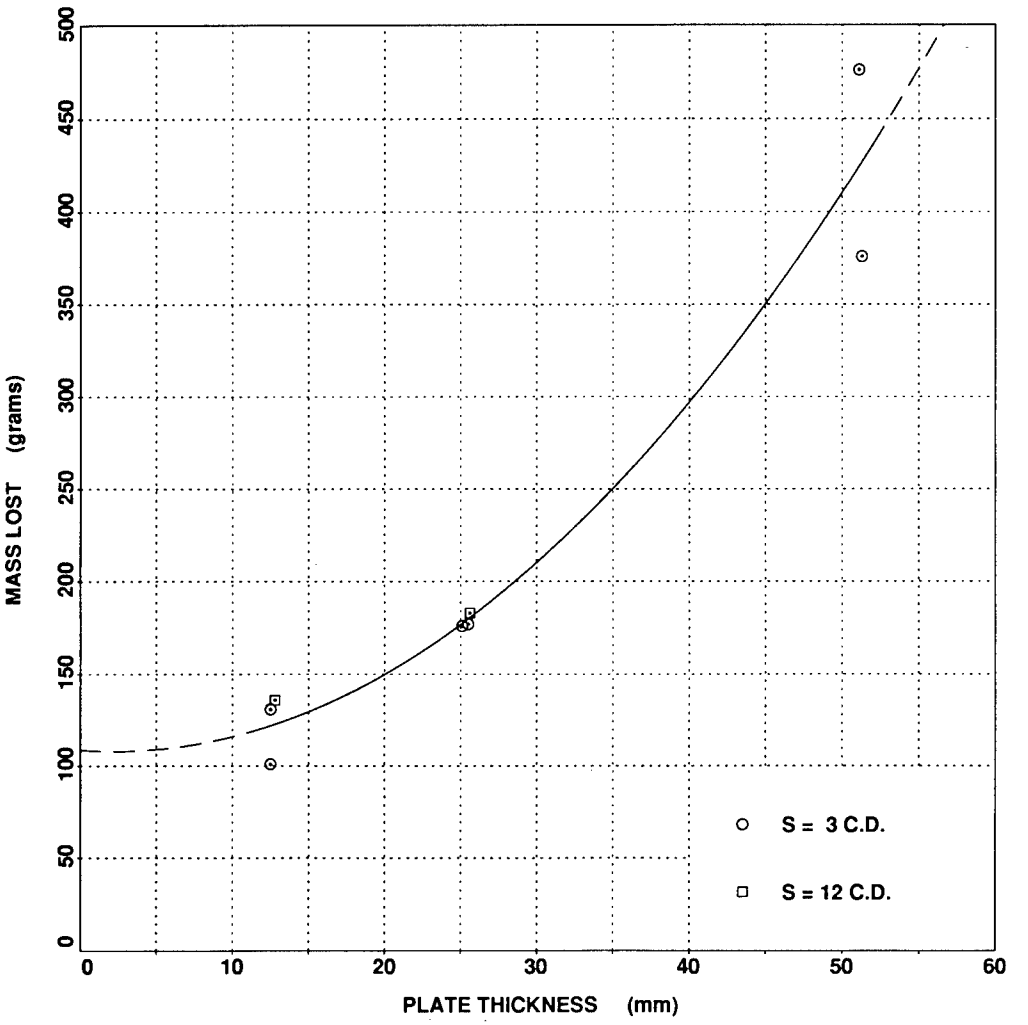

Figure 13. Total Mass Loss of Target Plate, ΔM, vs. Plate Thickness d with Standoff S a Parameter, Plust Least-Squares-Error Fit of Equation (5).

Penetration Analysis of HY100 Steel Plate

E. P. Chen
Sandia National Laboratories
Albuquerque, New Mexico 87185

Introduction

This investigation deals with the analysis of penetration processes in HY100 steel plates. The study is limited to 1.05-cm-thick and 30.48-cm-diameter HY100 steel plates being impacted by 3-cm-diameter and 28.15-cm-long maraging steel rods (T-250) at 100 to 400 m/s impact velocities. The impact conditions correspond to a series of experiments reported in Reference [1]. The analysis is numerical in nature. The transient dynamic finite element code PRONTO 2D [2] is used to perform the numerical simulations.

Experimental evidence [1] suggests that under the above impact conditions, little or no damage is inflicted on the maraging steel rods while the targets fail by shear induced plugging. Based on these observations and limited material test data [3], the rod is modeled as an elastic/perfectly plastic solid while the target is approximated as an elastic/plastic hardening material. A maximum equivalent plastic strain criterion is used to govern the progressive failure process in the target plate. The element death option in PRONTO 2D is used to simulate the plug formation by removing failed elements. A special dissipative viscous pressure was introduced in [2] to allow energy to be dissipated as new surfaces are formed by deletion of failed elements. Complete details of the calculation procedure are presented. Comparisons between calculated and measured data are made. Good agreement is observed.

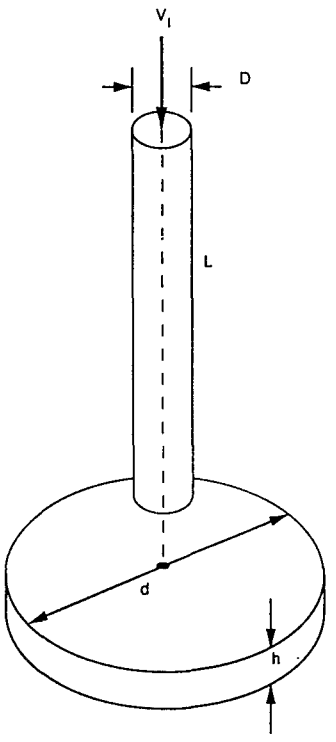

Figure 1. Schematic view of test condition.

Finite Element Analysis

A schematic view of the experiment is shown in Figure 1 where a cylindrical rod is impacting normally onto a circular plate. The rod is made of maraging steel (T-250) with length L = 28.15 cm and diameter D = 3.0 cm. The circular target plate is made of HY100 steel with diameter d = 30.48 cm and thickness h = 1.05 cm. The edge of the target plate is clamped, and the impact velocity varies approximately from 100 to 400 m/s.

Figure 2 shows the finite element model of the experimental geometry. Due to axisymmetry, only half of the actual geometry needs to be included.

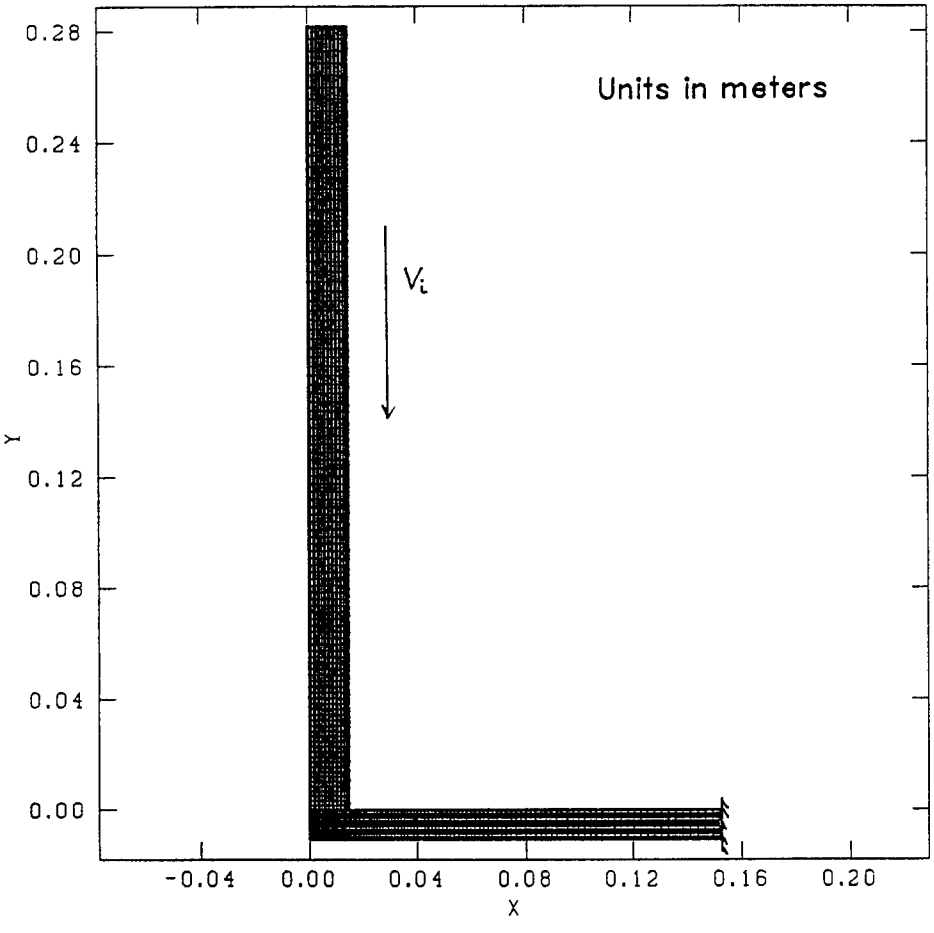

Figure 2. Finite element mesh.

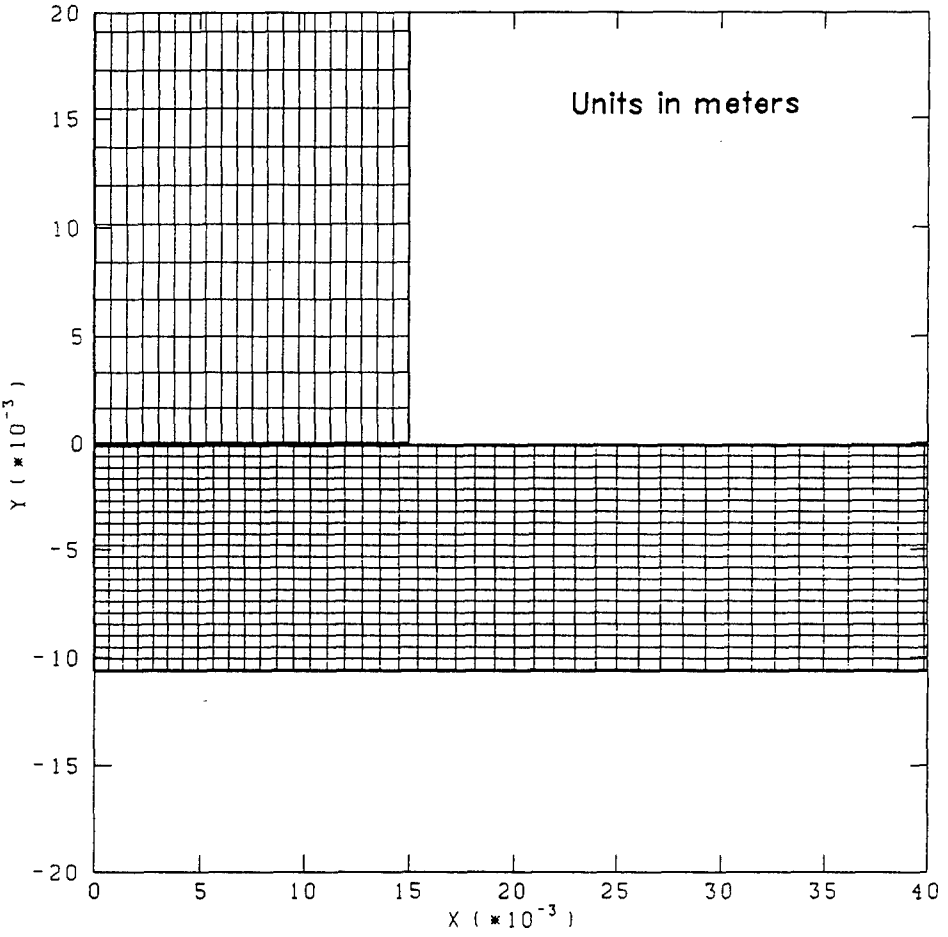

Figure 3. Expanded view of the mesh near the interface.

The mesh in Figure 2 has 4000 quadrilateral elements and 4242 nodes . The edge of the target plate is fixed. The rod and the plate are in contact at time t = 0 with the rod approaching the plate at the impact velocity. The contact surfaces at the interface between the rod and the target are taken to be slideline pairs to transfer momentum from the impacting rod to the target. An expanded view of the mesh near the interface between the rod and the plate is shown in Figure 3 to show relative element sizes in the rod and in the plate.

Limited material property measurements on both maraging and HY100 steel were obtained [3] which exhibited elastic/plastic behavior for both materials. Moreover, observations from the present series of experiments

[1] indicated a ductile response for both steels. As a first order approximation, the penetrator is modeled as an elastic/perfectly plastic material while the target behaves as an elastic/plastic hardening solid. For maraging steel (T-250), the material properties can be taken from [3] as: mass density ρ = 8000.0 kg/m^3, Young's modulus E = 206.9 GPa, Poisson's ratio ν = 0.3, and yield stress σ_Y = 1.724 Gpa. For HY100 steel, the material properties are taken from [3] as: mass density ρ = 7830.0 kg/m^3, Young's modulus E = 206.9 GPa, Poisson's ratio ν = 0.3, yield stress σ_Y = 1.034 Gpa and tangent modulus E_t = 2.069 GPa. Experimental evidence [1] shows that except in areas near the interface, the rod sustains little or no damage and the plate fails by shear induced plug formation. Because failure did not occur in the rod, no failure criterion is required in its numerical treatment. For the target plate, failure is assumed when the maximum equivalent plastic strain exceeds 15%. This corresponds to the strain level measured in uniaxial tension tests. The progressive plugging sequence is numerically modeled as follows. Failure initiation occurs at element locations which have reached 15% equivalent plastic strain. These elements are then deleted from the mesh to simulate material fracturing. As the rod penetrates into the target, more elements fail and are deleted. This process is repeated until a block of target material under the rod is completely separated from the rest of the plate to form a plug. The rigid-body velocity of the rod decreases initially due to target resistance until the plug is formed. At this time, the rod penetrates and exits the target at a constant residue velocity since the target can no longer offer any resistance. At the same time, the plug is also ejected from the target plate. The calculated residue velocity of the penetrator and the ejection velocity of the plug will be compared to the measured data to validate the numerical procedure.

Presentation of Results

Nineteen different impact velocities have been included in the numerical computations. These velocities are: 78, 93, 94, 95, 100, 110, 120, 127, 140, 150, 162, 180, 200, 230, 258, 300, 350, 370, and 400 m/s. For the first two velocities, the rod does not perforate the target plate. Perforation of the target plate occurs for all the remaining impact velocities. Figures 4-5 show the penetration process at 78 m/s rod velocity in terms of the equivalent plastic strain contour plots. The maximum equivalent plastic

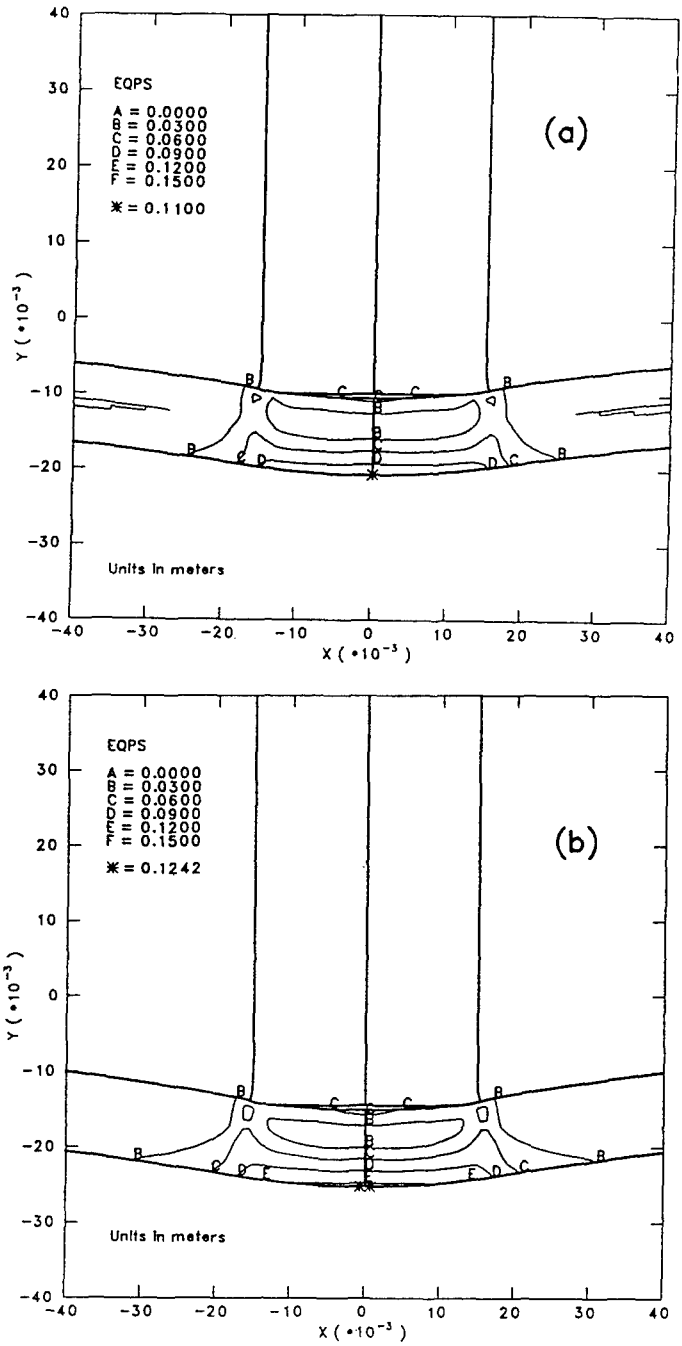

Figure 4. Equivalent plastic strain contour plot for 78 m/s impact velocity. (a) 0.2 ms, and (b) 0.4 ms after impact.

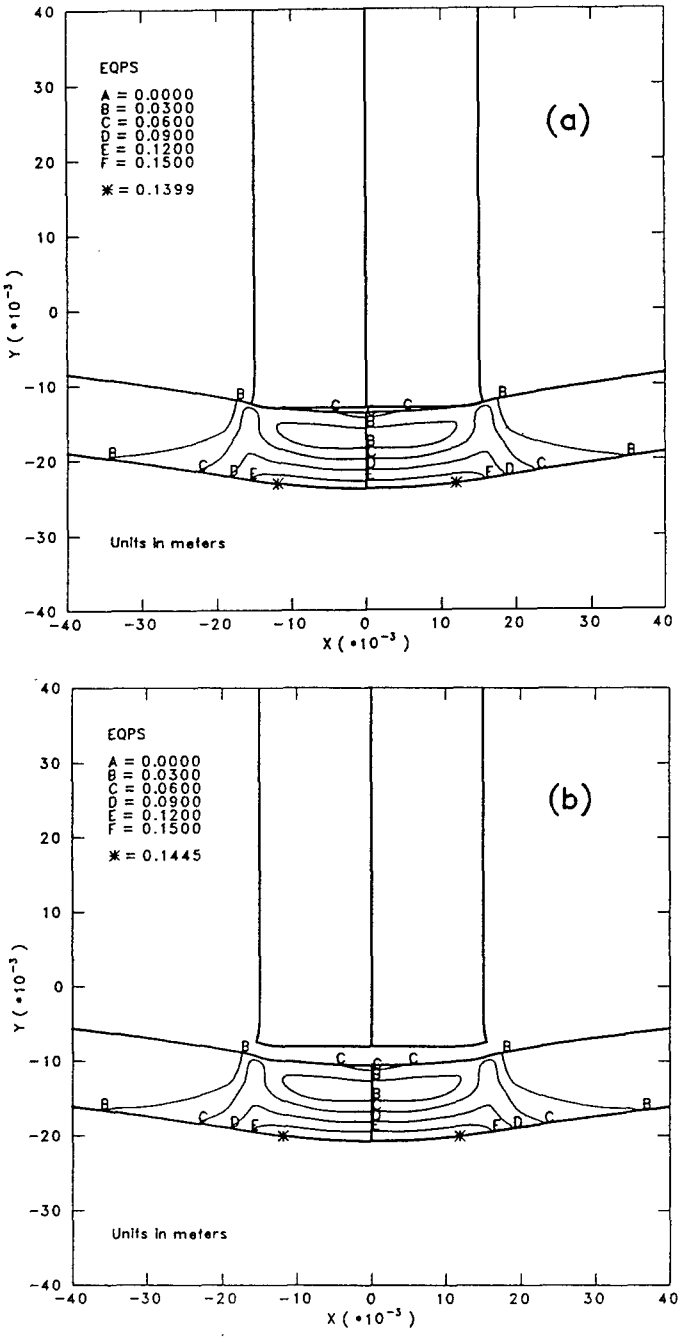

Figure 5. Equivalent plastic strain contour plot for 78 m/s impact velocity. (a) 0.6 ms, and (b) 0.8 ms after impact.

strain reaches only 14.45%, and consequently, no plugging occurs. At 0.8 ms, the numerical solution predicts rebounding of the penetrator as shown in Figure 5. This has also been observed in the experiment. For impact velocities of 93 m/s, similar behavior to that of Figures 4-5 is predicted.

For higher impact velocities, plate perforation occurs. As an illustration, Figures 6-7 show the penetration process in terms of the deformed mesh at 127 m/s impact velocity. The plugging sequence is clearly demonstrated. Failure initiates from the bottom of the plate at 70 μs after impact. Failure progresses until complete separation of the plug from the plate occurs at about 110 μs. At 180 μs, Figure 7, the penetrator has just about cleared the plate and the plug has been ejected. Figure 8 shows the axial velocity history of the penetrator for 127 m/s impact velocity. It is seen that at about 110 μs after impact, when the plug has separated completely from the plate (Figure 7), the axial velocity of the penetrator attained a constant magnitude for the rest of the penetration event. This constant velocity is interpreted to be the residue velocity of the penetrator. Similar penetration processes are predicted for all other impact velocities equal or higher than 94 m/s. Comparison between calculated and measured residue velocities are shown in Figure 9. The residue velocities are taken to be zero when plate perforation did not take place. The dotted line in Figure 9 provides a reference indicating equal impact and residue velocities. For the range of impact velocities studied, excellent agreement is observed. Finally, Figure 10 compares the calculated and measured plug velocities for impact velocities equal to 127, 258, 162, and 370 m/s. The calculated results include velocity histories while measured data from [1] provide only one value for each impact velocity. The calculated results show that at later times, the plug velocity oscillates about a constant value. By interpreting these constant values to be the long term steady-state velocities of the plug and comparable to the measured data, good agreements are again obtained.

Summary

Numerical analysis of a series of penetration experiments in which maraging steel rods impact HY100 steel plates at various impact velocities is presented. Using a maximum equivalent plastic strain criterion for the HY100 steel and the element deletion capability in the PRONTO 2D code, the analysis simulates successfully the observed plugging failure sequence in the target plate. Quantitatively, moreover, calculated penetrator residue

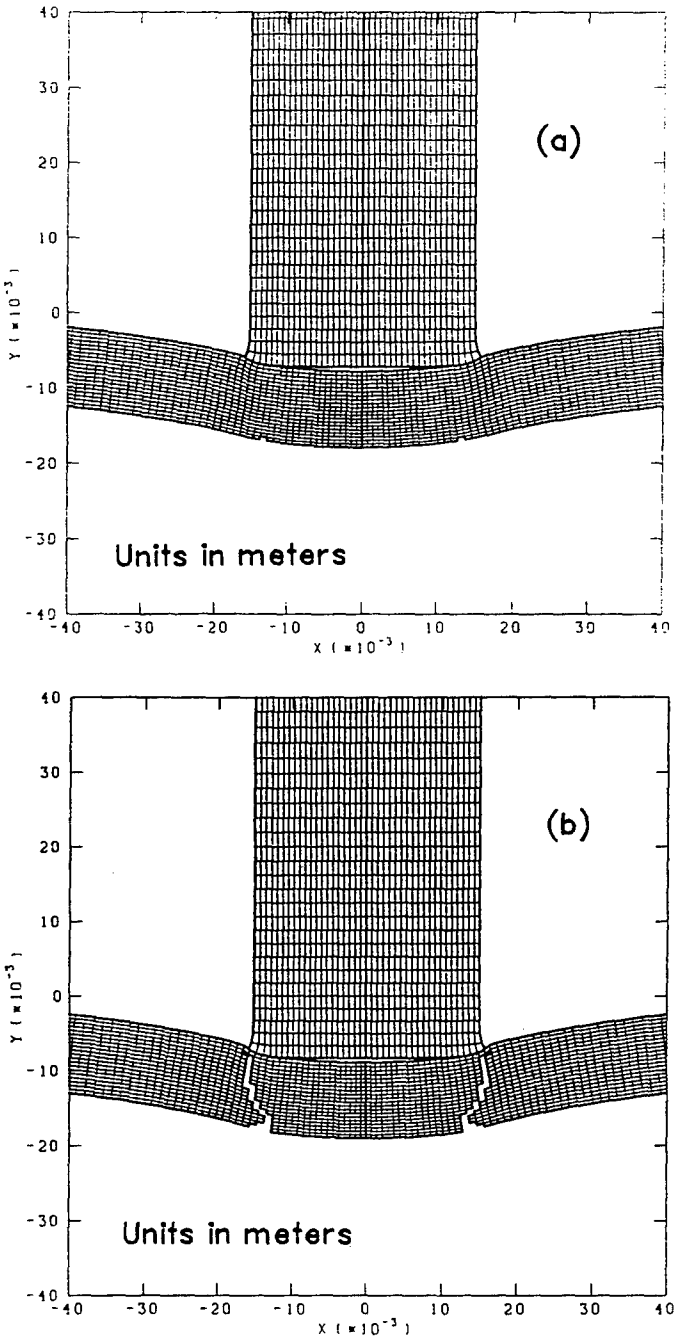

Figure 6. Plugging sequence for 127 m/s impact velocity. (a) 70 μs, and (b) 80 μs after impact.

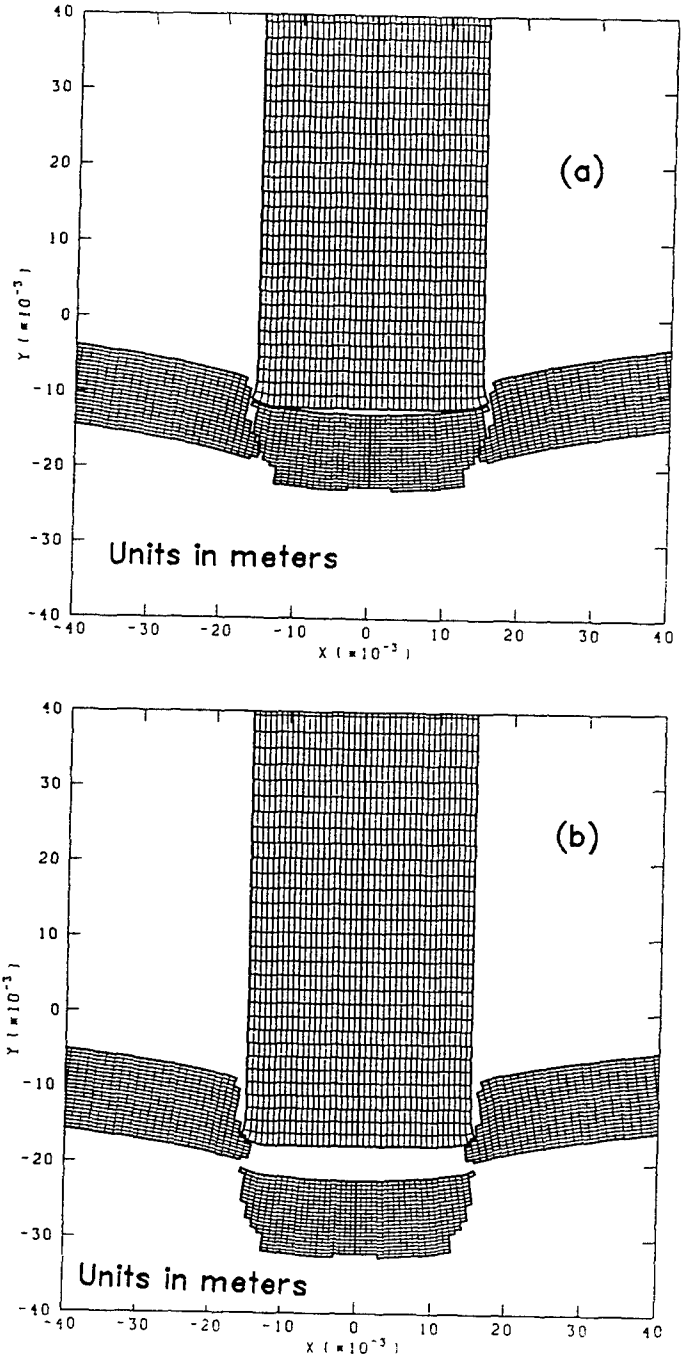

Figure 7. Plugging sequence for 127 m/s impact velocity. (a) 110 μs, and (b) 180 μs after impact.

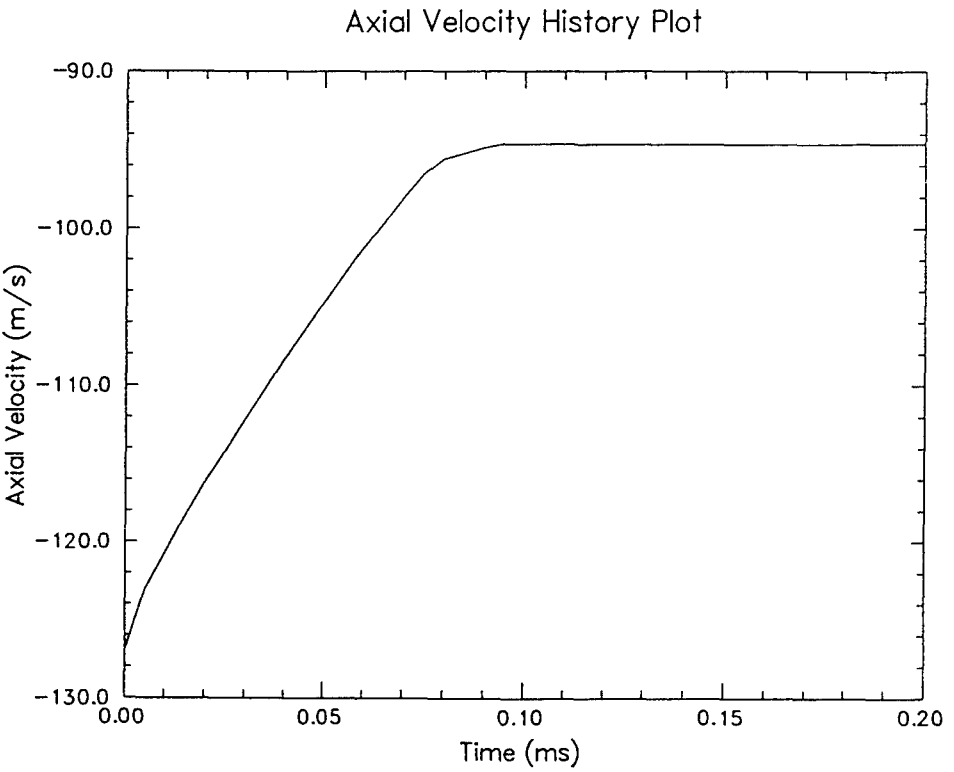

Figure 8. Penetrator axial velocity history at 127 m/s impact velocity.

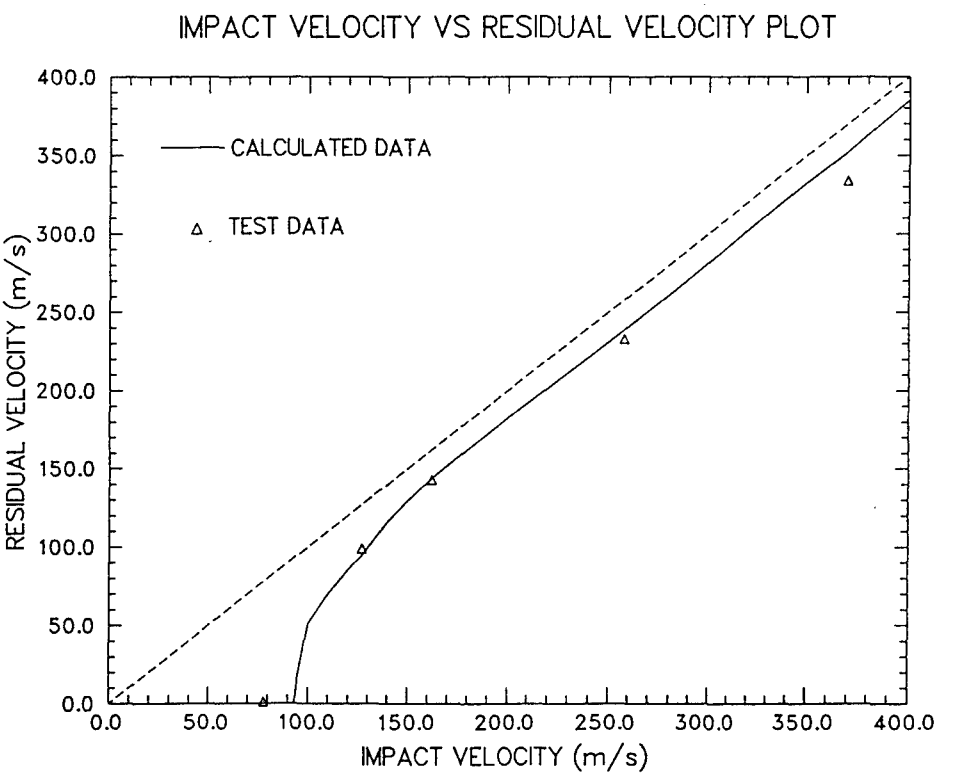

Figure 9. Comparison between calculated and measured data.

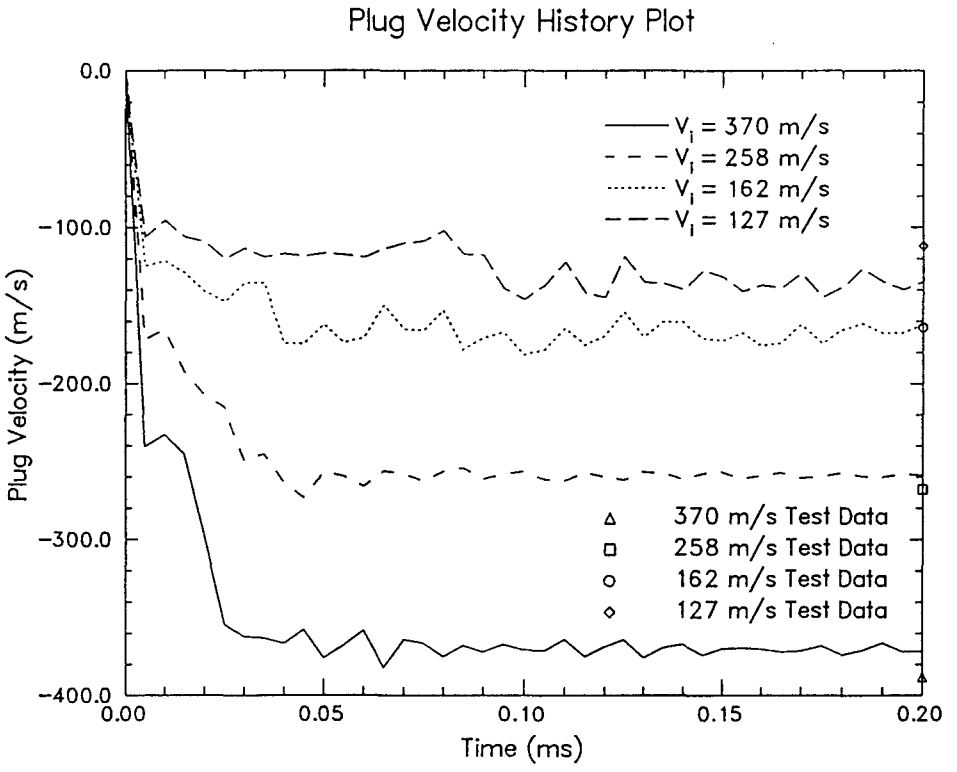

Figure 10. Plug velocity history plot and comparison with measured data.

velocities and plug velocities are in excellent agreement with measured data.

Acknowledgement

This work was performed at Sandia National Laboratories and was supported by the U. S. Department of Energy under contract number DE-AC04-76DP00789.

References

[1] S. J. Hanchak, Penetration Study of HY100 Steel Plate, UDR-TR-90-76, The University of Dayton, Dayton, Ohio, 1990.

[2] L. M. Taylor and D. P. Flanagan, PRONTO 2D, A Two Dimensional Transient Solid Dynamics Program, SAND86-0594, Sandia National Laboratories, Albuquerque, New Mexico, 1987.

[3] M. J. Forrestal, Private communication, 1991.

Determination of the Contact Forces Between a Projectile and a Hard Target *

R. K. Thomas
Structural and Solid Mechanics Department 1540
V. I. Bateman
T. G. Carne
Experimental Mechanics Department 2740
Sandia National Laboratories
Albuquerque, New Mexico 87185

Introduction

The determination of the contact forces at impact between a deformable projectile and a hard target is required for the design of energy absorbing features which limit the shock loads experienced by critical onboard components carried by the projectile. In this paper we present both analytical and experimental methods to obtain the force-displacement history of the impact event. The immediate application of these methods is toward the design of energy absorbing noses for laydown bombs. Upon impact, the desired performance of the deformable nose is to absorb the kinetic energy of the laydown bomb and smoothly decelerate the motion to near-zero velocity. This attenuates the shock loads to internal electronic components which must function after the impact event. The example we have chosen is the axial impact of a 670 lb projectile, travelling at a velocity of 125 ft/sec, onto a hard concrete target. In general, this technology falls within the area of crash worthiness, and thus has further application to transportation vehicles and shipping containers.

*This work was performed at Sandia National Laboratories and was supported by the U. S. Department of Energy under contract number DE-AC04-76DP00789.

Analytical Method

The analytical approach to the impact problem of a deformable projectile consists of using finite element methods. PRONTO2D [1] is a finite element code for large deformations of nonlinear materials subjected to high strain rates. It contains algorithms for sliding material interfaces and rigid boundaries, which are required for this type of contact problem.

The projectile test unit is 100 *in* long, has a 13.3 *in* diameter, and weighs approximately 670 *lbs*. The computational model is shown in Figure 1. The forward section is composed of the energy absorbing nose, while the aft section contains two cylindrical blivets which model the overall mass properties of the test unit. A detailed model of the nose geometry is shown in Figure 2. Of importance is the geometric step which is introduced in the nose shell at approximately the midlength. This rolling plastic hinge causes the shell aft of the step to roll inward during axial impact. By varying the shell thickness aft of the geometric step, the strain energy of deformation can be tailored to absorb the kinetic energy of the projectile. The use

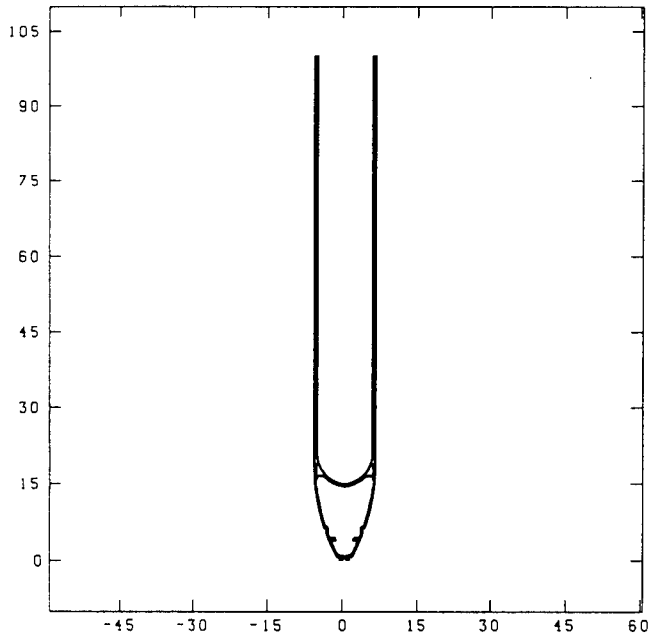

Figure 1. Projectile Model for Axial Impact Calculations (Units in Inches)

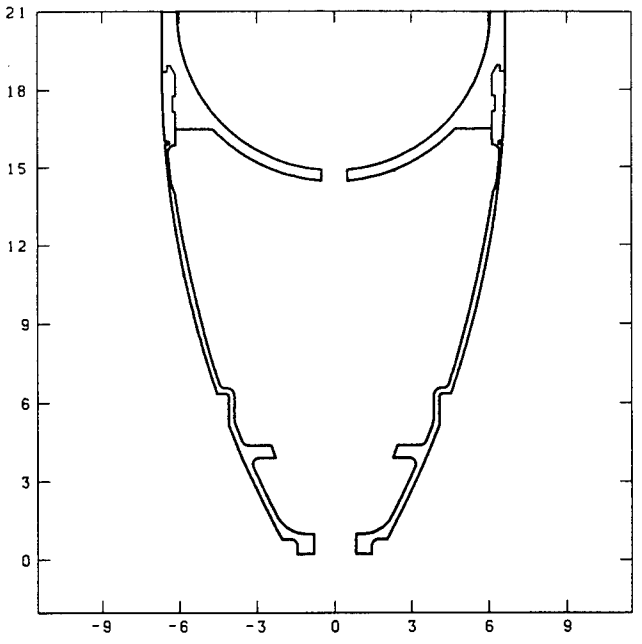

Figure 2. Detailed Model of Energy Absorbing Nose (Units in Inches)

of rolling plastic hinges is an effective method to absorb large energies in a small volume of material. The other geometric features internal to the nose shell are required for mounting components contained within the nose. The thin-walled section at the rear of the nose is required for oblique impacts, and will not be discussed in this paper. However, this aft feature is important to the axial impact problem in that energy is not being absorbed during the collapse of this region.

The mesh for the axisymmetric geometry, not shown, is composed of 1144 four-node quadrilateral elements and 1487 nodes. Four materials are employed: 21-6-9 stainless steel for the nose, 7075 aluminum for the forward flange region, and two fictitious materials for the aft cylindrical sections. Mechanical property data for these materials are given in Table 1. The data for 21-6-9 SS were taken at a strain rate of $10^{-3}/sec$ [2]. The implications of using material data at this strain rate are discussed later in this paper.

The target is assumed to be unyielding, and the coefficient of friction between the projectile and the target is assumed to be negligible. The

Table 1. FE Model Material Properties

	21-6-9 SS	7075 AL	MAT 1	MAT 2
Material Model	Elastic-Plastic	Elastic	Elastic	Elastic
Density, lbs/in^3	0.283	0.100	1.13	0.205
Elastic Modulus, psi	29.0×10^6	10.0×10^6	30.0×10^6	30.0×10^6
Poisson's Ratio	0.33	0.30	0.30	0.30
Yield Stress, psi	54.0×10^3			
Hardening Modulus, psi	240.0×10^3			

contact force is obtained by summing external forces, for each computational time step, on those nodes in contact with the target. The computed deformed shapes of the nose for an impact velocity of 125 ft/sec are shown in Figure 3 at selected times. The effectiveness of the rolling plastic hinge is clearly evident. One can also observe the collapse of the aft thin-walled section between 3.0 and 4.0 ms.

Experimental Method

The experimental method employs the Sum of Weighted Accelerations Technique (SWAT) to construct the contact forces. This method was first described by Gregory, et al., [3] and has successfully been applied to the impact of large nuclear transportation casks [4]. A detailed report on the use of SWAT methods for projectile impact is given by Bateman, et al., [5].

In general, the force is constructed from accelerometer measurements,

$$\mathbf{F} = \sum_{i=1}^{N} w_i \mathbf{a}_i \tag{1}$$

where $\mathbf{a}_i$ are measured accelerations, w_i are weighting factors, and the products are summed over N measurements. The weighting factors are determined a priori by imposing orthogonality between the rigid body modes and the flexible modes of a structure with free boundary conditions. In this manner the vibratory response of the structure is eliminated, without having to filter the raw accelerometer data, and the single sum in (1)

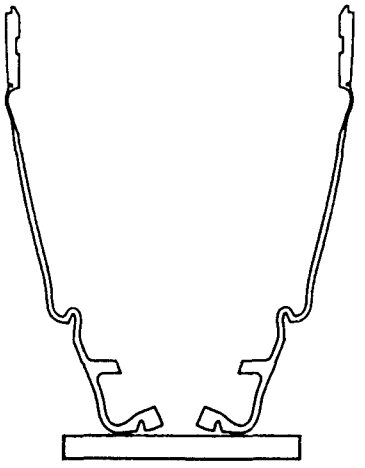

2.0 ms

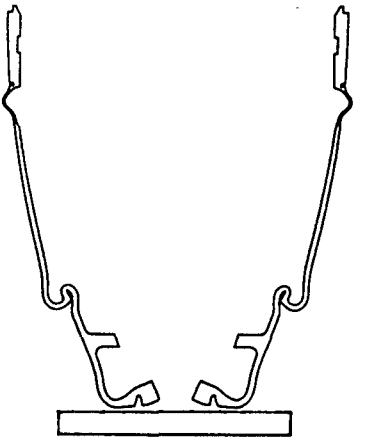

3.0 ms

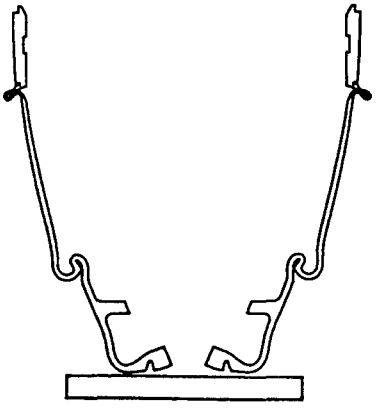

4.0 ms

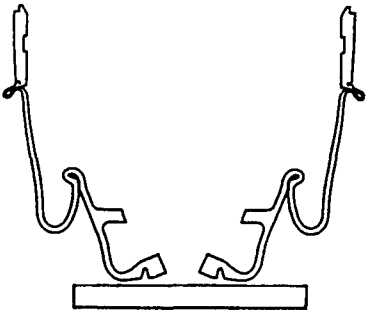

8.0 ms

Figure 3. Computed Shapes of Energy Absorbing Nose

yields the applied contact force. A detailed discussion of the relationships between the weighting factors, the mode shapes, and the contact forces can be found in [3,4,5].

Only the axial modes need to be considered for axial impact of the projectile test unit. The first three modes of the cylindrical section aft of the nose were determined by modal testing. These have frequencies of approximately 1800 Hz, 3500 Hz, and 4800 Hz. The weights for the SWAT algorithm were computed using these three modes. Note that SWAT is a linear method of force reconstruction. Therefore the nose, which undergoes highly nonlinear deformations during the impact event, could not be attached to the projectile test unit for evaluation of the modes. This means that the forces constructed by the SWAT method are actually those that are transmitted from the nose to the aft cylindrical section.

In order to measure the contribution of the three modes during the impact event, individual accelerometers were mounted on the ends of the cylindrical section and pairs of accelerometers were mounted on the sides at approximately the 1/4, 1/2, and 3/4 length positions. The data were digitally filtered with a cutoff frequency of 4500 Hz and an attenuation of 120 $dB/octave$. Pairs of accelerometer measurements at the same axial positions were averaged to eliminate any bending response. The resulting five accelerometer signals were combined with the weighting factors to determine the contact force.

The impact test was conducted at the Sandia Rail Launch Facility. The projectile was mounted to a carriage on a horizontal I-beam and accelerated to a velocity of 125 ft/sec using a solid rocket motor. The motor and carriage were stopped and separated from the projectile at the end of the I-beam. The projectile then traveled about 20 ft before impacting a 5 ft concrete cube backed by a packed earth berm. The instrumentation was hard-wired to recording equipment in a nearby instrumentation trailer.

Results

A comparison of the computed and experimental deformed shapes of the nose after impact is shown in Figure 4. The asymmetric deformation of the experimental shape was caused by the projectile impacting the target slightly off the normal direction. This qualitative comparison shows

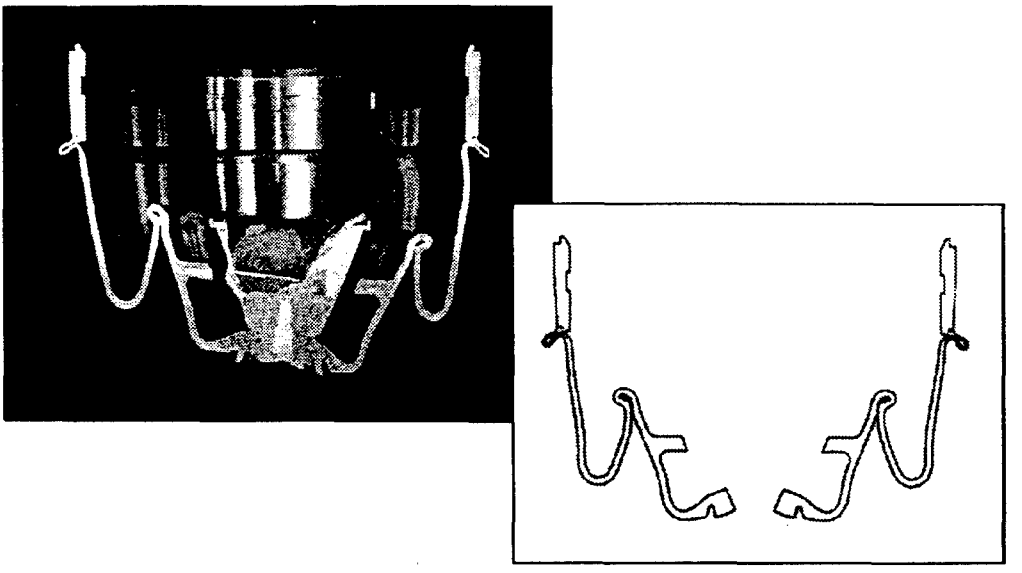

Figure 4. Computed and Experimental Deformed Nose Shapes.

excellent agreement between calculation and experiment. Of particular importance is the prediction of the extent of roll of the plastic hinge, and the final radius of curvature. These are the quantities of interest for energy absorber design.

A comparison of the computed and experimental contact forces is shown in Figure 5. The computed forces are those transmitted from the nose to the aft cylindrical section in order to be comparable with the experimental values. These forces are obtained by summing the product of the finite element axial stresses multiplied by the corresponding areas at a cross section just aft of the nose. They have also been low pass filtered with a cutoff frequency of 4500 Hz. Note the excellent agreement between 4.0 and 5.0 in of displacement where the aft thin-walled section is collapsing.

During the initial deformation the peak value of the computed force is slightly less than the experimental force. This can result from many causes. The plastic behavior of 21-6-9 SS was modelled using a bi-linear stress-strain curve, and perhaps a more realistic model (Johnson-Cook, for example) would yield better agreement. In the experiment the concrete target was not rigid as assumed in the computations. And clearly a strain-rate

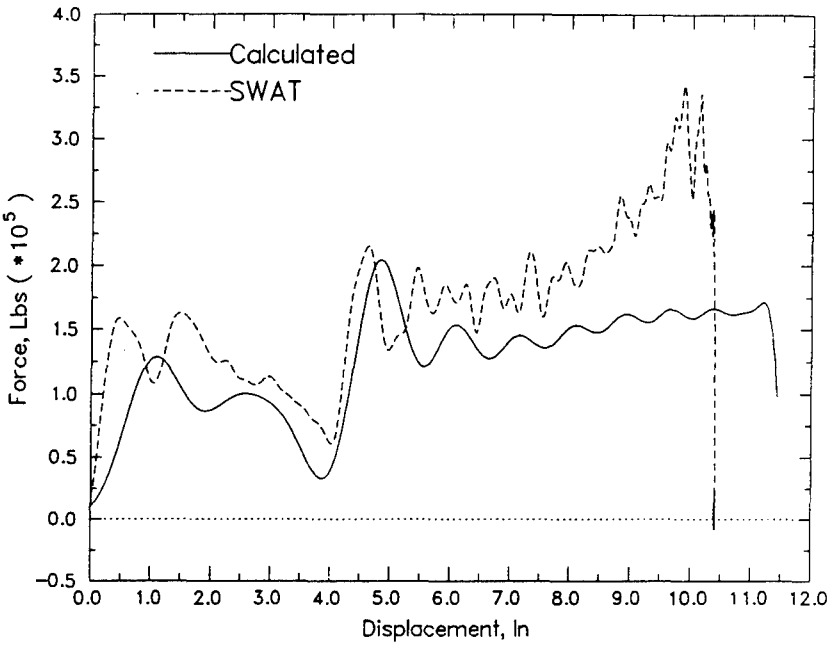

Figure 5. Computed and Experimental Contact Forces.

dependent model of 21-6-9 SS would yield larger predicted forces. During the late deformation the discrepancy between computed and experimental forces is caused by components located in the nose of the test unit projectile, but which were not included in the computational model. Crushing these components increases the stiffness of the nose structure, and thus increases the contact force. Overall, the agreement is excellent for purposes of characterizing the energy absorption behavior of this complex projectile structure.

It is generally accepted that the yield strength of 21-6-9 stainless steel increases with strain rate [6]. This is a necessary consideration at the higher impact velocities. For the projectile geometry and velocity under consideration in this paper, the peak strain rate is on the order of $10^{+2}/sec.$ At this rate the yield strength is about 84 ksi, compared to 54 ksi at $10^{-3}/sec.$ Computations were conducted with a rate-dependent material model, and yet only a modest increase in the peak contact forces were computed. This is attributed to the fact that rate-dependent effects would most likely be observed in the high frequency portion of the response, however this portion has been filtered to under 4500 Hz. It is concluded that for higher

frequencies of interest, and for much greater impact velocities, the rate-dependent models would be required.

References

[1] L. M. Taylor and D. P. Flanagan, *PRONTO2D: A Two Dimensional Transient Solid Dynamics Program*, SAND86-0594, Sandia National Laboratories, Albuquerque, New Mexico, 1987.

[2] W. A. Kawahara, *21-6-9 High Rate Tensile Data*, Internal memorandum, Sandia National Laboratories, Albuquerque, NM, March 19, 1980.

[3] D. L. Gregory, et al., *Experimental Determination of the Dynamic Forces Acting on Non-Rigid Bodies*, SAE Tech Series, Paper No. 861791, Aerospace Technology Conference and Exposition, Long Beach, CA, October 1986.

[4] V. I. Bateman, et al., *Force Reconstruction for Impact Tests*, Journal of Vibration and Acoustics, Trans ASME, vol 113, April 1991, pp. 192-200.

[5] V. I. Bateman, et al., *Force Reconstruction for Impact Tests of an Energy-Absorbing Nose*, Sixty-First Shock and Vibration Symposium, Pasadena, CA, vol 4, October 1990, pp. 127-136.

[6] M. E. Kessner, *A Simple Constitutive Equation to Model the Low Temperature Yield Strength of Type 21-6-9 Stainless Steel*, Journal of Engineering Materials and Technology, vol 105, July 1983, pp. 231-233.

Modeling Deformation and Damage in Armor Ceramics

Charles S. White
James J. McLaughlin

Materials Dynamics Branch
U.S. Army Materials Technology Laboratory
Watertown, MA 02172-0001

ABSTRACT

Ceramic materials have become extremely important as integral components of modern armor systems. The high compressive strength and low density compare well with traditional metal armor. Previous analysis and modeling techniques for penetrator/armor interactions have been based upon ideas from metal plasticity. In recognizing that different physical phenomena occur in ceramic based armor as compared with metals, the task of constructing suitable material constitutive relations has begun. This paper reports the first step in building a material model for use with armor ceramics. The ideas of metal plasticity are extended to evaluate their suitablility for modeling ceramics. Normal plate impact and instrumented ballistic experiments are modeled. The results show that elastic-plastic models can predict the first stress pulse in a ballistic event well.

INTRODUCTION

The nature of the impact geometry and rate is such that only limited details can be directly measured such as impact velocity, residual velocity, crater geometry and limited free surface velocities. Other phenomena must be inferred from more indirect observations (Shockey et al., 1990). The understanding of ballistic events requires the contributions of the experimentalist, the material scientist, the material modeller, and the hydrocode user.There needs to be interaction of the material scientist with the experimentalist to identify and understand the physical phenomena, the material modeller with the material scientist to build the physics into the constitutive relations, and the hydrocode user with

the material modeler and experimentalist to iterate on the material model until the experiments can be satisifactorily simulated.

The approach taken in this paper is to take uniaxial plate impact experiments, apply simple elastic-plastic modeling ideas and apply to predictions of complicated, projectile-plate impact experiments. The desire is to explore the limits of applying elastic-plastic modeling in these senarios.

Experimental results for the high deformation rate, material behavior of ceramics has been limited. The recent publication of a series of symmetric plate impact tests by Sandia (Kipp and Grady, 1989) has provided the most complete data base for dynamic behavior of armor ceramics. These tests apply to one cycle of load-unload for shocking of the material and should be quite useful for developing models of and obtaining fitting constants for the initial pulse level and fracturing of the material. These experiments are less useful for later time behavior of the fracture ceramic. These tests have recently been modeled by Furlong et al. (1990) and also by Steinberg (1990) using damage and elastoviscoplastic theories, respectively. Both of these models are able to give good matching of the rear surface velocity profiles from the experiments. They do so through the expense of many material parameters. These analyses are useful for showing the ability to curve fit the experiemental profiles but not for demonstrating predictive capabilities.

The suitability of using these one dimensional results for general ballistic applications has yet to be established. Recent experimental results (Vincent and Chang, 1990) seek to aid in addressing this problem. They have obtained recordings of stress as a function of time at certain points along interfacial boundaries in ceramic targets during ballistic impact. Piezo-resistive pressure gauges were placed at either one or two locations along the line of sight of the incoming projectile at the interfaces of the different plates of the target system. These stress history results were only obtained for the first 10 microseconds after impact.

MATERIAL MODELING

The deformation behavior of ceramics in armor applications has been modeled with concepts originally developed for metals. These have been available in the computer codes since their inception. The earliest large scale numerical modeling of ceramic armor was by Wilkins (Wilkins, 1968). His fracture model caused an element to fail when the principal stress in the plane of motion exceeded a critical value. Certain limitations were put into place such that the fracture had to initiate at a surface and could only move into an adjacent element when sufficient time had elapsed for a running crack to have reached that loca-

tion. The element (zone) was failed by relaxing the material strength to zero. This brittle fracture model does reproduce certain observed phenomena including the fracture conoid from a point nosed projectile impact.

Gordon Johnson and coworkers (Johnson and Stryk, 1990) have developed a phenomenological ceramic model which includes more observed phenomena. This model includes damage and fracture in both compression and tension. After fracture a pressure increment is given to the element corresponding to dilatational effects and the flow strength becomes a function of pressure. This model has been incorporated into the EPIC code.

As mentioned above, R&D Associates (Furlong et al., 1990) have developed a model which introduces fracture via damage accumulation which can occur both in tension and compression. In tension, the material behaves elastically but its bulk and shear moduli are degraded linearly by the accumulated damage. The damage accumulates in tension as a function of strain rate and hydrostatic tension (negative pressure). One implication of this model is that spall does not occur if the hydrostatic stress is compressive no matter how large the maximum principal stress. In compression, the ceramic behaves in an elastic-plastic manner following a damage-degraded Johnson-Cook flow stress where damage accumulates as a function of plastic work.

Steinberg's recent ceramic model (Steinberg, 1990) falls into the class of elastoviscoplastic models. It gives a very good match with experiments for symmetric plate impact. The model has a temperature and pressure dependent shear modulus and adds strain rate dependence to these variables for the flow stress. The Cochran-Banner spall model is incorporated as the failure mechanism (Cochran and Banner, 1977).

In the simulations reported in this paper, several variations of the elementary elastic-plastic theory originally developed for metals will be used. The ceramics in the experiments that were modeled (Al_2O_3 and SiC) are known to exhibit Hugoniot behavior that resembles the results for elastic-plastic behavior of metals (Kipp and Grady, 1989; Mashimo et al., 1987). The basic structure of the model that was used includes three major components: the hydrostatic behavior, the flow stress behavior, and the fracture criterion.

The hydrostatic behavior was modeled using a polynomial equation of state:

$$p = c_1\mu + c_2\mu^2 + c_3\mu^3 \qquad (1)$$

where p is the pressure (positive for compression), and μ is given by $\mu = \rho/\rho_o - 1$, where ρ is the density.

The initial yield stress of the ceramic is determined from the Hugoniot elastic limit. For the simulations shown here the material was modeled as perfectly-plastic prior to fracture (no strain hardening) although strain-rate dependence

was allowed. After the material exceeded the fracture criterion the model allowed for the flow stress behavior to be pressure dependent such as observed by Arrowood (1987). The general form for the flow stress is shown in equation 2, where ε° is the normalized strain rate. The coefficients can be different before and after fracture.

$$\sigma_y = \sigma_{yo}(1 + c_5 ln\varepsilon^{\circ}) + c_4 p \qquad (2)$$

The fracture criterion that was used is among the very simplest. The material was considered to have fractured when the maximum principal stress exceeded a critical value, σ_{crit}. When the material fractures, the flow stress is set to the value given above and the pressure is not allowed to be negative. If the pressure is negative it is set to zero. This model is very elementary, yet as will be shown, reproduces a number of the important early-time stress and velocity results.

SIMULATION OF SANDIA EXPERIMENTS

The Sandia experiments (Kipp and Grady, 1989) did not examine Al_2O_3, so silicon carbide results for symmetric plate impact were simulated using the material model described above. A 4 mm thick SiC tile was used to impact a target consisting of an 8.9 mm thick SiC tile backed by a 25.4 mm thick lithium-flouride window. The lithium-flouride window is placed on the back of the target plate to provide a suitable window for the VISAR velocity interferometer. The output from the experiment is a recording of the velocity of the interface between the SiC target plate and the backup window. The data is only available for the first 2.5 microseconds after impact but this is long enough for the impacting plate to send one loading wave followed by an unloading wave. The experimental results show the two-wave loading profile reminiscent of elastic-plastic waves in metals followed by the elastic-type unloading profile and subsequent dispersion.

These tests were simulated using the DYNA2D finite element code (Hallquist, 1987). The mesh and boundary conditions were configured to give one-dimensional straining in the impact direction. The three plates (projectile, target, window) were discretized by 160, 358 and 81 elements, respectively. The projectile plate elements were given an initial velocity of 0.21 cm/microsecond, corresponding to the experiment CE 5 (Kipp and Grady, 1989).

The first simulation was done using the simple elastic-plastic model with no fracture. The comparison with experiment is shown in Figure 1.. Notice that

the timing of the arrival of the loading and unloading waves is well predicted as is the peak velocity. The shape of the loading and unloading profiles is not well modeled. The elastic-perfectly plastic simulation gives a distinctive two wave structure while the experimental result exhibits possible hardening and rate effects. The timing and peak levels, being in good agreement, indicate that the equations of state give good results.

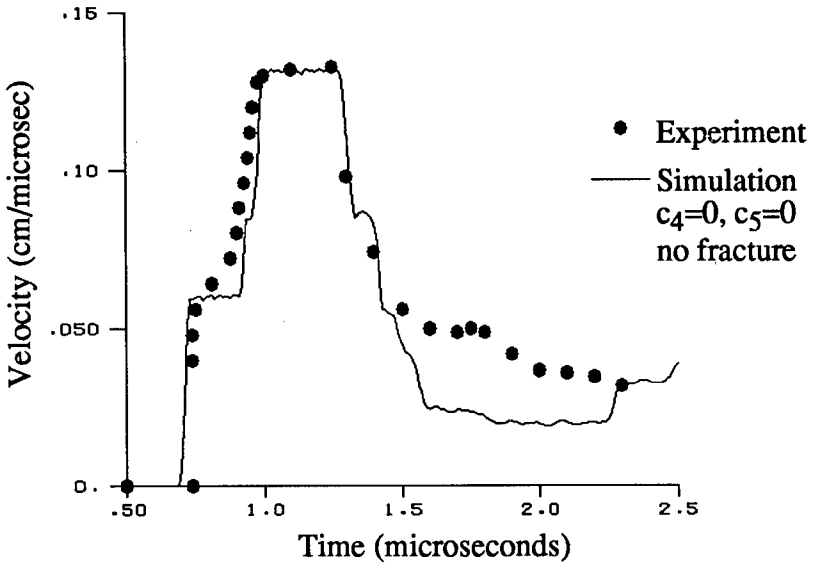

Figure 1, Elastic perfectly-plastic simulation of SiC experiment CE 5.

In White et al. (1991), the effect of adding the strain rate dependence and fracture are systematically shown for modeling this experiment. Here we give just the result showing the good correlation with experiment of the simple elastic-plastic model (Figure 2). The largest difference with experiment occurs at the top of the loading wave where the experiment shows a well defined plateau of constant velocity. The simulation does not rise as quickly as the experiment and display as sharp a corner. This is believed to be a result of neglecting strain hardening of the ceramic and not of major consequence in ballistic applications. Overall, we see that a very good match is obtained with a very simple model, having only a few material constants. The constants used in the simulation were: c_1=2.3 Mbar, c_2=0., c_3=0., c_4=0., c_5=0.02, and σ_{y_o}= 0.16 Mbar

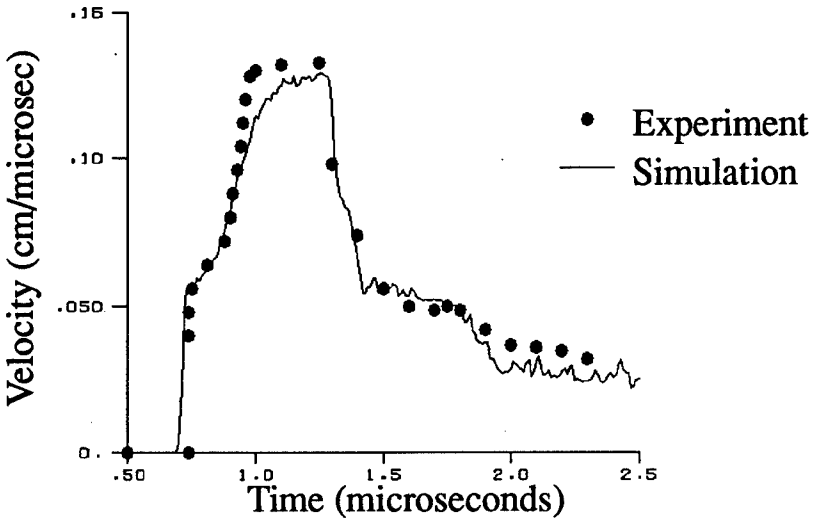

Figure 2, Simulation of SiC symmetric plate impact at 2.1 km/se using strain rate dependence and fracture

Using these constants, a lower velocity experiment was simulated. Although it is certainly from the same class as the one used to determine these constants it provides a verification of some of the features of the model. The experiment had the same geometry as the one considered above. The difference was that the impact velocity of the flyer plate was reduced from 2.1 km/sec to 1.54 km/sec. The simulation of this experiment is shown in Figure 3. Notice again that the major features are captured by the simple model. No adjustment of any parameters was made. The utility of simple elastic-plastic ideas for modeling certain ceramics is shown here.

SIMULATION OF BALLISTIC EXPERIMENTS

The experiments of (Vincent and Chang, 1990) were simulated with various of the modeling techniques previously discussed. Figure 4 shows a schematic of the target for one of the two experiments considered here. A front tile of Al_2O_3 (Coors AD85) is followed by a thin layer of Isodamp shock absorbing material. For high velocity impacts involving blunt projectiles, the Isodamp was necessary to reduce the initial stress pulse so that it remained in the range that the stress gauges could measure (less than 100 kbar). Following the Isodamp is a second tile of Al_2O_3 (Coors AD94). Finally, the arrangement is backed up by a plate of 5083 aluminum. The ceramic, Isodamp, and aluminum

plates were all bonded together with an epoxy patch kit. The stress gauges were firmly bonded to the ceramic plates.

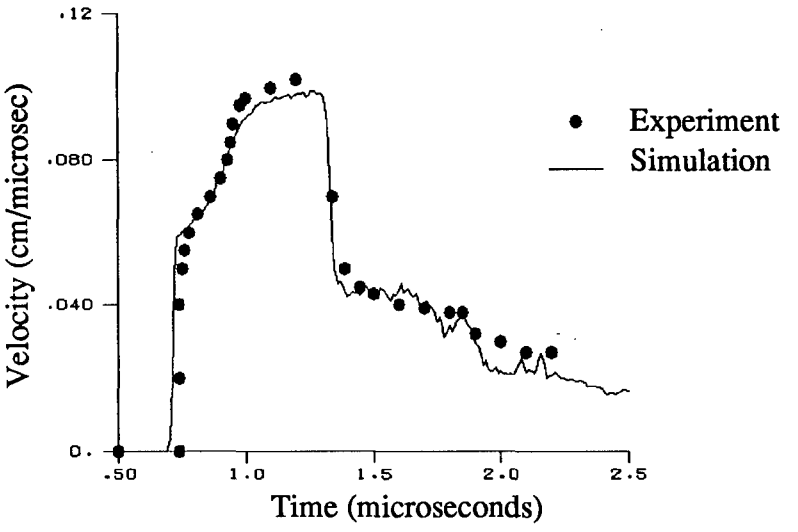

Figure 3, Simulation of SiC symmetric plate impact at 1.54 km/ sec.

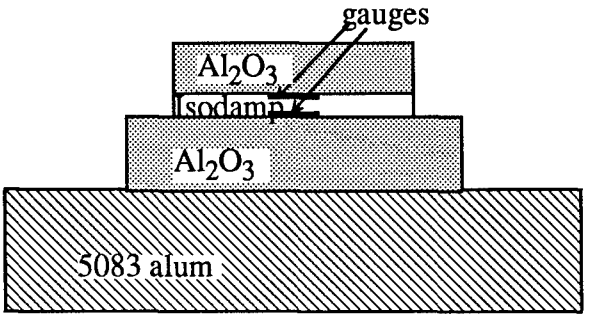

Figure 4, Instrumented ballistic test target

In the first experiment the above target assembly was impacted by a 20mm blunt nose steel projectile at 2602 ft/sec. In the second experiment, a 90 degree conical nosed projectile was impacted upon the target as shown above with the exception that the Isodamp layer was not present. In that test the two alumina plates were directly adhered to each other with the stress gauge in between them.

The blunt nose projectile experiment, Saturn 3, was analyzed with the DYNA2D finite element code. The projectile and target were discretized into 1943 elements. The axial stress measured at the second interface between the Isodamp and ceramic is compared with the simulation in Figure 5. The simulation result is taken from the element stress in the ceramic at the closest position to the interface with the Isodamp. The fracture stress was chosen to be 3 kbar (Rosenberg et al., 1985) and the deformation parameters for the Al_2O_3 (estimated from Johnson and Stryk (1990) were: $c_1 = 1.621$ Mbar, $c_2 = 1.945$ Mbar, $c_3 = 1.929$ Mbar, $c_4 = 0.$, $c_5 = 0.$, $\sigma_{yo} = 39$ kbar. Results are shown for two cases: elastic-plastic with no fracture, and elastic-plastic with fracture (setting $\sigma_{yo} = 0$ after fracture)

In Fig. 5, the general experimental trend is predicted but there are substantial differences observed as well. The experiment quickly loads to about 36 kbar and maintains that approximate stress for 2-3 microseconds. It then relaxes to about 10 kbar, shows evidence of a secondary loading wave and finally drops to zero. The finite element solutions show much more wave interaction than the experiment. The models predict both the initial stress peak and second peak (at ~3.5 microseconds) but recover to the 20-25 kbar range for the time between. The model which allows fracture predicts a lower stress throughout the history as expected. The difference between the simulation with fracture and the experimental curve is indictitive of the post fracture strength of the ceramic. The elastic-plastic simulation without fracture provides the better prediction here since it has strength throughout the event.

Leaving the ceramic intact increases the stresses relative to the simple fracture model predictions but it is physically unreasonable. Rather, consider the observation that ahead of the penetrator the ceramic fractures into fine rubble. It is believed that as this confined rubble is deformed the granules will slide over one another creating free space between them. As in all granular materials, both the shear stress and dilitation rate of a granular material are pressure dependent, hence, the c_4 term in equation 2.

In order to include this post-fracture, pressure dependent strength a simulation was conducted with the flow stress constant before fracture ($\sigma_y = 39$ kbar) but after fracture the flow stress depends upon pressure according to $\sigma_y = 0.45$ kbar + 1.61 p. This expression was derived from Arrowood's data for slow strain rate confined compression of powered alumina (Arrowood, 1987). The results, shown in Figure 6, do not differ very much from the elastic-plastic without fracture result from Figure 5. The pressure dependent flow stress after fracture raises the stress signal after the initial peak and provides better agreement with experiment than the model which has no .post-fracture strength. The later time stresses were overpredicted though.

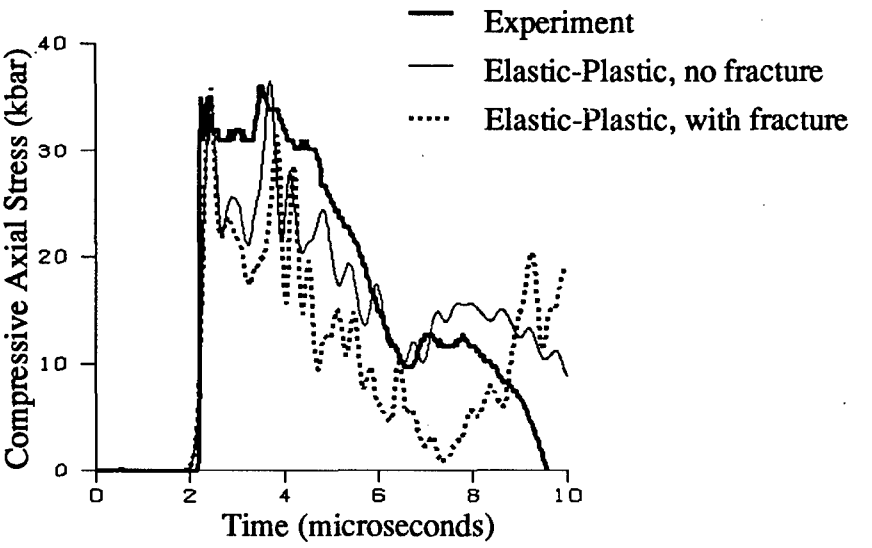

Figure 5, Comparison of experiment Saturn 3 with simple elastic-plastic fracture model.

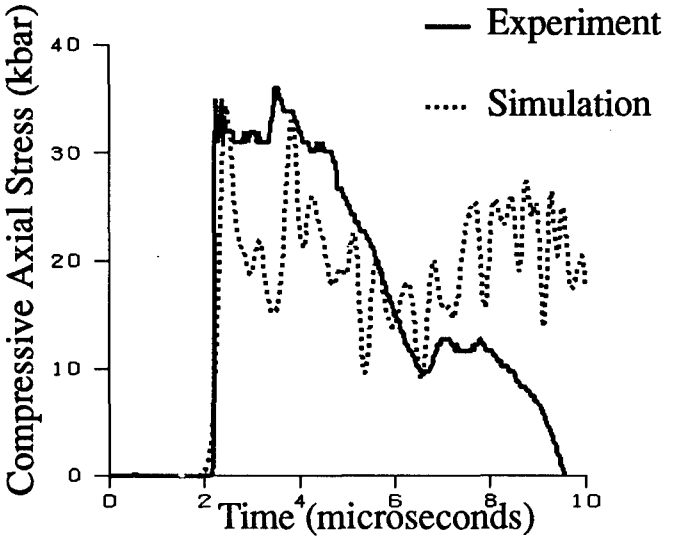

Figure 6, Simulation of Saturn 3 experiment with model having post-fracture, pressure dependent flow stress.

A major deficiency in these simulations of the blunt nose impact test is the failure to keep the stress level in the 30 kbar range during the 2 to 4 microsecond time frame.

The second ballistic experiment (Uranus 6) involved the impact of a coni-

cally nosed, steel projectile at 2540 ft/sec. The target assembly was similar to Figure 4 with the exception that the Isodamp layer was removed. The pointed nose of the projectile produced a more gradual loading wave for the ceramic material away from the impact point. The experimental curve in Figure 7 shows the gradual load and unload profile for the stress at the ceramic tile interface.

This experiment was simulated with two hydrocodes. The DYNA2D code as used with the same material model as discussed above (equations 1 and 2) and the CALE code was used with just perfectly elastic-plastic behavior (no fracture or rate dependence). It was necessary to use the Eulerian capabilities of CALE to be able to run the simulation to 14 microseconds. The DYNA2D code, being a Lagrangian formulation, developed highly distorted elements in the penetrator that did not allow the solution to proceed beyond about 10 microseconds. These distorted elements could be removed using an erosion algorithm but that gave spurious stress history results due to the jackhammer effect. Large stress spikes were calculated with surfaces coming into and out of contact as elements were deleted. Not only did this make it difficult to compare the stress history with the experiment but the effect of these nonphysical stress spikes on the fracture behavior could be severe. Having stress history data illustrates the importance for having a continuous Eulerian calculation for these brittle materials and not being satisified with just being able to push a calculation to show penetration.

The elastic-plastic result from CALE is shown in Figure 7. The loading ramp is predicted very well. The peak stress is overshot by a little and the unloading ramp is delayed relative to experiment. Overall, the simulation gives a very good prediction. The maximum stress overshoot and delay in unloading can, perhaps, be attributed to the neglect of fracture in the calculation.

Since the CALE code does not currently have any fracture models, the DYNA2D (Lagrangian) code was used to simulate the first 10 microseconds of the impact. The material model was the same as that used in the blunt nose projectile simulation reported in Figure 5. The flow stress was constant before fracture (σ_y = 39 kbar) but after fracture the flow stress depends upon pressure according to σ_y = 4.5 kbar + 1.61 p.

The result in Figure 8 was taken for the third element away from the centerline. The stress response for the blunt nose projectile was found to be insensitive to slight gauge misalignment away from the line of sight of the projectile. For the pointed nose projectile, the stress response did vary with position away from the centerline. It was observed in post-mortum examination of Uranus 6 that the stress gauge was slightly off line of the center of the projectile impact. Hence, the simulation result was also taken from a position slightly off the centerline. Again we observe that modeling the alumina with these techniques gives satisfactory prediction of stress history during the initial phase of impact.

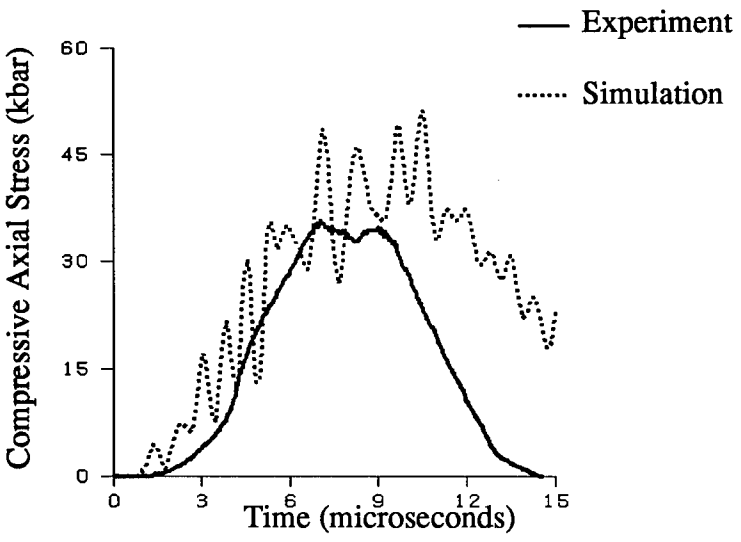

Figure 7, CALE simulation of Uranus 6 experiment.

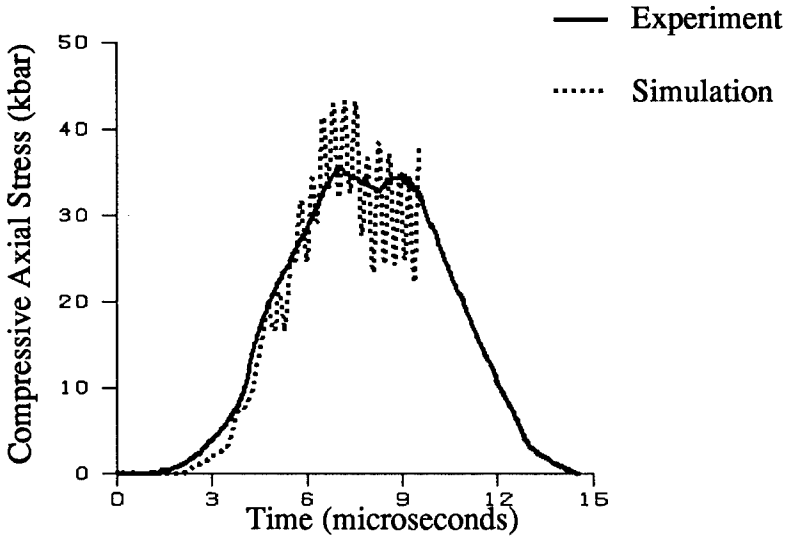

Figure 8, DYNA simulation of Uranus 6 experiment using fracture and pressure dependent flow stress

CONCLUSIONS

Simple elastic-plastic modeling techniques were shown to effectively model the behavior of silicon carbide under impact conditions. It was shown to behave like a rate dependent elastic-plastic material in the one dimensional experiments of (Kipp and Grady, 1989). A simple maximum stress fracture criterion adequately reproduced the unloading wave behavior.

The ballistic experiments of (Vincent and Chang, 1990) provided stress versus time profiles useful for modeling of alumina. The elastic-plastic model predicted the general trends and intial pulse magnitude quite well. The model did not fully predict the stress magnitude after fracture. This is attributed to the need for a post-failure damage model. This is the direction of future research. It is recognized that elastic-plastic modeling should be more satisifactory for the ceramics considered here (SiC and alumina) than for all other ceramics but this work does show a place for elastic-plastic modeling.

Acknowledgment

The authors would like to thank L. Chiu for help with the CALE simulation reported in this paper.

REFERENCES

Arrowood, R. and J. Lankford. 1982. "dynamic characterization of an Alumina Ceramic." SwRI Report 6724, ONR Contract N0014-81-C-0745.

Cochran, S. and D. Banner. 1977. Journal of Applied Physics, 48, p. 2729

Furlong, J.R.; M.L. Alme; and J.F. Davis. 1990. "Modeling the Dynamic Load/Unload Behavior of Ceramics Under Impact Loading (U)." RDA-TR-0030-0001-001. R & D Associates, Arlington, VA (July).

Hallquist, J.O. 1987. "User's Manual for DYNA2D -- An Explicit Two-Dimensional Hydrodynamic Finite Element Code With Interactive Rezoning and Graphical Display." Lawrence Livermore National Laboratory Report UCID-18756, Rev. 3, Livermore, CA (February).

Johnson, G.R. and W.J. Cook. 1983. "A Constitutive Model and Data for Metals Subjected to Large Strains, High Strain Rates and High Temperatures."

In Proceedings of Seventh International Symposium on Ballistics (The Hague, The Netherlands, April).

Johnson, G.R. and R.A. Stryk. 1990. "User Instructions for the 1989 Version of the EPIC-2 Code." Report Number AFATL-TR-90-07, Honeywell Incorporated, Brooklyn Park, MN.

Kipp, M.E. and D. E. Grady. 1989. "Shock Compression and Release in High-Strength Ceramics." Sandia Report SAND89-1461. Sandia National Laboratories, Albuquerque, NM (July).

Mashimo, T.; Y. Hanaoka; and K. Nagayama. 1987. "Elastoplastic Properties Under Shock Compression of Al_2O_3 Single Crystal and Polycrystal." Journal of Applied Physics, 63, No. 2, 327-336.

Rosenberg, Z., Yeshurun, Y. and D.G. Brandon. 1985. "Dynamic Response and Microstructure of Commercial Alumina." Journal de Physique, C5, pp. 331-341.

Shockey, D.A.; A.H. Marchand; S.R. Skaggs; G.E. Cort; M.W. Burkett; and R. Parker. 1990. "Failure Phenomenology of Confined Ceramic Targets and Impacting Rods." International Journal of Impact Engineering 9, no. 3, pp. 263-275.

Steinberg, D. 1990. "Computer Studies of the Dynamic Strength of Ceramics." Lawrence Livermore National Laboratory report UCRL-ID-106004. (Sept. 24).

Vincent, P.M. and A.L. Chang. 1990. "Ballistic Impact Pressure Pulse Measurement." presented at the 41st Meeting of the Aeroballistic Range Association." (San Diego, CA, October 22-25).

White, C.S., Chang, A.L., McLaughlin, J.J., Ofstedahl, K.E. and P.M. Vincent. 1991. "An Investigation of Ceramic Behavior During Impact." Ballistics Simulation, Michael Chinni, ed., Proceedings of the SCS Simulaiton MultiConference on Ballistics Simulation and Simulation Work and Progress, 1-5 April 1991, New Orleans, LA.

Wilkins, M.L. 1968. "Third Progress Report of Light Armor Program." Lawrence Radiation Laboratory Report UCRL-50460. University of California, Livermore, CA (July 9).

SESSION V: PLASTICITY

Session Chairman: *Prof. P. Symonds*

Dynamic Ductile Rupture in a Spheroidized 1045 Steel

M. Zhou and R. J. Clifton
Division of Engineering
Brown University
Providence, RI-02912

Abstract

A plate impact experiment has been used to study dynamic ductile rupture at strain rates up to 10^5 s^{-1} in a spheroidized 1045 steel. Plane strain tensile loading is generated by impacting a deeply notched specimen by a thin elastic flyer plate. The notch, parallel to the impact plane and extending halfway through the diameter, is filled with steel shims to transmit compressive waves. The tensile wave reflected from the rear surface causes tensile loading at the blunt notch tip, resulting in ductile void nucleation and growth. Free surface velocities are monitored at three points by means of a normal velocity interferometer. Extensive void growth is observed as the impact velocity is increased. Relative notch opening displacement is found to depend on the initial notch width as well as the impact velocity. At impact velocities above 0.14 $mm/\mu s$, void nucleation due to the reflected tensile wave is also observed along a plane parallel to the rear surface. This spallation is studied in one version of the plate impact experiment that does not involve a notch. Scanning electron microscopy of the rupture surface shows that spallation occurs mainly by cleavage of the ferrite grains and is assisted by void nucleation and growth on separated void sheets. A dynamic finite element method based on a constitutive law proposed by Gurson for porous materials is used to simulate the plate impact experiment.

1. Introduction

While second phase precipitates or particles greatly enhance the strength of materials by acting as obstacles to dislocation movement, see, *e.g.*, Dew-Hughes and Robertson (1960)[1], Meiklejohn and Skoda (1960)[2], Ashby (1964)[3], Kocks (1966)[4], Foreman and Makin (1966)[5], Liu and Gurland (1968)[6], they also provide sites for the initiation of microvoids during plastic deformation. The nucleation, growth and subsequent coalescence of voids play the most important role in the process of ductile failure, (Gurland and Plateau (1963)[7], Thomson and Hancock (1984)[8], and Thompson (1987)[9]). Voids nucleate through particle-matrix debonding and through particle cracking, (Gurland and Plateau (1963)[7]). The early studies by McClintock (1968)[10] for a cylindrical

void and Rice and Tracey (1969)[11] for a spherical void focused on the quasi-static growth kinetics of a single cavity in an infinite elastic-plastic matrix. Their work showed the dependence of void growth on the triaxiality of the stress state. Brownrigg *et al* (1983)[12] found that the superposition of pressure severely retards the nucleation and growth of voids at carbide particles and that fracture strain increases linearly with pressure in a spheroidized 1045 steel. Void initiation and growth are explained by Gurland and Plateau (1963)[7] and Broek (1973)[13] as a result of dislocation loop pile-ups against particles. The study by Park and Thompson (1988)[14] showed that void nucleation appears to be controlled by a stress-based criterion and that void growth and coalescence are controlled predominantly by plastic strain in tensile tests. Fisher and Gurland (1981)[15] found that larger particles and grain boundaries are more favorable sites for void nucleation.

There have been extensive studies of the ductile rupture process based on the continuum theory of plasticity. Berg (1962)[16] described the motion of an elliptical cavity in a plane viscous body by a conformal transformation. The deformation and conditions under which an isolated void may become ellipsoidal and collapse into the shape of a crack or needle were studied by Budiansky, Hutchinson and Slutsky (1982)[17] and Budiansky (1983)[18]. Based on the hypothesis that coalescence is the result of internal necking of adjacent cavities, Thomason (1968)[19] analyzed the evolution of a regular array of cavities subjected to plane strain triaxial stress states. Blume (1988)[20] studied the interaction between two contiguous spherical voids under radially symmetric remote loading in a hyperelastic solid and found that the voids are attracted to each other for most remote load triaxialities; separation is predicted only under stress states which are nearly uniaxial along the line of centers of the voids. The interactions between periodically distributed voids and their growth and collapse have also been analyzed by Nemat-Nasser and Iwakuma (1982)[21] and Nemat-Nasser, Iwakuma and Accorsi (1986)[22].

Gurson (1975,1977)[23,24] developed a phenomenological constitutive relation by introducing a plastic potential depending on the material strength, the void volume fraction and the hydrostatic stress. The effects of voids are represented by a single parameter, the void volume fraction, through which materials with any porosity exibit macroscopic dilatancy and pressure sensitivity. Tvergaard (1981, 1982)[25,26] modified the Gurson model by amplifying the void volume fraction and hydrostatic stress in order to bring the predictions closer to the results of full numerical analyses at small void volume fractions. Tvergaard and Needleman (1984)[27]

further modified the yield condition to model the loss of macroscopic stress-carrying capacity associated with void coalescence.

Several investigators have considered the effects of crystalline slip on the deformation of voids. Nemat-Nasser and Hori (1987,1988)[28,29] showed that, as a result of the local anisotropic plastic flow by slip on crystallographic planes, an initially circular (2D) or spherical (3D) void quickly deforms into a noncircular (2D) or nonspherical (3D) shape even under all-around uniform tension or pressure.

Hori and Nemat-Nasser (1988)[30] studied the dynamic response of crystalline solids with micro-cavities based on an approximate method for calculating void deformation in crystalline bodies. They found that the global response of the material toughens as the loading rate increases. Studies on void nucleation, growth and coalescence under dynamic conditions are reviewed by Curran, Seaman and Shockey (1987)[31]. One of the experimental configurations used to study ductile rupture under dynamic conditions involves impacting a flyer plate against a target specimen of the same or different material. Upon reflection from the rear surface of the target the compressive wave becomes a tensile wave propagating in the opposite direction. This tensile wave causes initiation, growth and coalescence of voids, leading to spallation. Thorough reviews of spallation have been reported by Meyers and Aimone (1983)[32] and Asay and Kerley (1987)[33]. Continuum mechanics modeling of spallation based on void nucleation and growth has been done by Rajendran (1988)[34] and Eftis *et al* (1991)[35] with finite difference methods.

The objective of the current study is to obtain dynamic rupture at strain rates up to 10^5 s^{-1} caused by the non-uniform stress and strain fields resulting from the diffraction of a tensile plastic stress wave by a precut notch in the middle of a specimen in a plate impact experiment. The experiment is simulated by means of a dynamic finite element method.

2. Material

The material is 1045 steel obtained in the form of cold drawn bars 2.5 inches in diameter. Its chemical composition is given in Table 1. The spheroidizing treatment involves austenitizing at 900^oC for 1 hour, quenching in agitated ice water and normalizing at 700^oC for (A) 24 hours, (B) 48 hours and (C) 120 hours. To obtain a fullly martensitic structure as required for obtaining a uniform distribution of carbide spheroids during normalization, the material is cut into circular disks 62.5 *mm* in diameter and 10 *mm* in thickness to ensure a sufficiently

high cooling rate. After normalization, the specimens are air-cooled to room temperature. Figure 1 shows the microstructure produced by normalization A. The microstructure is that of a spheroidized steel consisting of a fine dispersion of cementite particles embedded in a ferrite matrix. The particle size distributions are measured by an interception line method which involves recording the number of particles intercepted by randomly placed test lines and the corresponding intercept lengths, for a plane section of the specimen. The particle volume fraction f is obtained by dividing the number of grid points falling in areas occupied by the particles by the total number of grid points in the area covered by a uniform test grid. The microstructural parameters obtained by these means are listed in Table 2. These parameters obey the relations

$$f = N_l \cdot L = N_l \cdot \sqrt{\frac{2}{3}} d_s = N_l \cdot \frac{2}{3} d, \tag{2.1}$$

which are exact for uniform particles which are spherical and randomly distributed, Ashby (1964)[3] and Underwood (1970)[36]. In eqns. (2.1), N_l is the number of intersections with the particles per unit test line, L is the mean particle intercept length, d_s is the mean particle diameter on a random section and d is the three-dimensional particle diameter. Also in Table 2, σ_n denotes the standard deviation of the particle diameter d, λ is the mean surface-to-surface particle distance calculated from $\lambda = L(1-f)/f$.

Table 1 Chemical Composition of the 1045 steel, wt%;

Fe	C	S	Mn	P
98.74	0.47	0.028	0.75	0.012

Table 2 Microstructural Parameters;

Heat Treatment	f %	d μm	σ_n μm	λ μm
A	6.54	0.54	0.43	5.14
B	6.52	0.84	0.75	8.03
C	6.58	1.18	0.90	11.17

Pressure-shear plate impact experiments, described by Clifton and Klopp, (1985)[37] were conducted to study the material response under high strain rates of the order of 10^5 s^{-1}. By measuring the transverse

particle velocity at the rear surface of the anvil plate v_{fs}, the shear stress τ and nominal shear strain rate $\dot{\gamma}$ are obtained as $\tau = (\rho c_2) v_{fs}/2$, and $\dot{\gamma} = (V_0 \sin\theta - v_{fs})/h$, where ρc_2 is the shear impedance of the anvil plate, V_0 is the projectile velocity, θ is the skew angle of the specimen, and h is the initial thickness of the specimen. The shear strain rate is integrated to yield the shear strain $\gamma(t) = \int_0^t \dot{\gamma}(\tau) d\tau$.

The resulting dynamic stress-strain curves are shown in Figure 2 together with those obtained at a lower strain rate of 4.05×10^3 s^{-1} in torsional Kolsky bar tests and in quasi-static torsional tests by Walter and Duffy (1990)[38] for a spheroidized 1045 steel with a microstructure similar to that produced by normalization C above. Clearly, the materials show a strong strain-rate sensitivity over the rate regime studied.

Longer normalization times produce coarser carbide particles and lower flow stress levels. The stress level however, does not change significantly with an increase in the normalization time from 48 hours to 120 hours (mean particle diameters 0.84 μm to 1.18 μm) whereas a significant reduction is noticed between the 24 and 48 hour treatments (particle diameters from 0.54 μm to 0.84 μm).

Over the range of strain rates from 10^{-4} s^{-1} to 3.0×10^3 s^{-1} the material response can be characterized by an empirical visco-plastic constitutive relation of the form

$$\dot{\gamma}_1 = \dot{\gamma}_0 \left[\frac{\tau}{g(\gamma^p)} \right]^m, \tag{2.2}$$

where $\dot{\gamma}_1$ is the shear strain rate, τ is the shear stress, $\dot{\gamma}_0 = 1 \times 10^{-4}$ s^{-1} is a reference strain rate, $m = 75$ is a rate sensitivity parameter and

$$g(\gamma^p) = \tau_0 [1 + \exp(\omega - \gamma^p/\gamma_r)](1 + \gamma^p/\gamma_0)^n, \tag{2.3}$$

represents the stress-strain relation at a constant shear strain rate of $\dot{\gamma} = \dot{\gamma}_0$. In Eqn. (2.3), γ^p is the plastic shear strain, $\tau_0 = 179$ MPa is a reference shear stress, $\gamma_0 = \tau_0/E$ is a reference shear strain, $n = 0.13$ is the strain hardening exponent, parameters $\omega = 0.65$ and $\gamma_r = 0.0043$ are introduced to model the higher flow stress levels at small strains due to the lack of a large mobile dislocation density in the annealed material. These parameters are chosen by fitting the initial part of the velocity profiles at the rear surface from the normal impact experiment of unnotched specimens.

In order to account for the behavior at higher strain rates the relation (2.2) is modified to

$$\dot{\gamma}^p = \frac{\dot{\gamma}_1 \dot{\gamma}_2}{\dot{\gamma}_1 + \dot{\gamma}_2}, \tag{2.4}$$

where $\dot{\gamma}^p$ is the plastic shear strain rate and

$$\dot{\gamma}_2 = \dot{\gamma}_m \exp\left[-\frac{\alpha g(\gamma^p)}{\tau}\right], \tag{2.5}$$

is a mathematical model of the limiting viscoplastic response at very high strain rates. In Eqn. (2.5) $\alpha = 15$ is a strain rate sensitivity parameter for strain rates above, say, 3×10^3 s^{-1}. The form (2.4) limits the strain rate to values less than $\dot{\gamma}_m$. It also provides a smooth transition between the measured response $\dot{\gamma}^p = \dot{\gamma}_1(\tau, \gamma^p)$ at strain rates less than, say, 10^3 s^{-1}, and the limiting behavior $\dot{\gamma}^p = \dot{\gamma}_2(\tau, \gamma^p)$ at strain rates greater than, say, 10^5 s^{-1}. The value of $\dot{\gamma}_m$ is not available from experiments; a value of 5×10^8 s^{-1} is chosen, primarily for the numerical purpose of avoiding the need for unreasonably small time steps at early times when the shear stresses are large.

Stress-strain curves in shear, predicted by Eqns. (2.2-2.5) for constant strain rates are compared with those obtained from the experiments in Figure 2. All the parameters are chosen to best fit the material response for specimens with normalization A, which are used in the subsequent dynamic ductile rupture experiments. Because the quasi-static curves and the torsional Kolsky bar curves were obtained from a spheroidized 1045 steel with a microstructure similar to that produced by normalization C which has a larger mean particle size and lower flow stress level, the parameters in the formulation are intentionally chosen to produce slightly higher flow stresses at the corresponding strain rates. It should be recalled that pressure-shear plate impact tests and torsional tests provide more accurate measures of the material response at strains greater than a few percent than at very small strains.

3. Experiment

The experimental configuration for the dynamic ductile rupture experiment is shown in Figure 3. The specimen is a circular disk, 59 *mm* in diameter and 8 *mm* in thickness. The notch has a width of approximately 0.35 *mm* and is cut halfway through the diameter of the disk by electrical

discharge machining (EDM). The notch is filled with stainless steel shims to transmit the compressive pulse. The experiment involves plane strain loading of the notched specimen by impacting it with a thin elastic flyer plate and reflecting the compressive pulse from the rear surface of the specimen. The flyer plate has a thickness of 3 *mm* and the same diameter as the specimen. The impact results in the loading of the specimen by a plastic wave whose main pulse has a duration of approximately 1 microsecond. Figure 4 shows the time-distance diagram for the main wave fronts that traverse the specimen and flyer. Upon arrival at the notch the reflected tensile wave is diffracted, causing straining at high rates around the notch tip. The reflected tensile wave and its diffraction by the notch causes dynamic ductile void nucleation, growth and coalescence in the specimen. To study the plastic wave profiles that propagate through the specimen and the ductile rupture (or spallation) caused by the tensile wave in the absence of the notch, one version of the experiment involves the impact of an un-notched specimen of the same dimensions. These two types of experiments allow comparison of the ductile rupture processes initiated by a tensile plane plastic wave alone and by its diffraction from a blunt notch.

The motion at three separate points on the rear surface is monitored by a multi-beam displacement or velocity interferometer system. By relating the motion of the rear surface at several points to the void nucleation and growth near the notch tip, and the initiation and propagation of the spalling cracks, a better understanding can be obtained of the various stages of void nucleation, growth and coalescence and their effects. The multi-beamsplitting scheme used in the system has been described in detail by Mello *et al* (1991)[39]. Each leg of the system is a normal velocity interferometer described by Barker (1968)[40].

A quadrature optical setup, similar to but different from those described by Hemsing (1979)[41] and Bouricius and Clifford (1970)[42], is used for one of the points to obtain two interference signals which are 90^o out of phase to allow unambiguous identification of the absolute phase of the interference signals.

4. Numerical Simulation

Finite element simulation of the impact experiments is conducted by a finite deformation formulation by Needleman *et al* (*e.g.*, 1982, 1988, 1990).[26,43–45] The principal feature of this formulation that is of interest in the present investigation is the modeling of viscoplastic deformation

and material failure due to the nucleation and growth of voids. The flow rule for a material containing voids is derived from a plastic potential introduced by Gurson (1975, 1977)[23,24] and modified by Tvergaard (1981)[25] and Tvergaard and Needleman (1984)[27],

$$\Phi = \frac{\sigma_e^2}{\bar{\sigma}^2} + 2q_1 f^* \cosh\left(\frac{3q_2\sigma_h}{2\bar{\sigma}}\right) - 1 - {q_1}^2 f^{*2} = 0. \tag{4.1}$$

In (4.1) σ_e and σ_h are the macroscopic equivalent Cauchy stress and the macroscopic hydrostatic stress, respectively, *i.e.*

$$\sigma_e^2 = \frac{3}{2}\boldsymbol{\sigma}' : \boldsymbol{\sigma}'; \qquad \sigma_h = \frac{1}{3}\boldsymbol{\sigma} : \mathbf{I}, \tag{4.2}$$

where $\boldsymbol{\sigma}$ and $\boldsymbol{\sigma}' = \boldsymbol{\sigma} - \sigma_h \mathbf{I}$ are the Cauchy and the deviatoric Cauchy stress tensors, respectively; $\mathbf{I}$ is the second order identity tensor and $\boldsymbol{\sigma}' : \boldsymbol{\sigma}'$ denotes the dyadic product $\boldsymbol{\sigma}'^{ij}\boldsymbol{\sigma}'_{ij}$. The stress $\bar{\sigma}$ is an equivalent stress in the matrix material. Parameters q_1 and q_2 are dilatancy and pressure sensitivity parameters introduced by Tvergaard (1981,1982)[25,26]. The quantity f^* is a function of the void volume fraction f defined as

$$f^* = \begin{cases} f & f \le f_c; \\ f_c + \frac{f_u^* - f_c}{f_f - f_c}(f - f_c) & f \ge f_c, \end{cases} \tag{4.3}$$

where $f_u^* = 1/q_1$ is the value of f^* when the material loses all stress carrying capacity, corresponding to the rapid void coalescence in the final stages of ductile rupture; as $f \to f_f$, $f^* \to f_u^*$; f_c is the critical void volume fraction after which the material loses its strength at accelerated rates. Values for the parameters f_c, f_f, q_1, q_2 that are used in the simulation reported here are $f_c = 0.07$, $f_f = 0.15$, $q_1 = 1.25$, and $q_2 = 1.3$.

The plastic flow rule is obtained from (4.1) by writing the plastic part of the rate-of-deformation tensor, $\mathbf{D}^p$, as

$$\mathbf{D}^p = \dot{\Lambda}\frac{\partial\Phi}{\partial\boldsymbol{\sigma}} = \dot{\Lambda}\left[\frac{3\boldsymbol{\sigma}'}{\bar{\sigma}^2} + 3q_1 q_2 f^* \sinh\left(\frac{3q_2\sigma_h}{2\bar{\sigma}}\right)\mathbf{I}\right], \tag{4.4}$$

where the proportionality factor $\dot{\Lambda}$ is obtained by equating the plastic work rate to the matrix energy disspation rate.

The damage parameter or the void volume fraction f evolves through the initiation of new voids and the growth of existing voids according to

$$\dot{f} = \dot{f}_{nucleation} + \dot{f}_{growth}. \tag{4.5}$$

To model void nucleation through both a strain-controlled mechanism and a stress-controlled mechanism the nucleation rate is taken to have the form

$$\dot{f}_{nucleation} = \mathcal{D}\dot{\bar{\epsilon}} + \mathcal{B}(\dot{\bar{\sigma}} + \dot{\sigma}_h), \tag{4.6}$$

where

$$\mathcal{D} = \frac{f_N}{s_N\sqrt{2\pi}}\exp\left[-\frac{1}{2}\left(\frac{\bar{\epsilon} - \epsilon_N}{s_N}\right)^2\right], \tag{4.7}$$

$$\mathcal{B} = \frac{f_N}{\sigma_0 s_N\sqrt{2\pi}}\exp\left[-\frac{1}{2}\left(\frac{(\bar{\sigma} + \sigma_h) - \sigma_N}{\sigma_0 s_N}\right)^2\right]. \tag{4.8}$$

The parameter f_N is the volume fraction of void nucleating particles, σ_N is the mean void nucleation stress, s_N is the standard deviation of nucleation, ϵ_N is the mean void nucleation strain and $\sigma_o s_N$ is the standard deviation of stress-controlled nucleation. Values used for the respective parameters are: $f_N = 0.06$, $\sigma_N = 2700\ MPa$, $s_N = 0.01, \epsilon_N = 0.041$ and $\sigma_o = \sqrt{3}\tau_o = 217\ MPa$.

The growth rate of existing voids is determined from the plastic incompressibility of the matrix material as

$$\dot{f}_{growth} = (1 - f)\mathbf{D}^p : \mathbf{I}. \tag{4.9}$$

The numerical implementation of the material model has been described by Needleman and Tvergaard (1990)[44].

5. Results and Discussion

The experiments are summarized in Table 3 for the un-notched specimens and Table 4 for the notched specimens. All experiments are conducted with impactors made of a Hampden high carbon tool steel which has a proportional limit of 1600 MPa in shear and remains elastic throughout the experiment.

Table 3 Experiments with un-notched Specimens;

Shot #	V_0 $mm/\mu s$	T_f mm	T_s mm	d mm
9006	0.155	3.12	8.12	2.34
9101	0.141	3.08	8.05	*
9102	0.138	3.08	8.01	**

*: no spall; **: void initiation observed in locations 2-2.4 mm from rear surface.

Table 4 Experiments with notched Specimens;

Shot #	V_0 $mm/\mu s$	W_0 mm	W mm	$\Delta W/W_0$ %	T_f mm	T_s mm	d mm
9002	0.140	0.372	0.438	17.6	3.06	7.98	*
9003	0.196	0.336	**	**	3.06	7.98	2.39
9004	0.150	0.343	0.521	52.0	3.18	8.05	2.22
9005	0.156	0.413	0.593	43.6	3.12	8.12	2.03

* No spall, void initiation observed; ** Spall crack connected with notch; V_0: projectile velocity; W_0: average notch width before experiment; W: notch width at middle section after experiment; T_f: flyer thickness; T_s: specimen thickness; d: distance between spall plane and rear surface of specimen.

The relative notch opening $\Delta W/W_0$ in Table 4 can be used as an approximate measure of the amount of plastic deformation that the notch tip material undergoes. As predictable intuitively, the relative notch openning depends on the impact velocity as well as the initial notch width W_0 — the smaller the notch width the larger the relative notch opening $\Delta W/W_0$. At impact velocities of approximately $V_0 = 0.140\ mm/\mu s$ the tensile wave, reflected from the rear surface of the specimen begins, to cause void nucleation at $2-2.4\ mm$ from the rear surface. As the impact velocities are increased this tensile wave causes the material to fail. Scanning electron microscopic examination shows that the spallation initiates as cleavage of the ferrite matrix grains and is assisted by void coalescence as discussed in section 5.1.

5.1 Scanning Electron Microscopy

The impacted specimens are sectioned along a plane perpendicular to the impact face and the notch front. The revealed surface is ground, polished, etched with 4% picral and examined in a JEOL 840F scanning

electron microscope (SEM). Figures 5(a–b) show the notch tip region of the specimen from shot 9002. Voids are found in a region within about 5–10 μm in front of the notch tip. Nucleation occurs through (a) particle-matrix debonding; (b) particle cracking and (c) particle–particle separation as shown in Figure 5(b). The voids show apparent growth after nucleation. The notch width, which was approximately 372 μm wide initially, increased by 17.6% to 438 μm after the impact. As the impact velocity is increased to 0.156 $mm/\mu s$ (shot 9005) voids are found in a larger region, approximately $30 - 40$ μm in front of the notch tip. The voids show substantial growth, and begin to coalesce, as shown in Figure 6. This is the result of the increased amount of plastic straining indicated by the relative notch width increase of 43.6% at this impact velocity. The growth and coalescence of voids lead to the onset of ductile rupture at the immediate notch tip region where severe plastic straining occurs, as shown in Figure 6. Figure 7 shows that void growth tends to localize in areas at the notch tip region. These areas often appear as bands extending from the notch tip where a cavity is formed. The voids inside the bands undergo substantial growth and coalescence. The formation of these void bands may be related to notch surface defects existing before the experiments.

Voids also appear in a strip about $2 - 2.4$ mm from the rear surface in the un-notched lower half of the specimen. These are initiated by the reflected tensile wave. The voids in the strip do not show substantial growth at impact velocities of the order of $V_0 = 0.140$ $mm/\mu s$. As the impact velocity is increased the material ruptures along a plane parallel to the rear surface in a predominantly brittle manner. Impact experiments of un-notched specimens as well as notched specimens show that when the tensile wave is not sufficient to spall the specimen, voids can initiate during the tensile pulse, but they are relatively small. Spallation results if the impact velocity is increased to a value higher than 0.150 $mm/\mu s$. Figure 8 shows the typical morphology of the spalled regions. Only a few voids are observed along the spall plane. It appears that spallation initiates as cleavage fracture fragments. These segments link by lateral shear, which involves void growth and coalescence, (Figure 8). This observation is supported by a study of the spall plane which shows transgranular cleavage of the ferrite matrix and cleavage facets connected by ductile necking of the matrix material. The transgranular cleavage planes link up via inclined void sheets, (Figure 9), which are formed through the lateral shear seen in Figure 8. These void sheets appear to form primarily at grain boundaries.

The void band is observed only on the un-notched half of the specimen; a small number of nucleating voids are observed at the same distance from the rear surface on the notched half. The explanation may be that the reflected tensile wave is reflected back toward the rear surface, by the notch surface, as a compressive wave, thereby reducing the duration of the tensile loading and keeping the putative spall plane in compression for most of the loading time.

5.2 Free Surface Velocity–Time Profiles

Figure 10 shows the free surface velocity profiles from the experiments with un-notched specimens listed in table 3, and finite element simulations. The parts of the profiles corresponding to the different wave fronts shown in the x–t diagram (Figure 6) are labeled as: A–Arrival of the compressive wave at the rear surface; B–unloading of the main compressive pulse at the rear surface; C–tensile damage location (Figure 4) and its arrival at the rear surface (Figure 10); D–damage signal at the rear surface; and E–reflected compressive pulse arriving at the rear surface; The initial part of the experimental curves is used to determine the material parameters ω and γ_r in Eqn. (2.3). These two parameters are introduced to model the higher flow stresses at small strains due to the lack of a large mobile dislocation population in the annealed material.

The calculated profiles shown in Figure 10, both without voids and with the inclusion of void nucleation and growth, are simulations of the experiments with an impact velocity of $V_0 = 0.140\ mm/\mu s$. Comparisons of the experimental profiles with those from the calculation indicate that the 'bumps' at about 2900 ns correspond to tensile damage located approximately $2.0 - 2.4\ mm$ from the rear surface. This interpretation is confirmed by the SEM observation, described above, that void nucleation occurs at these locations for impact velocities of the order of $0.140\ mm/\mu s$ and that spallation occurs at higher impact velocities through transgranular cleavage and ductile rupture by void growth and coalescence.

Figure 11 shows the free surface velocities at three points, located at 0.7 mm, 1.0 mm and 1.4 mm in front of the notch tip, for shot 9002. Only the time interval after the the arrival of the main compressive wave is shown. Point D corresponds to the arrival of the diffracted wave reflecting from the impingement of the tensile wave on the notch. For the calculation shown, void nucleation and growth have been suppressed. Thus the computed profiles represent velocity profiles without damage. Further simulations will be conducted to study the effect of void nucleation and growth on the free surface velocity profiles.

6. Concluding Remarks

Dynamic ductile rupture has been obtained in plate impact experiments of both notched and un-notched specimens. Ductile void nucleation and growth occur due to the reflected tensile wave alone and to its diffraction from a blunt notch. Void growth and coalescence are observed to occur with increased plastic straining resulting from increased impact velocities. As the impact velocity is increased, the tensile wave induced spall appears to be transgranular cleavage of the ferrite matrix assisted by ductile rupture through void growth and coalescence on separated void sheets.

Numerical simulations of the impact experiments have produced free surface velocity profiles that agree with the measured profiles except for features that can be attributed to the ductile nucleation and growth of voids. Further efforts will be directed toward better simulation of void nucleation, growth and coalescence under the dynamic conditions obtained in the experiments.

7. Acknowledgement

This research is supported by the Army Research Office. Computations described here were carried out on the CRAY Y-MP8/864 at the San Diego Supercomputer Center. We wish to thank Professors A. Needleman and V. Tvergaard for providing the finite element program on which the simulation is based. Thanks are due to M. C. Mello for his assistance in the experiments.

8. References

[1] Dew-Hughes, D. and Robertson, W. D., (1960), "Dispersed Particle Hardening of Aluminum-Copper Alloy Single Crystals", *Acta Metall.*, Vol. **8**, March, pp. 147-155.

[2] Meiklejohn, W. H. and Skoda, R. E., (1960), "Dispersion Hardening", *Acta Metall.*, Vol. **8**, pp. 773-780.

[3] Ashby, M., (1964), "The Hardening of Metals by Non-Deforming Particles", *Z. Metallk.*, Vol. **55**, pp. 5-17.

[4] Kocks, U. F., (1966), "A Statistical Theory of Flow Stress and Workhardening", *Phil. Mag.*, Vol. **13**, pp. 541-566.

[5] Foreman, A. J. E. and Makin, M. J., (1966), "Dislocation Movement Through Random Arrays of Obstacles", *Phil. Mag.*, Vol. **13**, pp. 911-924.

[6] Liu, C. T. and Gurland, J., (1968), "The Strengthening Mechanism in Spheroidized Carbon Steels", *Trans. Metall. Soc. AIME*, Vol. **242**, pp. 1535-1542.

[7] Gurland, J. and Plateau, J., (1963), "The Mechanism of Ductile Rupture of Metals Containing Inclusions", *Trans. ASM*, Vol. **56**, pp. 442-456.

[8] Thomson, R. D. and Hancock, J. W., (1984), "Ductile Failure by Void Nucleation, Growth and Coalescence", *Int. J. Frac.*, Vol. **26**, pp. 99-112.

[9] Thompson, A. W., (1987), "Modeling of Local Strains in Ductile Fracture", *Metall. Trans.* A, Vol. **18A**, pp. 1877-1886.

[10] McClintock, F. A., (1968), "A Criteria for Ductile Fracture by the Growth of Holes", *J. Applied Mech.*, Vol. **35**, pp. 363-371.

[11] Rice, J. R. and Tracey, D. M., (1969), "On the Ductile Enlargement of Voids in Triaxial Stress Fields", *J. Mech. Phys. Solids*, Vol. **17**, pp. 201-217.

[12] Brownrigg, A., Spitzig, W. A., Richmond, O., Teirlinck, D. and Embury, J. D., (1983), "The Influence of Hydrostatic Pressure on the Flow Stress and Ductility of a Spheroidized 1045 Steel", *Acta Metall.*, Vol. **31**, No. 8, pp.1141-1150.

[13] Broek,D., (1973), "The Role of Inclusions in Ductile Fracture and Fracture Toughness", *Eng. Frac. Mech.*, Vol. **5**, pp. 55-66.

[14] Park, In-Gyu and Thompson, A. W., (1988), "Ductile Fracture in Spheroidized 1520 Steel", *Acta Metall.*, Vol. **36**, No. 7, pp. 1653-1664.

[15] Fisher, J. R. and Gurland, J., (1981), "Void Nucleation in Spheroidized Carbon Steels", Parts I and II, *Metal Science*, May, 1981, pp. 185-202.

[16] Berg, C. A., (1962), "The Motion of Cracks in Plane Viscous Deformation", *Proceedings of the 4th U.S. National Congress on Applied Mechanics*, Vol. **2**, pp. 885-892.

[17] Budiansky, B., Hutchinson, J. W. and Slutsky, S., (1982), "Void Growth and Collapse in Viscous Solids", In *Mechanics of Solids, The Rodney Hill 60th Anniversary Volume*, edited by H. G. Hopkins and M. J. Sewell, pp. 13-45. Pergamon, Oxford.

[18] Budiansky, B., (1983), "Micromechanics", *Computers & Structures*, Vol. **16**, pp. 3-12.

[19] Thomason, P. F., (1968), "A Theory for Ductile Fracture by Internal Necking of Cavities", *J. Inst. Metals*, Vol. **96**, pp. 360-365.

[20] Blume, J. A., (1988), "The Finite Deformation and Stress Fields Near a Pair of Spherical Cavities in a Nonlinearly Elastic Solids", *Proc. Symposium on Three-dimensional Fracture Processes*, Berkeley, CA, June.

[21] Nemat-Nasser, S. and Iwakuma, T., (1982), "NASA Conference Publication No. 2271, 113.

[22] Nemat-Nasser, S., Iwakuma, T. and Accorsi, M., "Cavity Growth and Grain Boundary Sliding in Polycrystalline Solids", *Mechanics of Materials*, Vol. **5**, pp. 317-329.

[23] Gurson, A. L., (1975), "Plastic Flow and Fracture Behavior of Ductile Materials Incorporating Void Nucleation, Growth and Interaction", Ph.D. Thesis, Brown University.

[24] Gurson, A. L., (1977), "Continuum Theory of Ductile Rupture by Void Nucleation and Growth – I. Yield Criteria and Flow Rules for Porous Ductile Materials, *J. Eng. Mat. Tech.*, Vol. **99**, pp. 2-15.

[25] Tvergaard, V., (1981), "Influence of Voids on Shear Band Instabilities under Plane Strain Conditions", *Int. J. Frac.*, Vol. **17**, pp. 389-407.

[26] Tvergaard, V., (1982), "On Localization in Ductile Materials Containing Spherical Voids", *Int. J. Frac.*, Vol. **18**, pp. 237-252.

[27] Tvergaard, V. and Needleman, A., (1984), "Analysis of the Cup-Cone Fracture in a Round Tensile Bar", *Acta Metallurgica*, Vol. **32**, pp. 157-169.

[28] Nemat-Nasser, S. and Hori, M., (1987), "Void Collapse and Void Growth in Crystalline Solids", *J. Appl. Phys.*, Vol. **62**, pp. 2746-2755.

[29] Hori, M. and Nemat-Nasser, S., (1988), "Mechanics of Void Growth and Void Collapse in Crystals", *Mechanics of Materials*, Vol. **7**, pp. 1-13.

[30] Hori, M. and Nemat-Nasser, S., (1988), "Dynamic Response of Crystalline Solids with Microcavities", *J. Appl. Phys.*, Vol. **64**, pp. 856-863.

[31] Curran, D. R. and Seaman, L., (1987), "Dynamic Failure of Solids", *Physics Reports*, Vol. **147**, Nos. 5 & 6, pp. 255-388.

[32] Meyers, M. A. and Aimone, C. T., (1983), "Dynamic Fracture (Spalling) of Metals", *Progress in Material Science*, Vol. **28**, pp. 1-96.

[33] Asay, J. R. and Kerley, G. I., (1987), "The Response of Materials to Dynamic Loading", *Int. J. Impact Eng.*, Vol. **5**, pp. 69-99.

[34] Rajendran, A. M., (1988), "A Void Growth Based Failure Model to Describe Spallation", *Dynamic Constitutive/Failure Models*, Rajendran, A. M. and Nicholas, T., Eds., Dayton, OH, May, 1988, pp. 111-144.

[35] Eftis, J., Nemes, J. A. and Randles, P. W., (1991), "Viscoplastic Analysis of Plate-Impact Spallation", *Int. J. Plasticity*, Vol. 7, pp. 15-39.

[36] Underwood, E. E., (1970), "Quantitative Stereology", *Addison-Wesley.*

[37] Clifton, R. J. and Klopp, R. W., (1985) "Pressure-Shear Plate Impact Testing", *Metals Handbook*, Vol. 8, Amer. Soc. Metals, Metals Park, 9th ed., pp. 230-239.

[38] Walter, M. and Duffy, J., (1990), Thesis, Brown University, April.

[39] Mello, M. C., Prakash, V. and Clifton, R. J., (1991), "Multi-Point Interferometer for Monitoring Two Dimensional Wave motions", *APS Topical*

Conference on Shock Compression of Condensed Matter, June 17-20, Williamsburg, Va.

[40] Barker, L. M., (1968), "Behavior of Dense Media Under High Dynamic Pressures", Gordon and Breach, NY, p. 483.

[41] Hemsing, W. F., (1979), "Velocity Sensing Interferometer (VISAR) Modification", *Rew. Sci. Instrum.*, Vol. **50**, No. 1, pp. 73-77.

[42] Bouricius, G. M. B. and Clifford, S. F., (1970), "An Optical Interferometer Using Polarization Coding to Obtain Quadrature Phase Components", *Rew. Sci. Instrum.*, Vol. **41**, No. 12, pp. 1800-1803.

[43] Tvergaard, V. and Needleman, A., (1988), "An Analysis of Temperature and Rate Dependence of Charpy V-Notch Energies for a High Nitrogen Steel", *Int. J. Frac.*, Vol. **37**, pp. 197-215.

[44] Needleman, A. and Tvergaard, V., (1990), "An Analysis of Dynamic, Ductile Crack Growth in a Double Edge Cracked Specimen", *To be published in the International J. of Fracture.*

[45] Needleman, A. and Tvergaard, V., (1990), "A Numerical Study of Void Distribution Effects on Dynamic, Ductile Crack Growth", *Eng. Frac. Mech.*, in press.

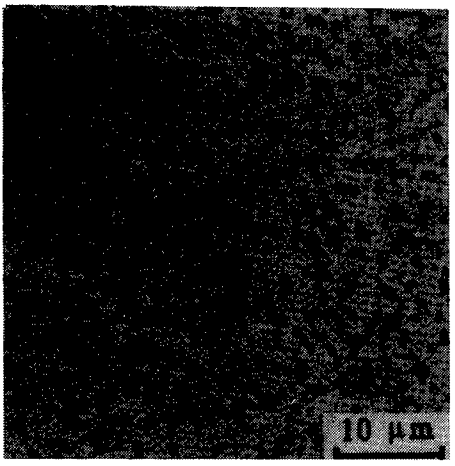

(A), 24 hours

Fig. 1 Microstructure of Spheroidized 1045 Steel

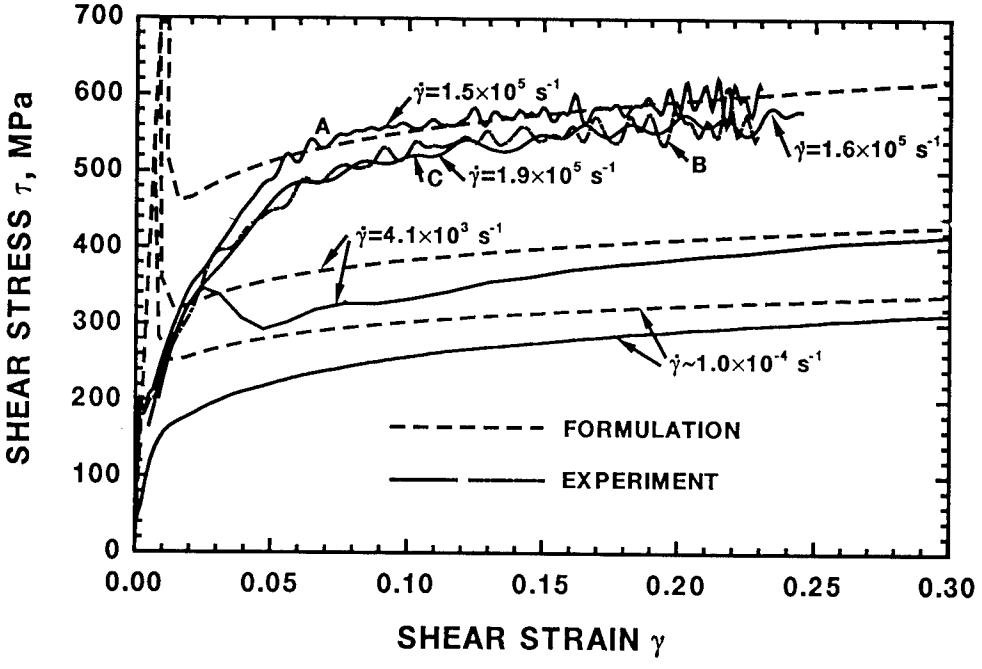

Fig. 2 Stress-Strain Curves of Spheroidized 1045 Steel

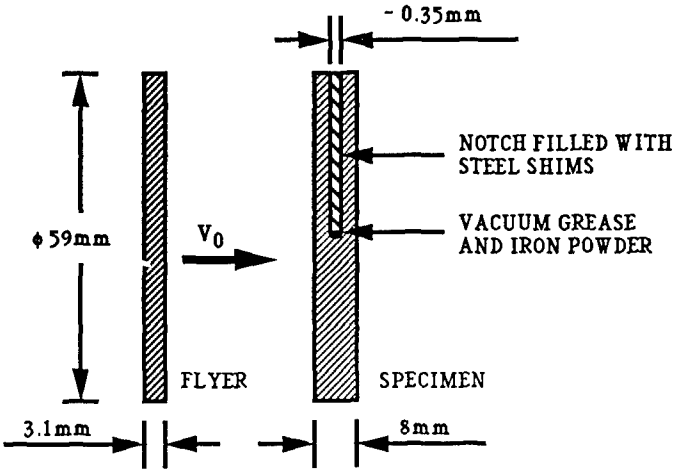

Fig. 3 Configuration of Dynamic Ductile Rupture Experiment

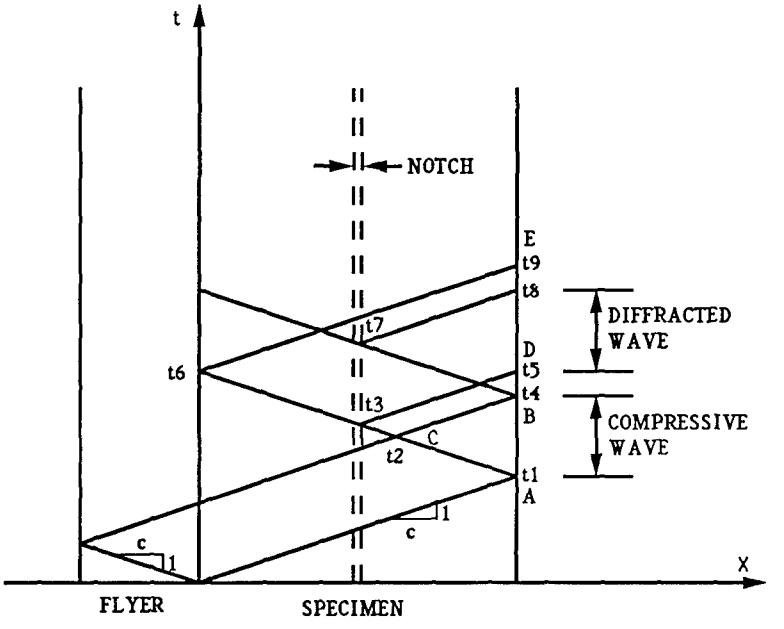

Fig. 4 t–x Diagram for Dynamic Ductile Rupture Experiment of Spheroidized 1045 Steel

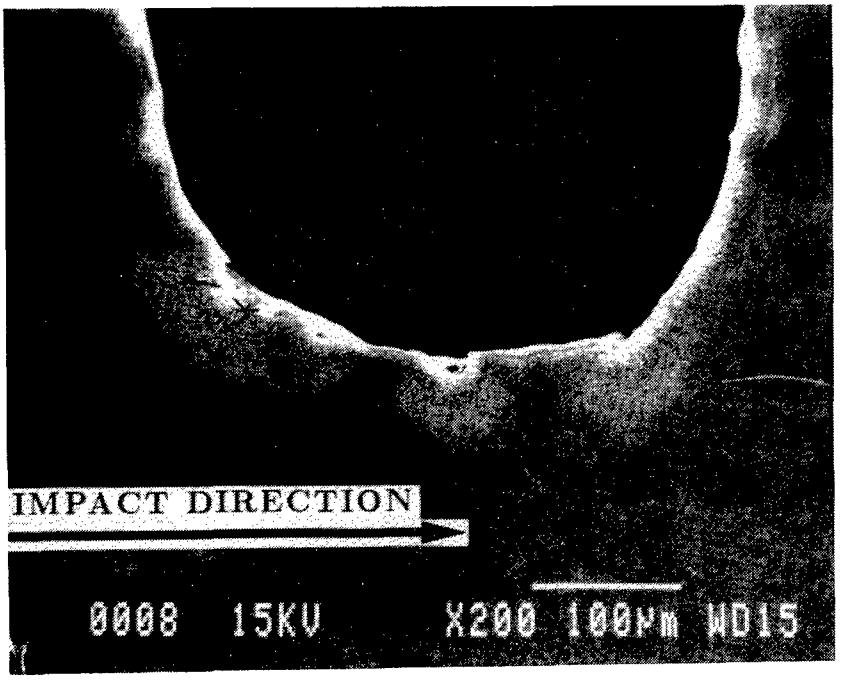

(a) Notch Tip Region

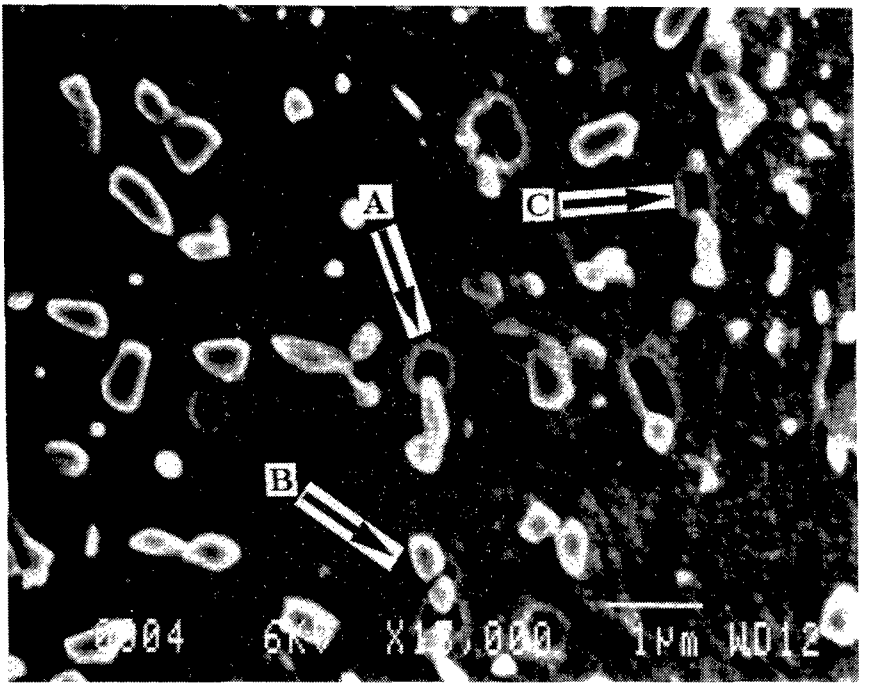

(b) Void Nucleation at the Notch Tip

Fig. 5 Void Nucleation in the Notch tip Region
Shot 9002, Impact Velocity $V_0 = 0.140\ mm/\mu s$

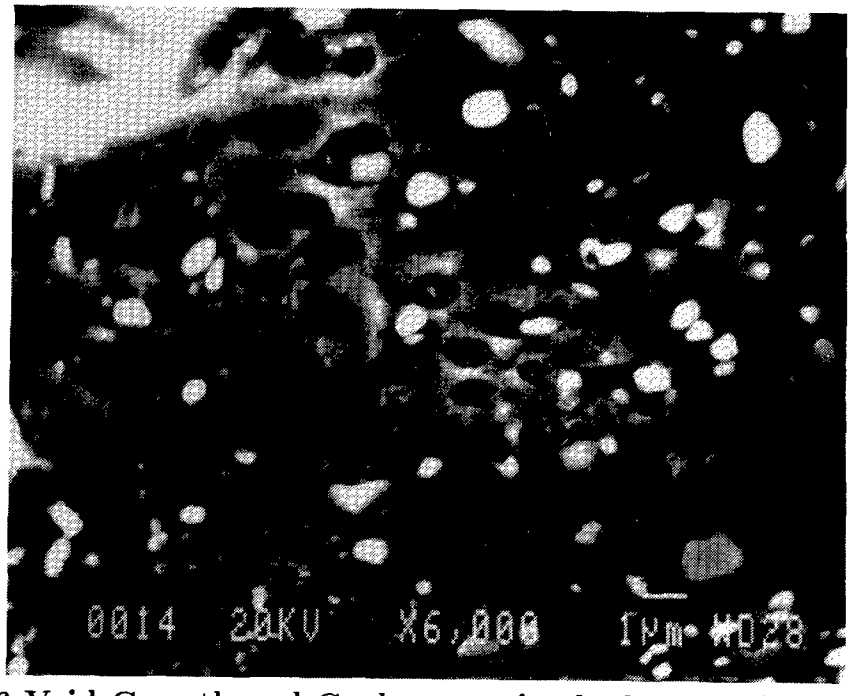

Fig. 6 Void Growth and Coalescence in the Notch Tip Region Shot 9005, Impact Velocity $V_0 = 0.156\ mm/\mu s$

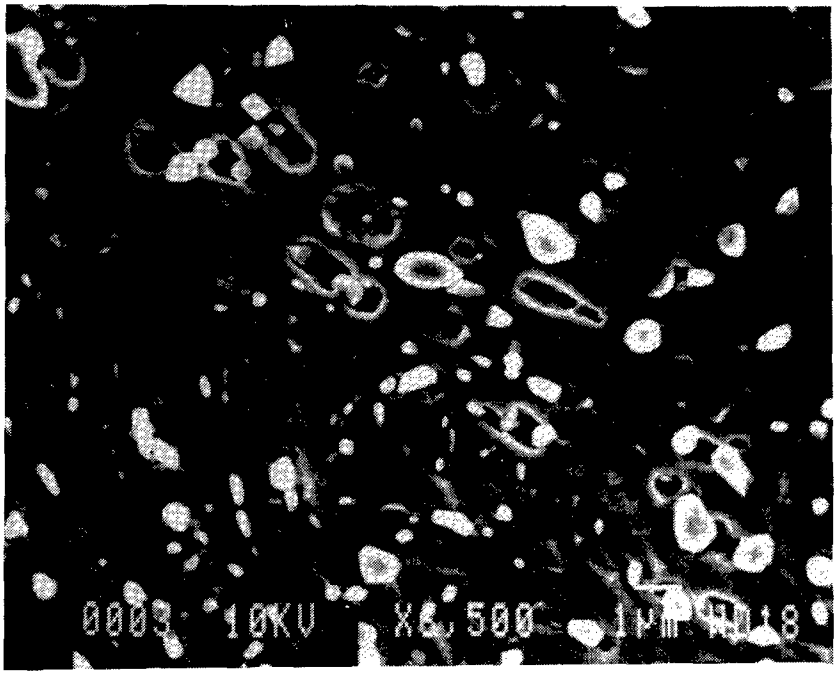

Fig. 7 A Void Band at the Notch Tip, (Shot 9005)

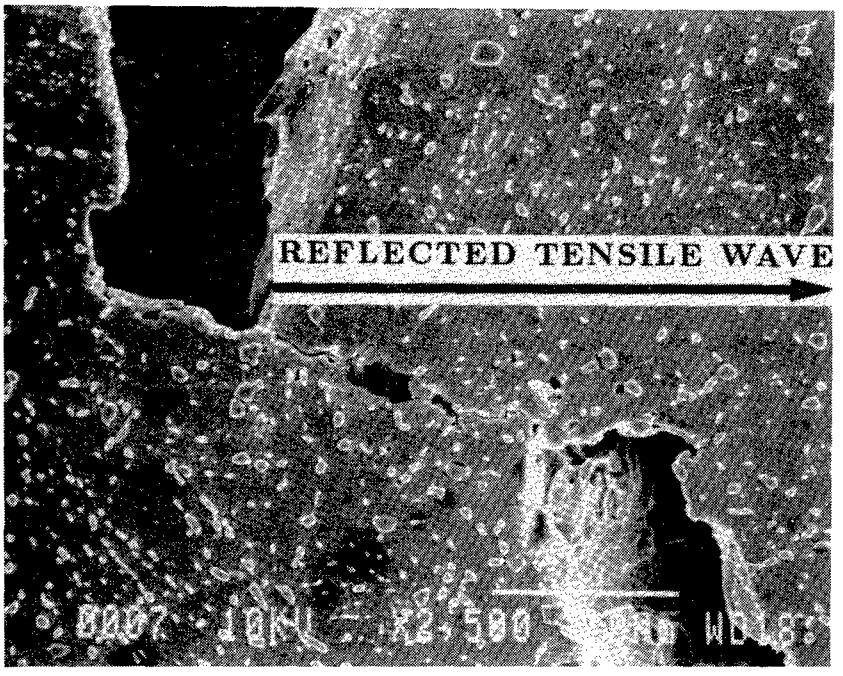

Fig. 8 Linkage of Cleavage Fracture Segments through Lateral Shear, (Shot 9005)

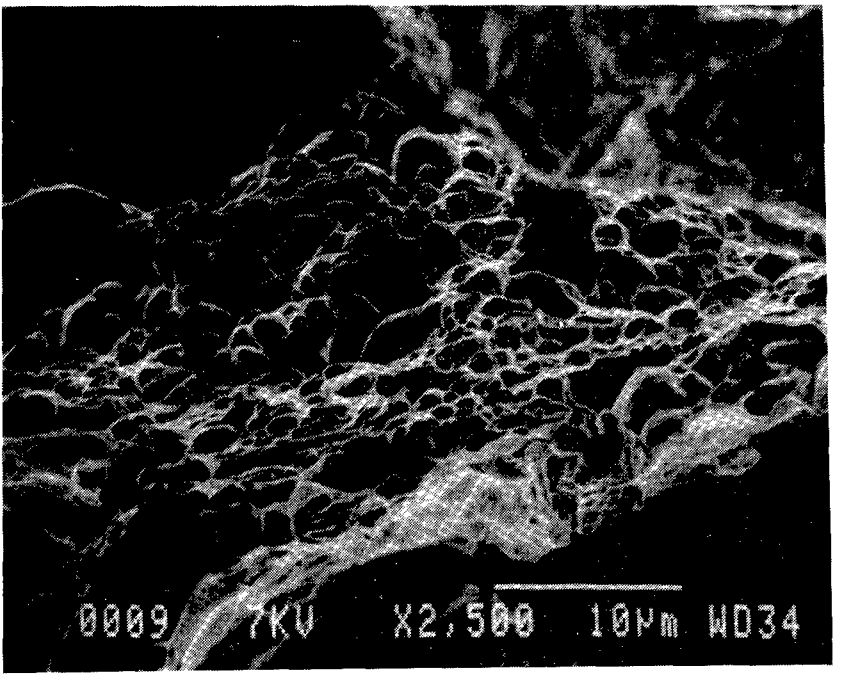

Fig. 9 Void Sheet at a Grain boundary between Cleaved Ferrite Grains (Shot 9006, $V_0 = 0.155\ mm/\mu s$)

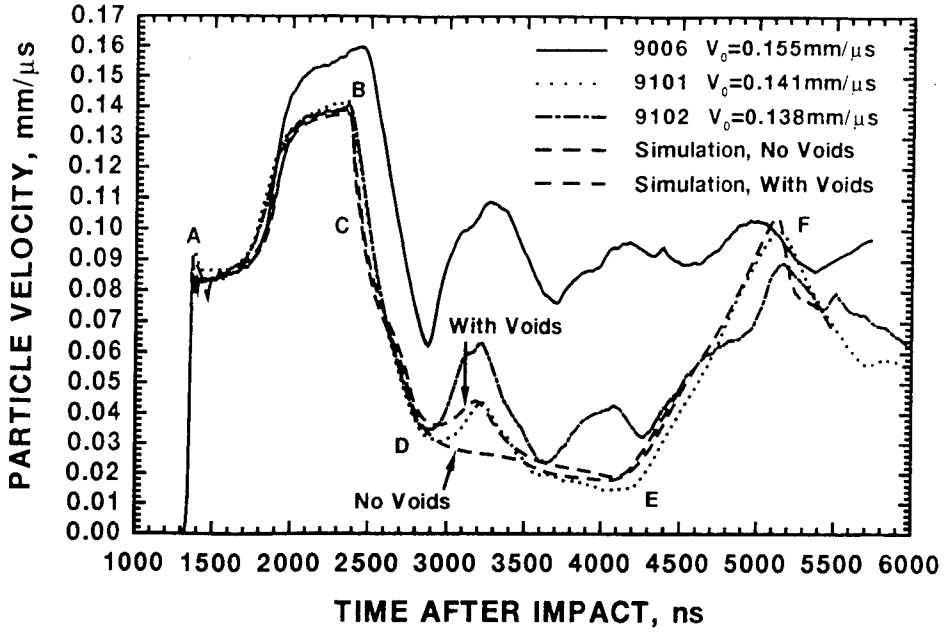

Fig. 10 Free Surface Velocity Profiles for Un-notched Specimen (Experiments and Calculations)

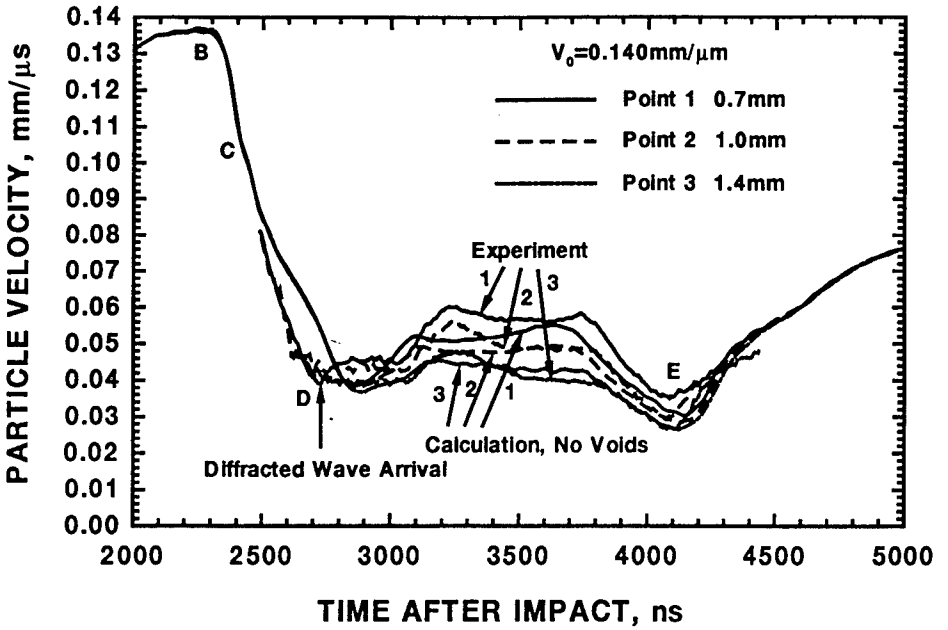

Fig. 11 Free Surface Velocity Profiles for Notched Specimen (Experiment (9002) and Calculation without Voids)

Plastically Induced Surface Roughness: Phenomena and Mechanism

Y.Z. Dai *
Brown and Sharpe Co., North Kingstown, RI 02852

F.P. Chiang
SUNY at Stony Brook, Stony Brook, NY 11794

Abstract

The surface roughness of a metallic material varies as a function of the plastic deformation it has experienced. Investigations on plastically induced surface roughness in literature are incomplete because the roughness parameter used can not define the surface roughness completely. Furthermore the mechanism of plastically induced surface roughness is, to a large extent, unknown. The purpose of this work is therefore twofold: First, a clearer picture of the phenomena is provided through a more detailed description of surface roughness and its relation to material property, stress mode, and strain path. Second, the mechanism of the plastically induced surface roughness is experimentally studied on both macroscopic and microscopic scales.

Introduction

Studies on the roughening of free surfaces of metallic materials due to plastic deformation have been reported.[1-8] These studies discussed the influence of stress mode,[1,2,4,5,8] grain size,[1,2,7] material property,[4,5,8] temperature,[7] strain rate,[7] and hydrastatic pressure[7] on the characteristics of surface roughness. Models relating surface roughness and some of the factors mentioned above have been propose.[1,3,6,9] Despite differences in test conditions such as the initial surface roughness, some conclusions have been

*Formerly a graduate student at SUNY, Stony Brook.

drawn. For room temperature tests, the major conclusion is that the vertical roughness of the surface increases linearly to the magnitude of plastic deformation and to the average grain size of the test specimen, but it is independent of stress mode, hydrastatic pressure, strain rate, and material property.

This conclusion was made based on some experimental observations and the resulting empirical relations. No investigations, to the authors' knowledge, have been devoted to the mechanism of surface roughness induced by plastic deformation. Besides, almost all the studies only discussed the surface vertical characteristics. Thus the behavior of surface horizontal characteristics during plastic deformation is, to a large extent, still unknown.

This work is designed to investigate the surface roughness response to plastic deformation of different materials and to study its mechanism by using coarse grained specimens such that the deformation of each individual grain due to plastic deformation may be revealed and characterized. It is hoped that this approach will provide an explanation to the roughening mechanism induced by plastic deformation.

Roughening Phenomena

Plastic deformation roughens free surfaces of metallic material by producing, among other things, slip bands within grains, and relative rotation and sliding among grains as shown in Fig.1. A rough surface may be completely described by two parameters: one vertical(root-mean-square roughness σ) and the other horizontal(correlation length T). These parameters may be approximately evaluated by using the profiles measured by a mechanical profilometer such as that shown in Fig.2. (A measured actual surface profile is shown in Fig.6a.) For a surface profile represented by discrete values $h(i)$ measured by such a system, these two parameters are defined as

$$\sigma = \sqrt{\frac{1}{N}\sum_{i=1}^{N} h^2(i)} \tag{1}$$

and

$$\frac{\sum_{i=1}^{N-T} h(i) \times h(i+T)}{\sum_{i=1}^{N} h^2(i)} = \frac{1}{e} \tag{2}$$

where N is the number of sampling points, and e is equal to 2.718.

Surface roughness response to plastic deformation was studied on four different materials, namely: copper, aluminum, stainless steel, and hot-rolled steel. The specimens were cut along the rolling direction into a 'dog-bone' shape with dimensions of $2.15mm$ thick, $20.00mm$ wide and $125mm$ long. The surfaces of the specimens were then polished by a cloth buffer wheel and aluminum powder to an initial surface finish of $\sigma < 0.05\mu m$. Specimens were loaded on a universal testing machine to plastic deformation at incremental steps. At each step, the specimens were unloaded for surface roughness measurements. Surface roughness was measured using a system as schematically shown in Fig.2 with a stylus having a tip radius of 5 μm. The plastic deformation was evaluated in terms of true strain which is defined as

$$\epsilon_t = \ln(l/l_o) \tag{3}$$

where ϵ_t is the true plastic strain; l_o and l are the specimen gage length before and after plastic deformation, respectively.

Figure 3 shows the experimental results of both the vertical and the horizontal surface roughnesses values versus true strain ϵ_t for the four materials. As a first approximation the vertical roughness σ is seen to increase linearly to true plastic strain (Fig.3a); and the horizontal parameter, the correlation length T decreases with the increasement of tue strain(Fig.3b). These relations may be characterized by simple mathematical models as following

$$\sigma = a\epsilon_t + b \tag{4}$$

and

$$T = \frac{c}{\epsilon_t + d} + e \tag{5}$$

where a, b, c, d and e are constants.

As shown in Fig.3 the surface vertical roughness seems to be independent of material property(Fig.3a); whereas the surface horizontal roughness seems to be dependent of material property(Fig.3b).

The influence of stress mode in terms of the ratio of principal stresses, which varied from -0.577 to -3.732 in a study, was investigated previously using specimens made of copper alloy in a disk shape as shown in Fig.4. Experimental results[8] suggest that the surface roughness is independent of stress mode.

The strain path effect on surface roughness was also investigated using the set-up as schematically shown in Fig.4. Different strain paths in terms of principal strain ratio, which varied from -3.1 to 0.233 in the present work, were obtained by loading the specimen through different angle α. Figure 5 shows some of the strain paths achieved in the test, some of which were achieved by a one-step, while the others by a two-step loading to the final effective strain of 2.3%. Observations made on copper alloy material show that surface roughness is dependent on strain path. However, if no reverse yielding occurs, the process is virtually independent of strain path. (A strain path with reverse yielding is shown in the Fig.5 for $\alpha = 115^{\circ} \rightarrow -15^{\circ}$).

A Model for Roughening Mechanism

The surface roughening mechanism induced by plastic deformation was experimentally investigated using aluminum specimens with a grain size of 1.4 millimeters. Microscopically, the fundamental cause to surface rougheness is due to dislocation movement. Macroscopically, the process manifests itself in a number of ways: First, more and more slip bands come into being within each individual grain. Second, grains rotate with respect to each other and the resulting out-of-plane component of the relative rotation contributes to surface roughness. Third, neighboring grains may slide relatively to each other forming steps at the grain boundaries as can be seen in Fig.6a. Some other mechanisms, such as the bending of a single grain (section A-B in Fig.6a) and the rotation of multi-grains (section C-D in Fig.6a), may also come into play.

In order to provide an understanding to the roughening phenomenon, it is necessary that the dominant mechanism be isolated among the less significant factors. It was done by decomposing a measured profile into low and high spatial frequency components, and then comparing the surface roughness calculated for each component with that of the original profile. An example showing the decomposed low frequency component(Fig.6b), and the high frequency component(Fig.6c) is also given in Fig.6. Experimental evidence suggests that both the horizontal and vertical surface roughness phenomena σ, T for the low frequency component are almost the same as that for the actual measured profile . Thus we may conclude that the low frequency component is the dominant factor.

Specimens with grain sizes of the order of millimeter were used to study the plastically induced relative grain rotation. The grain boundaries in

each specimen's surface was marked and the specimen was then polished to almost mirror finish. The relative grain rotation was measured by using a set-up which consists of a laser, a partial mirror, a translation stage and an observation screen as schematically shown in Fig.7. The laser beam was directed to a grain on the specimen surface and the specular reflection point was marked on the observation plane. The specimen was then translated such that the neighboring grain was now under illumination and the specular reflection point from this grain was then determined. The relative angle between the two grains was determined by the distance between the two marks and the distance between the observation plane and the specimen. The relative grain rotating angle at each plastic deformation level was the average of rotating angles from ten pairs of grains. Figure 8 shows the average grain rotation θ versus true plastic strain for specimens with four different grain sizes. They all appear to increase linearly with plastic strain.

Based on the experimental evidence mentioned above, a tentative explanation to the plastically induced roughening may be given as follows. For $0 < \epsilon_t < 3.5\%$: At the begining the surface polishing process has rendered all the grains on a specimen surface to be approximately on a plane. As a result, the initial *rms* roughness σ is small and the correlation length T is large. As the plastic deformation increases, slip bands come into being and grains begin to rotate with respect to each other. Because plastic deformation is small, some grains tend to be bonded together to rotate as a group with respect to the other grains or grain groups. With the progression of plastic deformation less and less grains remain bonded resulting in the correlation length T becoming smaller and smaller. The combined effect of change in correlation length and grain rotation results in a increase of σ when ϵ_t is increased.

For $3.5\% < \epsilon_t < 18\%$: At this stage, almost all the grains have been involved in the relative rotation with their neighboring grains. This results in a slower generation rate of new low frequency profile components rendering the correlation length T being saturated. The relative grain rotation still increases linearly with respect to plastic stain making the surface vertical roughness σ increase approximately linearly with plastic strain.

Conclusion

Based on the evidence we have gathered for the material studied we may conclude that: 1. surface vertical roughness increases linearly with respect to plastic strain; that 2. surface horizontal correlation length de-

creases with respect to plastic strain; that 3. surface vertical roughness is independent of material property, stress mode, but dependent on strain path; that 4. surface horizontal correlation length is dependent of material property; that 5. plastic deformation roughens surface by introducing slip bands within grains and relative rotation and sliding between grains; that 6. the low frequency component of a surface profile contributes dominantly to surface roughness parameters σ and T; that 7. the horizontal surface roughness parameter in terms of correlation length is proportional to a material's average grain size and it becomes saturated at a certain plastic deformation; that 8. relative rotation between grains increases linearly to the amount of plastic deformation; and that 9. surface vertical *rms* roughness is mainly due to grain rotation.

Acknowledgment

We would like to thank the Army Research Office, Engineering Science Division for financial support through contract No.DAA03-88-K-0033.

References

[1] Osakada, K., Oyane, M. (1971), On the roughening of free surface in deformation process, *Bulletin of the JSME* **14**, p.171-177.

[2] Fukuda, M., Yamaguchi, K., Takakura, N., Sakano, Y. (1974), Roughening phenomenon on free surface of products in sheet metal forming, *J. Jap. Soc. Technol. Plast.*, **15**, p.994-1002.

[3] Parmar, A., Mellor, P.B. (1977), A new model for the prediction of instability and limit strains in thin sheet metal, *Int. J. Mech. Sci.*, **19**, p.389-398.

[4] Thomson, P.F., Nayak, P.U. (1980), The effect of plastic deformation on the roughening of free surfaces of sheet metal, *Int. J. of Mach. Tool Des. Res.*, **20**, p.73-86.

[5] Thomson, P.F., Shafer, B.V. (1982), The roughening of free surface during plastic working, *Int. J. of Mach. Tool Des. Res.*, **22**, p.261-264.

[6] Dautzenberg, J.H., Kals, J.A.G. (1984), Stress state and surface roughness, *Adv. Technol. of Plasticity*, **1**, p.186-191.

[7] Azushima, A., Miyagawa, M. (1986), Effect of working factors and metallurgical factors on roughening phenomenon on free surface of sheets, *J. of the Jap. Soc. for Technol. of Plasticity*, **27**, p.1261-1267.

[8] Chiang, F.P., Dai, Y.Z., Xu, B.Q., Kato, A. (1990), Study of surface roughening under different stress modes by correlation, in: *Hologram Interferometry and Speckle Metrology*, p.36-42, Baltimore.

[9] Dai, Y.Z., Chiang, F.P. (1990), Application of scattering theory to plastic strain estimation, in: *The 4th Int. Sympo. on Nondestructive Characterization of Materials*, Annapolis.

[10] Bennett, J.M., Mattsson, L. (1989), *Introduction to Surface Roughness and Ccattering*, Optical Society of America, Washington D.C.

[11] Dieter, G.E. (1968), *Mechanical Metallurgy*, Mc-Graw-Hill, New York.

[12] Li, X.M., Chiang, F.P. (1990), High temperature creep crack growth in coarse-grained aluminum, in: *ASME 1990 Winter Annual Meeting*, Dalas

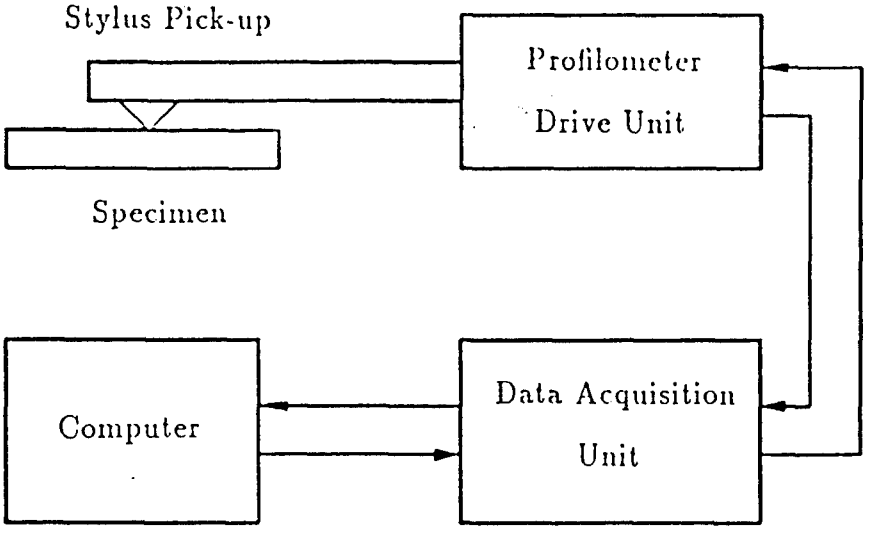

Figure 2 Set-up for surface roughness study

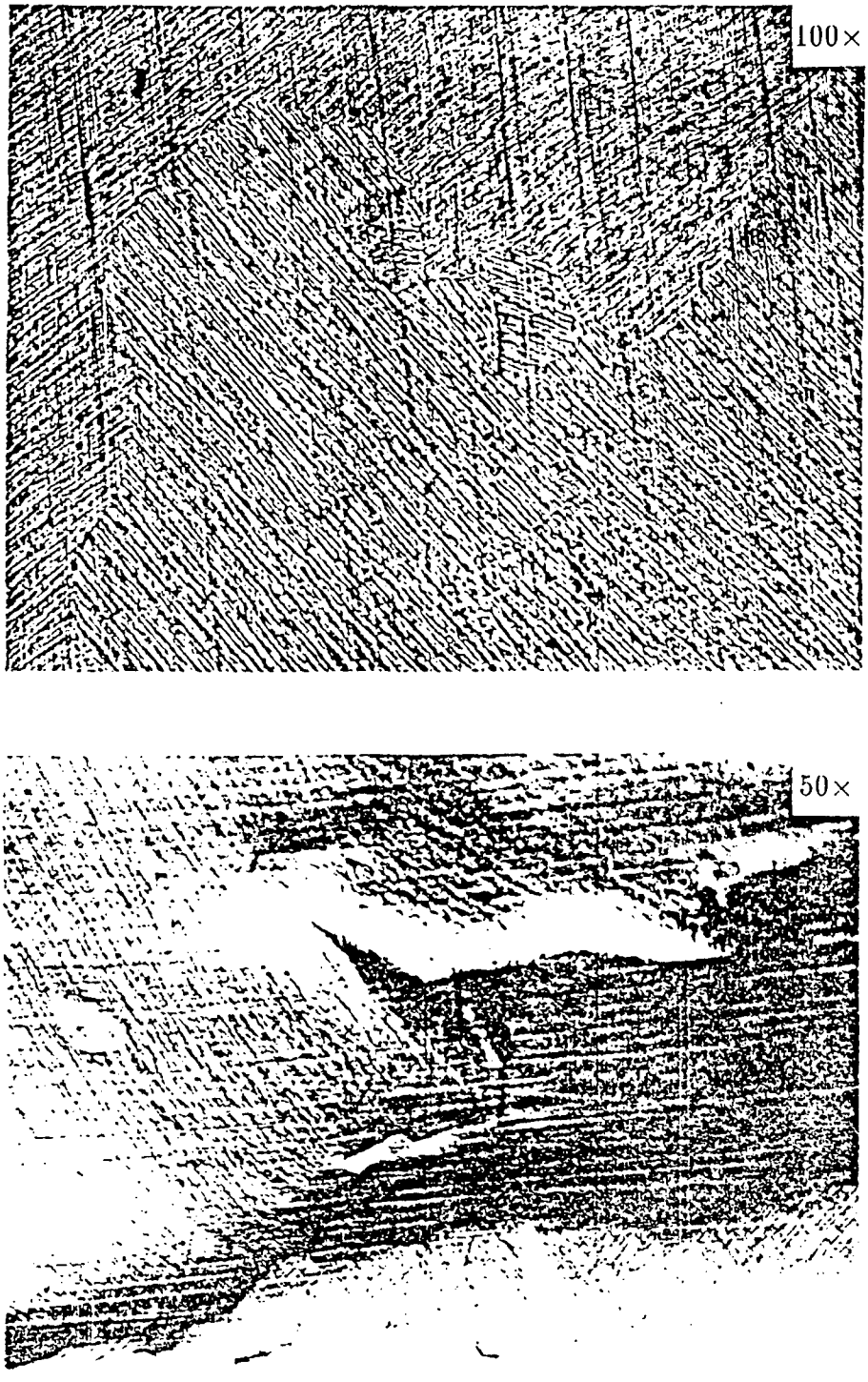

Figure 1 Plastically roughened surfaces revealing (a) slip bands within individual grains (b) grain rotation, grain boundary sliding among grains

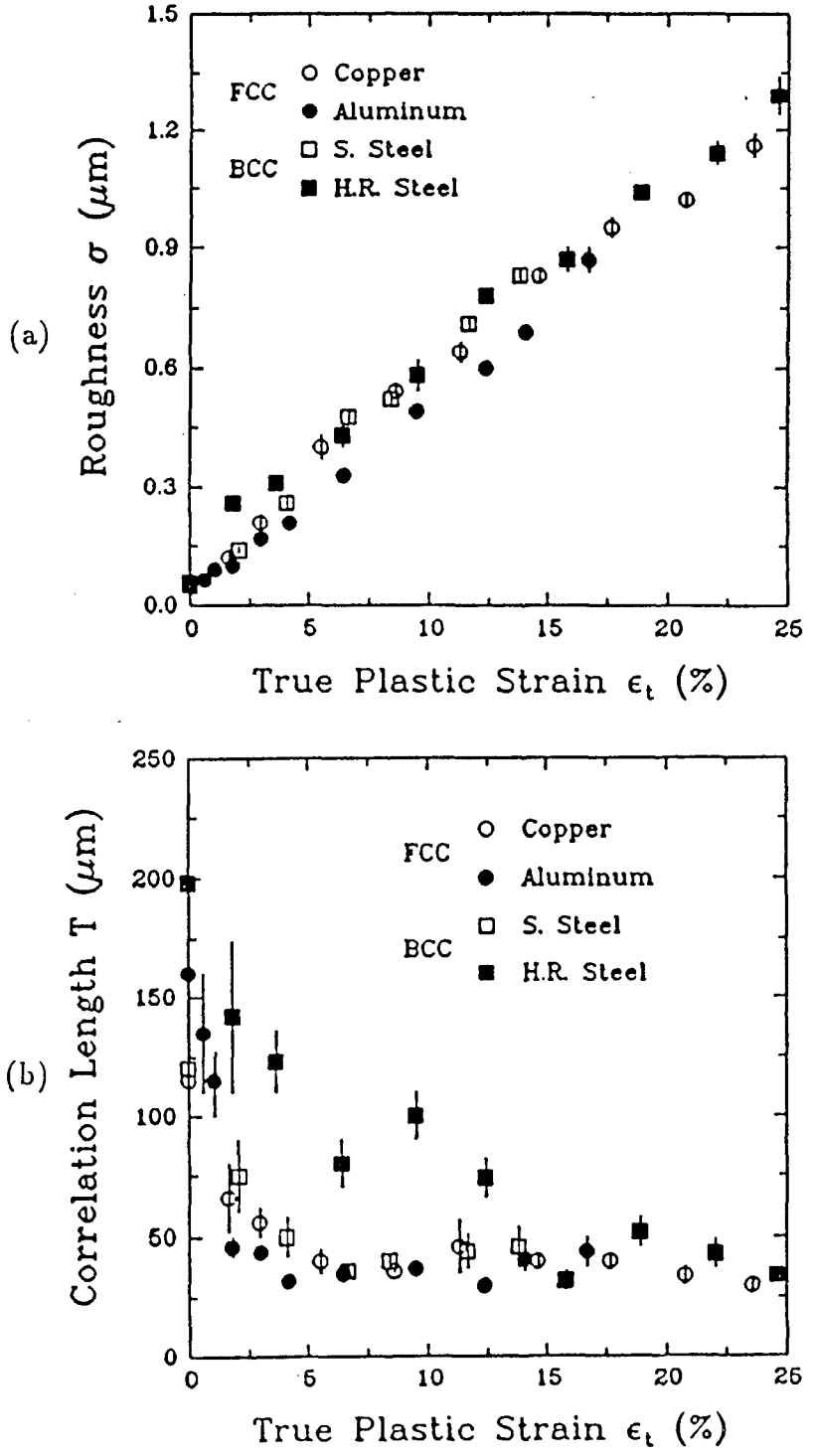

Figure 3 Relation between surface roughness and plastic strain

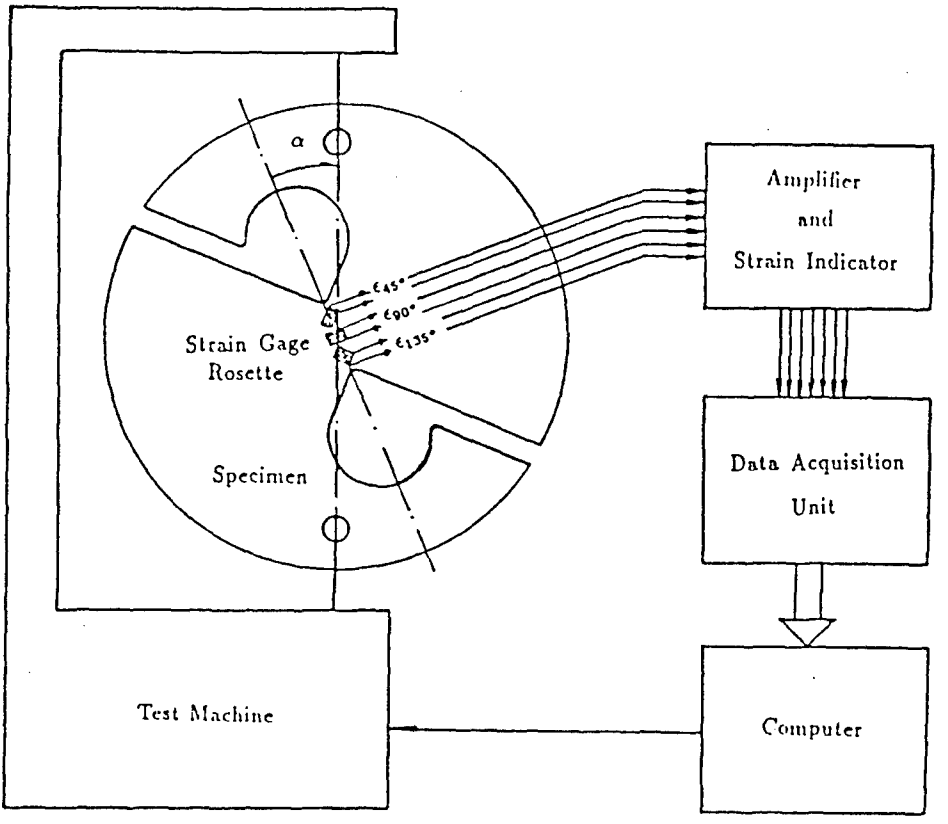

Figure 4 Schematic set-up for strain path effect study

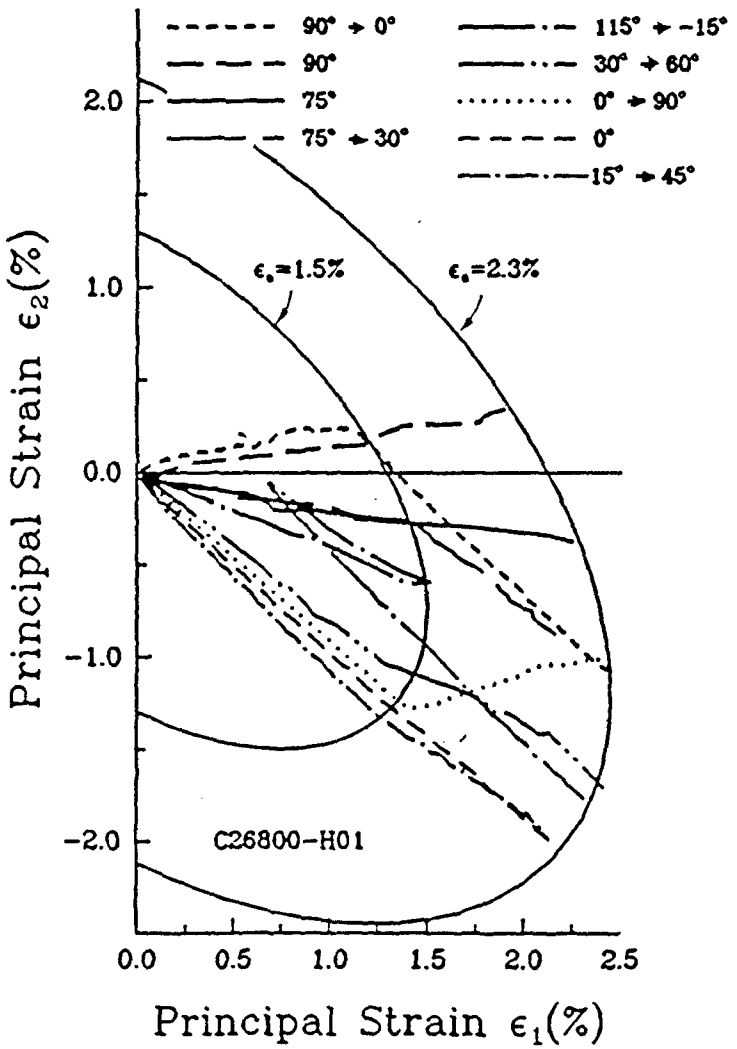

Figure 5 Stain path effect on surface roughness

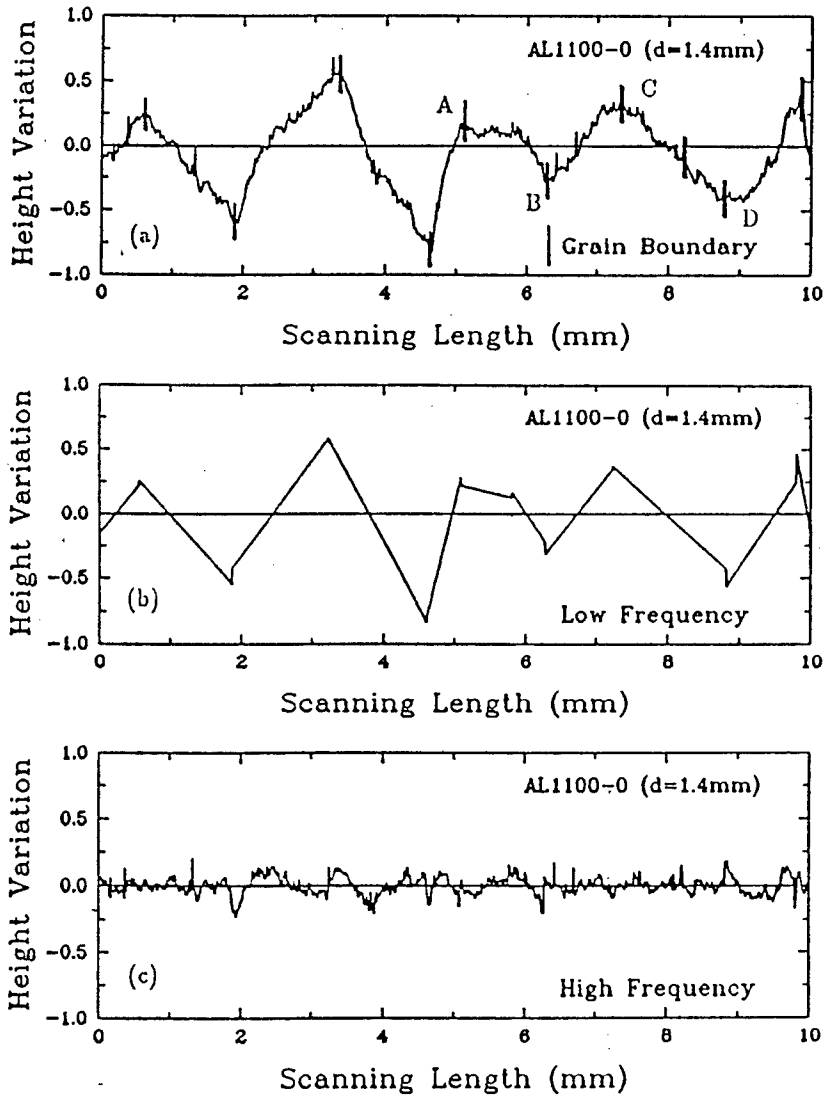

Figure 6 Decomposition of a profile (a) measured surface profile (b) low frequency component (c) high frequency component

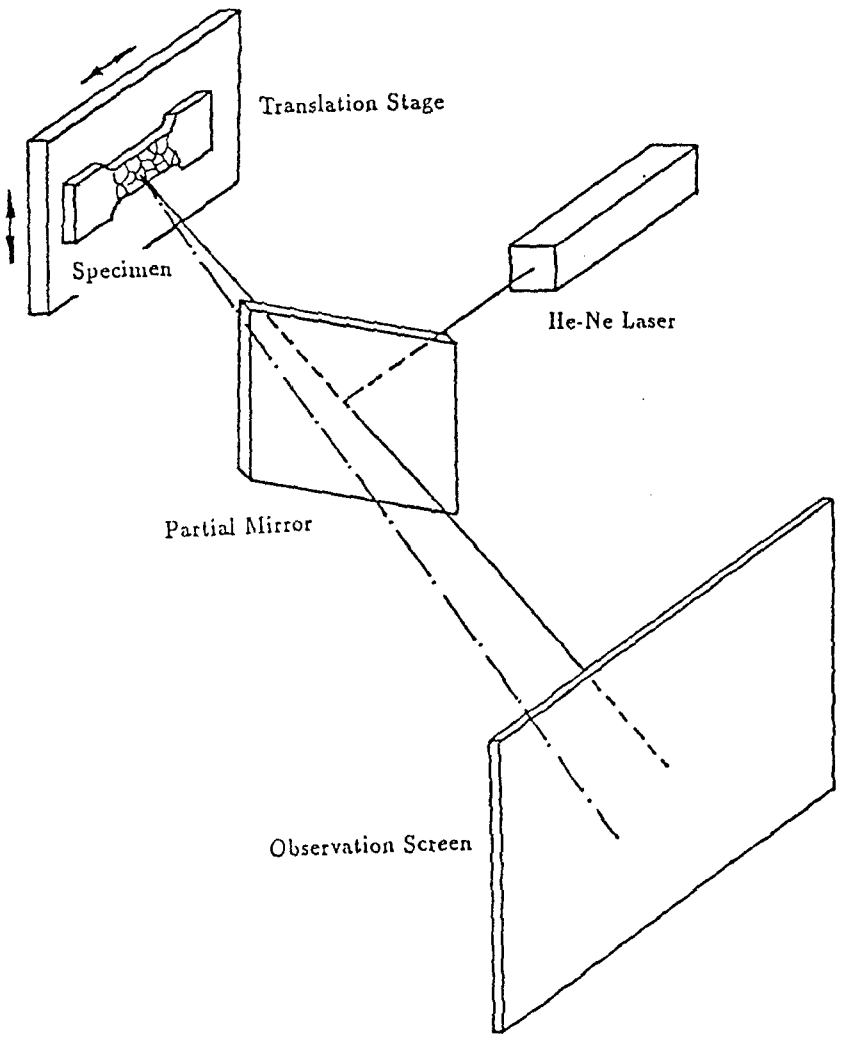

Figure 7 Set-up for relative grain rotation measurement

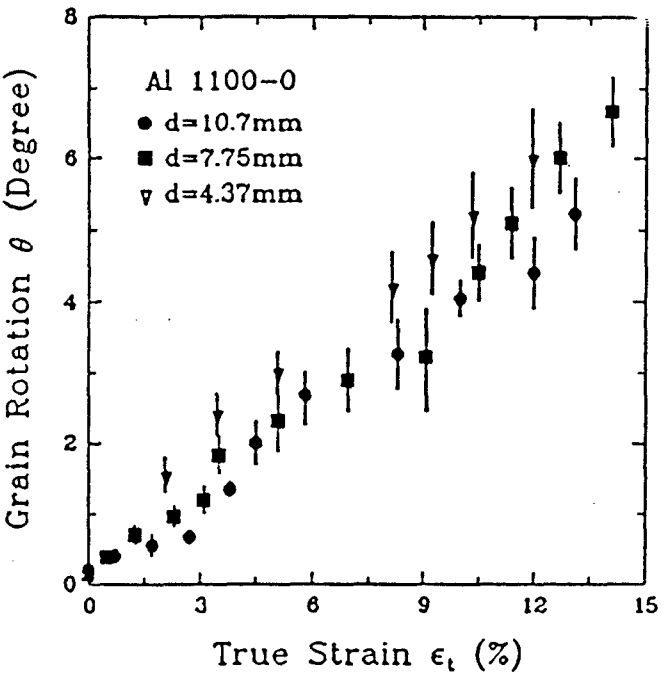

Figure 8 Relation between the relative grain rotation and plastic deformation

ELASTO-PLASTIC FINITE ELEMENT ANALYSIS OF 2-D ROLLING PLUS SLIDING CONTACT WITH TEMPERATURE DEPENDENT BEARING STEEL MATERIAL PROPERTIES

Vikas Gupta
Pedro Bastias
George T. Hahn
Carol A. Rubin

Center for Materials Tribology, Vanderbilt University
Nashville, TN 37235

INTRODUCTION

Poorly lubricated bearings exposed to rolling and sliding contact are subjected to localized frictional heating caused by relative slip between the two sliding surfaces. This heating leads to a rise in temperature, thermal stresses and changes in the elastic, plastic strength and thermo-physical properties of the material. The changes in the properties, in turn, alter the stress state, the displacement field and the temperature rise itself. Thus the problem of rolling-sliding contact is a coupled one and extremely difficult to be studied analytically. To effectively design components such as the roller bearings there is a need for realistic characterization of the deformations, plastic strain distributions and residual stresses in the material.

A large amount of literature in this area deals with theoretical treatments and is mostly confined to the elastic case. The mechanics of elasto-plastic contact with friction, but in the absence of heating, have been examined [12,13]. A bulk of the existing literature deals with surface limited analyses [2,3, 10] and the contact of rough surfaces, such as flash temperatures [7,8,14], the transient temperatures and thermal deformations due to frictional heating and asperity contact [1,17]. Newman [18] developed an elasto-plastic finite element model to study the stress fields in welded plates. Muro et al. [16] have studied the residual stresses in roller bearings by X-ray measurements. Kulkarni et al. have put forward a finite element model incorporating the effects of frictional heating for elastic-perfectly plastic material behavior. But it has been shown that material behavior in repeated rolling contacts is not perfectly plastic but comes close to elastic-linear-kinematic-hardening-plastic (ELKP) behavior.

This paper extends the coupled mechanical and thermal loading

finite element analysis of line contact, carried out by Kulkarni, to a kinematically hardening material with temperature dependent strength properties.

ANALYTICAL PROCEDURE

The 2-D finite element mesh employed in the present study consists of 285 elements and 919 nodes (see Fig. 1). Eight noded isoparametric plane strain elements, which are biquadratic in displacement and linear in temperature are used. The mesh is 24w long (in the circumferential or x-direction) and 12w deep (in the radial or y-direction), where w is the half contact width. The z- direction (out of plane) is the axial direction. The

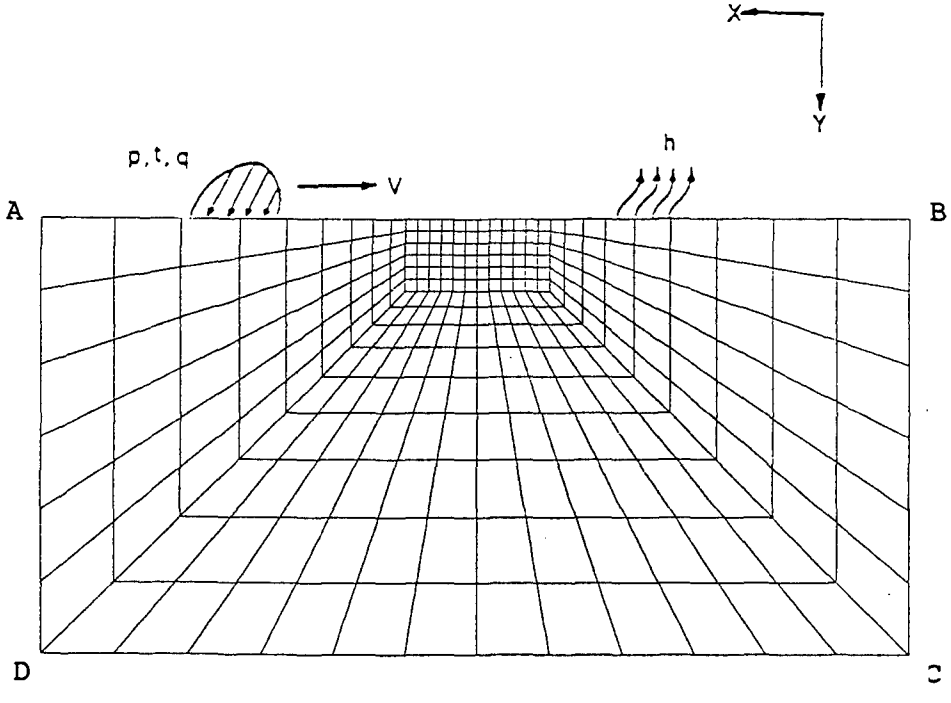

Figure 1. Finite element mesh used for the 2-dimensional calculations accounting for rolling-plus-sliding with frictional heat generation and temperature dependent material properties.

mesh generation and analysis has been carried out using the finite element code 'ABAQUS'.

To simulate frictional rolling contact a thermo-mechanical load is repeatedly translated across the free surface, AB (see Fig. 1). The mechanical loading is a combination of a normal Hertzian pressure distribution, p, a tangential surface component, t and thermal load, q, given by,

$$p = p_o[1- (x^2/w^2)]^{1/2}$$

$$t = \mu p_o[1- (x^2/w^2)]^{1/2}$$

$$q = 0.5p_oV\mu[1- (x^2/w^2)]^{1/2}$$

Where V is the sliding velocity, μ is the coefficient of friction, p_0 is the peak normal pressure and x is the coordinate measured from the center of the pressure distribution. The temperature dependent strength and thermo-physical properties namely, elastic modulus, E, kinematic yield strength, σ_k, Plastic modulus, M, coefficient of thermal expansion, α, thermal conductivity, K and specific heat C_p are listed in Table 1 [9,11,19]. Side AB loses heat by convection. The film coefficient h is selected to be 150 W/m^2°C. The present calculations have been performed for p_0/k_k=

Table 1. Temperature dependence of strength and thermo-physical properties.

Temp (°C)	E (GPa)	σ_k (GPa)	M (GPa)	α x10^6/°C	K W/m	C_p KJ/Kg°K
0.0	207.0	1.05	188.0	13.05	20.0	450.0
25.0	205.0	1.01	185.0	13.89	21.6	458.0
93.3	201.0	0.96	180.3	14.22	22.1	626.0
204.4	196.0	0.91	175.3	15.30	22.9	640.0
315.6	190.0	0.77	169.4	16.20	23.4	690.0
426.7	183.3	0.75	162.9	16.83	24.0	745.0
537.8	170.4	0.53	150.7	17.46	24.8	798.0

5.0 ($k_k = \sigma_k/\sqrt{3}$) and half contact width w = 0.5 mm (assumed constant with temperature).

The non-surface boundaries are displaced elastically to make the mesh behave as a semi-infinite half space. The normal load is applied as an elliptical pressure distribution whereas the traction load is applied as concentrated consistent nodal forces. The applied Hertzian pressure distribution and the traction loads are discretized into several concentrated forces. Elastic displacements due to each of these forces are calculated at the non-surface boundary nodes using closed form solutions and superposed. For the bottom surface DC, both the X and Y displacements are prescribed, while for sides AD and BC only X displacements are prescribed.

It is seen that thermal gradients are insignificant below a depth of 2w and hence the temperatures at the bottom surface of the mesh are set equal to the ambient value. For the sides AD and BC the temperatures are not fixed but thermal gradients are set equal to zero.

The heat fraction generated due to inelastic strains has not been accounted for. However, this should not create any significant error because the amount of cyclic plasticity for ELKP materials has been found to be very small. Also Kumar et al. (1988) have calculated the total plastic energy dissipated during rolling sliding ($p_0/k=6$, $\mu=0.2$) for 52100 steel using finite element calculations and have estimated a 0.6°C rise in temperature per contact, which is insignificant considering the 100°C rise in temperature per pass for this study.

Three different cases have been studied:

1. Rolling and Sliding without any heat effects. Normal pressure p and traction t are applied.
2. Rolling, sliding and frictional heat generation with temperature independent material and thermo-physical properties. Thermal flux q, along with mechanical loads p and t, is applied.
3. Rolling, Sliding and frictional heat generation with temperature dependent material and thermo-physical properties. Mechanical loads p and t and thermal flux q are applied.

In each case two passes were made. The loads are translated from one end of the mesh to the other to complete one pass. The same properties are used for cases one and two; these are the same as the initial properties (at 0°C) in case three. The three cases are compared to study the effects of frictional heating and temperature dependent properties.

RESULTS

Figures. 2 and 3 show the normalized circumferential and axial residual stresses (after unloading followed by cooling to ambient temperature) as a function of normalized depth, y/w. For cases 2 and 3, both the circumferential and axial residual stresses are tensile to a depth of about 0.5w and compressive after that. For case 1, circumferential residual stresses are slightly tensile near the surface, but axial residual stresses are compressive throughout. For all the three cases, the residual stresses are not very different below a depth of 1.5w. Figures. 4, 5 and 6 illustrate the magnitude of cyclic plasticity during pass 2 for the three cases. These show the variation of the equivalent plastic strain amplitude, $\Delta\epsilon^p_{eq}/2$, shear plastic strain range, $\Delta\gamma^p_{xy}$ and the radial plastic strain range, $\Delta\epsilon^p_{yy}$ respectively. The location of peak plastic activity shifts from a depth of 0.7 y/w in case 1 to 0.3 y/w in cases 2 and 3. Fig. 7 shows the residual equivalent plastic strains for the three cases.

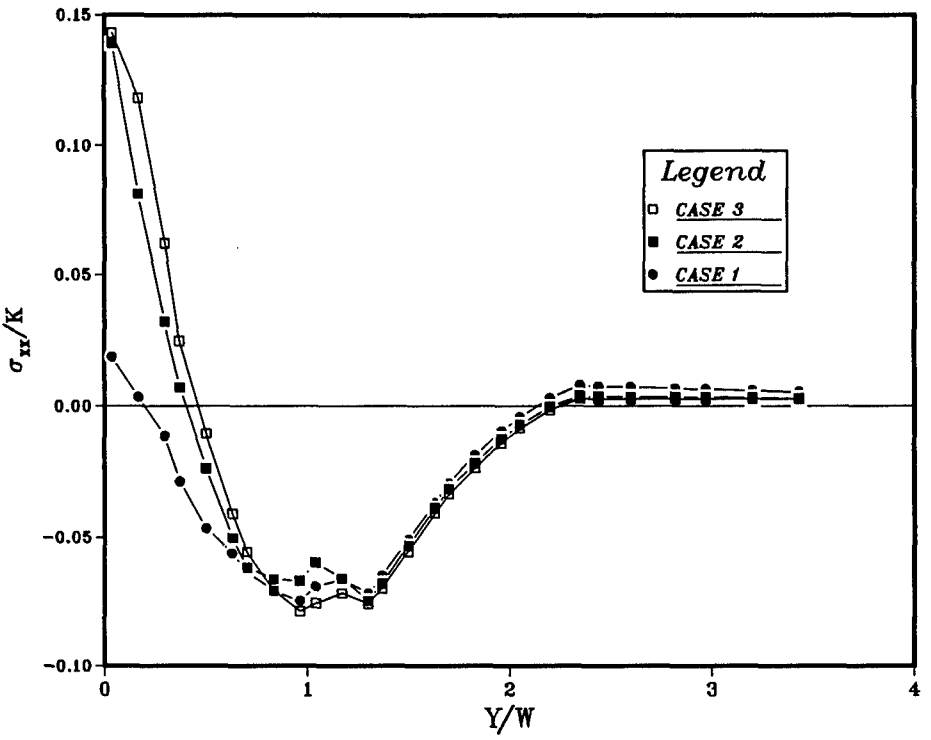

Figure 2. Normalized circumferential residual stresses as a function of normalized depth, y/w, for the three cases.

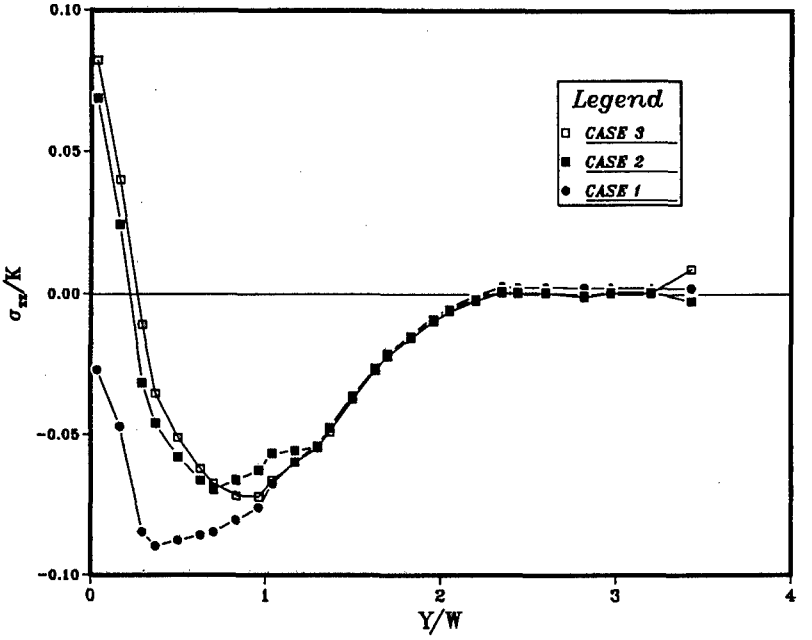

Figure 3. Normalized axial residual stresses as a function of normalized depth.

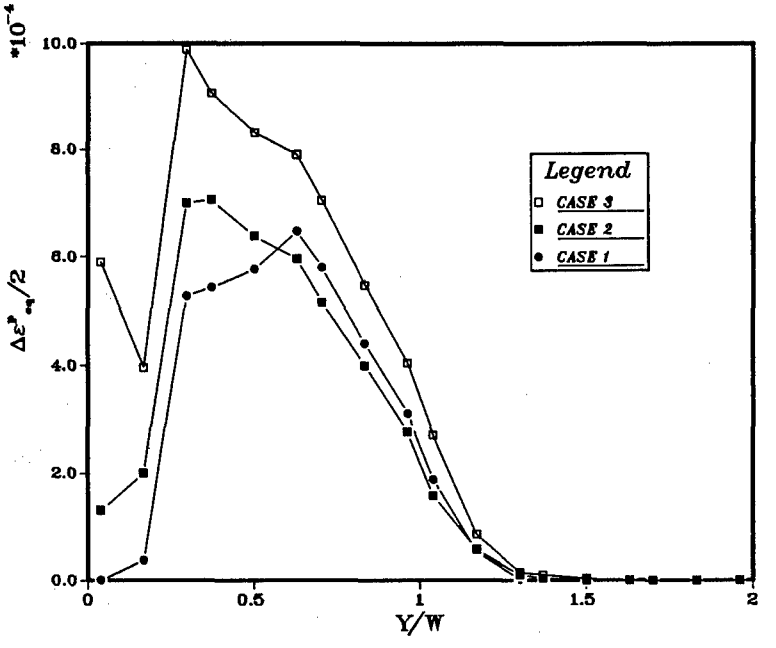

Figure 4. Equivalent plastic strain amplitude variation with depth for a point located at the center of the mesh.

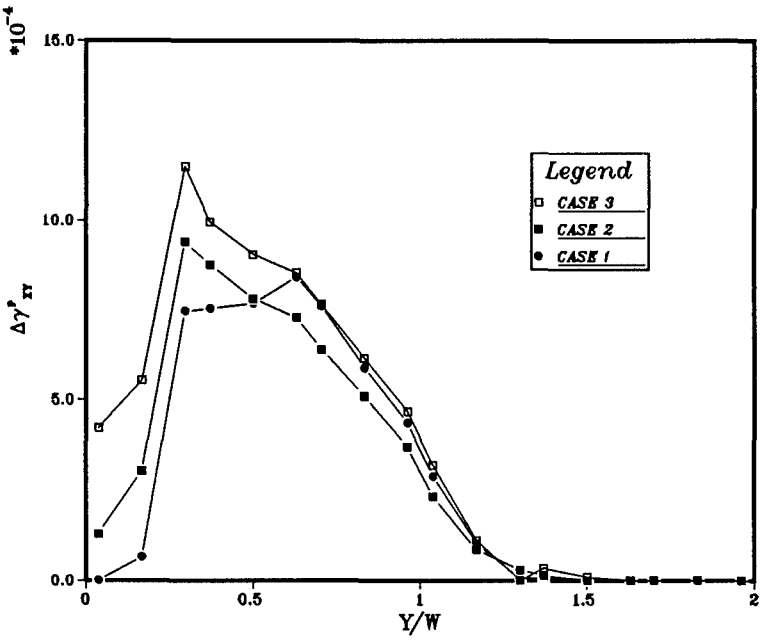

Figure 5. Variation of plastic shear strain range, $\Delta\gamma^{p}_{xy}$, with depth at the center of the mesh.

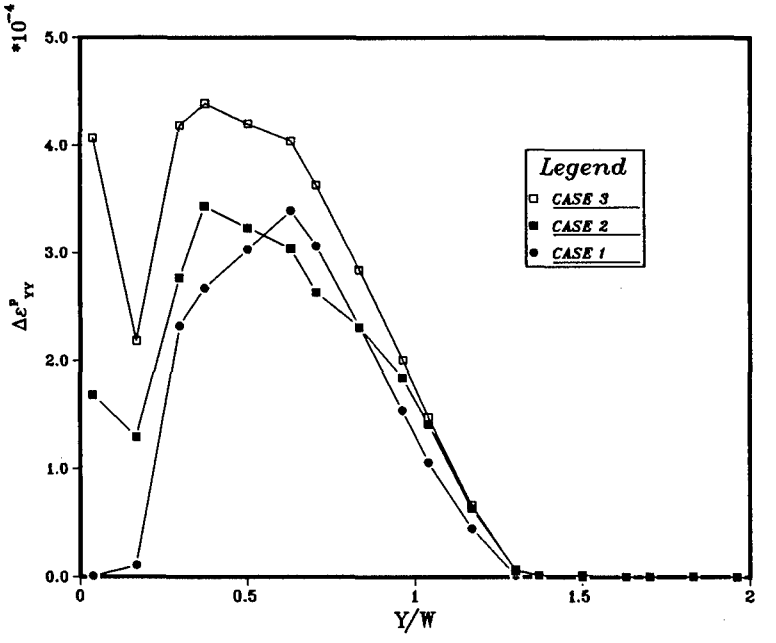

Figure 6. Variation of plastic radial strain range, $\Delta\epsilon^{p}_{yy}$, with depth at the center of the mesh.

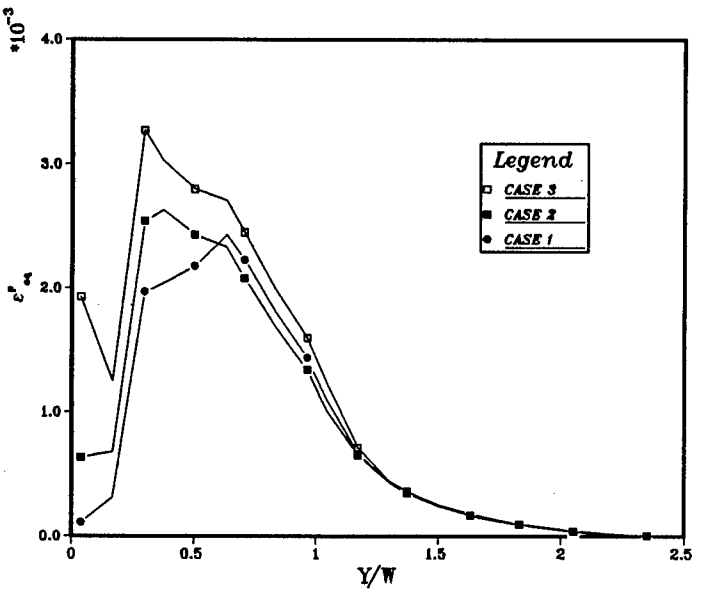

Figure 7. Residual plastic equivalent strain (ϵ^{p}_{eq}) as a function of depth at the center of the mesh.

Figures. 8 and 9 show the surface temperatures half way through the first and second passes, for cases 2 and 3, respectively. The

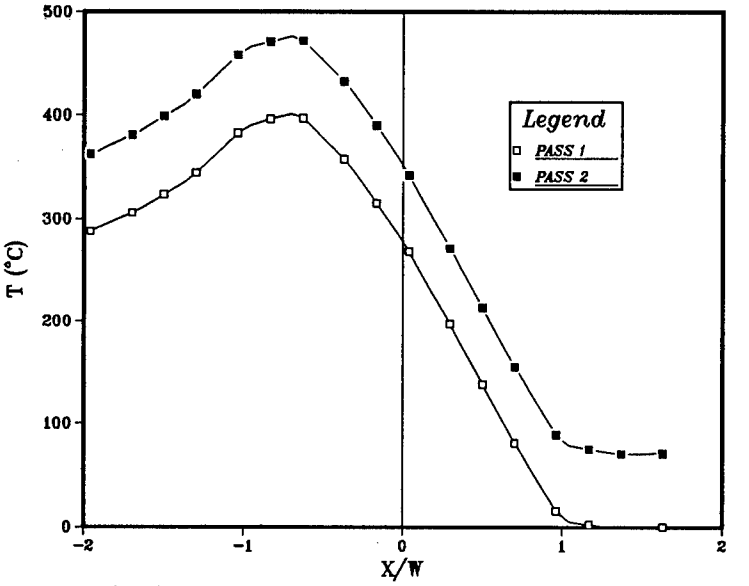

Figure 8. Distribution of surface temperature for case 2, halfway through the pass, for different passes.

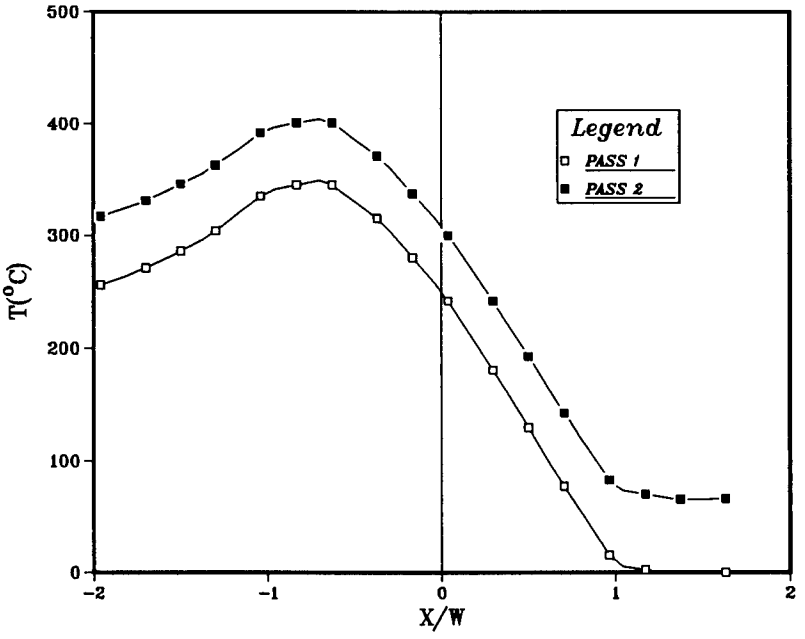

Figure 9. Distribution of surface temperature for case 3, halfway through the pass, for different passes.

temperature distribution is asymmetric about x/w=0.0. The highest temperature attained is higher in case 2 than case 3. This is because the heat influx remains the same in the two cases but thermal conductivity and specific heat increase in case 3 with increase in temperature, thereby reducing the peak temperature. Fig. 10 shows the temperature contours in a section of the mesh, halfway through the third pass, for case 3. It is seen that the thermal gradients are steep near the surface but die out quickly with depth.

Figure 11 shows the cyclic stress strain hysteresis loops for pass 2 for case 2. The loop is found to be closed indicating fully reversed plasticity.

DISCUSSION

The analyses reveal that the incorporation of ELKP material properties greatly reduces the plastic strains generated, relative to those expected for perfect plasticity. The peak residual equivalent plastic strain (ϵ^p_{eq}) obtained here for case 2: 2.5e-03 ($p_o/k=5.0$, $\mu=0.1$), is $1/25^{th}$ of the

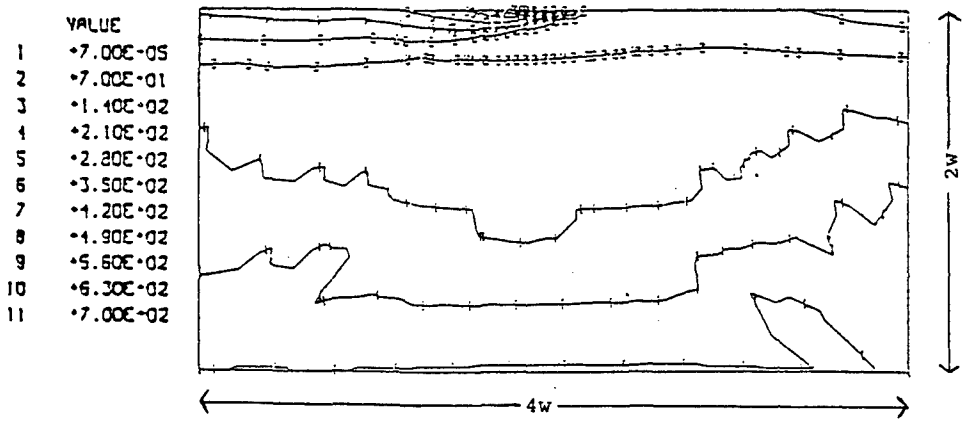

Figure 10. Temperature contours half way through the third pass, in a section of the mesh, for case 3.

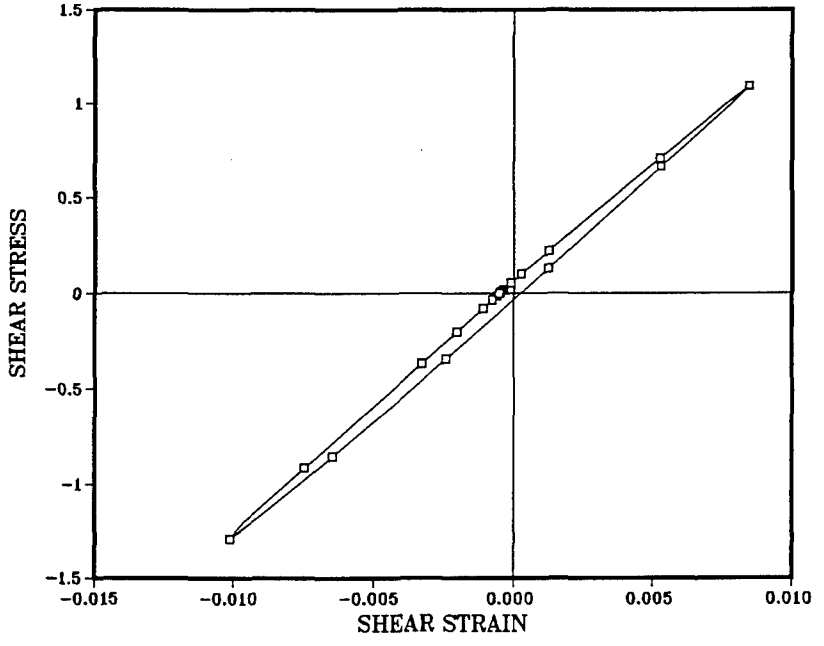

Figure 11. Hysteresis loop, shear stress versus shear strain, for second pass of case 2.

value obtained by Kulkarni et al. (1989): 6.0E-02 ($p_o/k=5.0$, $\mu=0.1$), for elastic perfectly plastic behavior for the same conditions. From Fig. 7 it can be seen that frictional heating and temperature dependence of properties has a large effect on the residual strains. The peak equivalent plastic strain increases by 10 percent from case 1 to case 2 and by 30 percent from case 1 to case 3. It should be noted that the peak strain occurs nearer to the surface in cases 2 and 3, as compared to case 1. Figures 4, 5 and 6 indicate that a large difference in cyclic plasticity is obtained due to heating and temperature dependent properties. The peak equivalent plastic strain amplitude increases 40 percent from case 1 to case 2. Important changes in plasticity occur very near the surface. Equivalent plastic strain amplitude changes from zero in case 1 to 6.0e-04 in case 3, which is very significant considering the peak value of 10.0e-04. This high amount of plasticity near the surface could be the reason for formation of near surface cracks.

The normalized residual stresses are found to be tensile near the surface, consistent with the findings of Kulkarni et al. (finite element model, 1988) and Muro et al. (X-ray measurements, 1973). But the magnitudes are far less than those obtained by Kulkarni et al. (elastic perfectly plastic material properties) who reported a peak normalized circumferential residual stress of 1.7 compared to 0.14 for case 3 in this study (ELKP properties). The difference is clearly due to the different material property representations. The residual stresses in cases 2 and 3 are found to be highly tensile and less compressive as compared to case 1.

The ratio of peak tensile stress to peak compressive stress is close to 2.5 for circumferential residual stresses and 2.0 for axial residual stresses for cases 2 and 3. A value of 2.0 has been reported by Muro et al. (1973) determined by X-ray measurements (see Figs. 2 and 3). The peak circumferential residual stresses are found to be about 1.4 times the peak axial residual stresses for case 3.

There is an appreciable difference in the magnitude of the residual stresses for cases 2 and 3. The magnitudes are increased by 5 to 10 percent due to the introduction of temperature dependent properties (Figs. 2 and 3). This is as expected, because the material becomes softer with increase in temperature and hence deforms more under the same amount of load, leading to higher residual stresses.

Also as seen in Figs. 2 and 3, the residual stresses for all three cases are almost the same at a depth greater than 1.5 w. This is because the temperature gradients vanish at a depth of 1.5 w and the temperature is close to ambient below that depth. This steep temperature gradient

produces very high compressive stresses. This, followed by non uniform thermal contraction during cooling, appears to be the reason for the residual tensile stresses. These transient residual tensions (due to translating thermo-mechanical loads) suggest a possible mechanism for thermo-cracking.

CONCLUSION

1. A transient translating elasto-plastic thermo-mechanical finite element model is used to study 2-D frictional rolling plus sliding contact with kinematically hardening and temperature dependent material properties. Residual stresses, temperature and plastic strain distributions are evaluated.

2. ELKP material properties greatly reduce the plastic strains and residual stresses generated, as compared to elastic-perfectly plastic material properties.

3. Incorporating the frictional heating makes the residual stresses highly tensile and less compressive. Residual tensile stresses are the result of compressive thermal stresses due to the steep temperature gradients followed by the non uniform thermal contraction (during cooling). However they do not effect the residual plastic strains significantly.

4. The incorporation of temperature dependent material properties highly increases the cyclic plasticity and also increases the residual stresses. This increase in plasticity is drastic very near the surface and could be a possible mechanism for formation of near surface cracks.

5. The residual tension and the transient tension (associated with the translating thermo-mechanical loads) may be a possible source of thermal cracking.

Several approximations have been made-

1. Arbitrarily selected heat transfer coefficient h.
2. No heat generation due to inelastic straining.
3. Representation of the bearing material as a continuum (not considering the metallurgical transformations accompanying the

high temperatures).

4. Results have been obtained in the transient state, i.e., before a steady state temperature was reached. It should be pointed out that the results of Kulkarni [15] with which comparisons are made in this paper, were also reported before the steady state was reached.

The convection coefficient for forced convection, h(T), is an important thermal parameter. It varies from 10 to more than 10^4 $W/m^2°K$ and depends on geometry, flow conditions and physical properties. An attempt at a boundary layer analysis to solve the heat transfer problem and define h(T) for specific contact situations is recommended.

ACKNOWLEDGMENTS

The authors express their thanks to Hibbitt, Karlsson and Sorensen, Inc. for making possible the use of their finite element code ABAQUS. The calculations were performed on the Cray Y-MP8/646 at the San Diego supercomputer center and on the Cray-2 at the National Center for Supercomputing Applications,IL. The computer time allocation at SDSC was supported by National Science Foundation under grant number DMR-8721915.

REFERENCES

1. Archard, J.F., 1959, "The Temperature of Rubbing Surfaces, "Wear, Vol. 2, pp. 438-455.

2. Barber, J.R., 1971b, "The Effect of Thermal Distortion on Constriction Resistance", *International Journal of Heat and Mass Transfer*, Vol. 14, pp. 751-766.

3. Barber, J.R., 1972, "Distortion of the Semi-infinite Solid due to Transient Surface Heating", *International Journal of Mechanical Science*, Vol. 14, pp. 377-393.

4. Bhargava, V., Hahn, G.T., Ham, G., Kulkarni, S.M., and Rubin, C.A., 1986, "Influence of Kinematic Hardening on Rolling Contact Deformation", *Proceedings of the 2nd International Symposium on Contact Mechanics and Rail/Wheel Systems,* Kingston, R.I, University of Waterloo Press.

5. Bhargava, V., Hahn, G.T., and Rubin, C.A., 1988, "Analysis of Rolling Contact with Kinematic Hardening for Rail Steel Properties", *Wear*, Vol. 122, pp. 267-283.

6. Bhat, B.N., and Dolan, F.J., 1983, "Analysis of Cryogenic Turbopump Bearing Service life, *"A Collection of Technical Papers: 24th Structures, Structural Dynamics and Materials Conference,* May 2-4, 1983, Lake Tahoe, Nevada, sponsored by AIAA.

7. Blok, H., 1937, "Theoretical Study of Temperature Rise at Surface of Actual Contact under Oiliness Lubricating Conditions, "General Discussion on Lubrication, Inst. Mech. Eng., Vol. 2, pp. 222-235.

8. Blok, H., 1963, "The Flash Temperature Concept, "Wear, Vol. 6, pp. 483-494.

9. Bradley, E.F., 1979, "Source Book on Materials for Elevated Temperature Applications", *American Society of Metals,* Metals Park, Ohio.

10. Comminou, M., Dundurs, M., and Barber, J.R., 1981, "Planar Hertz Contact with Heat Conduction, *Journal of Applied Mechanics,* Vol. 48, pp. 549.

11. Clauss, F.J., 1969, "Engineers Guide to High Temperature Materials", *Addison Wesley Publishing Co.,* Reading, Ma.

12. Ham, G.L., Hahn, G.T., Rubin, C.A. and Bhargava, V., 1989, "Finite Element Analysis of the Influence of Kinematic Hardening in Two-Dimensional Repeated, Rolling-Sliding Contact", *Tribology Transactions,* Vol 32, pp. 311-316.

13. Johnson, K.L., and Jefferies, J.A., 1963, "Plastic Flow and Residual Stresses in Rolling and Sliding Contact" *Proceedings of the Institute of Mechanical Engineering*, London, Vol. 177, pp. 54-65.

14. Kuhlmann-Wilsdorf, D., 1985, "Flash Temperature due to Friction and Joule Heat at Asperity Contact", *Wear*, Vol. 105, pp. 187-198.

15. Kulkarni, S.M., 1989, Ph.D. Dissertation: "Elasto-Plastic Finite Element

Analyses of 3-D and 2-D Repeated Rolling Contact", *Vanderbilt University*, 1989.

16. Muro, H., Tsushima, N. and Nunome, K., 1973, "Failure Analysis of Rolling Bearings by X-Ray Measurement of Residual Stress", *Wear,* 25, pp. 345-356.

17. Nagaraj, H.S., Sanborn, D.M., and Winer, W.O., 1978, "Direct Surface Temperature Measurement by Infrared Radiation in Elasto-hydrodynamic contacts and the correlation with Blok Flash Temperature Theory", *Wear,* Vol. 49, pp. 43-59.

18. Newman, S.Z., 1986, "FEM Model of 3-D Transient Temperature and Stress Fields in Welded Plates", Ph.D. Dissertation, *Carnegie Mellon University.*

19. Toulaukian, Y.S., 1967, "Thermophysical Properties of High Temperature Solid Materials", Vol. 3, *Macmillan, New York.*

THE INFLUENCE OF PRESTRAIN ON THE STRESS RESPONSE OF AN Al/Mg ALLOY TO A POLYGONAL STRAIN PATH

Erhard Krempl
Shiyuan Cheng

Mechanics of Materials Laboratory
Rensselaer Polytechnic Institute
Troy, NY 12180–3590

Introduction

Plastic strain induced anisotropy is of great interest in the formulation of constitutive equations for metals and alloys. This paper presents experiments depicting the response of an Al alloy to a nonproportional, polygonal loading path in strain space.

Experimental Arrangements

A servohydraulic, computer–controlled MTS axial–torsion testing machine with a biaxial clip–on extensometer is used to test thin–walled tubes of an Al–Mg alloy under nonproportional straining. Digital data acquisition is used to record axial and shear stress as well as axial and shear strain. The influence of three levels of prestrain (0, 1 and 12%) on the subsequent stress response to a regular, 16–sided, polygonal strain path is investigated. At each corner of the polygon, yield surface probings were performed in most of the tests before straining continued to the next corner. Straining and yield surface probing were done under computer control with no human interaction. The alloy was donated by ALCOA and has a tensile ductility of about 16%.

Experimental Results

Figure 1 depicts the polygonal strain path imposed on the specimens (the square path following the polygonal path and identified by the numbers 19 through 26 was not used for the results reported in this paper). The axial prestrain level X was changed from specimen to specimen and amounted to zero, to 1% and to 12%. After prestraining the polygonal strain path was imposed. At each station, identified by numbers 1 through 18 yield surface probing was conducted before straining continued to the next station. Details can be found in Cheng [1].

Figure 2 shows the stress response to the polygonal strain path at three levels of prestrain. With an increase of prestrain

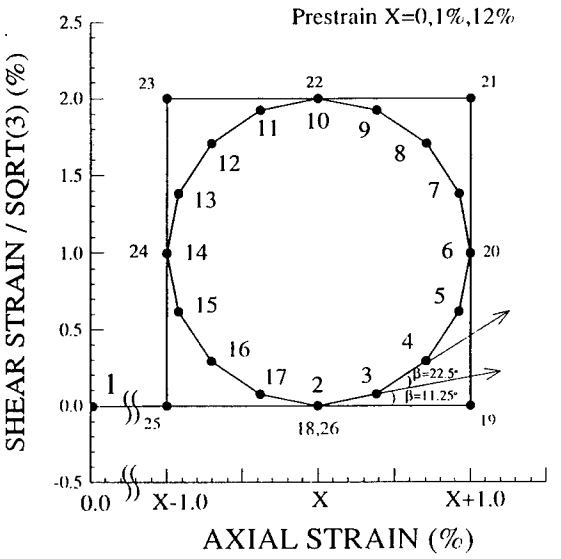

Figure 1. Polygonal strain path imposed on specimens. Numbers 1-18 indicate the stations at which yield surface probing was performed. x is the tensile prestrain level (0 for ALD1, 1% for ALG4, 12% for ALH2).

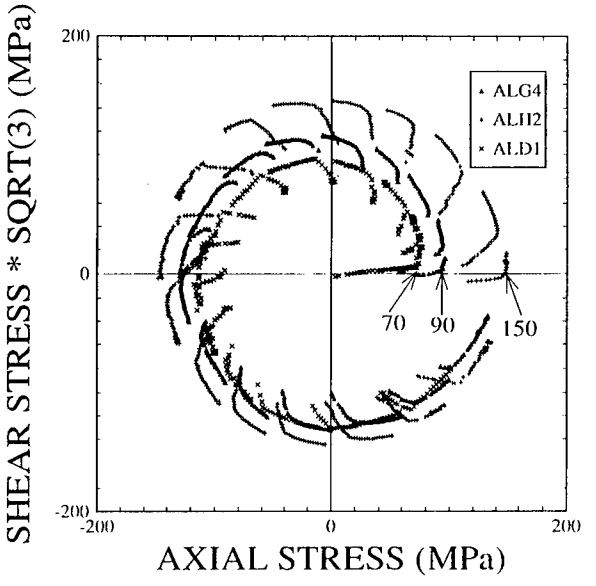

Figure 2. Stress responses to polygonal strain path (70, 90, 150 indicate the stress level reached at the end of prestraining). The nearly radial stress paths correspond to elastic behavior; inelastic behavior is predominant after the bends when the stress paths are nearly circumferential.

(ALD1–0%, ALG4–1%, ALH2–12%) the size of the stress response increases. For each specimen the response is akin to a spiral with an initial radial path. (During yield surface probing the stress pertaining to the same strain drops due to small accumulated inelastic strains and due to time dependent effects such as relaxation, see Cheng and Krempl [2] and Cheng [1]. As a consequence the stress at the beginning and at the end of the yield surface probing is different.) The initial radial path is associated with elastic deformation and inelastic deformation sets in at the pronounced bends. For zero prestrain, specimen ALD1, the growth of the radius of the spiral is initially rapid but levels off as straining continues. There is less of a radial growth for the stress path of specimen ALG4 and its stress response finally coincides with that of specimen ALD1. The stress responses for inelastic deformation of specimen ALH2, 12% prestrain, are nearly on a circle with radius 150 MPa. The tensile prestraining has diminished the capacity for hardening, taken here as an increase of the radius of the stress response. The final radius of specimen ALH2 is larger than those of the other two specimens which is taken to be an indication of specimen–to–specimen variation. The ultimate engineering tensile strength of this material is approximately 150 MPa. It is seen that the effect of tensile prestraining is primarily to increase the initial radius and to decrease the rate of radius increase under subsequent straining.

It can be argued that the response depicted in Figure 2 might be influenced by yield surface probing and the attendant stress drop. Figure 3 compares the response of specimen ALG4 with that of specimen ALF7 which was only subjected to continuous loading until station 13 when yield surface probing commenced. It is obvious that the response associated with inelastic deformation is unaltered by yield surface probing.

Returning to the results of Figure 2 it is reasonable to suggest that the material hardens until the stress response reaches a radius equivalent to the ultimate tensile strength of the material. The effect of prestraining is primarily an increase of the initial radius of the spiral. Ultimately the growth levels off at the same radius as for the specimen without prestrain. It seems that an ultimate surface with a radius equal to the ultimate strength can be postulated. For the present tests at least, this surface is unaffected by prior deformation.

When the effective stresses pertaining to the corners of the polygon are plotted vs. accumulated inelastic strain, an effective stress–strain curve is obtained within a reasonable scatter, see Figure 4. It contains the results of seven specimens including a

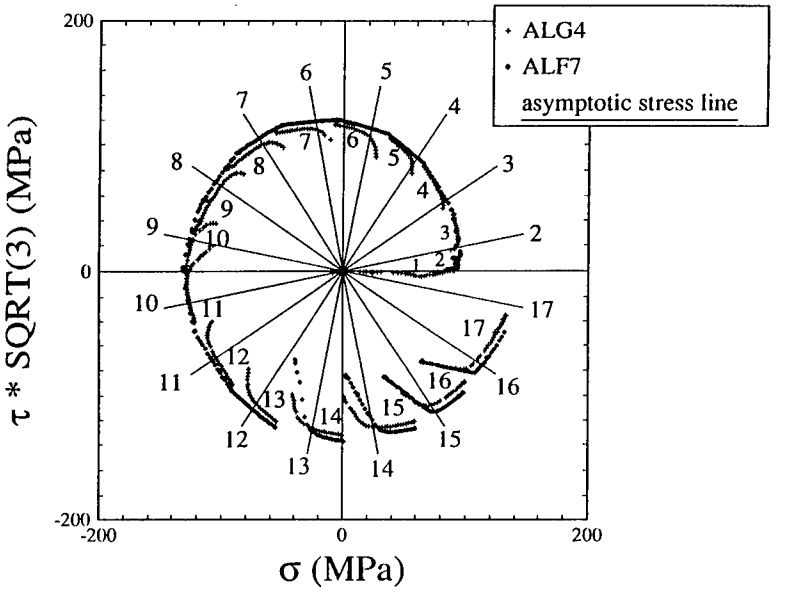

Figure 3. Comparison of the stress responses of specimens ALG4 (yield surface probing at every station) and ALF7 (no yield surface probing until station 13).

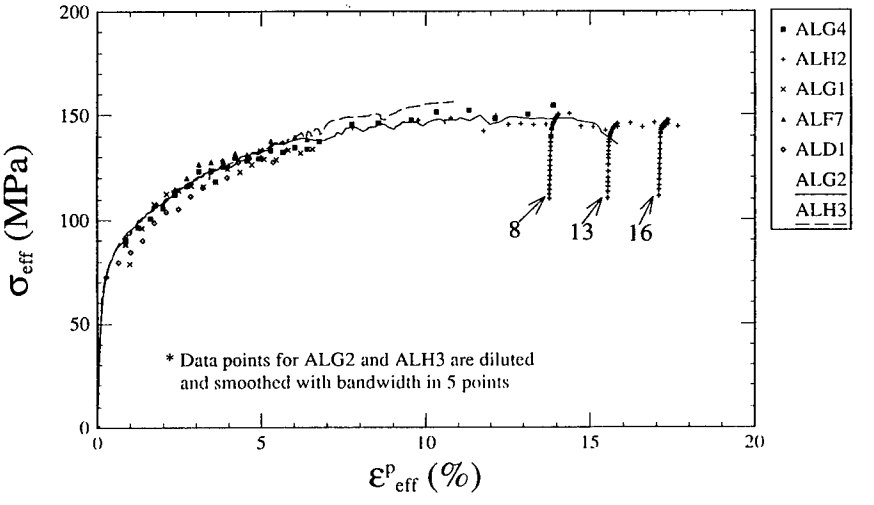

Figure 4. Effective stress vs. accumulated inelastic strain for various specimens.

tensile test, ALG2 and a torsion test, ALH3. The strain path for specimen ALF7 is identical to that of specimen ALG4. For specimen ALG1 the one percent prestrain was followed by the polygonal strain path which in this case was traversed in clock–wise direction. It is seen that the ultimate responses to the polygonal strain path lie on a nearly unique effective stress–accumulated inelastic strain graph. The transient responses are generally not included. They deviate from the effective stress–strain diagram as seen for the responses of stations 8, 13 and 16 of specimen ALH2. It is seen that only the final points of the stress response are on the curve.

Discussion

The present results suggest that after sufficient inelastic straining the response of this material to the employed nonproportional loading paths is independent of prior history. Also an ultimate surface with center at the origin appears to exist. Its radius is independent of prior history and equal to the ultimate engineering strength of the material. The transient effects have been investigated, Cheng and Krempl [2], and have been used in formulating constitutive laws for deformation induced anisotropy, see Lee and Suh [3].

Acknowledgement

This research was supported by ARO Grant DAAL03–88–K–0041. The test material was donated by ALCOA.

References

[1] S. Cheng, PhD dissertation, Rensselaer Polytechnic Institute, December 1991.

[2] S. Cheng and E. Krempl, "Experimental Determination of Strain–Induced Anisotropy During Nonproportional Straining of an Al/Mg Alloy at Room Temperature," to appear International Journal of Plasticity, 1991.

[3] E. H. Lee and Y. S. Suh, "Development and Application of an Elastic–Plastic Constitutive Relation Involving Strain–Induced Anisotropy Based on Nonproportional Straining Experiments," Proceedings Army Symposium on Solid Mechanics, Plymouth, MA, November 4–7, 1991.

A REEXAMINATION OF THE PLASTIC FLOW CRITERION FOR COPPER

Norris J. Huffington, Jr.

U.S. Army Ballistic Research Laboratory
Aberdeen Proving Ground, Maryland 21005-5066

SUMMARY: It was found impossible to reconcile discrepancies between uniaxial and torsion test data for copper within the framework of the von Mises yield function; use of a more general function employing both the second and third invariants of the stress deviator was studied and certain limitations on use of such functions are discussed.

INTRODUCTION

While finite element hydrocodes can predict the contours of finitely deforming metals with reasonable accuracy, their ability to determine local strain and stress states leading to catastrophic failure by such mechanisms as adiabatic shear banding and void openings leaves much to be desired. An improvement in the ability to compute such local state histories would significantly enhance the design of warheads and predictions of armor penetration and behind-armor debris formation. In recognition that better material characterization was an essential ingredient of the desired improvement, a joint BRL/MTL program entitled Advanced Constitutive Models was initiated several years ago. This paper reports on one facet of this investigation.

At BRL, it was decided to employ the DYNA3D hydrocode [1] in connection with this study. This is a Lagrangian finite element computer program currently in widespread use which employs an adequate finite deformation formulation and features a choice of approximately 30 constitutive models*. However, only a few of these models are suitable for the large strain, low rate applications to be discussed in sequel. These

*This term is used to identify a mathematical function or algorithm which determines stress tensor components from the current rate-of-deformation components, some past history data, and possibly temperature through an incremental plasticity time marching process.

models generally* employ the von Mises yield condition $J_2 - k^2 = 0$, where J_2 is the second invariant of the stress deviator tensor, as the plastic potential function and use the Jaumann stress rate to account for the rigid body rotation of elements.

QUASI-STATIC MATERIAL PROPERTIES

For an evaluation of material constitutive behavior, it is necessary to have test data for the specific lot of material to be characterized. It was decided that this investigation would commence with a study of OFHC copper and MTL was tasked to perform the necessary experimentation. Dr. Tusit Weerasooriya has reported [3] data from two types of quasi-static (isothermal) tests on annealed copper:

(1) Uniaxial compression stress-strain curves for the range $-1.30 < \varepsilon < 0$.

(2) Torsional shear stress-strain data from twist tests on modified Lindholm-type thin-walled tubular specimens for the range $0 < \varepsilon < 1.4$ (tensor) shear strain. These tests were performed for two conditions of axial restraint: (a) almost total axial restraint in which case the induced axial force was recorded and (b) no applied axial restraint where the axial displacement was monitored.

Also, Dr. Weerasooriya provided the author a curve for reversed loading of a torsion specimen which permitted an assessment of the Bauschinger effect for this material.

CONSTITUTIVE MODELING CONSIDERATIONS

The compression test data cited above reveal that the stress-strain curve for annealed copper is nonlinear over the entire range, the elastic portion being of negligible size. For a curve of this form, a bilinear representation (such as DYNA3D Material 3) is unsatisfactory. Material 10 of the DYNA code, which permits input of up to 16 stress-strain points and interpolates linearly for intermediate values, is more appropriate but only treats isotropic hardening.

---

*The exception is the model of D. Bammann [2] as incorporated by M. Chiesa of Sandia Livermore which is a multi-parameter micromechanically-based constitutive system which uses the Green-Naghdi stress rate.

The Lindholm-type torsion specimen does not result in a homogeneous state of stress in the thin-walled test section; also, the shearing strain and plastic deformation extend into the transition section. For this reason, various investigators have resorted to 3-D finite element modeling of the whole specimen (using an assumed constitutive model) to provide a basis for interpretation of test data. Lipkin et al. [4] reported a DYNA3D calculation using an earlier version of the Bammann constitutive model in which a twist rate high enough to predict adiabatic shear banding was used. The present author performed a DYNA3D analysis for the MTL geometry using Material 3 and found this geometry was prone to premature torsional buckling. It was recommended that a thicker wall be used since an interpretive analysis would be required in any event. Dr. C. S. White [5] reported an ABAQUS analysis of a geometric configuration closely corresponding to that used by Weerasooriya and has concluded that "about 78% of the twist that is applied at the grips actually goes into the deformation in the gauge section." Although White's calculations were made for a different material, it was decided to multiply Weerasooriya's shear strain data by a factor of 0.78.

USE OF EXPERIMENTAL DATA; DISCREPANCIES

If the compression test data are used as input to DYNA3D Material 10 and a calculation is made for an element constrained to deform uniaxially with no lateral restraints, the code predictions are (naturally) in excellent agreement with the experimental values. (It is necessary to choose an equation-of-state which permits specifying the pressure to be proportional to the volumetric strain {proportionality constant = bulk modulus}, use the hourglass viscosity type 3 {Flanagan-Belytschko [6] with exact volume integration}, and to set the Gruneisen coefficient = 0 for an isothermal calculation.) Similarly, when torsion test data are inserted in DYNA3D Material 10 and a simple shear problem is run for an element, there is no discrepancy.

However, when compression test data are used in Material 10 to predict the stresses in an element subjected to increasing simple shear the result shown in Figure 1 is obtained, where the overprediction of the shear stress σ_{zx} is as great as 30%. Not surprisingly, the converse is also true: use of the torsion test data as input for a uniaxial compression calculation results in a significant underprediction of the axial stress σ_x as shown in Figure 2.*

This phenomenon is no new discovery and has been discussed in the literature by Prager [7], Drucker [8], Edelman and Drucker [9], and many others. The basic problem is that use of the von Mises condition as

* While strain data input to the DYNA3D code is in terms of logarithmic strains, the abscissas of Figures 1 and 2 are in terms of engineering strain tensor components.

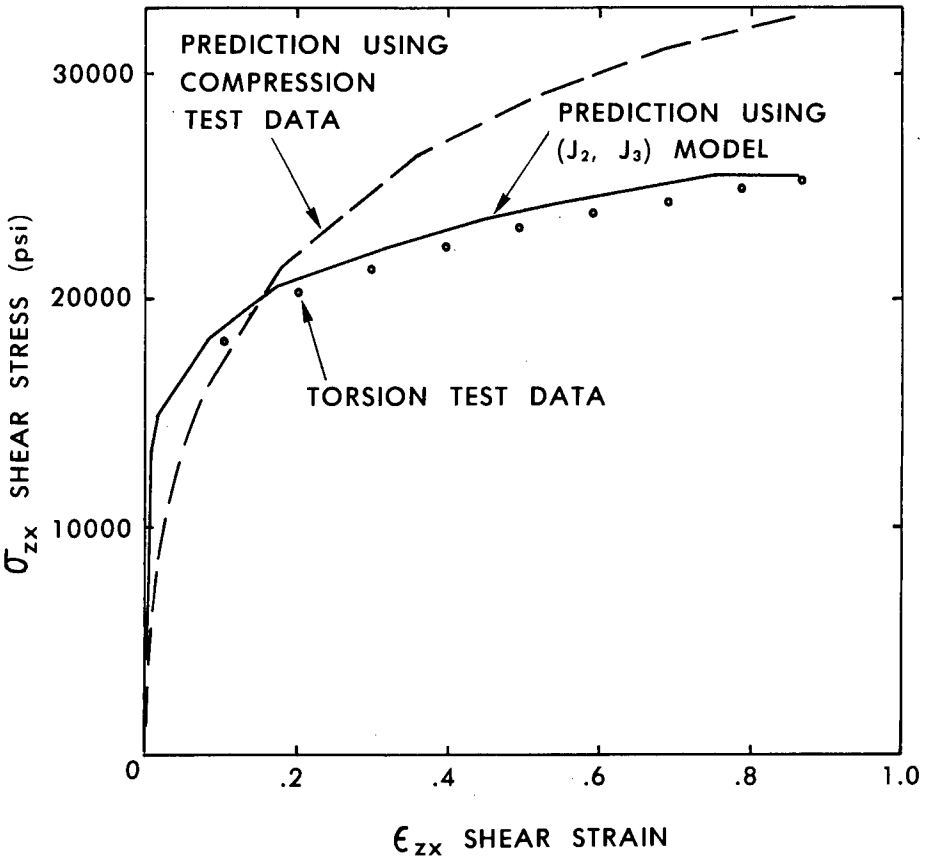

Figure 1. Simple Shear Calculation (Geometric Constraints, Material Type 10).

a loading function for work hardening materials does not closely describe the plastic deformation of many materials (even though it is widely employed for this purpose in most currently used hydrocodes). According to the authors just cited, the problem can be resolved by use of a loading function depending on both the second and third invariants of the stress deviation; i.e., a (J_2, J_3) theory. Although such theories seem to have fallen into disuse, perhaps this approach should be considered for applications involving large strains, where the discrepancies are greatest.

IMPLEMENTATION OF A (J_2, J_3) THEORY

It was decided to employ the function quoted by Malvern [10]:

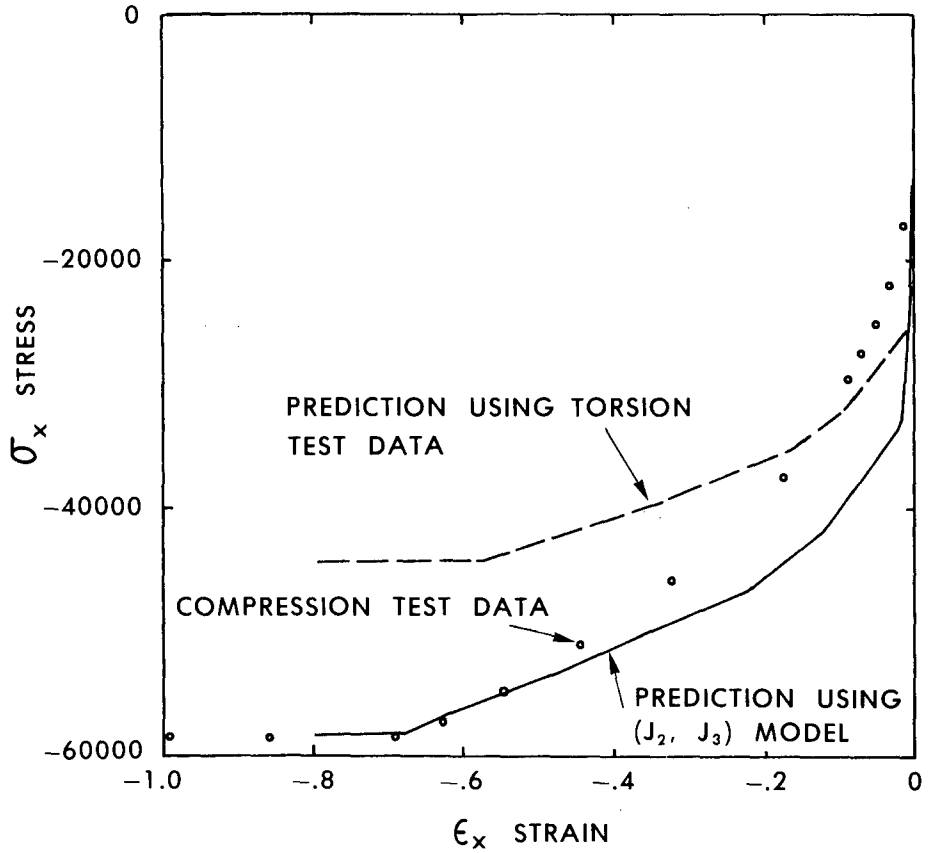

Figure 2. Uniaxial Compression Calculation (Geometric Constraints, Material Type 10).

$$f(J_2,J_3) \equiv J_2\left[1 - \frac{c(J_3)^2}{(J_2)^3}\right] - k^2 = 0 \qquad (1)$$

where $J_2 = \frac{1}{2}(S_{11}^2 + S_{22}^2 + S_{33}^2) + S_{12}^2 + S_{23}^2 + S_{31}^2 = \frac{1}{2}(S_1^2 + S_2^2 + S_3^2)$ (2)

$$J_3 = S_{11}\,S_{22}\,S_{33} + 2S_{12}\,S_{23}\,S_{31} - S_{11}\,S_{23}^2 - S_{22}\,S_{31}^2 - S_{33}\,S_{12}^2$$
$$= S_1\,S_2\,S_3 \qquad (3)$$

k = yield stress in pure shear, variable for a work hardening material

c = nondimensional parameter to be adjusted to provide match of post yield flow data

S_{ij} = deviatoric stress components

S_k = principal deviatoric stresses

Installation of Equation (1) as the load function in DYNA3D was easily accomplished since current values of all required quantities are available in the stress evaluation subroutine. Because J_3 vanishes for pure shear, it is attractive to insert the tabular data from the shear tests in Material 10 and then determine the parameter c to provide correspondence to the compression test data for uniaxial stress calculations. For the present application, the peak stress was employed because the uniaxial stress-strain curve appears to level off at this value and the interest is in large strain plasticity. Of course, other matching criteria could be adopted for other strain ranges. Only a few trials were required to obtain c = 2.83; this value was used in DYNA3D to obtain the solid curves displayed in Figures 1 and 2.

GEOMETRIC REPRESENTATION

It is instructive to view the (J_2, J_3) yield function in principal stress space, where it may be recalled that the von Mises function is represented by a circular cylinder coaxial with the hydrostatic line $\sigma_1 = \sigma_2 = \sigma_3$. To achieve this, the following orthogonal coordinate transformation was made:

$$\sigma_1 = -\frac{\tau_1}{\sqrt{6}} + \frac{\tau_2}{\sqrt{2}} + \frac{\tau_3}{\sqrt{3}}$$

$$\sigma_2 = -\frac{\tau_1}{\sqrt{6}} - \frac{\tau_2}{\sqrt{2}} + \frac{\tau_3}{\sqrt{3}}$$

$$\sigma_3 = \frac{2\tau_1}{\sqrt{6}} + \frac{\tau_3}{\sqrt{3}} \qquad (4)$$

With this transformation, the τ_3 axis coincides with the hydrostatic line and the τ_1 axis is aligned with the projection of the σ_3 axis on the deviatoric plane $\sigma_1 + \sigma_2 + \sigma_3 = 0$. Using Equations (4), one obtains

$$J_2 = \frac{1}{2}(\tau_1^2 + \tau_2^2) \qquad (5)$$

$$J_3 = \frac{1}{\sqrt{6}} \left(\frac{\tau_1^3}{3} - \tau_1\tau_2^2\right) \tag{6}$$

and, substituting these values in Equation (1), there results

$$27\tau_2^6 + \left\{(81-36c)\tau_1^2 - 54k^2\right\}\tau_2^4 + \left\{(81 + 24c)\tau_1^4 - 108k^2\tau_1^2\right\}\tau_2^2 + (27-4c)\tau_1^6 - 54k^2\tau_1^4 = 0 \tag{7}$$

which defines the contour of the yield function in the τ_1, τ_2-plane.

As noted by Hill [11], it is only necessary to compute coordinates for a 30° segment of this plane, the remainder of the locus being determined by the symmetry constraints for an isotropic material. This locus for c = 2.83 is displayed in Figure 3 as a solid line. It is seen that the (J_2, J_3) surface is a fluted cylinder with the von Mises cylinder inscribed. For Material 10 which provides only for isotropic hardening, these surfaces would expand uniformly as plastic deformation progresses. It should be mentioned that DYNA3D presently uses only the Krieg-Key radial return algorithm [12] to return the stress state to the updated yield surface each cycle. This algorithm is clearly more appropriate for the J_2 surface than for the (J_2, J_3) function. However, it is still attractive due to its simplicity and the assurance that the yield surface will be intersected, although for the latter it corresponds to a nonassociated flow rule. A "normal return" algorithm would seem preferable or perhaps the recently published Nemat-Nasser algorithm [13], but either of these would require more extensive calculations per cycle. These matters may be academic in view of the following discussion.

MATERIAL STABILITY, CONVEXITY REQUIREMENTS

It is clear from inspection that the c = 2.83 loading function in Figure 3 violates the requirement that the surface be convex, as deduced by Drucker [14,15] from his postulates for material stability. Although the author has made a considerable number of computer runs using this value of c with no evidence of instability, these cases were not designed to test all types of loading and unloading. Thus, it is appropriate to ask: Can any (J_2, J_3) load function satisfy the convexity requirement? The answer is yes and the limitation on c is determined by evaluating the curvature of the load function at its point of tangency to the von Mises circle. Thus, at $\tau_1 = 0$,

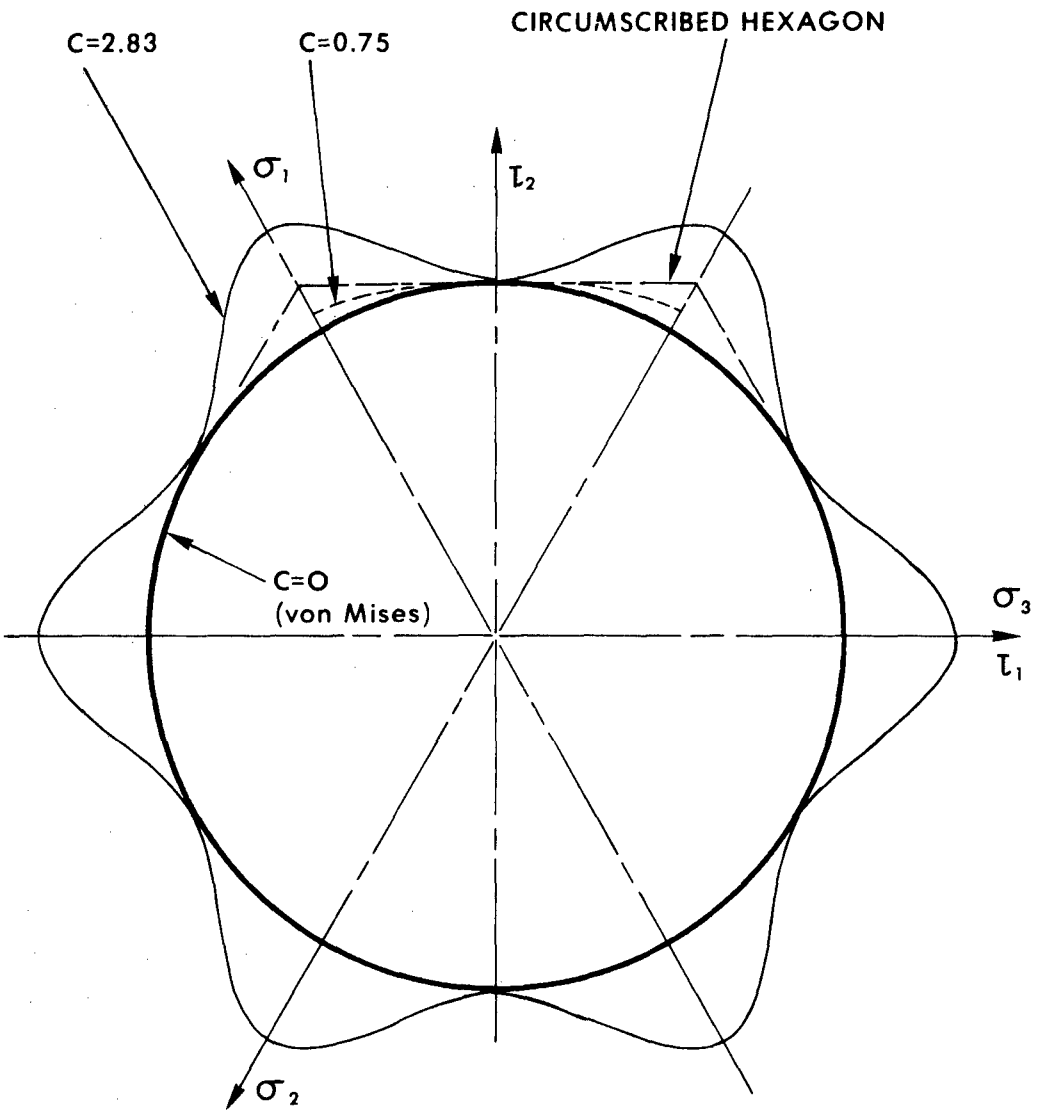

Figure 3. Axial View of Yield Loci.

$$\frac{d^2\tau_2}{d\tau_1^2} = \frac{1 - \frac{4}{3}c}{\sqrt{2}\,k} \tag{8}$$

This happens to be the exact curvature since $\frac{d\tau_2}{d\tau_1} = 0$ at this location.

Therefore, the transition in sign of the curvature occurs at c = 0.75 and the load function is everywhere convex for this or lesser values of c. The form of the load function for c = 0.75 is plotted in the upper sextant of Figure 3. Unfortunately, for this value of c, the percentage difference between the maximum and minimum radii of the load function is only about 6%. It can now be seen that the greatest percentage difference in radii consistent with convexity requires a load function in the form of a hexagon circumscribed about the von Mises circle, as shown in the upper portion of Figure 3. Even for this form of yield function (with its attendant analytical complexities), the percentage difference in radii is only 15.5%, about half of what is needed to reconcile the discrepancies associated with experimental data.

CONCLUDING REMARKS

It is realized that other investigators [16,17,3] have treated the subject matter of this paper by micromechanical modeling and have attributed the cited discrepancies to formation of texture. However, the end objective of such research does not appear to be the identification of load functions appropriate to classical plasticity.

This author is convinced that material behavior must be modeled within the framework of continuum mechanics if efficient, large-scale computations are to yield valid results for engineering purposes. While the study reported herein may seem inconclusive, it is believed that use of a nonconvex loading function may be permissible for certain classes of problems, especially if the computer program is modified to test on the sign of the plastic work increment in each element and to terminate the calculations if a negative work increment is predicted. It is very desirable to resolve this matter before proceeding to studies of strain-rate effects, stress rate models, etc., where uncertainties regarding the loading function may obscure interpretation of other types of experimental results.

It should be mentioned that the author has added a new subroutine to a research version of DYNA3D which includes many effects previously not present in a single material model, specifically:

1. Finite elastoplastic straining.

2. Mixed kinematic/isotropic hardening, as recommended by Hodge [18].

3. Arbitrary shape of uniaxial stress-strain function through input of tabular data.

4. Choice of stress rate formulation (Jaumann [19] or Green-Naghdi [20,21]).

5. Choice of several equation-of-state models.

It is planned to use this tool to study finite plasticity for various proportional and nonproportional loading paths.

ACKNOWLEDGEMENT

The author benefitted from several stimulating discussions with Dr. Joseph M. Santiago, Jr., of BRL.

REFERENCES

1. J. O. Hallquist, "Theoretical Manual for DYNA3D," University of California, Lawrence Livermore National Laboratory, Rept. UCID-19401 (1983).

2. G. C. Johnson and D. J. Bammann, "A Discussion of Stress Rates in Finite Deformation Problems," Int. J. Solids Structures, vol. 20, no.8, 1984, pp. 725–737.

3. T. Weerasooriya and R. A. Swanson, "Experimental Evaluation of the Taylor-Type Polycrystal Model for the Finite Deformation of an FCC Metal (OFHC Copper)," U.S. Army Materials Technology Laboratory, MTL TR 91-20, 1991.

4. J. Lipkin, M. L. Chiesa, and D. J. Bammann, "Thermal Softening of 304L Stainless Steel: Experimental Results and Numerical Simulations," Proc. of IMPACT'87, Bremen, Germany, 1987.

5. C. S. White, "An Analysis of the Torsion Specimen Used in Constitutive Modeling," presented at the Eighth Army Conference on Applied Mathematics and Computing, Cornell U., 1990.

6. D. P. Flanagan and T. Belytschko, "A Uniform Strain Hexahedron and Quadrilateral and Orthogonal Hourglass Control," Int. J. Numer. Meths. Eng., vol. 17, 1981, pp. 679–706.

7. W. Prager, "Strain Hardening Under Combined Stresses," J. Appl. Physics, vol. 16, 1945, pp. 837–840.

8. D. C. Drucker, "Relation of Experiments to Mathematical Theories of Plasticity," Journal of Applied Mechanics, vol. 16, no. 4, 1949, pp. 349–357.

9. F. Edelman and D. C. Drucker, "Some Extensions of Elementary Plasticity Theory," Journal of the Franklin Institute, vol. 251, 1951, pp. 581–605.

10. L. E. Malvern, "Introduction to the Mechanics of a Continuous Medium," Prentice-Hall, 1969, p. 355.

11. R. Hill, "The Mathematical Theory of Plasticity," Oxford, 1950, p. 18.

12. R. D. Krieg and S. W. Key, "Implementation of a Time Independent Plasticity Theory Into Structural Computer Programs," Constitutive Equations in Viscoplasticity, ASME, AMD - Vol. 20, 1976.

13. S. Nemat-Nasser, "Rate-Independent Finite-Deformation Elastoplasticity: A New Explicit Constitutive Algorithm," to be published.

14. D. C. Drucker, "A More Fundamental Approach to Plastic Stress-Strain Relations," Proc. First U. S. Natl. Cong. Appl. Mechanics, ASME, 1951, pp. 487–491.

15. D. C. Drucker, "A Definition of Stable Inelastic Material," Journal of Applied Mechanics, vol. 26, 1959, pp. 101–106.

16. S. C. Shrivastava, J. J. Jonas, and G. Canova, "Equivalent Strain in Large Deformation Torsion Testing: Theoretical and Practical Considerations," J. Mech. Phys. Solids, vol. 30, 1982, pp. 75–90.

17. R. J. Asaro and A. Needleman, "Texture Development and Strain Hardening in Rate Dependent Polycrystals," Acta Metall., vol. 33, 1985, p. 923.

18. P. G. Hodge, Jr., Discussion of Prager (1956), Journal of Applied Mechanics, vol. 24, no. 3, 1957, pp. 482–483.

19. G. Jaumann, "Grundlagen der Bewegungslehre", Leipzig, 1905.

20. A. E. Green and P. M. Naghdi, " A General Theory of an Elastic-Plastic Continuum," Arch. Rat. Mech. Anal., vol. 18, 1965, pp. 251–281.

21. A. E. Green and B. C. McInnis, "Generalized Hypo-Elasticity," Proc. Roy. Soc. Edinburgh, A57, 1967, p. 220.

A CLASS OF CONSTITUTIVE MODELS FOR RATE-DEPENDENT INELASTICITY IN METALS

M. M. Rashid†

Center of Excellence for Advanced Materials
Department of Applied Mechanics and Engineering Sciences
University of California, San Diego
9500 Gilman Drive
La Jolla, CA 92093-0411

ABSTRACT

A general thermomechanical framework for the inelastic response of solids is presented. The formalism makes use of the state-variable concept, but differs from other such constructs in two important ways. Restrictions on the response functions imposed by the second law of thermodynamics are derived, and correspondence with familiar concepts in metal plasticity is discussed. A special case of the general theory, suitable for metals and involving only a single state variable, is developed. Although this special model is necessarily isotropic, it is capable of capturing some aspects of the Swift effect (i.e. length changes observed in twisted tubes). A simple procedure for experimentally determining the two hardening functions that appear in the model is also described.

† Present address: Division 1561, Sandia National Laboratories, Albuquerque, NM 87185

1. Introduction

A large body of literature now exists wherein the broad discipline of inelastic behavior of solids is unified and rationalized by means of general constitutive formalisms. These theoretical constructs have taken the form of both memory-functional and state-variable formulations. In the latter approach it is assumed that, insofar as future thermomechanical response is concerned, all relevant aspects of a given material's previous history may be expressed through the values of a finite collection of state variables.

In this paper, this state-variable approach is adopted, but with two important differences in relation to what has gone before. First, the usual (but not universal) practice of including, in the description of state, some measure of the total deformation with respect to a reference configuration is not followed here. Such a dependence is not always natural or desirable, and may be awkward to compensate for in some cases. Secondly, with a view toward maintaining contact with conventional concepts in metal inelasticity theory, the present formalism allows for an explicit decomposition of the type $\mathbf{F} = \mathbf{F}^e \mathbf{F}^p$ of the total deformation gradient into elastic and plastic parts, *when this is appropriate to the material under consideration.* However, such a decomposition does not here constitute a basis for the development; rather it has the status of an *interpretive aid* to which the constitutive modeler may or may not appeal, according to taste. Accordingly, all of the discussion that has appeared in the literature relating to the admissibility of such a multiplicative decomposition has no relevance here.

The concept of state is discussed in Section 2, followed by a development of the general constitutive framework. Appeal is made to a statement of the second law of thermodynamics in order to establish relationships among the thermomechanical response functions. In Section 3, the general constitutive equations are reduced to a simple model for rate-dependent plasticity in metals. This model is arrived at following the introduction of a number of plausible physical assumptions regarding the behavior of metals, and has as a special case the classical J_2-viscoplasticity theory.

Notation is conventional, with Cartesian tensors being employed throughout. Where component notation is used, summation is implied by repeated indicies.

2. General Theory

2.1. concept of state

Central to the development of the general theory for inelastic solids is the concept of *state.* Here, the *state of a material element* at time t refers to the collection of all information that, once known, allows the response of the element to be determined for times greater than t, given the applied stimuli for times greater than t. In this intuitive definition of state, the *response* of a material element refers to the time-histories of Cauchy stress $\mathbf{T}$, specific entropy η, heat flux vector $\mathbf{q}$, and specific Helmhlotz free energy ψ ($\psi = \varepsilon - \eta\theta$, where ε is the internal

energy per unit mass and θ is the temperature). The *stimuli* are the time histories of temperature θ, spatial temperature gradient $\nabla\theta$, and deformation gradient $\mathbf{F}$ with respect to a reference configuration at which the state is known. The constitutive relations, then, become a set of rules by which the response $\{\mathbf{T}, \eta, \mathbf{q}, \psi\}$ and the state at time t_2 of a material element may be determined, given the state at time t_1 and the stimuli for times greater than t_1 and up to and including t_2.

It will further be assumed that the state of a material element is expressible through the values of a finite collection of *state variables*, which in general may have tensorial character. Besides allowing for the development of a quite detailed theoretical framework, this assumption leads to enormously practical constitutive descriptions for particular materials.

The incorporation of the concept of state into a constitutive framework is formally distinct from the "memory-functional" approach to constitutive theory. The memory-functional approach is exemplified by the work of Coleman [1], who carefully laid out a general memory-functional formalism in the context of continuum thermodynamics. In this approach, the response of a material element is regarded as a (generally nonlinear) functional of the past history of stimuli. Constitutive descriptions of this kind suffer from the practical difficulties of constructing realistic and meaningful memory functionals, and of accounting for the fact that the stimuli and state history in the infinite past can never be known.

In the present formulation, the state variables will be used in a slightly different manner than they are in other, more conventional formulations. In particular, in the work of, e.g., Coleman and Gurtin [2], Rice [3], Kestin and Rice [4], Kratochvil [5], Lubliner [6], and Valanis [7], the response of a material element is assumed to be a function of the state (or "internal") variables *and* what Lubliner [6] refers to as "external" variables. These external variables are usually taken to be the deformation gradient, the temperature, and the temperature gradient, the time histories of which are here regarded as stimuli. No distinction is made in the present formulation between "external" variables and "state" variables, so that if, e.g., the response depends explicitly upon the deformation gradient (as it does in the case of thermoelasticity), then this must be explicitly provided for by including a state variable whose value is that of the appropriate deformation gradient. The present formulation is similar to the purely mechanical theories of Dashner [8] and of Onat [9] in this respect. The purpose of this feature is to remove from the constitutive relations any extraneous (and perhaps awkward) dependence on a particular reference configuration, in accord with the conceptual role of the constitutive relations as stated in the first paragraph of this subsection.

2.2. state evolution

The collection of state variables will be denoted by S. In what follows, it will be convenient to work with a single, typical state variable $\mathbf{S} \in S$ which will be taken to be a second-rank tensor; the analogous expressions for $\mathbf{S}$ of other than second rank, and for multiple state variables, may usually be written immediately.

Before discussing the thermomechanical response itself, the issue of state-variable evolution will be addressed. In line with the statements of the previous subsection, and using the single state variable S as an example, the state of a material element is regarded to evolve according to

$$S(t+s) = \Sigma(S(t),\, s;\, \mathbf{F}_t(\alpha),\, \theta_t(\alpha),\, \mathbf{g}_t(\alpha)) \;, \quad s > 0 \;. \tag{2.1}$$

In (2.1), Σ is a function of its first two arguments and a *functional* of its last three, and s is any real number greater than zero. Also, $\mathbf{F}_t(\alpha)$ is the time-varying deformation gradient with respect to the configuration at time t, i.e.

$$\mathbf{F}_t(\alpha) = \mathbf{F}(t+\alpha)\,\mathbf{F}^{-1}(t) \;, \quad 0 < \alpha \le s \;; \tag{2.2}$$

and $\theta_t(\alpha)$ and $\mathbf{g}_t(\alpha)$ are defined by

$$\theta_t(\alpha) = \theta(t+\alpha) - \theta(t) \;, \quad \mathbf{g}_t(\alpha) = \nabla\theta_t(\alpha) \;, \quad 0 < \alpha \le s \;, \tag{2.3}$$

where ∇ represents the spatial gradient operator $\partial / \partial \mathbf{x}$. (Here and throughout, the spatial position $\mathbf{x}$ is not explicitly included among the arguments of functions for brevity.) The notation of (2.1) is meant to indicate that the functional Σ depends on the functions $\mathbf{F}_t(\alpha)$, $\theta_t(\alpha)$, and $\mathbf{g}_t(\alpha)$ for $0 < \alpha \le s$. It is assumed that $\mathbf{F}$ and θ are continuously differentiable functions of time, so that $\mathbf{F}_t(\alpha)$, $\theta_t(\alpha)$, and $\mathbf{g}_t(\alpha)$ are also continuously differentiable with respect to α for all $\alpha > 0$ and all t. Equation (2.1) is essentially a mathematical statement of what is meant by the "state" of a material element; it is similar to that employed by Dashner [8] in the context of a purely mechanical theory.

Our aim now is to reduce the functional expression (2.1) to a rate equation for $\mathbf{S}$ by introducing certain plausible assumptions. To this end, the notation $\mathbf{Q}(\alpha)[\mathbf{S}(t+\alpha)]$ for the transformation of $\mathbf{S}(t+\alpha)$ under a superposed rigid-body rotation $\mathbf{Q}(\alpha)$ is introduced. In this notation, $\mathbf{Q}(\alpha)$ is a proper orthogonal rotation tensor with $\mathbf{Q}(\alpha) = \mathbf{1}$ for $\alpha \le 0$ (otherwise arbitrary), so that $\mathbf{Q}(\alpha)\,\mathbf{F}(t+\alpha)$ corresponds to a motion that differs from the given motion by a rigid rotation for times greater that t. For example, if $\mathbf{S}$ is known to transform objectively under superposed rigid rotations, then $\mathbf{Q}(\alpha)[\mathbf{S}(t+\alpha)] = \mathbf{Q}(\alpha)\,\mathbf{S}(t+\alpha)\,\mathbf{Q}^T(\alpha)$. Equation (2.1) must hold for all motions; therefore

$$\mathbf{Q}(s)[\mathbf{S}(t+s)] = \Sigma(\mathbf{S}(t),\, s;\, \mathbf{Q}(\alpha)\,\mathbf{F}_t(\alpha),\, \theta_t(\alpha),\, \mathbf{Q}(\alpha)\,\mathbf{g}_t(\alpha)) \;, \quad s > 0 \;. \tag{2.4}$$

Since $\mathbf{Q}(\alpha)$ is arbitrary for $\alpha > 0$, it may be chosen so that

$$\mathbf{Q}(\alpha) = \mathbf{R}_t^T(\alpha) \;, \quad 0 < \alpha \le s \;, \tag{2.5}$$

where $\mathbf{R}_t$ arises from the polar decomposition $\mathbf{F}_t = \mathbf{R}_t\mathbf{U}_t$. Equation (2.4) then becomes

$$\mathbf{R}_t^T(s)[\mathbf{S}(t+s)] = \Sigma(\mathbf{S}(t),\, s;\, \mathbf{U}_t(\alpha),\, \theta_t(\alpha),\, \mathbf{R}_t^T(\alpha)\,\mathbf{g}_t(\alpha)) \;, \quad s > 0 \;. \tag{2.6}$$

One method of deducing a rate equation for S from (2.6) would be to simply take the material rate of both sides of this equation. However, it appears that some knowledge of the functional Σ is required to proceed in this direction.

Instead, attention is simply restricted to cases in which the functional Σ may be written in *differential form* [24]. That is, it is presumed that the value of Σ for any $s > 0$ may be regarded as the solution to an initial value problem in which $\mathbf{S}(t)$ represents the initial value, and the last three arguments (and possibly their rates of some order) form the "forcing functions." Clearly a very large class of functionals may be represented in this way. Equation (2.1) may be written as an initial value problem as follows:

$$D_\alpha\{\mathbf{F}_t(\alpha), \theta_t(\alpha), \mathbf{g}_t(\alpha), \mathbf{S}(t+\alpha), \alpha\} = 0\ , \quad \mathbf{S}(t+\alpha)\Big|_{\alpha=0} = \mathbf{S}(t). \tag{2.7}$$

In (2.7), D_α represents a continuous ordinary differential operator with respect to α; i.e. D_α is a continuous function of its arguments and their derivatives, of some order, with respect to α. The initial value problem (2.7) is solved, and the solution evaluated at $\alpha = s$ to yield $\mathbf{S}(t+s)$.

The order of the rates involved in the differential operator D_α may be deduced as follows. First, D_α must involve only zero- and first-order derivatives of $\mathbf{S}(t+\alpha)$, since the single initial condition given in (2.7) must be sufficient to yield a unique solution. The "smoothness" of the solution $\mathbf{S}(t+\alpha)$ will be determined by the order of the derivatives of the first three arguments appearing in D_α; e.g. if only zero- and first-order derivatives are present, then continuously differentiable stimuli will result in a continuously differentiable $\mathbf{S}(t+\alpha)$. Intuitively, "solids-type" behavior is associated with a response and a state that change abruptly with abruptly changing stimuli. Accordingly, it is assumed that D_α involves only zero- and first-order derivatives with respect to α of its first three arguments. With very little loss in generality, then, (2.7) may be replaced by

$$\dot{\mathbf{S}}(t+\alpha) = \mathbf{E}\ (\mathbf{F}_t, \theta_t, \mathbf{g}_t, \dot{\mathbf{F}}_t, \dot{\theta}_t, \dot{\mathbf{g}}_t, \mathbf{S}, \alpha)\ , \quad \mathbf{S}(t+\alpha)\Big|_{\alpha=0} = \mathbf{S}(t)\ . \tag{2.8}$$

In (2.8), $\mathbf{E}$ is a continuous function of its arguments, and an overdot denotes derivative with respect to α.

Equation (2.8) may be transformed under superposed rigid-body motions of the type considered in connection with (2.6) to obtain

$$\frac{d}{d\alpha}\left[\mathbf{R}_t^T(\alpha)[\mathbf{S}(t+\alpha)]\right] = \mathbf{E}\ (\mathbf{U}_t, \theta_t, \mathbf{R}_t^T\mathbf{g}_t, \dot{\mathbf{U}}_t, \dot{\theta}_t, d(\mathbf{R}_t^T\mathbf{g}_t)/d\alpha\ , \mathbf{R}_t^T[\mathbf{S}], \alpha)\ , \tag{2.9}$$

$$\mathbf{R}_t^T(\alpha)[\mathbf{S}(t+\alpha)]\Big|_{\alpha=0} = \mathbf{S}(t)\ .$$

Finally, equation (2.9) is evaluated at $\alpha = 0$, and the facts that $\dot{\mathbf{U}}_t(\alpha = 0) = \mathbf{D}(t)$, $\mathbf{U}_t(\alpha = 0) = \mathbf{1}$, $\theta_t(\alpha = 0) = 0$, $\mathbf{g}_t(\alpha = 0) = \mathbf{0}$, and $\mathbf{R}_t^T(\alpha = 0) = \mathbf{1}$ are used to obtain

$$\overset{\circ}{\mathbf{S}}(t) = \mathbf{E}\ (\mathbf{D}(t), \dot{\theta}(t), \overset{\circ}{\mathbf{g}}(t), \mathbf{S}(t))\ . \tag{2.10}$$

In (2.10), $\mathbf{D}$ denotes the symmetric part of the spatial velocity gradient $\mathbf{L}$, and $\overset{\circ}{\mathbf{S}}$ represents the left-hand side of (2.9) evaluated at $\alpha = 0$. For example, for the case in which $\mathbf{S}$ transforms objectively under superposed rigid rotations (i.e. $\mathbf{S}^+ = \mathbf{Q}\mathbf{S}\mathbf{Q}^T$), then

$$\overset{\circ}{\mathbf{S}} = \dot{\mathbf{S}} + \mathbf{S}\mathbf{W} - \mathbf{W}\mathbf{S}\ , \tag{2.11}$$

where $\mathbf{W}$ is the antisymmetric part of $\mathbf{L}$. (That $\dot{\mathbf{R}}_t(\alpha = 0) = \mathbf{W}(t)$ is easily seen by taking the derivative with respect to α of (2.2) and evaluating at $\alpha = 0$.) Similarly, $\overset{\circ}{\mathbf{g}} = \dot{\mathbf{g}} - \mathbf{W}\mathbf{g}$.

It bears emphasis that the rate $\overset{\circ}{(\ )}$ is obtained as follows: first, the argument "( )" is transformed under a superposed rigid rotation $\mathbf{R}_t^T$ [see equation (2.5)], then the material rate of the transformed quantity is taken, and finally the result is evaluated at the instant $\alpha = 0$ when $\mathbf{R}_t = \mathbf{1}$. In the language of general tensor analysis on manifolds, the rate $\overset{\circ}{(\ )}$ is a special case of the *Lie derivative* (see Marsden and Hughes [25] for a discussion of tensor analysis on manifolds as it relates to continuum mechanics). It is further emphasized that the particular form of the rate $\overset{\circ}{(\ )}$ [e.g. see equation (2.11)] depends on the manner in which the argument transforms under superposed rigid rotations. Indeed, the rate $\overset{\circ}{(\ )}$ is equivalent to the familiar Jaumann rate only for the case in which the argument transforms objectively under superposed rigid rotations. For tensors that transform differently, the corresponding rate expression must be obtained by resorting to the definition as described at the beginning of this paragraph.

Equation (2.10) is the desired rate equation for the typical state variable $\mathbf{S}$. As a further simplifying restriction, it is assumed that the dependence of $\mathbf{E}$ on $\mathbf{D}$, $\dot{\theta}$, and $\overset{\circ}{\mathbf{g}}$ is *linear*. Even with this restriction, the resulting theory will be seen to encompass most of the usual concepts encountered in the modeling of rate-dependent-solid behavior. In this connection, Lubliner [6] notes that linear dependence of this kind results in "reversible" behavior in a sense defined by him. In line with the assumed linearity of $\mathbf{E}$, (2.10) may be written

$$\overset{\circ}{\mathbf{S}} = \mathbf{A} \cdot \mathbf{D} + \mathbf{Z}\,\dot{\theta} + \mathbf{P} \cdot \overset{\circ}{\mathbf{g}} + \boldsymbol{\sigma}\,, \tag{2.12}$$

where $\mathbf{A}$, $\mathbf{Z}$, $\mathbf{P}$, and $\boldsymbol{\sigma}$ are, respectively, fourth-, second-, third-, and second-rank tensor functions of the state if $\mathbf{S}$ is a second-rank tensor. Of course, these tensor functions must transform properly under superposed rigid-body rotations, consistent with (2.12) and the transformation rule for $\mathbf{S}$.

As mentioned in the previous subsection, the response $\{\mathbf{T}, \psi, \eta, \mathbf{q}\}$ is assumed to depend exclusively upon the state, the evolution of which is exemplified by (2.12) for the typical state variable $\mathbf{S}$. Before proceeding to deduce restrictions on the response functions, three special state variables will be introduced whose utility will be demonstrated subsequently. First, the absolute temperature θ itself may be recovered as a state variable by simply choosing

$$\mathbf{A} = 0\,, \quad Z = 1\,, \quad \mathbf{P} = \mathbf{0}\,, \quad \sigma = 0\,. \tag{2.13}$$

(Note that Z and σ are scalars in this case.) Similarly, the spatial temperature gradient may be recovered as a state variable by choosing

$$\mathbf{A} = 0\,, \quad \mathbf{Z} = \mathbf{0}\,, \quad \mathbf{P} = \mathbf{1}\,, \quad \boldsymbol{\sigma} = \mathbf{0}\,, \tag{2.14}$$

in which $\mathbf{P}$ is now a second-rank tensor. In view of (2.13) and (2.14), and the fact that it is generally convenient to have the response depend directly on the temperature and the temperature gradient, θ and $\mathbf{g}$ will henceforth be explicitly

included among the state variables.

The final special state variable that will be considered is a second-rank tensor $\mathbf{H}$, which obeys the evolution equation

$$\overset{\circ}{\mathbf{H}} = \mathbf{D}\,\mathbf{H} - \boldsymbol{\beta}\,\mathbf{H}\,, \tag{2.15}$$

which is clearly a special case of (2.12). Under superposed rigid-body rotations, $\mathbf{H}$ is specified to transform according to $\mathbf{H}^+ = \mathbf{Q}\mathbf{H}$, which can be motivated by appeal to the primitive constitutive form (2.8). With this transformation law, it is clear that $\overset{\circ}{\mathbf{H}} = \dot{\mathbf{H}} - \mathbf{W}\mathbf{H}$, so that $\overset{\circ}{\mathbf{H}}{}^+ = \mathbf{Q}\overset{\circ}{\mathbf{H}}$ and $\boldsymbol{\beta}^+ = \mathbf{Q}\boldsymbol{\beta}\mathbf{Q}^T$ (note that $\boldsymbol{\beta}$ is, in general, a function of the state). It bears emphasis that the rate $\overset{\circ}{\mathbf{H}}$ is not of the "Jaumann rate" form (2.11), owing to the manner in which $\mathbf{H}$ transforms under superposed rigid rotations. The significance of $\mathbf{H}$ will be discussed subsequently; however, here it is mentioned that $\mathbf{H}$ equals the deformation gradient of the current configuration with respect to the initial configuration if $\boldsymbol{\beta}$ is set to zero.

2.3. thermomechanical response

Attention is now focused on the task of deducing restrictions on the thermomechanical response $\{\mathbf{T}, \psi, \eta, \mathbf{q}\}$, which is now assumed to be a function of $\mathbf{H}$, θ, $\mathbf{g}$, and any other state variables that may exist. The additional state variables will again be exemplified by the single variable $\mathbf{S} \in S$. The idea is to find restrictions on the response functions that are demanded by the requirement that the second law of thermodynamics must be satisfied for all possible stimuli. If one accepts the Clausius-Duhem inequality as an adequate statement of the second law, then the deduction of these restrictions follows a well-known procedure (see [10]). Without indulging in a discussion of the various approaches to continuum thermodynamics that one may take, it is here remarked that objections have been raised to the Clausius-Duhem inequality as a basis for continuum thermodynamics (e.g. [11]), and that alternatives have been proposed (e.g. [12] and [13]).

The Clausius-Duhem inequality may be written in the form

$$\rho\dot{\psi} + \rho\eta\dot{\theta} - \mathbf{T}\cdot\mathbf{D} + \theta^{-1}\,\mathbf{q}\cdot\mathbf{g} \leq 0\,, \tag{2.16}$$

where ρ is the current-configuration mass density. In the present context, the procedure referred to above consists of substituting the response functions into (2.16) and carrying out the indicated material rates with the help of (2.12) and (2.15). The resulting inequality is then required to hold for all arbitrary and independent choices of $\mathbf{L}$, $\dot{\theta}$, and $\dot{\mathbf{g}}$, which could, at least in principle, be brought about by suitable body force and radiative heat supply fields. The resulting restrictions are as follows:

$$\eta = -\frac{\partial\psi}{\partial\theta} - \frac{\partial\psi}{\partial S_{ij}} Z_{ij}\,, \tag{2.17}$$

$$T_{ij} = \rho\left[\frac{\partial\psi}{\partial H_{ik}} H_{jk}\right]_s + \rho\left[\frac{\partial\psi}{\partial S_{kl}} A_{klij}\right]_s\,, \tag{2.18}$$

$$\frac{\partial \psi}{\partial S_{ij}} P_{ijk} + \frac{\partial \psi}{\partial g_k} = 0 , \tag{2.19}$$

$$\left[\frac{\partial \psi}{\partial H_{ik}} H_{jk} \right]_a + 2 \left[\frac{\partial \psi}{\partial S_{ik}} S_{jk} \right]_a - \left[\frac{\partial \psi}{\partial S_{kl}} P_{kli} g_j \right]_a = 0 . \tag{2.20}$$

In (2.17)-(2.20), Cartesian components of the relevant tensors are employed for clarity, and subscripts $[\ ]_s$ and $[\ ]_a$ are used to denote the symmetric and antisymmetric parts; e.g., $[B_{ij}]_s = \frac{1}{2}(B_{ij} + B_{ji})$. Expressions analogous to (2.17)-(2.20), but for state variables of other than second tensorial rank, and for multiple state variables, may be deduced in a similar manner.

After using (2.17)-(2.20) in the Clausius-Duhem inequality, one obtains

$$-\rho \frac{\partial \psi}{\partial H_{ij}} \beta_{ik} H_{kj} + \rho \frac{\partial \psi}{\partial S_{ij}} \sigma_{ij} + \theta^{-1} q_i g_i \leq 0 . \tag{2.21}$$

We define the *dissipation rate* γ per unit mass by

$$\gamma = \frac{\partial \psi}{\partial H_{ij}} \beta_{ik} H_{kj} - \frac{\partial \psi}{\partial S_{ij}} \sigma_{ij} , \tag{2.22}$$

so that (2.21) becomes $\rho\gamma - \theta^{-1} \mathbf{q} \cdot \mathbf{g} \geq 0$. Manipulation of (2.22) together with (2.18) results in the alternative expression

$$\gamma = \rho^{-1} T_{ij} \beta_{ij} + \frac{\partial \psi}{\partial S_{ij}} \left\{ [\beta_{kl}]_s A_{ijkl} + [\beta_{kl}]_a P_{ijk} g_l - 2[\beta_{ik}]_a S_{kj} - \sigma_{ij} \right\} . \tag{2.23}$$

Now, the first law of thermodynamics (i.e. conservation of energy) may be written

$$\rho \dot{\varepsilon} = T_{ij} D_{ij} + \rho r - q_{i,i} , \tag{2.24}$$

where ε is the internal energy per unit mass, and r is the radiative heat supply per unit mass. Use of (2.23) and (2.17)-(2.20) in (2.24) results in the two alternative statements of conservation of energy

$$\rho \theta \dot{\eta} = \rho\gamma + \rho r - q_{i,i} \quad \text{and} \tag{2.25a}$$

$$\rho^{-1} T_{ij} D_{ij} = \dot{\psi} + \eta \dot{\theta} + \gamma . \tag{2.25b}$$

From (2.25a) and (2.25b), the following special forms of the energy equation, which hold for restricted classes of processes as noted, may be deduced:

$$\theta \dot{\eta} = \gamma \qquad \text{adiabatic (i.e. } \rho r - q_{i,i} = 0) , \tag{2.26a}$$

$$\mathbf{T} \cdot \mathbf{D} = \rho \dot{\psi} + \rho\gamma \qquad \text{isothermal (i.e. } \dot{\theta} = 0) , \tag{2.26b}$$

$$0 = \rho\gamma + \rho r - q_{i,i} \qquad \text{isentropic (i.e. } \dot{\eta} = 0) . \tag{2.26c}$$

Equations (2.26) lend motivation to the term "dissipation rate" for the quantity γ. (The definition of dissipation rate used here is somewhat different from that of Coleman's [1] "internal dissipation." The motivation for introducing the definition (2.22) is that, under certain conditions, γ so-defined is analogous to the "rate of plastic work" encountered in isothermal theories of plasticity and viscoplasticity.)

Finally, it is noted that, if the state (and therefore the response) depends on the temperature gradient $\mathbf{g}$ only through its current value (and not its past history), then $\mathbf{P} = 0$ and $\mathbf{A}$, $\mathbf{Z}$, and $\boldsymbol{\sigma}$ are independent of $\mathbf{g}$. In this case, it is clear from (2.19) that ψ is independent of the current value of $\mathbf{g}$, and consequently that $\mathbf{T}$ and η are also independent of $\mathbf{g}$ by (2.18) and (2.17). In this case, it is clear that $\gamma \geq 0$ holds in addition to (2.21), since (2.21) must hold for $\mathbf{g} = \mathbf{0}$. It bears mentioning that, in most applications, it is further assumed that $\mathbf{q} \cdot \mathbf{g} \leq 0$ always, so that

$$\gamma \geq 0 \quad \text{and} \quad \mathbf{q} \cdot \mathbf{g} \leq 0 \tag{2.27}$$

hold separately.

Before closing this section, the physical significance of the state variable $\mathbf{H}$ will be discussed. With reference to (2.15), and as mentioned previously, if $\boldsymbol{\beta} = 0$ then $\mathbf{H}$ is equal to the deformation gradient of the current configuration with respect to the initial configuration (or the configuration at which the initial condition $\mathbf{H} = \mathbf{1}$ applies). It is therefore immediately seen that the constitutive equations for thermoelasticity may be recovered by stipulating that the state is given by $\{\mathbf{H}, \theta, \mathbf{g}\}$ only, that $\boldsymbol{\beta} = \mathbf{0}$, that $\mathbf{H} = \mathbf{1}$ when $\mathbf{T} = 0$, and finally that only $\mathbf{q}$ depends on $\mathbf{g}$ as described in the previous paragraph.

For cases in which $\boldsymbol{\beta} \neq \mathbf{0}$, $\boldsymbol{\beta}$ can be interpreted as a *plastic velocity gradient* and $\mathbf{H}$ as an *elastic deformation gradient* under certain conditions. In particular, and omitting the mathematical details, a process which takes the deformation gradient $\mathbf{F}$ from $\mathbf{F}_1$ at time t_1 to $\mathbf{F}_2$ at time t_2 can be shown to approach arbitrarily closely an *elastic process* when the time scale is compressed. (Loosely, the term "elastic process" here refers to processes in which the sequence of states is retraced if the process is followed by another process that is derived from the first by reversing the direction of time. It is easily shown that thermoelastic materials are capable of sustaining only elastic processes. Additionally, if the state is independent of the history of the temperature gradient as described above, then $\gamma = 0$ at each instant during an elastic process.) In other words, the present constitutive framework exhibits what many authors have called "instantaneously elastic" response. The physical basis for this behavior is that all microscale processes associated with departures from elastic response must necessarily proceed at finite rates; an intuitively appealing conjecture for solids. This point is also related to what Lubliner [6] calls "reversible behavior," as mentioned in Subsection 2.2. Looking at (2.18), if the function ψ is such that $\mathbf{T} = 0$ when $\mathbf{H} = \mathbf{1}$ and $\theta = \theta_0$ (a reference temperature) for all values of the other arguments, then the stress may be reduced to zero by undergoing an elastic process in which the deformation gradient is taken from its current value $\mathbf{F}$ to $\mathbf{Q}^T\mathbf{H}^{-1}\mathbf{F}$, and θ is taken to θ_0, in a vanishingly small time interval. Here, $\mathbf{Q}$ is an arbitrary rotation tensor.

In metal plasticity, it has become almost standard to decompose the total deformation gradient $\mathbf{F}$ into elastic and plastic parts as $\mathbf{F} = \mathbf{F}^e\mathbf{F}^p$, obtained by imagining an "instantaneous elastic unloading" from the current configuration at each instant. Typically, the stress is then assumed to depend only upon $\mathbf{F}^e$. Much discussion has appeared in the literature concerning the applicability and propriety of

such a multiplicative decomposition (see, e.g., [14] and [15]). Here the view is taken that the decomposition $\mathbf{F} = \mathbf{F}^e \mathbf{F}^p$ should not play the part of a primitive concept, or starting point, of a constitutive theory; rather it should serve only as an interpretive aid in existing theoretical frameworks. In other words, if $\mathbf{F} = \mathbf{F}^e \mathbf{F}^p$ is applicable to a particular material, then it should be possible to execute an unloading at any instant to zero stress *using the material model*, and thereby interpret some of the state variables appearing in the model in terms of elastic and plastic deformation gradients. With reference to the previous paragraph, it is clear that the tensor $\mathbf{HQ}(t)$ ($\mathbf{Q}(t)$ an arbitrary, time-varying rotation tensor), may be interpreted as an elastic deformation gradient if the stated condition is met. Accordingly, $\boldsymbol{\beta} - \dot{\mathbf{H}}\mathbf{Q}\mathbf{Q}^T\mathbf{H}^{-1}$ may be interpreted as a "plastic velocity gradient." On the other hand, if ψ is such that $\mathbf{H} = \mathbf{1}$ and $\theta = \theta_0$ does *not* imply $\mathbf{T} = \mathbf{0}$ for all values of the other state variables, then the interpretation of $\mathbf{HQ}(t)$ as an "elastic deformation gradient" looses some of its utility. This may be the case, for example, in metals that exhibit a strong Bauschinger effect, and in some kinds of polymers. In such cases, however, it may still be useful to consider "fast" processes (although perhaps not involving unloading to zero stress) for the purpose of assigning a physical interpretation to $\mathbf{H}$. These issues will be addressed in a detailed manner in a forthcoming article.

Before proceeding to the specific example of the next section, some further comments are made regarding the relation between the present formulation and those based on $\mathbf{F} = \mathbf{F}^e \mathbf{F}^p$. In formulating plasticity theories based on a multiplicative decomposition of the total deformation gradient, many authors have appealed to well-established concepts of plastic flow in metallic single crystals for motivation. In metallic single crystals, there exists a readily identifiable substructure, or *lattice*, that may be said to distort elastically, and through which the material may be said to flow plastically. Typically, developments of the theory of single crystal plasticity produce a rate expression for stress that involves stress rate corotational with the lattice. At first glance, it appears that the present framework, and in particular (2.15), is incapable of representing single crystal behavior since the rate $\overset{\circ}{(\ )}$ involves the *total* spin $\mathbf{W}$. This, however, is not the case. Indeed, a properly invariant function $\boldsymbol{\beta}$ may be chosen so that the theory of single crystal plasticity is recovered. Correspondence between the resulting theory and the familiar concepts of single crystal behavior may then be made by performing instantaneous unloadings using the constitutive equations themselves, as discussed above.

3. An Application: Isotropic Viscoplasticity

The above-described constitutive framework may be specialized to describe a very large range of inelastic behavior in solids, including virtually all of the familiar concepts of isotropic and anisotropic viscoplasticity (including crystal viscoplasticity), and much of nonlinear viscoelasticity. Indeed, corresponding models for rate-independent plasticity, and for linearly viscous, fluids-type behavior, may be recovered by applying appropriate limiting processes to suitable models for viscoplasticity. In this section, a specialization of the general theory presented in

Section 2 will be considered, in which only a single scalar state variable exists in addition to $\mathbf{H}$, θ, and $\mathbf{g}$. This model is necessarily isotropic, and includes the usual J_2-viscoplasticity theory as a special case. However, it will be shown that some types of physically relevant behavior not predicted by J_2-viscoplasticity theory can be recovered as well.

Consider the theory of Section 2, with the state specified by $\{\mathbf{H}, \theta, \mathbf{g}, \alpha\}$, where α is a scalar state variable. Focusing on the mechanical response, our aim is to construct the function $\boldsymbol{\beta}$ and the evolution equation for α in accord with a set of simple, plausible assumptions that are representative of the behavior of metals. First, it is assumed that the conditions leading up to (2.27) are met, so that (2.27) holds. Next, it is assumed that the Helmholtz free energy ψ is independent of α. This is consistent with the notion that α is a hardening parameter whose change leaves the crystalline lattice, and therefore the material's ability to store elastic strain energy, essentially unchanged. According to (2.23) and (2.18), then, the dissipation rate is

$$\gamma = \rho^{-1}\, \mathbf{T} \cdot \boldsymbol{\beta}\,, \tag{3.1}$$

and the Cauchy stress is given by

$$\mathbf{T} = \rho \left[\frac{\partial \psi}{\partial \mathbf{H}} \mathbf{H}^T \right]_s . \tag{3.2}$$

In what follows, it will be assumed that the "plastic deformation" is volume-preserving. In anticipation of this, ψ is written as $\psi = \rho\, W(\mathbf{H}, \theta)$, from which it can be shown that

$$\mathbf{T} = J^{-1} \left[\frac{\partial W}{\partial \mathbf{H}} \mathbf{H}^T \right]_s . \tag{3.3}$$

In (3.3), $J = \det \mathbf{F} = \det \mathbf{H}$ [see equation (3.6)], where $\mathbf{F}$ is the total deformation gradient.

In view of (3.3) and the invariance requirements on $W(\mathbf{H}, \theta)$ and $\boldsymbol{\beta}(\mathbf{H}, \theta, \alpha)$, the function $\boldsymbol{\beta}(\mathbf{H}, \theta, \alpha)$ can always be written as a function of $\mathbf{T}$, θ, and α with mild restrictions on W. Since both $\boldsymbol{\beta}$ and $\mathbf{T}$ transform objectively under superposed rigid-body rotations, $\boldsymbol{\beta}$ must be an isotropic function of $\mathbf{T}$, so that $\boldsymbol{\beta} = \bar{\mu}_0 \mathbf{1} + \bar{\mu}_1 \mathbf{T} + \bar{\mu}_2 \mathbf{T}^2$ by the Cayley-Hamilton theorem. Alternatively, this expression may be written in terms of the Cauchy stress deviator $\mathbf{T}' = \mathbf{T} - 1/3\ (\mathrm{tr}\ \mathbf{T})\mathbf{1}$ as

$$\boldsymbol{\beta} = \mu_0 \mathbf{1} + \mu_1 \mathbf{T}' + \mu_2 \mathbf{T}'^2 . \tag{3.4}$$

Here, μ_0, μ_1, and μ_2 are functions of α, θ, and the three invariants of $\mathbf{T}$

$$J_1 = \mathrm{tr}\ \mathbf{T}\,, \quad J_2 = \tfrac{1}{2}\left[(\mathrm{tr}\ \mathbf{T})^2 - \mathrm{tr}\ \mathbf{T}^2\right], \quad J_3 = \det \mathbf{T}\,. \tag{3.5}$$

As a matter of convenience, the equivalent set of invariants J_1, J'_2, and J'_3 will be used in what follows, where prime indicates invariant of $\mathbf{T}'$.

As is usual in metal plasticity, it is assumed that unloading a material element to zero stress from any state returns the element to a volume that depends

only on the temperature. It can be shown that a necessary and sufficient condition for this to hold is that

$$\operatorname{tr} \boldsymbol{\beta} = 0 . \tag{3.6}$$

Condition (3.6), together with (3.4), implies the restriction

$$3\mu_0 - 2J'_2 \, \mu_2 = 0 \tag{3.7}$$

Using (3.7), the second-law restriction (2.27) requires that

$$\rho\gamma = -2J'_2 \, \mu_1 + 3J'_3 \, \mu_2 \geq 0 . \tag{3.8}$$

Also, (3.7) and (3.4) combine to yield

$$\boldsymbol{\beta} = \frac{2}{3} J'_2 \, \mu_2 \mathbf{1} + \mu_1 \mathbf{T}' + \mu_2 \mathbf{T}'^2 . \tag{3.9}$$

Certain assumptions concerning the mechanical behavior are now introduced in order to further reduce the form (3.9). If $W(\mathbf{H}, \theta)$ is specified such that $\mathbf{T} = \mathbf{0}$ when $\mathbf{H} = \mathbf{1}$ and $\theta = \theta_0$ (a reference temperature), then $\mathbf{HQ}$ may be interpreted as an elastic deformation gradient, as described previously. Accordingly, the deformation gradient of a material element in the elastically unloaded (or "plastically deformed") configuration with respect to a fixed reference configuration is $\mathbf{Q}^T\mathbf{H}^{-1}\mathbf{F}$. Here, $\mathbf{F}$ is the total deformation gradient with respect to a reference configuration, and $\mathbf{Q}$ is again an arbitrary, time-varying rotation tensor. It is emphasized that consideration of this unloaded configuration is not mandatory and is purely an aid to the mathematical formulation of certain physical assumptions.

To proceed further, it is assumed that $\mathbf{H}$ represents "small" elastic deformations in the sense that $\mathbf{Y}$, in the polar decomposition

$$\mathbf{H} = \mathbf{P}(\mathbf{1} + \mathbf{Y}) , \tag{3.10}$$

is small. Here, $\mathbf{P}$ is a rotation tensor and $\mathbf{Y}$ is symmetric. The logarithmic plastic extension rate corresponding to a material direction $\mathbf{m}$ is

$$\dot{\lambda}_p \, \lambda_p^{-1} = \mathbf{m} \cdot \boldsymbol{\beta} \, \mathbf{m} + O(\mathbf{Y}) , \tag{3.11}$$

in which λ_p is the stretch of a material line element in the *unloaded* configuration, whose direction in the *current* configuration is along the unit vector $\mathbf{m}$. Now, it is always possible to find an orthonormal triad $\{\mathbf{v}_1, \mathbf{v}_2, \mathbf{v}_3\}$ such that

$$\mathbf{v}_i \cdot \mathbf{T}' \, \mathbf{v}_i = 0 , \quad i = 1, 2, 3 ; \tag{3.12}$$

i.e. such that the normal deviatoric stress is zero on planes whose normals are $\mathbf{v}_i$. One possible physical assumption that might be made is that the plastic extension rates are also zero, to $O(1)$, in these directions. Clearly the condition $\mu_0 = \mu_2 = 0$ is sufficient for this to hold; it turns out that it is also necessary. In other words, if

$$\boldsymbol{\beta} = \mu_1(J_1, J'_2, J'_3, \alpha) \, \mathbf{T}' , \tag{3.13}$$

then any cubic material element that suffers only deviatoric shear stresses on its

faces will likewise plastically deform exclusively by *shearing* on face-planes, and conversely. Additionally, for metals it is reasonable to remove the dependence of μ_1 in (3.13) on J_1 (i.e. pressure-independence of plastic flow). Having done this, (3.13) represents the classical J_2-viscoplasticity theory, except for the dependence of μ_1 on J'_3.

Equation (3.13) represents perhaps the simplest reasonable model for rate-dependent inelasticity in metals. However, it is well-known that the physical assumptions leading to this expression are not realized in most metals at large strains. In particular, large-strain twisting of thin-walled tubes generally results in the development of either axial deformation or axial stress, depending on whether the tube length is held fixed or not. This phenomenon is known as the *Swift effect*, following the original investigation by Swift [16] using solid bars.

The Swift effect is generally associated with anisotropy due to developing texture [17]. However, for some applications it may be desirable and practical to retain the isotropy of the present model, but still capture the Swift effect. If μ_0 and μ_2 in (3.4) are *not* zero, then some aspects of the Swift effect are exhibited by the present model. In particular, any material direction $\mathbf{v}$ such that $\mathbf{v} \cdot \mathbf{T}' \mathbf{v} = 0$, suffers the (approximate) logarithmic plastic extension rate

$$\mathbf{v} \cdot \boldsymbol{\beta}\, \mathbf{v} = \mu_2 (2/3\, J'^2_2 + \tau^2)\,. \tag{3.14}$$

Here, $\tau^2 = (\mathbf{T}'\mathbf{v}) \cdot (\mathbf{T}'\mathbf{v})$ (i.e. τ is the magnitude of the shear stress on the plane whose normal is $\mathbf{v}$). From (3.14) it is clear that a pure shear stress state, such as exists in a free-end torsion test of a thin-walled tube, produces axial plastic deformation. Also, since $J_1 = J'_3 = 0$ in a pure shear stress state, and since J'_2 is an even function of stress, the axial deformation rate must be an even function of the shear stress. This is consistent with the isotropy of the material model. Indeed, in the context of isotropic, rate-independent plasticity, both Hill [18] and Billington [21] note that the assumption of isotropy demands that the axial plastic deformation rate be an even function of the shear stress. They further note that classical isotropic plasticity, with a normality flow law, predicts nonzero axial plastic deformation in free-end torsion only if the yield function depends on J'_3.

In line with these observations, the following "generalized isotropic" model for rate-dependent metal plasticity is proposed:

$$\mu_1 = \frac{\dot{\varepsilon}_0}{\sqrt{-J'_2}} \left[\frac{\sqrt{-3\, J'_2}}{g_1(\alpha)} \right]^M, \quad \mu_2 = \frac{-\dot{\varepsilon}_0\, g_2(\alpha)}{J'_2} \left[\frac{\sqrt{-3\, J'_2}}{g_1(\alpha)} \right]^M; \tag{3.15}$$

$$\dot{\alpha} = [\, \mu_2 (4/27\, J'^2_2\, \mu_2 + 4/3\, \mu_1\, J'_3) - 4/9\, J'_2\, \mu_1^2 \,]^{1/2}\,. \tag{3.16}$$

In (3.15), $\dot{\varepsilon}_0$ is a constant and M is a rate-dependence exponent; rate-independent behavior is approached as $M \to \infty$. It should be noted that $J'_2 \le 0$ always, and that the hardening function $g_1(\alpha) > 0$ whereas $g_2(\alpha)$ may be positive, negative, or zero. The factor 3 under the radical in (3.15) is included so that the term $\sqrt{-3\, J'_2}$ would equal the axial stress in a uniaxial stress state; $g_1(\alpha)$ may therefore be regarded as a "flow stress" in uniaxial tension. The origin of (3.16) is that $\dot{\alpha}$ is

proportional to the root-mean-square of the principal plastic stretch rates. That is,

$$\dot{\alpha} = \frac{\sqrt{6}}{3}\left[\sum_{i=1}^{3}(\mathbf{a}_i \cdot \boldsymbol{\beta}\,\mathbf{a}_i)^2\right]^{1/2}, \tag{3.17}$$

where the $\mathbf{a}_i$'s are the principal directions of $\boldsymbol{\beta}$ (and of $\mathbf{T}$), and where the constant of proportionality was chosen so that $\dot{\alpha}$ would equal the axial plastic stretch rate in uniaxial tension. Finally, it is noted that the second-law restriction (3.8) requires that

$$-\sqrt{3} \le g_2(\alpha) \le \sqrt{3}\,. \tag{3.18}$$

Assuming isotropic elastic response (i.e. W in (3.3) is an isotropic function of $\mathbf{H}^T\mathbf{H}$), and employing the small-elastic-strain approximation (3.10), the stress response is given by

$$\overset{\circ}{\mathbf{T}}' = 2G(\mathbf{D}' - \boldsymbol{\beta})\,, \quad J_1 = 3\kappa\,\mathrm{tr}\,\mathbf{D} \tag{3.19}$$

to first order in $\mathbf{Y}$. Here, G is the shear modulus and κ is the bulk modulus. The $\boldsymbol{\beta}$ appearing in (3.19) is given by (3.9), where μ_1 and μ_2 are in turn as given in (3.15).

4. Discussion and Conclusions

With regard to the first of (3.19), it bears emphasizing that the corotational rate of Cauchy stress that appears is the Jaumann rate (i.e. that involving $\mathbf{W}$), and that this is the *only* corotational rate consistent with the assumptions made in this single-state-variable formulation. In conventional formulations that begin with an *ad hoc* decomposition of $\mathbf{D}$ into elastic and plastic parts, it is generally necessary to make some choice for the corotational stress rate. For example, the corotational rate involving $\dot{\mathbf{R}}\mathbf{R}^T$ (where $\mathbf{F} = \mathbf{RU}$ is the right polar decomposition of the total deformation gradient) is often preferred over the Jaumann rate, since its use eliminates the aphysical stress oscillations present when the Jaumann rate is used in conjunction with kinematic hardening [19]. It is, in fact, possible to formulate a model within the present framework in which the Jaumann rate in (3.19) is replaced by the rate involving $\dot{\mathbf{R}}\mathbf{R}^T$. However, to do so it is necessary to include among the state variables both the left stretch tensor $\mathbf{V}$ (from $\mathbf{F} = \mathbf{VR}$), and another second-rank tensor whose evolution equation depends on $\mathbf{V}$ in a complicated manner. It is difficult to justify such state variables on physical grounds. Indeed, an attraction of the present constitutive framework is that the influence of any past configuration or history must be accounted for *explicitly*, by inclusion of appropriate state variables. Within this framework, the physical phenomena associated with the notion of kinematic hardening may be modeled by including one or more physically meaningful, tensorial state variables. Dafalias [20] has made points similar to the forgoing in a slightly different context.

An advantage of the "generalized isotropic" viscoplasticity model of Section 3 is that the hardening functions $g_1(\alpha)$ and $g_2(\alpha)$ may be easily measured with just a single material test. Specifically, $g_1(\alpha)$ may be determined from the shear-stress

response in monotonic, free-end torsion of a thin-walled tube, whereas $g_2(\alpha)$ may be obtained from the axial extension that occurs during the test. Indeed, from (3.19), (3.9), and (3.15), it is easily seen that

$$g_2(\alpha) = \frac{3G\,D_{33} - 3D_{23}\,\tau}{G\,D_{23} - \tfrac{1}{2}\,\dot{\tau}} \approx \frac{3D_{33}}{D_{23}} \quad \text{and} \tag{4.1}$$

$$g_1(\alpha) = \sqrt{3}\,\tau\left[\frac{\dot{\varepsilon}_0}{D_{23} - \dot{\tau}/2G}\right]^{1/M} \approx \sqrt{3}\,\tau\,. \tag{4.2}$$

In (4.1) and (4.2), τ is the torsional (i.e. shear) component of Cauchy stress, whereas D_{33} and D_{23} are the axial and torsional components of the deformation rate. Typically, D_{23} would be prescribed, and τ and D_{33} would be measured. The approximations indicated in (4.1) and (4.2) are related to the fact that $G >> \tau$; in (4.2) the fact that (typically) $M > 50$ has also been used. In addition to (4.1) and (4.2), there also holds

$$\dot{\alpha} = 2/3\,(D_{23} - \dot{\tau}/2G)\,\{[g_2(\alpha)]^2/3 + 1\}^{1/2} \approx 2/3[3(D_{33})^2 + (D_{23})^2]^{1/2}\,. \tag{4.3}$$

The stress response in uniaxial tension and in fixed-end torsion, which depends on $g_1(\alpha)$ and $g_2(\alpha)$ in a more complicated way than in the free-end-torsion case, may then be used to assess the validity of the model's predictions.

As mentioned above, the isotropy of the model requires that a stress reversal in free-end torsion does *not* reverse the sense of the axial deformation rate. If the Swift effect were due entirely to texture formation, then such a stress reversal should result in a reversal of axial deformation rate. (In this connection, see [22], in which an analytical solution is given for the stress response of an idealized polycrystal with developing texture in simple shear.) However, in their study using aluminum, Freudenthal and Ronay [23] report that the axial deformation continues in the same sense in reversed torsion after small amounts of additional strain have accumulated. This suggests that the present "generalized isotropic" model may be useful for many purposes over a fairly large range of strain, particularly for metals that do not exhibit a strong Bauschinger effect.

The development of Section 2 demonstrates the feasibility of formulating a general constitutive framework of practical significance, starting with only a small set of conceptually clear assumptions and definitions. The resulting construct then serves to define the state and the response at future times, given the state at the current time and the future stimuli. The generalized isotropic model presented in Section 3 represents an example of the usefulness of the general theoretical framework. Ideally, one may choose the type and number of state variables, decide on the nature of the dependencies in (2.17)-(2.20), and then appeal to physical reasoning to define the remaining constitutive functions. This process has been completed for metallic single crystals, and for a class of strongly cross-linked polymers. These cases will be presented in future articles.

ACKNOWLEDGEMENT

This work was supported by the U.S. Army Research Office under Contract No. DAAL-03-86-K-0169 with the University of California, San Diego, for which the author is grateful.

REFERENCES

[1] B. D. Coleman, *Arch. Rational Mech. Anal.* **17**, pp. 1-46 (1964).

[2] B. D. Coleman and M. E. Gurtin, *J. Chem. Phys.* **47,** pp. 597-613 (1967).

[3] J. R. Rice, *J. Mech. Phys. Solids* **19,** pp. 433-455 (1971).

[4] J. Kestin and J. R. Rice, in *A Critical Review of Thermodynamics* (ed. by E. B. Stuart *et al.*), p. 275. Mono Book Corp., Baltimore (1970).

[5] J. Kratochvil, *Acta Mech.* **16,** pp. 127-142 (1973).

[6] J. Lubliner, *Acta Mech.* **17,** pp. 109-119 (1973).

[7] K. C. Valanis, *J. Math. and Phys.* **45,** pp. 197-212 (1966).

[8] P. A. Dashner, *Int. J. Solids Structures* **22,** pp. 571-592 (1986).

[9] E. T. Onat, in *IUTAM Symposium on Thermoinelasticity,* East Kilbride, U.K., 1968, pp. 213-225. Springer Verlag, Wien (1970).

[10] B. D. Coleman and W. Noll, *Arch. Rational Mech. Anal.* **13,** pp. 167-178 (1963).

[11] W. A. Day, *Acta Mech.* **27,** pp. 251-255 (1977).

[12] A. E. Green and P. M. Naghdi, *Proc. Royal Soc. London A.* **357,** pp. 253-270 (1977).

[13] W. A. Day, *The Thermodynamics of Simple Materials with Fading Memory,* Springer Verlag, Berlin (1972).

[14] P. A. Dashner, *J. Appl. Mech.* **53,** pp. 55-60 (1986).

[15] D. J. Bammann and G. C. Johnson, *Acta Mech.* **70,** pp. 1-13 (1987).

[16] H. W. Swift, *Engineering* **163,** pp. 253-257 (1947).

[17] F. Montheillet, M. Cohen, and J. J. Jonas, *Acta Metall.* **32,** pp. 2077-2089 (1984).

[18] R. Hill, *The Mathematical Theory of Plasticity,* p. 37. Clarendon Press, Oxford (1950).

[19] Y. F. Dafalias, *J. Appl. Mech.* **50,** pp. 561-565 (1983).

[20] Y. F. Dafalias, in *Plasticity Today* (ed. by A. Sawczuk and G. Bianchi), pp. 135-151. Elsevier Applied Science Publishers, Essex (1985).

[21] E. W. Billington, *J. Phys. D: Appl. Phys.* **9,** pp. 533-552 (1976).

[22] M. M. Rashid, submitted to *J. Mech. Phys. Solids.*

[23] A. M. Freudenthal and M. Ronay, *Proc. Royal Soc. London A.* **292,** pp. 14-50 (1966).

[24] W. Noll, *Arch. Rational Mech. Anal.* **48,** pp. 1-50 (1972).

[25] J. E. Marsden and T. J. R. Hughes, *Mathematical Foundations of Elasticity,* Prentice-Hall, Englewood Cliffs, NJ (1983).

SESSION VI:
STRUCTURAL MECHANICS

Session Chairman: *Dr. R. Singleton*

Predicting Low-Velocity Impact Damage in Organic Matrix Laminated Composites

By

H.Y. Choi, S. G. Lee, and F.K. Chang
Department of Aeronautics and Astronautics
Stanford University, Stanford, California 94305

ABSTRACT

An investigation was performed to study the damage resistance of organic matrix laminated composites to low-velocity impact. Matrix cracking and delaminations were the major concern of the failure modes. T300/976 and T800H/3900-2 graphite/epoxy laminated composites were selected for the study. The surfaces of the T800H/3900-2 prepreg contain thermoplastic polyamide particulates for toughening the laminate interface. Both analytical and experimental work were performed to evaluate the impact damage resistance of the composites. A computer code, "3DIMPACT", was developed for predicting the impact velocity threshold corresponding to the initial impact damage and estimating the extent of delaminations after impact. Tests were also performed to generate test data for verifying the predictions from the code.

I. INTRODUCTION

Organic matrix fiber-reinforced laminated composites have been known susceptible to transverse impact, especially at low velocities which can cause significant internal damage such as matrix cracks and delaminations. Numerous investigations have been conducted in this area [1 – 22] and extensive impact test data are available from the literature. It has been observed that the impact damage resistance strongly depended upon many factors including material systems, ply orientation, laminate thickness, as well as the mass of the impactor, etc.

Several analytical models [15-22] have been developed to study the transient dynamic response of composites due to impact. However, most of the analytical studies were primarily focused either on modelling the impact force distribution during impact [15-17] or on determining the response of the plates without consideration of the damage which may be induced during impact[18-22].

Recently, extensive studies on impact damage mechanism and mechanics were performed by Choi et al [23 – 26]. A line-nosed impactor was used to simplified the impact damage and to characterize the damage mechanism and mechanics. A two-dimensional transient dynamic analysis was also developed for understanding the damage mechanism of laminated composites subjected to line-nosed impact.

Based on these studies, an investigation was conducted by the authors to develop a model as well as a computer code for predicting impact velocity threshold corresponding to the initial impact damage and estimating the extent of delaminations resulting from transverse low-velocity impact [27, 28]. In this presentation, composites with two different material systems, T300/976 and T800/3900-2 prepregs, were studied. The computer code was utilized to characterize the impact resistance of the materials. Experiments were also performed to generate test data for verifying the predictions from the code.

II. IMPACT DAMAGE MECHANISM

Since impact damage is a very complicated phenomenon, predicting impact damage requires a thorough understanding of the basic damage mechanism and mechanics governing the impact damage event. In order to achieve such understanding, Chang et al[23-25] performed a series of extensive studies on impact damage mechanism and mechanics of laminated composites. Based on the these studies and the work done by others [2, 4, 9, 11] , the basic damage mechanism resulting from low-velocity impact can be in general summarised as follows:

(1) impact damage is initiated from an intraply matrix crack(s).

(2) the initial matrix crack(s) can produce delaminations along the neighboring interfaces with the dissimilar materials.

(3) the propagation of the delaminations during impact can generate extensive multiple micro-cracks.

The initial matrix cracks which produce delamination failure can be classified by their location into two types: one is referred to as "the shear crack" and the other is "the bending crack". A shear matrix crack appears inside the materials and is located a distance from the center of impact. It can generate an extensive delamination along the bottom interface and a small, confined delamination along the upper interface of the cracked ply (see Figure 1). However, a bending matrix crack is located right beneath the center of impact and mostly appears on the bottom surface ply of a composite (see Figure 1).

Chang et al [23 – 25] have shown that the interlaminar transverse shear stress and in-plane stress normal to the fiber direction are the major stress components contributing the initial impact damage. Excessive interlaminar shear stress will initiate shear cracks and high transverse in-plane normal stress will most likely produce a bending crack. However, once the matrix cracking is initiated, the occurrance and

growth of a delamination strongly depend upon the type of the matrix crack.

A recent study by Liu and Chang, et al [29 – 31] has shown that for a shear crack-induced delamination, the interlaminar longitudinal shear stress (along the fiber direction) in the layers right below the interface and the interlaminar transverse shear stress (normal to the fiber direction) right above the interface govern the delamination growth (Mode II and III fractures). A schematic description of the delamination growth mechanism induced by a shear crack is shown in Figure 2. However, for a bending crack-induced delamination, the in-plane transverse normal stress and the interlaminar logitudinal shear stress (Mode I and II fractures) in the layer right below the interface control the delamination propagation. A schematic description of the delamination growth mechanism is shown in Figure 3.

III. THE MODEL

Based on the aformentioned damage mechanism, a model will be presented for predicting low-velocity impact damage in fiber-reinforced, epoxy matrix laminated composites. The model consists of a stress analysis for determining the stress distributions inside the laminates during impact and a failure analysis for predicting the initiation and the extent of the impact damage.

3.1 STRESS ANALYSIS

The finite element analysis developed by Wu and Chang [18] was adopted in the model for calculating the stresses and strains inside the composites during impact resulting from a spherical-nose impactor. The analysis was based on a three-dimensional linear elasticity theory, and the materials in each layer were considered homogeneous and orthotropic. Accordingly, the equilibrium equations at instant time t in a variational form can be expressed as [28]

$$0 = \int_{\Omega} w_i \rho u_{i,tt} dv + \int_{\Omega} e_{ij} E_{ijkl} \epsilon_{kl} dv - \int_{\Gamma} w_i \sigma_{ij} n_j dA \tag{1}$$

where σ_{ij} are the stresses, ϵ_{kl} are the strains, ρ is the density, $u_{i,tt}$ are the accelerations ($u_{i,tt} = \partial^2 u_i / \partial t^2$), w_i are the arbitrary variational displacements, e_{ij} are the strains from the arbitrary variational displacements, Ω is the entire plate volume, Γ is the surface of the plate, n_j is the outward unit normal vector on the plate surface, and E_{ijkl} are the material properties of the laminate, which vary from layer to layer according to the ply orientation of the composite.

In order to solve Eq.(1), the distribution of the contact force, $F(= \sigma_{ij} n_j)$, between the impactor and the impacted laminate must first be known. The projectile was modeled as an elastic body with a spherical nose. The contact force distribution during impact was simulated according to loading and unloading processes.

Upon loading (the contact force was increased), the contact force distribution was determined using the Hertzian contact law [28]. Thus, the contact force F can be related to the indentation depth α (the distance between the center of the projectile's nose and the mid-surface of the plate) by the expression [28]

$$F = \kappa \alpha^{1.5} \tag{2}$$

where κ is the modified constant of the Hertz contact theory proposed by Sun et. al. [15, 16] and

$$\kappa = \frac{4}{3} \sqrt{r} \, \frac{1}{[(1 - \nu_s^2)/E_s + 1/E_{yy}]} \tag{3}$$

where r, ν_s, and E_s are the local radius, the Poisson's ratio, and the Young's modulus of the impactor, respectively. E_{yy} is the transverse modulus normal to the fiber direction in the upper most composite layer.

Upon unloading, the contact force is simulated by the following relation developed by Sun et. al. [15,16]

$$F = F_m \left[\frac{\alpha - \alpha_o}{\alpha_m - \alpha_o} \right]^{2.5} \tag{4}$$

where F_m is the maximum contact force just before unloading, α_m is the maximum indentation corresponding to F_m, and α_o is the permanent indentation during the loading/unloading process. The permanent indentation can be determined from the following expression [15,16]

$$\begin{aligned} \alpha_o &= 0 && \text{when } \alpha_m < \alpha_{cr} \\ \alpha_o &= \alpha_m \left[1 - \left(\frac{\alpha_{cr}}{\alpha_m} \right)^{2/5} \right] && \text{when } \alpha_m \geq \alpha_{cr} \end{aligned} \tag{5}$$

where α_{cr} is the critical indentation, and is approximately 0.004 inches for glass/epoxy and 0.00316 inches for graphite/epoxy.

An eight-node brick element incorporating incompatible modes developed previously by Wu and Chang [18] was used in the finite element calculations. The inclusion of incompatible modes was to improve the accuracy in calculating the bending stiffnesses and the interlaminar shear stresses. The accuracy of the computer code was verified by comparing with the existing analytical and numerical solutions [18]. For instance, consider an isotropic rectanglular steel plate rigidly fixed on its four edges. The plate was subjected to an impact induced by a steel ball to its center. The analytical solutions of the contact force, displacements, and velocity of the center of the plate and impactor are presented in Figure 4 as compared to the numerical solutions calculated by the code. As shown from the figure, excellent agreement can be found between the analytical solutions and the calculated results.

3.2 FAILURE ANALYSIS

Based on the impact damage mechanism discussed in Section II, two failure criteria, critical matrix cracking criterion and impact-induced delamination criterion,

were proposed in the model. The former was proposed to predict the initiation of the impact damage, and the latter was for predicting the extent of the delaminations in composites resulting from the low-velocity impact.

Critical Matrix Cracking Criterion

In order to predict the occurrence of the critical matrix cracks, the matrix failure criterion proposed previously by the authors [24] was selected and can be expressed as

$$\left(\frac{{}^n\overline{\sigma}_{yy}}{{}^nY}\right)^2 + \left(\frac{{}^n\overline{\sigma}_{yz}}{{}^nS_i}\right)^2 = e_M^2 \qquad \begin{cases} e_M \geq 1 & \text{Failure} \\ e_M < 1 & \text{No failure} \end{cases} \qquad \begin{cases} {}^nY = {}^nY_t & \text{if } \overline{\sigma}_{yy} \geq 0 \\ {}^nY = {}^nY_c & \text{if } \overline{\sigma}_{yy} < 0 \end{cases} \tag{6}$$

where the subscript of x and y are the local coordinates of the n-th layer parallel and normal to the fiber directions, respectively, and z is the out-of-plane direction. S_i is the in situ interlaminar shear strength within the laminate under consideration, and Y_t and Y_c are the in situ ply transverse tensile and compressive strength, respectively [24].

Unfortunately, the interlaminar shear strength within the laminate has not been well characterized in the literature and was frequently taken to be associated with in-plane shear strength. Therefore, the values of Y_t and S_i of n-th ply were determined from the empirical expressions proposed previously by Chang and Lessard [32]. $\overline{\sigma}_{yz}$ and $\overline{\sigma}_{yy}$ are the averaged interlaminar and in-plane transverse stresses, respectively, within the n-th ply which can be expressed as

$${}^n\overline{\sigma}_{yz} = \frac{1}{h_n}\int_{t_{n-1}}^{t_n} \sigma_{yz}\, dz \tag{7}$$

and

$${}^n\overline{\sigma}_{yy} = \frac{1}{h_n}\int_{t_{n-1}}^{t_n} \sigma_{yy}\, dz \tag{8}$$

where t_n and t_{n-1} are the upper and lower interfaces of the n-th ply in the laminate and h_n is the thickness of the ply.

Whenever the calculated averaged stresses in any one of the plies in the laminate first satisfy the criterion ($e_M = 1$) during impact, initial impact damage is predicted. It was assumed then that the matrix crack would propagate throughout the thickness of the ply group which contained the cracked ply. The time t corresponding to the initial damage is designated as t_M. A delamination could be immediately induced from the location of the matrix crack along the interfaces of the ply group. As the time increases ($t > t_M$) during impact, additional matrix cracking could be produced in the other layers. Hence, the criterion should continuously be applied to the other layers for determining any additional matrix failure. If no additional matrix cracking is found at any other layers during impact, then the impact velocity associated with the first matrix cracking is referred to as the impact velocity threshold which is the velocity required to just cause the initial impact damage of the laminate.

Impact-Induced Delamination Criterion

Based on the consideration of the aformentioned delamination growth mechanism, the distributions of the interlaminar longitudinal shear stress σ_{xz} and transverse in-plane stress σ_{yy} throughout the thickness of the bottom layer of the interface and the interlaminar transverse shear stress σ_{yz} in the upper layer contribute significantly to the delamination growth resulting from impact. Therefore, an impact-induced delamination growth criterion for low-velocity impact was proposed in the model [27, 28] which can be expressed as

$$D_a\left[\left(\frac{{}^n\overline{\sigma}_{yz}}{{}^nS_i}\right)^2+\left(\frac{{}^{n+1}\overline{\sigma}_{xz}}{{}^{n+1}S_i}\right)^2+\left(\frac{{}^{n+1}\overline{\sigma}_{yy}}{{}^{n+1}Y}\right)^2\right]=e_D^2 \qquad \begin{cases} e_D \geq 1 & \text{Failure} \\ e_D < 1 & \text{No failure} \end{cases} \qquad \begin{cases} {}^{n+1}Y = {}^{n+1}Y_t & \text{if } \overline{\sigma}_{yy} \geq 0 \\ {}^{n+1}Y = {}^{n+1}Y_c & \text{if } \overline{\sigma}_{yy} < 0 \end{cases} \tag{9}$$

where D_a is an empirical constant which has to be determined from experiments. Once chosen, it was found to be quite insensitive to the ply orientation and thickness of the laminates, and primarily dependent only on the material system used [27, 28]. The subscripts x, y, and z are the local material coordinates of an individual ply within the laminate, and the superscripts n and $n+1$ correspond to the upper and lower plies of the nth interface, respectively. $\overline{\sigma}_{yz}$, $\overline{\sigma}_{yy}$, and $\overline{\sigma}_{xz}$ are the averaged interlaminar and in-plane transverse stresses within the n-th and $n+1$th ply (see definition in Equations 7 and 8).

Accordingly, once a critical matrix crack is predicted in a layer, the delamination criteron is then applied to estimate the extent of the delamination along the interface of the cracked ply in the laminate. It is noted that only the delaminations along the bottom interface (see Figure 1) induced by shear cracks or along the upper interface induced by a bending crack are included in the analysis. The small, confined delamination along the upper interface induced by shear cracks (see Figure 1) is ignored in the present model.

A computer code, designated as "3DIMPACT", was developed based on the model. In summary, the procedures for determining the extent of the impact damage in the code can be described as follows:

(1) Calculating transient dynamic stresses within each layer as a function of time.

(2) Applying the matrix failure criterion for predicting the critical matrix cracks in each layer for determination of the extent of delaminations.

(3) If matrix cracking is predicted in a layer of the laminate, then applying the delamination criterion subsequently in the upper and bottom layer of the interface during the entire period of impact.

The sequence of the above impact damage mechanism is essential for the predicting the impact damage. The procedure has to be repeated at the other layers during

impact for determining any additional matrix cracking and delaminations. The final size of each delamination is determined by the area within the stress components satisfy the delamination failure criterion during the entire duration of impact. No material degradation was considered in the model, and it is also noted that the model doesn't take into account the delamination interaction during impact which may be important for multiple delaminations.

IV. COMPARISONS AND DISCUSSIONS

In this section, numerical results generated from the computer code will be compared with the impact test data obtained during the investigation. T300/976 and T800H/3900-2 graphite/epoxy composites were selected for the study. Although both composites have thermoset resins, T800H/3900-2 prepreg is coated with thermoplastic polyamide particulates to toughten the laminate interface. The mechanical properties of an unidirectional composite for both materials are listed in Table 1. Due to the presence of polyamide particulates, the thickness of a single ply of T800H/3900-2 was slightly thicker than that of T300/976.

The configuration of the specimens are given in Figure 5, and the experimental setup is shown in Figure 6. A spherical-nose steel impactor with a radius of 0.25 inches was used in the tests. All the specimens were only tested once, and then followed by an x-ray examination for determination of internal damage. In this presentation, only selected test data will be presented. More test data and the comparisons between the model prediction and the data can be found in [28].

T300/976 Graphite/Epoxy Composite

Figure 7 shows three X-radiographs $[45_4/-45_8/45_4]$ composites tested at three different velocities. The top X-radiograph was taken from the laminate subjected to impact at a velocity slightly above the impact velocity threshold of the laminate. Two distinct, parallel, short matrix cracks which were located near the area of impact

within the middle −45 degree ply group of the laminate were clearly shown in the Figure 7. A long matrix crack aligned in the 45 degree fiber direction and located in the bottom 45 degree ply group was also clearly indicated. These cracks were most likely assocated with the critical matrix cracks from which delamination was initiated. A white color area in a peanut shape oriented along the 45 degree fiber direction showed that a delamination existed at the interface between the middle −45 degree ply group and the bottom 45 degree ply group.

As the impact velocity increased, the first delamination found at the last interface between −45/45 ply groups was increased substantially as shown in the X-radiograph located at the middle of Figure 7. At a much higher velocity, as given in the X-radiograph at the bottom of Figure 7, the first delamination at the last interface measured from the top surface always governed the major delamination size, meanwhile, a relatively smaller delamination at the first interface between $45/-45$ ply groups was also observed near the impact area, in addition to a considerable amount of microcracks in the 45 and −45 degree ply group. However, the second delamination was confined to the impact area and kept within two parallel matrix cracks. Apparently, it seemed to indicate that the second delamination was generated along the upper interface of the cracked ply group by the shear cracks in the −45 degree plies (referred to Figure 1).

A summary of the measured delamination sizes in $[45_4/-45_8/45_4]$ composites as a function of the velocity of the impactor with 0.16 kg is shown in Figure 8. Solid circular and rectangular symbols represent the measured delamination length and width in the longitudinal and transverse directions as a function of the impact velocity, respectively. The top figure corresponds to the first delamination along the interface of the −45/45 degree plies, and the bottom one relates to the second delamination which occurred at the first interface of the laminate measured from the top surface.

Clearly, there existed an impact velocity threshold for the laminate. The first

delamination seemed to appear earlier than the second delamination. It is worth noting that no matrix cracks or delamination was found in the laminate from the X-radiographs when the impact velocity was less than 3.3 m/s.

The predicted delamination sizes at the last interface as a function of the impact velocity are also presented by the solid and dashed lines in Figure 8. The impact velocity threshold was slightly underestimated but still agreed with the data reasonably well. The first critical matrix cracking was predicted at the middle -45 degree layer of the laminate. The predicted delamination length and width also correlated well with the data. However, no delamination was predicted along the first interface within the range of the selected test velocities. This was becuase the model could not be applied to estimate the second, small delamination induced by a shear matrix crack.

Although the test data was quite scattered, a relationship which was quite consistent with the predictions seemed to exist between the delamination size and the velocity of the impactor. The longitudinal length of the delamination seemed to be more sensitive than the transverse width to the increase of the impact velocity. The longitudinal length of the delamination was always oriented along the fiber direction of the bottom ply below the delamination interface.

As a comparison, the numerical simulations of the delamination size of the composites subjected to impact at the velocities corresponding to the ones given in Figure 7 were generated, and the results of the predictions were presented in Figure 9. The "asterisk" symbol in the figure indicates the location where the stresses were calculated and satisfied the impact-induced delamination criterion. The area covered by the asterisks gives the estimation of the delamination size. Corresponding to each velocity given in Figure 7, the predicted shape and size of the first delamination shown in Figure 9 were reasonably consistent with the results of the X-radiographs givn in Figure 7. However, no delamination was predicted in the sencond interface.

The test results of quasi-isotropic laminates are shown by X-radiographs in Figure 10 corresponding to two different impact velocities. Multiple delaminations were found in the laminates along the interfaces where the neighboring plies have different ply orientations. In Figure 10, the predicted overall delamination sizes of the composites corresponding to the test condition were also presented. The predictions were apparently quite consistent with the test data obtained from X-radiographs.

Delamination was predicted at each interface except the first one between 45^o and -45^o ply groups measured from the impact surface. The calculated delamination size and shape at each delaminated interface corresponding to the impact velocity of 7.8 m/s are presented in Figure 11. It is interesting to point out that each predicted delamination was oriented itself along the fiber direction of the bottom ply group below the delaminated interface.

T800H/3900-2 Graphite/Epoxy Composite

Figure 12 summarizes the measured delamination length and width as a function of the impact velocity for T800H/3900-2 $[0_6/90_3]_s$ laminates. The initial impact damage was found to be a bending crack in the bottom 90^o ply group at the impact velocity near $3m/s$. However, unlike T300/976 composite, no delamination was found accompanying with the matrix crack from the specimens, until the impact velocity was increased up to $4m/s$ which produced a delamination along the interface between the 90^o and the central 0^o ply groups. As the impact velocity continued to increase, the size of the delamination increased as well.

The predictions based on the model are also shown in the figure by solid lines. The predictions correlated very well with the data. Only one delamination was predicted on the second interface between 90^o and 0^o ply groups measured from the impact surface, which was also confirmed from the experiment.

Apparently, based on the above comparisons, the code can provide reasonable prediction on the initiation and the extent of delaminations in both composites with

different material systems. To further compare the impact damage resistance between the two materials, the overall delamination area as a function of the impact velocity for the laminates with $[0_2/-45_2/45_2/90_2]_s$ ply orientation were calculated from the code. The calculations are presented in Figure 13. It shows that T800H/3900-2 composite has a higher impact velocity threshold and can resist delamination growth much more effectively than T300/976. At the impact velocity of $7.0m/s$, the overall size of the delaminations in T300/976 composite is about four times bigger than that in T800H/3900-2 composite.

V. CONCLUSION

An investigation was performed to study impact damage resistance of organic matrix laminated composites. T300/976 and T800H/3900-2 graphite/epoxy composites were studied. A model based on the impact damage mechanism was developed. The predictions obtained from the 3DIMPACT computer code compared favorably with the test data performed during the investigation. The code can be used to predict the initiation of damage and the extent of delaminations in laminated composites resulting from low-velocity impact.

VI. ACKNOWLEDGEMENT

The support of Army Research Office for the investigation is greatly appreciated. Dr. Gary L. Anderson was the Contract Monitor. The authors would also like to acknowledge the support of Boeing Company for providing T800H/3900-2 composite.

VII. REFERENCES

[1]. Guynn, E. G., and O'Brien, T. K., "The Influence of Lay-up and Thickness on Composite Impact Damage and Compression Strength," Proceedings of AIAA /ASME/ASCE/AHS, 26th SDM Conference, Orlando, FL, (1985), pp. 187–196.

[2]. Joshi, S. P. and Sun, C. T., "Impact-Induced Fracture in Quasi-Isotropic Laminate," J. Composite Technology and Research, Vol. 19, (1986), pp. 40–46.

[3]. Cantwell, W. J. and Morton, J., "Geometrical Effects in the Low Velocity Impact Response of CFRP," Composite Structures, Vol. 12, (1989), pp. 39–59.

[4]. Sjoblom, P. O., Hartness, J. T. and Cordell, T. M., "On Low-Velocity Impact Testing of Composite Materials," J. Computers and Structures, Vol. 22, (1988), pp. 30–52.

[5]. Greszczuk, L. B., "Foreign Objects Damage to Composites," ASTM STP 568, (1973).

[6]. Chamis, C. C. and Sinclair, J. H., "Impact Resistance of Fiber Composites: Energy-Absorbing Mechanisms and Environmental Effects," Recent Advances in Composites in the United States and Japan, ASTM STP 864, (Vinson and Taya, Eds.), (1983), pp. 326–345.

[7]. Wu, H. T. and Springer, G. S., "Measurements of Matrix Cracking and Delamination Caused by Impact on Composite Plates," J. of Composite Materials, Vol. 22, (1988), pp. 518–532.

[8]. Gosse, J. H. and Mori, P. B. Y., "Impact Damage Characterization of Graphite/ Epoxy Laminates," Proceedings of the Third Technical Conference of the American Society for Composites, Seattle, WA, (1988), pp. 334–353.

[9]. Joshi, S. P., "Impact-Induced Damage Initiation Analysis: An Experimental Study," Proceedings of the Third Technical Conference of the American Society

for Composites, Seattle, WA, (1988), pp. 325–333.

[10]. Sun, C. T. and Rechak, S., "Effect of Adhesive Layers on Impact Damage in Composite Laminates," Composite Materials: Testing and Design (Eighth Conf.), ASTM STP 972 (J. D. Whitcomb, Ed.), American Society for Testing and Materials, Philadelphia, PA, (1988), pp. 97–123.

[11]. Clark, G., "Modelling of Impact Damage in Composite Laminate," Composites, Vol. 20, (1988), pp. 209–214.

[12]. Reed, P. E. and Turner, S., "Flexed Plate Impact, Part 7. Low Energy and Excess Energy Impacts on Carbon Fiber-Reinforced Polymer Composites," Composites, Vol. 19, (1988),pp. 193–203.

[13]. Liu, D. and Malvern, L. E., "Matrix Cracking in Impacted Glass/Epoxy Plates," J. Computers and Structures, Vol. 21, (1987), pp. 594–609.

[14]. Chen, J. K. and Sun, C. T., "'Analysis of Impact Response of Buckled Composite Laminates," Composite Structures, Vol. 3, (1985), pp. 97–118.

[15]. Sun, C. T. and Yang, S. H., "Contact Law and Impact Responses of Laminated Composites," NASA CR-159884, National Aeronautical and Space Administration, Washington, D.C., (1980).

[16]. Tan, T. M. and Sun, C. T., "Use of Statical Indentation Laws in the Impact Analysis of Laminated Composite Plates," J. of Applied Mechanics, Vol. 52, March 1985, pp. 6–12.

[17]. Kubo, J. T. and Nelson, R. B., "Analysis of Impact Stresses in Composite Plates," American Society for Testing and Materials, Special Technical Publication 568, Philadelphia, Pa, (1975), pp. 228–244.

[18]. Wu, H. T. and Chang, F. K., "Transient Dynamic Analysis of Laminated Composite Plates Subjected to Transverse Impact," J. of Computers and Structures,

Vol. 31, (1989), pp. 453–466.

[19]. Ross, C. A. and Malvern, L. E., Sierakowski, R. L. and Taketa, N., "Finite-Element Analysis of Interlaminar Shear Stress Due to Local Impact," Recent Advances in Comp. in the United States and Japan, ASTM STP 864, (J. P. Vinson and M. Taya, Eds.) American Society for Testing and Materials, Philadelphia, PA, (1985), pp. 335–367.

[20]. Aggour, H. and Sun, C. T., "Finite Element Analysis of a Laminated Composite Plate Subjected to Circularly Distributed Central Impact Loading," J. Computers and Structures, Vol. 28, (1988), pp. 729–736.

[21]. Ross, C. A., Malvern, L. E., Sierakowski, R. L. and Takeda, N., "Finite-Element Analysis of Interlaminar Shear Stress Due to Local Impact," Recent Advances in Composites in the United States and Japan, ASTM STP 864, (Vinson and Taya, Eds.), (1983), pp. 355–367.

[22]. Sun, C. T. and Chattopadhyay, S., "Dynamic Response of Anisotropic Laminated Plates Under Initial Stress to Impact of a Mass," J. of Applied Mechanics, Vol. 42, (1975), pp. 693–698.

[23]. Choi, H. Y., Downs, R. J., and Chang, F. K., "A New Approach Toward Understanding Damage Mechanisms and Mechanics of Laminated Composites Due to Low-Velocity Impact, Part I–Experiments," J. of Composite Materials, Vol. 25, August, 1991, pp. 992-1011.

[24]. Choi, H. T., Wu, H. Y. T., and Chang, F. K., "A New Approach Toward Understanding Damage Mechanisms and Mechanics of Laminated Composites Due to Low-velocity Impact, Part II–Analysis," J. of Composite Materials, Vol. 25, August, 1991, pp. 1012-1038.

[25]. Choi, H. Y., Wang, H. S. and Chang, F. K., "Effect of Laminate Configuration and Impactor's Mass on the Initial Impact Damage of Composite Plates Due

to Line-Loading Impact," J. of Composite Materials, (to appear in June 1992 issue).

[26]. Chang, F. K., Choi, H. Y. and Wang, H. S., "Damage of Laminated Composites Due to Low Velocity Impact," 31st AIAA/ASME/ASCE/AHS/ASC Structures, Structural Dynamics and Materials (SDM) Conference, April 2–4, (1990), Long Beach, CA.

[27]. Choi, H. Y. and Chang, F. K.,"A Model for Predicting Impact Damage in Graphite/Epoxy Laminated Composites Resulting from A point-Nose Impact," J. of Composite Materials (submitted).

[28]. Choi, H. Y.,"Impact Damage In Laminated Composites due to Low-velocity Impact," Ph.D. dissertation, Stanford University, 1991.

[29]. Liu,S., Kutlu, Z., and Chang, F. K.," Matrix Cracking and Delamination Propagation in Laminated Composites Subjected to Quasi-static Transveresely Concentrated Loading," J. of Composite Materials,(to appear).

[30]. Liu,S., Kutlu, Z., and Chang, F. K.," Matrix Cracking and Delamination Propagation in Laminated Composites Subjected to Quasi-static Transveresely Concentrated Loading," AFOSR Progress Report, 1990.

[31]. Liu,S. and Chang, F. K.," Matrix Cracking and Delamination Propagation in Laminated Composites Subjected to Quasi-static Transveresely Concentrated Loading," 33st AIAA/ASME/ASCE/AHS/ASC Structures, Structural Dynamics and Materials (SDM) Conference, April 13-16, (1992), Dallas, TX.

[32]. Chang, F. K. and Lessard, L. B., "Damage Tolerance of Laminated Composites Containing an Open Hole and Subjected to Compressive Loading: Part I–Analysis," J. of Composite Materials, Vol. 25, January, 1991, pp. 2-43.

Table 1 Material Properties of $T300/976$ and $T800H/3900-2$ Unidirectional Composites

Property	T300/976	T800H/3900-2
Longitudinal Young's Modulus E_{xx} (GPa)	156.0	159.6
Transverse Young's Modulus E_{yy} (Gpa)	9.09	9.14
Shear Modulus G_{xy} (GPa)	6.96	6.21
Poison's Ratio υ_{xy}	0.23	0.28
Poison's Ratio υ_{yz}	0.40	0.28
Longitudinal Tensile Strength X_T (MPa)	1520	2841
Longitudinal Compressive Strength X_C (MPa)	1590	1313
Transverse Tensile Strength Y_T (MPa)	44.5	44.1
Transverse Compressive Strength Y_C (MPa)	252.0	167.5
Shear Strength S (MPa)	35.6	121.3
Ply Thickness h_O (m)	1.44e-4	1.66e-4
Density ρ (kg/m^3)	1540	1518
Delamination parameter D_a	1.80	0.45

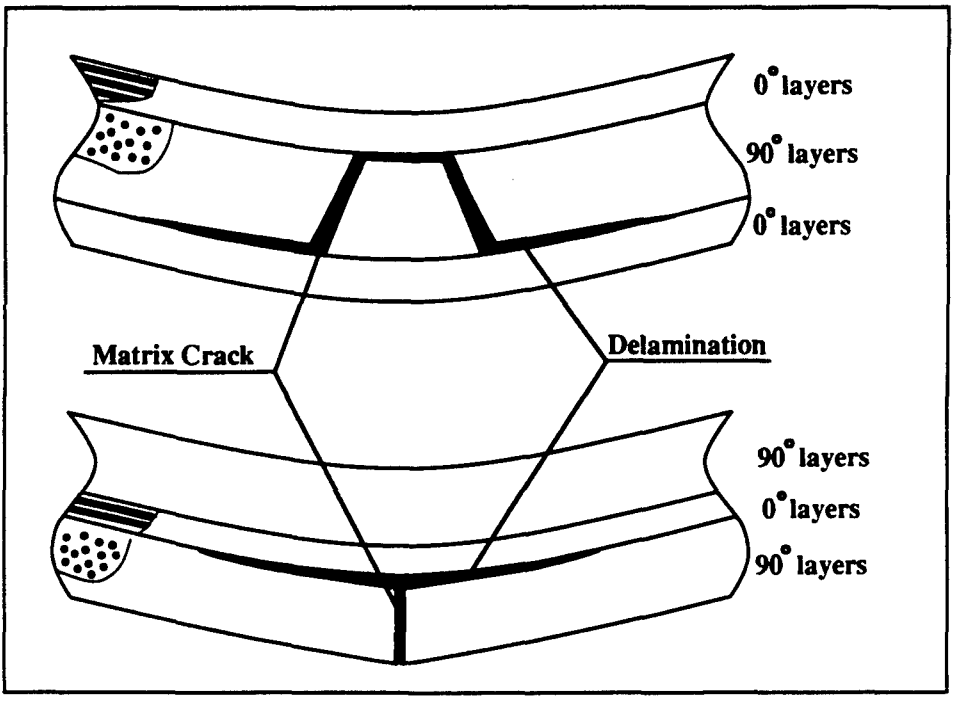

Figure 1 Basic impact damage mechanism of fiber-reinforced laminated composites subjected to low-velocity impact. (top): Delamination induced by inner transverse shear matrix cracks, (bottom): Delamination induced by a surface bending crack.

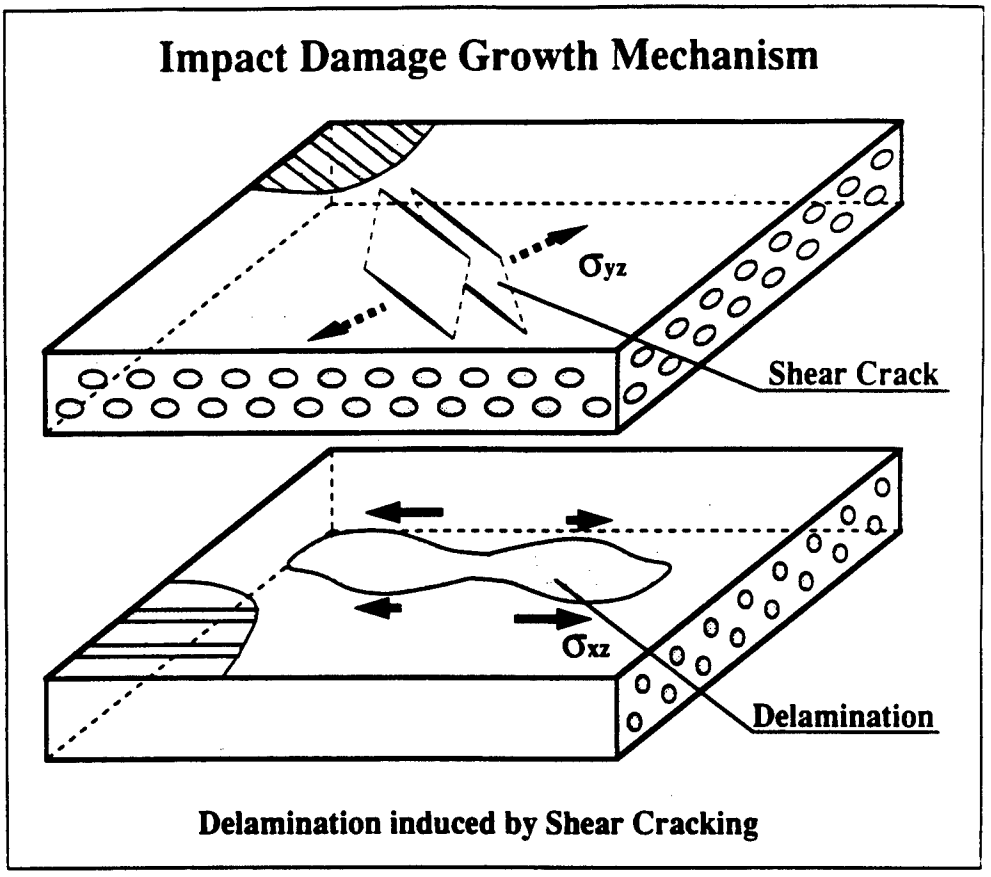

Figure 2 Schematic description of delamination growth mechanism induced by a shear crack in laminated composite due to impact.

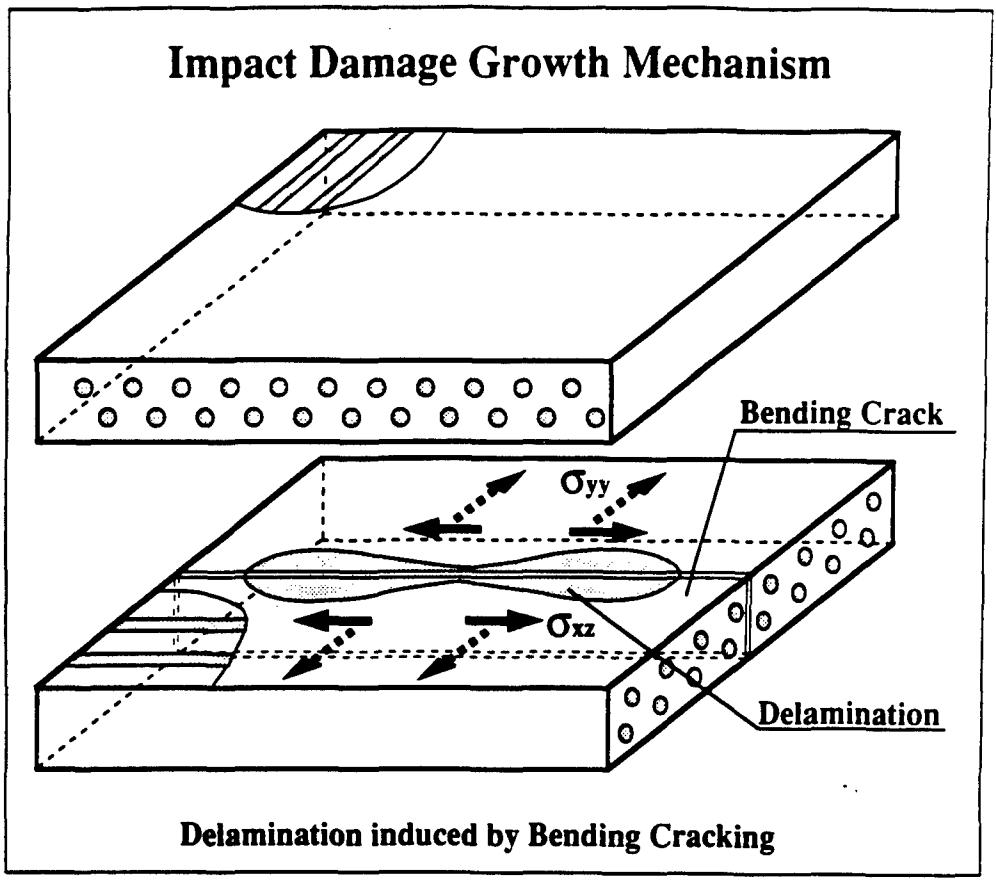

Figure 3 Schematic description of delamination growth mechanism induced by a bending crack in laminated composite due to impact.

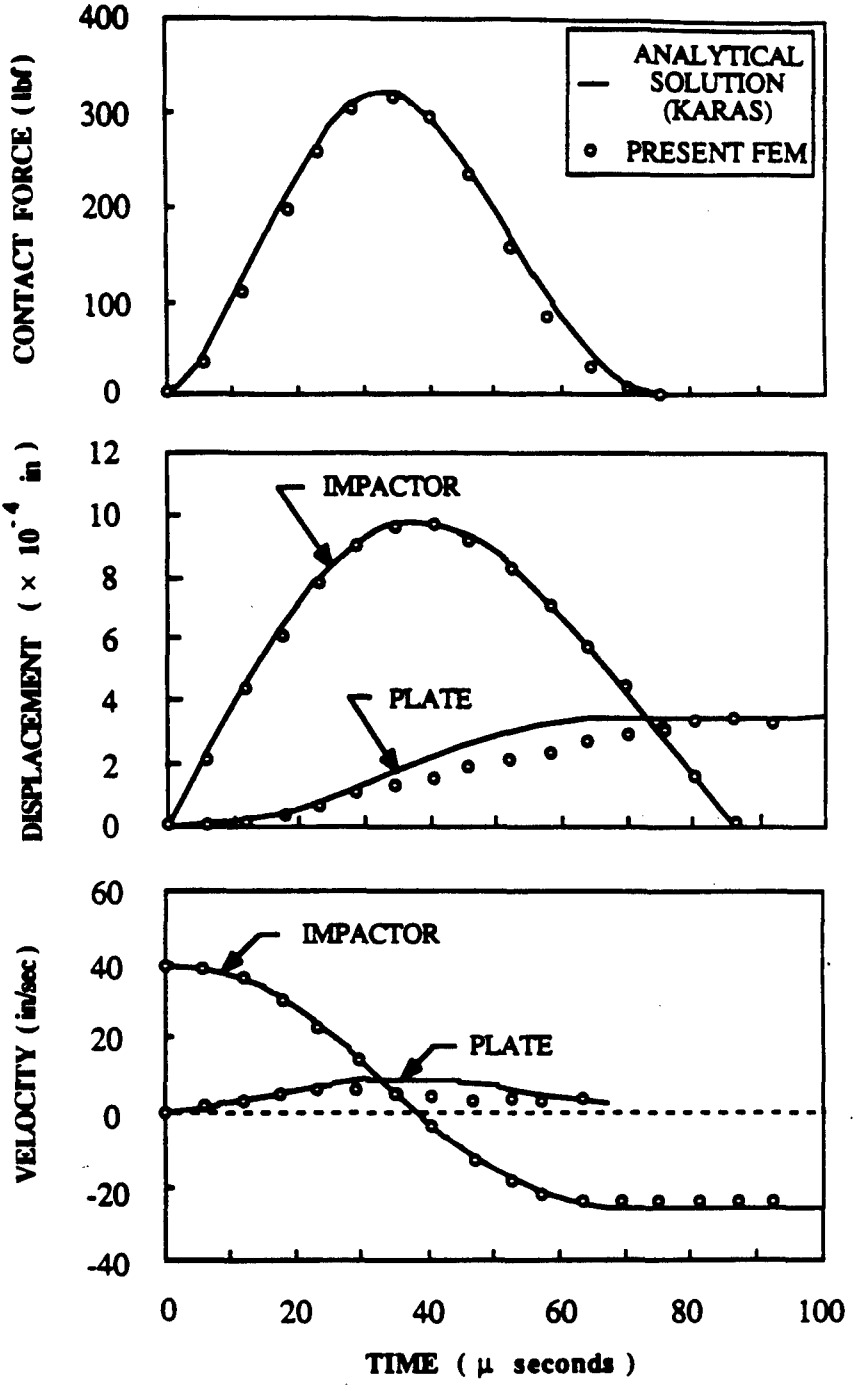

Figure 4 Comparison between the predictions based on the present method and Karas' analytical solutions [18] for contact force, displacement, and velocity of a steel plate subjected to transient dynamic impact.

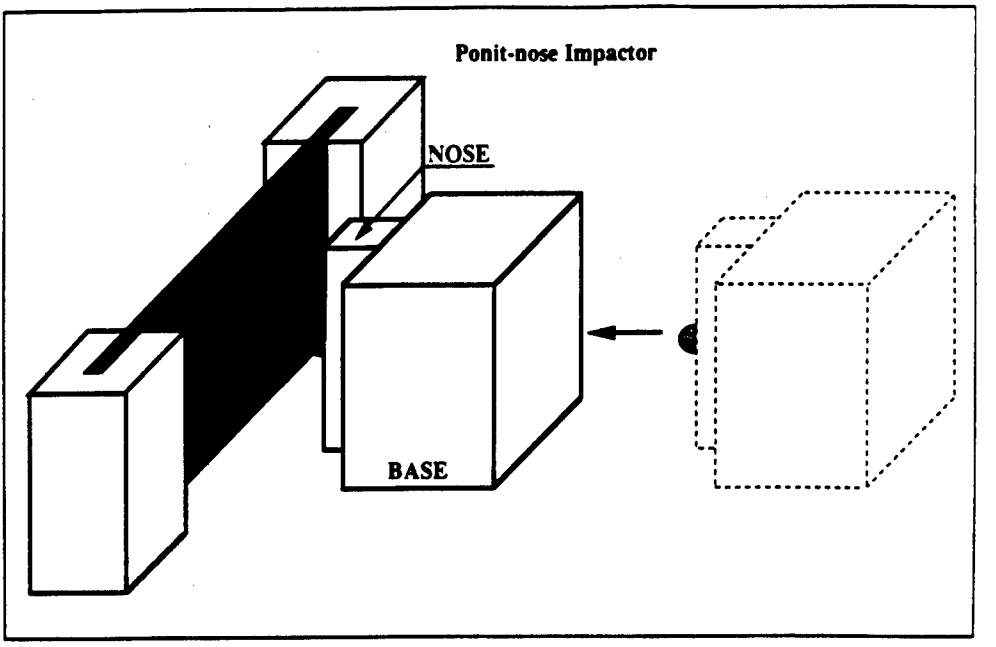

Figure 5 A schematic description of the test impactor and the specimen setup used in the experiments. A spherical steel ball of 0.635 cm radius mounted to a rectangular base.

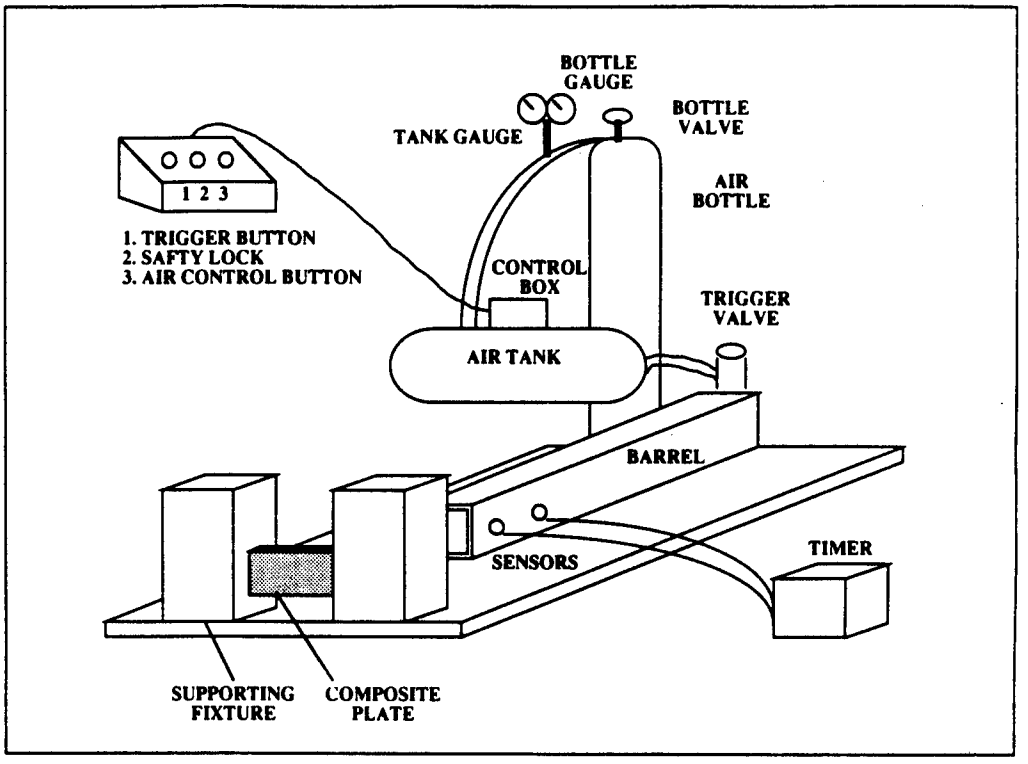

Figure 6 A schematic description of the impact test facility.

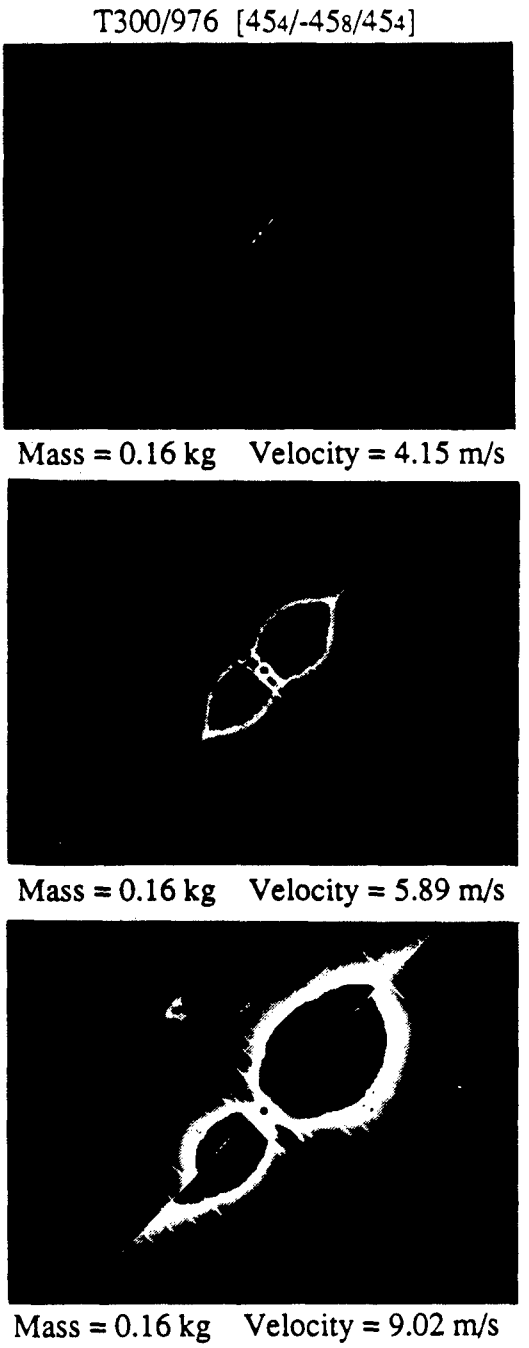

Figure 7 X-radiographs of $[45_4/-45_8/45/_4]$ composites subjected to impact by a spherical indenter at three different velocities.

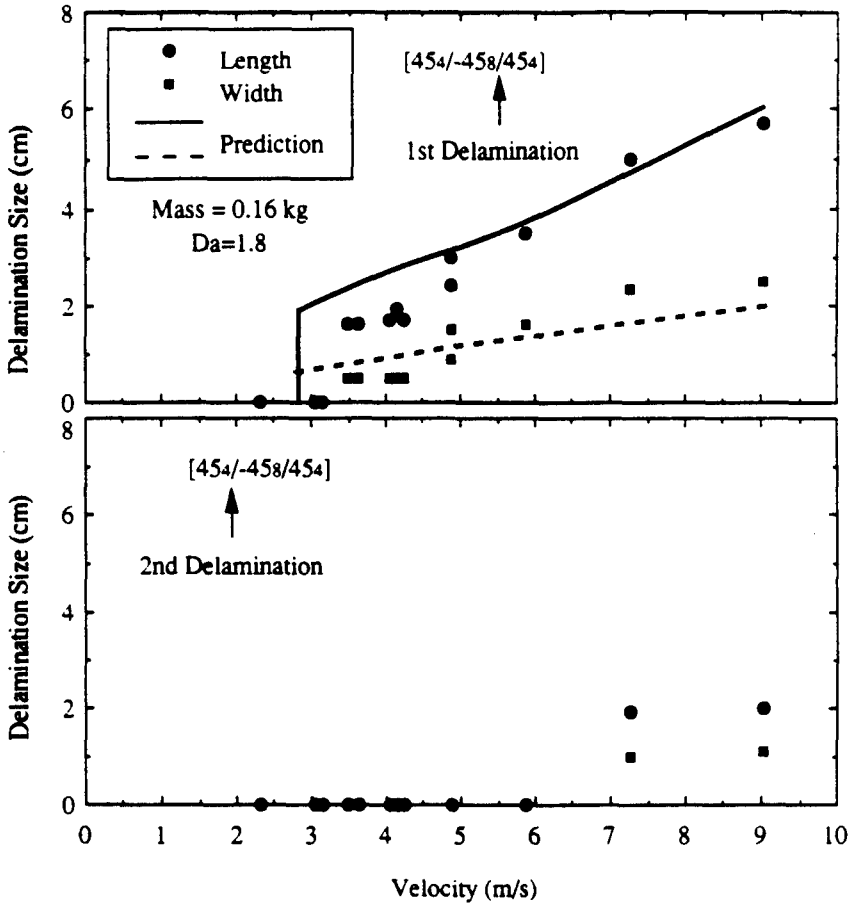

Figure 8 Comparison of delamination sizes of $T300/976$ $[45_4/-45_8/45_4]$ composites between the measurements from the experiments and the calculations based on the model.

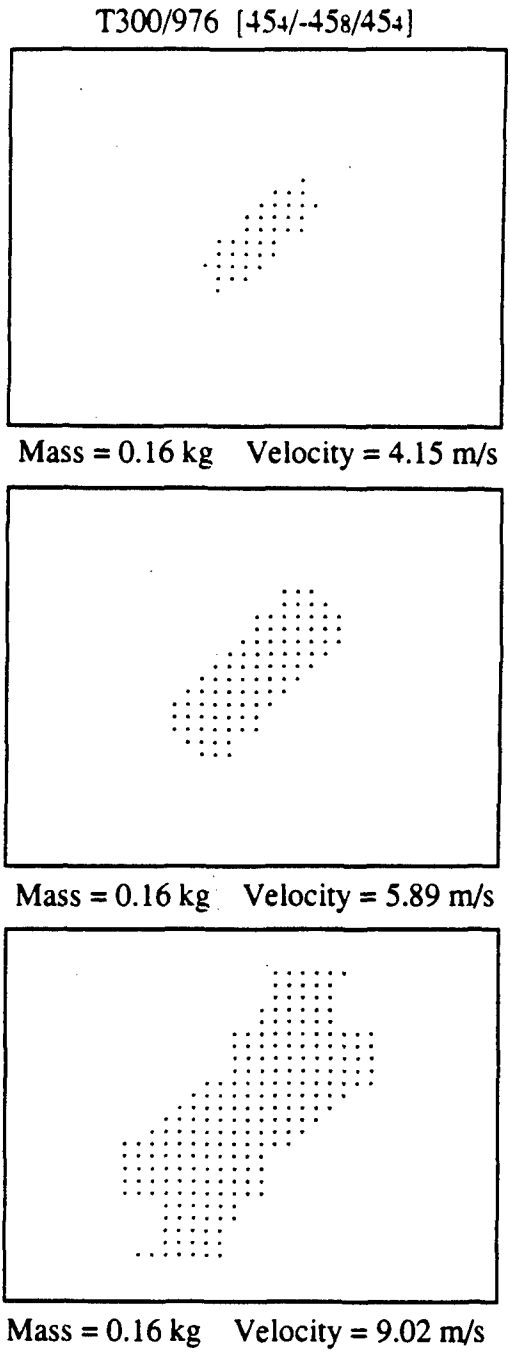

Figure 9 Predicted delamination sizes of $T300/976$ $[45_4/-45_8/45_4]$ composites corresponding to the impact condition given in Figure 7.

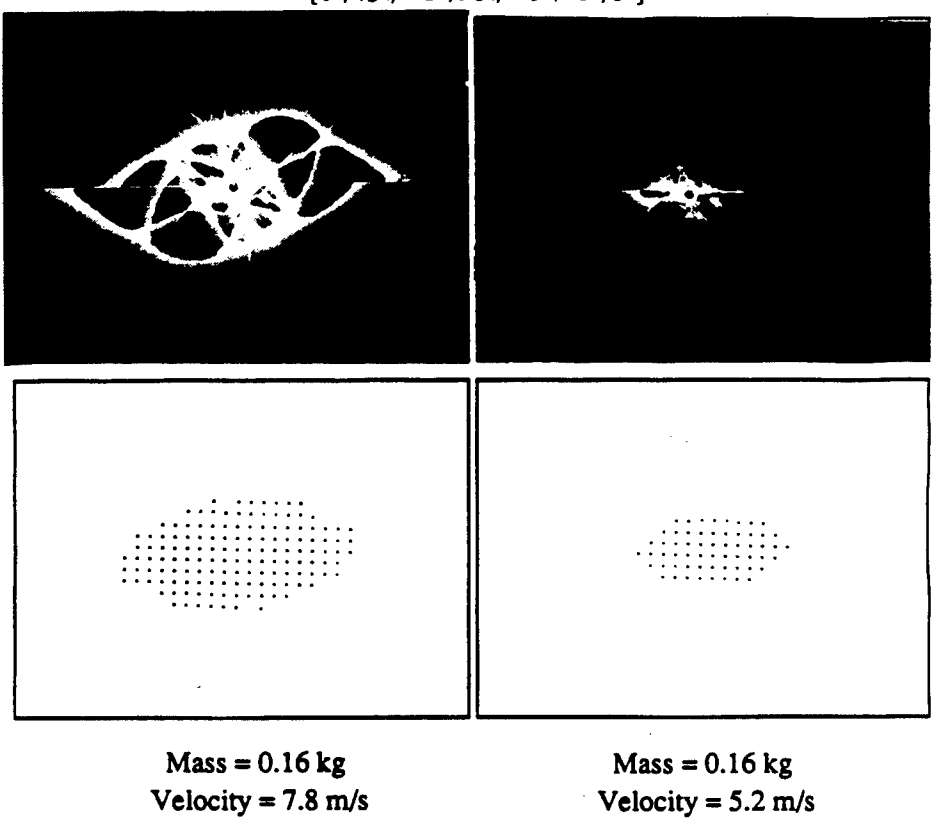

Figure 10 Comparison of delamination sizes and shapes of $T300/976$ $[0_4/45_4/-45_4/90_2]_s$ composites between the X-radiographs taken from the experiments and the calculations based on the model.

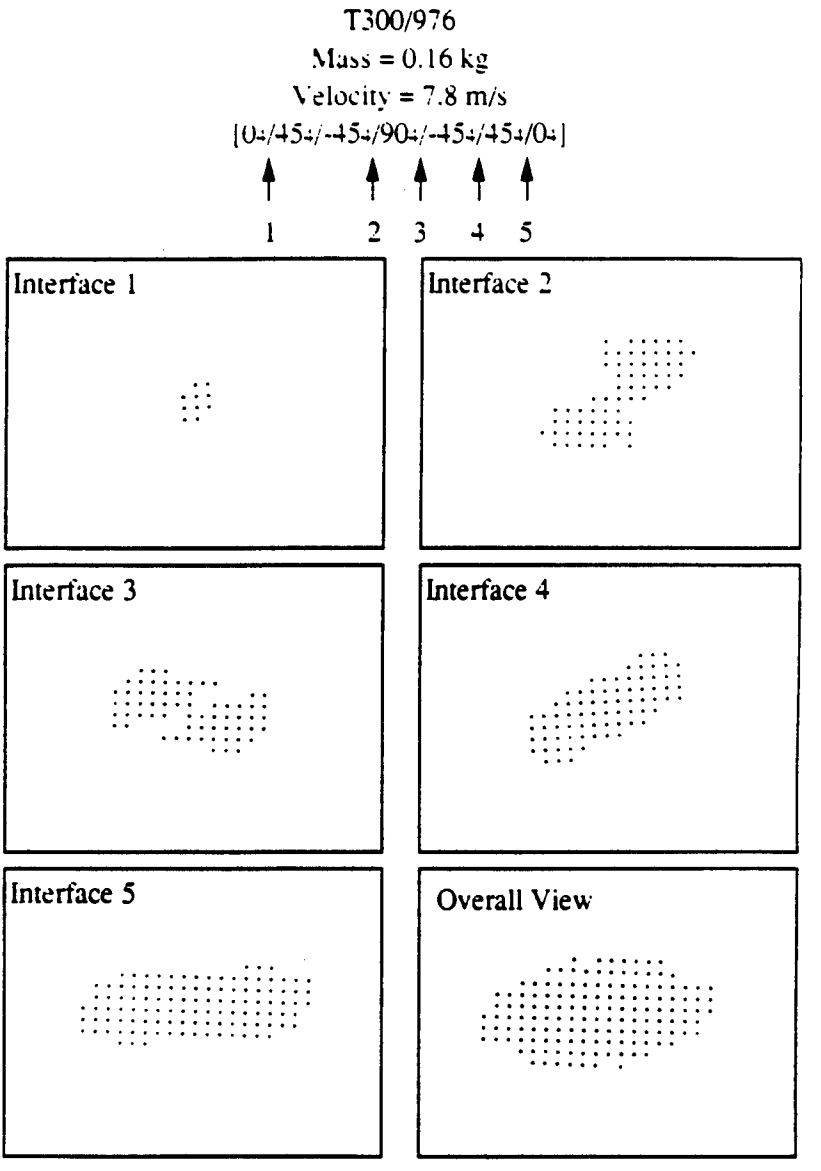

Figure11 Predicted delamination sizes and shapes of $T300/976$ $[0_4/45_4/-45_4/90_2]_s$ composites at different interfaces.

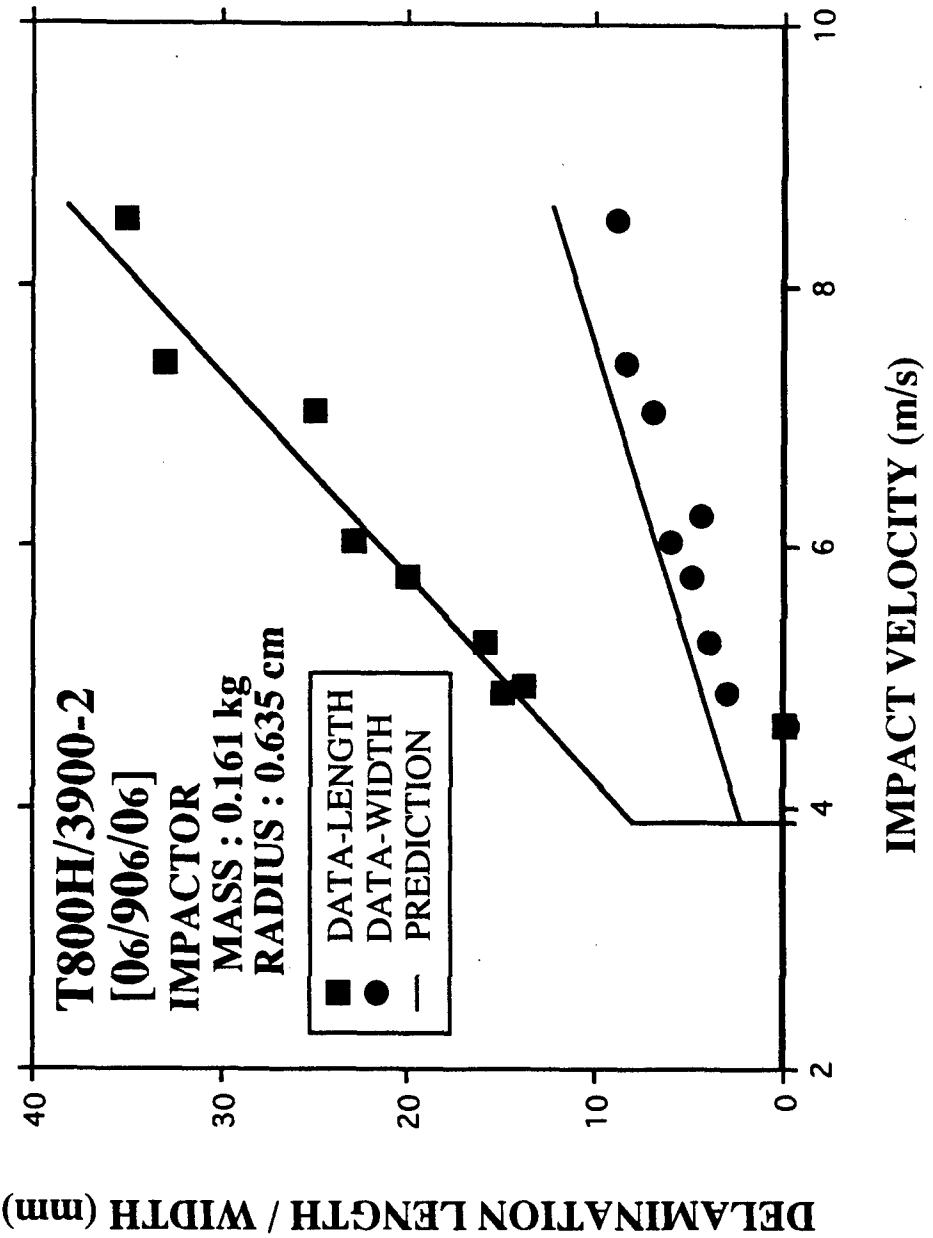

Figure 12 Comparison of delamination sizes of $T800H/3900-2\ [0_6/90_3]_s$ composites between the measurements from the experiments and the calculations based on the model.

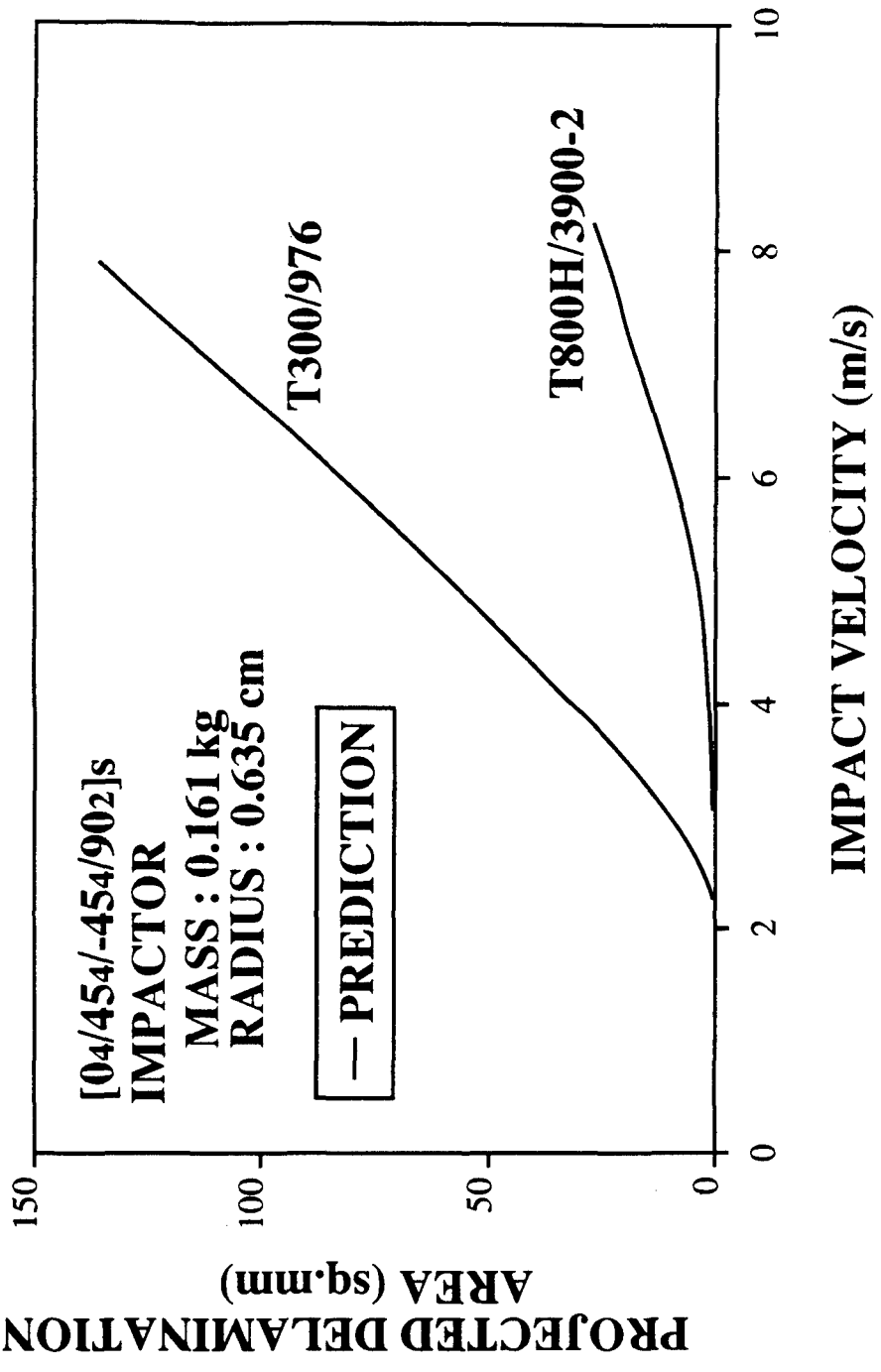

Figure 13 Comparison of predicted delamination area between $T300/976$ and $T800H/3900-2$ composites.

THE EFFECT OF LOW TEMPERATURE ON THE FLEXURAL FATIGUE AND FRACTURE OF UNIDIRECTIONAL GRAPHITE/EPOXY COMPOSITES

Piyush K. Dutta

U.S. Army Cold Regions Research and Engineering Laboratory
Hanover, New Hampshire 03755.

INTRODUCTION

This paper deals with the behavior of unidirectional graphite/epoxy composites in flexural fatigue and fracture over a temperature range of 20° to –40°C. Fatigue behavior and damage accumulation in fiber composites have been well studied for room temperature and higher service temperatures, but very few data exist for low temperature regimes. Basic failure mechanisms in composite laminates include inter- or intra-laminar matrix cracking, interface failure, and fiber fracture. Temperature reductions result in a stiffer and more brittle matrix and can potentially influence these failure mechanisms. The objective of this study is to understand the damage state, stiffness, strength, and fatigue properties of composite laminates as a function of reduced temperatures.

The yield strength of a composite laminate is a reliable measure of the internal damage as proven by Roylance et al. [1]. Hence, in this study the yield point was used as the basis for damage development comparisons under different temperatures. The specimens were subjected to 10^5 flexural load cycles between 20 and 80% of the expected yield strength. Modulus changes were determined at several intervals as the fatigue cycling progressed. The bending strength was determined upon completion of 10^5 cycles. Variables used to describe the specimen's fatigue and post-fatigue behavior are defined according to Figure 1. Failure surfaces were examined under a scanning electron microscope (SEM) to detect failure modes. Results of tests performed at different temperatures were then compared to determine temperature effects.

EXPERIMENTAL PROGRAM

Specimens prepared for this investigation were cut from 305- × 305-mm (12- × 12-in.) T300/Fiberite-975 graphite/epoxy panels of unidirectional lay-up. Completed specimens measured 229 × 17.8 mm (9 × 0.7 in.) and were 16 plies

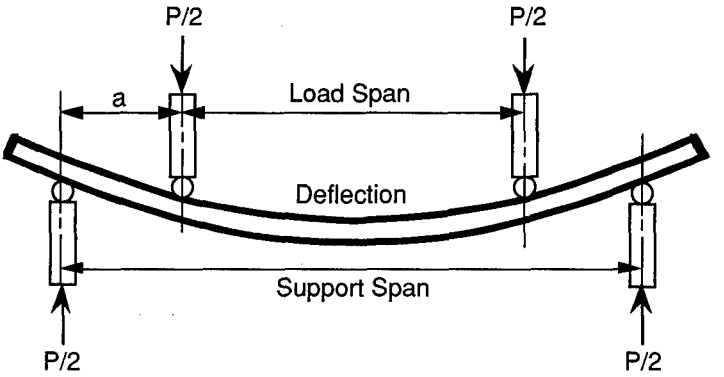

Figure 1. Test schematic.

in thickness. The fibers were oriented in the longitudinal direction of the specimens. After cutting, all specimens were X-rayed to ensure that they were free from internal defects. Because moisture content can dramatically affect the strength and failure mode of composites, specimens were maintained in a sealed container until testing. Small samples were tested periodically to ascertain that the moisture content was unaltered.

Four-point bending tests were performed at 20°, 0°, –20°, and –40°C to establish the bending modulus and loads associated with yield and failure. A photograph of the test setup is provided in Figure 2. All tests were performed in

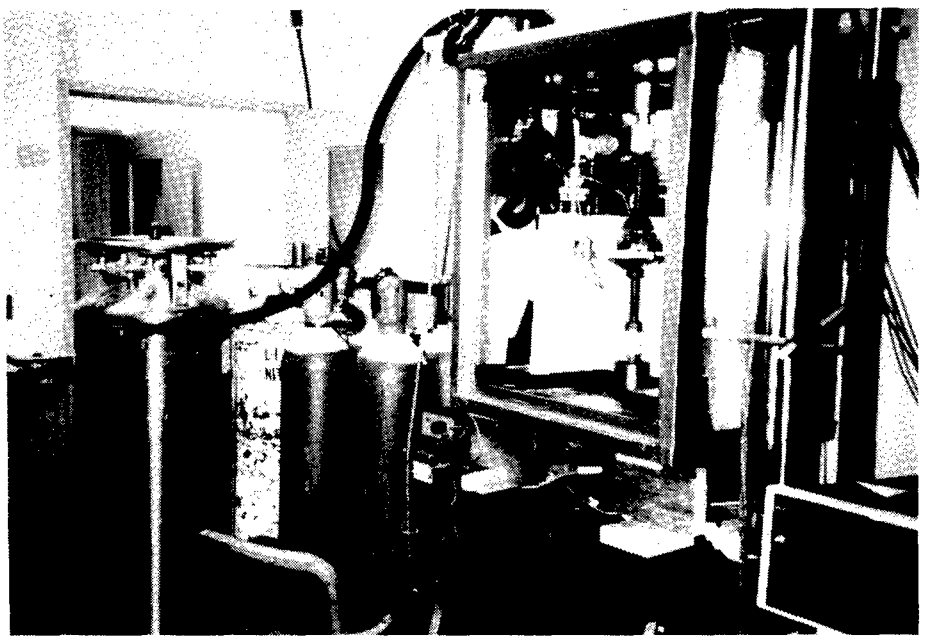

Figure 2. Setup for low temperature testing.

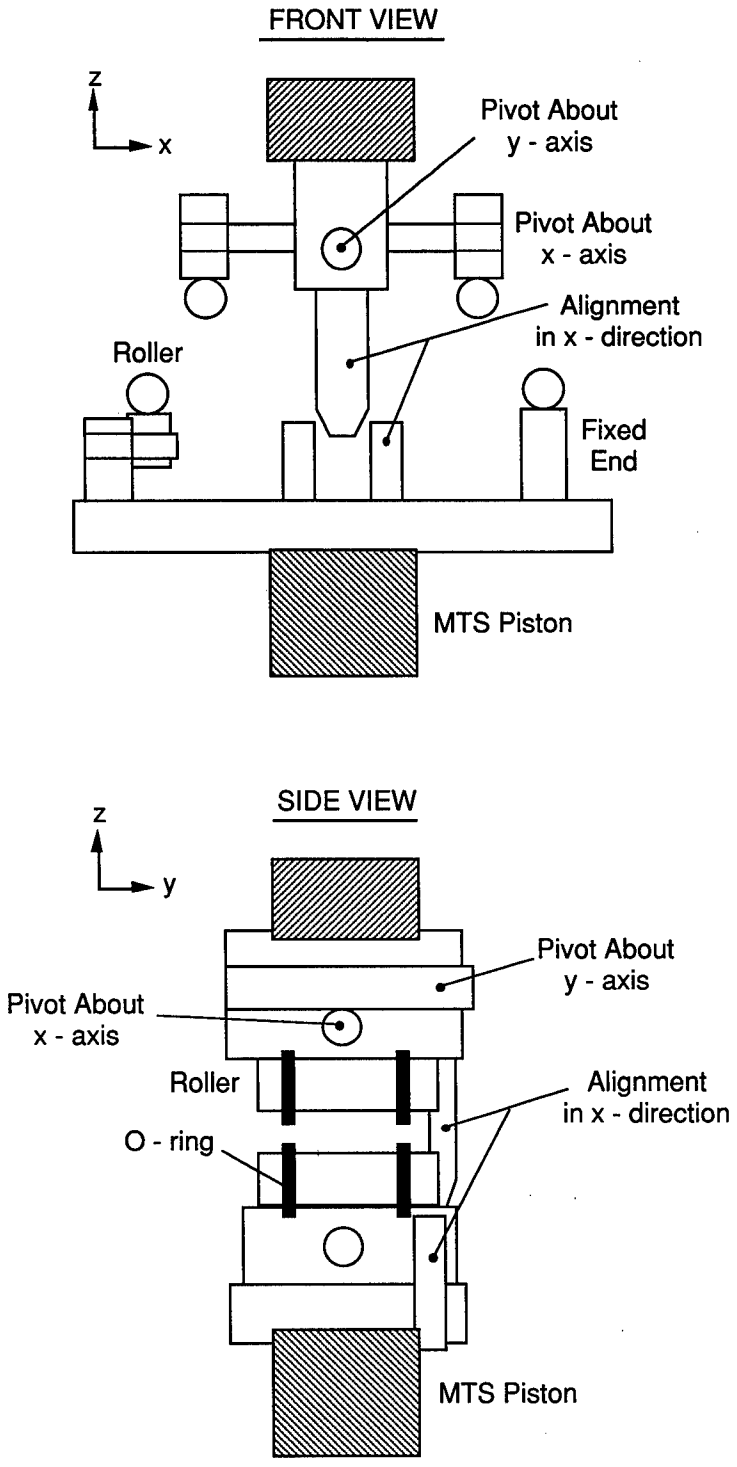

Figure 3. Loading arrangement used for four-point flexure test.

a nitrogen-gas-cooled environmental chamber. Temperatures within the chamber were controlled by a cooled nitrogen gas flow (varied by a thermostatically controlled solenoid valve). The loading system was actuated by a computer-controlled electrohydraulic machine. The four-point loading apparatus consisted of four 6.35-mm (0.25-in.) diameter rollers. Although the lower two rollers were fixed, the upper two were free to pivot about the x-axis (parallel to the length of the specimen, see Fig. 3). This configuration ensured that any twisting of the specimen was not transmitted as a side load, and it also accounted for any small deviations in thickness across the sample.

The bending modulus of elasticity E and the breaking strength S were calculated from the following equations:

$$E = Pa(3L^2 - 4a^2)/4bh^3d \tag{1}$$

$$S = 3Pa/bh^2 \tag{2}$$

where

P = load (N)
a = distance between the closest support and the load roller (m)
L = support span (m)
b = specimen width (m)
h = specimen thickness (m)
d = vertical deflection of the specimen center (m)

Flexural fatigue tests were conducted over the same temperature range as the four-point bending tests. For all low temperature testing, specimens were placed in the environment chamber and allowed to cool to the desired temperature for at least one hour before testing. Each specimen was subjected to 10^5 sinusoidal loadings at a frequency of 4 Hz within the limits of 20% and 80% of the yield load. This frequency is well below 10 Hz, at which hysteresis heating develops. To obtain damage accumulation estimates through stiffness data, load–deflection characteristics were recorded from separate quasi-static tests performed on the samples at the beginning, midpoint, and end of the fatigue cycle. Load applied during the quasi-static tests was 80% of yield. Upon completion of the fatigue cycle and corresponding quasi-static test at 10^5 cycles, bending tests to failure were performed at the specified temperatures.

Load and deflection for all quasi-static tests were recorded on a Nicolet 4094A digital oscilloscope at a rate of 200 samples/second. The cross-head speed was 1.22 mm/s (0.05 in./s). Load was was recorded directly as voltage outputs

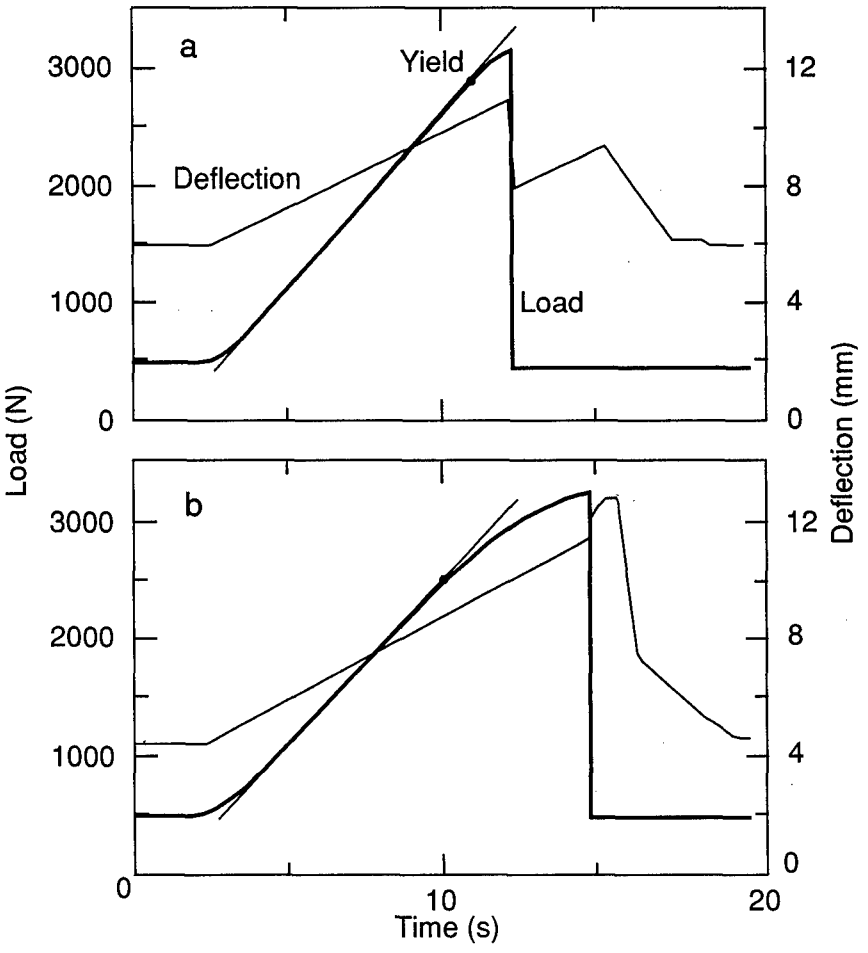

Figure 4. Load and deflection results in four-point flexure tests.
a. Failure in static flexure test at –20°C (non-fatigued specimen)
b. Failure in static flexure test at –20°C (fatigued specimens).

from the electrohydraulic loading system, and the deflection was read through a specially fabricated cantilever extensometer calibrated at low temperatures.

DISCUSSION AND ANALYSIS OF RESULTS

At all temperatures, load cycling proved to reduce the elastic modulus and shift the the yield point to a lower value, in effect toughening the material. These effects can be observed by comparing the data presented in Figures 4a and 4b.

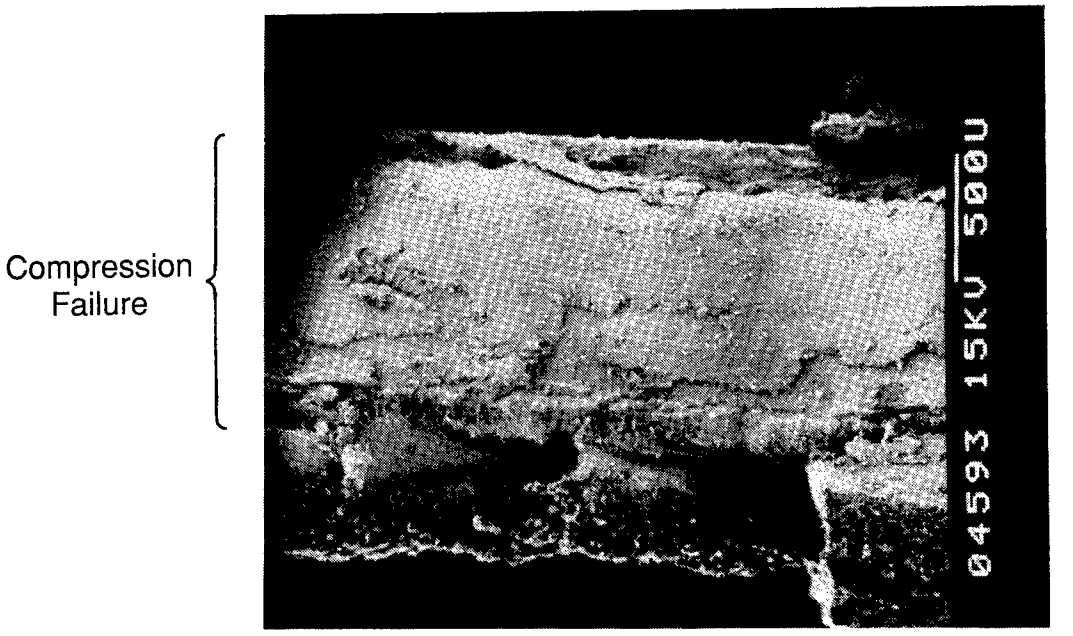

Figure 5. Failed surface of the fatigued GR/EP lamina specimen (SEM).

Yielding occurs at approximately 2900 N for the non-fatigued specimens, as compared to 2400 N for fatigued specimens. Note also that although both types of specimens experience failure at approximately 3200 N, the fatigued specimens exhibit plastic behavior over a greater range of deflections.

Specimen yielding (for non-fatigued and fatigued conditions) began with the growth of an incipient interlaminar crack in the upper compressive region, close to the neutral axis. Final failure occurred suddenly with a through-the-thickness crack generated between load rollers. Observed under the scanning electron microscope (Fig. 5), 60–70% of the fracture surface exhibited compression failure. This type of failure is recognized by a light and smooth texture with clumps of short broken fibers lodged in a disorderly fashion within the substrate of well-ordered material. In contrast, the tensile failure zone is darker with abundant evidence of fiber pullouts. The relatively large surface area under compressive failure was expected due to the strength being substantially lower in compression than in tension. Failure was initiated on the compressive surface by local fiber buckling. Owen and Morris [2] observed initiation of similar failures on the compressive surface of four-point bending tests involving high-modulus graphite/epoxy fibers. Successive buckling of adjacent layers shifted the neutral axis farther down to bring more areas of the section under compressive stress.

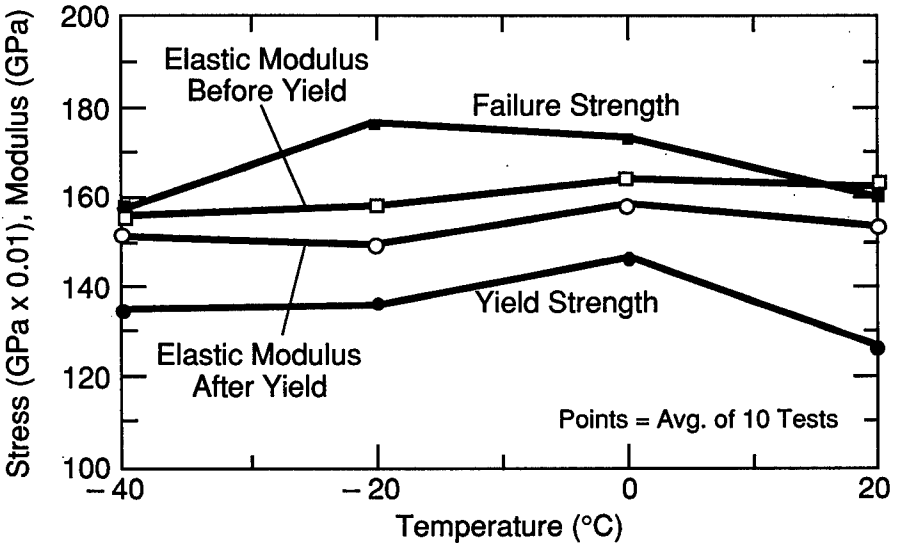

Figure 6. Effect of low temperatures on non-fatigued GR/EP 0-degree laminates under flexural test. (Each data point is the average of 10 tests.)

Initial portions of all load deflection curves exhibited a slight but discernible stiffness increase, possibly due to fiber straightening when subjected to tension. The next portion of the load deflection curve was essentially linear to the yield point. Beyond yield, stiffness continued to decrease until failure occurred.

When the specimens were cooled to 0°C, the stiffness (before and after the yield point), yield strength, and failure strength increased, but on further cooling to –40°C, they decreased. The behavior of the matrix, which became stiffer as temperatures are decreased, is responsible for the initial stiffness increase. According to Rosen's extensional or shear buckling theory of compressive failure [3], this matrix stiffness increase may have contributed to the strength increase. With further cooling, the thermoelastic residual stress (resulting from the thermal expansion mismatch between the fibers and the matrix) may have exceeded the matrix strength and allowed microcracks to develop. The effect of these microcracks would be a reduction of the laminate's stiffness and yield strength, as shown in Figure 6.

At room temperature, the strength associated with fatigued panels was nearly identical to that of the non-fatigued specimens. As temperatures decreased, however, dramatic differences in strength became apparent (Fig. 7). Microdamage produced during the fatigue process seems to strengthen the material. An examination of the failure mode revealed that in all cases fracture was initiated

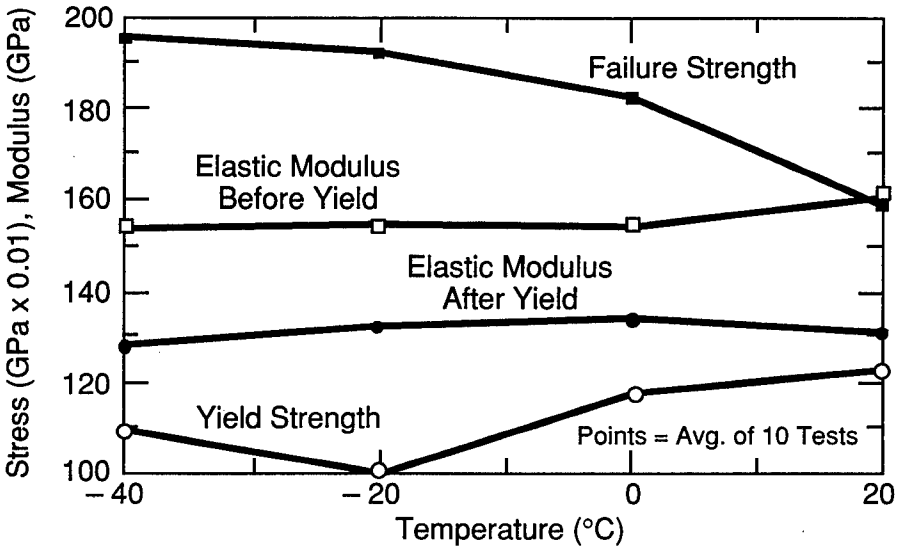

Figure 7. Effect of low temperatures on GR/EP 0-degree laminates under flexural test following 10^5 cycles of fatigue loading. (Each data point is the average of 10 tests.)

with the growth of interlaminar cracks tending to split the specimen horizontally in layers. The onset of these cracks corresponded to the yield point. In post-fatigue tests (for all temperatures), yield loads proved lower than the corresponding loads for non-fatigued specimens, which suggests that microdamage influenced the yield. Microdamage was also noted to have lowered stiffness both before and after yield. The final failure, however, would require through-the-thickness fiber fracture in tensile and compressive modes. (Compressional fracture by itself will not cause complete failure.) It is not totally inconceivable that following cyclic loading the reduction in matrix stiffness allowed the fibers to attain more uniform stress distribution, therefore allowing higher failure loads. More microdamage is expected at lower temperatures because of the higher residual thermoelastic stresses resulting from the thermal expansion mismatches. Larger reductions in pre-yield and post-yield stiffnesses support this observation (Fig. 7).

CONCLUSIONS

Various models of damage mechanisms and accumulation under fatigue loading are available in composites literature. Most, however, do not account for the influence of lower temperatures. The results from flexural fatigue tests,

presented here, show evidence of non-monotonic changes in residual strength and stiffness upon progressive cooling. Strength increased but stiffness degraded with lower temperatures. The constituent's low temperature properties and thermoelastic stresses seem to be the factors for such paradoxical results. These influences must be considered to apply damage models to low temperature regimes. Moreover, because the compressive strength is much lower than the tensile strength, flexural fatigue is controlled by the compressive strength. Low temperature enhances the strength and stiffness of the matrix, and thus provides overall beneficial effects on flexural fatigue.

Acknowledgements: The author thanks Martin Jan Kryska and Dr. Ian Baker of the Thayer School of Engineering, Dartmouth College, for their participation in this research and test program.

REFERENCES

1. Roylance, M.E.,Houghton, W.W., Foley, G.E., Shuford, R.J., and G.R. Thomas (1983) Characterization, analysis, and significance of defects in composite materials. In *Proceedings, Meeting of the Structures and Materials Panels (56th), London,12–14 April,* p. 7-1–7-14, NTIS AD -D134058.

2. Owen, M.J. and Morris, S. (1970b) Fatigue resistance of carbon fiber reinforced plastics. *Modern Plastics*, **47** (4): 158–173.

3. Rosen, B.W. (1965) Mechanics of composite strengthening. In *Fiber Composite Materials,* Am. Soc. Metals Seminar, p.37–75.

COUPLED HYDRO-STRUCTURAL ANALYSIS OF NON-PERFORATING IMPACTS

Nasit Ari and David Gray
Kaman Sciences Corporation
Colorado Springs, Colorado 80933-7463

I. INTRODUCTION

Standard methodologies exist to evaluate damage from penetrating impacts and blast/shock loads on structures. Penetration phenomena and structural response to impulsive loads are simulated with high fidelity by using Eulerian hydrocodes and Lagrangian structural finite element codes. In the case of non-perforating impacts, however, no established techniques exist to simulate the coupled phenomena of ballistic penetration shocks and late time structural response. This work-in-progress paper describes an attempt to establish a robust coupling methodology.

The impact domain consists of stress levels significantly higher than the yield stress and of extreme deformations such as jetting, erosion and cavity formation. Eulerian hydrocodes are equipped with the appropriate equations of state and advection routines to represent material flow and failure in an efficient way. The response time of interest in impact problems and, hence, hydrocode simulation durations are typically in the microseconds. As hydrocodes employ a very large number of cells, it is computationally impractical to utilize them to simulate late time response. Structural codes on the other hand can model the geometry in more detail with fewer complex elements and simulate structural response into much later time. These Lagrangian codes, however, are not most suitable for modelling the early impact regime: their elements may not accommodate severe geometric distortions due to penetration and erosion, or they might require excessive remeshing.

There is considerable effort to extend the range of applicability of both hydrocodes and structural codes. Eulerian codes are augmented with coupled Lagrangian elements and structural codes are modified with slide-line and erosion algorithms. A special evolution of these efforts is toward the so-called Arbitrary Lagrangian Eulerian (ALE) codes where the character of elements are automatically adjusted depending on distortion levels (e.g. CALE, AUTODYN). However, computational burdens associated with these modifications could be significant. Nevertheless they

can be efficient analytic tools for a restricted class of problems where impact is well localized.

However, for 3-D simulations of high momentum transfer, massive shock impacts into large targets, these tools might be inadequate. A logical alternate approach would then be to simulate the initial cratering with an Eulerian hydrocode and the late time structural response with a Lagrangian finite element code.

In Section II we briefly describe the present approach to a strongly coupled impact/structural response problem and its numerical implementation. Computational validation of the approach is described in Section III. Section IV discusses application of the methodology to lethality assessment studies and concludes the paper.

II. METHODOLOGY

Hydrocodes compute for each cell the strain and stress tensors, their time rates of change and cell-centered velocities. Thus, at an appropriate transition time they can supply the initial values for a structural code computation. The critical issues are selection of the handover time and self-consistency (compatibility) of initial stress and velocity fields. The time of coupling should be selected such that the transferred stress and deformation levels are within the domain of applicability of the constitutive equations present in the structural codes. In addition the stress or strain fields should not violate the compatibility conditions. Otherwise artificial dislocation and stress singularities might be introduced into the structural code computation which would cause numerical instabilities. Further, the interpolation of nodal velocities should give special consideration to boundaries and interfaces.

If one of the impacting bodies completely erodes or bounces back during the initial phase, then the structural mesh will consist of target elements only. If, however, there is a residual projectile mass still imparting momentum, then the initial setting of the structural computation will be more complex. Either a sliding surface has to be utilized or the residual momentum has to be applied as a surface pressure. Finally the structural mesh should account for the crater and the deformed geometry. The crater surface will include mixed and eroded cells and the representation of this region might not be complete in a structural mesh. It is assumed however that this deficiency will not affect the overall structural response.

Impulsive loads from impacts lead to fast running elastic shock waves, slower but higher amplitude plastic shocks, spallation and late time low frequency structural response. Each of these damage

mechanisms could be dominant for different subcomponents at various times depending on their distance from the hit location.

Thus multiple handover times could be utilized for different substructure analyses. For example, some sensitive equipment far from the hit point could be influenced by elastic shocks. The early time hydrocode computations could provide the proper initial and boundary conditions for this subregion even though a structural code might not be able to continue a full mesh transition.

Hydrocodes could also be utilized to determine the total forcing function applied during the penetration phase by monitoring the total momentum deposited on the target. This load history then could be applied over the proper loading region within a structural code. This approach indeed has been validated for simple plate targets by Quigley[1]. The hydrocode and structural code results have shown close agreement except for high frequencies and locations near the hit point.

The decision as to which coupling strategy to apply depends on the impact configuration and relative locations of critical components with respect to the hit point. This selection process could be supported with a systematic iterationas follows:

1. Run an initial hydrocode with a rough mesh of the full structure to establish the extent and timing of various shock fronts and to identify structurally vulnerable components. Determine the hydrocode and structural analysis domains.

2. Model the hydrocode domains in more detail and finer mesh. Establish the proper boundary conditions for the structural domains.

3. Decide what coupling method to apply to assess damage for subcomponents.

4. Accordingly, provide to the structural code the initial stress and velocity state and/or the impulse history on substructures.

The current approach is implemented at Kaman in a HULL[2]/ABAQUS[3] computing environment. The mesh geometry, stress, and velocity fields from HULL dumps generate ABAQUS input files automatically. If meshing of two codes are different, then rezoning routines and super element techniques could be utilized to map the fields properly. The automated coupling process should, however, be checked for self-consistency. A typical computational loop in a structural code would obtain accelerations from initial stress distributions and then determine by time integration

velocities and displacements which in turn yield the next cycle of strain and stress values. Whether this iteration works numerically through the coupling (i.e. changes in mesh and equation of state) however, needs to be tested. In the next section, a proof-of-principle simulation serves to illustrate various facets of the present coupling approach.

III. NUMERICAL EXAMPLE

The computational example given below is a representation of a massive rod impact into an armored vehicle at ordnance velocities. Figure 1 shows density maps from a full geometry hydrocode simulation during the penetration phase. Though the mesh is coarse, the model manages to deliver an image of essential shock distribution as shown in Figure 2. It also helps to visualize structurally vulnerable areas even though no low frequency structural modes are observable yet. A subsequent finer resolution simulation then focuses near the front region. Pressure maps of the penetration phase at t = 200, 650, and 1000 microseconds are shown in Figure 3.

A successful and efficient coupling requires a transition time around which element (cell) deformations and stress levels first become appropriate for the structural code. Too early of a coupling, at shock pressure levels well above the yield stress, might lead to numerical instabilities (either due to limitations in constitutive equations or due to severe element distortions). Too late of a transition would waste computational resources. Figure 4 shows the initial ABAQUS stress distributions after an early handover at 200 microseconds. The structural code can handle the transition mechanically but the time steps go down drastically to 0.1 microseconds, one tenth of the hydrocode time increments, possibly due to reasons cited above.

In contrast to this premature transition, the coupling at 650 microseconds is more promising (Figure 5) and structural code time steps increase compared to hydrocode time increments. Increased cell (element) size and consequently larger time steps are the expected benefits of the transition to the structural code. Indeed a Von Mises map at 5 and 12 microseconds after the handover (Figure 6) shows a relatively smooth continuation.

Another check for a successful coupling is to let the hydrocode and the structural code run for a short time interval Δt after the transition time t_1, and compare the results at time $t_2 = t_1 + \Delta t$. If the results are comparable, the transition time and domain are appropriately selected. A successful comparison indicates a stable handover and validates the coupling process. Utilization of this

technique is certainly facilitated by automated handling of the mapping between codes.

IV. APPLICATION OF THE METHODOLOGY TO LETHALITY ASSESSMENT STUDIES

In a recent BRL report, Walbert[4] elucidated reasons for incorporating ballistic shock effects in vulnerability/lethality analysis. Non-perforating impacts where substantial momentum transfer is involved are one of the primary examples for such a shock and late time structural damage analysis. The assessment of the Energy Deposition Lethality (EDL) could be based on the presented methodology. For a specific projectile/target configuration, one needs first to establish the set of perforating impact shotlines. For these cases, no further EDL analysis is necessary. For non-perforating impacts, one utilizes a Standard Damage Assessment List (SDAL) and selects components vulnerable to shock/structural effects. Then, depending on the mission requirements of the armored vehicle for non-perforating shotlines, a set of critical impact configurations could be identified for further EDL analysis. For these limited number of cases then, with the help of the present coupling methodology one can compute probabilities of kill (P_k) depending on total specific impulse delivered and distance of critical components from the impact area.

V. ACKNOWLEDGEMENTS

The authors acknowledge the valuable contributions of Messrs. Dick Keeffe, Jim Eamon, and Steve Diehl in technical discussions of this paper. Also, the help of Mrs. Eleanor Ellis in preparing this manuscript is greatly appreciated. Finally, we are indebted to the referee for the careful critique.

VI. REFERENCES

1. Quigley, E.F., "Finite Element Analysis of Ballistic Shock Using Hydro-Code Generated Loading History", Combat Vehicle Survivability Symposium Proceedings, Vol. II., March 1990, Sponsored by TACOM and ADPA, pp 176-183.
2. Matuska, D.A. and Osborn, J.J. (1986a). HULL Technical Manual, vol I, Orlando Technology Incorporated.
3. ABAQUS Finite Element Code, Hibbitt, Karlsson & Sorensen, Inc., Providence, RI
4. Walbert, J.N., "A Proposed Method for Incorporating Ballistic Shock Effects in Vulnerability/Lethality Analyses", BRL-MR-3930, August, 1991.

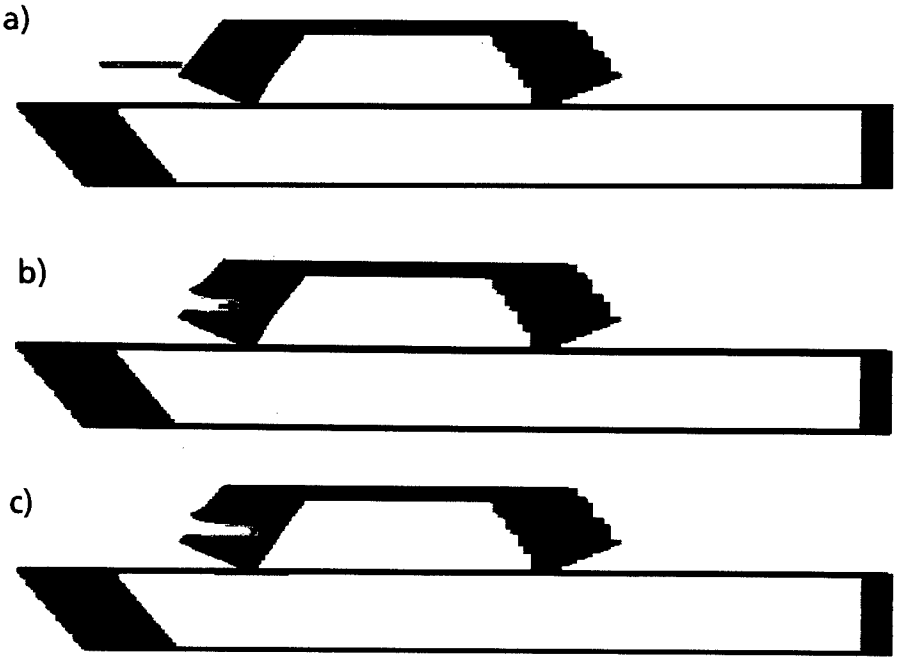

Figure 1. Density maps from the coarse mesh hydrocode simulation on the symmetry plane at a) t = 0 μsec, b) t = 700 μsec, c) t = 1100 μsec

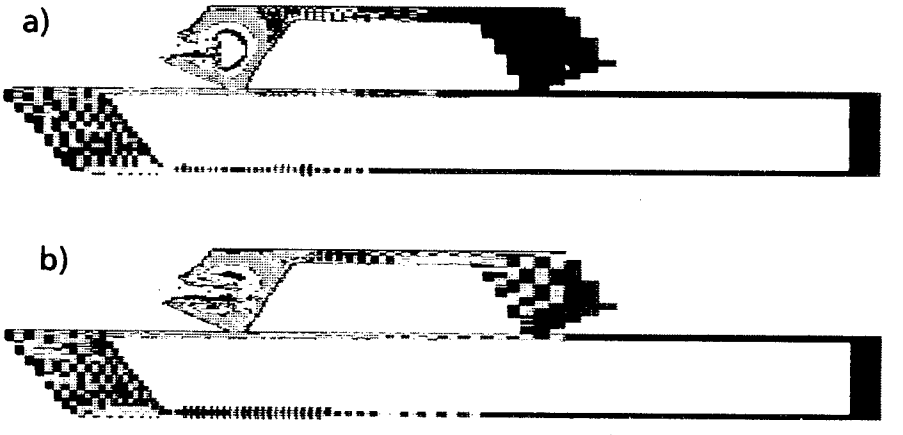

Figure 2. Pressure maps corresponding to density maps given in a) Fig. 1b and b) Fig. 1c.

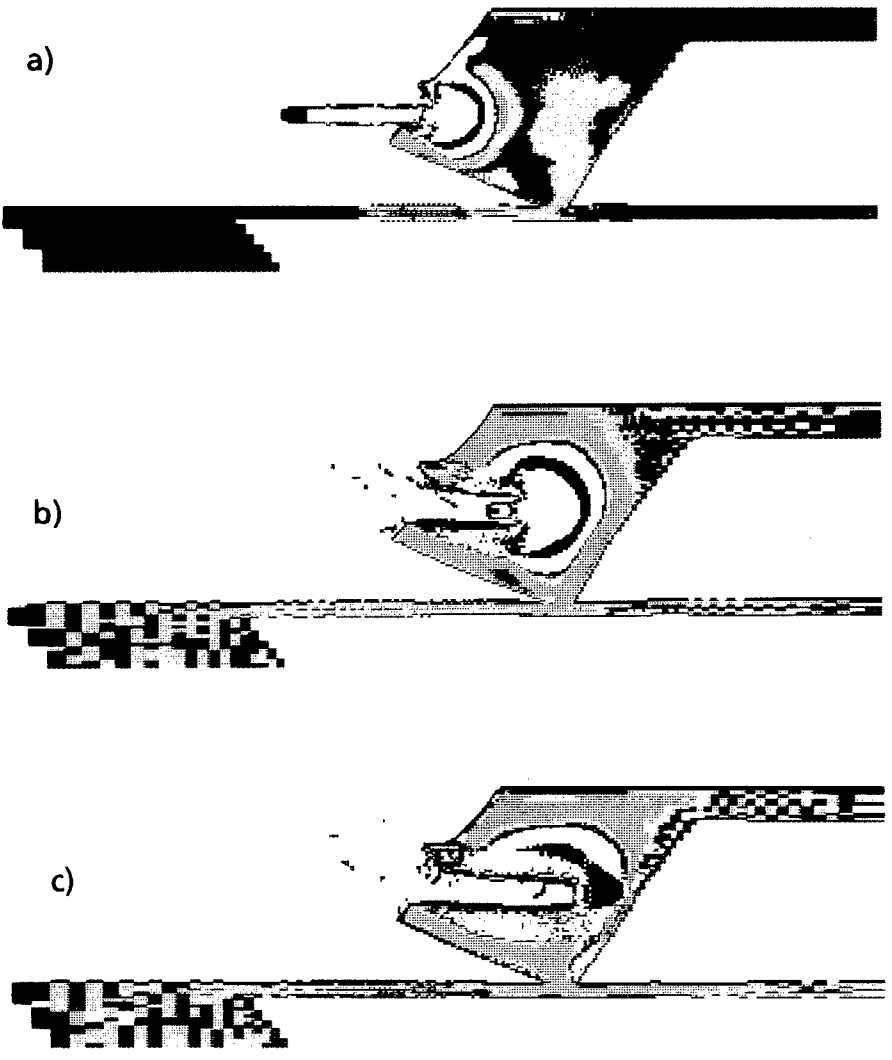

Figure 3. Pressure maps from the finer mesh hydrocode simulation on the symmetry plane at a) t = 200 μsec, b) t = 650 μsec, and c) t = 1000 μsec

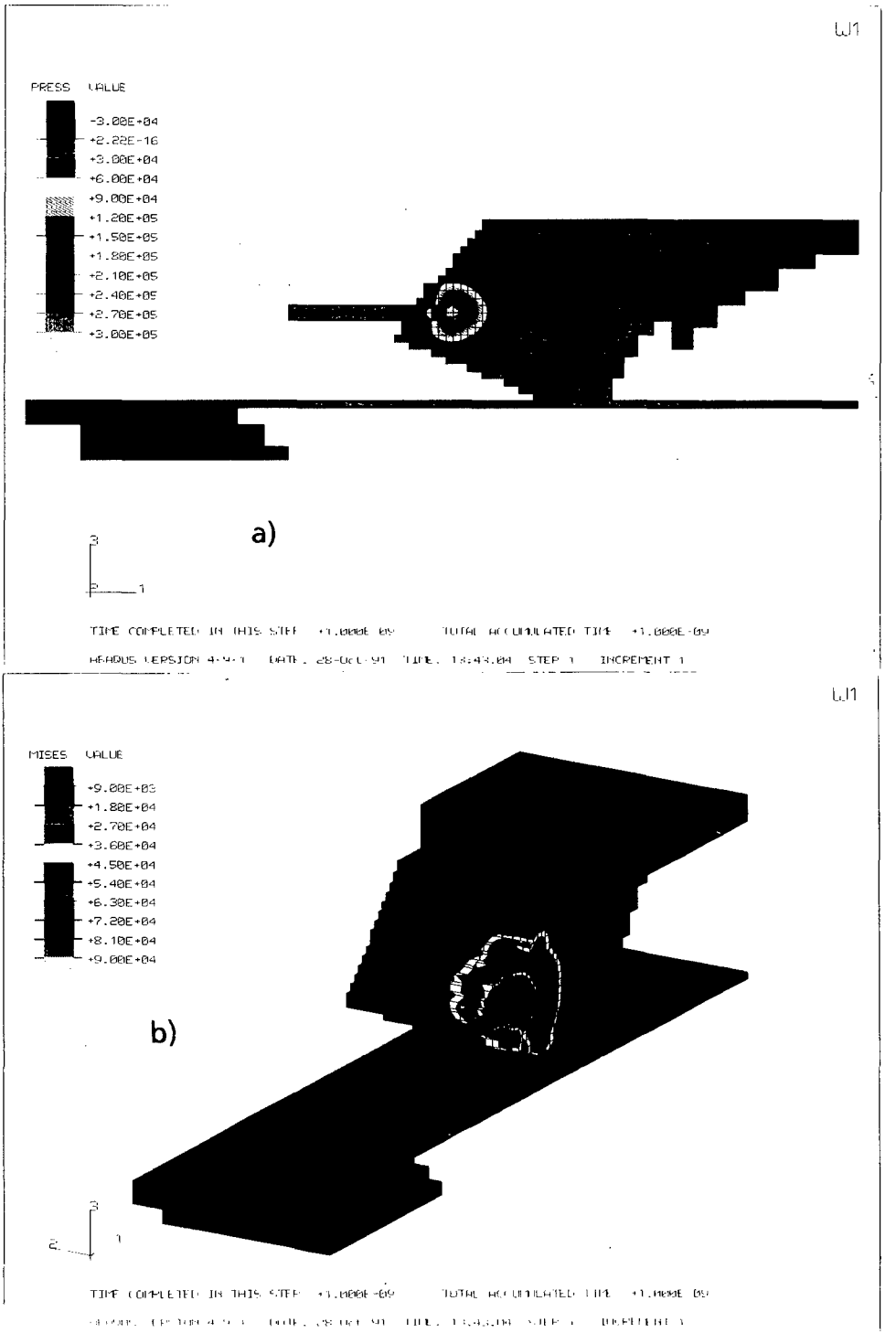

Figure 4. ABAQUS initial stress states at t = 200 μsec handover: a) pressure, b) Von Mises stress

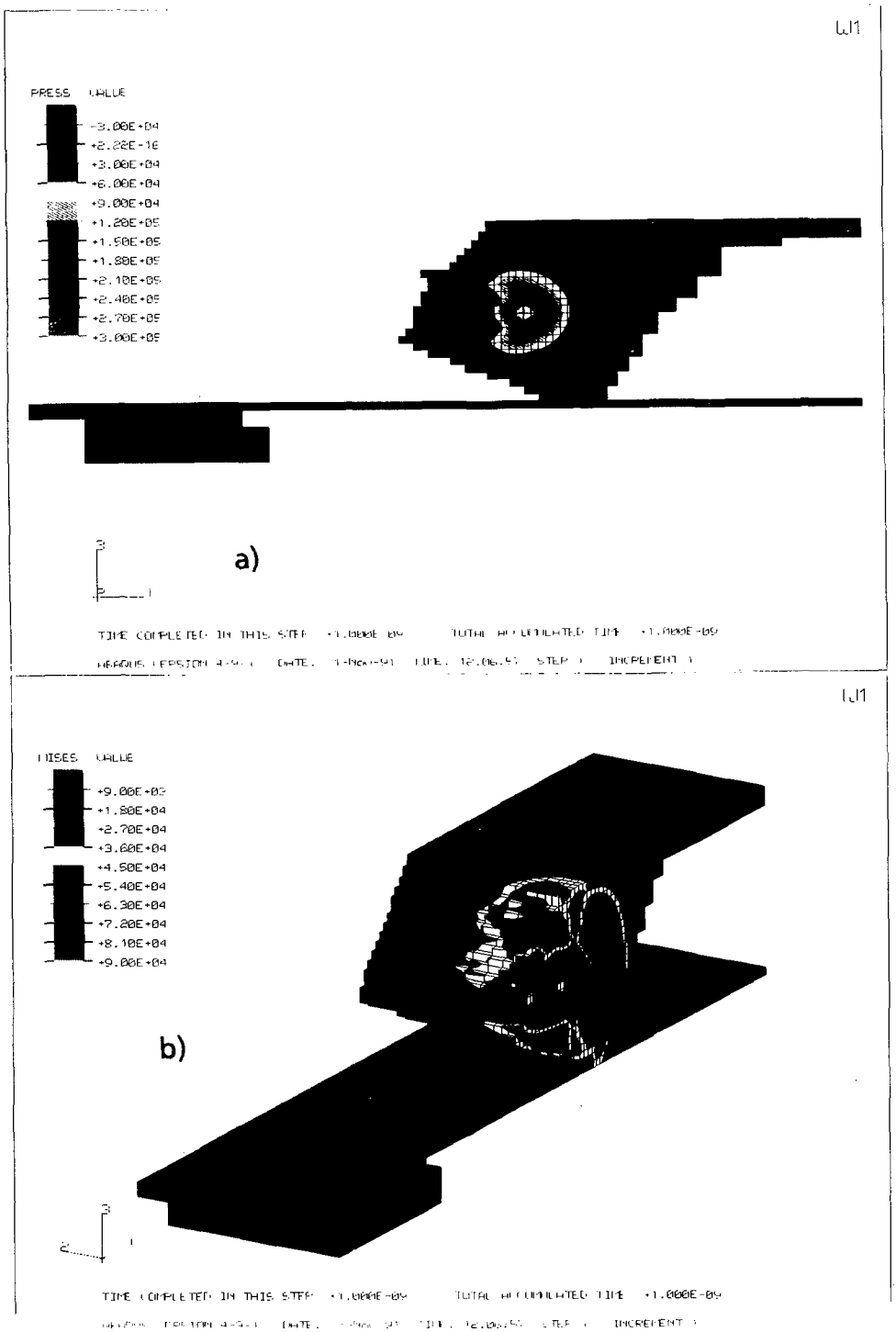

Figure 5. ABAQUS initial stress states at t = 650 µsec handover: a) pressure, b) Von Mises stress

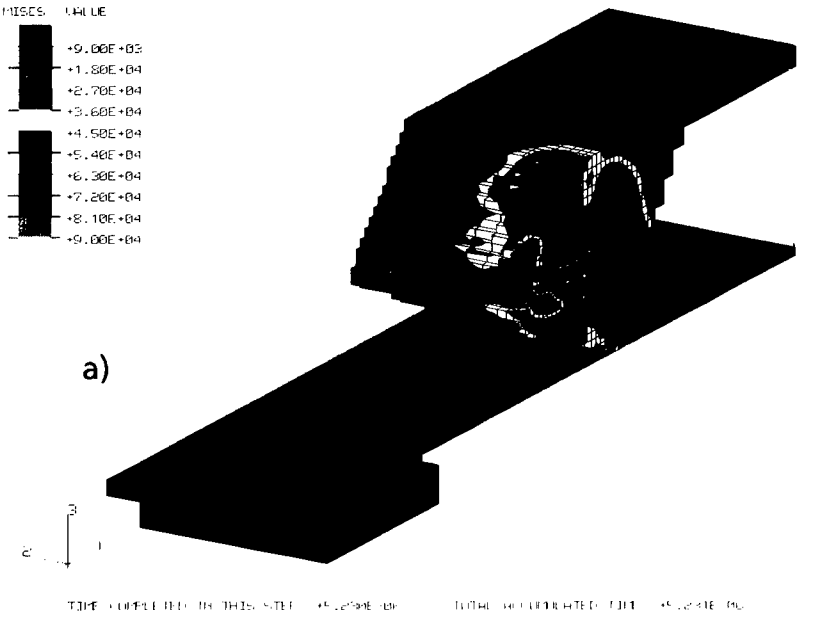

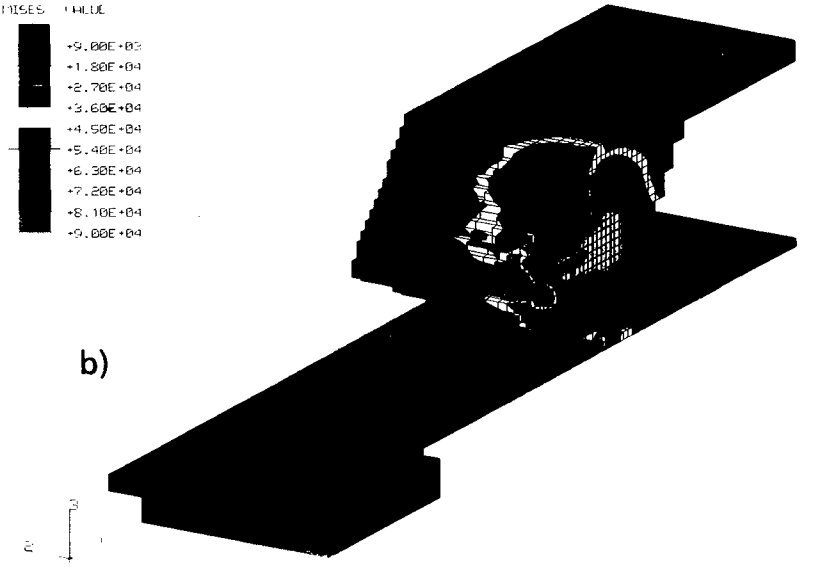

Figure 6. ABAQUS Von Mises map
a) 5 µsec after the handover
b) 12 µsec after the handover

CONTINUUM AND MOLECULAR MODELS FOR RUBBER VISCOELASTICITY

Arthur R. Johnson
Ross G. Stacer

Army Materials Technology Laboratory
Watertown, MA 02172

ABSTRACT

In the linear theory of viscoelasticity, the modulus is defined as the time-dependent proportionality constant relating stress to strain, independent of strain level. Although this definition is useful mathematically and provides a wide range of predictive capabilities, it is almost never observed in real polymeric materials. For these materials, mechanical behavior is both time and strain-level dependent. This nonlinear response to imposed deformations is discussed in this paper in terms of two models, one based on continuum mechanics and the other on molecular dynamics. First, we review a large deformation continuum mechanics model recently presented for nearly incompressible materials. Large cyclic deformations of filled elastomers are modelled in this approach using viscohyperelastic internal solids. Secondly, we present an analysis of the same behavior from the perspective of molecular mechanics. This later model is based upon a topological constraint system in which relaxations between entanglement junctions are treated via polymer tube dynamics. Finally, it is shown that a close relationship exists between the predictions of these two models.

INTRODUCTION

Response properties of elastomers are extremely dependent upon material deformation history [1-5]. This history dependent behavior is generically termed the Mullins effect. Although a number of definitions and observed phenomena are associated with the Mullins effect, it is most often discussed for crosslinked materials in terms of stress-softening and subsequent recovery. The latter feature is important since it differentiates the process from micromechanical damage and plasticity effects, to which the

process is often erroneously attributed. This is because given appropriate conditions, in terms of both time and temperature, an elastomer can be expected to recover most, if not all, of its original properties [1,2]. The rate of recovery, however, can vary significantly depending on which property is under consideration [6]. Other observational features of the Mullins effect which have been investigated include extension beyond earlier cyclic limits [2,3], change in volume when nonreinforcing fillers are used [2,7,8], alternate loading histories [9], and the role of various formulating ingredients [2].

A large deformation computational scheme has recently been proposed [10,11] which models these behaviors as a continuum. The one dimensional model was shown to predict literature data, and finite element analyses were carried out to compare the one dimensional model to its corresponding finite element model. This nonlinear model was first constructed for large cyclic deformations of a filled elastomer by superimposing a hyperelastic solid with a special internal viscohyperelastic solid-fluid [11]. Since filled elastomers are often slightly compressible, total Lagrangian minimal potential energy finite element models were developed even earlier and used to predict their static deformations [12,13].

In addition to briefly reviewing the above model, we also introduce in this paper a molecular dynamics model developed in parallel to account for many of the same phenomena. This approach is based on the reptation/tube model of polymer dynamics [14,15]. In this model, deformation behavior of the polymeric network is divided into two components. The first arises from the affine deformation of the network junctions while the second embodies network inhomogeneities such as entanglements, unattached chain ends, and segments between crosslink sites sufficiently far away from said sites that they relax independently. Contributions of these latter features to the

overall deformation behavior are combined and modelled by a simple topological constraint system. Within this system, individual chain segments are allowed to adjust or equilibrate themselves to a reduced energy state via reptation, thus relaxing their deformed length. A solution for the response of such a network under constant strain rate is developed.

Finally, both the continuum and the molecular models are brought together and their respective responses compared. It is the purpose of this paper to show that both lead to complementary rather than conflicting predictions, with the continuum model deemed more appropriate for structural analysis and the molecular model better to guide the development of new materials with superior properties.

CONTINUUM MODEL

We begin our brief review of the continuum model of Johnson and Quigley [10,11] by considering the nonlinear Maxwell model made from the four elements shown in Figure 1. The stretch ratio and energy function for the nonlinear elastic element in the middle leg are λ_E and W_E, respectively. A nonlinear loss element with energy function W_L is shown on the right. Constants to be used in the flow laws for the two nonlinear dashpots are η and η_L. At any time t the total stress σ is given by

$$\sigma(t) = \sigma_E(t) + \sigma_\eta(t) + \sigma_L(t) \qquad (1)$$

where σ_E and σ_L are the stresses in the nonlinear elastic and loss elements, respectively, and σ_η is the stress obtained from the nonlinear dashpot on the left side.

We assume that the nonlinear elastic and loss elements have their stresses determined from hyperelastic energy functions. The loss element's undeformed length is assumed to change according to a flow law described in Reference 10.

The dashpot in series with the loss element is used to symbolically indicate a flow law is active. In the case of a quasistatic deformation, the leg without a dashpot provides the expected nonlinear (long term) hyperelastic response. After a suddenly applied step displacement (relaxation test) the hyperelastic loss element provides the additional viscous stress above the long term stress. For a creep test or a continuous moving boundary, the single nonlinear dashpot on the left side in Figure 1 provides an additional viscous stress.

In this paper we use the three nonlinear Maxwell legs described above to model the exponential-rate stretching experiment of McGuirt and Lianis [16] for an SBR elastomer. Computations were first made with $\eta = 0.0$ for which the maximum difference between the computed stresses and those reported by McGuirt and Lianis was about 0.138 MPa. Selecting $\eta = 2/3$ s reduced the errors and the result is shown in Figure 2. Good agreement is found between the viscohyperelastic Maxwell model and the literature data. The material constants describing the model's elements were determined by standard methods (Mooney plots, etc.). Data required included a series of step relaxation tests to determine W_L, W_E and η_L, along with several different constant strain-rate tests or a single variable-rate test (to select η for the range of stain-rates expected). Next, we describe a finite element extension of this rubber viscoelasticity model.

The one dimensional model described above can be converted to a three dimensional solid model by superposing a nonlinear loss solid onto the hyperelastic storage solid. This requires the reference shape of the loss solid to change with t according a simple flow law. We use the loss solid's reference shape, the storage solid's deformed shape, and the loss solid's hyperelastic energy function to compute viscous forces (or stresses) on the storage solid's deformed shape similar to the one dimensional case [10]. Additional

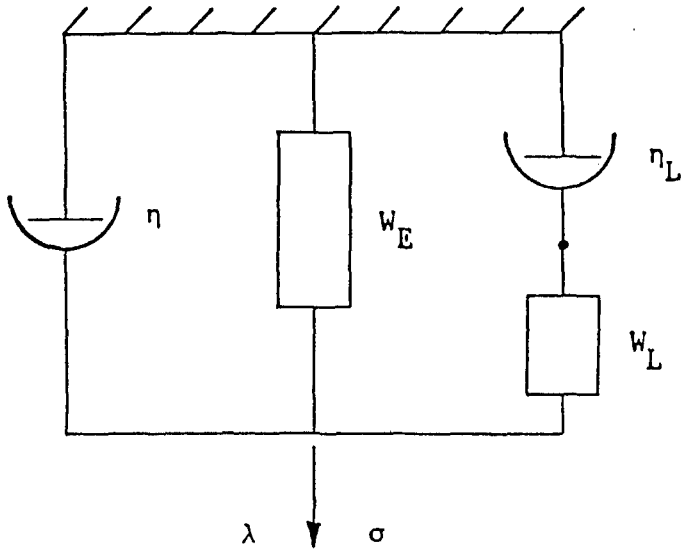

Figure 1. - Nonlinear Maxwell Model.

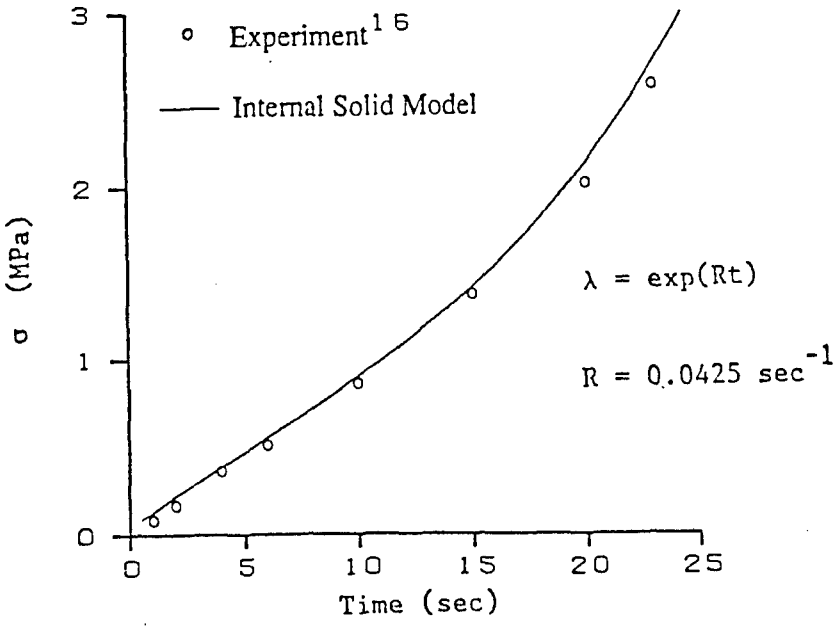

Figure 2. - Uniaxial Exponential Rate Loading at 0.0425 sec^{-1}.

viscoelastic or loss forces acting on the storage solid's deformed shape are determined through equations describing the damping in the nonlinear dashpots.

For a two dimensional finite element model, consider the solid configurations shown in Figure 3. The coordinate systems $\{X_1, X_2\}$, $\{Y_1(t), Y_2(t)\}$ and $\{x_1(t), x_2(t)\}$ describe the reference configuration for the hyperelastic storage solid, the reference configuration of the hyperelastic loss solid, and the deformed configuration of the elastic solid, respectively. Indicated time dependencies illustrate that the shape in the latter two coordinate systems change with t. Next, these shapes are discretized using the finite element method with the nodal locations indexing them given as in Figure 3, where the i subscripts refer to the node number. A complete description of the governing equations can be found in References 10 and 11 along with several analyses to compare the one dimensional solid-fluid model to its corresponding finite element version.

MOLECULAR MODEL

As mentioned in the Introduction, deformation of a polymeric network can be discussed from the perspective of a two-component system. Figure 4 illustrates how such a system would respond to an instantaneous step strain in simple extension. The left side of the figure shows the deformation of the unit cube with a single chain attached at two junction (crosslink) sites. In the kinetic theory of rubberlike elasticity [17], an assumption of affine deformation of these sites leads to an expression for the nominal stress

$$\sigma = \tfrac{1}{2}\nu kT(\lambda - 1/\lambda^2) \qquad (2)$$

where ν is number of crosslink sites per unit volume or

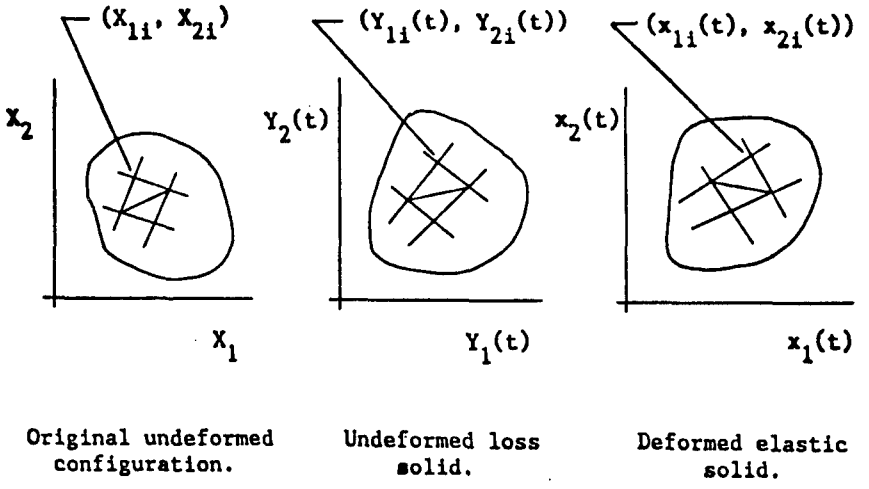

Figure 3. - Two Dimensional Configurations.

crosslink density, k is Boltzmann's constant, and T is temperature.

For purposes of this discussion, the chief limitation of Equation (2) is that it describes an ideal equilibrium condition and does not consider any time-dependent relaxation processes that may occur at other locations within the network. These relaxation processes are highlighted in Figure 4 through the deformation of the unit sphere, shown to the right as a chain segment responding independently of network junction after the initial deformation. In physical terms, these relaxations arise from a variety of network inhomogeneities including entanglements, loose chain ends, unattached molecules, etc. We combine all these processes together mathematically by defining an effective crosslink density ν_e for introduction later into equations similar to (2) via a volume rule of additivity

$$\nu_e = \nu_c + \nu_p \qquad (3)$$

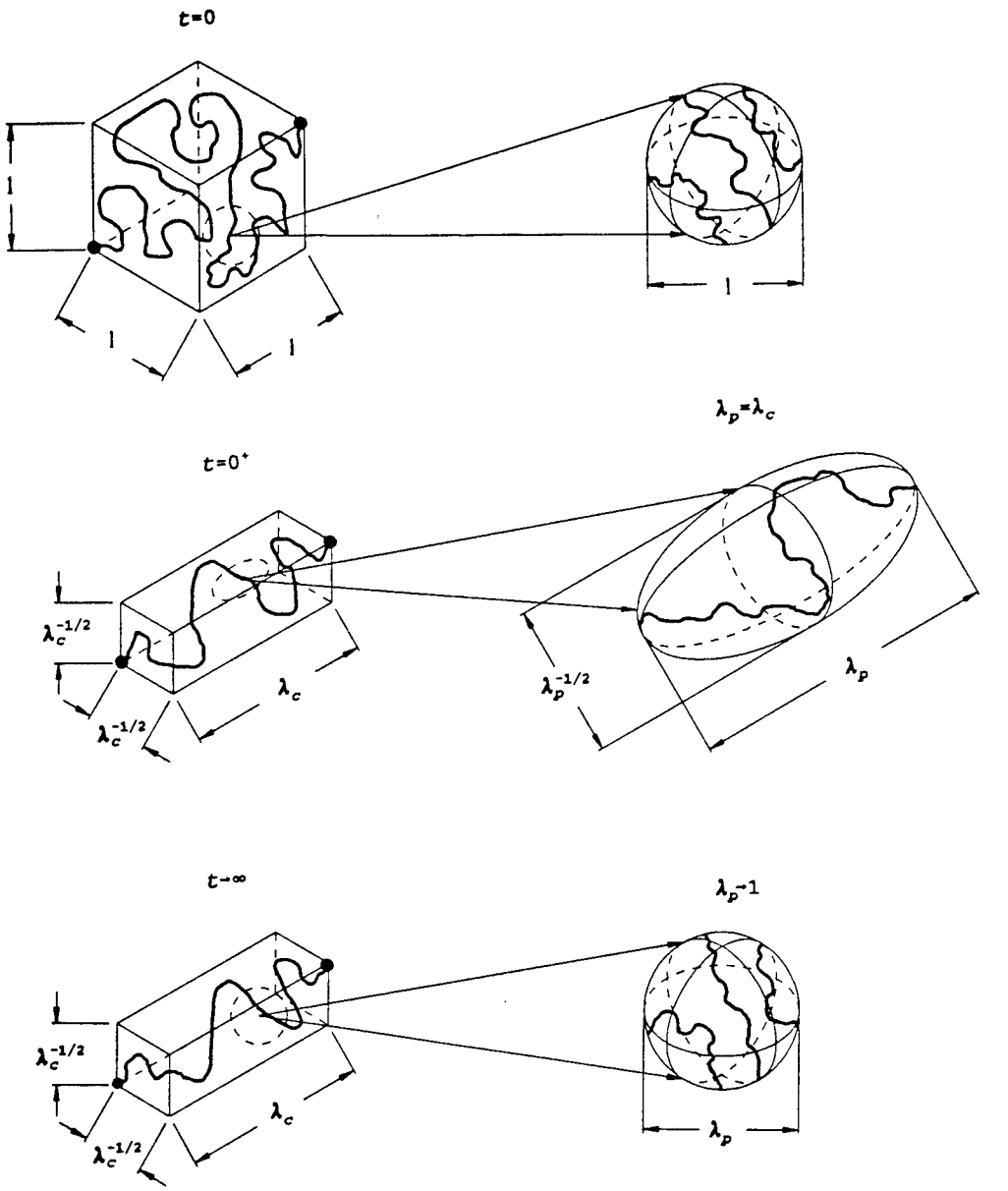

Figure 4. - Response of Unit Cube to Instantaneous Step-Strain, Illustrating Relaxation as Function of Time at Locations Away from Crosslink Sites.

where the subscripts c and p refer to chemical and physical (nonpermanent) crosslinks, respectively. From the brief description of the model given above, we see that ν_c describes a time independent process while ν_p is associated with time dependent effects.

An idealized response to cyclic deformation at a constant rate of strain for a single chain segment allowed to relax within its tube and thus representing molecules contributing to ν_p is illustrated in Figure 5. The tube, or topological constraint system, is defined in the customary fashion after DeGennes [14] and Edwards [15]. The arc length of the tube is designated as L while ℓ denotes the arc length of the constrained chain segment. At t = 0, both tube and segment are in their equilibrium state with $L_o = \ell_o$. Upon imposition of the triangular strain pulse, we assume L deforms in an affine fashion

$$L(t) = (\dot{\varepsilon}t + 1)L_o. \qquad (4)$$

Since the chain segment is not anchored at the tube ends, it immediately begins to relax within the deforming tube. Consequently, for finite rates of strain, at the conclusion of the first half cycle, $L_o < \ell(t') < L(t')$. This relaxation process continues during the first unloading cycle and as a result when the strain returns to zero, $\ell(2t') < \ell_o$. Given sufficient recovery time, $t_r > \tau$ where τ is the characteristic relaxation time for the chain, ℓ will again approach ℓ_o. However, for times shorter than τ, a new reference condition is established which propagates through subsequent cycles. The resultant response curves for $\ell(t)$ display all the features for the stress-softening behavior discussed at the beginning of this paper.

Quantification of the behavior illustrated in Figure 5 may be obtained by assumption of the mathematical form of the hierarchical constraint release process in response to an instantaneous step strain corresponding to ℓ^*

$$\ell(t) = \ell_o + (\ell^* - \ell_o)\exp(-t/\tau) \qquad (5)$$

which merely states that the length of the chain segment decays exponentially from ℓ^* to ℓ_o with relaxation time τ. Following the classic derivation of the Hereditary Integral of linear viscoelasticity [18,19], Equation (5) may be used to construct a series of infinitesimal step strains which approximate the relaxation that occurs continuously during a constant strain rate test. This approach leads to an ordinary differential equation with the general solution given by Equation (6).

$$\ell(t) = C(1 + \dot{\varepsilon}t)\exp(-t/\tau) + \ell_o/[\tau g(t)] \qquad (6)$$

where

$$g(t) = 1/\tau - \dot{\varepsilon}/(1 + \dot{\varepsilon}t).$$

Substituting this time dependent chain length into Equations (2 and 3) gives

$$\sigma(t) = \tfrac{1}{2}\nu_c kT(\lambda_c - 1/\lambda_c^2) + \tfrac{1}{2}\nu_p kT[\lambda_p(t) - 1/\lambda_p^2(t)] \qquad (7)$$

where λ_c denotes the affine deformation of the network junctions, and $\lambda_p(t) = \ell(t)$ quantifies the time-dependent relaxation processes occurring away from the fixed junctions. Figure 6 shows the results of applying this model to stress softening in a polybutadiene elastomer at five temperatures as indicated. Experimental data [20] are from a uniaxial tensile cycle consisting of N = 10 regular, triangular strain pulses with strain $\varepsilon = 0.02$ and rate $\dot{\varepsilon} = 0.05\ s^{-1}$. Individual data points represent peak stresses expressed as a percentage of the corresponding stress during the first cycle. Predictions of the model for $\nu_c = 1.30 \times 10^{-26}\ m^{-3}$ and $\nu_p = 0.24 \times 10^{-26}\ m^{-3}$ are shown as continuous curves. As can be seen, good general agreement exists between the model

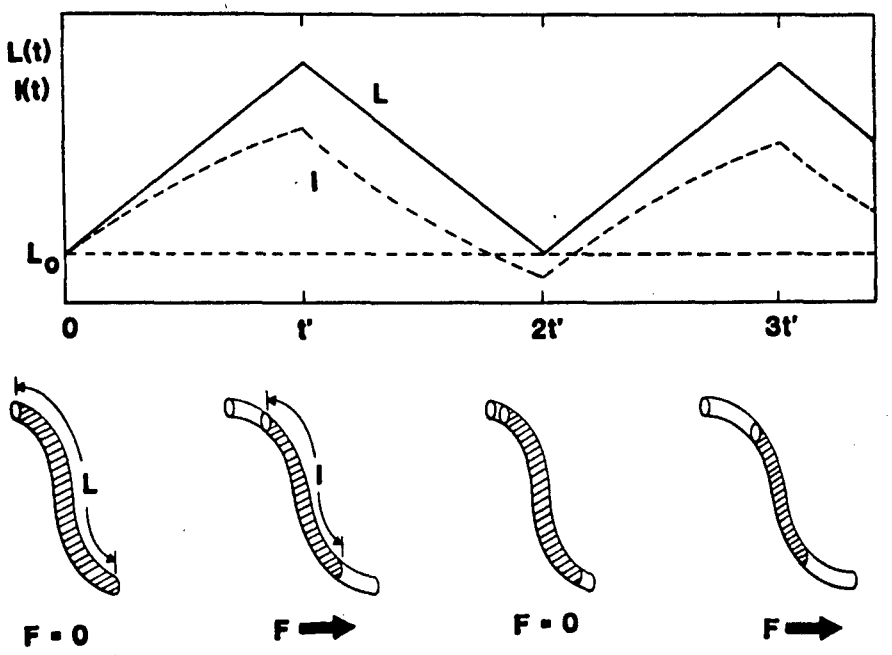

Figure 5. - Response of Single Chain in Tube.

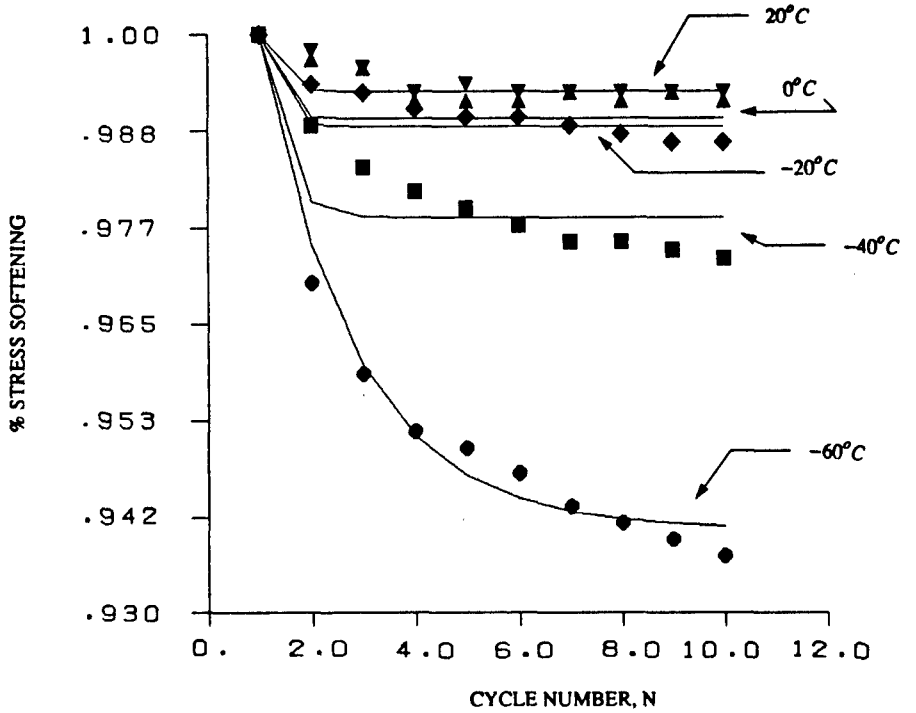

Figure 6. - Predicted vs. Observed Stress Softening Effects.

and the experimental data, with the best fit occurring at the lowest temperature. Differences between the individual temperatures were obtained by fitting reasonable values [21] of τ for the material. Fitted values ranged from a high of τ = 36 s for T = -60°C to τ = 4 s for T = 20°C.

ANALYSIS OF STEP-STRAIN RELAXATION

Although at first glance the two models discussed above may appear incompatible, further study reveals many similarities in their predictive capabilities. Space does not allow a complete comparison for a variety of deformation modes so the presentation below will be limited to the case of a simple step-strain relaxation. For generalization purposes, we introduce the first strain invariant

$$I_1 = \lambda_1^2 + \lambda_2^2 + \lambda_3^2. \tag{8}$$

Introduction of I_1 into the Neohookean version of the continuum model discussed above [10,11] gives an internal energy density function

$$W = \tfrac{1}{2}\nu_c kT(I_{1c} - 3) + \tfrac{1}{2}\nu_p kT(I_{1p}^* - 3) \tag{9}$$

where I_{1c} is the first invariant of the deformation mapping between the original reference configuration and the deformed elastic solid (chemically crosslinked molecules), and I_{1p}^* is the corresponding deformation mapping between the time-dependent reference loss solid (ν_p molecules) and the deformed elastic solid (see Figure 3). Likewise, a similar internal energy density function for the molecular model may be expressed as

$$W = \tfrac{1}{2}\nu_c kT(I_{1c} - 3) + \tfrac{1}{2}\nu_p kT(I_{1p} - 3) \qquad (10)$$

where I_{1p} ($= I^{*}_{1p}$) is a local measure of the time-dependent first invariant of the deformation mapping for the convected physically crosslinked molecules, see Figure 4.

Application of a step strain to a fully relaxed material yields

$$W = \tfrac{1}{2}kT(\nu_c + \nu_p)(I_{1c} - 3) \qquad (11)$$

from both Equations (9 and 10) since $\lambda_p(t = 0^+) = \lambda_c$ = the applied stretch. Also, as time becomes large (infinite) we have $\lambda_p \to 1$ for both models and both internal energies become

$$W(t \to \infty) = \tfrac{1}{2}\nu_c kT(I_{1c} - 3) \qquad (12)$$

Thus, both the continuum and molecular models will have the same shear moduli ($\nu_c kT$ and $\nu_p kT$) which are determined by step strain relaxation experiments [10].

The models do not, however, imply the same recovery mechanism for the molecules contributing to ν_p. In the continuum mechanics model, it is assumed that they adjust their structure with time to adapt to the macroscopic deformation configuration. This is accomplished in the model by applying deformation forces to them (i.e., to their time-dependent reference solid-fluid geometry [10]). Conversely, the molecular model assumes that the ν_p molecules deform immediately in response to the macroscopic strain and then relax back to their equilibrium energy state (or original contour length) with time according to Equation (5). The continuum model's relaxation equation for a tensile step strain test is

$$d\ell/dt = -(\ell^{*}/\eta)\,[\Lambda^2 - (1/\Lambda)]/[2\Lambda + (1/\Lambda^2)] \qquad (13)$$

where $\Lambda = \ell/\ell^*$.

Given ℓ^* in a step strain experiment, Equations (5 and 13) determine the length of the molecules free to reestablish their equilibrium state, $\ell(t)$, with time for the molecular and continuum models, respectively. Then, Equation (7) is used with $\lambda_c = L/\ell$ and $\lambda_p = \ell/\ell^*$ for both models to determine the time-dependent stress. Figure 7 contains plots of the predictions for the physically crosslinked network of Equations (5, 7 and 13) for a step strain relaxation experiment. As can be seen, both models produce the characteristic exponential decay in stress with time.

REFERENCES

1. F. Bueche, "Physical Properties of Polymers," Wiley, New York, 1962.
2. L. Mullins, Rubber Chem. Technol. 42, 339 (1969).
3. A.N. Gent, J. Appl. Polym. Sci. 18, 1397 (1974).
4. R.A. Schapery, Eng. Fracture Mech. 25, 845 (1986).
5. C.M. Roland, J. Rheol. 33, 659 (1989).
6. R.J. Farris, "Recovery of Strain Induced Daamage in ANB-3066 Propellant," AFRPL-TR-75-11, 1975.
7. R.J. Farris, Trans. Soc. Rheol. 12, 315 (1968).
8. H.P. Kugler, R.G. Stacer and C. Steimle, Rubber Chem. Technol. 63, 473 (1990).
9. G.B. McKenna and L.J. Zapas, Rubber Chem. Technol. 54, 718 (1981).
10. A.R. Johnson and C.Q. Quigley, Rubber Chem. Technol. 65, 137 (1992).
11. A.R. Johnson, C.Q. Quigley, C. Cavallaro and K.D. Weight, in "The Mathematics of Finite Elements and Applications VII - MAFELAP 1990," J.R. Whiteman, Ed., Academic Press, New York, 1991.
12. I. Fried and A.R. Johnson, Comput. Meths. Appl. Mech. Engng. 67, 241 (1988).
13. I. Fried and A.R. Johnson, Comput. Meths. Appl. Mech. Engng. 69, 53 (1988).
14. P.G. DeGennes, "Scaling Concepts in Polymer Physics," Cornell, Ithaca, 1979.
15. M. Doi and S.F. Edwards, "The Theory of Polymer Dynamics," Oxford, 1986.
16. C.W. McGuirt and G. Lianis, Trans. Soc. Rheol. 14, 117 (1970).
17. L.R.G Treloar, "The Physics of Rubber Elasticity, 3rd Edition," Oxford, 1975.
18. W. Flügge, "Viscoelasticity, 2nd Edition,"

Springer-Verlag, New York, 1975.
19. N.W. Tschoegl, "The Phenomenological Theory of Linear Viscoelastic Behavior," Springer-Verlag, New York, 1989.
20. R.G. Stacer, A.R. Johnson and Ch. Hübner, in preparation.
21. D.J. Plazek, G.-F. Gu, R.G. Stacer, L.-J. Su, E.D. von Meerwall and F.N. Kelley, J. Mater. Sci. 23, 1289 (1988).

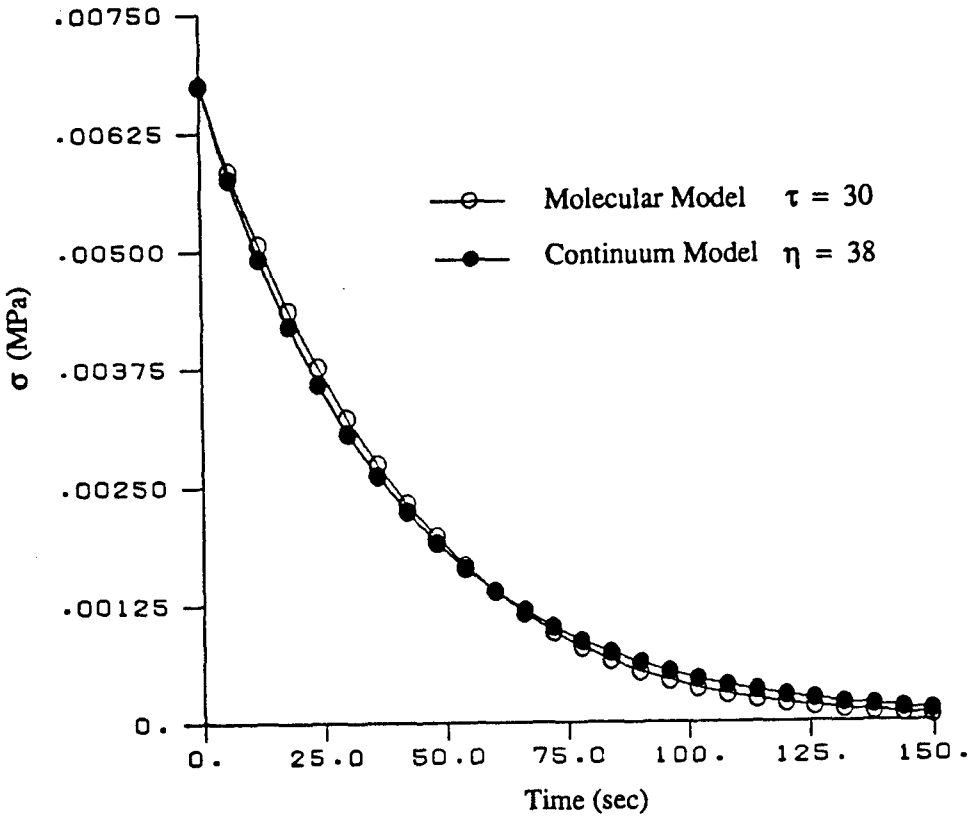

Figure 7. - Predictions of Continuum and Molecular Models of Instantaneous Step-Strain Responses

{1,2}-ORDER THEORY FOR HOMOGENEOUS ORTHOTROPIC SHELLS

T. Tsui and A. Tessler
Mechanics and Structures Branch
U.S. Army Materials Technology Laboratory
Watertown, Massachusetts

Nomenclature

A_1, A_2	surface metrics
A_{ij}	membrane shell rigidities
B_{ij}	membrane-bending coupling shell rigidities
C_{ij}	elastic stiffness coefficients
D_{ij}	bending shell rigidities
G_{ij}	transverse shear shell rigidities
C^0	the class of continuous functions possessing discontinuous derivatives at element nodes
C^{-1}	the class of continuous functions that are discontinuous at element nodes
I_i	inertial coefficients
G	shear modulus
L	length of clylider
$\boldsymbol{K}_{cyl}$	stiffness matrix for cylindrical shell
$\boldsymbol{M}_{cyl}$	mass matrix for cylindrical shell
a	cylindrical shell radius
$2h$	shell thickness
m, n	axial and circumferential wave numbers
u, v	midplane displacement along α_1 and α_2 directions
u_1, u_2, u_3	orthogonal displacement components
w, w_i	components of the transverse displacement
x, θ, ζ	cylindrical coordinates
t	time variable
Ω_i	normalized frequency
δ	variational operator
$\epsilon_{ij}, \kappa_{ij}$	strain and curvature components
$\theta_i \ \ (i = 1, 2, \text{or } x, \theta)$	bending cross-sectional rotations

ξ	dimensionless thickness coordinate
σ_{ij}, τ_{ij}	stress components
α	$m\pi/L$
$\alpha_1, \alpha_2, \zeta$	orthogonal curvilinear coordinates
ρ	material density
ω_i	circular frequency
$\dot{()}$	differentiation with respect to time
$()_{,i}$	partial differentiation with respect to α_i spatial coordinate

1 Introduction

The increasing applications of laminate composites in the design of various thick-section shell type structures necessitate the need for the development of a simple and accurate theory for the analysis of thick shells. The theory should include the effects of transverse shear and transverse normal deformations which can be particularly pronounced in thick shells and those subject to higher vibrational modes. Such a theory should also be amenable to finite element approximations.

In the case of thin shells, the refined two dimensional theories, which include the initial curvature effect (e.g. the Sanders - Koiter theory [1-2]), provide good predictions for shell response. When applied to thick shells, however, significant errors may result. This is because the shell deformations are constrained by the Kirchoff - Love assumption ignoring transverse shear and transverse normal deformations.

Numerous higher-order theories have been proposed for the analysis of thick laminated shells (e.g. [3-7]). These theories either neglect the effects of transverse normal deformation or their accuracies as well as computational simplicity and suitability need to be demonstrated. In certain relatively simple cases, three-dimensional elasticity solutions have been obtained [8,9].

The focus of this effort is to derive an accurate general shell theory for the analysis of thick orthotropic shells which is particularily suited for finite element application. The methodology is an extension of the {1,2}-order plate theory by Tessler [10-12]. The shell theory accounts for the effects of transverse shear and transverse nomal deformations.

The theory is evaluated via an analytic solution for a free vibration problem of isotropic cylindrical shells. The natural frequencies of vibrations

are determined for a wide range of geometric parameters and the results are compared with the three-dimensional elasticity solutions.

2 Foundation of {1,2}-Order Shell Theory

Let $(\alpha_1, \alpha_2, \zeta)$ denote the orthogonal curvilinear coordinate system of the shell element where α_1 - and α_2 - curves are lines of curvature on the reference midsurface of the shell and ζ are lines perpendicular to the midsurface ($\zeta = 0$). The principal radii of curvature of the reference surface are R_1 and R_2, and the thickness of the shell is $2h$.

The present {1,2}-order shell theory is a direct analogue of the plate theory of Tessler [10 - 12]. The displacement components are expanded in terms of the dimensionless thickness coordinate $\xi = \zeta/h \in [-1, 1]$ and the seven kinematic variables $\{u, v, w, \theta_1, \theta_2, w_1, w_2\}$ as:

$$\begin{aligned} u_1(\alpha_1, \alpha_2, \zeta, t) &= u(\alpha_1, \alpha_2, t) + h\xi\theta_1(\alpha_1, \alpha_2, t) \\ u_2(\alpha_1, \alpha_2, \zeta, t) &= v(\alpha_1, \alpha_2, t) + h\xi\theta_2(\alpha_1, \alpha_2, t) \\ u_3(\alpha_1, \alpha_2, \zeta, t) &= w(\alpha_1, \alpha_2, t) + \xi w_1(\alpha_1, \alpha_2, t) \\ &\quad + \left(\xi^2 - 1/5\right) w_2(\alpha_1, \alpha_2, t) \end{aligned} \tag{1}$$

The displacement expansions allow the inclusion of both transverse shear and transverse normal deformations.

The strains are related to the stresses through the 3-D Hooke's law as

$$\boldsymbol{\sigma} = C\boldsymbol{\epsilon} \tag{2}$$

where $C = [C_{ij}]$ is a 6×6 matrix of elastic material constants, and $\boldsymbol{\sigma}$ and $\boldsymbol{\epsilon}$ are vectors of stress and strain components, respectively.

The shell formulation employs the following shell strain and curvature variables.

$$\boldsymbol{\epsilon}_o^T = [\epsilon_1^0, \epsilon_2^0, \epsilon_n^0, \beta_1^0, \beta_2^0], \quad \boldsymbol{\kappa}_o^T = [\kappa_1^0, \kappa_2^0, \kappa_n^0, \beta_1', \beta_2'], \quad \boldsymbol{\gamma}_o^T = [\mu_1^0, \mu_2^0] \tag{3}$$

where $(\epsilon_1^0, \epsilon_2^0, \epsilon_n^0)$, $(\beta_1^0, \beta_2^0, \mu_1^0,$ and $\mu_2^0)$ represent the normal and shear strains of the reference surface; κ_1^0, κ_2^0, and κ_n^0 denote the changes of curvature of the reference surface; β_1' and β_2' indicate the twist of the reference surface. The relationships of these quantities to the kinematic variables in (1) are summarized in the Appendix.

The inplane strains, obtained from (1) in accordance with three-dimensional elasticity theory, are

$$\begin{aligned} \epsilon_i &= [\epsilon_i^0 + h\xi\kappa_i + h\xi\epsilon_n^0/R_i + h^2(\xi^2 - 1/5)\kappa_n^0/R_i]/L_i \quad (i = 1,2) \\ \gamma_{12} &= (\beta_1^0 + h\xi\beta_1')/L_1 + (\beta_2^0 + h\xi\beta_2')/L_2 \end{aligned} \tag{4}$$

where $L_i = 1 + h\xi/R_i \ \ (i = 1,2)$.

The transverse shear strainγ_{in} $(i = 1,2)$ and the transverse normal strain ϵ_n are respectively derived from independent quadratic and cubic polynomial expansions. The coefficients of the polynomials are determined by requiring the stress field to satisfy physical boundry conditions at the top and bottom shell surfaces.

$$\tau_{in}(\alpha_1, \alpha_2, \pm h, t) = \sigma_{n,\xi}(\alpha_1, \alpha_2, \pm h, t) = 0 \quad (i = 1,2) \tag{5}$$

and the transverse strain compatibility in the mean. This is achieved by minimizing the following expressions with respect to the unknown expansion coefficients:

$$\begin{aligned} &minimize \ \int_{-h}^{h} \left\{\gamma_{in} - [A_i\mu_i^0 + \xi w_{1,i} + (\xi^2 - 1/5)w_{2,i}]\right\}^2 A_i^2 L_i^2 d\zeta \\ &minimize \ \int_{-h}^{h} \left[\epsilon_n - (\epsilon_n^0 + 2\xi h\kappa_n^0)\right]^2 d\zeta \end{aligned} \tag{6}$$

The resulting transverse strains have the form

$$\begin{aligned} \gamma_{in} &= \frac{5}{4}(1 - \xi^2)\mu_i^0/L_i \quad (i = 1,2) \\ \epsilon_n &= s_1\epsilon_1^0 + s_2\epsilon_2^0 + s_3\epsilon_n^0 + s_4\beta_1^0 + s_5\beta_2^0 + \\ &\quad s_6\kappa_1^0 + s_7\kappa_2^0 + s_8\kappa_n^0 + s_9\beta_1' + s_{10}\beta_2' \end{aligned} \tag{7}$$

where $s_j(\xi) \ \ (j = 1,2,3,...,10)$ are cubic functions in ξ [14]. The equations of motion together with the natural boundry conditions are derived via Hamilton's variational principle. The resulting two-dimensional variational statement has the form

$$\begin{aligned} &\delta \int_{t_0}^{t_1} \{\frac{1}{2} \int_S \left[N^T\epsilon_o + M^T\kappa_o + Q^T\gamma_o\right] d\alpha_1 d\alpha_2 \\ &-K(\dot{u}, \dot{v}, \dot{w}, \dot{\theta}_1, \dot{\theta}_2, \dot{w}_1, \dot{w}_2) - W_e(u, v, w, \theta_1, \theta_2, w_1, w_2)\} dt = 0 \end{aligned} \tag{8}$$

where K and W_e denote the kinetic energy and the work done by external forces, respectively; $\boldsymbol{N}$, $\boldsymbol{M}$, and $\boldsymbol{Q}$ are vectors continuing the shell

stress resultants which are related to the shell strains (3) via the following constitutive relation

$$\left\{ \begin{array}{c} \boldsymbol{N} \\ \boldsymbol{M} \\ \boldsymbol{Q} \end{array} \right\} = \left[\begin{array}{ccc} \boldsymbol{A} & \boldsymbol{B} & \mathbf{o} \\ \boldsymbol{B}^T & \boldsymbol{D} & \mathbf{o} \\ \mathbf{o} & \mathbf{o} & \boldsymbol{G} \end{array} \right] \left\{ \begin{array}{c} \boldsymbol{\epsilon}_o \\ \boldsymbol{\kappa}_o \\ \boldsymbol{\gamma}_o \end{array} \right\} \tag{9}$$

where $\boldsymbol{A} = [A_{ij}]$, $\boldsymbol{B} = [B_{ij}]$, $\boldsymbol{D} = [D_{ij}]$, and $\boldsymbol{G} = [G_{ij}]$ are the shell constitutive matrices [14].

3 Free Vibration of Cylindrical Shells

To evaluate the present {1,2}-order shell theory, the free vibrations of infinitely long isotropic cylindrical shells are considered. The field equations in the orthogonal curvilinear coordinate system $(\alpha_1, \alpha_2, \zeta)$ are specialized for the case of cylindrical shells [14]. The equations of motion in terms of the displacement variables take the form

$$\begin{aligned}
&A_{11}u_{,xx} + A_{55}u_{,\theta\theta}/a^2 + (A_{12} + A_{54})v_{,x\theta}/a + B_{11}\theta_{\theta,xx} \\
&B_{55}\theta_{\theta,\theta\theta}/a^2 + (B_{12} + B_{54})\theta_{x,x\theta}/a + A_{12}w_{,x}/a + \\
&A_{13}w_{1,x}/h + B_{13}w_{2,x}/h^2 = \rho h(I_0\ddot{u} + I_1 h\ddot{\theta}_\theta) \\
\\
&(B_{54} + B_{12})u_{,x\theta}/a + B_{44}v_{,xx} + B_{22}v_{,\theta\theta}/a^2 + (D_{45} + D_{21})\theta_{\theta,x\theta}/a + \\
&D_{44}\theta_{x,xx} + D_{22}\theta_{x,\theta\theta}/a^2 + (B_{22} - aG_{44})w_{,\theta}/a^2 + B_{32}w_{1,\theta}/ha + \\
&D_{23}w_{2,\theta}/h^2a + G_{44}(v - a\theta_x)/a = \rho h(hI_1\ddot{v} + hI_2\ddot{\theta}_x) \\
\\
&G_{55}w_{,xx} + G_{44}w_{,\theta\theta}/a^2 - A_{21}u_{,x}/a - (A_{22} + G_{44})v_{,\theta}/a^2 - \\
&(B_{21} - aG_{55})\theta_{\theta,x}/a - (B_{22} - aG_{44})\theta_{x,\theta}/a^2 - A_{22}w/a^2 - A_{23}w_1/ah \\
&-B_{23}w_2/ah^2 = \rho h[I_0\ddot{w} + I_1\ddot{w}_1 + (-I_0/5 + I_2)\ddot{w}_2] \\
\\
&(A_{45} + A_{21})u_{,x\theta}/a + A_{44}v_{,xx} + A_{22}v_{,\theta\theta}/a^2 + (B_{45} + B_{21})\theta_{\theta,x\theta}/a + \\
&B_{44}\theta_{x,xx} + B_{22}\theta_{x,\theta\theta}\ a^2 + (A_{22} + G_{44})w_{,\theta}/a^2 + A_{23}w_{1,\theta}/ha + \\
&B_{23}w_{2,\theta}/h^2a - G_{44}(v - a\theta_x)/a^2 = \rho h(I_0\ddot{v} + I_1 h\ddot{\theta}_x) \\
\\
&B_{11}u_{,xx} + B_{55}u_{,\theta\theta}/a^2 + (B_{21} + B_{45})v_{,x\theta}/a + D_{11}\theta_{\theta,xx} + \\
&D_{55}\theta_{\theta,\theta\theta}/a^2 + (D_{12} + D_{54})\theta_{x,x\theta}/a + (B_{21} - aG_{55})w_{,x}/a + \\
&B_{31}w_{1,x}/h + D_{13}w_{2,x}/h^2 - G_{55}\theta_\theta = \rho h(hI_1\ddot{u} + h^2I_2\ddot{\theta}_\theta)
\end{aligned} \tag{10}$$

$$-[A_{31}u_{,x} + A_{32}(v_{,\theta} + w)/a + A_{33}w_1/h + B_{31}\theta_{\theta,x} + B_{32}\theta_{x,\theta}/a +$$
$$B_{33}w_2/h^2]/h = \rho h[I_1\ddot{w} + I_2\ddot{w}_1 + (-I_1/5 + I_3)\ddot{w}_2]$$

$$-[B_{13}u_{,x} + B_{23}(v_{,\theta} + w)/a + B_{33}w_1/h + D_{31}\theta_{\theta,x} + D_{32}\theta_{x,\theta}/a +$$
$$D_{33}w_2/h^2]/h^2 = \rho h[(-I_0/5 + I_2)\ddot{w} +$$
$$(-I_1/5 + I_3)\ddot{w}_2 + (I_0/25 - 2I_2/5 + I_4)\ddot{w}_2]$$

where I_i $(i = 0, 1, ..., 4)$ are constants [14].

For free vibration, the displacements are expanded in a modal series as

$$\begin{aligned}
u(x,\theta,t) &= \sum_{m=n=1}^{\infty} U_{mn} \sin\alpha x \cos n\theta e^{i\omega_{mn}t} \\
v(x,\theta,t) &= \sum_{m=n=1}^{\infty} V_{mn} \cos\alpha x \sin n\theta e^{i\omega_{mn}t} \\
w(x,\theta,t) &= \sum_{m=n=1}^{\infty} W_{mn} \cos\alpha x \cos n\theta e^{i\omega_{mn}t} \\
\theta_x(x,\theta,t) &= \sum_{m=n=1}^{\infty} \phi_{mn} \cos\alpha x \sin n\theta e^{i\omega_{mn}t} \\
\theta_\theta(x,\theta,t) &= \sum_{m=n=1}^{\infty} \psi_{mn} \sin\alpha x \cos n\theta e^{i\omega_{mn}t} \\
w_1(x,\theta,t) &= \sum_{m=n=1}^{\infty} W^1_{mn} \cos\alpha x \cos n\theta e^{i\omega_{mn}t} \\
w_2(x,\theta,t) &= \sum_{m=n=1}^{\infty} W^2_{mn} \cos\alpha x \cos n\theta e^{i\omega_{mn}t}
\end{aligned} \tag{11}$$

For the special case $n = 0$, the displacement expansions are obtained by interchanging $\sin n\theta$ and $\cos n\theta$ in (11). Substituting (11) into (10), results in the eigenvalue matrix equation

$$(\boldsymbol{K}_{cyl} - \omega^2 \boldsymbol{M}_{cyl})\boldsymbol{\Delta} = \boldsymbol{0} \tag{12}$$

with

$$\boldsymbol{\Delta}^T = \{U_{mn}, V_{mn}, W_{mn}, \phi_{mn}, \psi_{mn}, W^1_{mn}, W^2_{mn}\}$$

where the coefficients of the stiffness $\boldsymbol{K}_{cyl}$ and mass $\boldsymbol{M}_{cyl}$ matrices are summarized in [14].

Tables 1-4 show comparisons between the natural frequencies predicted by the present theory and the three dimensional elasticity solutions [9] for

two circumferential mode numbers. The frequencies, $\Omega_i = \omega_i/\omega_{ref}$ $(i = 1,2,3,4)$ where $\omega_{ref} = \pi\sqrt{G/\rho}/2h$, correspond, in the ascending order, to the flexural mode, associated with large radial displacements; axial shear mode, associated with large axial displacements; thickness-shear mode, associated with motions in the axial directions, and thickness-stretch mode with predominantly radial displacements [9]. The results are seen to be in excellent agreement with the exact solutions except for the thickness-stretch mode where the present predictions are consistently higher than the exact solutions. The largest error is about 10% corresponding to a thick cylinder ($2h/L = 0.40$ and $2h/a = .3$) and $n = 3$. Note that the thickness-stretch frequencies cannot be computed by the {1,0}-order theories.

Table 1: Normalized Natural Frequencies for Homogeneous Isotropic Cylinders
$2h/a = .01,\ \ m = 1,\ \ n = 1$

$2h/L$	Ω_1		Ω_2		Ω_3		Ω_4	
	Exact	Present	Exact	Present	Exact	Present	Exact	Present
.01	.0046	.0046	.01069	.01069	1.0001	1.0001	1.8706	1.8708
.10	.0160	.0159	.1001	.1001	1.0050	1.0050	1.8498	1.8726
.20	.0577	.0576	.2000	.2000	1.0198	1.0198	1.8121	1.8779
.40	.1989	.1973	.4000	.4000	1.0771	1.0771	1.7520	1.9020

Table 2: Normalized Natural Frequencies for Homogeneous Isotropic Cylinders
$2h/a = .01,\ \ m = 1,\ \ n = 3$

$2h/L$	Ω_1		Ω_2		Ω_3		Ω_4	
	Exact	Present	Exact	Present	Exact	Present	Exact	Present
.01	.0026	.0026	.0142	.0142	1.0001	1.0001	1.8704	1.8709
.10	.0160	.0160	.1005	.1005	1.005	1.005	1.8496	1.8726
.20	.0579	.0577	.2002	.2002	1.0199	1.0199	1.8120	1.8779
.40	.1990	.1974	.4001	.4001	1.0771	1.0771	1.7520	1.9021

Table 3: Normalized Natural Frequencies for Homogeneous Isotropic Cylinders
$2h/a = .3,\ \ m = 1,\ \ n = 1$

$2h/L$	Ω_1		Ω_2		Ω_3		Ω_4	
	Exact	Present	Exact	Present	Exact	Present	Exact	Present
.01	.0012	.0012	.0972	.0972	1.0083	1.0086	1.8583	1.8676
.10	.0616	.0616	.1648	.1648	1.0183	1.0185	1.8423	1.8693
.20	.1266	.1269	.2375	.2375	1.0383	1.0381	1.8100	1.8747
.40	.2440	.2440	.4142	.4142	1.0970	1.0965	1.7551	1.8992

Table 4: Normalized Natural Frequencies for Homogeneous Isotropic Cylinders
$2h/a = .3, \quad m = 1, \quad n = 3$

$2h/L$	Ω_1		Ω_2		Ω_3		Ω_4	
	Exact	Present	Exact	Present	Exact	Present	Exact	Present
.01	.0957	.0951	.2875	.2875	1.0455	1.0458	1.7865	1.8814
.10	.1064	1.060	.3095	.3095	1.0517	1.0519	1.7812	1.8833
.20	.1455	.1451	.3613	.3612	1.0692	1.0693	1.7681	1.8895
.40	.2792	.2772	.5018	.5017	1.1303	1.1305	1.7439	1.9171

4 Concluding Remarks

A general shell theory of order {1,2} for homogeneous orthotropic shells was developed following the basic methodology established in [10]. Parabolic transverse shear and cubic transverse normal strains were derived allowing vanishing shear traction boundary conditions to be satisfied. These strains are also compatible in the least-square sense with those obtained directly from displacements. The governing equations were formulated in terms of an orthogonal curvilinear coordinate system which permits the analysis of various types of shells such as circular cylindrical, spherical, conical, etc. Furthermore, the initial curvatures were retained throughout.

The shell theory results for the natural frequencies of free vibration infinitely long, isotropic cylindrical shells were found to be in close agreement with the three-dimensional elasticity solutions. The theory provides a convenient framework for the development of simple and computationally efficient finite element models. In addition, it serves as a foundation for a laminate shell theory to be addressed in a future effort.

5 Acknowledgements

The authors would like to thank their colleagues, Erik Saether, for his computational support and, Trevor Rudalevige, for manuscript preparation in this effort.

References

[1] Sanders, J. L. " An Improved First Approximation Theory of Thin Shells", NASA Report 24, 1959.

[2] Koiter, W. T. "A Consistent First Approximation in General Theory of Thin Elastic Shells", Theory of Thin Elastic Shells, First IUTAM Symp. (ed. W. T. Koiter) 1960, p. 12-33.

[3] Reddy, J. N., and Liu, C. F. "A Higher-Order Shear Deformation Theory of Laminated Elastic Shells", Internatioanl Journal of Engineering Science, v. 23, No. 3, 1985, p. 319-330.

[4] Whitney, J. M., and Sun, C. T. "A Refined Theory for Laminated Anisotropic, Cylindrical Shells", Journal of Applied Mechanics, v. 41, 1974, p. 471-476.

[5] Doxsee, L. E. Jr. "A Higher-Order Theory of Hygrothermal Behavior of Laminated Composite Shells", International Journal of Solids and Structures, v. 25, No. 4, 1989, p. 339-355.

[6] Lo, K. H., Christensen, R. M., and Wu, E. M. " A Higher-Order Theory of Plate Deformation. Part 1: Homogeneous Plates, and Part 2: Laminated Plates", Journal of Applied Mechanics, v. 44, 1977, p. 663-676.

[7] Voyiadjis, G. S. and Shi, G. "A Refined Two-Dimensional Theory for Thick Cylindrical Shells", Internation Journal of Solids and Structures, v. 27, No. 3, 1991, p. 261-282.

[8] Nelson, R. B., Dong, S. B., and Kalra, R. D. "Vibrations and Waves in Laminated Orthotropic Circular Cylinders", Journal of Sound and Vibration, v. 18, 1971 p. 429-444.

[9] Armenakas,A. E., Gazis, D. C., and Herrmann, G. "Free Vibrations of Circular Cylindrical Shells", Pergamon Press, Oxford, 1969.

[10] Tessler, A. "A Higher-Order Plate Theory with Ideal Finite Element Suitability", Comput. Meths. Appl. Mech. Eng. v. 85, No. 2 1991 p. 183-205.

[11] Tessler, A. "A Higher-Order Plate Theory with Ideal Finite Element Suitability", U.S. Army Material Technology Laboratory, MTL TR 89-85, September 1989.

[12] Tessler, A. " An Improved Higher-Order Theory for Orthotropic Plates", Proc. 13th Annual Composites Review, 1988, p. 59-65.

[13] Tessler, A. and Saether, E. " A Computationlly Viable Higher-Order Theory for Laminated Composite Plates", International Journal for Numerical Methods in Engineering, v. 31, 1991 p. 1069-1086.

[14] Tsui, T. Y., and Tessler, A. "An Improved Theory of Order {1,2} for Stress Analysis of Thick Orthotropic Shells", MTL Technical Report, November, 1991.

Appendix: Definitions of Shell Strain Variables

$$
\begin{aligned}
\epsilon_1^0 &= u_{,1}/A_1 + vA_{1,2}/A_1A_2 + w/R_1 \\
\epsilon_2^0 &= v_{,2}/A_2 + uA_{2,1}/A_1A_2 + w/R_2 \\
\epsilon_n^0 &= w_1/h \\
\beta_1^0 &= v_{,1}/A_1 - uA_{1,2}/A_1A_2 \\
\beta_2^0 &= u_{,2}/A_2 - vA_{2,1}/A_1A_2 \\
\kappa_1^0 &= \theta_{1,1}/A_1 + \theta_2 A_{1,2}/A_1A_2x \\
\kappa_2^0 &= \theta_{2,2}/A_2 + \theta_1 A_{2,1}/A_1A_2 \\
\kappa_n^0 &= w_2/h^2 \\
\beta_1' &= \theta_{2,1}/A_1 - \theta_1 A_{1,2}/A_1A_2 \\
\beta_2' &= \theta_{1,2}/A_2 - \theta_2 A_{2,1}/A_1A_2 \\
\mu_1^0 &= -u/R_1 + \theta_1 + w_{,1}/A_1 \\
\mu_2^0 &= -v/R_2 + \theta_2 + w_{,2}/A_2
\end{aligned}
$$

where A_1 and A_2 are the surface metrics

$$A_1^2 = \boldsymbol{r}_{,1} \cdot \boldsymbol{r}_{,1} \ , \qquad A_2^2 = \boldsymbol{r}_{,2} \cdot \boldsymbol{r}_{,2}$$

$\boldsymbol{r}$ is the position vector of a point on the middle surface of the shell.

PLY CRACKS AND LOAD REDISTRIBUTION IN LAMINATED COMPOSITES

Sailendra N. Chatterjee
Chian-Fong Yen

Materials Sciences Corporation,
Blue Bell, PA 19422

INTRODUCTION

Consider a laminate coupon under uniaxial loading, say for example, tension. If the laminate contains one or more laminae with fiber direction inclined to the direction of loading (30° to 90°), a nonlinear response of the coupon is often observed. If these off-axis laminae are considered to be elastic but susceptible to deterioration caused by constrained transverse cracking, then the decrease in strain energy U ($=\rho\psi$, ψ being the Helmholtz free energy) or increase in complementary energy (Figure 1) from their elastic values may be considered to be used in the creation of ply cracks.

Phenomenological as well as fracture mechanics based approaches have been used in the past to model stiffness loss in cross ply and angle ply laminates due to transverse ply cracks. In these approaches, the change in strain (or complementary) energy is estimated via approximate stress analyses or other assumptions. In the phenomenological model an additional assumption of dilute concentration of cracks is usually employed. In this work we first discuss some phenomenological considerations for dilute as well as nondilute concentration of cracks. Next we report some results from mechanics based models and finite element calculations to choose some constants and functions required in the phenomenological model. Finally we compare results from the model with test data and other calculations reported in literature.

PHENOMENOLOGICAL CONSIDERATIONS

Phenomenological approaches for modeling growth of distributed microcracks of many orientations (and the resulting stress-strain response) have been proposed [1, 2]. The model described in [1], which is based on strain formulation, has been modified [3, 4] to consider dilute concentration of such microcracks parallel to fibers in each lamina employing a stress formulation (Figure 1). Nonlinear responses of angle ply laminates predicted by the use of incremental laminate analysis have been correlated with test data in the same works. These results and other analytical and experimental studies [5-10] indicate that increasing number of ply cracks perpendicular to the planes of lamination is the dominant mechanism governing the stiffness loss. These cracks may start as microcracks but very quickly grow in the z-direction to the full thickness of the

ply (or layer) as shown in Figures 2 and 3 and become quite long in the x-direction (average length b >> 2a). Generation of increasing number of ply cracks in cross ply laminate coupons under tensile load occurs due to cleavage type fracture under transverse tensile stress. In general, in-plane shear stresses may also exist in a ply. The phenomenological formulation in [4] can be extended to consider the general situation of a balanced midplane symmetric laminate under in-plane loading. In a laminate coupon loaded in tension, plycracks are likely to appear in all the layers, whose fiber directions are inclined to the direction of loading. Figure 3 illustrates the situation in each of the cracked layers, the fiber direction of the layer coinciding with the x-axis in the figure. ΔU_L, the change in the energy density in a representative volume element of a laminate (decreases in strain energy or increase in complementary energy) due to a system cracks in one layer (one or more plies lumped together) with thickness fraction V_c can be written as

$$\Delta U_L = V_c \, \Delta U_c \tag{1}$$

$$\Delta U_c = \frac{1}{2} \omega^* \{C_1 \sigma_o^2 f_1(\omega^*) + C_2 \tau_o^2 f_2(\omega^*) + 2C_3 \sigma_o \tau_o f_3(\omega^*)\} \tag{2}$$

In equation (2) C_i (i = 1, 2, 3) are constants with a dimension which is the inverse of stress or modulus. σ_o, τ_o are the transverse tensile and in-plane shear stresses in the layer in absence of cracks. If a strain energy formulation is to be employed, these stresses should be expressed in terms of average laminate strains. On the other hand, for evaluating change in complementary energy they should be evaluated from average laminate stresses. f_i (i = 1, 2, 3) are nondimensional functions of ω^*, which is a nondimensional measure of the loss in load bearing volume or the crack density in the layer. Replacing these functions by unity gives us the form of the energy change due to dilute concentration of cracks discussed in [3, 4], which is a modified version of the expression suggested in [1] involving squares of the strains on the crack planes instead of the stresses σ_o, τ_o. Without any loss in generality we can, therefore, consider values of these functions to be equal to unity when $\omega^* = 0$ and further choose ω^* as

$$\omega^* = \alpha\omega \tag{3}$$

$$\omega = a/\ell \tag{4}$$

where $2a$ = thickness of the cracked layer

ℓ = average spacing of cracks perpendicular to crack planes, i.e., in direction y (Figure 2)

α = b/B, the ratio of average length of cracks to the spacing in x (fiber) direction

We note that for large b/a, most of the load near a crack is transferred to the adjoining layers (Figure 2) and for equally spaced cracks ω^* is a measure of the assumed loss of load bearing volume (denoted by the shaded area in Figure 3 multiplied by b) of the cracked layer

$$\omega^* = \left(\sqrt{2}\,a\right)^2 b/2\,a\,\ell\,B \tag{5}$$

In cross ply laminate coupons under tension, the ply cracks usually grow through the full width of the coupon. Thus, one may chose $\alpha = 1$ and

$$\omega^* = \omega = a/\ell \tag{6}$$

On the other hand when in-plane shear stresses dominate (as in $(\pm 45^\circ)_{ns}$ coupons under tension), microcracks start at an angle to the xz plane (since maximum tensile stresses are not perpendicular to the fibers) and there is not much evidence to show that the cracks grow to the full width before final failure and, therefore, α is expected to be less than unity.

In a phenomenological model, the constants C_i and the functional forms of $f_i(\omega^*)$ are estimated by fitting predictions to test data. Effective (reduced) laminate stiffnesses A_{ij}^* for a balanced symmetric laminate containing N cracked layers can then be obtained as (ϵ_i, i = 1, 2 and γ are extensional and shear strains)

$$U_L = U_L^o - \sum_{k=1}^{N} \Delta U_L^k = \frac{1}{2}\left(A_{11}^* \epsilon_1^2 + 2A_{12}^* \epsilon_1 \epsilon_2 + A_{22}^* \epsilon_2^2 + A_{66}^* \gamma^2\right) \quad (7)$$

Each of the effective stiffness has to be evaluated by considering one specific type of loading (for example, $\gamma \neq 0$, $\epsilon_1 = \epsilon_2 = 0$ for determining A_{66}^*). ΔU_L^k is the decrease in strain energy density due to the cracks in the k^{th} cracked layer. U_L and U_L^o are the strain energy densities in the cracked and uncracked laminate, respectively. Note that equation (7) is an approximate result if cracks exist in many layers, since interaction of cracks in different layers is not considered in equation (2).

To estimate the growth of cracks, the concept of strain energy release rate has been proposed [1, 3]. According to this concept, a measure of the energy release rate in a layer k is given by (the superscript k is omitted)

$$R = \frac{1}{V_c} \frac{\partial(\Delta U_L)}{\partial \omega^*} = \frac{\partial(\Delta U_c)}{\partial \omega^*} \quad (8)$$

where ΔU_L and ΔU_c are given by equations (1) and (2) with $f_i(\omega^*) = 1$ (the case of dilute concentration). Damage initiates when R reaches a critical value R_o and a power law type relation can be used [1] to predict growth of cracks when R exceeds R_o.

$$\omega^* = \Delta\left[(R/R_o)^\lambda - 1\right] \quad (9)$$

where the exponent λ (usually small compared to unity) and the constant Δ can be determined by fitting predicted stiffness loss [3, 4] (or crack growth) versus applied load data to those measured in tests. It may be noted that equation (9) simulates the reduction in the rate of increase in crack density with applied load. It has been shown in [4] that if $f_i(\omega^*)$ in (2) are decreasing functions of ω^*, then it is possible to model observed crack growth data by retaining $f_i(\omega^*)$ in the expression for ΔU_c in (8) and using the criterion

$$R = R_o \tag{10}$$

R_o may be easily shown to be related to an average measure of critical strain energy release rate (G_{cr}) used in linear fracture mechanics.

$$R_o \approx G_{cr}/a \tag{11}$$

Equation (11) implies that thicker layers will crack easier than thinner ones, which has been observed experimentally. Use of (10) and (11) in conjunction with (8) is conceptually similar to fracture mechanics based models [7, 8].

USE OF MECHANICS BASED MODELS

Determining all the quantities required in the phenomenological model from test data is a difficult task. Mechanics based approaches can be of some help as discussed in this section. Since $b >> a$, the constants C_i can be determined by considering the crack energy (work done by the applied tractions on the crack faces) for a single ply crack in the laminate which deforms in a quasi-three dimensional manner, i.e., all displacements are independent of x coordinate (Figure 2). Let us denote ad_{11} and ad_{12} as the average crack opening and tearing displacements due to constant unit pressure on the crack faces. Also, let ad_{21} (note that $d_{21} = d_{12}$) and ad_{22} denote the same average displacements due to applied unit in-plane shear traction on the crack faces, then the crack energy W^o due to tractions σ_o and τ_o can be written as

$$W^o = \frac{1}{2} \cdot 2a^2 \cdot \left(d_{11}\sigma_o^2 + d_{22}\tau_o^2 + 2d_{12}\sigma_o\tau_o\right) \tag{12}$$

The change in energy density for $\ell \to \infty$ is, therefore,

$$\Delta U_L = \frac{W^o \cdot b}{2a\ell \cdot B} \tag{13}$$

Using (12), (13) and (3) and comparing the result with (2) one obtains

$$C_1 = d_{11}, \quad C_2 = d_{22}, \quad C_3 = d_{12} \tag{14}$$

Similarly the functions $f_i(\omega^*)$ can be estimated from the crack energy for equally spaced cracks (with varying spacing ℓ) in a layer in the laminate undergoing quasi-three dimensional deformations as discussed above. The average crack opening and tearing displacements under unit pressure will yield values of $C_1 f_1(\omega^*)$ and $C_3 f_3(\omega^*)$. $C_2 f_2(\omega^*)$ (and also $C_3 f_3(\omega^*)$) can be obtained from the solution for unit shear traction. It may be noted that because of assumed quasi-three dimensional deformation state

$$f_i(\omega^*) = f_i(\omega) = f_i(a/\ell) \tag{15}$$

We note that the constants C_i and $f_i(\omega)$ are determined from solutions of crack problems in the laminate and thus quantify the process of load redistribution from the cracked layers to the adjoining layers for all crack densities. In the crack problems discussed above (for determining $f_i(\omega)$), the boundary conditions at $y = \pm \ell/2$ will be different, depending on whether one wants to obtain the change in strain or complementary energy. For evaluation ΔU_c (equation (2)), one may impose appropriate symmetry (for the problem of prescribed pressure) or antisymmetry (for in-plane shear) conditions. For obtaining estimates of change in complimentary energy, other boundary conditions have to be prescribed.

Solutions of the crack problems for each of the layers which are susceptible to cracking are required. Further, results will differ depending on the laminate. However, some approximations have been suggested in [3, 4] for the case of laminates with laminae which have fibers in two mutually perpendicular directions (cross ply or ± 45 arrangement). For such laminates

$$C_3 = d_{12} = 0 \tag{16}$$

In this section we report some results for cracks in the 90° layers in $(0/90_3)_s$ glass/epoxy and $(0/90)_s$ graphite/epoxy laminates, compare with the estimates obtained in [3, 4] and discuss some general nature of the required quantities which may be useful in other situations. The ply properties used for calculations are given in Table 1. Note that values of a for $(0/90_3)_s$ glass/epoxy and $(0/90)_s$ graphite/epoxy are 0.609 mm and 0.127 mm, respectively. The representative volume element of length ℓ containing one crack in the 90° layer (Figure 3) with the uncracked 0° layers above and below it was modeled with a sufficiently fine

mesh using rectangular four noded constant strain elements. Average crack opening displacements were calculated for each case of loading ($\sigma_o = 1$, $\tau^o = 0$ for d_{11} and $\sigma_o = 0$, $\tau_o = 1$ for d_{22}). C_1 and C_2 were obtained from the solutions when $\ell = 20$ a ($\omega = .05$).

Table 2 compares the values of C_1 and C_2 obtained from finite element results and the estimates suggested in [3, 4]. The two values of C_1 for glass/epoxy are practically identical since the estimate is obtained by integrating accurate values of energy release rates for various lengths (up to 2a) of cracks in an isotropic layer located between two thin stringers reported in [11]. Therefore, the estimation procedure using the results in [11] will be useful for problems of a thick cracked layer sandwiched between two thin laminae.

For graphite/epoxy, the estimate of $C_1 E_T$ (E_T = transverse modulus of the lamina) in [3, 4] is based on the assumption that the cracked layer is located between two layers which are very stiff as compared to the cracked layer. The finite element result is higher because of finite stiffnesses of the outer layers. Therefore, if the outer layers are stiffer (or thicker) the value of $C_1 E_T$ will be between the two values in Table 2. However, if they are more flexible and/or thinner, the value will be higher than 2.22 as evident from the result for glass/epoxy. Finite element results for a few other cases will be helpful to obtain accurate quantitative estimates of C_1 for various cases. The results given here show some trends.

The value of C_2 for graphite/epoxy estimated in [3, 4] is obtained for a single crack in an isotropic medium with shear modulus G_A, which is the axial shear modulus of the lamina. The finite element result is slightly different because the outer layers are of finite thickness. The transverse shear modulus of the layers is also lower than G_A, the axial shear modulus. We note that if each of the outer layers is replaced by an isotropic layer with shear modulus G_A but of thickness h^1, which is G_A/G_T times the actual thickness, then we obtain the case of a single crack in an isotropic strip. The modification of the thickness is motivated by the fact the shear stresses τ_{xz} in the original and modified layers are $G_T \frac{\partial U_1}{\partial z}$ and $G_A \frac{\partial U_1}{\partial z^1}$, respectively. The stresses at the outer surfaces and at the interfaces must be identical in the two systems and, therefore, the coordinate z^1 in the modified system should be chosen equal to $z \cdot G_A/G_T$. With the modified system and using the results for an isotropic strip, we obtain

$$G_A C_2 = -\frac{4}{\pi}\left(\frac{a+h^1}{a}\right)^2 \ell n\left[\cos\frac{\pi a}{2(a+h^1)}\right] \qquad (17)$$

The right hand side of (17) yields values of $\frac{\pi}{2}$ and 1.69 for $h^1 \to \infty$ (infinite medium case in the estimate [3, 4]) and for the $(0/90)_s$ laminate, modeled in finite element calculations. The procedure described above can, therefore, be used to obtain accurate values of C_2. We also note that for layers which are well inside a laminate, C_2 may be chosen equal to $\pi/2\, G_A$.

The values of $f_i(\omega)\ \left(\approx f_i(\omega^*)\right)$ obtained from finite element results are shown in Table 3. An approximate estimate of $f_i(\omega)$ suggested in [4] is given by

$$f_i(\omega) \approx \tanh\left[\frac{\beta_1}{\omega}\right] \qquad (18)$$

with

$$\begin{aligned}\beta_1 &= \pi/4\sqrt{2(1+\nu_t)} \\ &= 0.487 \text{ for } \nu_T = 0.3\end{aligned} \qquad (19)$$

The representation (18) yields the following limiting forms.

$$\begin{aligned} f_i(\omega) &\to 1 \quad ; \quad \omega \to 0 \\ f_i(\omega) &\to \frac{\beta}{\omega} \quad ; \quad \omega \to \infty \end{aligned} \qquad (20)$$

We calculated β_1 to fit (18) to the results in Table 3 and obtained

$$\begin{aligned}\beta_1 &= 0.32 \text{ for } (0/90)_{3s} \text{ glass/epoxy} \\ &= 0.419 \text{ for } (0/90)_s \text{ graphite/epoxy}\end{aligned} \qquad (21)$$

These values yield the product $\beta_1 C_1$ for both systems given by

$$\beta_1 C_1 \approx 0.9/E_T \tag{22}$$

which implies that a residual stiffness of 10 percent of the original value will remain at large values of ω (of the order $\omega \approx 2.0$). Note that a complete loss in stiffness implies $\beta_1 C_1 \approx 1/E_T$. Thus, if C_1 is known then $f_1(\omega)$ can be estimated pretty well by (18) and (22). At $\omega = 0.5$ the cracked layers retain more than 20% of the original stiffness.

A fit of the form (18) can also be attempted for $f_2(\omega)$ in the last column of Table 3. However, a better fit may be obtained with

$$f_2(\omega) = \frac{2}{\beta_2^2 \omega^2} \ell n \left(ch \beta_2 \omega\right) \tag{23}$$

with

$$\beta_2 \approx 2 C_2 G_A = 3.88 \text{ for graphite/epoxy} \tag{24}$$

We note that f_2 has the correct limiting forms, $f_2 = 1$ for $\omega = 0$ and for large ω, $C_2 f_2(\omega) \rightarrow 1/G_A \omega$. The results are also valid for a single stack of cracks in an isotropic medium. For this geometry, however, $\beta_2 = \pi$ in equation (23) and $C_2 = \pi/2 G_A$. At $\omega = 2.0$, about 3 percent of the original stiffness of the cracked layers remains as per (23). However, substantial stiffness (of the order of 40 percent) remains at $\omega = 0.5$, i.e., when the crack spacing is of the order of the thickness of the cracked layer. It may be noted that under in-plane shear the layers which have been considered to be uncracked are also susceptible to cracking in yz planes. Thus, at comparatively high crack densities, cracks in the two sets of layers will interact creating a complex situation which cannot be modeled in the fashion discussed here. However, at such a stage, delaminations are expected to develop at the interfaces which may cause failure of the system.

Delaminations have been observed to grow from ply cracks in cross ply laminates under tension and such delaminations can also contribute to stiffness loss. When the layers adjacent to the cracked plies are very stiff, then a simple

estimate of additional reduction in strain energy density can be obtained by a simple approximate model. We consider a cell of length ℓ containing a single ply crack (Figure 3) with two delaminations at each interface (one on each side of the crack starting from the crack tip). We thus have four delaminations. Let e be the length of each of these delaminations. If we assume the delaminated parts of the cracked layer to be stress free, then the change in energy density is given by

$$\Delta U_c^d \approx \frac{1}{2}\, \omega_2^*\, C_4 \sigma_o^2$$

where

$$\omega_2^* = \alpha \omega_2 = \alpha 2e/\ell \qquad (25)$$

$$C_4 \approx \frac{1}{E_T}$$

As discussed earlier, α may be chosen equal to unity. This term ΔU_c^d must be added to ΔU_C in equation (2) to evaluate the stiffness loss. We can also define a strain energy release rate corresponding to delamination density ω_2^* using a concept similar to (8), which indicates that it will remain constant for all ω_2^*. Actually, the expression for ΔU_c^d is an approximate one and it is valid when e comparable to a. Further, the addition of ΔU_c^d to ΔU_c is valid when e is small compared to ℓ. The expressions may be modified further, but we will not pursue this here.

RESULTS

We made use of equations (1), (2), (6), and (7) to predict the ratio of effective to original stiffness of the two laminates considered in the previous section, when subjected to uniaxial tension. Values of C_i and $f_i(\omega)$ obtained from finite element results (Tables 2, 3) were used. The results are compared in Figures 4 and 5 with some test data [10, 12] and some other analytical results. It may be seen that graphite epoxy systems do not show significant stiffness loss (Figure 4) and, therefore, it is difficult to conclude anything about the accuracy of the model. For the glass/epoxy laminate, the present results are higher than test data as well as the lower bound results in [5, 8] and the difference increases for larger ω. We note that the lower values obtained from tests may be attributed to growth of delaminations at interfaces originating from the ply cracks. Using the concept of additional energy loss due to such delaminations described in equation (25), we find that to match the test data at $\omega \approx 0.5$, it is necessary to choose

$$\omega_2 = 2e/\ell \approx 0.15 \tag{26}$$

which indicates that (since $\omega = 0.5$)

$$e/a \approx 0.15 \tag{27}$$

Thus, the total delamination length 2e at each interface near a crack is about 0.15 times the thickness of the cracked layer. Delaminations are expected to become larger at higher loads and cause complete separation of the cracked layers.

Using the concept of energy release rate described by equations (8), (10) and (11) we find

$$G_c \approx 210 \text{ Joules/m}^2$$
$$R_o \approx 345 \times 10^3 \text{Pa} \tag{28}$$

to match the test data for increase in crack density with applied stress. The comparison of experimental values with the prediction is shown in Figure 6. The results [8] are based on $G_c = 330$ Joules/m^2, but an assumed value of residual transverse tensile stress in the 90° layer.

DISCUSSIONS

We have shown that phenomenological considerations, when supported by some mechanical models, can provide simple yet very accurate representation of the phenomenon of ply crack growth. Suitable modifications may also be included, if desired, for considering delamination growth from such ply cracks. The model (for dilute concentrations) has also been used for simulating the responses of angle ply laminates [3, 4], but utilizing a fitted power law type relation between crack density and energy release rate. Use of the fracture mechanics concept (equations (8) and (10) as used here for $(0/90_3)_s$ glass/epoxy laminate under tension) to angle ply and other laminate configurations should be attempted in future studies.

ACKNOWLEDGEMENT: This work was supported by AMTL Contract No. DAAL04-89-C-0023. The authors express their sincere appreciation to Mr. D.W. Oplinger of AMTL for helpful suggestions.

REFERENCES

1. R. Ilankamban and D. Krajcinovic, "A Constitutive Theory for Progressively Deteriorating Brittle Solids", International Journal of Solids and Structures, Vol. 23, No. 11, p. 1521, 1987.
2. J.L. Chaboche, "Continuum Damage Mechanics: Part I and Part II", ASME Journal of Applied Mechanics, Vol. 55, No. 1, p. 59 and p. 65, March, 1988.
3. S.N. Chatterjee, E.C.J. Wung, V. Ramnath, and C.F. Yen, "Composite Specimen Design Analysis - Volume I: Analytical Studies', MTL TR 91-5, January, 1991.
4. S.N. Chatterjee, E.C.J. Wung, and C.F. Yen, "Modeling Ply Crack Growth in Laminates Under Combined Stresses", Presented at ASTM Fourth Symposium on Composite Materials, Fatigue and Fracture, May 6-7, 1991, to appear in STP, ASTM, Philadelphia.
5. Z. Hashin, "Analysis of Cracked Laminates: A Variational Approach", Mechanics of Materials, Vol. 4, p. 121, 1985.
6. N. Laws and G.J. Dvorak, "Progressive Transverse Cracking in Composite Laminates", J. of Composite Materials, Vol. 22, p. 900, 1988.
7. S.C. Tan and R.J. Nuismer, "A Theory of Matrix Cracking in Composite Laminates", J. Composite Materials, Vol. 23, p. 1009, 1989.
8. J.A. Nairn, "The Strain Energy Release Rate of Composite Microcracking: A Variational Approach", Journal of Composite Materials, V. 23, p. 1106, 1989.
9. J. Lee, D.H. Allen, and C.E. Harris, "Internal State Variable Approach for Predicting Stiffness Reductions in Fibrous Laminated Composites with Matrix Cracks", Journal of Composite Materials, V. 23, p. 1273, 1989.
10. A.L. Highsmith and K.L. Reifsnider, "Stiffness Reduction Mechanisms in Composite Laminates", Damage in Composite Materials, ASTM STP 775, p. 103, 1982.
11. M. Isida, in "Mechanics of Fracture", Vol. 1, edited by G.C. Sih, Noordhoff, 1973.
12. S.E. Groves, "A Study of Damage Mechanics in Continuous Fiber Composite Laminates", Dissertation, Texas A&M University (1986) - as reported in [9].

Table 1. Material Properties

Property	Glass/Epoxy	Graphite/Epoxy
$E_A = E_{11}$	41.7 GPa	130 GPa
$E_T = E_{22} = E_{33}$	13.0 GPa	10.5 GPa
$\nu_A = \nu_{12} = \nu_{13}$	0.3	0.35
$\nu_T = \nu_{23}$	0.3	0.31
$G_A = G_{12} = G_{13}$	3.4 GPa	6.0 GPa
$G_T = G_{23}$	5.0 GPa	4.0 GPa
h = Ply thickness	0.203 mm	0.127 mm
a	0.609 mm	0.127 mm

NOTE: A and T denote axial and transverse directions

Table 2. Values of $E_T C_1$ and $G_A C_2$ *

Quantity	Method	$(0/90)_{3S}$ Gl/Ep	$(0/90)_s$ Gr/Ep
$E_T C_1$	Finite Element	2.78	2.22
	Estimated [4]	2.8	1.98
$G_A C_2$	Finite Element	--	1.69
	Estimated [4]	--	$\frac{\pi}{2} = 1.57$

*E_T, G_A are the transverse Young's modulus and axial shear modulus of the laminae listed in Table 1.

Table 3. Values of $f_1(\omega)$ and $f_2(\omega)$

ω	$f_1(\omega)$		$f_2(\omega)$
	$(0/90)_{3s}$ Gl/Ep	$(0/90)_s$ Gr/Ep	$(0/90)_s$ Gr/Ep
0	1	1	1
0.05	≈ 1	≈ 1	≈ 1
0.1	≈ 1	≈ 1	0.971
0.3	0.768	0.890	0.827
0.5	0.564	0.685	0.694
2.0	0.165	0.210	0.262

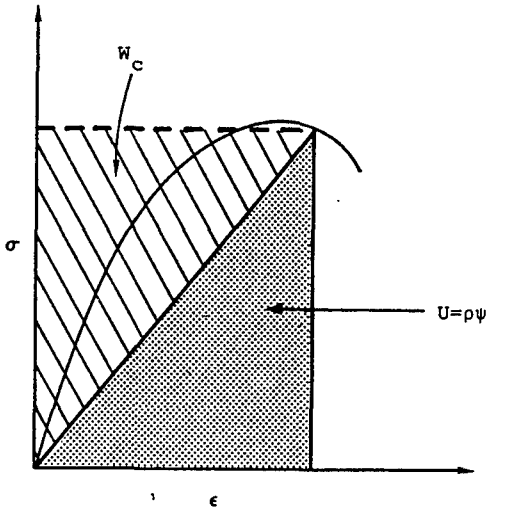

Figure 1. Stored Strain and Complementary Energies

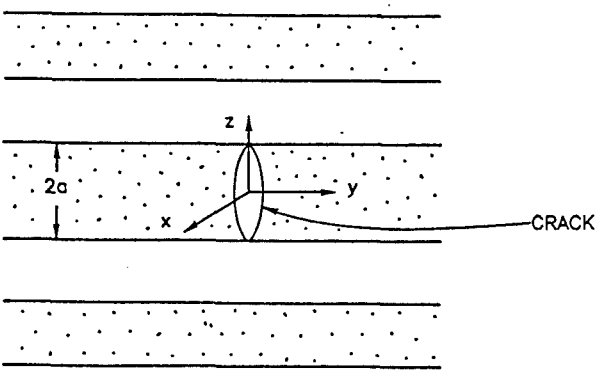

Figure 2. A Cracked Layer in a Laminate-Dilute Concentration

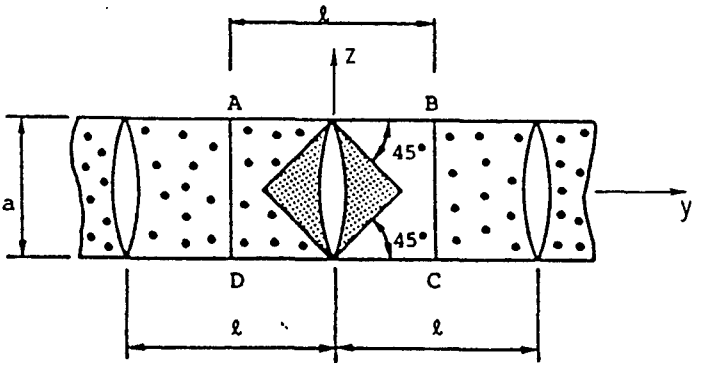

Figure 3. Equally Spaced Ply Cracks in a Layer

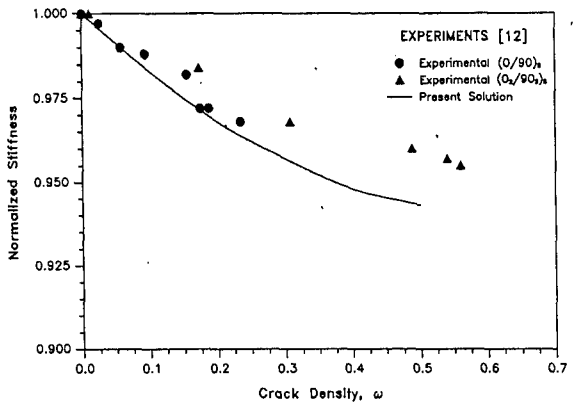

Figure 4. Stiffness Reduction in Graphite/Epoxy Laminates

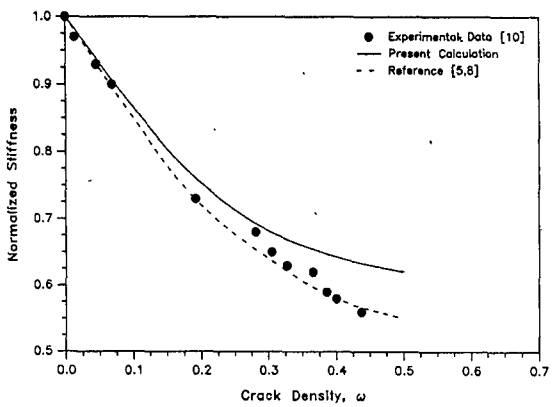

Figure 5. Stiffness Reduction in $(0/90_3)_s$ Glass/Epoxy

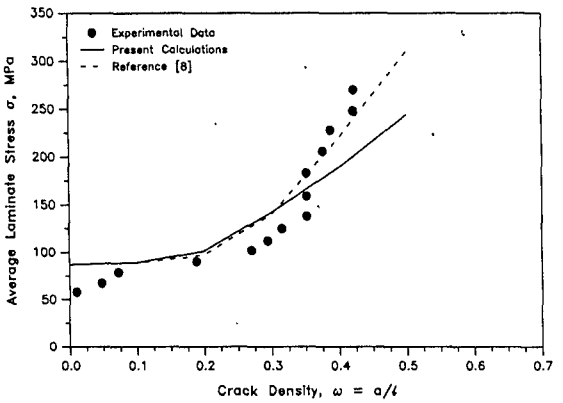

Figure 6. Crack Density vs. Applied Stress $(0/90_3)_s$ Glass/Epoxy

ATTENDANCE LIST

MR ROBERT P BAMBERG
US ARMY
MATLS TECH LAB
SLCMT-MSB
WATERTOWN MA 02172-0001
(617)-923-5272
FAX: ( )- -

DR ROMESH C BATRA
UNIV OF MISSOURI-ROLLA
MECH & AEROSPACE ENGRG
125 ME ANNEX
ROLLA MO 65401-0249
(314)-341-4589
FAX: (314)-341-4607

DR JOHN H BEATTY
RES MATLS ENGR
US ARMY
MATLS TECH LAB
SLCMT-EMM
WATERTOWN MA 02172-0001
(617)-923-5212
FAX: (617)-923-5477

DR G BISHOP
US ARMY
MATLS TECH LAB
SLCMT-MR
WATERTOWN MA 02172-0001

FAX: ( )- -

MR ANDREAS BLANAS
US ARMY
NATICK RD&E CTR
KANSAS ST
NATICK MA 01760-0001
(508)-651-5079
FAX: (508)-651-5000

DR GORDON A BRUGGEMAN
ARMY MATLS TECH LAB
SLCMT-DA
WATERTOWN MA 02172-0001
(617)-923-5351
FAX: ( )- -

MR PAUL V CAVALLARO
US ARMY
MATLS TECH LAB
SLCMT-MRS
WATERTOWN MA 02172-0001
(617)-923-5166
FAX: ( )- -

PROF CHING S CHANG
DEPT OF CIVIL ENGRG
UNIV OF MASSACHUSETTS
MARSTON HALL
AMHERST MA 01003-0001
(413)-545-5401
FAX: (413)-545-2840

PROF FU-KUO CHANG
STANFORD UNIV
DEPT OF AERONAUTICS
& ASTRONAUTICS
STANFORD CA 94305-4035
(415)-723-3466
FAX: (415)-725-3377

DR SAILLNDRA N CHATTERJEE
MATLS SCIENCE CORP
STE 300
930 HARVEST DR
BLUE BELL PA 19422-0001
(215)-542-8400
FAX: (215)-542-8401

DR ER-PING CHEN
SANDIA NATL LABS
ENGRG STRUCT MECH
DIV 1514
PO BOX 5800
ALBUQUERQUE NM 87185-5800
(508)-846-2400
FAX: (508)-846-9833

DR SHIYUAN CHENG
RENSSELAER POLYTECHNIC INST
TROY NY 12180-3540
(518)-276-8655
FAX: (518)-276-2623

DR FU-PEN CHIANG
STATE UNIV OF NEW YORK
DEPT OF MECH ENGRG
STONY BROOK NY 11794-2300
(516)-632-8311
FAX: (516)-632-8720

DR SHUN-CHIN CHOU
US ARMY
MATLS TECH LAB
SLCMT-MRD
WATERTOWN MA 02172-0001
(617)-923-5115
FAX: (617)-923-5065

PROF RODNEY J CLIFTON
DIV OF ENGRG
BROWN UNIV
182 HOPE ST
PO BOX D
PROVIDENCE RI 02912-0001
(401)-863-2855
FAX: (401)-863-1157

DR DATTATRAYA P DANDEKAR
US ARMY
MATLS TECH LAB
SLCMT-MRD
WATERTOWN MA 02172-0001
(617)-923-5704
FAX: ( )- -

MR ROBERT B DOOLEY
US ARMY
MATLS TECH LAB
SLCMT-MRD
WATERTOWN MA 02172-0001

FAX: ( )- -

PROF JACQUES DUFFY
BROWN UNIV
DIV OF ENGRG
PO BOX D
PROVIDENCE RI 02912-0001

FAX: ( )- -

DR PIYUSH K DUTTA
APPLIED RES BR
US ARMY
COLD REGIONS RES & ENGRG
72 LYME RD
HANOVER NH 03755-1290

FAX: ( )- -

MR HORACIO ESPINOSA
BROWN UNIV
PO BOX D
PROVIDENCE RI 02912-0001
(401)-273-4948
FAX: ( )- -

DR CHARLES C FENG
US ARMY
ARDEC BLDG 355
SMCAR-AET-M
PICATINNY ARSENAL NJ 07806-5000
(201)-724-3037
FAX: (201)-361-7378

DR LUTHER D FLIPPEN JR
US NAVY
NRL-CODE 6386
4555 OVERLOOK AVE SW
WASHINGTON DC 20375-5000
(202)-404-7182
FAX: (202)-404-7176

MR DANIEL FREDERICK
DEPT OF ENERGY
19901 GERMANTOWN RD
GERMANTOWN MD 20874-0001
(301)-353-5822
FAX: (301)-353-6594

MR COLIN FREESE
US ARMY
MATLS TECH LAB
SLCMT-MRS
WATERTOWN MA 02172-0001
(617)-923-5442
FAX: ( )- -

MR JEFF GORDON
US DEPT OF TRANS
VNTSC
M/S DTS 76
55 BROADWAY
CAMBRIDGE MA 02142-0001
(617)-494-2254
FAX: (617)-494-3066

MR DAVID L GRAY
KAMAN SCIENCES CORP
1500 GARDEN OF THE GODS RD
COLORADO SPRINGS CO 80907-0001

FAX: ( )- -

DR VIKAS GUPTA
VANDERBILT UNIV
PO BOX 1593-B
NASHVILLE TN 37235-0001
(615)-322-7220
FAX: (615)-343-8645

PROF MORTON E GURTIN
CARNEGIE MELLON UNIV
DEPT OF MATH
PITTSBURGH PA 15213-3890
(412)-268-2545
FAX: (412)-268-6380

DR WALTER HERRMANN
SANDIA NATL LABS
M/S 1600
PO BOX 5800
ALBUQUERQUE NM 87185-5800
(505)-844-2158
FAX: (505)-844-2415

PROF YUKI HORIE
NORTH CAROLINA STATE UNIV
DEPT OF CIVIL ENGRG
PO BOX 7908 CE
RALEIGH NC 27695-0001
(919)-515-7696
FAX: (919)-515-7908

DR SHIH L HUANG
US NAVY
NADC CODE 604
WARMINSTER PA 18974-5000
(215)-441-1561
FAX: (215)-956-4005

DR NORRIS J HUFFINGTON JR
US ARMY
BALLISTIC RES LAB
SLCBR-TB-W
APG MD 21005-0001
(301)-278-6556
FAX: (301)-278-6952

DR KAILASAM R IYER
US ARMY RESEARCH OFFICE
SLCRO-MS
PO BOX 12211
RES TRIANGLE PK NC 27709-2211
(919)-549-4258
FAX: (919)-549-4310

DR DAVID A JABLONSKI
INSTRON CORP
100 ROYALL ST
CANTON MA 02021-0001

FAX: ( )- -

DR D Y JEONG
US DEPT OF TRANS
M/S DTS-76
55 BROADWAY
CAMBRIDGE MA 02142-0001
(617)-494-2687
FAX: (617)-494-3066

DR ARTHUR R JOHNSON
US ARMY
MATL TECH LAB
SLCMT-MRS
WATERTOWN MA 02172-0001
(617)-923-5272
FAX: ( )- -

PROF MARK KACHANOV
TUFTS UNIV
DEPT OF MECH ENGRG
MEDFORD MA 02155-0001

FAX: ( )- -

MS KAREN A KALOOSTIAN
PROTOCOL OFCR
US ARMY MATLS TECH LAB
SLCMT-DPT
WATERTOWN MA 02172-0001
(617)-923-5043
FAX: (617)-923-5477

PROF ROBERT V KOHN
NEW YORK UNIV
COURANT INST
251 MERCER ST
NEW YORK NY 10012-0001
(212)-998-3217
FAX: (212)-995-4121

PROF DUSAN KRAJCINOVIC
ARIZONA STATE UNIV
MECH AND AEROSPACE ENGRG
M/S 6106
TEMPE AZ 85287-6106
(602)-965-8656
FAX: (602)-965-1384

PROF ERHARD KREMPL
RENSSELAER POLYTECHNIC INST
DEPT OF MECH ENGRG
TROY NY 12180-3590
(518)-276-6351
FAX: (518)-276-2623

DR ERIC B KULA
US ARMY
MATLS TECH LAB
SLCMT-EM
WATERTOWN MA 02172-0001
(617)-923-5295
FAX: (617)-923-5477

DR JAMES LANKFORD
SOUTHWEST RES INST
6220 CULEBRA RD
PO DRAWER 28510
SAN ANTONIO TX 78228-0510
(512)-522-2317
FAX: (512)-522-5122

DR DAVID H LASSILA
LAWRENCE LIVERMORE NATL LAB
M/S L-342
PO BOX 808
LIVERMORE CA 94550-0001
(510)-423-9537
FAX: (510)-422-2438

PROF ERASTUS H LEE
RENSSELAER POLYTECHNIC INST
ME DEPT
TROY NY 12180-3590
(518)-276-6301
FAX: (518)-276-2623

DR ULRIC S LINDHOLM
SOUTHWEST RES INST
6220 CILEBRA RD
PO DRAWER 28510
SAN ANTONIO TX 78228-0001
(512)-522-2500
FAX: (512)-522-5122

DR ARNOLD H MAYER
US AIR FORCE
WL/FIV
WRIGHT-PATTERSON AFB OH 45433-0001
(513)-255-3311
FAX: (513)-255-3717

MR MICHAEL MELLO
BROWN UNIV
PO BOX D
PROVIDENCE RI 02912-0001
(401)-863-3034
FAX: ( )- -

PROF GRAEME MILTON
NEW YORK UNIV
COURANT INST MATH SCIENCE
251 MERCER ST
NEW YORK NY 10012-0001
(212)-998-3155
FAX: (212)-995-4121

MS GRETCHEN MURRI
NASA LANGLEY
M/S 188E
HAMPTON VA 23665-0001
(804)-864-3466
FAX: ( )- -

MR DONALD M NEAL
US ARMY
MATLS TECH LAB
SLCMT-MRS-MM
WATERTOWN MA 02172-0001
(617)-923-5259
FAX: (000)-000-0001

PROF SIA NEMAT-NASSER
UNIV OF CALIFORNIA
DEPT APPLIED MECH
9500 GILMAN DR
MC 0411 RM 4207 EBU1
LA JOLLA CA 92093-0411
(619)-534-4772
FAX: (619)-534-7078

PROF STEVEN NUTT
BROWN UNIV
DIV OF ENGRG
PO BOX D
PROVIDENCE RI 02912-9000
(714)-856-6353
FAX: (714)-856-8585

DR OSCAR ORRINGER
US DEPT OF TRANS
DTS-744
55 BROADWAY
CAMBRIDGE MA 02142-0001

FAX: ( )- -

MR BLANAS PANAGIOTIS
US ARMY
MATLS TECH LAB
SLCMT-MEC
WATERTOWN MA 02172-0001
(617)-923-5421
FAX: ( )- -

MS MARY ANN PARTRIDGE
KAMAN SCIENCES CORP
83 SECOND AVE
BURLINGTON MA 01803-4479
(617)-272-1990
FAX: (617)-273-0944

PROF A B PERLMAN
TUFTS UNIV
DEPT OF MECH ENGRG
MEDFORD MA 02155-0001

FAX: ( )- -

PROF THEODORE H H PIAN
MASSACHUSETTS INST OF TECH
DEPT OF ASTRO & AERO
BLDG 33 RM 413
CAMBRIDGE MA 02139-0001
(617)-253-2425
FAX: (617)-253-7397

MR VIKAS PRAKASH
BROWN UNIV
ENGRG DEPT
PO BOX D
PROVIDENCE RI 02912-0001
(401)-863-3034
FAX: ( )- -

PROF VINCENT C PRANTIL
CORNELL UNIV
112 UPSON HALL
PO BOX 39
ITHACA NY 14853-7501

FAX: ( )- -

DR WILLIAM W PREDEBON
MICHIGAN TECH UNIV
DEPT MECH ENGRG
1400 TOWNSEND DR
HOUGHTON MI 49931-1295
(906)-487-2158
FAX: (906)-487-2822

MRS CLAUDIA J QUIGLEY
US ARMY
MATLS TECH LAB
SLCMT-MRS
WATERTOWN MA 02172-0001
(617)-923-5152
FAX: (617)-923-5154

MR MARTIN RAFTENBERG
US ARMY
TERMINAL BALLISTICS DIV
SLCBR-TB-W
BRL
APG MD 21005-0001
(301)-278-6075
FAX: ( )- -

MR GEORGE F RAISER
BROWN UNIV
ENGRG DEPT
PO BOX D
PROVIDENCE RI 02912-0001
(401)-863-3034
FAX: (401)-863-1157

DR A M RAJENDRAN
UNIVERSITY OF DAYTON
M/S JPC #201
DAYTON OH 45469-0120
(513)-229-4479
FAX: (513)-229-4251

DR MARK M RASHID
SANDIA NATL LAB
PO BOX 5800
ALBUQUERQUE NM 87185-0001
(505)-844-3136
FAX: ( )- -

DR MICHAEL SCHEIDLER
US ARMY
BALLISTIC RES LAB
BRL-TBD
APG MD 21005-5066
(301)-278-6836
FAX: (301)-278-6952

DR STEVEN SERABIAN
US ARMY
MATLS TECH LAB
SLCMT-MRS
WATERTOWN MA 02172-0001
(617)-923-5260
FAX: ( )- -

MR LUKA SERDAR JR
KAMAN SCIENCES CORP
83 SECOND AVE
BURLINGTON MA 01803-4479
(617)-272-1980
FAX: (617)-273-0944

DR ROBERT SINGLETON
US ARMY
SLCRO-ES
PO BOX 12211
RES TRIANGLE PARK NC 27709-2211
(919)-549-4250
FAX: ( )- -

DR ROSS STACER
US ARMY
MATLS TECH LAB
SLCMT-MRS
WATERTOWN MA 02172-0001
(617)-923-5025
FAX: ( )- -

MR JAMES M STAEHLER
MICHIGAN TECH UNIV
DEPT MECH ENGRG
1400 TOWNSEND DR
HOUGHTON MI 49931-1295
(906)-487-2009
FAX: (906)-487-2822

PROF SUBRA SURESH
BROWN UNIV
DIV OF ENGRG
BOX D
PROVIDENCE RI 02912-0001

FAX: ( )- -

PROF P S SYMONDS
BROWN UNIV
DEPT OF ENGRG
BOX D
PROVIDENCE RI 02912-0001
(401)-863-1484
FAX: (401)-863-1157

MS YIM HAR TANG
US DEPT OF TRANS
M/S SQUARE DTS-76
55 BROADWAY
CAMBRIDGE MA 02142-0001

FAX: ( )- -

DR ROBERT K THOMAS
SANDIA NATL LABS
APPLIED MECH DIV 1544
PO BOX 5800
ALBUQUERQUE NM 87185-5800
(505)-844-7450
FAX: (505)-846-9833

DR DOUGLAS THOMSON
FOSTER-MILLER INC
350 SECOND AVE
WALTHAM MA 02154-0001

FAX: ( )- -

PROF THOMAS C T TING
UNIV OF IL AT CHICAGO
CEMM DEPT (M/C246)
PO BOX 4348
CHICAGO IL 60680-0001
(312)-996-2429
FAX: (312)-996-2426

DR DENNIS TRACEY
NORTON CO
GODDARD RD
NORTHBORO MA 01532-1545
(508)-351-7811
FAX: (508)-351-7700

DR AMPERE A TSENG
DREXEL UNIV
COLLEGE OF ENGRG
DEPT OF MECH ENGRG
PHILADELPHIA PA 19104-0001
(215)-895-2370
FAX: ( )- -

DR TIEN TSUI
US ARMY
MATLS TECH LAB
SLCMT-MRS
WATERTOWN MA 02172-0001
(617)-923-5165
FAX: (617)-923-5154

MS KELLIE UNSWORTH
US ARMY
SAVRT-TY-ASV
FT EUSTIS VA 23604-5577
(804)-878-5838
FAX: (804)-878-3108

MS MELANIE G VIOLETTE
RPI
RD4 BOX 5A
HUDSON NY 12534-0001
(518)-851-3503
FAX: ( )- -

DR TUSIT WEERASOORIYA
US ARMY
MATLS TECH LAB
SLCMT-MRD
WATERTOWN MA 02172-0001

FAX: ( )- -

DR CHARLES S WHITE
US ARMY
MATLS TECH LAB
BLDG 39
SLCMT-MRD
WATERTOWN MA 02172-0001
(617)-923-5404
FAX: ( )- -

MR MICHAEL W WICKS
US ARMY
AMSMI-RD-ST-SA
BLDG 5400
REDSTONE ARSENAL AL 35898-5247
(205)-876-7459
FAX: (205)-876-9861

MR JONG-HO WOO
US ARMY
BLDG 1065
SLCBR-VLD-A
APG MD 21005-5066
(301)-278-2329
FAX: (301)-278-7266

DR JULIAN J WU
US ARMY RES OFC
MATH SCIENCE DIV
SLCRO-MA
PO BOX 12211
RES TRIANGLE PARK NC 27709-2211

FAX: ( )- -

MS MARGARET M ZAMORA
US DEPT OF TRANS
DYNATREND
55 BROADWAY
CAMBRIDGE MA 02142-0001
(617)-494-3448
FAX: (617)-494-2569

MR MIN ZHOU
BROWN UNIV
PO BOX D
PROVIDENCE RI 02912-0001
(401)-863-3034
FAX: (401)-863-1157